Ponnadurai Ramasami
Minu Gupta Bhowon
Sabina Jhaumeer Laulloo
Henri Li Kam Wah *Editors*

Emerging Trends in Chemical Sciences

Springer

Emerging Trends in Chemical Sciences

Ponnadurai Ramasami • Minu Gupta Bhowon •
Sabina Jhaumeer Laulloo • Henri Li Kam Wah
Editors

Emerging Trends in Chemical Sciences

Springer

Editors
Ponnadurai Ramasami
Dept. of Chem., Fac. of Science
University of Mauritius
Reduit, Mauritius

Minu Gupta Bhowon
Dept. of Chem., Fac. of Science
University of Mauritius
Reduit, Mauritius

Sabina Jhaumeer Laulloo
Dept. of Chem., Fac. of Science
University of Mauritius
Reduit, Mauritius

Henri Li Kam Wah
Dept. of Chem., Fac. of Science
University of Mauritius
Reduit, Mauritius

ISBN 978-3-319-60407-7 ISBN 978-3-319-60408-4 (eBook)
DOI 10.1007/978-3-319-60408-4

Library of Congress Control Number: 2017952931

Printed on acid-free paper

This Springer imprint is published by Springer Nature
The registered company is Springer International Publishing AG
The registered company address is: Gewerbestrasse 11, 6330 Cham, Switzerland

Preface

The fourth edition of the International Conference on Pure and Applied Chemistry (ICPAC 2016) was held from 18 to 22 July 2016 at Sofitel Mauritius l'Impérial Resort & Spa, Wolmar, Flic en Flac, in Mauritius. The theme of the conference was "Emerging Trends in Chemical Sciences". ICPAC 2016 was attended by 210 participants coming from 43 countries. The conference featured 90 oral and 80 poster presentations. The keynote lecture was addressed by Mr Philippe Denier, Director of Verification Division of the Organisation of the Prohibition of Chemical Weapons (OPCW). OPCW was awarded the 2013 Nobel Peace Prize.

The participants of ICPAC 2016 were invited to submit full papers. The latter were subsequently peer reviewed, and the selected papers are collected in this book of proceedings. This book encloses 24 chapters covering a wide range of topics from fundamental to applied chemistry.

In the first chapter, Stephen and Ramracheya reviewed the controversies, challenges and future directions of the modulation of the pancreatic hormone, glucagon, by the gut peptide. Nete et al. analysed tantalite minerals by glow discharge optical emission spectrometry. Mlala et al. investigated the chemical composition and antioxidant activity of the essential oil extracted from *Tagetes minuta* L. Babu and Gupta reported on the emerging therapeutic compounds used for treating the different devastating neurological disorders. Sekwati-Monang et al. investigated on the potential health risks of heavy metals in vegetables irrigated with treated wastewater. Chakraborty focused on the removal of fluoride ion from groundwater by adsorption using fly ash. Masesane et al. provided a comparative review of the synthesis of flavanones via two different pathways. Moyo et al. studied the use of calcium alginate–*Mangifera indica* seed shell composite as potential biosorbent for electroplating wastewater treatment. Nyamai and Oballa reported on the nitrogen absorption and immobilization patterns as catalysed by the roots of *Acacia* plants. Mashile and coworkers studied the ultrasonic-assisted dispersive solid-phase microextraction using silica@multiwalled carbon nanotube hybrid nanostructure sorbent for preconcentration of trace Aflatoxin B_1 in liquid milk samples. Pholosi et al. studied the mechanism for the removal of Ni(II) and Co(II) from aqueous

solution using pine cone. Nomngongo developed a simple, sensitive and selective method for speciation analysis of Sb, Se and Te in environmental samples using modified TiO_2 multi-walled carbon nanotube nanocomposite packed microcolumn prior to hydride generation inductively coupled plasma optical emission spectrometry. Ross and Iwuoha functionalized lithium manganese oxide cathodes with nanotransition metal alloy to enhance lithium-ion battery power densities. Khalid et al. synthesized 5-substituted 1,3,4-oxadiazole-2-yl-4-(piperidin-1-ylsulfonyl) benzyl sulfide and reported on their spectral and biological characteristics. Lötter et al. studied the influence of cation on zirconium/hafnium fluoride coordination. Nete and Purcell reported on the beneficiation of niobium and tantalum from tantalite ore using physical and chemical processes including magnetic separation, leaching, solvent extraction and ion exchange methods. Koloti et al. reviewed the recent applications of laccase-modified membranes in the removal of bisphenol A and other organic pollutants. Taka et al. synthesized and characterized a novel bio-nanosponge filter as potential adsorbent for wastewater purification. Forbes reviewed some novel approaches to environmental monitoring such as use of denuders, lichens and fluorescence sensors. Mhlongo et al. isolated endosymbiotic bacteria from Algoa and Kalk Bay in South Africa as source of antimicrobial compounds. Rahman et al. synthesized and characterized Pd-MCM-41 and Ni-boride-silica catalysts for reducing substituted aromatics. Ndinteh investigated the antidiabetic potential of *Erythrina abyssinica* via protein tyrosine phosphate 1B inhibitory activity. Mmonwa and Mphahlele studied the use of 2-amino-5-bromo-3-iodoacetophenone and 2-amino-5-bromo-3-iodobenzamide as synthons for novel polycarbo-substituted indoles and their annulated derivatives. The last chapter by Jeng and Krisnamoorthy related to processability issue in inverted organic solar cells.

We would like to thank all those who submitted full manuscripts for consideration and the reviewers for their timely help in assessing these manuscripts for publication.

We would also like to pay a special tribute to all the sponsors of ICPAC 2016.

We hope that this collection of papers will serve as a useful resource for researchers.

Reduit, Mauritius
June 2017

P. Ramasami
M. Gupta Bhowon
S. Jhaumeer-Laulloo
H. Li Kam Wah

Contents

Chapter 1
Modulation of the Pancreatic Hormone, Glucagon by the Gut Peptide, GLP-1: Controversies, Challenges and Future Directions

Sam Stephen and Reshma Ramracheya

Abstract Type 2 diabetes (T2D) is a chronic disease characterised by a combination of insufficient insulin release and an excess of glucagon secretion. The gut hormone glucagon-like peptide-1 (GLP-1) is a successful therapy for the treatment of diabetes as it can both potentiate glucose-induced insulin secretion as well as inhibit glucagon secretion from the pancreatic alpha cells. Another major gut hormone called peptide tyrosine tyrosine (PYY) has recently been reported to restore impaired insulin and glucagon secretion in islets from severely diabetic rats and humans. Whilst the mechanism by which both PYY and GLP-1 normalise insulin secretion is well characterised, to date the regulation of glucagon release by the two gut hormones remains unclear. Given that the GLP-1 receptor is expressed at extremely low levels on alpha-cells, it has been argued that the effects of GLP-1 may be mediated by paracrine (indirect) mechanisms. In contrast, there is also evidence that GLP-1 directly regulates glucagon secretion in isolated alpha-cells, excluding the possibility of islet cross-talk. Likewise, no receptors for PYY have been demonstrated in the alpha-cells that can explain the robust effects of the hormone on glucagon release. Elucidation of the mechanism of GLP-1 (and PYY) action on alpha cells necessitates further work. Specifically it will be important to determine if GLP-1 can mediate its effects via another receptor on alpha-cells.

1.1 Introduction

The classical definition of T2D is an inadequate beta-cell response to increased insulin resistance in peripheral tissues. However, accumulating evidence demonstrates that glucagon secretion from the alpha-cells is also impaired in patients with

S. Stephen • R. Ramracheya (✉)
Oxford Centre for Diabetes, Endocrinology and Metabolism, Radcliffe Department of Medicine, University of Oxford, Oxford OX3 7LJ, UK
e-mail: reshma.ramracheya@ocdem.ox.ac.uk

P. Ramasami et al. (eds.), *Emerging Trends in Chemical Sciences*,
DOI 10.1007/978-3-319-60408-4_1

the disease. T2D should therefore be classed as a *bihormonal* disease characterised by both insufficient insulin secretion and excess of glucagon release. Importantly, the role of glucagon in the pathophysiology of T2D had been mainly overlooked.

The function of glucagon is to enhance glucose production in the liver via suppression of glycogenesis and stimulation of gluconeogenesis and glycogenolysis. In healthy people, glucagon is released when plasma glucose levels fall and is reduced when plasma glucose levels rise. Thus, glucose homeostasis is tightly regulated by the joint actions of both glucagon and insulin in maintaining blood glucose levels within a narrow physiological range of 4–6 mmol/L. In diabetes, there is marked dysregulation of glucagon secretion such that there is a paradoxical increase in plasma glucagon levels during fasting (or absence of glucose) and a lack of suppression of glucagon secretion in the presence of glucose [1]. Thus, glucagon dysregulation plays a critical role in the hyperglycaemic phenotype.

Food intake triggers the release of gastrointestinal hormones known as incretins, which can modulate glucose homeostasis. Generally, incretin hormones potentiate glucose-stimulated insulin secretion (GSIS) from pancreatic beta-cells but can influence glucagon release differentially. For instance, the gastrointestinal factor, glucose-dependent insulinotropic peptide (GIP), stimulates glucagon secretion whereas GLP-1 released from the intestinal L cells, strongly suppresses glucagon release. Consequently, GLP-1 analogues have become successful diabetes therapy. Presently, GLP-1-based drugs are the only available therapeutics which can reduce blood glucose levels by both enhancing insulin secretion and suppressing glucagon release in patients with T2D. However, their application is severely restricted due to significant poor tolerance and side effects such as nausea and vomiting [2, 3]. We have recently demonstrated that the rapid remission of diabetes following weight-loss surgery is associated with a marked increase in the levels of another major incretin hormone called PYY [4]. We report that in addition to restoring impaired insulin secretion in diabetes, PYY can also potently inhibit glucagon secretion [4]. These results strongly suggest that drugs promoting PYY release or action can potentially address both insulin and glucagon impairments and may constitute an efficient treatment for T2D. Therefore, further studies are warranted to explore the therapeutic potential of PYY.

Several studies have demonstrated that GLP-1 can modulate alpha-cell function and glucagon secretion. However, whether the glucagon-suppressing actions of GLP-1 are mediated by a direct action on the alpha-cell, or via a paracrine mechanism remains essentially unexplored. It is well documented that GLP-1 potentiates insulin and somatostatin secretion from the pancreatic beta and delta cells respectively. Both of these hormones have been shown to directly suppress glucagon secretion and therefore it has been hypothesised that GLP-1-evoked inhibition of glucagon secretion occurs via a paracrine interaction.

However, there is some compelling data in support of a direct (autocrine) effect of GLP-1 on the suppression of glucagon secretion from the alpha-cells, as opposed to a paracrine mechanism. In this paper, we first discuss evidence for and against this theory, highlight the challenges faced when elucidating the underlying

mechanisms of GLP-1 action on alpha-cells and finally discuss the major questions which remain to be answered in the field to date.

1.2 Expression of GLP-1 Receptor on Pancreatic Alpha-Cells

In the search for the mechanism underlying the action of GLP-1 on glucagon release, efforts have focussed on investigating whether the pancreatic alpha-cells express the putative GLP-1 receptor (GLP-1R).

The GLP-1R belongs to the glucagon receptor family of G-protein coupled receptors (GPCRs). Originally cloned from a rat pancreatic cDNA library in 1992, the receptor has since been identified in several human tissues including the lung, heart, and GI tract. However, whether or not the alpha-cells express the GLP-1R has been specifically hard to demonstrate, despite the application of several experimental approaches.

GLP-1 has been shown to bind to pancreatic alpha- and delta-cells by means of radiographic density measurements from freshly (within 2 h) isolated islets. Interestingly, binding was enhanced in insulin-positive cells, demonstrating that beta-cells express higher levels of GLP-1R. However, there was a three-fold reduction in the signal in all cell types following 12–24 h culture of the islets, indicating that GLP-1R expression in islets is sensitive to culture (reviewed in [1]).

Whilst GLP-1R expression has been reproducibly shown in beta-cells at both the gene and protein level, expression on alpha-cells has been inconclusive. By means of in-situ hybridisation and double and triple immunofluorescence, Tornehave and colleagues have demonstrated localisation of GLP-1R in rodent and human beta-cells [5].

Recent approaches have been based on antibody-independent methods to determine the expression profile of the receptor in islets. By means of a transgenic mouse model expressing the Venus fluorescent protein under the proglucagon promoter and flow-sorting of the isolated islets to obtain pure alpha cells, it has been demonstrated that both alpha and beta-cells express the GLP-1R, but expression levels in alpha cells were only 0.2% of those in beta-cells [6]. There have also been remarkable efforts in identifying more specific antibodies against the GLP-1R. Thus, Pyke et al. have reported that by using a monoclonal antibody in healthy monkey and human pancreas, GLP-1R co-localisation was observed almost exclusively with insulin, although some expression was also documented in a very small subset of non-beta cells [7].

A major challenge in the determination of GLP-1R expression has been poor sensitivity and specificity of antibodies used to date. Concerns have also been raised regarding data generated by means of gene expression studies based on the use of quantitative real-time PCR (RT-PCR). Collectively, differences in experimental approaches and species tested can account for the discrepancies in the literature.

However, currently the consensus is that alpha-cells do express GLP-1Rs but at significantly reduced levels than in other islet-cell types.

1.3 Involvement of Paracrine Processes in GLP-1 Effects on Glucagon Suppression

With the prevailing lack of consensus on GLP-1R expression on pancreatic alpha-cells, the involvement of paracrine effects from the neighbouring beta- and delta-cells has been proposed. Both the beta- and delta-cells express very high levels of GLP-1Rs and cross-communication arising from the secretion of insulin and somatostatin respectively, would potentially affect how GLP-1 influences glucagon release. However, the role of insulin as a paracrine mediator is unlikely since infusion of GLP-1 in type 1 diabetic patients without detectable levels of C-peptide, led to a suppression in glucagon secretion. The level of glucagon inhibition was consistent with that observed in patients with T2D, who responded with a 20-fold potentiation in plasma insulin and C-peptide, implying that GLP-1-induced inhibition of glucagon release was independent of insulin secretion [1]. In addition, persistence of the inhibitory effect of GLP-1 on glucagon secretion in the absence of any insulin under a low glucose condition has also been documented [6].

The involvement of somatostatin released from the pancreatic delta-cells, as a potential paracrine modulator has subsequently been postulated. Alpha-cells express somatostatin receptors (SSTRs), of which the subtype 2 (SSTR2) is highly dominant. The effect of somatostatin on GLP-1-evoked suppression of glucagon secretion has been investigated in a whole rat pancreas perfusion system. Pharmacological antagonism of the SSTR2 was shown to reverse the inhibitory effects of GLP-1 on glucagon secretion, demonstrating involvement of somatostatin.

However, immunoneutralisation of somatostatin could not fully reverse the inhibitory effects of GLP-1 on glucagon, pointing to the involvement of additional factors [6].

1.4 Can the Effects on Glucagon Release Be Explained by a Direct Action of GLP-1?

Further work by De Marinis and colleagues has indicated that the action of GLP-1 on glucagon secretion cannot be accounted for fully by a paracrine effect mediated by somatostatin. Thus, the authors have demonstrated that in the absence of glucose, when there is no insulin and somatostatin secretion, GLP-1 retains its ability to inhibit glucagon secretion by ~50%. They also report preservation of the inhibitory effects of GLP-1 during blockade of the somatostatin receptor 2 (SSTR2). Finally, the

authors demonstrate that glucagon secretion can still be suppressed by GLP-1 in dispersed mouse islet cells, lacking cell-to-cell communication. Collectively, these findings rule out the involvement of somatostatin or insulin as paracrine mediators of the effects of GLP-1 on alpha-cell [6].

Thus, we hypothesise that the GLP-1-induced suppression of glucagon release is a consequence of a direct effect of GLP-1 on the alpha-cell. The binding of GLP-1 to its receptors (expressed at very low levels) activates Gs-coupled membrane receptors, resulting in a small increase in intracellular cAMP and activation of the intracellular secondary messenger protein kinase A (PKA). These events subsequently lead to PKA-dependent phosphorylation of P/Q-type Ca^{2+} channels [8] and suppression of their activity, resulting into reduced exocytosis of glucagon-containing granules.

It is known that in mice, both glucose and GLP-1 inhibit glucagon secretion via the P/Q-type Ca^{2+}-channels. However, the effects of GLP-1 occur independently of the ATP sensitive potassium channels (K_{ATP}). Thus, the K_{ATP} channel activator, diazoxide, reverses the inhibitory effects of glucose but is unable to block GLP-1 action. These results imply that glucose regulates P/Q-type Ca^{2+} channels by an indirect mechanism induced by changes in the alpha-cell membrane potential arising from closure of the K_{ATP} channels, whereas GLP-1 suppresses alpha-cell secretion by a direct effect on Ca^{2+} channel activity and glucagon exocytosis [6].

Given the reported physiological differences in rodent and human islets, it is critical to validate these reports in human studies. Early findings from our group point to a direct effect of GLP-1 on glucagon release in donor human islets. Thus, our data demonstrate that the action of GLP-1 on glucagon secretion can only be partially accounted for by somatostatin, and is sensitive to GLP-1R blockade (Ramracheya, unpublished).

1.5 Facing Challenges in the Field

Elucidation of the process by which GLP-1 regulates glucagon secretion is faced with countless challenges. First and foremost, highly specific and sensitive detection systems are needed for measuring islet hormones in supernatant samples. Second, more robust techniques are required to explore receptors/mechanisms involved in incretin biology and action.

Despite the elapse of more than 50 years since the development of glucagon radioimmunoassay (RIA), there are still significant concerns regarding antibody sensitivity for glucagon, GLP-1 and GLP-1R due to structural overlap. These limitations may be responsible for the lack of consensus in the field.

1.6 Future Directions

1.6.1 Improving Methods for GLP-1R Detection

Among differences in experimental approaches, concerns have been raised on the reliability of both commercial and in-house detection assays. Thus, non-specific bands were reported in lysates from GLP-1R knockout mice from pre-validated antisera, whereas application on lysates over-expressing the GLP-1R did not detect any immunoreactivity [9]. More recently, out of three commercial antibodies for the GLP-1R, a study was unable to confirm the specificity or sensitivity of all three antibodies in the determination of GLP-1R expression in positive and negative control samples [9]. To address this shortcoming, Pyke and colleagues have generated their own monoclonal antibody. However, this is also likely to be challenging due to high levels of homology between GPCRs and their low cellular density [7].

1.6.2 Need for More Specific Antibodies for GLP-1 and Glucagon

There is presently a lack of highly specific antibodies available for GLP-1 and glucagon. This is mainly due to the fact that both GLP-1 and glucagon are synthesised from the same precursor protein, proglucagon. Proglucagon is a 158 amino acid peptide, synthesised in intestinal L-cells and the pancreatic alpha-cells. Cell-specific cleavage events subsequently generate protein moieties unique to each cell type. Thus, breakdown by the enzyme prohormone convertase 2 (PC2) in alpha-cells leads to the formation of glucagon and major proglucagon fragment (MPGF) whereas breakdown by another enzyme PC1/3 in L-cells gives rise to GLP-1, GLP-2 and glicentin, which can be further processed to GRPP and oxyntomodulin.

L-cells and alpha-cells process the proglucagon peptide into GLP-1 and glucagon respectively. Both glucagon and GLP-1 are secreted in human serum or plasma. Therefore, the formation of multiple proteins from a single precursor peptide necessitates stringent antibody selection due to potential cross-reactivity. It is thought that antibodies targeted to the N-terminus (amino acid 33) or to the C-terminus (amino acid 61) would constitute more precise quantification of circulating glucagon in circulation. However, this entails the risk that N-terminal glucagon antibodies can also detect oxyntomodulin produced in the intestine whilst C-terminal glucagon antibodies can cross-react with proglucagon 1–61. As for GLP-1, antibodies directed to the N-terminus can cross-react with MPGF secreted from the alpha-cells whereas it would not be possible for C-terminal antibodies to distinguish between the active (7–36) and inactive (9–36) forms of the peptide. Thus, antibodies designed to recognise one end of the peptide may not provide specific detection in plasma. Sandwich assays based on antibodies targeting both

ends of GLP-1 and glucagon may constitute a reliable and robust means of detection.

1.6.3 Reconciling Species Differences and Dealing with Major Challenges

Important differences in islet cell density and configuration, complement of ion channels and signalling cascades are known to exist between mice and man (reviewed in [10]). However, to date, most of GLP-1 based studies have been conducted in mouse islets and human data is missing. Given the compelling differences, data cannot be directly extrapolated between the species. Therefore, key observations made in animal studies necessitate validation in human models, which will aid development of novel treatments for diabetes in humans.

1.6.4 How Are the Effects of GLP-1 on Glucagon Release Mediated?

It is well-established that GLP-1 can suppress glucagon release from alpha-cells despite the fact that these cells express less than 1% of GLP-1Rs detected in beta-cells. This discrepancy has also been reported in other tissues such as the liver, adipose tissue and skeletal muscle where GLP-1Rs have not been conclusively demonstrated. Moreover, Ramracheya et al. have observed retention of the inhibitory effects of GLP-1 on glucagon secretion in islets obtained from mice lacking the GLP-1R (Ramracheya et al., unpublished). This raises the possibility of another receptor or mechanism for GLP-1 which operates in the alpha-cells. GLP-1R is a member of the glucagon receptor family of GPCRs. These receptors are known to exhibit similar conformations and can therefore be activated by ligands generated from the same proglucagon precursor. This is exemplified by oxyntomodulin, derived from proglucagon, which has been demonstrated to act as a partial agonist for the GLP-1R. Therefore, future work should investigate the potential existence of new/novel receptors for GLP-1, which may explain its effects on the alpha-cells and other tissues.

1.6.5 Does the Metabolite GLP-1(9–36) Play a Role in Islet Physiology?

GLP-1 (7–36) constitutes the active form of GLP-1, which has a half-life of less than 2 min. In circulation, GLP-1 (7–36) is rapidly broken down to GLP-1 (9–36)

by the proteolytic enzyme dipeptidyl peptidase-IV (DPP-IV). Although GLP-1 (9–36) constitutes ~80% of circulating GLP-1, this metabolite is thought to be biologically inactive. Moreover, unlike its active counterpart, GLP-1 (9–36) has been reported to have no effects on insulin secretion in mouse islets and in healthy volunteers (Rolin et al., reviewed in [11]).

However, there have since been a number of studies reporting biological effects of GLP-1 (9–36) in organs/tissues such as the heart, liver and adipose tissue. More recently, a study by Robinson and colleagues has shown that GLP-1 (9–36) can confer protection against post myocardial infarction remodelling [10]. Moreover, GLP-1 (9–36) infusion has been reported to enhance glucose clearance in anaesthetised pigs by an insulin independent process, implying that the metabolite may exert glucose-lowering effects (reviewed in [11]). Likewise, several other studies have explored the action of GLP-1 (9–36) on peripheral tissues [12].

Thus, based on evidence from recent studies, it is clear that the breakdown product of GLP-1 is not biologically inactive and may have important physiological roles. Findings from our own laboratory indicate that GLP-1 (9–36) has no effect on glucose-induced insulin secretion but it can suppress glucagon release in both mouse and human islets as strongly as active GLP-1 (Ramracheya et al., unpublished). Elucidating the mechanism by which GLP-1 (9–36) can affect glucagon secretion remains an important puzzle to solve as it will lend insight into the processes via which active GLP-1 influences alpha-cell function. Given the role of glucagon in the pathophysiology of diabetes, understanding its regulation by GLP-1 and GLP-1 (9–36) may facilitate the generation of effective anti-diabetic therapies. However, if GLP-1 (9–36) regulates glucagon levels in the body, this argues against the use of DPP-IV inhibitors as a diabetes therapy.

References

1. Holst JJ, Christensen M, Lund A, de Heer J, Svendsen B, Kielgast U et al (2011) Regulation of glucagon secretion by incretins. Diabetes Obes Metab 13(Suppl 1):89–94
2. Xue X, Ren Z, Zhang A, Yang Q, Zhang W, Liu F (2016) Efficacy and safety of once-weekly glucagon-like peptide-1 receptor agonists compared with exenatide and liraglutide in type 2 diabetes: a systemic review of randomised controlled trials. Int J Clin Pract 70:649–656
3. Samson SL, Garber AJ (2016) A plethora of GLP-1 agonists: decisions about what to use and when. Curr Diab Rep 16:120
4. Ramracheya RD, McCulloch LJ, Clark A, Wiggins D, Johannessen H, Olsen MK et al (2016) PYY-dependent restoration of impaired insulin and glucagon secretion in Type 2 diabetes following Roux-En-Y gastric bypass surgery. Cell Rep 15:944–950
5. Tornehave D, Kristensen P, Rømer J, Knudsen LB, Heller RS (2008) Expression of the GLP-1 receptor in mouse, rat, and human pancreas. J Histochem Cytochem 56:841–851
6. De Marinis YZ, Salehi A, Ward CE, Zhang Q, Abdulkader F, Bengtsson M et al (2010) GLP-1 inhibits and adrenaline stimulates glucagon release by differential modulation of N- and L-type Ca^{2+} channel-dependent exocytosis. Cell Metab 11:543–553
7. Pyke C, Heller RS, Kirk RK, Orskov C, Reedtz-Runge S, Kaastrup P et al (2014) GLP-1 receptor localization in monkey and human tissue: novel distribution revealed with extensively validated monoclonal antibody. Endocrinology 155:1280–1290

8. Rorsman P, Ramracheya R, Rorsman NJ, Zhang Q (2014) ATP-regulated potassium channels and voltage-gated calcium channels in pancreatic alpha and beta cells: similar functions but reciprocal effects on secretion. Diabetologia 57:1749–1761
9. Drucker DJ (2013) Incretin action in the pancreas: potential promise, possible perils, and pathological pitfalls. Diabetes 62:3316–3323
10. Robinson E, Tate M, Lockhart S et al (2016) Metabolically-inactive glucagon-like peptide-1 (9–36)amide confers selective protective actions against post-myocardial infarction remodelling. Cardiovasc Diabetol 15:65
11. Rorsman P, Braun M (2013) Regulation of insulin secretion in human pancreatic islets. Annu Rev Physiol 75:155–179
12. Baggio LL, Drucker DJ (2007) Biology of incretins: GLP-1 and GIP. Gastroenterology 132: 2131–2157

Chapter 2
Analysis of Non-Conducting Tantalite Minerals by Glow Discharge Optical Emission Spectrometry

M. Nete, W. Purcell, and J.T. Nel

Abstract Capabilities of the radio frequency glow discharge optical emission spectroscopy (RF-GD-OES) for analysis of Ta_2O_5/Nb_2O_5 and tantalum and niobium in electrically non-conducting geological samples were investigated. The metal pentoxides (Ta_2O_5 and Nb_2O_5) and the tantalite mineral powders were mixed with a thermally conductive copper powder in ratios of up to 1:10 sample: copper and pressed into a disc sample for glow discharge sputtering. Studies were carried out to determine and optimize all the parameters affecting the analyses by the RF-GD-OES technique. This included the determination of the ability of the methodology to generate usable analytical curves for the target elements. Good calibration curves which were used for analyses of Ta and Nb in the tantalite minerals were obtained at optimized experimental conditions. Respective tantalum and niobium recoveries were in the order of 99.78–104.91% and 98.34–102.03% from the mineral analyses.

Keywords Tantalite • Tantalum oxide • Niobium oxide • Glow discharge • Analysis

M. Nete (✉)
Department of Chemistry, University of the Free State, Bloemfontein 9300, South Africa

The South African Nuclear Energy Corporation SOC Ltd. (Necsa), P.O. Box 582, Pretoria 0001, South Africa
e-mail: netem@ufs.ac.za

W. Purcell
Department of Chemistry, University of the Free State, Bloemfontein 9300, South Africa
e-mail: purcellw@ufs.ac.za

J.T. Nel
The South African Nuclear Energy Corporation SOC Ltd. (Necsa), P.O. Box 582, Pretoria 0001, South Africa
e-mail: johann.nel@necsa.co.za

P. Ramasami et al. (eds.), *Emerging Trends in Chemical Sciences*,
DOI 10.1007/978-3-319-60408-4_2

2.1 Introduction

Tantalum and niobium are group VB elements with very similar chemical properties and as such they are always found together in nature. These elements have recently been found to have a great potential for use in strategic energy technologies such as nuclear, solar, carbon capture and capacitor manufacturing [1]. Tantalum is used for manufacturing of capacitors [2, 3], which offer high capacitance density needed in the smallest possible size. Niobium oxide is used in the manufacturing of high refractive index lenses as well as high dielectric and multilayer ceramic capacitors [3, 4]. Niobium oxide powder material has many desirable properties as a solid electrolyte capacitor. These properties include a better load resistance, reduced costs and significant reduction in ignition failure [5].

The demand for highly precise quantitative methods for accurate characterization of niobium and tantalum in various sample matrices has increased significantly due to their importance in the production of modern industrial products [1]. Conventional wet analytical methods such as inductively coupled plasma spectroscopy (ICPS) and flames which require complete sample dissolution are the most successful and commonly used techniques. However, the different sets of impurities in natural samples such as tantalite mineral can alter the performance of the dissolution method and thereby require a modification of the already existing methods or even developing a new alternative dissolution method.

The use of glow discharge spectrometry (GDS) for bulk analysis of mineral samples has been relatively poorly explored. The general challenge in using solid analysis techniques such as GDS and X-ray fluoresence (XRF) is the sample preparation, especially for powder samples which require homogenization of the sample prior to analysis. In addition, the most limiting factor is the requirement that the samples be electrically conductive for successful measurements using GDS analysis. Challenging as the sample preparation may be, the direct analysis of solid samples is important for the reduction of acidic liquid waste which in turn ensures a safe environment free of chemical contamination. Compared to XRF, glow discharge optical emission spectroscopy (GD-OES) has a higher sensitivity for the light metals such as B, Be and Li (ppm range), better precisions and lower %RSD values [6].

Compared to wet spectrometric methods, such as AAS and ICPS, GDS has advantages of being partially non-destructive, multi-elemental, fast and requiring simpler sample preparation [7]. Moreover, the GD-OES analysis is non-destructive; hence the samples can be stored and reused for other investigations at a later stage or be kept as archival samples [8]. GDS is superior for rapid depth profiling [9], surface, interface and bulk qualitative and quantitative analyses of solids [10]. Metallic bar or disc samples can be analyzed directly without any preparation or slightly polished to ensure that they are vacuum-tight when pressed against a silicone O-ring. Powdered conductive samples on the other hand need to be pressed into discs for analysis by GDS. Non-conductive powders such as metal oxides and minerals are either pressed into very thin discs that can be analyzed using the radio

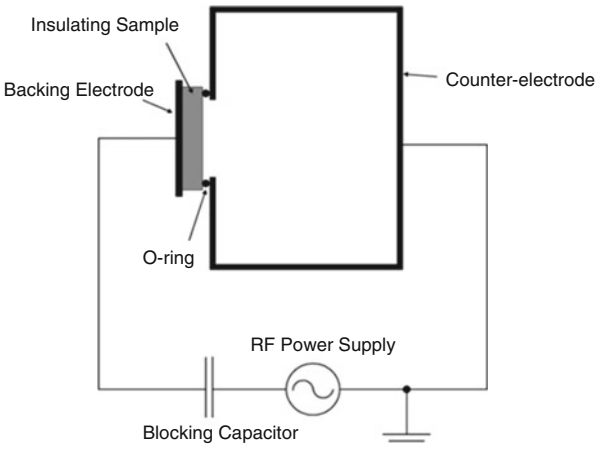

Fig. 2.1 Diagrammatic representation of a radio frequency glow discharge (RF GD) sample introduction system [11]

frequency GD lamp or mixed with conductive host material such as copper powder (to make them electrically conductive) and then pressed into a disc [7]. The main challenge in this method of sample preparation is obtaining a homogenous mixture. The accuracy of analysis depends strongly on the even distribution of the particles of the analyte. These requirements cannot always be fulfilled, especially when the amount of sample is very small.

The sample introduction into the GD-OES instrument involves mounting of the sample over an O-ring at the lamp opening (Fig. 2.1) where it is held in place by vacuum. This method of sample introduction into the system requires preparation of non-porous and flat polished sample surfaces. Once the sample is properly mounted the next requirement is the production of sufficiently energetic ions by the lamp to sputter the atoms on the sample surface.

The aim of this study was to investigate the capability of the GD-OES in quantitative and accurate determination of Ta and Nb in tantalite minerals. Samples were prepared for analysis by mixing the non-conductive metal oxide and mineral samples with the conductive copper powder. Optimum experimental conditions were investigated extensively during the developments to obtain a good calibration curve. These included the determination of an optimum sample:host material ratio, preburn times as well as optimal voltage and current.

2.2 Experimental

2.2.1 Reagents and Equipment

Tantalite samples (manganotantalite (Tan A) and ferrocolumbite (Tan C)) were sourced from Mozambique. High purity Ta_2O_5, Nb_2O_5 and 99.5% copper powder (particle size <425 μm) were purchased from Sigma Aldrich South Africa.

Powdered samples were mixed using a Retsch mixer mill MM 200 and the mixtures were pressed into discs using an Altech hydraulic press. Sample discs were analyzed by a LECO GDS850A glow discharge optical emission spectrometer (GD-OES).

2.2.2 Sample Preparation

Calibration samples were prepared by mixing the non-conducting $(Ta/Nb)_2O_5$ mixture with the host (conductive) copper powder. Samples were mixed in ratios ranging between 1:99 and 1:1 m/m (sample to host) with copper powder. The mixture was shaken for 10 min using a Retsch mixer mill MM 200. Samples were pressed into 2.0 mm × 25 mm discs at a pressure of at least 10 MPa for 30 s with a hydraulic press (Fig. 2.2). The mineral samples (maximum particle sizes = 250 μm) were prepared in a similar manner to the calibration samples. The sample discs were analyzed using GD-OES. Experimental factors which were investigated include the influence of sample to host material ratio, power effects and pre-burn time.

2.3 Results and Discussion

2.3.1 Optimization of the Sample Preparation

The development of the sample preparation method was begun by investigation of the niobium/tantalum pentoxide:copper mixtures at ratios ranging between 1:99 and 1:1. The experimental results indicated that at higher relative metal pentoxide concentrations sample discs were not vacuum-tight. The results indicated that the porosity of the discs increased as the sample content was above the 15% concentration. Another observation which was made was the obvious segregation between the metal oxide particles and those of the copper metal at 10% metal oxide and above. Lastly, metal oxide concentrations between 10 and 15% were not sputtered even though they were vacuum-tight on the instrument (Fig. 2.3). The observed particle separation between the oxide materials and the copper metals could be due to the difference in the densities and/or the particle sizes of these samples. This could also be due to the diffusional migration of the non-conducting metal oxide and copper particles [12] which may occur during the pressing of the samples. This separation may be occurring even at lower metal pentoxide concentrations but only become visible at relatively higher metal pentoxide concentration which would imply potentially poor homogeneity of the discs.

Fig. 2.2 Hydraulic press for preparation of pellets for analysis by GD-OES

2.3.2 Calibration Curves

The limit of detection (LOD) estimates of 0.0024% for Nb and 0.0028% for Ta (which were comparable and in the same magnitude to those of inductively coupled plasma optical emission spectroscopy (ICP-OES)) were obtained by using a copper powder sample (~7 g) as blank in this study. The copper powder (host matrix), which is responsible for the spectral background has a different sputtering rate from the oxide materials to be analyzed. The analytical calibration curve was investigated for the metal pentoxide with concentrations of less than 10%. Measurements were initially performed under default instrument conditions of 700 V, 20 mA and 1 min pre-burn time at three different positions (to determine the reproducibility of intensities) of each standard and a plot of intensities against concentrations was

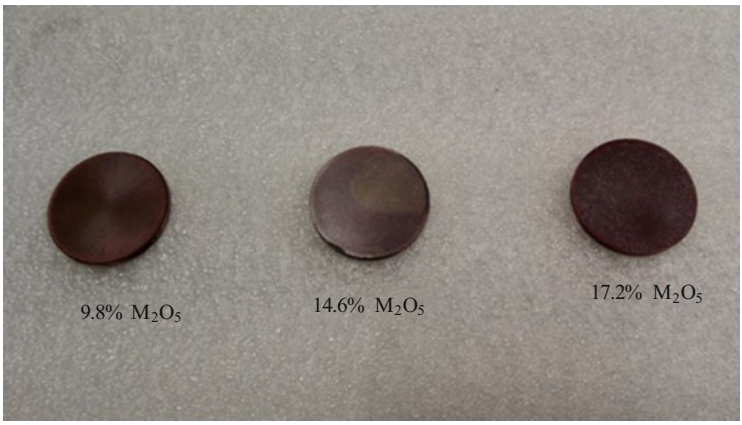

Fig. 2.3 Influence of sample concentration on the homogeneity and porosity of the sample/copper powder mixture

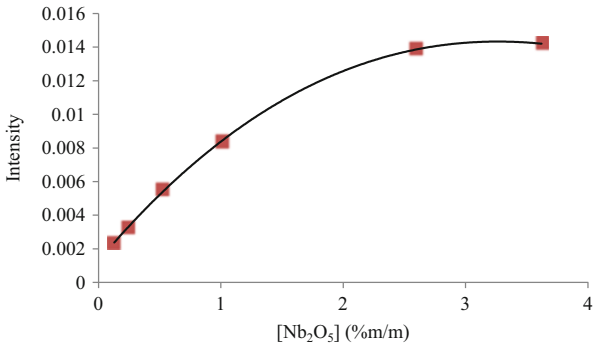

Fig. 2.4 Standard curve for intensity versus concentration for analysis of Nb_2O_5 by RF-GD-OES under default instrument conditions

established. The calibration curves (Figs. 2.4 and 2.5) exhibited good linearity in the ranges of 0.13–1.01% of niobium and 0.15–4.20% of tantalum. At these lower concentrations correlation coefficient values (R^2) for Ta and Nb linear curves were 0.988 and 0.990 respectively. Above the 1.01% Nb_2O_5 concentration there is a clear loss of linearity in the calibration curve but generally good reproducibility of the signal intensities for all the standard samples.

Literature study has indicated that this loss of linearity with the Nb_2O_5 concentration increase could be due to the slow sputtering rate of the oxide material [13]. Another literature study has shown that the increase in oxide concentration leads to decrease in discharge voltage and subsequently to decreased sputter yields [14]. The stronger molecular bonding in oxide material is responsible for the slower sputtering of these materials compared to metals. The Ta_2O_5 calibration curve on the other hand displayed less or no loss of linearity over a concentration of 0.15–4.20% Ta_2O_5. The linear calibration curves (0.13–1.01% Nb_2O_5 and

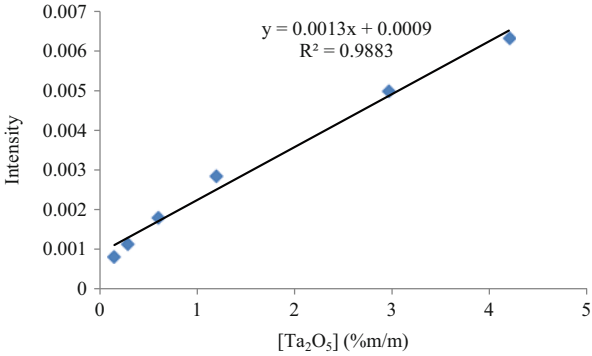

Fig. 2.5 Standard curve for intensity versus concentration for analysis of Ta_2O_5 by RF-GD-OES under default instrument conditions

Table 2.1 Quantities and %RSD values of Ta_2O_5 and Nb_2O_5 in tantalite minerals determined by RF-GD-OES under default instrument conditions and comparison to ICP-OES results

	ICP-OES [15]		RF-GD-OES		Average % recovery	
Sample ID	Ta_2O_5	Nb_2O_5	Ta_2O_5	Nb_2O_5	Ta_2O_5	Nb_2O_5
Tan A	27.8(3)	27.0(2)	23(1)	9(1)	82.73	34.02
%RSD			4.94	13.34		
Tan C	33.0(2)	13.7(2)	29(2)	6(1)	87.88	46.50
%RSD			6.94	20.96		

0.15–4.20% Ta_2O_5) were used for quantification of Ta and Nb in the tantalite minerals, under the default instrument conditions. The results were compared to the previous ICP-OES analysis results [15] and unsatisfactory recoveries of less than 90% Ta_2O_5 and 50% Nb_2O_5 were obtained (Table 2.1) in this study. In addition to the poor analyte recoveries were the high %RSD values (up to 20.96%) which indicated poor reproducibility of the data points.

In the next step, it was decided to investigate the effect of the pre-burn time to try and improve the recovery of the analytes during the mineral analysis. The influence of the pre-burn time was studied at the current of 23 mA, voltage of 700 V and the pre-burn times of 1, 2 and 5 min (Fig. 2.6). Experimental results obtained in this part of the study indicated a significant improvement of Nb_2O_5 recoveries from 34.02 to 76.40% when the pre-burn time was increased from 1 to 5 min. The Ta_2O_5 recoveries also increased from 82.73 to 98.17% during the same pre-burn time increase. The %RSD of Nb_2O_5 analysis improved from 13.34 to 2.52% and 4.94 to 3.44% for Ta_2O_5 for the 1 to 5 min pre-sputtering times during analysis of Tan A. The longer pre-sputtering maximizes the sputtering of the oxide material thereby improving the stability of the RF power discharge which results in achievement of reproducible intensities.

The influence of power was studied to improve both the linear range of the standard curves as well as the recovery of the analytes. The influence of power on the intensities obtained was studied by analyzing three Nb_2O_5 standard samples (each sample disc was sputtered at three different positions) at a current of 23 mA and 5 min pre-burn time while changing the discharge voltage from 600 to 900 V (Fig. 2.7). The results obtained in this part of the study indicated an increase in the

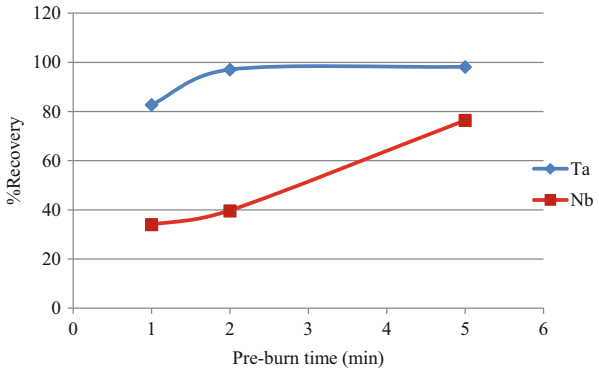

Fig. 2.6 Elemental recoveries versus pre-burn time for analysis of tantalite A mineral by RF-GD-OES at 23 mA and 700 V

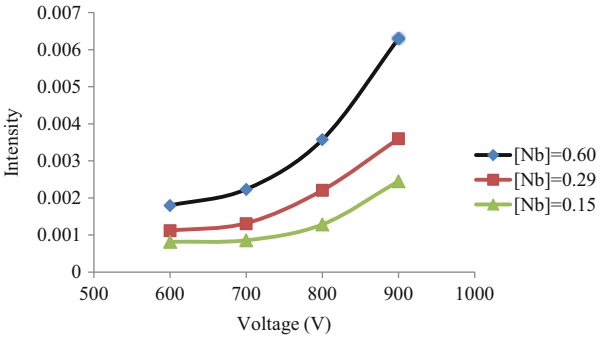

Fig. 2.7 Intensities versus voltage for analysis of Nb_2O_5 standard samples by RF-GD-OES at 23 mA and 5 min pre-burn time

intensities of the standard samples with increasing discharge voltage. Similar results were also obtained for Ta_2O_5 standard samples under the same experimental conditions. It is clear from these results that more power and pre-sputtering time are essential for better sputter rates of the oxide materials. A higher power is mainly required to break the stronger molecular bonds of the oxide material while longer pre-burn times are important for stable RF power discharge and steady sputter rates and excitations.

The combination of longer pre-burn times and a higher discharge voltage was used to establish the calibration curves of both Ta and Nb (Figs. 2.8 and 2.9). As previously, measurements were performed in triplicate for each standard and the lowest and highest data values are indicated by vertical error bars. These calibration curves (Figs. 2.8 and 2.9) exhibit improved linear range (0.13–2.6%) and good linear regression (R^2 value = 0.9992) for Nb_2O_5. The Ta_2O_5 calibration curve was not studied beyond the 0.15–4.20% range due to the fear of particle segregation and poor sputtering, which were previously observed for higher oxide concentrations. However, the new experimental conditions greatly improved the linear regression of the standard curve ($R^2 = 0.9995$).

Percentage recoveries of the analytes in the two minerals also improved significantly (Table 2.2) under these new set of experimental conditions (23 mA, 900 V and 5 min pre-burn time). The %RSD values of the analytes' recoveries were less than 5%.

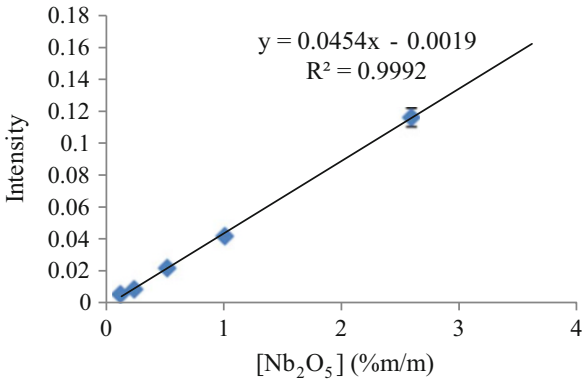

Fig. 2.8 Standard curve for intensity versus concentration for analysis of Nb_2O_5 by RF-GD-OES at optimum conditions

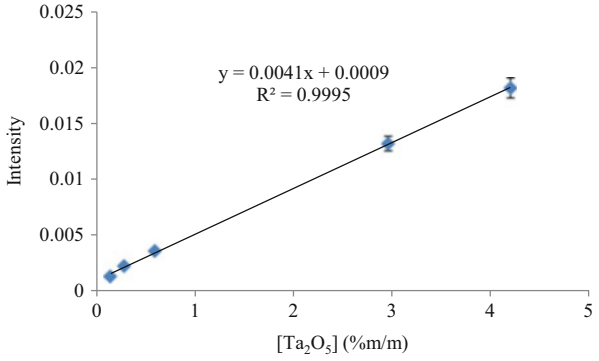

Fig. 2.9 Standard curve for intensity versus concentration for analysis of Ta_2O_5 by RF-GD-OES at optimum conditions

Table 2.2 Quantities and %RSD values of Ta_2O_5 and Nb_2O_5 in tantalite minerals determined by RF-GD-OES under optimized experimental conditions and comparison to ICP-OES results

	ICP-OES [15]		RF-GD-OES		Average % recovery	
Sample ID	Ta_2O_5	Nb_2O_5	Ta_2O_5	Nb_2O_5	Ta_2O_5	Nb_2O_5
Tan A	27.8(3)	27.0(2)	28.1(9)	26.8(5)	101.08	99.26
%RSD			1.55	1.99		
Tan C	33.0(2)	13.7(2)	32.7(9)	12.9(8)	99.09	94.16
%RSD			3.19	1.65		

2.4 Conclusion

The analytical capabilities of RF-GD-OES for tantalum and niobium analyses in powdered tantalite minerals were investigated. Studies were carried out to develop a sample preparation method for successful analysis of non-conducting $(Ta/Nb)_2O_5$ and Ta/Nb in tantalite samples. Optimization of sample preparation and analytical parameters was successfully achieved for satisfactory determination of Ta/Nb in

non-conducting tantalite samples. Good calibration curves were obtained using a RF lamp at lower sample:copper ratios. The figures of merit (R^2 and standard deviations indicated by error bars) obtained for the standard curves were highly satisfactory. Studies were carried out to investigate the influence of operating parameters such as the applied voltage and the pre-sputtering time. At optimal conditions the respective tantalum and niobium recoveries from the mineral analyses were in the order of 99.78–104.91% and 98.34–102.03% respectively. The %RSD values were decreased from 13.34 to 1.99% for Nb_2O_5 and 4.94 to 1.55% for Ta_2O_5 by increasing both the pre-burn time and the applied voltage during analysis of Tan A sample. Comparison of the mean results obtained in this study to those recorded using ICP-OES analysis indicated high comparable values. The Student t-test gave t values which ranged from 0.391 and 2.191 and which were all below the tabulated value of 2.447 at the 95% confidence level.

Acknowledgements The authors thank the Research Fund of the University of the Free State, the National Research Foundation of SA, the South African Nuclear Energy Corporation Ltd (Necsa) and the New Metals Development Network (NMDN) of the Advanced Metals Initiative (AMI) of the Department of Science and Technology of South Africa (DST) for financial support. The authors also wish to thank Dr Steven Lötter for his assistance on the operation of the GD-OES instrument.

References

1. Moss RL, Tzimas E, Kara H, Willis P, Kooroshy J (2011) Critical metals in strategic energy technologies: assessing rare metals as supply-chain bottlenecks in low-carbon energy technologies. JRC Scientific and Technical Reports. https://setis.ec.europa.eu/system/files/CriticalMetalsinStrategicEnergyTechnologies-def.pdf
2. Prymak J (2008) Update – comparison of ceramic and tantalum capacitors. KEMET update, Nov 2008
3. Zednicek T, Gill J (2003) Voltage derating rules for solid tantalum and niobium capacitors. In: Proceedings of CARTS EUROPE, Stuttgart, Germany
4. Polyakov EG, Polyakova LP (2003) Current trends in the production of tantalum and niobium. Metallurgist 47:33–41
5. Zednicek T, Vrana B, Millman WA, Gill J, Reynolds C (2002) Tantalum and niobium technology roadmap. AVX Corporation. http://www.avx.com/docs/techinfo/TantalumandNiobiumTechnologyRoadmap.pdf
6. Anfone AB, Marcus KR (2001) Radio frequency glow discharge optical emission spectrometry (RD-GD-OES) analysis of solid glass samples. J Anal At Spectrom 16:506–513
7. Marcus RK, Broekaert JAC (2003) Glow discharges plasmas in analytical spectroscopy. Wiley, Chichester
8. Betti M, de las Heras LA (2004) Glow discharge spectrometry for the characterization of nuclear and radioactively contaminated environmental samples. Spectrochim Acta B 59: 1359–1376
9. King FL, Teng J, Steiner RE (1995) Glow discharge mass spectrometry: Trace element determinations in solid samples. J Mass Spectrom 30:1061–1075
10. Suzuki S, Kakita K (2005) A comparative study of GDOES, SIMS and XPS depth profiling of thin layers on metallic materials. J Surf Anal 12:174–177

11. Winchester RM, Payling R (2004) Radio-frequency glow discharge spectrometry: a critical review. Spectrochim Acta B 59:607–666
12. Marcus RK (1993) Modern analytical chemistry: glow discharge spectroscopies. Plenum, New York
13. Gonzalez-Gago C, Smid P, Hofmann T, Venzago C, Hoffmann V, Gruner W (2014) The use of matrix-specific calibrations for oxygen in analytical glow discharge spectrometry. Anal Bioanal Chem 406:7473–7482
14. De Gryse R, Depla D, Haemers J The discharge voltage behaviour during reactive sputtering of oxides. Ghent University, Krijgslaan 281 (S1), B-9000 Ghent, Belgium. http://www.aimcal.org/uploads/4/6/6/9/46695933/degryse.pdf
15. Nete M, Purcell W, Snyders E, Nel JT, Beukes G (2012) Characterization and alternative dissolution of tantalite mineral samples from Mozambique. J S Afr Inst Min Metall 112: 1079–1086

Chapter 3
Chemical Composition and Antioxidant Activity of *Tagetes minuta* L. in Eastern Cape, South Africa

Sithenkosi Mlala, Opeoluwa Oyehan Oyedeji, Constance Rufaro Sewani-Rusike, Adebola Omowunmi Oyedeji, and Benedicta Ngwenchi Nkeh-Chungag

Abstract The purpose of this study was to determine the chemical composition of essential oils from *Tagetes minuta* from the Eastern Cape of South Africa and evaluate their antioxidant potential for medicinal end use. The essential oils were extracted by hydrodistillation method from fresh and dry parts (stem, leaves and flowers) of *Tagetes minuta* collected from Komga, Eastern Cape Province, South Africa and analyzed by gas chromatography coupled with mass spectrometry (GC-MS) and gas chromatography (GC). This analysis has led to the identification of 12, 31, 10, 37, 4 and 39 compounds representing 99.16, 98.07, 98.86, 98.30, 100 and 97.66% of fresh stem (TMFS), dry stem (TMDS), fresh leaves (TMFL), dry leaves (TMDL), fresh flower (TMFF) and dry flower (TMDF) essential oil respectively. The major components were identified to be *cis*-*β*-ocimene (38.03%) for TMFS; caryophyllene oxide (18.04%) for TMDS; *trans*, *cis*-alloocimene (25.35%) for TMFL; isopropyl tetradecanoate (17.02%) for TMDL; *cis*-*β*-ocimene (38.14%), for TMFF and *trans*-*β*-ocimene (37.03%), for TMDF. The dry parts (TMDS, TMDL and TMDF) essential oil were evaluated for antioxidant activity using DPPH and FRAP bioassays. Standard equivalent values from DPPH assay were

S. Mlala • O.O. Oyedeji (✉)
Faculty of Science and Agriculture, Department of Chemistry, University of Fort Hare, Private Bag X1314, Eastern Cape Province, Alice 5700, South Africa
e-mail: ooyedeji@ufh.ac.za

C.R. Sewani-Rusike
Faculty of Health Sciences, Department of Human Biology, Walter Sisulu University, Private Bag X1, Eastern Cape Province, Mthatha, South Africa

A.O. Oyedeji
Department of Chemistry and Chemical Technology, Walter Sisulu University, Private Bag X1, Eastern Cape Province, Mthatha 5117, South Africa

B.N. Nkeh-Chungag
Faculty of Natural Sciences, Department of Biological and Environmental Sciences, Walter Sisulu University, Private Bag X1, Eastern Cape Province, Mthatha 5117, South Africa

P. Ramasami et al. (eds.), *Emerging Trends in Chemical Sciences*,
DOI 10.1007/978-3-319-60408-4_3

between 6.74 ± 0.27 and 18.7 ± 0.35 μg/mL AAE with scavenging ability in descending order: TMDF > TMDL > TMDS. Standard equivalent values from FRAP assay were between 26.30 ± 0.41 and 113.0 ± 1.2 μg/mL AAE with antioxidant activity in descending order: TMDF > TMDL > TMDS. These results suggest that *T. minuta* may be used as a potential natural source of antioxidant.

Keywords *Tagetes minuta* • Hydrodistillation • Essential oil • GC-MS • GC • DPPH • FRAP

3.1 Introduction

Most essential oils are reported to possess antioxidant, anti-inflammatory and antimicrobial activities [1]. Natural antioxidants are known to display an extensive range of biological properties such as antibacterial, anti-inflammatory, antiallergic, antithrombotic and vasodilatory activities [1, 2]. Hypertensive effects of oxidative stress are typically caused by endothelial dysfunction resulting from disturbances of vasodilator system, mainly degradation of nitric oxide (NO) by oxygen free radicals [3]. The increase in reactive oxygen species (ROS) may lead to the reduction of nitric oxide levels which could be part of the mechanism that leads to hypertension and other oxidative stress related diseases [4]. Antioxidants are able to trap ROS and thus reduce their ability to induce oxidative damage and may therefore be useful in preventing oxidative stress and consequently chronic diseases such as hypertension [5]. Therefore, it is important to investigate the antioxidant activity of essential oils from *Tagetes minuta*. To the best of our knowledge, there have not been any literature evidence reporting about isolation of essential oil from *Tagetes minuta* in the Eastern Cape Province, South Africa.

Tagetes genus consists of 56 different species, of which 29 grow perennially and 27 grow annually [6]. This genus belongs to the Asteraceae family with some common species such as *Tagetes tenuifolia*, *Tagetes erecta*, *Tagetes minuta* and *Tagetes patula* [7]. *T. minuta* traditionally known as nukayo in Xhosa [8] is native to the temperate grasslands and mountains of the southern part of South America and North America. It was introduced to Europe, Asia, Africa, India, Australia, Madagascar and Hawaii [9]. *T. minuta* is one of the annual plants of 1–2 m in height, with upright erect stems that bear leaves of up to 15 cm in length that are glossy green in colour with 17–19 leaflets and creamy-yellow flowers of 10 mm long and 2 mm wide in size [10]. *T. minuta* is used for wound healing, bronchodilatory, microbial and anti-inflammatory problems, kidney trouble, piles and muscular pain. It is also used for fevers, indigestion, gastritis and as a mild laxative [11].

It has been reported that *T. minuta* contains a varying number of secondary metabolites that include flavanoids, terpenoids, saponins, thiophenes, monocyclic, bicyclic and acyclic monoterpenes [11, 12]. Previous phytochemical analysis of essential oils from *T. minuta* showed that the major components were *cis*-ocimene,

β-ocimene, rosefuran, limonene, dihydrotagetone, *trans*-tagetone, *cis*-tagetone and *cis*-tagetenone [11, 13]. Previous studies showed high antioxidant capacity (LC_{50} of 1.49 g/L) of essential oil from *T. minuta* collected in Uganda when assessed using the stable free radical DPPH [14]. *T. minuta* essential oil (from Iran) also showed potency in vitro reactive oxygen species (ROS), reactive nitrogen species (RNS) and hydrogen peroxide (H_2O_2) scavenging activity with IC_{50} of 12–15 μg/mL [15]. *T. minuta* essential oil (from Iran) also showed a concentration dependent ROS and RNS scavenging ability. Inhibition concentration (IC_{50}) were reported to be 12 ± 2 and 13 ± 4 μg/mL for ROS and RNS, respectively [16]. To the best of our knowledge, as literature is concerned, this research study represents a first report on chemical composition and antioxidant activity from *T. minuta* in the Eastern Cape Province, South Africa. Therefore, our primary aim was to determine the chemical composition of essential oil from the selected plant and evaluate their antioxidant activity in an attempt to contribute to their uses as alternatives in hypertension and other oxidative related diseases.

3.2 Materials and Methods

3.2.1 Chemicals

Hexane, DPPH (2,2-diphenyl-1-picrylhydrazyl), ascorbic acid, methanol, ferric tripyridyltriazine (Fe^{3+}-TPTZ), sodium acetate trihydrate, and hydrochloric acid were all purchased from Sigma-Aldrich (Germany) except for n-hexane which was purchased from Merck-Schuchardt (Germany).

3.2.2 Plant Material

Tagetes minuta was collected on March 2014 along Komga road, and deposited at Selmar Schonland Herbarium, Rhodes University for identification by T. Dold and deposition of voucher specimen (MS/PL4).

3.2.3 Isolation of Essential Oil

Hydrodistillation is a simple form of steam distillation which is often used to isolate volatile compounds. 300 g of fresh and dry plant material were subjected to the hydrodistillation set-up using Clevenger apparatus as prescribed by British pharmacopeae [17]. Two litres distilled water were poured to 300 g of either fresh or dry plant material and boiled at 100 °C for 4 h consecutively; the essential oils were

collected into hexane and transferred to a dark vial which is stored at 4 °C in a refrigerator.

3.2.4 Gas Chromatography-Mass Spectrometry

An HP 5890 Series II gas chromatograph equipped with an Agilent mass spectrometry detector was used. The mass spectrometer (MS) was operated in the full scan mode from 30 to 350 amu. Helium was used as a carrier gas at constant pressure of 100 kPa, and flow of 1.2 mL/min with linear velocity 30.1 cm/s. A 1 μL volume of sample was injected at a temperature of 280 °C. An HP-5MS fused silica column with 30 m length by 0.25 mm internal diameter and 0.25 μm film thickness capillary was used. The oven temperature was programmed from 40 °C for 2 min and at 10 °C/min to 280 °C with split ratio of 1:30.

3.2.5 Gas Chromatography

An HP 5890 Series II gas chromatograph equipped with a flame ionization detector (FID) was used. The detector was operated in the full scan mode from 30 to 350 amu. Helium was used as a carrier gas at constant pressure of 100 kPa, and flow of 1.2 mL/min with linear velocity 30.1 cm/s. A 1 μL volume of sample was injected at a temperature of 280 °C. An HP-5MS fused silica column with 30 m length by 0.25 mm internal diameter and 0.25 μm film thickness capillary was used. The oven temperature was programmed from 40 °C for 2 min and at 10 °C/min to 280 °C with split ratio of 1:30.

3.2.6 DPPH Assay

The scavenging reaction between DPPH (2,2-diphenyl-1-picrylhydrazyl) radical and an antioxidant (H-A) is expressed as:

$$\underset{\text{(Purple)}}{\text{DPPH}} + (\text{H-A}) \rightarrow \underset{\text{(Yellow)}}{\text{DPPH-H}} + (\text{A})$$

This test is based on the principle that antioxidants react with DPPH, which is a stable free radical and is reduced to DPPH-H and as a result the absorbance decreases. Ascorbic acid (standard) stock was prepared by dissolving 0.1 g of ascorbic acid in 100 mL of dH_2O (distilled water). The working solution was obtained by diluting 640 μL of ascorbic acid with 3360 μL to give a concentration of 160 μg/mL which was then double diluted serially into several concentrations

(160, 80, 40, 20, 10, and 5 µg/mL). 0.01 mmol/L DPPH (MW = 394.32 g/mol) was dissolved in 500 mL methanol to make up to 0.01 mM and the absorbance (OD) was 1.5 at 517 nm. Prepared DPPH was kept in the dark covered in aluminium foil. TMDS, TMDL, and TMDF essential oil stocks were prepared by dissolving 300 µL of oil which is equivalent to 0.3 g in 0.2 mL Tween 80 and diluted to 5 mL by dH_2O. 120, 60, 30 and 15 µg/mL for TMDS, TMDL and TMDF were prepared in duplicates for each essential oil. Three millilitres DPPH were added to the sample/standard and 1 mL methanol was used as blank. The solutions were incubated in the dark for 30 min and absorbance was read at 517 nm [2].

3.2.7 Ferric Reducing Antioxidant Power (FRAP) Assay

The FRAP assay evaluates antioxidants according to their reducing activity in a redox-linked colorimetric method which is a direct indicator of total antioxidant power [18]. Reduction of a ferric tripyridyltriazine (Fe^{3+}-TPTZ) complex which is a FRAP agent results in a ferrous complex which produces an intense blue color to confirm its formation. Absorption of FRAP reagent was read at 593 nm. FRAP reagent is made up of acetate buffer, $FeCl_3$ (20 mM) and TPTZ. Acetate buffer was prepared by dissolving 3.1 g of sodium acetate trihydrate ($C_2H_9NaO_5$) in 500 mL dH_2O; afterwards 16 mL of glacial acetic acid was added to the mixture which was made up to 1 L with dH_2O and stored at room temperature. $FeCl_3$ (20 mM) was prepared by dissolving 1.1 g in 200 mL dH_2O. 0.156 g TPTZ was dissolved in 50 mL HCl (40 mM). FRAP reagent was prepared by combination of 100 mL acetate buffer, 10 mL TPTZ and 10 mL $FeCl_3$. Ascorbic acid (AA) stock was prepared by dissolving 0.1 g of ascorbic acid ($C_6H_8O_6$) in 100 mL dH_2O. The working solution was prepared by adding 640 µL of AA stock to 3360 µL of dH_2O to give a concentration of 80 µg/mL which was then double diluted serially to the following concentrations: 160, 80, 40, 20, 5 and 2.5 µg/mL. A 1 mg/mL of TMDS, TMDL, and TMDF essential oils were prepared respectively by dissolving 300 µL which is equivalent to 0.3 g in 0.2 mL Tween 80 and diluted to 5 mL by dH_2O.

A procedure for standard curve and sample/standard was started by pipetting 100 µL of sample into labeled test tube. Three millilitres of freshly mixed FRAP reagent were added to 100 µL of samples/standard and the prepared solutions were incubated in a water bath at 40 °C for 4 min. The absorbance was read at 593 nm. A standard curve was drawn and the antioxidant activity of samples was extrapolated (as ascorbic acid equivalent/mg) from the standard curve [2].

3.2.8 Statistical Analysis

The data were analyzed using Graphpad Prism (v5). Analysis of variance (ANOVA) followed by Dunnet's post-hoc test were used to compare the

Table 3.1 Percentage yield (w/w) of essential oil extracted from *Tagetes minuta*

	Stem	Leaves	Flowers
Fresh oil (%)	0.20	0.65	1.12
Dry oil (%)	0.20	0.91	1.10

differences between fractions of *T. minuta*. Data was expressed as mean ± standard error of mean. P values lower than 0.05 will be considered significant.

3.3 Results

Essential oils from fresh and dry materials of *T. minuta* were extracted and analysed by GC-MS and GC. The essential oils extracted from this plant were yellow in color with a pleasant herbal odor and have thick viscosity. The oils were stored in a refrigerator before analysis. The percentage yields of essential oil in the present study are reported (Table 3.1).

3.3.1 Essential Oil Composition

The identification of 12, 31, 10, 37, 4 and 39 compounds representing 99.2, 98.1, 98.9, 98.3, 100 and 97.7% of fresh stem (TMFS), dry stem (TMDS), fresh leaves (TMFL), dry leaves (TMDL), fresh flower (TMFF) and dry flower (TMDF) essential oil respectively was achieved. The major components were identified to be *cis*-*β*-ocimene (38.0%), *trans*,*cis*-alloocimene (12.3%), spathulenol (12.1%) and *α*-cadinol (5.89%) for TMFS; *β*-caryophyllene (8.38%), *α*-caryophyllene (6.58%), elemol (9.31%), spathulenol (10.7%) and caryophyllene oxide (18.0%) for TMDS; *trans*-*β*-ocimene (7.39%), *trans*,*cis*-alloocimene (25.4%), *β*-caryophyllene (22.9%), caryophyllene oxide (15.81%), octadecanoic acid (5.88%) and tricosane (5.80%) for TMFL; *cis*-*β*-ocimene (6.73%), *trans*-tagetone (7.01%), terpin-4-ol (10.2%) and isopropyl tetradecanoate (17.0%) for TMDL; *cis*-*β*-ocimene (38.1%), valeric acid (30.9%), limonene (19.1%) and linalool (11.9%) for TMFF; *cis*-*β*-ocimene (6.53%), *trans*-*β*-ocimene (37.0%), *trans*,*cis*-alloocimene (12.3%) and m-tert-butylphenol (5.94%) for TMDF as displayed in Table 3.2.

3.3.2 Antioxidant Activity

The free radical scavenging ability of TMDS, TMDL and TMDF essential oil from *T. minuta* was determined from reduction absorbances of DPPH radical at 517 nm. The capacity of natural products to donate electrons can be measured by DPPH

Table 3.2 Essential oil composition of *Tagetes minuta*

Compound	RI	Formula	Composition (%)						Identification
			TMFS	TMDS	TMFL	TMDL	TMFF	TMDF	
Monoterpene hydrocarbons and their oxygenated derivatives									
α–Pinene	932	$C_{10}H_{16}$	–	1.41	–	–	–	0.11	GC-MS, GC
Camphene	953	$C_{10}H_{16}$	–	–	–	–	–	0.10	GC-MS, GC
Sabinene	976	$C_{10}H_{16}$	–	0.28	–	–	–	0.56	GC-MS, GC
β-Pinene	980	$C_{10}H_{16}$	–	3.38	–	–	–	3.08	GC-MS, GC
Myrcene	991	$C_{10}H_{16}$	–	–	–	–	–	0.16	GC-MS, GC
α-Phelladrene	1005	$C_{10}H_{16}$	–	–	–	–	–	0.20	GC-MS, GC
n-Octanal	1023	$C_8H_{16}O$	–	–	–	–	–	0.15	GC-MS, GC
p-Cymene	1026	$C_{10}H_{16}$	–	0.53	–	0.38	–	–	GC-MS, GC
Limonene	1031	$C_{10}H_{16}$	4.79	3.67	4.94	2.74	19.1	4.75	GC-MS, GC
cis-β–Ocimene	1040	$C_{10}H_{16}$	38.0	–	–	6.73	38.1	6.53	GC-MS, GC
trans-β–Ocimene	1043	$C_{10}H_{16}$	3.26	2.06	7.39	2.47	–	37.0	GC-MS, GC
α-Ocimene	1056	$C_{10}H_{16}$	–	–	–	–	–	0.72	GC-MS, GC
E,Z-Alloocimene	1128	$C_{10}H_{16}$	12.3	–	25.4	–	–	12.3	GC-MS, GC
Neo-Alloocimene	1129	$C_{10}H_{16}$	–	0.66	–	–	–	–	GC-MS, GC
Dihydrotagetone	1061	$C_{10}H_{18}O$	–	–	–	4.90	–	5.11	GC-MS, GC
Diethyl-carbitol	1081	$C_8H_{18}O_3$	–	–	–	2.58	–	–	GC-MS, GC
Methyl benzoate	1091	$C_8H_8O_2$	–	–	–	1.93	–	–	GC-MS, GC
Linalool	1100	$C_{10}H_{18}O$	–	–	–	–	11.9	–	GC-MS, GC
Nonanal	1107	$C_9H_{18}O$	–	–	–	1.45	–	–	GC-MS, GC
Filifolone	1108	$C_{10}H_{14}O$	–	–	–	–	–	0.10	GC-MS, GC
Thujone	1116	$C_{10}H_{16}O$	–	–	–	–	–	0.32	GC-MS, GC
Isophorone	1118	$C_9H_{14}O$	–	–	–	–	–	1.80	GC-MS, GC
Chrysathenone	1125	$C_{10}H_{16}O$	–	–	–	–	–	0.22	GC-MS, GC

(continued)

Table 3.2 (continued)

Compound	RI	Formula	Composition (%)						Identification
			TMFS	TMDS	TMFL	TMDL	TMFF	TMDF	
trans-Tagetone	1146	$C_{10}H_{16}O$	3.48	1.09	2.53	7.01	–	1.52	GC-MS, GC
Iso-Borneol	1155	$C_{10}H_{18}O$	–	0.57	–	–	–	–	GC-MS, GC
β-Phellandren-8-ol	1163	$C_{10}H_{16}O$	–	–	–	–	–	0.13	GC-MS, GC
Endo-Borneol	1165	$C_{10}H_{18}O$	–	–	–	–	–	0.10	GC-MS, GC
1-Nonanol	1171	$C_9H_{20}O$	–	–	–	0.27	–	–	GC-MS, GC
Terpin-4-ol	1177	$C_{10}H_{18}O$	–	0.70	–	10.2	–	0.11	GC-MS, GC
Octanoic acid	1179	$C_8H_{16}O_2$	–	–	–	2.82	–	–	GC-MS, GC
Dehydroelshotizia ketone	1180	$C_{10}H_{14}O_2$	–	–	–	–	–	0.12	GC-MS, GC
α-Terpinol	1189	$C_{10}H_{18}O$	–	2.11	–	0.44	–	3.10	GC-MS, GC
L-Camphor	1192	$C_{10}H_{16}O$	–	1.90	–	2.19	–	–	GC-MS, GC
Myrtenol	1194	$C_{10}H_{16}O$						2.10	GC-MS, GC
Decanal	1204	$C_{10}H_{20}O$	–	–	–	1.81	–	0.11	GC-MS, GC
Verbinone	1204	$C_{10}H_{14}O$	–	2.33	–		–	0.12	GC-MS, GC
m-tert-Butylphenol	1228	$C_{10}H_{14}O$	–	–	–	–	–	5.94	GC-MS, GC
Nerol	1228	$C_9H_{18}O$	–	–	–	1.20	–	–	GC-MS, GC
trans-Ocimenone	1235	$C_{10}H_{14}O$	–	–	–	–	–	3.11	GC-MS, GC
2-Phenoxyethanol	1245	$C_9H_{18}O_2$	–	–	–	0.37	–	–	GC-MS, GC
m-Thymol	1290	$C_{10}H_{14}O$	–	–	–	–	–	0.29	GC-MS, GC
Total%			**61.9**	**20.7**	**40.2**	**49.4**	**69.1**	**90**	
Sesquiterpenes hydrocarbons and their oxygenated derivatives									
Bicycloelemene	1337	$C_{15}H_{24}$	–	–	–	–	–	0.29	GC-MS, GC
β-Isocomene	1407	$C_{15}H_{24}$	–	–	–	–	–	0.10	GC-MS, GC
α-Gurjunene	1407	$C_{15}H_{24}$	–	2.77	–	2.10	–	0.17	GC-MS, GC
trans-Caryophyllene	1417	$C_{15}H_{24}$	5.46	–	–	–	–	–	GC-MS, GC

β-Caryophyllene	1418	$C_{15}H_{24}$	3.96	8.38	22.87	3.26	–	2.79	GC-MS, GC
γ-Elemene	1430	$C_{15}H_{24}$	4.20	–	–	0.60	–	–	GC-MS, GC
α-Guaiene	1439	$C_{15}H_{24}$	–	0.84	–	–	–	–	GC-MS, GC
α-Caryophyllene	1454	$C_{15}H_{24}$	3.10	6.58	–	2.28	–	1.39	GC-MS, GC
Germacrene-D	1480	$C_{15}H_{24}$	–	–	–	0.31	–	0.17	GC-MS, GC
α-Selinene	1493	$C_{15}H_{24}$	–	2.73	–	–	–	–	GC-MS, GC
Bicyclogemacrene	1494	$C_{15}H_{24}$	–	–	–	0.24	–	0.45	GC-MS, GC
Elixene	1514	$C_{15}H_{24}$	2.57	–	–	–	–	–	GC-MS, GC
Tridecanal	1511	$C_{13}H_{26}O$	–	–	–	1.56	–	–	GC-MS, GC
Elemol	1550	$C_{15}H_{26}O$	–	9.31	–	–	–	–	GC-MS, GC
trans-Nerolidol	1564	$C_{15}H_{26}O$	–	3.33	–	1.88	–	–	GC-MS, GC
Zierone	1574	$C_{15}H_{22}O$	–	1.01	–	–	–	–	GC-MS, GC
Spathulenol	1576	$C_{15}H_{24}O$	12.10	10.7	4.64	0.69	–	1.08	GC-MS, GC
Caryophyllene Oxide	1581	$C_{15}H_{24}O$	–	18.0	15.8	1.28	–	–	GC-MS, GC
Humelene epoxide II	1606	$C_{15}H_{24}O$	–	3.92	–	0.35	–	0.12	GC-MS, GC
Tetradecanal	1611	$C_{14}H_{28}O$	–	–	–	3.38	–	–	GC-MS, GC
Benzophenone	1621	$C_{13}H_{10}O$	–	–	–	0.67	–	–	GC-MS, GC
Alloaromadendrene epoxide	1639	$C_{15}H_{24}O$	–	1.21	–	–	–	–	GC-MS, GC
α–Cadinol	1647	$C_{15}H_{24}O$	5.89	–	–	–	–	–	GC-MS, GC
α–Eudesmol	1652	$C_{15}H_{26}O$	–	2.90	–	–	–	–	GC-MS, GC
Ledol	1665	$C_{15}H_{26}O$	–	1.00	–	3.66	–	–	GC-MS, GC
cis-α-Santalol	1678	$C_{15}H_{24}O$	–	1.07	–	–	–	–	GC-MS, GC
Benzyl benzoate	1762	$C_{14}H_{12}O_2$	–	–	–	2.14	–	–	GC-MS, GC
13-Hydroxy–valencene	1767	$C_{15}H_{24}O$	–	1.02	–	–	–	–	GC-MS, GC
Tetradecanoic acid	1780	$C_{14}H_{28}O_2$	–	–	–	2.25	–	–	GC-MS, GC
Isopropyl tetradecanoate	1824	$C_{17}H_{34}O_2$	–	–	–	17.02	–	–	GC-MS, GC
Methyl hexadecanoate	1926	$C_{17}H_{34}O_2$	–	–	–	0.44	–	–	GC-MS, GC

(continued)

Table 3.2 (continued)

Compound	RI	Formula	Composition (%)						Identification
			TMFS	TMDS	TMFL	TMDL	TMFF	TMDF	
Methyl stearate	2128	$C_{19}H_{38}O_2$	–	–	–	0.70	–	–	GC-MS, GC
Octadecanoic acid	2172	$C_{18}H_{36}O_2$	–	–	5.88	–	–	–	GC-MS, GC
1-Octadecanol	2082	$C_{18}H_{38}O$	–	–		4.03	–	–	GC-MS, GC
Total%			**37.3**	**74.8**	**49.2**	**48.9**	**–**	**6.56**	
Diterpene hydrocarbons									
Docosane	2200	$C_{22}H_{46}$	–	–	3.65	–	–	–	GC-MS, GC
Tricosane	2300	$C_{23}H_{48}$	–	–	5.80	–	–	–	GC-MS, GC
Total%			**–**	**–**	**9.45**	**–**	**–**	–	
Ester									
2-Acetylfuran	910	$C_6H_6O_2$	–	–	–	–	–	1.12	GC-MS, GC
(-)-Bornyl acetate	1284	$C_{12}H_{20}O_2$	–	1.56	–	–	–	–	GC-MS, GC
Total%			**–**	**1.56**	**–**	**–**	**–**	**1.12**	
Others									
Valeric acid	1084	$C_5H_{10}O_2$	–	–	–	–	30.9	–	GC-MS, GC
Octadecene	1800	$C_{18}H_{36}$	–	1.04	–	–	–	–	GC-MS, GC
Total%			**–**	**1.04**	**–**	**–**	**30.9**	–	
Overall Total%			**99.2**	**98.1**	**98.9**	**98.3**	**100**	**97.7**	

RI = Retention index of *T. minuta* composition, TMFS = *T. minuta* fresh stem, TMDS = *T. minuta* dry stem, TMFL = *T. minuta* fresh leaves, TMDL = *T. minuta* dry leaves, TMFF = *T. minuta* fresh flower and TMDF = *T. minuta* dry flower. GC: co-injection of known n-alkane standards (C_8-C_{24}) was used in order to calculate Kovat Index (KI) or Retention Index (RI) values using the equation:

$KI = 100 \times \left(n + (N - n)\left(\frac{tc - tn}{tN - tn}\right)\right)$

where KI = Kovat index for volatile compounds;
n = initial number of carbons of alkane standard;
N = next number of carbons of alkane standard;
t_c = retention time of unknown compound;
t_n = retention time of initial alkane; and
t_N = retention time of next alkane.

radical color change from purple to yellow DPPHH. In this assay, the color change was observed indicating reduction from purple DPPH to yellow DPPHH signifying that the tested essential oils have antioxidant activity. The TMDF essential oil (standard equivalent value = 18.7 ± 0.35 μg/mL AAE) has the highest radical scavenging ability as compared to the other essential oils in the descending order: TMDF > TMDL > TMDS as displayed in Table 3.3. Antioxidant activity of TMDF ($p < 0.001$) was recorded to be significantly better compared to the other essential oils.

The antioxidant activities of *T. minuta* essential oils (TMDS, TMDL and TMDF) were further established through their reducing power. In this assay, the reducing ability ($Fe^{3+} \rightarrow Fe^{2+}$) was established by the resulting noticeable intense blue colour indicating the formation of ferrous complex which further confirmed that *T. minuta* essential oils have antioxidant activity. The TMDF essential oil (standard equivalent value = 113.7 ± 1.2 μg/mL AAE) has highest reducing power and differs significantly ($p < 0.001$) in comparison with the other essential oils in the activity order: TMDF > TMDL > TMDS as shown in Table 3.3.

3.4 Discussion

In the present study, the essential oil content was higher in dry tissue parts than fresh tissue parts of the *T. minuta*. This could be due to the loss of water content during the drying process [19]. Essential oils from *T. minuta* were rich in terpenes, with monoterpene hydrocarbons more abundant than other secondary metabolites such as oxygenated sesquiterpenes, oxygenated monoterpenes, sesquiterpene hydrocarbons, diterpene hydrocarbons, esters and others. There is a chemical composition variation of essential oil from *T. minuta* amongst different parts namely stem, leaves and flowers as observed in Table 3.2. There is also a variation in chemical composition between fresh and dry parts essential oil. These variations may be due to a number of factors, namely type of soil, levels of nitrogen, amount of exposure to sunlight, age of a plant, climate changes, geographic origin/location, drying of plant prior to distillation of oils, plant parts distilled, hydrolysis and storage of oils prior to analysis [10, 20, 21]. The main constituents of essential oils isolated from *T. minuta* parts (stem, leaves and flowers) in the present study are in agreement with previous research. The previous study done in Pretoria, South Africa reported the main chemical components of *T. minuta* as *cis*-ocimene, *β*-ocimene, dihydrotagetone, piperitone and 3-methyl-2-(2-methyl-2-butenyl)-furan [22]. Another study in the United States reported the major components of leaves and flower essential oil extracts from *T. minuta* as *cis*-ocimene, dihydrotagetone, *trans*-tagetone, *cis*-tagetone and limonene [23]. The results in the present study are similar to the previous studies by Nchu et al. and Weaver et al. mentioned above although the composition and the number of major components slightly differ when compared to other provinces of South Africa and selected

Table 3.3 Antioxidant activity of essential oils from *Tagetes minuta*

	TMDS	TMDL	TMDF
DPPH (μg AAE/mL extract)	6.74 ± 0.27	14.4 ± 0.17*	18.7 ± 0.35*
FRAP (μg AAE/mL extract)	26.30 ± 0.41	63.56 ± 1.46	113.7 ± 1.2*

AAE = Ascorbic acid equivalent. Reported as mean ± standard error of mean (X ± SEM); $p^* < 0.001$ = statistically different

countries in the world and this may be due to the type of soil, climatic changes and geographical origin where the plant grows [22, 23].

The antioxidant activity may be due to the high percentage of oxygenated terpenes from the dry part essential oil as indicated in Table 3.2 [24]. The high percentage of the major components might also have significant input on *T. minuta* strong antioxidant activity. In general the antioxidant activity of essential oils depends on the phenolic compound content and the reaction of phenol compounds against chain-carrying peroxyl radicals [25]. Phenolic compounds are not fully responsible for antioxidant activity of plants but other constituents such as ascorbates, terpenes, carbohydrates, tocopherols, carotenoids, pigment and synergistic effect amongst others could possibly contribute to the total antioxidant activity [2]. The dry flower essential oil (TMDF) showed high antioxidant activity when evaluated by DPPH and FRAP biossays. The highest antioxidant activity on TMDF essential oil can be attributed to the presence of two phenolic compounds namely m-thymol and m-tert-butylphenol. Hence, TMDF essential oil may act as electron donor to react with free radicals to form suitable product and stop the free radical chain reaction [26]. Previously, Christine et al. reported that *T. minuta* exhibits strong antioxidant properties when measured by DPPH which is in agreement with this current study [14]. Another study showed that *T. minuta* essential oil possesses radical oxygen species (ROS), radical nitrogen species (RNS) and peroxide (H_2O_2) scavenging properties [15]. Shiraz et al. also reported that *T. minuta* essential oil showed ability to scavenge ROS and RNS [16]. In the current investigation, the essential oils (TMDS, TMDL and TMDF) from *Tagetes minuta* showed antioxidant properties with varying activity depending on the part of the plant as shown in Table 3.3.

However, the TMDF essential oil (standard equivalent value = 113.7 ± 1.2 μg/mL AAE) has highest reducing power and differs significantly ($p < 0.001$) in comparison with the other essential oils in the activity order: TMDF > TMDL > TMDS for both DPPH and FRAP assays as revealed in Table 3.3. Therefore, this plant could be a potential source of natural antioxidants which are more preferable as compared to the synthetic antioxidants.

3.5 Conclusion

The chemical composition of essential oils from *T. minuta* in the present study was different from previous studies in some of the major components. The use of DPPH and FRAP provide an easy and rapid way to determine antioxidant activity. *Tagetes minuta* essential oils (TMDS, TMDL and TMDF) showed strong antioxidant activity when evaluated by DPPH and FRAP assays which is in agreement with some of the previous reports. This can be attributed to the presence of oxygenated monoterpenes and sesquiterpenes which may act as free radical scavenging and reducing agents. *T. minuta* essential oil also showed the ability to reduce DPPH by donating hydrogen ions which are considered as antioxidant having free radical scavenging activity. Therefore, this study suggests that *T. minuta* could be used as a potential natural antioxidant source to treat various oxidative stress related diseases such as hypertension.

Acknowledgements The authors would like to thank DST/NRF—Sasol Inzalo Foundation scholarship, Govan Mbeki Research Centre (GMRDC), University of Fort Hare and Research Directorate Walter Sisulu University for financial support.

References

1. Imelouane B, El Bachiri A, Ankit M, Khedid K, Wathelet JP, Amhamdi H (2010) Essential oil composition and antimicrobial activity of Artemisia herba-alba Asso grown in Morocco. Banat's J Biotechnol 1:48–55
2. Fernandes de Oliveira A, Sousa Pinheiro L, Souto Pereira C, Neves Matias W, Albuquerque Gomes R, Souza Chaves O et al (2012) Total phenolic content and antioxidant activity of some Malvaceae family species. Antioxidants 1:33–43
3. Beg M, Sharma V, Akhtar N, Gupta A, Mohd J (2011) Role of antioxidants in hypertension. J Indian Acad Clin Med 12:122–127
4. Rodrigo R, González J, Paoletto F (2011) The role of oxidative stress in the pathophysiology of hypertension. Hypertens Res 34(4):431–440
5. Ceriello A (2008) Possible role of oxidative stress in the pathogenesis of hypertension. Diabetes Care 31(Supplement 2):181–184
6. Senatore F, Napolitano F, Mohamed MAH, Harris PJC, Mnkeni PNS, Henderson J (2004) Antibacterial activity of *Tagetes minuta* L. (Asteraceae) essential oil with different chemical composition. Flavour Frag J 19:574–578
7. Tahir L, Khan N (2012) Antibacterial potential of crude leaf, fruit and flower extracts of *Tagetes Minuta* L. J Public Health Biol Sci 1:74–78
8. Dold AP, Cocks ML (1999) A preliminary list of Xhosa plant names from the Eastern Cape, South Africa. Bothalia 29:267–292
9. Wang C, Chen C (2006) *Tagetes minuta* L (Asteraceae), a newly naturalized plant in Taiwan. Taiwania 51:32–35
10. Tankeu SY, Vermaak I, Viljoen AM, Sandasi M, Kamatou GPP (2013) Essential oil variation of *Tagetes minuta* in South Africa—A chemometric approach. Biochem Syst Ecol 51:320–327
11. Sadia S, Khalid S, Qureshi R, Bajwa AA (2013) *Tagetes minuta* L., a useful underutilized plant of family Asteraceae: a review. Pak J Weed Sci Res 19:179–189

12. Tankeu SY, Vermaak I, Viljoen AM, Sandasi M, Kamatou GPP (2010) Essential oil variation of *Tagetes minuta* in South Africa—A chemometric approach. Biochem Syst Ecol 51:320–327
13. Nchu F, Magano SR, Eloff JN (2003) In vitro anti-tick properties of the essential oil of *Tagetes minuta* L. (Asteraceae) on Hyalomma Rufipes (Acari : Ixodidae). AOSIS Open J:1–5
14. Christine K, Omolo IN, Kabasa JD, Nagawa CB, Wasswa J, Kikawa CR (2015) Evaluation of anti-oxidant properties in essential oil and solvent extracts from *Tagetes minuta*. Afr J Pure Appl Chem 9:98–104
15. Karimian P, Kavoosi G, Amirghofran Z (2014) Anti-oxidative and anti-inflammatory effects of *Tagetes minuta* essential oil in activated macrophages. Asian Pac J Trop Biomed 4:219–227
16. Shirazi MT, Gholami H, Kavoosi G, Rowshan V, Tafsiry A (2014) Chemical composition, antioxidant, antimicrobial and cytotoxic activities of *Tagetes minuta* and *Ocimum basilicum* essential oils. Food Sci Nutr 2:146–155
17. Anonymous (1980) British pharmacopoeia, vol 2. University Press, Cambridge, p 576
18. Moniruzzaman M, Khalil MI, Sulaiman SA, Gan SH (2012) Advances in the analytical methods for determining the antioxidant properties of honey: a review. Afr J Tradit Complem 9:36–42
19. Charles DJ, Simon JE (1990) Comparison of extraction methods for the rapid determination of essential oil content and composition of basil. J Am Hort Sci 115:458–462
20. Babu KGD, Kaul VK (2005) Variation in essential oil composition of rose-scented geranium (Pelargonium sp) distilled by different distillation techniques. Flavour Frag J 20:222–231
21. Saeb K, Gholamrezaee S (2012) Variation of essential oil composition of *Melissa officinalis* L. leaves during different stages of plant growth. Asian Pac J Trop Biomed 2:S547–S549
22. Nchu F, Magano SR, Eloff JN (2012) *In vitro* anti-tick properties of the essential oil of *Tagetes minuta* L. (Asteraceae) on Hyalomma rufipes (Acari: Ixodidae). Onderstepoort J Vet Res 79:1–5
23. Weaver DK, Wells CD, Dunkel V, Bertsch W, Sing SE, Sriharan S (1994) Insecticidal activity of floral, foliar, and root extracts of *Tagetes minuta* (Asterales: Asteraceae) against adult Mexican bean weevils (Coleoptera: Bruchidae). Entomol Soc Am 87(6):1718–1725
24. Saeed N, Khan MR, Shabbir M (2012) Antioxidant activity, total phenolic and total flavonoid contents of whole plant extracts of *Torilis leptophylla* L. BMC Complement Altern Med 12:221
25. Ćavar S, Maksimović M, Vidic D, Parić A (2012) Chemical composition and antioxidant and antimicrobial activity of essential oil of *Artemisia annua* L. from Bosnia. Ind Crops Prod 37:479–485
26. Petricevich VL, Figueroa LA, Navarro LB, Vera MP (2014) Antioxidant activity, total phenolic and flavonoid contents, and cytotoxicity evaluation of *Bougainvillea xbuttiana*. Int J Phar Pharm Sci 6:497–502

Chapter 4
Therapeutics in Neurodegenerative Disorders: Emerging Compounds of Interest

G. Nagesh Babu and Manjeet Gupta

Abstract Neurodegenerative diseases are a heterogeneous group of disorders. They are characterized by progressive degeneration of the structure and function of the central nervous system or peripheral nervous system. Neurodegenerative diseases include Parkinson's Disease (PD), Alzheimer's Disease (AD), Amyotrophic Lateral Sclerosis (ALS) and Huntington's Disease (HD). Key characteristic feature of neurodegenerative diseases is aggregation of misfolded proteins in the cytoplasm and nucleus of central nervous system (CNS) neurons. In this review we discuss about the emerging therapeutic compounds and targets for treating these devastating neurological disorders. Oxidative stress appears to be a common denominator and transcription factors are also involved. Compounds that can scavenge free radicals showed some potential. Some protein and peptide compounds also exhibited good therapeutic activity. Ligand binding domains are targeted for efficacy and showed promise. Agonists and antagonists of receptors and enzyme inhibitors are playing a remarkable role in controlling the symptoms of these diseases. Chemical chaperones and compounds that can inhibit the protein aggregation are widely tried and showing therapeutic potential.

Keywords Neurodegenerative diseases • Parkinson's disease • Alzheimer's disease • Amyotrophic lateral sclerosis • Huntington's disease • Levodopa • Alpha-Synuclein • Reactive oxygen species • Receptor agonists and antagonists • Acetylcholinesterase • Antisense oligonucleotide • Therapeutic targets • Drugs • Glutamate

G. Nagesh Babu (✉) • M. Gupta
Department of Neurology, Sanjay Gandhi Post Graduate Institute of Medical Sciences, Lucknow 226014, India
e-mail: gnageshbabu@yahoo.com

P. Ramasami et al. (eds.), *Emerging Trends in Chemical Sciences*,
DOI 10.1007/978-3-319-60408-4_4

4.1 Introduction

4.1.1 Parkinson's Disease

Parkinson's Disease (PD) is a neurodegenerative disease that affects millions of people worldwide. Common symptoms are tremor, bradykinesia, rigidity and postural instability. These are due to the progressive loss of dopaminergic neurons in substantia nigra pars compacta (SNpc) [1, 2]. Neurodegeneration in PD is accompanied by the accumulation of Lewy bodies, which are abnormal aggregates of protein that develop inside nerve cells. Alpha-synuclein (α-syn) is the main component of Lewy bodies and it plays a major role in PD pathogenesis [3]. Homeostasis of intracellular protein is maintained by chaperone, ubiquitin proteasome, and autophagy system. But this homeostasis is found altered in this disease. Accumulation of α-syn reciprocally inhibits the protein control system [4]. Loss of SNpc dopaminergic neurons results in dopamine depletion and it leads to an impaired nigro-striatal system, thereby improper movement. PD till today is an incurable disease. The precursor of dopamine, Levodopa is given to the patients. Environmental toxins and aging are also risk factors for the onset of PD [5]. Oxidative stress also leads to the PD pathogenesis. Reactive oxygen species (ROS) generating enzymes, tyrosine hydroxylase and monoamine oxidase, are present in dopaminergic neurons [6]. Dopamine metabolism, inflammation, and mitochondrial dysfunction are the major sources of ROS in SNpc [7]. Neurotoxicity of glutamate is well known. It increases ROS and decreases the mitochondrial permeability and antioxidant glutathione [8]. But the same deleterious action is prevented by the treatment of acetyl-*l*-carnitine and –dl-α-lipoic in rat brain by altering mitochondrial function [9].

4.1.2 Alzheimer's Disease

In brain, Alzheimer's disease (AD) features as intracellular neurofibrillary protein aggregates called as neurofibrillary tangles (NFT), an accumulated form of hyperphosphorylated tau protein, amyloid-β (Aβ) and extracellular aggregates. Aβ peptide causes lipid destabilization and aggregation of Aβ into Ca^{2+} channels. It forms synapse-suppressing oligomeric complexes. Another AD pathogenesis is the abnormal proteolytic processing by β and γ secretase of amyloid precursor protein (APP) that increases the self-aggregating form of Aβ. Mutations in APP, PS1 and PS2, and in secretase enzymes involved in APP processing cause insoluble amyloid-β peptide (Aβ) aggregation resulting in massive accumulation of fibrillary protein. Amyloid peptides can also destroy the cell membrane integrity, disturb the influx of extracellular Ca^{2+} and interrupt the homeostasis. Aggregation of β-amyloid peptides compromises the acetylcholine (Ach) neurotransmission, and consequences are the AD neurological signs [10, 11].

4.1.3 Amyotrophic Lateral Sclerosis

Amyotrophic lateral sclerosis (ALS) is a neurodegenerative disease characterized by the death of motor neurons and skeletal muscle atrophy. Characteristic features of ALS are muscles stiffness, muscle twitching and weakness due to muscles decreasing in size. Prominent symptoms are difficulty in speaking, swallowing, and breathing. Familial ALS (FALS) is characterized by mutations in genes including superoxide dismutase 1 (SOD1), transactive response DNA-binding protein 43 kDa (TARDBP, TDP-43), fused in sarcoma (FUS) and chromosome 9 open reading frame 72 (C9ORF72). Levels of pro-inflammatory molecules like tumor necrosis factor-alpha (TNF-α), interferon-γ (IFN-γ) and nitric oxide (NO) were found increased in the patients of ALS [12]. Increase in lipid peroxidation was observed with decrease in catalase, glutathione reductase and glucose-6-phosphate dehydrogenase enzyme activities in the erythrocytes of ALS patients. These studies confirm the involvement of oxidative stress in the progression of ALS [13]. The ^{1}H NMR study of ALS serum revealed abnormal metabolite patterns in ALS patients and the observations could be used to monitor ALS disease progression [14].

4.1.4 Huntington's Disease

Huntington's disease (HD) is a neurodegenerative disorder caused by expansion in autosomal dominant huntingtin (HTT) gene, in short arm of chromosome 4 (4p63), protein encoded by CAG repeats. In normal population CAG repeat is polymorphic and varies from 10 to 35 repeats but in the expanded form it has about 36 to 120 repeats, which transcribe in the first exon of the HTT gene, an expanded polyglutamine (polyQ) at the N-terminus of HTT. It is also reported that higher the CAG expansion, the earlier the onset of HD symptoms. HTT is a protein composed of approximately 3100 amino acids with a molecular mass of 349 kDa and involved in many functions like protein trafficking, vesicle transport and anchoring to the cytoskeleton, clathrin-mediated endocytosis, postsynaptic signaling, transcriptional regulation, and anti-apoptotic function. Expansion in polyglutamine (polyQ) is a marker for mutant HTT (mHTT). The pathological hallmark of HD is the gradual atrophy of the striatum. Mutant huntingtin causes neuronal dysfunction and degeneration of striatal medium spiny neurons (MSNs) and cortical neurons resulting in the cardinal disease features of movement, cognitive, and psychiatric symptoms.

Two mechanisms have been suggested for the formation of aggregates of mutant huntingtin. HTT proteins are destabilized due to the expanded polyQ. First is polar zipper model which suggests about the formation of insoluble β-pleated sheets between the polyQ-bearing proteins and second is the transglutaminase model. Transglutaminases are cross-linking enzymes of glutamine residues and they are also involved in polyQ aggregation. HTT mutation and CAG repeat expansion are

not checked by DNA repair system. It is found that DNA methylation leads to the down regulation of DNA repair genes involved in mismatch/loop-out repair [15]. HTT promotes vesicular transport of brain-derived neurotrophic factor (BDNF) with microtubules. Huntingtin-associated protein-1 (HAP1) and the p150 glued subunit of dynactin are essential components of molecular motors [16].

4.2 Therapeutic Compounds in PD

4.2.1 Transcription Factors

As the oxidative stress is directly proportional to mitochondrial malfunction, it plays a major role in apoptosis, necrosis and neurodegeneration. Nrf2 is a transcription factor that regulates the expression of many antioxidant proteins. On depletion of GSNOR, Nrf2 upregulates its expression and protects against PD toxins-induced cell death [17]. The overexpression of Nrf2 has become a potential therapeutic avenue for various neurodegenerative disorders such as PD [18].

In an animal model of PD, Nurr1 agonists are used to enhance its function. Nurr1 is a transcription factor essential for maturation of dopaminergic neurons. Two drugs, Amodiaquine and Chloroquine are found to interact with ligand binding domain of Nurr1 and stimulate transcriptional activation of mid brain dopamine specific gene. It also suggests that Nurr1 could be a potential drug target [19].

4.2.2 Lipid Carriers for Levodopa Co-Drugs

Tristearin and Tricaprylin are used to constitute nanostructured lipid carriers (NLC) to encapsulate and for better delivery of lipophilic levodopa (LD) with co-drugs, named PDA (3,4-diacetyloxy-LD-caffeic acid co-drug), PDB (lipoic acid-dopamine co-drug), PDC (lipoic acid-3,4-diacetoxy-dopamine co-drug), and PDD (dimeric LD co-drug containing an alkyl linker), with therapeutic potential in Parkinson's disease [20].

4.2.3 Levodopa Adjuncts

Safinamide was found to be a safe and effective first adjunct therapy in Levodopa-treated patients and improved cardinal symptoms of PD while providing benefits to mild and non-mild fluctuators and patients receiving other concomitant dopaminergic therapies [21]. Treatment of Opicapone as adjunct to Levodopa helps in

significant reduction in mean daily off-time in Levodopa-treated patients with PD [22].

Oral medication may lose its effectiveness due to several reasons, like dysphagia, impaired absorption from the gastro-intestinal tract and delayed emptying of the stomach. Levodopa-Carbidopa intestinal gel is an effective treatment developed for patients with advanced PD. It provides a stable Levodopa plasma concentration compared with oral administration because of continuous infusion into the duodenum/jejunum by a portable pump [23].

4.2.4 Receptor Targets

Treatment with Rotigotine causes overexpression of dopamine transporter (DAT). DAT upregulation by rotigotine in an opposite direction with respect to early PD compensatory mechanisms might reduce the risk of dyskinesia, but it could imply less motor benefit because of less stimulation by the dopamine itself on dopaminergic receptors [24].

Mavoglurant is a subtype-selective, non-competitive antagonist at the metabotropic glutamate receptor-5 binding site. The efficacy of Mavoglurant in Levodopa-induced dyskinesia patients was assessed and failed to meet the primary objective of demonstrating improvement of dyskinesia [25].

Preladenant combined with Eltoprazine was found to counteract dyskinesia and maintain full therapeutic effects of a low dose of Levodopa in animal model [26]. Eltoprazine has been found to have beneficial antidyskinetic effects without altering normal motor responses to Levodopa. Eltoprazine inhibits the sensitization of striatonigral medium-sized Gamma-aminobutyric acid (GABA) spiny neurons to Levodopa and their over-activation associated with dyskinesias appearance [27, 28].

Enantiopure indolo[2,3-a]quinolizidine is synthesized from enantiopure tryptophanol. This compound was evaluated as NMDA receptor antagonist and found to be 2.9-fold more potent as NMDA receptor blocker amantadine [29].

Caffeine consumption was found associated with a reduced accrual of motor and non-motor disability in de novo PD, showing the rationale for using as adenosine A2A antagonists. C8 substitution on the caffeine core identified 8-(2-phenylethyl)-1,3,7-trimethylxanthine as a non-selective adenosine receptor antagonist. Various C8 two-chain-length linkers are applied to enhance adenosine receptor affinity. Benzyloxy linker displayed the highest affinity for the A1 adenosine receptor and the *para*-chloro-substituted phenoxymethyl linker showed the best A2A adenosine receptor affinity [30, 31].

Derivatives of 2-aminopyrimidine were synthesized. 4-(5-Methylfuran-2-yl)-6-[3-(piperidine-1-carbonyl) phenyl] pyrimidin-2-amine was found to have high affinity for antagonists of adenosine A1 and A2A receptors. In a molecular docking study, it was also revealed that the interactions between the synthesized compounds and the adenosine A2A binding site most likely involve Phenylalanine 168 and

Asparagine 253, interactions which are similar for structurally related adenosine A2A receptor antagonists [32]. Sulfanylphthalimide analogues were found to possess high binding affinity to adenosine A1 receptors as antagonists. These compounds are also reported to inhibit monoamine oxidase (MAO) B. Such dual-target-directed compounds are expected to be advantageous over single-target treatments of PD [33].

4.2.5 Supplements

Creatine and coenzyme Q10 combination therapy delays the decline of cognitive function in PD-mild cognitive impairment (MCI) patients and could lower their plasma phospholipid levels; therefore, this combination therapy may have a neuroprotective function [34]. It is reported that ubiquinol-10 (reduced form of Coenzyme Q10) may significantly improve PD with wearing off [35].

4.2.6 PEG Polymer

Fibrillation of α-syn plays an important role in PD. A hyperbranched PEG polymer containing dopamine is developed by RAFT polymerization and one-spot reaction. This can be used for anti-fibrillation activity as dopamine is an inhibitor of α-syn fibril formation. However, it may also alter biological activity [36].

4.2.7 Metabolites

^{1}H magnetic resonance spectroscopy has shown that the concentration of certain metabolites like 2-hydroxybutyrate, glutamine, and dimethyl sulphone are altered in sporadic and Leucine-rich repeat kinase 2 (LRRK2) Parkinson's disease. These three metabolites are involved in neurodegeneration. Glutamine removes excess nitrogen in brain; 2-hydroxybutyrate is a component in glutathione metabolism and dimethyl sulphone is an anti-inflammatory agent [37]. These metabolites could be used as therapeutic targets. We performed one dimensional ^{1}H NMR study in PD patients and observed that the peaks of glutamate are increased in the patients of multiple system atrophy (MSA), a disease control of PD (unpublished observations).

4.2.8 Protein Targets

α-Syn is a major constituent of Lewy bodies, protein clumps that are the pathological hallmark of PD. Immunization with monoclonal antibodies targeting the C-terminus truncation site of α-syn has therapeutic potential (in mouse model), not only as α-syn reducing agents, but also as inhibitors of its pathological propagation [38].

PD protein 7 (DJ-1) is a multifunctional protein, involved in transcriptional regulation, anti-oxidative stress reaction, chaperone, protease, and mitochondrial regulation [39]. Mutation in DJ-1 gene leads to early onset of PD, which is an autosomal recessive familial disorder. Chaperone activities of PARK 7 inhibit aggregation of α-syn and anti-oxidative action reduces neurodegeneration. A peptide ND-13 is created, which is a 13 amino acid fragment from DJ-1 protein and 7 amino acid fragment from protein transduction domain of Trans-Activator of Transcription (TAT), also known as cell penetrating peptide. By enhancing the Nrf2 activity, ND-13 is able to protect the cells against oxidative stress, neurotoxic compounds and promote cell survival [40]. Therapeutic effect of ND-13 is also evaluated against MSA and yielded positive results [41]. Another compound getting attention is compound 23. This is from Zinc compound library, identified as N-[4-(8-methyl(4-hydroimidazo[1,2-a]pyridin-2-yl))phenyl](3,4,5-trimethoxyphenyl) carboxamide, and is a DJ-1-binding compound. It has DJ-1 dependent activity, protects neuronal cell death, and supports anti-oxidative redox reaction [42]. Involvement of DJ-1 in the regulation of dopamine level is also observed. It interferes with the dopamine transporter (DAT) activity. It is shown by the co-expression of DAT and DJ-1 gene in HEK-293T cells [43].

Glia Maturation Factor (GMF) has a role in the induction of pro-inflammatory cytokines and granulocyte-macrophages in the CNS. This role of GMF is also involved in PD pathogenesis. It was shown that the decreased expression of GMF leads to decreased production of ROS and down regulation of nuclear factor-κβ (NF-κβ) mediated production of TNF-α and Interleukin 1 beta (IL1β). But the overexpression of GMF induces dopaminergic neurodegeneration, which makes GMF a target for PD therapeutics [44].

4.2.9 Other Potential Targets

Inosine, a nucleoside, increased plasma antioxidant capacity in PD [45]. Rasagiline, a mono amino oxidase-B inhibitor, showed improvement in motor symptoms of PD [46]. Zonisamide, a sulfonamide anticonvulsant, improved wearing-off in PD [47]. Dalframpidine is an organic compound with the chemical formula $C_5H_4N–NH_2$. This molecule is one of the three isomeric amines of pyridine. Dalframpidine completed phase 2 clinical trials for PD (US government data on clinical trials).

4.3 Therapeutic Compounds in AD

4.3.1 Anxiolytics

Clomethiazole (CMZ) is an anxiolytic and anticonvulsant with sedative and hypnotic effects; it allosterically increases the GABA receptor conductance and found to be neuroprotective. At the same time it potentiates the function of the inhibitory neurotransmitter GABA in the brain and therefore attenuates glutamate-induced excitotoxic cascade leading to mitochondrial damage and neuronal loss. CMZ is re-engineered to 4-methyl-5-(2-(nitrooxy) ethyl) thiazol-3-ium chloride (NMZ)**.** It can activate NO/cGMP/CREB signaling and also retains the activity of CMZ. The cAMP-response element binding protein (CREB) is required for the memory emergence and effective synapses. Phosphorylation and nitric oxide (NO) induced release of cyclic guanosine 3, 5-monophosphate (cGMP) is important for CREB [10].

4.3.2 Alginate-Derived Oligosaccharide

Well known AD pathogenesis is due to neuroinflammation and Aβ aggregation. Alginate-derived oligosaccharide (AdO) is found to be tackling both the conditions. It inhibits the microglia-mediated neuroinflammation and enhances the microglial phagocytosis of Aβ. The expression of nitric oxide synthase (iNOS) and cyclooxygenase (COX-2) produces NO and Prostaglandin E2 (PGE2) and these are involved in lipopolysaccharide (LPS) mediated neuroinflammation. It is found that AdO suppresses transcriptional activation of iNOS and COX-2 in BV2 microglial cells. Toll like receptor 4 (TLR4) is involved in NF-κB signaling pathway and plays a role in the neuroinflammatory responses. AdO treatment attenuates the nuclear translocation of the NF-κB p65 subunit. Aβ aggregates should be cleared and degraded by the microglia and macrophages, otherwise, impaired phagocytosis of Aβ is observed. The AdO-induced uptake of Aβ may be directly or indirectly involved in TLR4 actions [48].

4.3.3 Tricyclic Pyrones

In vivo treatment of animal models of AD by CP2, a member compound of tricyclic pyrone, resumes axonal trafficking and overcomes cognitive and motor deficit. CP2 enhances the mitochondrial function and restores the mitochondrial trafficking which protects against AD cognitive dysfunction [49].

4.3.4 Molecular Chaperones and Receptor Targets

Sigma-1 receptor (S1R), a molecular chaperone and M1 muscarinic receptor (M1R) are also major therapeutic targets in AD. M1R is a subclass of G-protein-coupled receptors (GPCRs). Muscarinic receptors (mAChR) are common in cortex, hippocampus and striatum and play a role in cognitive processing. Agonists of M1R and S1R are developed. AF102B, AF267B and AF710B (bicyclic heterocyclic spiro compounds) are able to enhance the reduction of Tau-hyperphosphorylation, and Glycogen synthase kinase-3β (GSK-3β) activation. It reduces apoptosis and mitochondrial dysfunction by enhancing Bcl2/Bax [50].

H3 receptor is a G-protein coupled receptor. It is a presynaptic autoreceptor on histamine-containing neurons. H3 receptor regulates the release of histamine and several key neurotransmitters. Antagonists of H3 receptor cause increase in neurotransmitter levels in brain and may be beneficial for neurodegenerative diseases. A series of H3 receptor antagonists were designed by the incorporation of 1-phenyl-3-hydroxy-4-pyridinone and 3-hydroxy-4-pyridinone moiety (metal chelating). 5c is the most promising compound of these derivatives. 5c has shown good scavenging effect, copper and iron chelating properties and inhibits against self- and Cu^{2+}-induced Aβ1−42 aggregation. 5c also showed blood brain barrier penetration behavior in vivo [51].

4.3.5 Immunosuppressive Drugs

For amyloid-β plaque clearance, immunosuppressive drugs were used but were not successful. Pharmacological inhibition or depletion of Foxp3+ regulatory T cells (Tregs) helps in the clearance of amyloid-β plaque [52].

4.3.6 Tau-Centric Targets and Drugs

The failure of several Phase II/III clinical trials in Alzheimer's disease (AD) with drugs targeting β-amyloid accumulation in the brain drove attention to alternative treatments against tau pathology, including approaches targeting tau phosphatases / kinases, active and passive immunization, and anti-tau aggregation. The most advanced tau aggregation inhibitor (TAI) is methylthioninium (MT), a drug existing in equilibrium between a reduced (leuco-methylthioninium) and oxidized form (MT (+)). MT chloride (methylene blue) was investigated in a 24-week Phase II clinical trial in 321 patients with mild to moderate AD that failed to show significant positive effects in mild AD patients, although long-term observations (50 weeks) and biomarker studies suggested possible benefit [53].

4.3.7 Acetylcholinesterase and Other Compounds

Acetylcholinesterase (AChE) and butyrylcholinesterase (BChE) are the enzymes that hydrolyze acetylcholine and make cholinergic neurons to return to the resting state following activation. The *N*-methyl-D-aspartate (NMDA) receptor is a glutamate receptor that controls synaptic plasticity and memory function. Hence, AChE, BChE and NMDA receptors are targeted in AD patients. For AD treatment cholinesterase's inhibitors like Donepezil, Rivastigmine, Galantamine and Memantine are used; low-affinity antagonist is used for NMDA receptor [54].

4.3.8 Combination Drug Targets

Currently a combination of glutamatergic and cholinergic drugs are considered for the treatment of AD. The γ-carboline fragment of Dimebon (Latreperdine) and Phenothiazine core of Methylene Blue (MB) are conjugated to a single drug. These conjugates selectively inhibit BChE and block NMDA receptors. ACh interacts with amyloid peptide and disturbs its oligomerisation, thereby modulates cholinergic transmission. ACh could also be used in AD therapeutics [55].

AChE promotes the assembly of Aβ fibrils. NMDA receptor antagonist, Memantine, and three acetylcholinesterase inhibitors (AChEIs): Galantamine, Rivastigmine and Donepezil are the currently approved drugs for AD. AChEIs act on peripheral anionic site of AChE. In the same sequence, new multitarget-directed-ligands (MTDLs), benzochromenopyrimidinimines are developed for AD therapy. Benzochromenopyrimidinimine inhibits the AChE, Aβ1-42 aggregation, and is a strong antioxidant [56].

Triazolopyrimidine-quinoline and cyanopyridine-quinoline hybrids are also synthesized which can inhibit the AChE-induced Aβ aggregation [57].

4.3.9 Peptide Therapeutics

VDAC1-N-Ter peptide is a voltage-dependent anion channel 1 (VDAC1), which mediates the transport of many metabolites across the mitochondrial outer membrane. Overexpression of VDAC1 is observed in AD patients. Interaction of Aβ with VDAC1 increases its conductance about twofold and results in mitochondria-mediated cell death. But the VDAC1 N-terminal peptide (VDAC1-N-Ter) checks the Aβ interaction and mitochondria-mediated apoptosis. Thus the VDAC1-N-Ter peptide could be a therapeutic target for AD [58].

Deficiency of insulin and glucagon-like peptide-1 (GLP-1) signaling raises the risk of AD. Treatment with or an analog of GLP-1 prevents declination of glucose metabolism (CMRglc). It signifies the metabolic role of glucose in cognitive impairment and synaptic dysfunction [59].

4.3.10 Targetting RNA and MicroRNA

β-oligomers enhance endocytosis that reduces NMDA receptors (NMDAR) and long-term potentiation (LTP). At the same time it activates the metabotropic glutamate receptors (mGluRs), which induce long-term depression (LTD). Apolipoprotein E (ApoE) receptor, ApoER2 opposes the suppression of LTP and induction of LTD and strengthens the synapse. Alteration was found in ApoER2 exon 19 splicing in AD patients. ApoER2 splicing treated with single dose of antisense oligonucleotide (ASO) improves the synaptic function, learning and memory. These are the splicing therapeutics for AD [60].

Expression of MicroRNA (miR-29) is found to be decreased in AD patients and increased level of human β-secretase (hBACE1). So to prevent Amyloid-β (Aβ) peptide it is intended to employ miR-29 so as to suppress the hBACE1 expression. Highly pure and biologically active pre-miRNAs are purified by arginine-affinity chromatography and encapsulated in polyplexes for better delivery in cytoplasm [61].

4.4 Therapeutic Compounds in ALS

4.4.1 Riluzole

Currently Riluzole is the only FDA approved drug for ALS. It is a TTX-sensitive sodium channel blocker and also has anti-glutamatergic activity.

4.4.2 Dopamine D2 Receptor Agonists

Bromocriptine methylate (BRC) is a dopamine D2 receptor agonist, which protects against oxidative stress-induced cell death by upregulating neuronal apoptosis inhibitory proteins (NAIP) in a clinical trial [62].

4.4.3 Potassium Channel Blockers

4-Aminopyridine (4AP) is a potassium channel blocker. 4AP induced activity rescues hypoexcitable motor neurons from ALS patient-derived induced pluripotent stem cells by restoring ion-channel imbalances, decreasing endoplasmic reticulum (ER) stress and caspase activation [63].

4.4.4 Chemical Chaperone

Lead compound 14 (3-((5-((4,6-dimethylpyridin-2-yl)methoxy)-5-oxopentanoyl) oxy)-*N*,*N*-dimethylpropan-1-amine oxide) improved neurological functions in ALS mouse model. Compound 14 is a lipophilic derivative of TMAO and acts as a chemical chaperone. It decreases the misfolded aggregation [64].

4.4.5 H1 Receptor Antagonists

Clemastine is a well known H1 receptor antagonist. Histamine plays a major role in the pathogenesis of neuroinflammatory and neurodegenerative diseases. Microglial cells are sensitive to histamine. Administration of Clemastine in ALS mouse model reduces microgliosis and enhances motor neuron survival [65].

4.4.6 Bile Acids

Tauroursodeoxycholic acid (TUDCA) is a hydrophilic bile acid, produced by humans in the liver, by combination of taurine to ursodeoxycholic acid (UDCA). It has shown anti-apoptotic, immunomodulatory and antioxidant effects in ALS patients [66].

4.4.7 NOX Inhibitors

Thioridazine is found to improve motor performance in ALS mouse model. This compound inhibits NADPH oxidases (NOX) and reduces the oxidative stress [67].

4.4.8 New Drug Entities

Kenpaullone and Anacardic acid are newly discovered drugs for ALS but different ALS models showed different responses to these compounds [68].

4.4.9 Targetting Microtubules

Stathmin is a 17 kDa protein, which regulates microtubule dynamics. In ALS models, it is found that Stathmin triggers microtubule destabilization and causes Golgi fragmentation [69].

4.4.10 Natural Compounds

Ginsenosides (G-Re) are found to suppress the expression of pro-inflammatory proteins such as CD14 and TNF-α and inhibit TLR4 signaling pathway in ALS mouse model. G-Re are major bioactive components of Ginseng, 20(S)-protopanaxatriol, Re, Rg1, Rg2, and Rb3 [70]. Neuroinflammation and apoptosis are key players in the progressive damage of the neurons in AD and ALS.

4.4.11 AMPA Receptor Antagonists

Perampanel is a non-competitive antagonist of α-amino-3-hydroxy-5-methyl-4-isoxazole propionic acid (AMPA) receptor. Perampanel rescues neurons in ALS mouse model by maintaining Ca^{2+} influx through the abnormal AMPA receptors [71].

4.5 Therapeutic Compounds in HD

4.5.1 Natural Products

Xyloketal B, a natural product from mangrove fungus, has also shown protective effect against neurodegenerative diseases. Xyloketal B has unique bicyclic acetal moieties fused to its aromatic core structure and has the ability to hydrogen bond with mHTT proteins and disrupt the aggregation. In Caenorhabditis Elegans Huntington's disease model, Xyloketal B showed a protective effect [72].

4.5.2 Dopaminergic Stabilizers

Pridopidine is a new drug that helps in the reduction of involuntary movements in HD. But it is still in the developing stage. Mechanism of action is not clear but it is expected to regulate hypoactive and hyperactive function in areas of the brain that receive dopaminergic input. Observation from animal studies reflects it as a "dopaminergic stabilizer" [73].

4.5.3 Mitochondrial Targets

MitoQ (Mitoquinone) and SS31 are mitochondria targeting antioxidant molecules and are found to be protective against mHTT-induced mitochondrial and synaptic damage in HD neurons. MitoQ with the molecular formula $C_{37}H_{45}O_4PB_4$ and molecular weight of 665.65 is conjugated with antioxidants and positively charged lipophilic phosphonium cations. These moieties have the ability to reduce mitochondrial dysfunction by scavenging free radicals and maintain neuronal viability. SS31 has H-D-Arg-Dmt-Lys-Phe-NH_2 aromatic residues and basic amino acids. Because of the sequence motif, SS31 can target mitochondria and scavenge free radicals [74].

4.5.4 Peptides Targeting Proteins

To prevent misfolding and aggregation of the expanded polyQ protein, certain peptides are used that can interact with HTT protein. These therapeutic peptides have been found to significantly slow down the progression of HD in experimental models. They prevent the abnormal HTT protein from sticking together. P42 is a peptide which is derived from the 480–502 amino acid (aa) region of HTT. P42 interacts with the N17 domain of HTT and disturbs the aggregation process by inhibiting the initial step of nucleation of abnormal HTT.

4.5.5 Intracellular Antibodies

Many intracellular antibodies were identified, also known as intrabodies and they have specific binding affinity with the N-terminal HTT. Some bind on first 17aa of HTT, whereas some bind to proline rich region (PRR) domain. They amplify the degradation of mutant protein. PRR tract causes degradation by ubiquitin-proteasome system. It might also alter the conformation of mutant HTT [75].

4.5.6 Pro-Apoptotic Proteins

Pro-apoptotic proteins get influenced during mutation. Bax/Bak and Bcl-2/adenovirus E1B 19-kDa interacting protein 3 (BNip3) are the proteins whose activation triggers mitochondrial depolarization and fragmentation inducing cell death. In case of HTT mutation, its effect on mitochondrial dysfunction and cell death depends on BNip3 rather than Bax/Bak. Hence, BNip3 could be a potential target towards HD therapy [76].

4.5.7 Antisense Oligonucleotides

RNA interference (RNAi) technology is used to reduce the level of HTT mRNA. To make it more specific, single nucleotide polymorphisms (SNPs) are targeted. Many SNPs have been identified in the HTT gene that are associated with mutant huntingtin allele. For a long period effect, antisense oligonucleotides (ASOs) are chemically modified and administered intraventricularly in mouse models, YAC128 and BACHD. Zinc finger proteins (ZFPs) are shown to bind and repress the mHTT.

In humans it is difficult for ASO and siRNAs to cross the blood brain barrier. So to introduce RNAi, some delivery systems are used. Virus-coupled siRNAs have shown high efficiency in transducing cells in the striatum. Coupling siRNAs with lipids or cholesterol was also found to give good results. Adeno-associated virus (AAV2) vector expressing HTT-silencing micro RNA (miRNA) and intraventricular delivered ASOs are also being used [77].

4.6 Conclusion

Current approaches in neurodegenerative diseases are multi-targeted. Several studies are being carried out to find a cure to these diseases; some are successful at least in animal models. Proteins and other chemical compounds are used to target gene expression and oxidative stress. Nrf2, ND-3 and compound 23 are found to check oxidative stress in PD. In the case of AD, CWZ are re-engineered into NWZ to enhance its effect. AdO suppresses transcriptional activation of iNOS and subsequently oxidative stress and apoptosis. CP2 resumes axonal trafficking. AF102B, AF267B and AF710B are able to reduce Tau hyperphosphorylation. VDAC1 N Ter interferes with Aβ interaction and mitochondrial apoptosis. Compound 5c inhibits Aβ aggregation. In ALS, BRC, which is a dopamine D2 receptor agonist, is used with the only approved drug Riluzole. Compound 14 acts as a chemical chaperone and reduces aggregation. G-Re suppresses the expression of pro-inflammatory proteins. In HD, Xyloketal B has the ability to hydrogen bond with mHTT and

reduce the protein aggregation. Same is the case for P42 peptide. Pridopidine is found to be a dopaminergic stabilizer and MitoQ and SS31 are scavenging moieties for free radicals which are being explored for clinical efficacy.

Acknowledgments This study was funded by a research grant awarded to GNB by the Council of Science and Technology, UP, India.

References

1. Braak H, Del Tredici K, Rub U, de Vos RA, Jansen Steur EN, Braak E (2003) Staging of brain pathology related to sporadic Parkinson's disease. Neurobiol Aging 24:197–211
2. Rodriguez-Oroz MC, Jahanshahi M, Krack P, Litvan I, Macias R, Bezard E, Obeso JA (2009) Initial clinical manifestations of Parkinson's disease: features and pathophysiological mechanisms. Lancet Neurol 8:1128–1139
3. Spillantini MG, Schmidt ML, Lee VM, Trojanowski JQ, Jakes R, Goedert M (1997) Alpha-synuclein in Lewy bodies. Nature 388:839–840
4. Lim KL, Zhang CW (2013) Molecular events underlying Parkinson's disease—an interwoven tapestry. Front Neurol 4:33
5. Schapira AH, Jenner P (2011) Etiology and pathogenesis of Parkinson's disease. Mov Disord 26:1049–1055
6. Halliwell B (1992) Reactive oxygen species and the central nervous system. J Neurochem 59:1609–1623
7. Hwang O (2013) Role of oxidative stress in Parkinson's disease. Exp Neurobiol 22:11–17
8. Kumar A, Singh RL, Babu GN (2010) Cell death mechanisms in the early stages of acute glutamate neurotoxicity. Neurosci Res 66:271–278
9. Babu GN, Kumar A, Singh RL (2011) Chronic pretreatment with acetyl-L-carnitine and +/-DL-alpha-lipoic acid protects against acute glutamate-induced neurotoxicity in rat brain by altering mitochondrial function. Neurotox Res 19:319–329
10. Luo J, Lee SH, VandeVrede L, Qin Z, Piyankarage S, Tavassoli E, Asghodom RT, Ben Aissa M, Fa M, Arancio O, Yue L, Pepperberg DR, Thatcher GR (2015) Re-engineering a neuroprotective, clinical drug as a procognitive agent with high *in vivo* potency and with GABAA potentiating activity for use in dementia. BMC Neurosci 16:67
11. Procaccini C, Santopaolo M, Faicchia D, Colamatteo A, Formisano L, de Candia P, Galgani M, De Rosa V, Matarese G (2016) Role of metabolism in neurodegenerative disorders. Metabolism 65:1376–1390
12. Babu GN, Kumar A, Chandra R, Puri SK, Kalita J, Misra UK (2008) Elevated inflammatory markers in a group of amyotrophic lateral sclerosis patients from northern India. Neurochem Res 33:1145–1149
13. Babu GN, Kumar A, Chandra R, Puri SK, Singh RL, Kalita J, Misra UK (2008) Oxidant-antioxidant imbalance in the erythrocytes of sporadic amyotrophic lateral sclerosis patients correlates with the progression of disease. Neurochem Int 52:1284–1289
14. Kumar A, Bala L, Kalita J, Misra UK, Singh RL, Khetrapal CL (2010) Metabolomic analysis of serum by (1) H NMR spectroscopy in amyotrophic lateral sclerosis. Clin Chim Acta 411: 563–567
15. Mollica PA, Reid JA, Ogle RC, Sachs PC, Bruno RD (2016) DNA methylation leads to DNA repair gene down-regulation and trinucleotide repeat expansion in patient-derived Huntington disease cells. Am J Pathol 186:1967–1976
16. Gauthier LR, Charrin BC, Borrell-Pages M, Dompierre JP, Rangone H, Cordelieres FP, De Mey J, MacDonald ME, Lessmann V, Humbert S, Saudou F (2004) Huntingtin controls

neurotrophic support and survival of neurons by enhancing BDNF vesicular transport along microtubules. Cell 118:127–138
17. Rizza S, Cirotti C, Montagna C, Cardaci S, Consales C, Cozzolino M, Carri MT, Cecconi F, Filomeni G (2015) S-nitrosoglutathione reductase plays opposite roles in SH-SY5Y models of Parkinson's disease and amyotrophic lateral sclerosis. Mediators Inflamm 2015:536238
18. Joshi G, Johnson JA (2012) The NRF-2 ARE pathway: a valuable therapeutic target for the treatment of neurodegenerative diseases. Recent Pat CNS Drug Discov 7:218–229
19. Kim CH, Han BS, Moon J, Kim DJ, Shin J, Rajan S, Nguyen QT, Sohn M, Kim WG, Han M, Jeong I, Kim KS, Lee EH, Tu Y, Naffin-Olivos JL, Park CH, Ringe D, Yoon HS, Petsko GA, Kim KS (2015) Nuclear receptor Nurr1 agonists enhance its dual functions and improve behavioral deficits in an animal model of Parkinson's disease. Proc Natl Acad Sci USA 112:8756–8761
20. Cortesi R, Esposito E, Drechsler M, Pavoni G, Cacciatore I, Sguizzato M, Di Stefano A (2017) Levodopa co-drugs in nanostructured lipid carriers: a comparative study. Mater Sci Eng C Mater Biol Appl 72:168–176
21. Cattaneo C, Sardina M, Bonizzoni E (2016) Safinamide as add-on therapy to levodopa in mid- to late-stage Parkinson's disease fluctuating patients: post hoc analyses of studies 016 and SETTLE. J Parkinsons Dis 6:165–173
22. Lees AJ, Ferreira J, Rascol O, Poewe W, Rocha JF, McCrory M, Soares-da-Silva P, Investigators B-S (2016) Opicapone as adjunct to levodopa therapy in patients with Parkinson's disease and motor fluctuations: a randomized clinical trial. JAMA Neurol 74(2):197–206. doi:10.1001/jamaneurol.2016.4703
23. Senek M, Nielsen EI, Nyholm D (2016) Levodopa-entacapone-carbidopa intestinal gel in Parkinson's disease: a randomized crossover study. Mov Disord 32(2):283–286. doi:10.1002/mds.26855
24. Rossi C, Genovesi D, Marzullo P, Giorgetti A, Filidei E, Corsini GU, Bonuccelli U, Ceravolo R (2016) Striatal dopamine transporter modulation after rotigotine: results from a pilot single-photon emission computed tomography study in a group of early stage Parkinson disease patients. Clin Neuropharmacol 40(1):34–36. doi:10.1097/WNF.0000000000000198
25. Trenkwalder C, Stocchi F, Poewe W, Dronamraju N, Kenney C, Shah A, von Raison F, Graf A (2016) Mavoglurant in Parkinson's patients with Levodopa-induced dyskinesias: two randomized phase 2 studies. Mov Disord 31:1054–1058
26. Pinna A, Ko WK, Costa G, Tronci E, Fidalgo C, Simola N, Li Q, Tabrizi MA, Bezard E, Carta M, Morelli M (2016) Antidyskinetic effect of A2A and 5HT1A/1B receptor ligands in two animal models of Parkinson's disease. Mov Disord 31:501–511
27. Svenningsson P, Rosenblad C, Af Edholm Arvidsson K, Wictorin K, Keywood C, Shankar B, Lowe DA, Bjorklund A, Widner H (2015) Eltoprazine counteracts Levodopa-induced dyskinesias in Parkinson's disease: a dose-finding study. Brain 138:963–973
28. Paolone G, Brugnoli A, Arcuri L, Mercatelli D, Morari M (2015) Eltoprazine prevents levodopa-induced dyskinesias by reducing striatal glutamate and direct pathway activity. Mov Disord 30:1728–1738
29. Pereira NA, Sureda FX, Perez M, Amat M, Santos MM (2016) Enantiopure indolo[2,3-a] quinolizidines: synthesis and evaluation as NMDA receptor antagonists. Molecules 21:1027
30. van der Walt MM, Terre'Blanche G (2017) Selected C8 two-chain linkers enhance the adenosine A1/A2A receptor affinity and selectivity of caffeine. Eur J Med Chem 125:652–656
31. Moccia M, Erro R, Picillo M, Vitale C, Longo K, Amboni M, Pellecchia MT, Barone P (2016) Caffeine consumption and the 4-year progression of de novo Parkinson's disease. Parkinsonism Relat Disord 32:116–119
32. Robinson SJ, Petzer JP, Terre'Blanche G, Petzer A, van der Walt MM, Bergh JJ, Lourens AC (2015) 2-Aminopyrimidines as dual adenosine A1/A2A antagonists. Eur J Med Chem 104:177–188

33. Van der Walt MM, Terre'Blanche G, Petzer A, Petzer JP (2015) The adenosine receptor affinities and monoamine oxidase B inhibitory properties of sulfanylphthalimide analogues. Bioorg Chem 59:117–123
34. Li Z, Wang P, Yu Z, Cong Y, Sun H, Zhang J, Zhang J, Sun C, Zhang Y, Ju X (2015) The effect of creatine and coenzyme q10 combination therapy on mild cognitive impairment in Parkinson's disease. Eur Neurol 73:205–211
35. Yoritaka A, Kawajiri S, Yamamoto Y, Nakahara T, Ando M, Hashimoto K, Nagase M, Saito Y, Hattori N (2015) Randomized, double-blind, placebo-controlled pilot trial of reduced coenzyme Q10 for Parkinson's disease. Parkinsonism Relat Disord 21:911–916
36. Breydo L, Newland B, Zhang H, Rosser A, Werner C, Uversky VN, Wang W (2016) A hyperbranched dopamine-containing PEG-based polymer for the inhibition of alpha-synuclein fibrillation. Biochem Biophys Res Commun 469:830–835
37. Aasly JO, Saether O, Johansen KK, Bathen TF, Giskeodegard GF, White LR (2015) Changes to intermediary metabolites in sporadic and LRRK2 Parkinson's disease demonstrated by proton magnetic resonance spectroscopy. Parkinsons Dis 2015:264896
38. Games D, Valera E, Spencer B, Rockenstein E, Mante M, Adame A, Patrick C, Ubhi K, Nuber S, Sakayon P, Zago W, Seubert P, Barbour R, Schenk D, Masliah E (2014) Reducing C-terminal-truncated alpha-synuclein by immunotherapy attenuates neurodegeneration and propagation in Parkinson's disease-like models. J Neurosci 34:9441–9454
39. Ariga H, Takahashi-Niki K, Kato I, Maita H, Niki T, Iguchi-Ariga SM (2013) Neuroprotective function of DJ-1 in Parkinson's disease. Oxid Med Cell Longev 2013:683920
40. Lev N, Barhum Y, Ben-Zur T, Aharony I, Trifonov L, Regev N, Melamed E, Gruzman A, Offen D (2015) A DJ-1 based peptide attenuates dopaminergic degeneration in mice models of Parkinson's disease via enhancing Nrf2. PLoS One 10:e0127549
41. Glat MJ, Ben-Zur T, Barhum Y, Offen D (2016) Neuroprotective effect of a DJ-1 based peptide in a toxin induced mouse model of multiple system atrophy. PLoS One 11:e0148170
42. Takahashi-Niki K, Inafune A, Michitani N, Hatakeyama Y, Suzuki K, Sasaki M, Kitamura Y, Niki T, Iguchi-Ariga SM, Ariga H (2015) DJ-1-dependent protective activity of DJ-1-binding compound no. 23 against neuronal cell death in MPTP-treated mouse model of Parkinson's disease. J Pharmacol Sci 127:305–310
43. Khan MM, Zaheer S, Nehman J, Zaheer A (2014) Suppression of glia maturation factor expression prevents 1-methyl-4-phenylpyridinium (MPP(+))-induced loss of mesencephalic dopaminergic neurons. Neuroscience 277:196–205
44. Luk B, Mohammed M, Liu F, Lee FJ (2015) A physical interaction between the dopamine transporter and DJ-1 facilitates increased dopamine reuptake. PLoS One 10:e0136641
45. Bhattacharyya S, Bakshi R, Logan R, Ascherio A, Macklin EA, Schwarzschild MA (2016) Oral inosine persistently elevates plasma antioxidant capacity in Parkinson's disease. Mov Disord 31:417–421
46. Frakey LL, Friedman JH (2016) Cognitive effects of Rasagiline in mild-to-moderate stage Parkinson's disease without dementia. J Neuropsychiatry Clin Neurosci 29(1):22–25. doi:10.1176/appi.neuropsych.15050118
47. Murata M, Hasegawa K, Kanazawa I, Fukasaka J, Kochi K, Shimazu R, Japan Zonisamide on PDSG (2015) Zonisamide improves wearing-off in Parkinson's disease: a randomized, double-blind study. Mov Disord 30:1343–1350
48. Zhou R, Shi XY, Bi DC, Fang WS, Wei GB, Xu X (2015) Alginate-derived oligosaccharide inhibits neuroinflammation and promotes microglial phagocytosis of beta-amyloid. Mar Drugs 13:5828–5846
49. Trushina E, Zhang L, Zhang S, Trushin S, Hua D (2015) Mitochondria-targeted therapeutics for Alzheimer's disease. J Neurol Sci 357:e7–e9
50. Fisher A, Bezprozvanny I, Ryskamp D, Frenkel D, Rabinovich A, Bar-Ner N, Natan N, Brandeis R, Elkon H, Gershonov E, Laferla F, Mederios R (2016) A unique target for a comprehensive therapy of Alzheimer's disease: concomitant activation of sigma1/M1 muscarinic receptors. Neurobiol Aging 39:S5

51. Sheng R, Tang L, Jiang L, Hong L, Shi Y, Zhou N, Hu Y (2016) Novel 1-phenyl-3-hydroxy-4-pyridinone derivatives as multifunctional agents for the therapy of Alzheimer's disease. ACS Chem Neurosci 7:69–81
52. Baruch K, Rosenzweig N, Kertser A, Deczkowska A, Sharif AM, Spinrad A, Tsitsou-Kampeli-A, Sarel A, Cahalon L, Schwartz M (2015) Breaking immune tolerance by targeting Foxp3(+) regulatory T cells mitigates Alzheimer's disease pathology. Nat Commun 6:7967
53. Panza F, Solfrizzi V, Seripa D, Imbimbo BP, Lozupone M, Santamato A, Zecca C, Barulli MR, Bellomo A, Pilotto A, Daniele A, Greco A, Logroscino G (2016) Tau-centric targets and drugs in clinical development for the treatment of Alzheimer's disease. Biomed Res Int:3245935. doi:10.1155/2016/3245935
54. Makhaeva GF, Lushchekina SV, Boltneva NP, Sokolov VB, Grigoriev VV, Serebryakova OG, Vikhareva EA, Aksinenko AY, Barreto GE, Aliev G, Bachurin SO (2015) Conjugates of gamma-carbolines and phenothiazine as new selective inhibitors of butyrylcholinesterase and blockers of NMDA receptors for Alzheimer disease. Sci Rep 5:13164
55. Grimaldi M, Marino SD, Florenzano F, Ciotta MT, Nori SL, Rodriquez M, Sorrentino G, D'Ursi AM, Scrima M (2016) beta-Amyloid-acetylcholine molecular interaction: new role of cholinergic mediators in anti-Alzheimer therapy? Future Med Chem 8:1179–1189
56. Dgachi Y, Ismaili L, Knez D, Benchekroun M, Martin H, Szalaj N, Wehle S, Bautista-Aguilera OM, Luzet V, Bonnet A, Malawska B, Gobec S, Chioua M, Decker M, Chabchoub F, Marco-Contelles J (2016) Synthesis and biological assessment of racemic benzochromeno-pyrimidinimines as antioxidant, cholinesterase, and Aβ1-42 aggregation inhibitors for Alzheimer's disease therapy. Chem Med Chem 11:1318–1327
57. Kumar J, Meena P, Singh A, Jameel E, Maqbool M, Mobashir M, Shandilya A, Tiwari M, Hoda N, Jayaram B (2016) Synthesis and screening of triazolopyrimidine scaffold as multi-functional agents for Alzheimer's disease therapies. Eur J Med Chem 119:260–277
58. Smilansky A, Dangoor L, Nakdimon I, Ben-Hail D, Mizrachi D, Shoshan-Barmatz V (2015) The voltage-dependent anion channel 1 mediates amyloid beta toxicity and represents a potential target for Alzheimer disease therapy. J Biol Chem 290:30670–30683
59. Gejl M, Gjedde A, Egefjord L, Moller A, Hansen SB, Vang K, Rodell A, Braendgaard H, Gottrup H, Schacht A, Moller N, Brock B, Rungby J (2016) In Alzheimer's disease, 6-month treatment with GLP-1 analog prevents decline of brain glucose metabolism: randomized, placebo-controlled, double-blind clinical trial. Front Aging Neurosci 8:108
60. Hinrich AJ, Jodelka FM, Chang JL, Brutman D, Bruno AM, Briggs CA, James BD, Stutzmann GE, Bennett DA, Miller SA, Rigo F, Marr RA, Hastings ML (2016) Therapeutic correction of ApoER2 splicing in Alzheimer's disease mice using antisense oligonucleotides. EMBO Mol Med 8:328–345
61. Pereira PA, Tomas JF, Queiroz JA, Figueiras AR, Sousa F (2016) Recombinant pre-miR-29b for Alzheimer's disease therapeutics. Sci Rep 6:19946
62. Nagata E, Ogino M, Iwamoto K, Kitagawa Y, Iwasaki Y, Yoshii F, Ikeda JE, ALS Consortium Investigators (2016) Bromocriptine mesylate attenuates amyotrophic lateral sclerosis: a phase 2a, randomized, double-blind, placebo-controlled research in Japanese patients. PLoS One 11: e0152845
63. Naujock M, Stanslowsky N, Bufler S, Naumann M, Reinhardt P, Sterneckert J, Kefalakes E, Kassebaum C, Bursch F, Lojewski X, Storch A, Frickenhaus M, Boeckers TM, Putz S, Demestre M, Liebau S, Klingenstein M, Ludolph AC, Dengler R, Kim KS, Hermann A, Wegner F, Petri S (2016) 4-Aminopyridine induced activity rescues hypoexcitable motor neurons from amyotrophic lateral sclerosis patient-derived induced pluripotent stem cells. Stem Cells 34:1563–1575
64. Getter T, Zaks I, Barhum Y, Ben-Zur T, Boselt S, Gregoire S, Viskind O, Shani T, Gottlieb H, Green O, Shubely M, Senderowitz H, Israelson A, Kwon I, Petri S, Offen D, Gruzman A (2015) A chemical chaperone-based drug candidate is effective in a mouse model of amyotrophic lateral sclerosis (ALS). Chem Med Chem 10:850–861

65. Apolloni S, Fabbrizio P, Parisi C, Amadio S, Volonte C (2016) Clemastine confers neuroprotection and induces an anti-inflammatory phenotype in SOD1(G93A) mouse model of amyotrophic lateral sclerosis. Mol Neurobiol 53:518–531
66. Elia AE, Lalli S, Monsurro MR, Sagnelli A, Taiello AC, Reggiori B, La Bella V, Tedeschi G, Albanese A (2016) Tauroursodeoxycholic acid in the treatment of patients with amyotrophic lateral sclerosis. Eur J Neurol 23:45–52
67. Seredenina T, Nayernia Z, Sorce S, Maghzal GJ, Filippova A, Ling SC, Basset O, Plastre O, Daali Y, Rushing EJ, Giordana MT, Cleveland DW, Aguzzi A, Stocker R, Krause KH, Jaquet V (2016) Evaluation of NADPH oxidases as drug targets in a mouse model of familial amyotrophic lateral sclerosis. Free Radic Biol Med 97:95–108
68. Isobe T, Tooi N, Nakatsuji N, Aiba K (2015) Amyotrophic lateral sclerosis models derived from human embryonic stem cells with different superoxide dismutase 1 mutations exhibit differential drug responses. Stem Cell Res 15:459–468
69. Bellouze S, Baillat G, Buttigieg D, de la Grange P, Rabouille C, Haase G (2016) Stathmin 1/2-triggered microtubule loss mediates Golgi fragmentation in mutant SOD1 motor neurons. Mol Neurodegener 11:43
70. Cai M, Yang EJ (2016) Ginsenoside reattenuates neuroinflammation in a symptomatic ALS animal model. Am J Chin Med 44:401–413
71. Akamatsu M, Yamashita T, Hirose N, Teramoto S, Kwak S (2016) The AMPA receptor antagonist perampanel robustly rescues amyotrophic lateral sclerosis (ALS) pathology in sporadic ALS model mice. Sci Rep 6:28649
72. Zeng Y, Guo W, Xu G, Wang Q, Feng L, Long S, Liang F, Huang Y, Lu X, Li S, Zhou J, Burgunder JM, Pang J, Pei Z (2016) Xyloketal-derived small molecules show protective effect by decreasing mutant huntingtin protein aggregates in Caenorhabditis elegans model of Huntington's disease. Drug Des Devel Ther 10:1443–1451
73. Zielonka D, Mielcarek M, Landwehrmeyer GB (2015) Update on Huntington's disease: advances in care and emerging therapeutic options. Parkinsonism Relat Disord 21:169–178
74. Yin X, Manczak M, Reddy PH (2016) Mitochondria-targeted molecules MitoQ and SS31 reduce mutant huntingtin-induced mitochondrial toxicity and synaptic damage in Huntington's disease. Hum Mol Genet 25:1739–1753
75. Marelli C, Maschat F (2016) The P42 peptide and peptide-based therapies for Huntington's disease. Orphanet J Rare Dis 11:24
76. Sassone F, Margulets V, Maraschi A, Rodighiero S, Passafaro M, Silani V, Ciammola A, Kirshenbaum LA, Sassone JF (2015) Bcl-2/adenovirus E1B 19-kDa interacting protein (BNip3) has a key role in the mitochondrial dysfunction induced by mutant huntingtin. Hum Mol Genet 24:6530–6539
77. Stanek LM, Sardi SP, Mastis B, Richards AR, Traleaven CM, Tatyana T, Misra K, Cheng SH, Shihabuddin LS (2014) Silencing mutant huntingtin by adeno-associated virus-mediated RNA interference ameliorates disease manifestations in the YAC128 mouse model of Huntington's Disease. Human Gene Therapy 25:461–474

Chapter 5
Investigation of Heavy Metal Hazards Status and Their Potential Health Risks in Vegetables Irrigated with Treated Wastewater in Oodi Gardens

Bonno Sekwati-Monang, Kabelo Gilbert Gaboutloeloe, and Sello Alfred Likuku

Abstract This study was conducted in Oodi Village, Botswana to investigate human health risk associated with heavy metals: Mn, Fe, Cu, Ni and Zn intake via consumption of contaminated locally grown vegetable: *Spinacia oleracea* L. (spinach) collected from wastewater irrigated farms. The results showed that the highest concentrations of metals found in spinach at the study site were Fe and Mn whereas Ni and Cu were the lowest. Nickel was found to be 20 fold above the prescribed safe limit whereas all the other studied metals were below the prescribed safe limits by the international scientific expert committee administered jointly by the Food and Agriculture Organization of the United Nations and the World Health Organisation. Moderate to significant enrichment of Ni and Fe, respectively, were observed in spinach which suggested that the two metals were transferred from the soils to the edible parts of spinach. Based on the oral reference values for Mn, Fe, Cu, Ni and Zn, respectively, the estimated daily intake of metal values for Mn, Fe and Ni were greater than unity, suggesting that consumption of spinach irrigated with treated wastewater had the potential to pose health risk to consumers.

Keywords Human health • Risk assessment • Metal uptake • Vegetables • Daily intake of metals

B. Sekwati-Monang (✉)
Department of Food Science and Technology, Botswana University of Agriculture and Natural Resources, Private Bag, 0027 Gaborone, Botswana
e-mail: bmonang@bca.bw

K.G. Gaboutloeloe
Department of Agricultural Engineering and Land Planning, Botswana University of Agriculture and Natural Resources, Private Bag, 0027 Gaborone, Botswana
e-mail: ggaboutl@bca.bw; ggaboutloe@hotmail.com

S.A. Likuku
Department of Basic Sciences, Botswana University of Agriculture and Natural Resources, Private Bag, 0027 Gaborone, Botswana
e-mail: alikuku@bca.bw; likuku_as@yahoo.com

P. Ramasami et al. (eds.), *Emerging Trends in Chemical Sciences*,
DOI 10.1007/978-3-319-60408-4_5

5.1 Introduction

Botswana has over a decade experienced growing problems of water scarcity which has significant negative influence on economic development, human livelihoods, and environmental quality. Volumes of wastewater released from domestic use and industries are increasingly utilized as a valuable resource for irrigation particularly in peri-urban agriculture. Thus, it drives significant economic activity, supports countless livelihoods particularly those of poor farmers, and substantially changes the water quality of natural water bodies [1].

There is evidence to indicate that agricultural soil also has increased levels of heavy metals partly due to increased anthropogenic activities [2, 3]. Wastewater irrigation may also lead to accumulation of heavy metals in the soil [3–5]. Sewage waste has been implicated as a potential source of heavy metals in the edible and non-edible parts of vegetables [6] and it often carries appreciable amounts of trace toxic metals such as copper (Cu), cadmium (Cd), zinc (Zn), lead (Pb), nickel (Ni) and iron (Fe) which often lead to degradation of soil health and contamination of food chain mainly through the vegetable grown on such soils [7]. Although certain trace elements are essential in plant nutrition, plants growing in a polluted environment can accumulate trace elements at high concentrations causing a serious risk to human health when they are consumed [8]. The toxic elements accumulated in organic matter in soils are taken up by growing plants and ultimately exposing humans to this contamination [9], which becomes one of the most serious environmental concerns in terms of the food safety issues and potential health risks to man. A number of studies have been conducted worldwide and have reported the uptake of heavy metals in crops and vegetables irrigated with wastewater and/or grown in the vicinity of polluted areas.

It is a well-known fact that treated wastewater used for livelihood activities in many parts of Botswana, in particular, the urban and peri-urban areas, is a reality that planners and policy makers must face. The opportunities of treated wastewater cultivation include increased food production and improvement in the living standards of crop cultivators both through crop consumption and income generation. Although this might be of potential value for livelihood activities, there is inadequate information either by being under-reported or underestimated, on the temporal changes in the heavy metal concentration in treated wastewater irrigated crops and the potential health risks in the long term.

In general, heavy metals are not removed even after the treatment of wastewater at sewage treatment plants [10], and thus cause risk of heavy metal contamination of the soil and subsequently to the food chain [11]. Literature on heavy metal intake through the food chain by humans is widely available throughout the world [12]. Heavy metals are non-biodegradable and persistent in nature; thus, if ingested; they accumulate in vital organs in the human body such as the kidneys, bones and liver and are associated with numerous serious health disorders [13]. On an individual basis, each metal may exhibit specific signs of toxicity as listed in USEPA [14].

The objective of this investigation was to: (1) determine the concentrations of manganese, iron, copper, nickel and zinc in the vegetables grown under treated wastewater irrigation at Oodi vegetable gardens, and (2) assess the risk to human health through the intake of locally grown vegetables using spinach as a case study. This would provide knowledge that guides future research into protection of the environment and people from exposure to heavy metals through oral intake. Thus, the information would be useful from a policy point of view. This work supplements earlier findings by Likuku and Obuseng [15] who reported heavy metal concentrations and their potential health risks in vegetables cultivated at the Glen valley farms in Gaborone, Botswana.

5.2 Materials and Methods

5.2.1 Site Description

Oodi is a small village approximately 10 km from the south-eastern part of the capital city of Botswana, Gaborone, and located at 24.56 °S; 26.03 °E. Three cultivated vegetable farms were identified and selected. Two of the selected farms were irrigated with treated wastewater (WWI) and the other, located about 3 km from the river bank was irrigated with ground water (GWI) and used as a reference or control site. Figure 5.1 shows a map indicating the relative positions of the farms.

The two treated wastewater farms were located along the gently undulating terrain of about 2–5% slope of the Oodi river bed. The river flows through the village of Oodi, receiving secondary treated wastewater discharged from the Gaborone sewage ponds location, which is an effluent catchment from the city and its surroundings. Vegetables grown at the Oodi horticultural gardens include spinach (*Spinacia oleracea* L.), Rape (*Brassica rapa var. rapa*), green peppers (*Capsicum annuum* L.) and tomatoes (*Solanum lycopersicum* L.). The gardens are irrigated with hosepipes connected to pumps drawing water from the river. Irrigation is mostly done by hand sprinkling from the hosepipes. The vegetation is tree-shrub dominated by *Vachellia tortilis*, widely known as *Acacia tortilis* and the soil type is silty clay.

5.2.2 Sampling Strategy and Sample Preparation

Sampling expedition was conducted at Oodi Farms in September 2015. Samples of *Spinacia oleracea* were uprooted with the consent of the cultivators from a cluster of gardens located within the farms (see Fig. 5.1), and five other samples from the groundwater irrigated farm. Soil samples were obtained from each sampling site

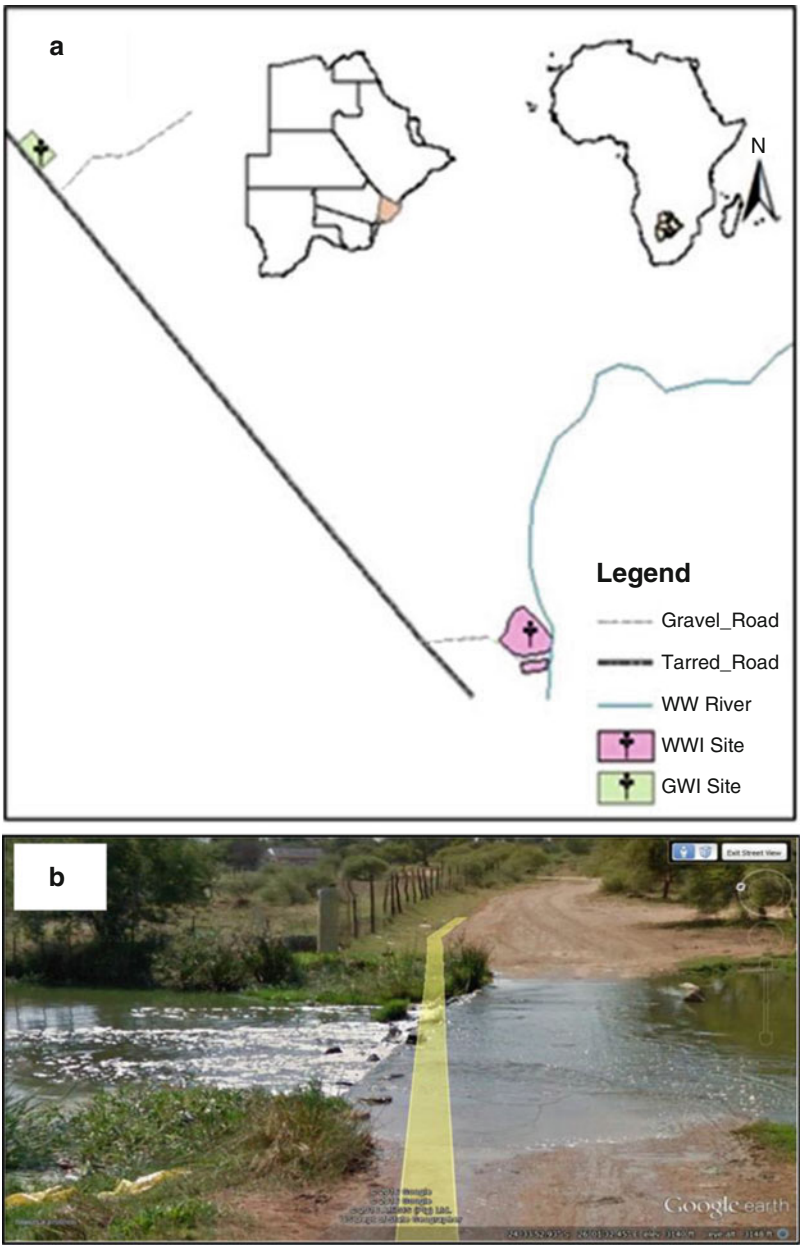

Fig. 5.1 Map of Botswana showing relative positions of wastewater irrigated (WWI) and ground water irrigated (GWI) farms. Photograph: (**a**) shows aerial view of some of the WWI farms and (**b**) a closer view the of the Oodi river carrying wastewater discharge

from the depth of 0–20 cm, the root penetration depth of the sampled vegetable. All

samples were transported in a cooler box to the laboratory for further analysis.

At the laboratory, the edible part of each spinach sample and the roots were sectioned out and thoroughly washed with water, and then rinsed three times with distilled water to remove the soils adhered to the samples. Soils were pre-sieved through 2 mm mesh sieve to remove stones, and roots that remained on the sieve were discarded.

Soil and vegetable samples were air dried at 50 °C to constant weight, homogenised and then transported to the Nation Environment Laboratory for elemental analysis.

5.2.3 *Quality Assurance, Quality Control and Heavy Metal Analysis*

At the fields, the sampling cores were first washed with tap water and then thoroughly rinsed with distilled water prior to each vegetable plot, to avoid cross-contamination. Similarly, the cutting knives used for harvesting were also thoroughly washed with distilled water prior to each harvesting to avoid cross-contamination from dust adhered on the cutting knives. Samples were transported in clean polyethylene unit-packs for laboratory analysis. The pestle and mortar used for grinding the samples were first blown with a high air pressure hose and then wiped with cleaning tissues in 70% ethanol to ensure effective sanitisation.

Implementation of laboratory methods and laboratory quality assurance included the use of standard operating procedures, calibration with standards and analysis of reagent blanks. Levels of Mn, Fe, Cu, Ni, and Zn in the solutions were determined by flame atomic absorption spectroscopy (FAAS) at the Department of Waste Management and Pollution Control. The AAS was optimised and a calibration curve was produced using standards prepared from pipetting of 5 µl each of the 1000 mg/L stock solutions of Cu, Mn, Zn, Ni and 10 µl Fe stock solutions (5 µg/ml for Cu, Mn, Zn, Ni;10 µg/ml for Fe). Calibration curves were then prepared using the stock solutions. The instrumental parameters were set depending on the type of analysis done and samples were analysed in triplicate.

5.2.4 *Analysis of Data*

Mobilisation of the measured metals from the root to the edible part of spinach was determined by means of Translocation Factor (*TF*), described as the ratio of heavy metals in plant shoot to that in plant root as defined in Eq. (5.1). Translocation Factor values greater than 1 infer effective metal transfer from the roots to shoot [16–18].

$$TF = \left(\frac{[Metals]_{\text{shoot}}}{[Metals]_{\text{root}}} \right)_{\text{Dry Weight}} \tag{5.1}$$

Accumulation of the measured metals in plant shoot from the soils is determined by means of Bioaccumulation Factor (*BAF*), described as the ratio of heavy metals in plant shoot to that in soil as defined in Eq. (5.2). Similarly, $BAF > 1$ would imply that the vegetable under study had accumulated metals from the soil.

$$BAF = \left(\frac{[Metals]_{\text{shoot}}}{[Metals]_{\text{soil}}} \right)_{\text{Dry Weight}} \tag{5.2}$$

The degree of soil contamination by heavy metals transfer from the soil to the edible portion of test plants was estimated by means of the Enrichment Factor (*EF*), calculated by using the formula given by Buat-Menard and Chesselet [19] [Eq. (5.3)]:

$$EF = \left(\frac{\text{Conc.in plant at WWI/Conc.in soil at WWI}}{\text{Conc.in plant at GWI/Conc.in soil at GWI}} \right)_{\text{Dry Weight}} \tag{5.3}$$

Enrichment factor categories proposed by Sutherland [20] were then used as follows:

EF $<$ 2 = deficient to minimal enrichment
2 $\leq$ EF $<$ 5 = moderate enrichment
5 $\leq$ EF $<$ 20 = significant enrichment
20 $\leq$ EF $<$ 40 = very high enrichment
EF $\geq$ 40 = extremely high enrichment.

Statistical tests of significance using *t*-tests and analysis of variance (ANOVA) to assess pairs of results in both soils and vegetables were performed. A two-tailed probability value less than 0.05 was considered to be statistically significant. Analysis was performed by IBM SPSS Statistics 24 software.

5.2.5 *Potential Health Risk from Consuming Vegetable*

The risk to human beings resulting from consumption of spinach grown from the area was calculated by employing the estimated daily intake of metals (*DIM*) and health risk index (*HRI*) described by Cui et al. [21], Zheng et al. [22] and Islam et al. [23] as shown in Eq. (5.4):

$$DIM = \frac{C_{\text{plant}}(\text{mg/kg}) \times \text{Intake (kg/person)}}{BM(\text{kg})} C_{\text{factor}} \tag{5.4}$$

where C_{plant} is the metal concentration of heavy metal in spinach,

Intake is the ingestion rate and
BM is the body mass in kilogram.

Literature reports average adult daily vegetable intake rate of 0.345 kg/person/day and body mass of 55.9 kg [24]. For the case of Botswana, the daily intake of vegetables was 0.116 kg/person and the body weight was 66.4 kg reported by Jackson et al. (2012) [25]. Thus, the *DIM* values in this study were determined based on vegetable consumption rate and body weight reported for the local population.

The health risk indexes (*HRI*) for Mn, Fe, Cu, Ni and Zn were determined from the ratio of the *DIM* to oral reference dose RfD_{o} values obtained from Integrated Risk Information Systems (IRIS) [26] and the Department of Environment, Food and Rural Affairs (DEFRA) [27] as shown in Eq. (5.5). The Oral Reference Dose (RfD_o) is used by the U.S. Environmental Protection Agency and is a measure of daily exposure that should not be associated with non-cancer adverse effects. The oral reference dose values used in this study for Mn, Fe, Cu, Ni and Zn were 0.014, 0.7, 0.04, 0.02 and 0.3 mg/kg body weight/day respectively (USEPA) [28].

$$HRI = \frac{DIM}{RfD_o\ (\text{mg/kg/day})} \tag{5.5}$$

If the value of *HRI* is above 1, it implies a high risk of non-carcinogenic effects, since the accepted standard is 1.0 at which there will be no significant health hazard [29].

5.3 Results and Discussion

5.3.1 Metal Concentrations, Uptake and Enrichment

The mean concentrations of Cu, Fe, Mn, Ni and Zn in soils and in sites where the spinach were irrigated with treated wastewater and ground water are presented in Table 5.1.

The magnitude of metal concentrations in soils compared to that in the vegetable varied greatly and there was no significant correlation ($P = 0.05$) in the shoot-root-soil system between the WWI and GWI sites. This was also explained by the varying degree in the translocation and bioaccumulation of individual metals in the plant system from both sites. Translocation and bioaccumulation of individual metals in plants are key parameters to the determination of the degree of human

Table 5.1 Metal concentration (mg/kg) and uptake in treated wastewater irrigated (WWI) and ground water irrigated (GWI) sites, metal uptake and enrichment factors

Metal	Sample	(WWI)	Metal uptake		(GWI)	Metal uptake		EF
		(mg/kg)	TF	BAF	(mg/kg)	TF	BAF	
Cu	Shoot	23 ± 6	0.9	0.9	19 ± 2	1.0	–	0.04
	Root	26 ± 4			20 ± 10			
	Soil	27 ± 9			ND			
Fe	Shoot	1727 ± 1403	0.4	0.4	413 ± 69	0.1	0.1	8.00
	Root	4855 ± 4146			6897 ± 1394			
	Soil	4109 ± 633			7859 ± 9069			
Mn	Shoot	158 ± 42	2.0	0.3	676 ± 400	10	8.0	–
	Root	67 ± 76			71 ± 21			
	Soil	551 ± 38			90 ± 11			
Ni	Shoot	30 ± 5	0.7	–	21 ± 1	0.6	3.0	4.74
	Root	44 ± 33			33 ± 5			
	Soil	ND			8 ± 1			
Zn	Shoot	65 ± 20	0.8	0.5	94 ± 8	2.0	1.0	0.50
	Root	77 ± 83			51 ± 9			
	Soil	124 ± 34			91 ± 20			

exposure through the food chain [30]. Moderate ($EF = 4.74$) to significant ($EF = 8.00$) enrichment of Ni and Fe, respectively, were however observed in spinach which suggested that the two metals were in overall, transferred from the soils to the edible parts of spinach as described by Eq. (5.3). Among all the metal concentrations in both soil and plant systems, Fe and Mn were highest whereas Ni and Cu were lowest. Nickel was found to be 20 fold above the prescribed safe limit whereas all the other studied metals were below the prescribed safe limits by the international scientific expert committee administered jointly by the Food and Agriculture Organization of the United Nations and the World Health Organisation.

Nickel is readily accumulated in different parts of plants due to its mobile nature in plants [31]. Exposure to Ni by humans through consumption may lead to lung fibrosis, cardiovascular and kidney diseases, among others [31].

The uptake mechanism of each element by the plant species was measured by means of the bivariate Pearson correlation coefficient, r and all elemental pairs except Zn and Cu ($r = 0.92$; $p < 0.01$) showed insignificant relationship with each other. This was possibly due to their differences in mechanisms controlling their bioavailability to the plant (Table 5.2).

Table 5.2 Pearson product moment correlation coefficient (r) among the metals in the plant

	Mn	Fe	Cu	Ni	Zn
Mn	1.00	−0.23	0.05	−0.30	0.24
Fe		1.00	0.34	0.18	0.28
Cu			1.00	0.06	0.92[a]
Ni				1.00	−0.13
Zn					1.00

[a]Correlation is significant at $p < 0.01$ (2-tailed)

Table 5.3 Daily intake of metals, *DIM* (mg/kg body weight/day) and the health risk index, *HRI* for individual trace metals in the plant

	Mn	Fe	Cu	Ni	Zn
DIM	1.18	0.72	0.03	0.04	0.16
HRI	19.8	4.3	1.0	2.6	0.4

5.3.2 Metal Daily Intake and Health Risk Assessment

The daily intake of metals provides an estimate of the degree of toxicity of heavy metals by human beings through consumption of the vegetable. Our estimated daily intake of all metals by humans were far below the tolerable daily intake for all the metals studied, as per the established reference values for tolerable intake published in the Joint FAO/WHO [32]. The *DIM* values (in mg/kg body weight /day) for the individual metals were: Mn (1.18), Fe (0.72), Cu (0.03), Ni (0.04) and Zn (0.16). Based on the oral reference values of 0.014, 0.7, 0.04, 0.02 and 0.3 mg/kg body weight/day for Mn, Fe, Cu, Ni and Zn, respectively, the *DIM* values suggest that consumption of spinach irrigated with the treated wastewater is free of risks of Cu and Zn, but not from Mn, Fe and Ni.

The *HRI* estimated from Eq. (5.5) for Mn, Fe, Cu, Ni and Zn were 19.8, 4.3, 1.0, 2.6 and 0.4 respectively. The results of *HRI* showed that Mn, Fe and Ni contamination in the plant had the potential to pose health risk to the consumers. Table 5.3 shows the measured *HRI* values.

5.4 Conclusion

This study was conducted to assess the risk to human health by Mn, Fe, Cu, Ni and Zn through the intake of locally grown vegetable: *Spinacia oleracea* L. (spinach) from treated wastewater irrigated site in Oodi Farms, in Botswana. The results showed that the highest concentrations of metals found in spinach at the study site were Fe and Mn, whereas Ni and Cu were the lowest. On comparison with the prescribed safe limits of heavy metal concentrations in plants, all except Ni, were found to be below the prescribed safe limits. Moderate and significant enrichment

of Ni and Fe, respectively, were observed in spinach which suggested that the two metals were transferred from the soils to the edible parts of spinach. Based on the oral reference values for Mn, Fe, Cu, Ni and Zn, respectively, the DIM values suggest that consumption of spinach irrigated with the treated wastewater is free of risks except from Mn, Fe and Ni. Therefore, based on the results from the *HRI* calculations, Mn, Fe and Ni had the potential to pose health risk to the consumers.

Acknowledgements The authors gratefully acknowledge the generosity of the farmers who donated vegetables used in this study.

References

1. Singh A, Sharma RK, Agrawal M, Marshall FM (2010) Health risk assessment of heavy metals via dietary intake of foodstuffs from the wastewater irrigated site of a dry tropical area of India. Food Chem Toxicol 48:611–619
2. McLaughlin MJ, Singh BR (1999) Cadmium in soil and plants: a global perspective. Kluwer Academic Publishers, Dordrecht, pp 13–21
3. Sharma RK, Agrawal M, Marshall F (2007) Heavy metal contamination of soil and vegetables in suburban areas of Varanasi, India. Ecotox Environ Safe 66:258–266
4. Singh KP, Mohan D, Sinha S, Dalwani R (2004) Impact assessment of treated/untreated wastewater toxicants discharged by sewage treatment plants on health, agricultural, and environmental quality in the wastewater disposal area. Chemosphere 55:227–255
5. Mapanda F, Mangwayana EN, Nyamangara J, Giller KE (2005) The effect of long-term irrigation using wastewater on heavy metal contents of soils under vegetables in Harare, Zimbabwe. Agr Ecosyst Environ 107:151–165
6. Sharma RK, Agrawal M, Marshall F (2006) Heavy metal contamination in vegetables grown in wastewater irrigated areas of Varanasi, India. Bull Environ Contam Toxicol 77:312–318
7. Rattan RK, Datta SP, Chonkar PK, Suribabu K, Singh AK (2005) Long term impact of irrigation with sewage effluents on heavy metal contents in soil, crops and ground water—a case study. Agr Ecosyst Environ 109:310–322
8. Voutsa D, Grimanis A, Samara C (1996) Trace elements in vegetables grown in an industrial area in relation to soil and air particulate matter. Environ Pollut 94:325–335
9. Khan S, Cao Q, Zheng YM, Huang YZ, Zhu YG (2008) Health risks of heavy metals in contaminated soils and food crops irrigated with wastewater in Beijing, China. Environ Pollut 152: 686–692
10. Chipasa K (2003) Accumulation and fate of selected heavy metals in a biological wastewater treatment system. Waste Manag 23:135–143
11. Fytianos K, Katsianis G, Triantafyllou P, Zachariadis G (2001) Accumulation of heavy metals in vegetables grown in an industrial area in relation to soil. Bull Environ Contam Toxicol 67: 423–430
12. Muchuweti M, Birkett JW, Chinyanga E, Zvauya R, Scrimshaw MD, Lister JN (2006) Heavy metal content of vegetables irrigated with mixtures of wastewater and sewage sludge in Zimbabwe: implication for human health. Agr Ecosyst Environ 112:41–48
13. Jaishankar M, Tseten T, Anbalagan N, Mathew BB, Beeregowda KN (2014) Toxicity, mechanism and health effects of some heavy metals. Interdiscip Toxicol 7:60–72
14. USEPA (US Environmental Protection Agency) (2002) Region 9, Preliminary Remediation Goals. 5 http://www.epa.Gov/region09/waste/sfund/prg. Accessed 20 Oct 2015

15. Likuku AS, Obuseng G (2015) Health risk assessment of heavy metals via dietary intake of vegetables irrigated with treated wastewater around Gaborone, Botswana. In: Rahman A, Ahmadi R (Eds). International Conference on Plant, Marine and Environmental Sciences (PMES-2015). Jan 1–2, 2015 Kuala Lumpur (Malaysia)
16. Baker AJM, Brooks RR (1989) Terrestrial higher plants which hyperaccumulate metallic elements. A review of their distribution, ecology and phytochemistry. Biorecovery 1:81–126
17. Zhang WH, Cai Y, Tu C, Ma QL (2002) Arsenic speciation and distribution in an arsenic hyperaccumulating plant. Sci Tot Environ 300:167–177
18. Fayiga AQ, Ma LQ (2006) Using phosphate rock to immobilize metals in soils and increase arsenic uptake in *Pteris vittata*. Sci Total Environ 359:17–25
19. Buat-Menard P, Chesselet R (1979) Variable influence of the atmospheric flux on the trace metal chemistry of oceanic suspended matter. Earth Planet Sc Lett 42:398–411
20. Sutherland RA, Tolosa CA, Tack FMG, Verloo MG (2000) Characterization of selected element concentration and enrichment ratios in background and anthropogenically impacted roadside areas. Arch Environ Con Tox 38:428–438
21. Cui YJ, Zhu YG, Zhai RH, Chen DY, Huang Y, Qiu Y, Liang JZ (2004) Transfer of metals from soil to vegetables in an area near a smelter in Nanning, China. Environ Int 30:785–791
22. Zheng N, Wang Q, Zhang X, Zheng D, Zhang Z, Zhang S (2007) Population health risk due to dietary intake of heavy metals in the industrial area of Huludao city, China. Sci Tot Environ *387*:96–104
23. Islam MS, Ahmed MH, Al-Mamun MH (2015) Apportionment of heavy metals in soil and vegetables and associated health risks assessment. Stoch Environ Res Risk Assess 30:365–377
24. Wang X, Sato T, Xing B, Tao S (2005) Health risks of heavy metals to the general public in Tianjin, China via consumption of vegetables and fish. Sci Tot Environ 350:28–37
25. Jackson MD, Motswagole BS, Kwape LD, Kobue-Lekalake RI, Takgantshwana TB, Mongwaketse T, Mokotedi M, Jackson-Malete J (2012) Validation and producibility of an FFQ for use among adults in Botswana. Public Health Nutr 16:1–10
26. IRIS, Integrated Risk Information System database (2003). US Environmental Protection Agency
27. DEFRA (Department of Environment, Food and Rural Affairs) (1999) Total diet study-aluminum, arsenic, cadmium, chromium, copper, lead, mercury, nickel, selenium, tin and zinc. The Stationery Office, London
28. USEPA (2005) Toxicological Review of Zinc and Compounds. Washington, DC. EPA/635/R-05/002, CAS NO.7440-66-6. http://www.epa.gov/iris/toxreviews/0426tr.pdf. Accessed 22 Oct 2015
29. Grzetic I, Ghariani RHA (2008) Potential health risk assessment for soil heavy metal contamination in the central zone of Belgrade (Serbia). J Serb Chem Soc 73:923–934
30. Prabu PC (2009) Impact of heavy metal contamination of Akaki river of Ethiopia on soil and metal toxicity on cultivated vegetable crops. EJEAFChe 8:818–827
31. Kamal AKI, Islam MR, Hassan M, Ahmed F, Rahman M, Muniruzzaman M (2016) Bioaccumulation of trace metals in selected plants within Amin Bazar landfill site, Dhaka, Bangladesh. Environ Processes 3:179–194
32. Joint FAO/WHO (1999) Evaluation of certain food additives and contaminants (Forty-ninth report of the Joint FAO/WHO Expert Committee on Food Additives). WHO Technical Report Series, No. 884

Chapter 6
Removal of Fluoride from Ground Water by Adsorption Using Industrial Solid Waste (Fly Ash)

Gargi Maitra Chakraborty, Saroj Kumar Das, and Sailendra Nath Mandal

Abstract The fluoride removal ability of industrial waste (fly ash) from ground water was studied at different concentrations, contact times, reaction temperatures, adsorbent dosage, coexisting anions and pH of the solution. The rate constants of adsorption, intraparticle transport, mass transfer coefficients and thermodynamic parameters have been calculated at 303 K, 313 K and 323 K. The empirical model has been tested at various concentrations for the present system. The removal of fluoride is favourable at low concentration (5 ppm), high temperature (313 K) and under highly acidic conditions. The batch adsorption process fitted well the Langmuir isotherm and the adsorption kinetics followed the pseudo-second-order rate equation. The physicochemical properties of fly ash were characterized by X-ray diffraction, Fourier Transform infrared spectroscopy and scanning electron microscopy.

Keywords Fluoride • Ground water • Fly ash • Adsorption • pH

G.M. Chakraborty (✉)
Department of Chemistry, NIT Agartala, Barjala, Jirania, Agartala 799055, Tripura, India

National Institute of Technical Teachers' Training and Research, Kolkata, Ministry of Human Resource Development, Govt. of India, Block-FC, Sector-III, Salt Lake City, Kolkata 700106, India
e-mail: gmaitra82@gmail.com

S.K. Das
Department of Chemistry, NIT Agartala, Barjala, Jirania, Agartala 799055, Tripura, India
e-mail: sdatnit@gmail.com

S.N. Mandal
National Institute of Technical Teachers' Training and Research, Kolkata, Ministry of Human Resource Development, Govt. of India, Block-FC, Sector-III, Salt Lake City, Kolkata 700106, India
e-mail: drsailen@hotmail.com

P. Ramasami et al. (eds.), *Emerging Trends in Chemical Sciences*,
DOI 10.1007/978-3-319-60408-4_6

Abbreviations

Nomenclature

a_1	Elovich constant which gives an idea of the reaction rate constant (mg/g/min)
b	Langmuir constant (L/mg)
b_1	Elovich constant and represents the rate of chemisorption at zero coverage (g/mg)
b_T	Temkin constant
C	Intra-particle diffusion constant
C_a	Amount of F^- (mg) adsorbed on the adsorbent per liter of the solution at equilibrium
C_{abs}	Amount of F^- ion adsorbed onto sorbent surface (mol/g)
C_e	F^- ion concentration in solution at equilibrium (mg/L)
C_0	Initial F^- ion concentration (mg/L)
C_t	F^- ion concentration at time t (mg/L)
D_e	Effective diffusion coefficient of adsorbates in the sorbent phase (m^2/s)
E	Mean sorption energy (kJ/mol)
ΔG°	Gibbs free energy (kJ/mol)
ΔH°	Enthalpy (kJ/mol)
K_1	Pseudo first-order rate constant (min^{-1})
K_2	Pseudo second-order rate constant (mg/g/min)
K_i	Intra-particle rate constant ($mg/g/min^{1/2}$)
K_{bq}	The constant obtained by multiplying q_{max} and b
K^o_c	Thermodynamic equilibrium constant
$K^{/}_c$	Apparent equilibrium constant
K_T	Temkin isotherm constant
M	Mass of the sorbent per unit volume (g/L)
K_f	Freundlich constants, intensity of sorption $(mg/g)/(mg/L)^{1/n}$
n	An integer
q_e	Amount adsorbed per gram of the sorbent at equilibrium (mg/g)
q_{max}	Maximum sorption capacity (mg/g)
q_t	Amount adsorbed per gram of sorbent at any time t (mg/g)
q_α	Amount adsorbed per gram of sorbent at infinite time (mg/g)
q_{tm}	Amount adsorbed per gram of adsorbent from model (mg/g)
r^2	Correlation coefficient
R	Ideal gas constant (J/mole/K)
R_L	Separation factor
R_a	Radius of the sorbent particle (m)
S_S	External surface area of the sorbent per unit volume (m^{-1})
ΔS°	Entropy [kJ/(mole K)]
t	Time (min)
T	Temperature (K)

t_0 Elovich constant equals to $1/(a_1 \cdot b_1)$
V Volume (mL)
W Amount of sorbent (g)
X_m Maximum sorption capacity of sorbent (mmole/g)

Greek Letters

β Mass transfer coefficient (cm/s)
λ Constant related to sorption energy (mol^2/kJ^2)
ε Polanyi potential (kJ^2/mol^2)
χ^2 Chi-square value

$$\chi^2 = \sum \frac{(q_t - q_{tm})^2}{q_{tm}}$$

6.1 Introduction

United Nations had declared 2005–2015 as the "*decade of water for life*". Fluoride is a persistent, non-biodegradable pollutant and an accumulative toxin. It is "*more toxic than Pb but less toxic than As*". Water (inherent ion dissolving capacity) picks up F^- from minerals and salts in the earth crust during runoff/percolation.

Fluoride is widely distributed in the geological environment [1] and is generally released into the ground water by slow dissolution from the fluorine-containing rocks [2]. The various fluoride minerals include Sellaite (MgF_2), Fluorspar (CaF_2), Cryolite (Na_3AlF_6), Topaz ($Al_2F_2SiO_4$), Fluoroapatite [$Ca_5F(PO_4)_3$], Apophyllite [$KFCa_4(Si_8O_{18})18H_2O$]. These are associated with the rocks of either igneous or metamorphic origin whereas fluoroapatite is associated with the rocks of sedimentary origin [3] and apophyllite is found in the inner lining of cavities of the amygduales in basaltic rocks [4, 5]. In streaming surface fresh water, fluoride concentrations are usually lower than in ground water because of the shorter contact time between water and the rocks. The natural concentration of fluoride depends on the geological, chemical and physical characteristics of the aquifer, the porosity and acidity of the soil and rocks, the temperature and the action of other chemical elements such as sulfate, phosphate, etc. [6]. However elevated fluoride concentrations in the ground water occur in various parts of the world [7–16] as shown in Table 6.1.

In India, the problem has reached alarming proportion affecting at least 19 states, with the highest value of fluoride of 48 mg/L being found in Haryana and the lowest in Jammu and Kashmir of 4.21 mg/L. Andhra Pradesh, Gujarat and Rajasthan have 50 to 100% of the districts affected by fluoride, whereas Bihar, Jharkhand, Haryana, Karnataka, Madhya Pradesh, Maharashtra, Orissa, Punjab, Tamil Nadu and Uttar Pradesh have 30 to 50% of districts affected. Chhattisgarh, Delhi, Jammu and Kashmir, Kerala and West Bengal have less than 30% of districts affected [17].

Table 6.1 Major fluoride affected regions in the world

Continent	North Africa	South Africa	Asia	Europe
Countries	Egypt, Libya, Nigeria	Zambia, Zimbabwe	China, Hong Kong, India, Israel, Japan, South Korea, Malaysia, Singapore, Vietnam	Austria, Belgium, Germany, Greece, France, Ireland, Sweden, Spain, Norway, Hungary, Latvia, Switzerland

Among the 25 districts of West Bengal, the prominent districts which are severely fluoride-affected are (i) Purulia; (ii) Bankura; (iii) Birbhum; (iv) South 24 Parganas (Baruipur); (v) Malda; (vi) Uttardinajpur; and (vii) Dakshindinajpur [17].

In West Bengal, during the pre-monsoon season, fluoride level was found lower as compared to other places in the newly developed areas or in those locations which are located at higher altitude. Fluoride level was found higher in thickly populated areas or nearer the populated zone of river or in slum area [18].

The fluoride levels of food depend upon the nature of soil and quality of water used for irrigation and thus vary from village to village and town to town [17].

Fluoride is attached to positively charged calcium in bones and teeth because of its strong electronegativity. Depending on the concentration and the duration of continuous uptake, the impact of fluoride in drinking water can be beneficial or detrimental to mankind. Small amounts in ingested water are usually considered to have a beneficial effect (concentration of fluoride range: 0.8–1.20 ppm) on the rate of occurrence of dental caries, particularly among children below 8 years old [19]. On the contrary, excess intake of fluoride leads to various diseases such as osteoporosis, arthritis, brittle bones, cancer, infertility, brain damage, Alzheimer syndrome and thyroid disorder [20, 21]. Fluorosis is a common symptom of high fluoride ingestion manifested by mottling of teeth in mild cases and embrittlement of bones and neurological damage in severe case [Dental caries ($\leq$0.5 ppm), optimum dental health (0.5–1.5 ppm), dental fluorosis (1.5–4.0 ppm), dental and skeletal fluorosis (4–10 ppm), cripping fluorosis ($\geq$10.0 ppm)] [22]. There are some reports indicating that fluoride may also interfere with DNA synthesis [23]. The excess concentration of fluoride can also interfere with carbohydrates, lipids, proteins, vitamins and mineral metabolism [24]. Pineal gland is a major site of fluoride accumulation within the body, with higher concentrations of fluoride than either teeth or bone [25]. Fluoride exposure has also been linked to bladder cancer, particularly among workers exposed to excess fluoride in the workplace [25]. According to human health demand WHO had set a limit to fluoride concentration in drinking water of 0.5–1.0 mg L^{-1} [26].

Various industries are also responsible towards fluoride pollution to a great extent [27]. The industries (including pharmacy) which discharge wastewater containing high fluoride concentrations into water bodies include glass and ceramic production, semiconductor manufacturing, electroplating, coal fired power stations, beryllium extraction plants, brick and iron works, rubber and fertilizer production

and aluminium smelters. Such excessive fluoride content has been drained into water bodies. USEPA has established the effluent standard of 4 mg L^{-1} for fluoride from wastewater treatment plants. Water resources substitution is impossible; so the removal of fluoride from aquatic environment is necessary.

Among various methods used for defluoridation of water, the adsorption process is widely used and offers satisfactory results in terms of economic feasibility, simplicity of design, high efficiency and easy operation [28, 29]. Coagulation methods have generally been found effective in defluoridation, but they are unsuccessful in bringing fluoride to the desired concentration levels [30]. Furthermore, membrane processes do not require additives but these are relatively expensive to install and operate and prone to fouling, scaling or membrane degradation [31]. Also, the electrochemical techniques, in general, suffer due to the high cost factor during installation and maintenance [30]. Nalgongda technique is widely used for defluoridation of water in developing countries but suffers from the disadvantage that the treated water has high residual aluminium concentration [30].

Fly ash, as a by-product of the burning of fossil fuels, is a particulate waste material originating in great amounts from the combustion of coal in thermoelectric power plants, steel mills, etc. Landfill of fly ash is the current management strategy (Fig. 6.1). Because of its spherical shape and pozzolanic properties, fly ash is a valuable and desirable additive to cement concrete and is effectively used in many other areas. It is an alternative to activated carbon or zeolites for adsorption in water pollution treatment. Raw fly ash usually has low adsorption capacity. Utilization of fly ash would help to reduce the environmental burden and enhance economic benefit.

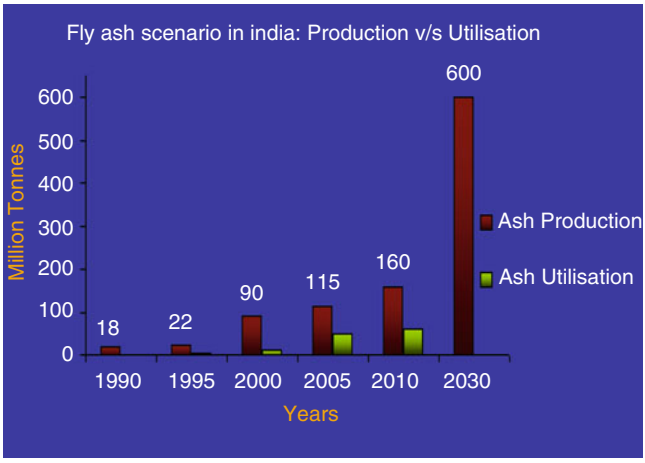

Fig. 6.1 Fly ash production and utilization in India from 1990 to 2030

6.2 Adsorption Experiments

6.2.1 Preparation of Adsorbent

Coal fly ash was collected from Bandel Thermal Power Station, near Kolkata, West Bengal, India. It was dried at 110 °C for 24 h to remove the adherent moisture. After drying, the sample was cooled at room temperature and was then sieved to obtain particle size of 100–150 μm prior to use for present studies. The anhydrous powdered adsorbent was stored in an airtight plastic container.

6.2.2 Preparation of Synthetic F^- Solution

An artificial 1000 ppm F^- solution was prepared by dissolving 2.21 g of amorphous anhydrous NaF (Merck Specialties Private Limited, Mumbai, India) in 1 L of ultrapure water.

This stock solution was subsequently diluted to the required concentrations for the adsorption experiments.

6.2.3 Reagents and Instruments

- All chemical reagents were of analytical grade (Merck Specialties Private Limited, Mumbai, India).
- Ultrapure water was used in all experiments.
- Only plastic wares and vials were used for handling fluoride solutions and for analysis.
- The pH of the solution was measured with a pH 5500 dual channel pH/ion (Eutech Instrument, Singapore) using FET solid electrode calibrated with standard buffer solutions.
- Electrically thermostatted reciprocating shaker.
- Fluoride ion selective electrode (HQ 40d) (Hach, USA) was used to measure the F^- ion concentration in solution.
- FTIR (Jasco FT/IR-670 Plus) studies were carried out for the fresh and fluoride loaded adsorbents to determine the type of functional group responsible for the adsorption process.
- XRD (Rigaku MiniFlex, Japan)
- SEM (HITACHI,S-530)

6.2.4 Adsorption Experiments and Analytical Method

Batch adsorption experiments were conducted to determine the optimum conditions. The effects of pH, adsorbent dosage, initial fluoride concentration and contact time on adsorption were studied by varying the pH, dose, concentration and contact time respectively. All the experiments were carried out in 250 mL conical flasks with 100 mL test solution at room temperature (30 °C). These stoppered flasks (6–9), along with desired test solution and fixed amount of adsorbent were shaken for the desired contact time in an electrically thermostatted reciprocating shaker at the rate of 110–125 strokes/min at desired temperature to study the various parameters. At regular interval of time the conical flasks from the shaker were withdrawn and allowed to stand for 5 min for the adsorbent to settle, then the adsorbent was separated from the F^- ion solution by filtration (Whatman filter paper No. 42), and the filtrate was analysed using a fluoride ion selective electrode. The initial pH of the F^- solution was adjusted by adding 0.1 M HCl or 0.1 M NaOH solutions as required. The amount of F^- (q_e, mg/g) retained in the adsorbent phase was estimated using Eq. (6.1):

$$q_e = \frac{(C_0 - C_e)V}{W} \tag{6.1}$$

The percentage removal of F^- ion from the solution is calculated using Eq. (6.2):

$$E = \left(\frac{C_0 - C_e}{C_0}\right)100 \tag{6.2}$$

The ground water sample collected from Baruipur, West Bengal (India) was studied for defluoridation, under the feasible optimized condition for justification of above experiment.

Our aim of the study is the removal of fluoride from ground water as per WHO guidelines and optimization of the other parameters.

6.3 Results and Discussion

6.3.1 Effects of Operating Parameters

6.3.1.1 pH

pH is a key factor affecting fluoride adsorption at the water adsorbent interface. The removal of fluoride by adsorption on fly ash was found to increase from pH 10 to pH 2. The optimum pH is 2 (% of fluoride removal is 99). The effect of pH was investigated by maintaining the other parameters (T = 303 K, W = 2.5 g L^{-1},

$C_0 = 10$ mg L^{-1}, t = 600 min). Such type of changes is particularly observed in the case of adsorption of strong hydrolyzable cations [31]. Fly ash contains metal oxides which are hydroxylated in aqueous solution. Such an interface on acid base dissociation develops positive and negative charges on the surface [32, 33] generating more H^+ ions which led to greater adsorption. Due to anionic adsorption, the removal of fluoride will be more at lower pH.

Causes for reduction of fluoride removal in alkaline medium:

- Increasing electrostatic repulsion between the fluoride ions and the negatively charged surface sites of fly ash
- On considering charge and ionic radii, F^- is similar to OH^-, leading to competition between them for the adsorption sites.

6.3.1.2 Contact Time

The adsorption capacity increased with time up to about 180 min (range 15–600 min) and then the reaction attained equilibrium. Hence the optimum time is found to be 180 min (T = 303K, W = 2.5 g L^{-1}, $C_0 = 10$ mg L^{-1}, pH = 2). If the adsorption process was only controlled by an ion exchange mechanism, equilibrium time would have been short [34].

6.3.1.3 Initial Fluoride Concentration

The adsorption of fluoride decreased with an increase in the fluoride concentration from 5 to 20 ppm. Further, it was observed that the removal efficiency is smooth and continuous indicating the possibility of the formation of monolayer coverage of fluoride ion at the interface of adsorbent.

6.3.1.4 Adsorbent Dosage

It had been observed that up to a certain level, higher doses of adsorbent resulted in higher removal of fluoride. This might be because of higher availability of surface and pore volume at higher doses. This fact has been well established in adsorption study. The fluoride removal efficiencies increased from 1.0 to 2.5 g L^{-1} dosage of adsorbent; from 2.5 to 3.0 g L^{-1} there was no significant change in the percentage removal of fluoride probably due to the overlapping of active sites at higher dosage, thus reducing the net surface area.

6.3.1.5 Coexisting Ions

The initial fluoride concentration in solution was fixed (10 mg/L) while the initial concentrations of the coexisting anions were 5, 10 and 20 mg/L. Decreasing order of co-existing anions was found to be as follows: comprehensive (mixture of sulfate, nitrate and dihydric phosphate in the concentration ratio 1:2:2) > dihydric phosphate > nitrate > bicarbonate > sulfate. This may be due to the competition between the fluoride anions and the coexisting anions for the active sites on the adsorbent surfaces.

6.3.2 Adsorption Kinetics Study

Different rate equations have been used to correlate the present experimental data of the adsorption processes. With the average shaking speed of 125 rpm, it was assumed to offer no mass transfer (both external and internal) resistance to the overall adsorption process. The equations used are:

6.3.2.1 Pseudo 1st-Order Model [34]

$$\log(q_e - q_t) = \log q_e - \frac{K_1}{2.303} t \tag{6.3}$$

The adsorption of fluoride from a liquid phase to solid phase can be considered as a reversible process with equilibrium being established between the solution and the solid phase. Adsorption phenomenon can be described as a diffusion controlled process, assuming a non-dissociation molecular adsorption of fluoride on fly ash. Eq. (6.3) is known as the Lagergren equation. The value of K_1 is determined from the slope of the linear plot of log ($q_e - q_t$) vs. time.

6.3.2.2 Pseudo 2nd-Order Model [35]

$$\frac{t}{q_t} = \frac{1}{K_2 q_e^2} + \frac{1}{q_e} t \tag{6.4}$$

This model is based on the assumption of the chemisorption of the adsorbate on an adsorbent. K_2 can be calculated from the slope and intercept of the linear plot $\frac{t}{q_t}$ vs. t (Fig. 6.2).

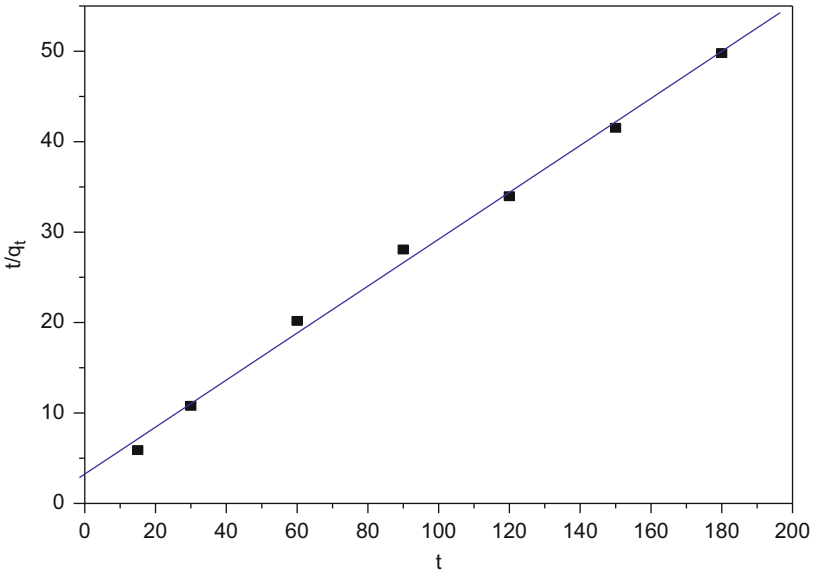

Fig. 6.2 Pseudo-second-order plot for fluoride adsorption by fly ash (pH = 2.0; T = 313 K; W = 2.5 g L^{-1})

6.3.2.3 Elovich Model [36]

$$q_t = \frac{1}{b_1} \ln (a_1 b_1) + \frac{1}{b_1} \ln (t + t_0) \tag{6.5}$$

6.3.2.4 Pore Diffusion, Intra-Particle Diffusion Model [37]

$$q_t = K_i t^{0.5} + C \tag{6.6}$$

The adsorbate transport from the solution phase to the surface of the adsorbent particles occurs in several steps; the overall adsorption process may be controlled either by one or more steps.

Table 6.2 Parameters and correlation coefficients of the different kinetic models

Pseudo 1st-order model	Pseudo 2nd-order model	Intra-particle diffusion	Elovich model	Mass transfer control process
K_1 (min^{-1}):	K_2 (mg/g/min):	r^2: 0.973	a_1: 0.49	β (cm/s) × 10^7:
0.041	0.027		b_1: 2.35	8.002
r^2: 0.7884	r^2: 0.996		r^2 : 0.96	r^2: 0.953

6.3.2.5 Mass Transfer Control Process [38]

$$\ln\left(\frac{C_t}{C_0} - \frac{1}{1+MK_{bq}}\right) = \ln\left(\frac{MK_{bq}}{1+MK_{bq}}\right) - \left(\frac{1+Mb_{bq}}{MK_{bq}}\right)\beta S_s t \qquad (6.7)$$

The mechanism of adsorption process depends on several factors including structure of the adsorbent, physical and chemical characteristics of solute and adsorbent. Pseudo 1st-order kinetic model was based on the assumption of physisorption process. Equation (6.3) was initially used successfully to describe the chemisorption of gas molecule onto the sorbent [39]. In this model, a variation in the energy of chemisorption is attributed to a change in the surface coverage or to a continuous and specific range of site reactivates. The Elovich equation is used to describe the sorption system if it is chemisorption [40]. Intra-particle diffusion in liquid-porous solid systems may be described by surface diffusion, pore-volume diffusion or both the processes. Equation (6.6) represents the intra-particle diffusion model. The diffusion of solute molecules through the liquid pores to the adsorption sites was known as pore-volume diffusion. Surface diffusion was described by the adsorption at the outer surface of the adsorbents [41]. The mass transfer coefficient is determined by applying Eq. (6.7) to identify the film mass transfer control process. The value of rate constants and statistical parameters for each model are shown in Table 6.2. Pseudo-2nd order model is more applicable for the adsorption process as evidenced from the statistical data.

6.3.3 Adsorption Mechanism

It is important to predict the rate-limiting step in the adsorption process to understand the adsorption mechanism. For a solid–liquid adsorption process, the solute transfer is characterized by either external mass transfer (boundary layer diffusion) or intra-particle diffusion or both.

6.3.3.1 Determination of Rate Limiting Step

The Fick's equation (Eq. (6.8)) was used to describe the rate limiting step of F^- ions adsorption as film diffusion, intra-particle diffusion or adsorption onto the active functional group in inner and outer surface of the adsorbent [42, 43].

$$\frac{q_t}{q_\alpha} = \frac{6}{R_a}\sqrt{\frac{D_e t}{\pi}} \tag{6.8}$$

The plot of (q_t/q_e) (q_α was replaced by q_e) vs. $\sqrt{t}$ represents the different stages of adsorption process.

6.3.4 *Adsorption Isotherm Study*

The four-parameter adsorption isotherm models were used to explain the F^- ion adsorption from aqueous solution. The applicability of the isotherm models was compared by judging the statistical parameters value. These four-parameter models are as follows:

(a) Langmuir isotherm model [44]

$$\frac{C_e}{q_e} = \frac{1}{q_{\max} b} + \frac{C_e}{q_{\max}} \tag{6.9}$$

The values of q_m and b are calculated from the slope and the intercept of the linear plot $\frac{C_e}{q_e}$ vs. C_e (Fig. 6.3).

(b) Freundlich isotherm model [45]

$$\log q_e = \log K_f + \frac{1}{n}\log C_e \tag{6.10}$$

(c) Temkin isotherm model [46]

$$q_e = b_T \ln K_T + b_T \ln C_e \tag{6.11}$$

(d) Dubinin–Radushkevich isotherm model

Sorption energy was calculated by Dubinin–Radushkevich [47] isotherm model to predict the nature of adsorption process, i.e. physical or chemical. The linear form of the model is described as:

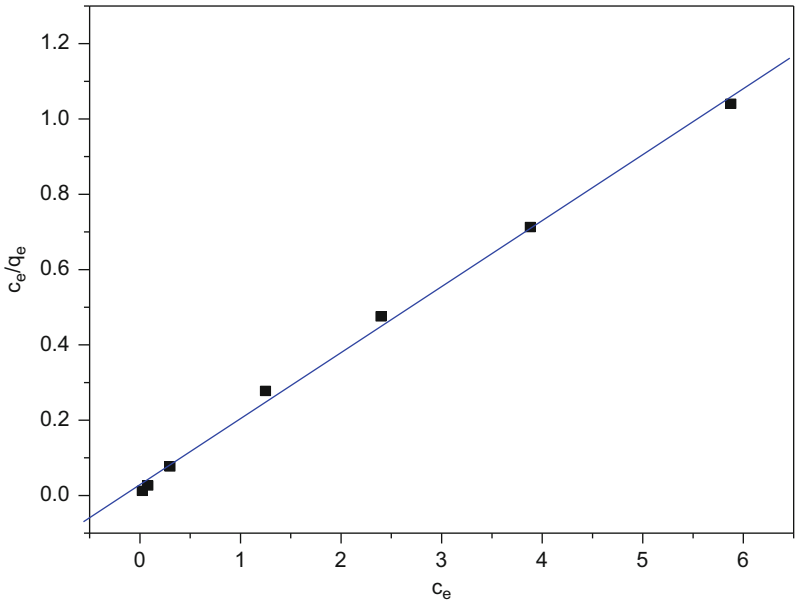

Fig. 6.3 Linearization of the Langmuir isotherm for fluoride removal (pH = 2.0; W = 2.5 g L^{-1}; t = 600 min)

$$\ln C_{abs} = \ln X_m - \lambda \in^2 \tag{6.12}$$

The Polanyi potential [48] is equal to:

$$\in = RT \ln\left(1 + \frac{1}{C_e}\right) \tag{6.13}$$

The plot of ln C_{abs} vs. ε^2 gave a straight line from which the values of λ and X_m for all the adsorbents were calculated. Using the value of λ, the mean sorption energy, E, was evaluated as:

$$E = \frac{1}{\sqrt{-2\lambda}} \tag{6.14}$$

The E (kJ/mole) value gives the information about sorption type: physical (E < 8 kJ/mole) or chemical (E = 8–16 kJ/mole). It was found to be chemical in nature in the present study [49].

The Langmuir isotherm best describes chemisorption processes. The Langmuir adsorption isotherm model was applied for the estimation of maximum adsorption capacity corresponding to complete monolayer coverage onto the adsorption surface of a finite number of the identical sites. Feasibility of the Langmuir isotherm in

Table 6.3 R_L values and isotherm type

R_L	Type of isotherm
$R_L > 1$	Unfavorable
$R_L = 1$	Linear
$0 < R_L < 1$	Favorable
$R_L = 0$	Irreversible

Table 6.4 Comparison of correlation coefficients and χ^2 values of the different isotherm parameters

Langmuir	Freundlich	Temkin	Dubinin–Radushkevich
q_{max} (mg/g): 5.70	K_f: 4.33	K_T: 5.01	$X_m \times 10^4$: 8.21
b (L/mg): 6.11	n: 5.61	b_T (kJ/mole): 6.02	E (kJ/mole): 10.51
r^2: 0.997	r^2: 0.963	r^2: 0.977	r^2: 0.996
χ^2: 0.12	χ^2: 0.62	χ^2: 0.32	

terms of a dimensionless constant was expressed by the separation factor or equilibrium parameter, R_L [50].

$$R_L = \frac{1}{1 + bC_0} \tag{6.15}$$

For favorable adsorption the value of R_L should lie in between 0 and 1 (Table 6.3). The R_L values for the adsorption process were estimated at lower initial concentration of 5 ppm and higher initial concentration of 20 ppm of F^- ion. All these values were found to lie between 0 and 1 and indicated favorable adsorption.

The Freundlich isotherm is based on an empirical equation where the adsorption took place on the heterogeneous surface of the adsorbent. The Freundlich isotherm constants n and K_f were empirical parameters that vary with the degree of heterogeneity and are related to adsorption capacity. The values of n should lie between 1 and 10 for the favorable adsorption process. Temkin isotherm model was applied to evaluate the adsorption potentials of adsorbents for adsorbates, i.e. F^- ion from aqueous solution. All the isotherm parameters along with correlation coefficient (r^2) and Chi-square (χ^2) are shown in Table 6.4, and it can be concluded that the Langmuir isotherm model was more applicable than other three isotherm models studied.

6.3.5 Thermodynamic Study

Different thermodynamic parameters for the adsorption process were studied at different initial F^- ion concentrations and temperature. The thermodynamic equilibrium constant (K_c^0) was obtained by calculating the apparent equilibrium constant

Table 6.5 Thermodynamic parameters of fluoride adsorption onto fly ash

Temperature (K)	ΔG° (kJ/mole)	ΔH° (kJ/mole)	ΔS° [kJ/(mole/K)]
303	−1.4	11.66	0.05
313	−1.9	11.66	0.05
323	−2.1	11.66	0.05

($K_c^{/}$) at different temperatures and initial F^- concentration for each system and extrapolating to zero [51]. Table 6.5 represented all the thermodynamic parameters. The negative value of Gibbs free energy at all temperatures indicated the spontaneous nature of the adsorption process. Decreasing values of ΔG° with increasing temperature indicated that higher adsorption occurred at higher temperatures. Positive values of ΔH^0 showed that the process was endothermic under the given conditions. The value of ΔS^0 was positive which indicated the increased randomness at the solid/solution interface during the adsorption process [52].

$$K_c^{/} = \frac{C_a}{C_0} \tag{6.16}$$

$$\Delta G^0 = -RT \ln K_c^0 \tag{6.17}$$

$$\ln K_c^0 = -\frac{\Delta H^0}{RT} + \frac{\Delta S^0}{R} \tag{6.18}$$

6.4 Properties of Fly Ash

SEM The fly ash had a uniform smooth surface (Fig. 6.4).

XRD In comparison to JCPDS standard cards, the approximate composition of fly ash was mainly composed of mullite ($Al_6Si_2O_{13}$) and sillimanite (Al_2SiO_5) in addition to the main amorphous glassy phase and quartz crystal (SiO_2) (Fig. 6.5).

FTIR The broad band around 3449.7 cm^{-1} was due to the stretching vibration of H_2O. A sharp band at 1084.1 cm^{-1} was related to the stretching vibrations of the Si-O groups and the band at 458.5 cm^{-1} is due to Si–O–Si bending vibrations. The bands centered at 795.7 cm^{-1} and 553.4 cm^{-1} are assigned to Al–O bending vibrations and Fe–O stretching vibrations (Fig. 6.6).

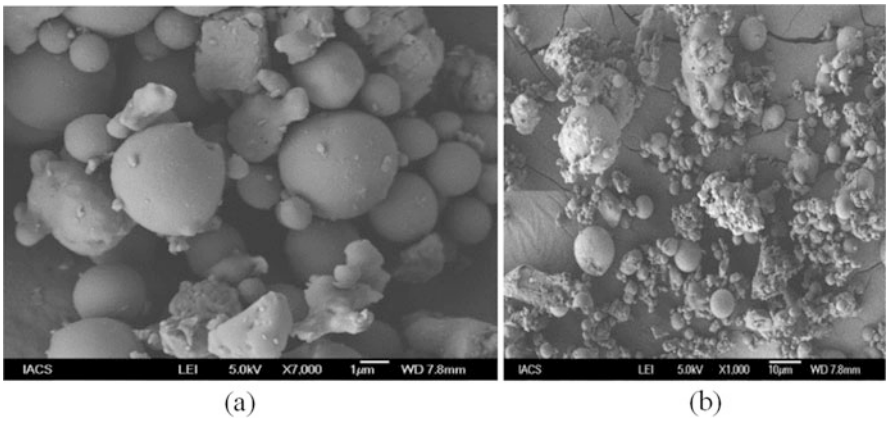

Fig. 6.4 SEM images of fly ash

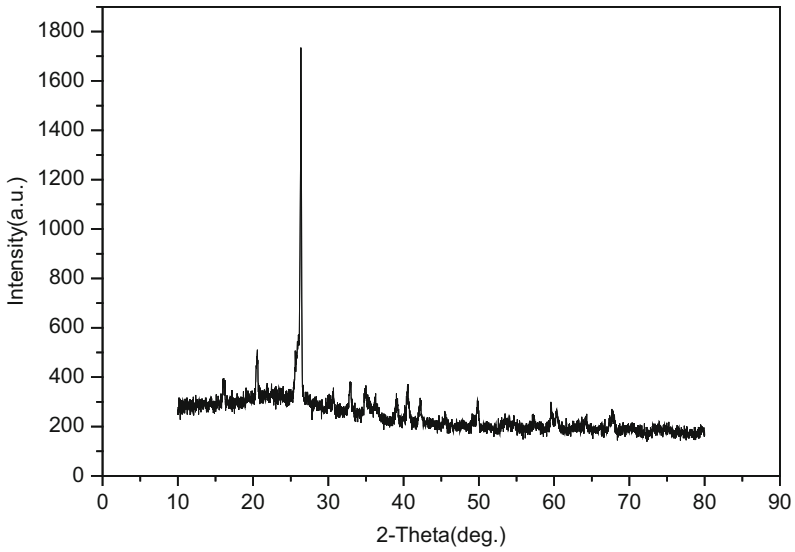

Fig. 6.5 XRD pattern of fly ash

6.5 Conclusions

Batch experiments have been carried out for the removal of F^- ion from synthetic solution and ground water using industrial waste (fly ash). The results obtained in this study indicated the ability of fly ash for the removal of F^- ion.

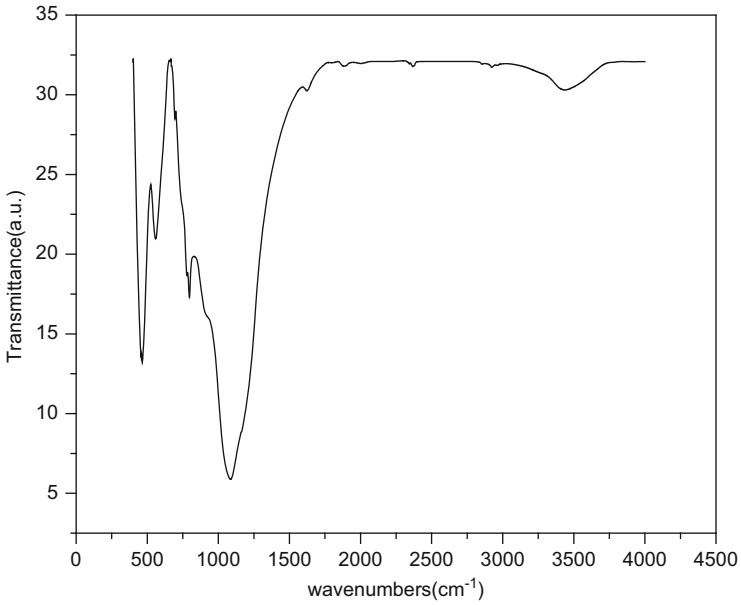

Fig. 6.6 FTIR spectrum of fly ash

- Maximum F^- ion adsorption occurred at the initial pH 2 for all the adsorbents.
- Percentage removal of F^- ion increases with the increase of contact time, adsorbent dosage but it is the reverse for initial fluoride ion concentration.
- Pseudo-2nd-order model was more applicable for the adsorption process as evidenced from the statistical parameters.
- Langmuir isotherm model was more applicable than the other isotherm models studied.
- The diffusion coefficient and sorption energy indicated that the interactions between F^- ion and natural sorbents were chemical in nature.
- The thermodynamic study indicated that the sorption process is spontaneous and endothermic in nature.
- Active functional groups for the F^- ion adsorption process were identified by FTIR studies.
- Industrial waste (fly ash) is suitable for F^- ion removal from aqueous solutions as well as from ground water at highly acidic condition but in neutral and less acidic conditions the removal efficiency is very low.

The present investigation thus indicates the ability of fly ash to remove fluoride from water in a simple way. However this may be slightly difficult for designing a treatment plant for the defluoridation of water due to highly acidic condition.

References

1. Abe I, Iwasaki S, Tokimoto T, Kawasaki N (2004) Adsorption of fluoride ions onto carbonaceous materials. J Colloid Interf Sci 275:35–39
2. Banks D, Reimann C, Røyset O, Skarphagen H (1995) Natural concentrations of major and trace elements in some Norwegian bedrock ground waters. Appl Geochem 10:1–16
3. Fawell J, Bailey K, Chilton J, Dahi E, Fewtrell L, Magara Y (2006) Fluoride in drinking water. WHO, IWA Publishing, London. ISBN 92-4156319-2
4. Biswas K, Gupta K, Goswami A, Ghosh UC (2007) Fluoride removal efficiency from aqueous solution by synthetic iron(III)-aluminum(III) mixed oxide. Ind Eng Chem Res 46: 5346
5. Singh R, Maheshwari RC (2001) Defluoridation of drinking water–a review. Ind J Environ Prot 21:983–991
6. UNICEF (2005) Unicef's position on water fluoridation; online database. www.unicef.org
7. Gaciri SJ, Davies TC (1993) The occurrence and geochemistry of fluoride in some natural waters of Kenya. J Hydrol 143:395–412
8. Czarnowski W, Wrześniowska K, Krechniak J (1996) Fluoride in drinking water and human urine in northern and central Poland. Sci Total Environ 191:177–184
9. Azbar N, Turkman A (2000) Defluorination in drinking waters. Water Sci Technol 42:403–407
10. Agarwal M, Rai K, Shrivastav R, Dass S (2003) Defluoridation of water using amended clay. J Clean Prod 11:439–444
11. Ayoob S, Gupta AK (2006) Fluoride in drinking water: a review on the status and stress effects. Crit Rev Environ Sci Technol 36:433–487
12. Wang LFM, Huang JZ (1995) Outline of control practice of endemic fluorosis in China. Social Sci Med 411:1191–1195
13. Mjengera H, Mkongo G (2003) Appropriate defluoridation technology for use in fluorotic areas in Tanzania. Phys Chem Earth 28:1097–1104
14. Ortiz-Pérez D, Rodríguez-Martínez M, Martínez F (1997) Endemic fluorosis in Mexico. Fluoride 30:233–239
15. Kruse E, Ainchil J (2003) Fluoride variations in groundwater of an area in Buenos Aires province, Argentina. Environ Geol 44:86–89
16. WRC (2001) Distribution of fluoride-rich groundwater in eastern and Mogwase region of northern and north-west province. WRC Report No. 526/1/01 1.1-9.85
17. Saxena KL, Sewak R (2015) Fluoride consumption in endemic villages of India and its remedial measures. Int J Eng Sci Invent 4:58–73
18. Bhattacharya J, Mandal SN (2014) Effect of nitrate, sulphate and fluoride of wastewater and groundwater. Res J Chem Environ 18:50–56
19. Mahramanlioglu M, Kizilcikli I, Bicer IO (2002) Adsorption of fluoride from aqueous solution by acid treated spent bleaching earth. J Fluorine Chem 115:41–47
20. Chinoy NJ (1991) Effects of fluoride on physiology of animals and human beings. Indian J Environ Toxicol 1:17–32
21. Harrison PTC (2005) Fluoride in water: a UK perspective. J Fluorine Chem 126:1448–1456
22. Fan X, Parker DJ, Smith MD (2003) Adsorption kinetics of fluoride on low cost materials. Water Res 37:4929–4937
23. Zhou Y, Yu C, Shan Y (2004) Adsorption of fluoride from aqueous solution on La^{3+} impregnated crosslinked gelatin. Sep Purif Technol 36:89–94
24. Islam M, Patel RK (2011) Thermal activation of basic oxygen furnace slag and evaluation of its fluoride removal efficiency. Chem Eng J 169:68–77
25. Online database: http://www.fluoridealert.org/health/
26. WHO (2004) Guidelines for drinking water quality, Geneva
27. Shen F, Chen X, Gao P, Chen G (2003) Electrochemical removal of fluoride ions from industrial wastewater. Chem Eng Sci 58:987–993

28. Mohapatra M, Anand S, Mishra BK, Giles DE (2009) Review of fluoride removal from drinking water. J Environ Manage 91:67–77
29. Miretzky P, Cirelli AF (2001) Fluoride removal from water by chitosan derivatives and composites: a review. J Fluorine Chem 132:231–240
30. Ayoob S, Gupta AK, Bhat VT (2008) A conceptual overview on sustainable technologies for defluoridation of drinking water and removal mechanisms. Crit Rev Environ Sci Technol 38:401–470
31. James RO, Healy TW (1972) Adsorption of hydrolysable metal ions at the oxide water interface. III. A thermodynamic model of adsorption. J Colloid Interf Sci 40:65–81
32. Panday et al (1983) Removal of metal ions from water and wastewater. Nat Acad Sci Lett 6:415–418
33. Chaturvedi AK, Pathak KC, Singh VN (1988) Fluoride removal from water by adsorption on china clay. Appl Clay Sci 3:337–346
34. Lagergren S (1898) Zur theorie der sogenannten adsorption geloster stoffe. Kungliga Svenska Vetenskapsakademiens Handlingar 24:1–39
35. Ho YS, McKay G (2000) Study of the sorption of divalent metal onto peat. Adsorp Sci Technol 18:639–650
36. Teng H, Hsieh CT (1999) Activation energy for oxygen chemisorption on carbon at low temperature. Ind Eng Chem Res 38:292–297
37. Weber WJ, Morris JC (1963) Kinetics of adsorption on carbon from solution. J Sanit Eng Div Am Soc Civ Eng 89:31–60
38. McKay G, Otterburn MS, Sweeney AG (1981) Surface mass transfer processes during colour removal from effluent using silica. Water Res 15:327–331
39. Low MJD (1960) Kinetics of chemisorption of gases on solids. Chem Rev 60:267–312
40. Ho YS, McKay G (2002) Application of kinetic models to the sorption of copper(II) onto peat. Adsorp Sci Technol 20:797–815
41. Reyes RBG, Mendez JRR (2010) Adsorption kinetics of chromium(III) ions on agrowaste materials. Bioresour Technol 101:8099–8108
42. Zaki AB, El-Sheikh MY, Evans J, El-Safty SA (2000) The sorption of some aromatic amines onto amberlite IRA-904 anion-exchange resin. J Colloid Interf Sci 221:58–63
43. Kalavathy MH, Karthikeyan T, Rajgopal S, Miranda LR (2005) Kinetic and isotherm studies of Cu(II) adsorption onto H_3PO_4-activated rubber wood sawdust. J Colloid Interf Sci 292: 354–362
44. Langmuir I (1918) The adsorption of gases on plane surfaces of glass, mica and platinum. J Am Chem Soc 40:1361–1368
45. Freundlich H (1906) Adsorption in solution. Phys Chem Soc 40:1361–1368
46. Temkin MJ, Pyzhev V (1940) Recent modifications of Langmuir isotherms. Acta Physiochim URSS 12:217–222
47. Dubinin MM, Zaverina ED, Radushkevich LV (1947) Sorption and structure of active carbons. Adsorption of organic vapors. Zhurnal Fizicheskoi Khimii 21:1351–1362
48. Polanyi M (1932) Theories of the adsorption of gases. A general survey and some additional remarks. Trans Faraday Soc 28:316–333
49. Naiya TK, Bhattacharya AK, Mandal S, Das SK (2009) The sorption of lead(II) ions on rice husk ash. J Hazard Mater 163:1254–1264
50. Webi TW, Chakravorty RK (1974) Ore and solid diffusion models for fixed bed adsorbers. AIChE J 20:228–238
51. Dakiky M, Khamis M, Manassra A, Mereb M (2002) Selective adsorption of chromium(VI) in industrial wastewater using low-cost abundantly available adsorbents. Adv Environ Res 6: 533–540
52. Malkoc E, Nuhoglu Y (2007) Determination of kinetic and equilibrium parameters of the batch adsorption of Cr(VI) onto waste acorn of *Quercus ithaburensis*. Chem Eng Process 46: 1020–1029

Chapter 7
Comparative Review of the Synthesis of Flavanones *via* the Reaction of Cinnamic Acids and Phenols and the Reaction of 2-Hydroxyacetophenones and Benzaldehydes

Ishmael B. Masesane, Kenamile Rabasimane, and Kibrom G. Bedane

Abstract This review compares the efficiency of a three-step procedure developed by the authors for the synthesis of flavanones that relied on the boron trifluoride diethyl etherate ($BF_3{\cdot}OEt_2$)-mediated reaction of cinnamic acid and phenols to the one-step or two-step procedures reported in literature involving the reaction of 2-hydroxyacetophenones and benzaldehydes. The three-step procedure was found to give the flavanones in comparable yields to both the one-step and the two-step literature methods.

7.1 Introduction

The isolation and characterization of flavonoids from medicinal and economically relevant plants has been the main focus of research in the Department of Chemistry, University of Botswana since the 1980s. These research endeavors have contributed several novel flavonoid structures and promising biological activities of these isolated compounds [1]. It however became evident that the limited quantities of compounds that are isolated from plants made it difficult to develop them further into useful chemicals.

In an effort to subvert the quantity problem mentioned above, we develop a synthetic method for the preparation of flavanones from the reaction of cinnamic acids and phenols. Flavanones are a class of flavonoids that has attracted our interest because of their presence in the genus *Erythrina*. The genus *Erythrina* has been at the centre of our phytochemical work for over a decade [2–4]. In this review, our cinnamic acid method for the synthesis of flavanones will be compared

I.B. Masesane (✉) • K. Rabasimane • K.G. Bedane
Department of Chemistry, University of Botswana, Private Bag, 00704 Gaborone, Botswana
e-mail: masesane@mopipi.ub.bw; krabasimane@gmail.com; kibromg09@gmail.com

P. Ramasami et al. (eds.), *Emerging Trends in Chemical Sciences*,
DOI 10.1007/978-3-319-60408-4_7

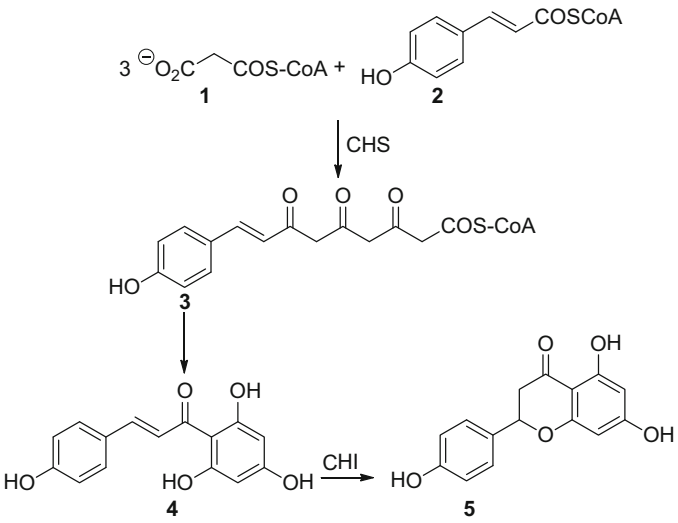

Scheme 7.1 Biosynthesis of flavanones

to the conventional methods that rely on the reaction of 2-hydroxyacetophenones and benzaldehydes.

At this juncture, it is instructive to draw attention to the fact that our cinnamic acid route for the synthesis of flavanones was inspired by the biosynthetic pathway. Flavanones biosynthesis involves the chalcone synthase(CHS)-catalyzed condensation of three molecules of malonyl-CoA **1** and one molecule of p-coumaroyl-CoA **2** to give the polyketide intermediate **3** that cyclizes and aromatizes to afford chalcone **4**. The chalcone is then cyclized to the corresponding flavanone **5** in a reaction catalyzed by the enzyme chalcone isomerase (CHI), as shown in Scheme 7.1 [5].

Section 7.2 of this chapter will discuss the authors' procedure for the synthesis of flavanones *via* the reaction of cinnamic acid derivatives with phenols. Section 7.3 will review the literature methods for the synthesis of flavanones *via* the reaction of 2-hydroxyacetophenone derivatives with benzaldehydes and compare the efficiency of these methods to the authors' procedure.

7.2 Preparation of Flavanones *via* the Reaction of Cinnamic Acids and Phenols

The preparation of flavanones that involves $BF_3{\cdot}OEt_2$-mediated reaction of cinnamoyl chlorides and phenols was recently reported by our group [6]. The procedure involved conversion of cinnamic acids into the corresponding cinnamoyl chlorides using thionyl chloride, reaction of the cinnamoyl chlorides with phenols

in the presence of $BF_3{\cdot}OEt_2$ to give chalcones and finally cyclisation of chalcones in the presence of a base to give the flavanones. For example, the reaction of cinnamic acid **6** with thionyl choride ($SOCl_2$) gave cinnamoyl chloride **7** which was not isolated. Excess $SOCl_2$ was removed under vacuum and cinnamoyl chloride **7** was reacted with resorcinol in the presence of $BF_3{\cdot}OEt_2$ under reflux to give chalcone **8** in 72% yield (Scheme 7.2). Cyclisation of chalcone **8** in the presence of NaOH gave flavanone **9** in overall yield of 68% [6].

Further reactions involving cinnamoyl chloride **7** and phenols **10**, **11** and **12** in the presence of $BF_3{\cdot}OEt_2$ followed by cyclisation using NaOMe instead of KOH gave flavanones **16**, **17** and **18** in 49, 57 and 36% yields respectively (Scheme 7.3) [6]. It is important to note that 4-nitrophenol and 3-nitrophenol failed to react with cinnamoyl chloride **7** to give the corresponding chalcones. The nitro group is a strongly electron-withdrawing group that deactivates the aromatic ring against

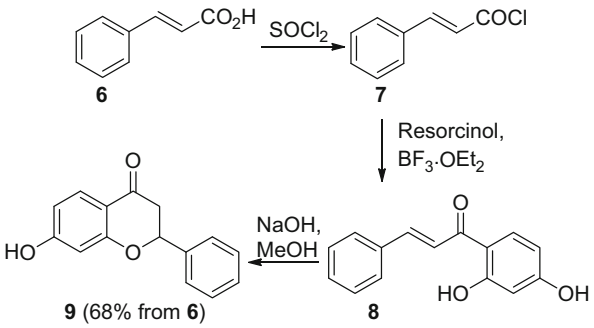

Scheme 7.2 Synthesis of flavanone **9** from cinnamic acid **6**

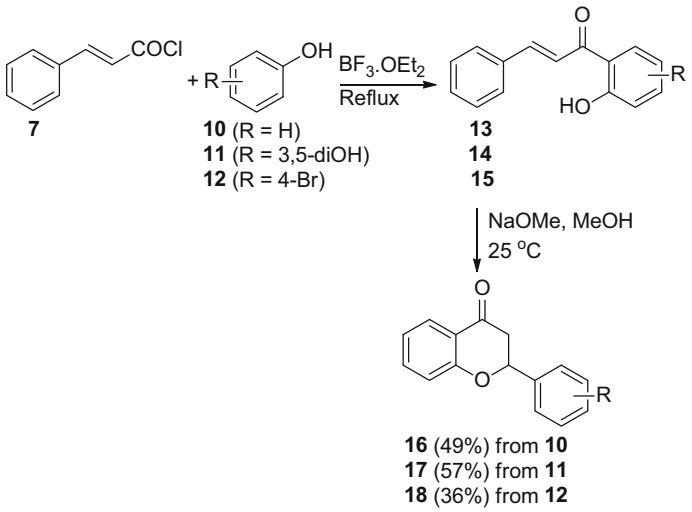

Scheme 7.3 Synthesis of flavanones **16**–**18**

electrophilic substitution reactions, therefore these results were not surprising. However, bromophenol **12**, a phenol with a less electron-withdrawing bromo group, reacted with acid chloride **7** to give chalcone intermediate **15** in lower yield of 42%. Cyclisation of chalcone **15** afforded flavanone **18** in 36% overall yield.

The effects of both electron donating and withdrawing groups attached to the cinnamic acid on the efficiency of the reaction were also investigated. Thus, 3-methoxycinnamic acid **19** was converted to its acid chloride using $SOCl_2$, reacted with resorcinol to give chalcone **24** in 75% yield and then cyclized using KOH to give flavanone **29** in 92% yield (Scheme 7.4) [6]. Interestingly, subjection of 4-methoxycinnamic acid **20** to the same reaction conditions failed to give the corresponding chalcone **25**. Similarly, 3-nitrocinnamic acid **21** was converted to chalcone **26** in 66% yield and chalcone **26** was subsequently cyclized in the presence of KOH to afford flavanone **30** in 90% yield. However, attempts to convert 4-nitrocinnamic acid **22** to the corresponding chalcone **27** under the same reaction conditions failed. 4-Chlorocinnamic acid **23**, on the other hand was successively converted to its acid chloride and reacted with resorcinol in the presence of $BF_3{\cdot}OEt_2$ to give chalcone **28** in lower yield of 44%. Cyclisation of chalcone **28** afforded flavanone **31** in 93% yield.

The logical explanation for the similar effect of 4-OMe and 4-NO_2 groups is that $BF_3{\cdot}OEt_2$ coordinates with the oxygen atom of the methoxy group and turns it into an electron-withdrawing group. The effect is less pronounced for 3-OMe and

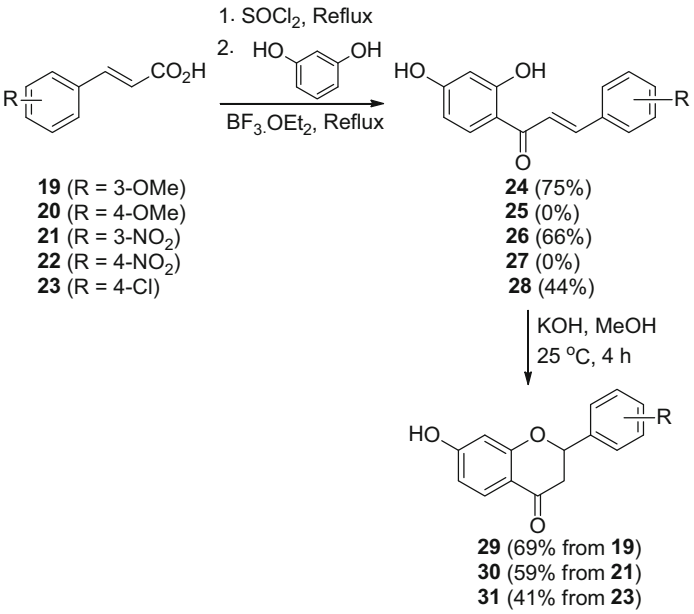

Scheme 7.4 Synthesis of flavanones **29**–**31**

3-NO_2 substituted cinnamic acid substrates because of lack of conjugation between the substituents and the acid carbonyl group.

To the best of the knowledge of the authors, this is the only method in the literature for the synthesis of flavanones from cinnamic acids. Flavanones were prepared in three steps in overall yields of 36–69%.

7.3 Preparation of Flavanones *via* the Reaction of 2-Hydroxyacetophenones and Benzaldehydes

Unlike the preparation of flavanones from the reaction of cinnamic acids and phenols described above, the synthesis of flavanones through the reaction of 2-hydroxyacetophenones and benzaldehydes has been reported extensively in the literature. The synthesis of flavanones through this route can be achieved either by a one-step process or a two-step procedure. Zhou and co-workers achieved the one-step synthesis of flavanones **37**–**40** in 54–68% yields from acetophenone **32** and benzaldehydes **33**–**36** in the presence of catalytic amount of pyrrolidine and $BF_3{\cdot}OEt_2$ (Scheme 7.5) [7]. The benzaldehydes **34**, **35** and **36** with electron-withdrawing groups afforded the corresponding flavanones in lower yields when compared to the benzaldehyde **33**. This procedure afforded flavanones with electron-withdrawing groups on ring B in better yields that the authors' procedure described in Sect. 7.2.

A one-step Julia-Kocienski olefination reaction was used by Kumar and co-workers in the synthesis of an array of flavanones. The reaction involved the refluxing of sulphone **41** with benzaldehydes **33**, **42**, **43** and **44** in the presence of the base 1,8-diazabicyclo[5.4.0]undec-7-ene (DBU) to give flavanones **45**, **46**, **47** and **48** respectively in 40–68% yields (Scheme 7.6) [8]. Benzaldehyde **43** with an unprotected hydroxyl group gave the flavanone with the lowest yield. It is important to note that the authors' procedure discussed in Sect. 7.2 tolerated free hydroxyl groups and afforded the corresponding flavanones in better yields.

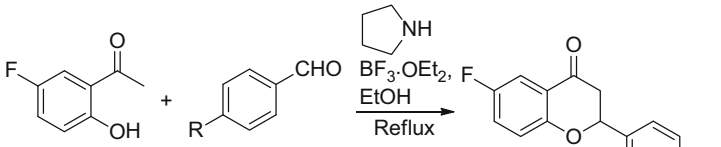

32

33 (R = H)
34 (R = NO_2)
35 (R = CO_2Me)
36 (R = CHO)

37 (68%)
38 (54%)
39 (60%)
40 (60%)

Scheme 7.5 One-step synthesis of flavanones **37**–**40** from **32**

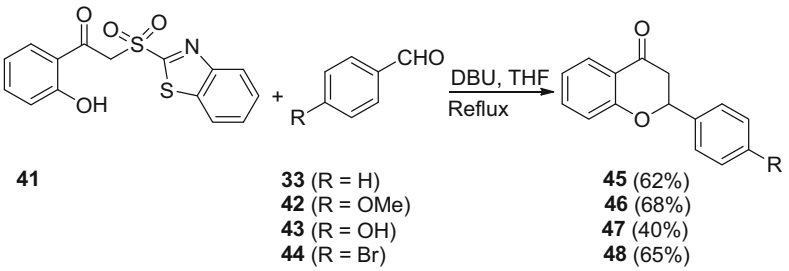

41

33 (R = H)
42 (R = OMe)
43 (R = OH)
44 (R = Br)

45 (62%)
46 (68%)
47 (40%)
48 (65%)

Scheme 7.6 One-step synthesis of flavanones **45**–**48**

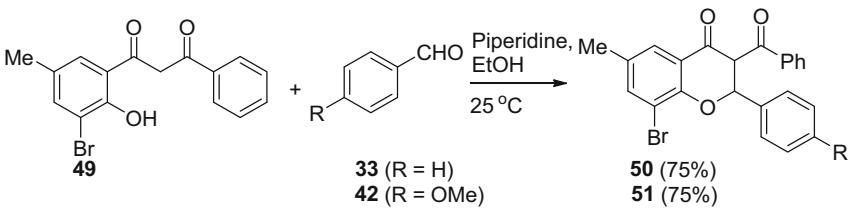

49

33 (R = H)
42 (R = OMe)

50 (75%)
51 (75%)

Scheme 7.7 One-step synthesis of flavanones **50** and **51**

In their one-step approach to flavanones **50** and **51**, Mahalle and Khaty relied on the reaction of diketone **49** with benzaldehydes **33** and **42** respectively in the presence of the base piperidine [9]. Thus, flavanones **50** and **51** were prepared in 75% yields by the condensation of diketone **49** with benzaldehydes **33** and **42** respectively in ethanol for two hours in the presence of catalytic amount of piperidine (Scheme 7.7). The products were purified by recrystallization and were afforded in slightly better yields than those achieved in the authors' procedure discussed in Sect. 7.2.

Albogami and co-workers have described the use of microwave irradiation in the one-step synthesis of flavanones. Their procedure involved reactions of acetophenones **52**–**54** with benzaldehyde **33** to give the corresponding flavanones **56**–**58** in 81–88% yield. Further reactions of 4-chlorobenzaldehyde **55** and acetophenones **52** and **53** afforded the corresponding flavanones **59** and **60** in 92 and 88% yield respectively (Scheme 7.8) [10]. This method showed an excellent tolerance of different functional groups on both the acetophenone and benzaldehyde reagents and gave yields of the flavanone that were considerably higher that those achieved by the authors' procedure discussed in Sect. 7.2.

It is important to note that the yields of the majority of the one step-procedures discussed above were not significantly different from those achieved in the authors' three-step procedure discussed in Sect. 7.2. The exceptions that gave significantly higher yields of the flavanones are the reactions catalyzed by an organic base and the one performed under microwave irradiation.

In addition to the one-step procedures discussed above, flavanones have been prepared *via* two-step procedures involving the reaction of 2-hydroxyacetophenones and benzaldehydes to give chalcones followed by cyclisation of the chalcones. The expedient synthesis of flavanone **64** for example

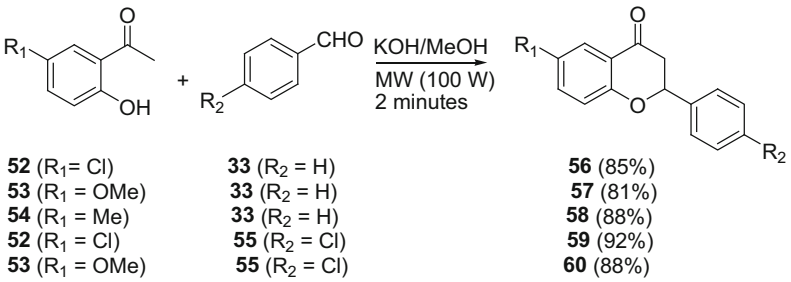

Scheme 7.8 Microwave mediated one-step synthesis of flavanones **56–60**

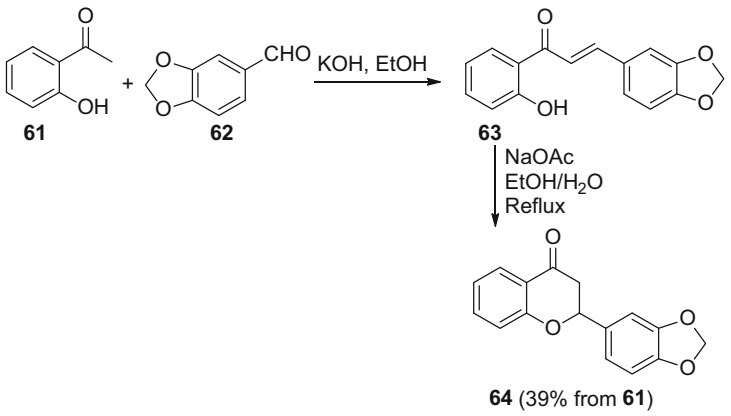

Scheme 7.9 Synthesis of flavanone **64** in two steps

was achieved by the condensation of 2-hydroxyacetophenone **61** and benzaldehyde **62** in the presence of KOH in ethanol to give chalcone **63** that was subsequently cyclized in the presence of sodium acetate (NaOAc) under reflux, Scheme 7.9 [11]. The overall percentage yield of this reaction was 39% and was significantly lower than that of the authors' three-step procedure discussed in Sect. 7.2.

A similar two-step procedure was used by Rao and co-workers in the preparation of the protected derivative of a prenylated flavanone isolated from *Dalea boliviana*. Condensation of 2-hydroxyacetophenone **65** and benzaldehyde **66** in the presence of KOH gave chalcone **67** that was cyclized in the presence of NaOAc under reflux to give flavanone **68** in overall yield of 38% (Scheme 7.10) [12]. The prenyl units did not significantly affect the yield of the reaction when compared to the reaction summarized in Scheme 7.9.

A third approach to flavanones in two steps by Mardjan and co-workers involved condensation of 2-hydroxyacetophenone **69** with benzaldehydes **42** and **70** to give the corresponding chalcones **71** and **72** in 81 and 71% yield respectively. Cyclisation of chalcones **71** and **72** in the presence of NaOAc gave the corresponding flavanones **73** and **74** in overall yields of 54 and 42% respectively (Scheme 7.11) [13]. The presence of the acid group in the 2-acetophenone reagent

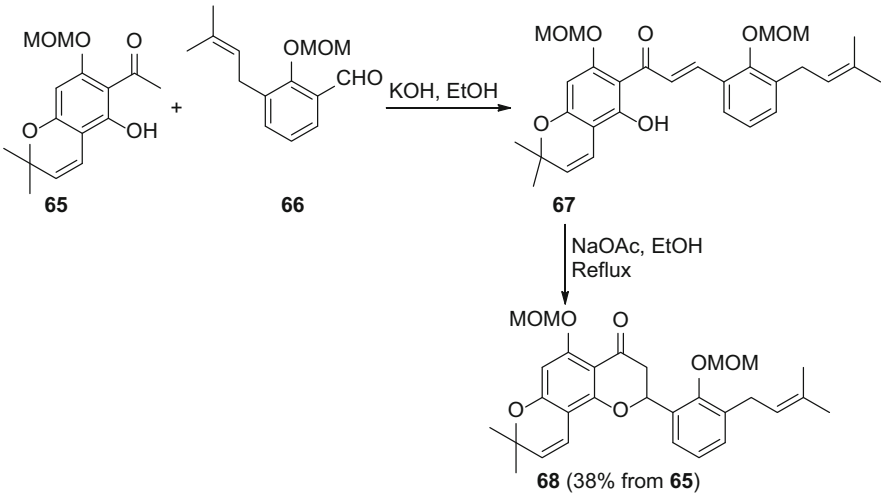

Scheme 7.10 Synthesis of flavanone **68** in two steps

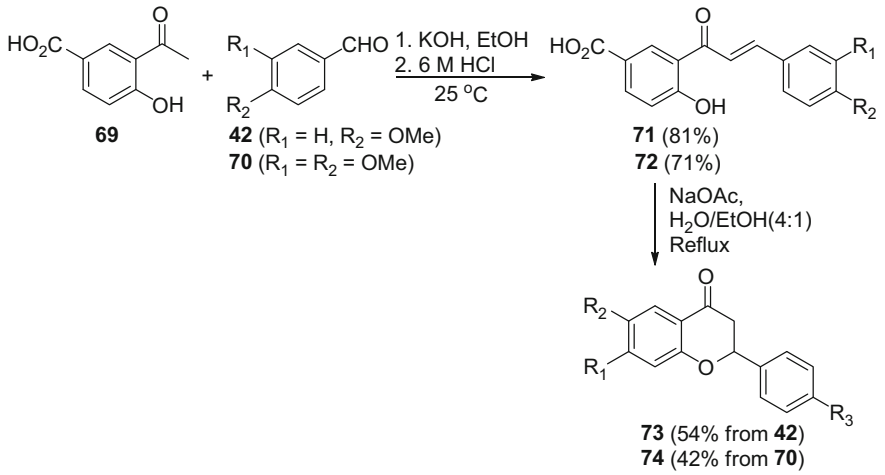

Scheme 7.11 Synthesis of flavanones **73** and **74** in two steps

is suspected to be responsible for the increase in the overall yield of this procedure. The overall yields are comparable to those achieved by the authors' procedure discussed in Sect. 7.2.

In another approach to the chalcone intermediate, Ketabforoosh and co-workers used NaOH instead of KOH as the base in the condensation of 2-hydroxyacetophenone and aldehydes as illustrated in Scheme 7.12. Reactions of 2-hydroxyacetophenone **61** and benzaldehydes **70**, **75** and **76** gave chalcone intermediates **77**, **78** and **79** respectively [14]. It is worth noting that the reaction

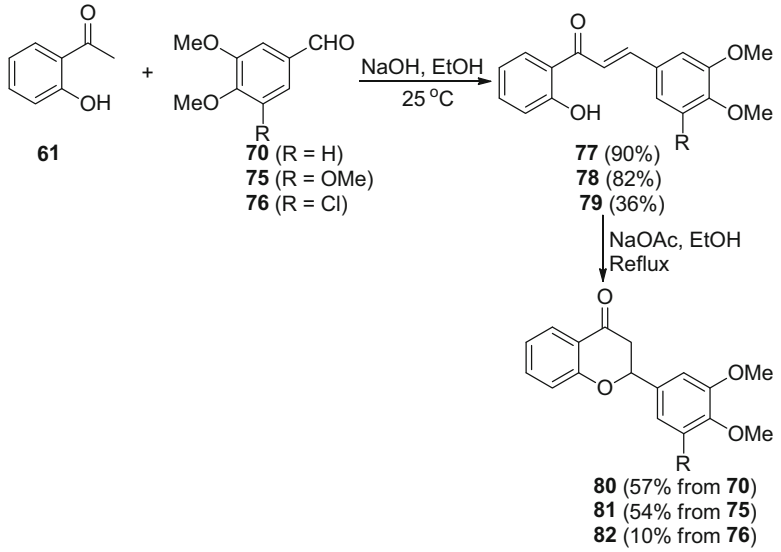

Scheme 7.12 Synthesis of flavanones **80**–**82** in two steps

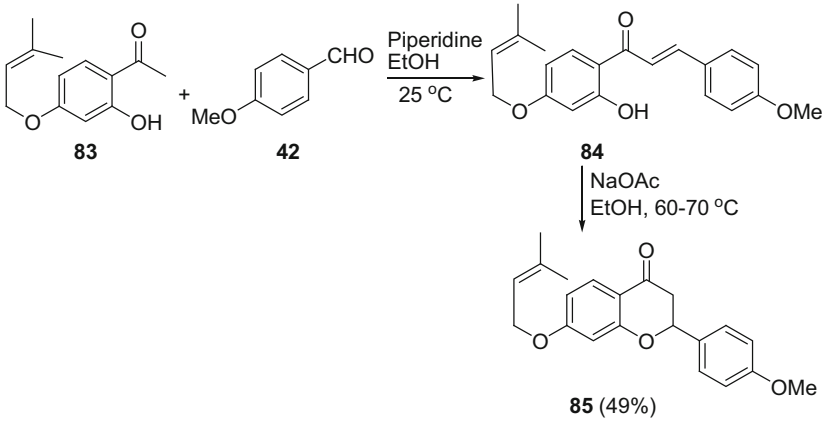

Scheme 7.13 Synthesis of flavanone **85** in two steps

that involved the chloro-substituted benzaldehyde **76** gave the corresponding intermediate **79** in a very poor yield of 36%. Subsequent cyclisation of the chalcone intermediates **77**–**79** afforded the corresponding flavanones **80**–**82** in overall yields of 57, 54 and 10% respectively.

Bhasker and co-workers have reported the piperidine-mediated condensation of 2-hydroxyacetophenone **83** and benzaldehyde **42** in the synthesis of chalcone intermediate **84** that was subsequently cyclized in the presence of NaOAc to give flavanone **85** in overall yield of 49% (Scheme 7.13) [15].

An interesting two-step procedure was reported by Lee and co-workers and it involved the lithium diisopropylamide (LDA)-mediated condensation of 2-hydroxyacetophenones **53**, **61** and **86** and benzaldehydes **22**, **33** and **42** in THF to give an array of 3-hydroxyketone intermediates that were subsequently cyclized to give flavanones [16]. The condensation of benzaldehyde **33** and 2-hydroxyacetophenones **53**, **61** and **86** under these conditions afforded the corresponding 3-hydroxyketone intermediates **89**, **87** and **88** respectively. Cyclisation of intermediates **87**, **88** and **89** by treating them with triphenylphosphine/diethyl azodicarboxylate (Ph_3P/DEAD) in CH_2Cl_2 at 0 °C afforded the corresponding flavanones **45**, **92** and **57** in overall yields of 63–69%, as shown in Scheme 7.14. In a parallel sequence of reactions, 2-hydroxyacetophenone **61** underwent condensation reactions with benzaldehydes **22** and **42** to give the corresponding hydroxyketone intermediates that were cyclised to afford flavanones **93** and **46** respectively.

In general, the two-step procedures involving the reaction of 2-hydroxyacetophenones or its derivatives and benzaldehydes afforded the flavanones in comparable yields to those achieved in the authors' three-step procedure for the synthesis of flavanones from cinnamic acids described in Sect. 7.2.

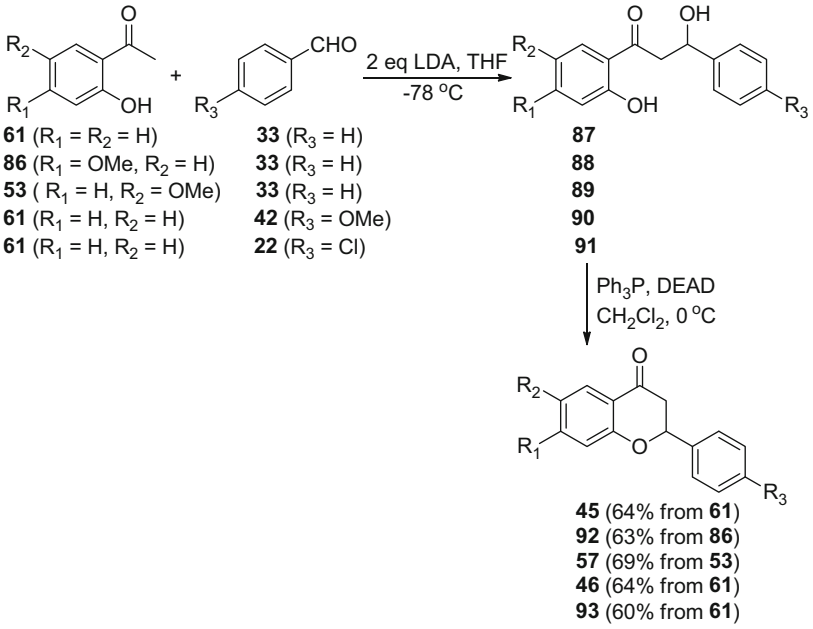

Scheme 7.14 Synthesis of flavanones **45**, **46**, **57**, **92** and **93**

7.4 Conclusion

A comparative review of the synthesis of flavanones via the reaction of cinnamic acids and phenols and via the reaction of 2-hydroxyacetophenones and benzaldehydes was achieved. Both methods afforded the flavanones in yields that were not in general significantly different. The two methods are highly complementary. Flavanones that are not accessed through one method are easily prepared using the other procedure.

References

1. Majinda RRT, Abegaz BM, Bezabih M et al (2001) Recent results from natural product research at the University of Botswana. Pure Appl Chem 73:1197–1208
2. Chacha M, Bojase G, Majinda RRT (2005) Antimicrobial and radical scavenging flavonoids from the stem wood of *Erythrina latissima*. Phytochemistry 66:99–104
3. Bedane KG, Kusari S, Eckelmann D et al (2015) Erylivingstone A–C with antioxidant and antibacterial activities from *Erythrina livingstoniana*. Fitoterapia 105:113–118
4. Bedane KG, Kusari S, Masesane IB et al (2016) Flavanones of *Erythrina livingstoniana* with antioxidant properties. Fitoterapia 108:48–54
5. Khan MK, Zill-E-Huma DO (2014) A comprehensive review on flavanones, the major citrus polyphenols. J Food Compos Anal 33:85–104
6. Bedane KG, Majinda RRT, Masesane IB (2016) Fast and efficient synthesis of flavanones from cinnamic acids. Synthetic Commun 46:1803–1809
7. Zhou S, Zhou Y, Xing Y, Wang N, Cao L (2011) Exploration on asymmetric synthesis of flavanone catalyzed by (S)-pyrrolidinyl tetrazole. Chirality 23:504–506
8. Kumar A, Sharma S, Tripathi VD, Srivastava S (2010) Synthesis of chalcones and flavanones using Julia-Kocienski olefination. Tetrahedron 66:9445–9449
9. Mahalle PR, Khaty NT (2010) Synthesis of some bromo-substituted 3-aroyl flavanones and flavones. E-J Chem 7:1359–1361
10. Albogami AS, Karama U, Mousa AA et al (2012) Simple and efficient one step synthesis of functionalized flavanones and chalcones. Orient J Chem 28:619–626
11. Murti Y, Mishra P (2014) Synthesis and evaluation of flavanones as anticancer agents. Indian J Pharm Sci 76:163–166
12. Rao BV, Ramanjaneyulu K, Rao TB, Rambabu T (2011) First total synthesis of three anti-tyrosinase activity prenylated flavanones from *Dalea boliviana*. J Chem Pharm Res 3:49–54
13. Mardjan MID, Ambarwati R, Matsjeh S et al (2012) Synthesis of flavanone-6-carboxylic acid derivatives from salicylic acid derivative. Indo J Chem 12:70–76
14. Ketabforoosh SHME, Kheirollahi A, Safavi M et al (2014) Synthesis and anti-cancer activity evaluation of new dimethoxylated chalcone and flavanone analogs. Arch Pharm Chem Life Sci 347:1–8
15. Bhasker N, Prashanthi Y, Subba Reddy BV (2015) Piperidine mediated synthesis of new series of prenyloxy chalcones, flavanones and comparative cytotoxic study. Pharm Lett 7:8–13
16. Lee JI, Jung MG, Jung HJ (2007) A novel synthesis of flavanones from 2-hydroxybenzoic acids. Bull Korean Chem Soc 28:859–862

Chapter 8
Calcium Alginate-*Mangifera indica* Seed Shell Composite as Potential Biosorbent for Electroplating Wastewater Treatment

Malvin Moyo, Vusumzi E. Pakade, and Sekomeng J. Modise

Abstract Surface functionalized biosorbent was developed from mango seed shell powder through ethylenediaminetetraacetic acid (EDTA) grafting and encapsulation in calcium alginate gel beads. Introduction of EDTA to the sorbent surface was established by elemental analysis and Fourier transform infra-red spectroscopic analysis. The performance of the composite biosorbent in the removal of copper, chromium, nickel and iron from electroplating wastewater was evaluated through consecutive batch column adsorption and desorption experiments. At innate initial pH of 3.4, metal removal varied within the following ranges: 5.5–12.3% for copper, 2.3–14.8% for chromium, 2.3–4.4% for nickel, and 2.3–13.8% for iron. Acidification of the wastewater to initial pH of 1.8 yielded generally higher metal removal. This hinted at chromic ester formation followed by a redox reaction involving oxidation of $–CH_2OH$ groups on the cellulosic components of the mango material to more potent –COOH groups simultaneously with reduction of chromium from hexavalent to trivalent state.

8.1 Introduction

Mango seeds constitute the bulk of solid waste from mango fruit processing in South Africa [1], hence massive potential for sustainable use of mango seed waste exists in the country's mango producing regions. Mango seed shells are typical lignocellulosic biomass that have lignin, cellulose and hemicelluloses as their major constituents [2]. These plant components possess hydroxyl, carbonyl and carboxyl functional groups capable of acting as metal ion binding sites.

M. Moyo • V.E. Pakade
Department of Chemistry, Vaal University of Technology, Vanderbijlpark 1911, South Africa

S.J. Modise (✉)
Institute of Chemical and Biotechnology, Vaal University of Technology, Vanderbijlpark 1911, South Africa
e-mail: joe@vut.ac.za

P. Ramasami et al. (eds.), *Emerging Trends in Chemical Sciences*,
DOI 10.1007/978-3-319-60408-4_8

In their natural state, however, lignocellulosic biosorbents often exhibit low sorption capacities and tend to increase the chemical oxygen demand and total organic content of treated water through leaching of water soluble organics [3]. Moreover, application of fine biosorbent powders in column mode presents problems of clogging and development of high pressure drop, sorbent swelling and poor regeneration for reuse.

To date, no literature is available on ligand grafted mango biosorbents for removal of metal ions from aqueous solutions. This paper reports the preparation of EDTA grafted mango seed shell biosorbent. The functionalized biomass was adapted for column adsorption by immobilization in calcium alginate. The biosorbent composite was applied to electroplating wastewater sample treatment in a preliminary study of its performance.

8.2 Materials and Methods

8.2.1 Mango Seed Shell Preparation and Characterization

Waste mango seeds obtained from a farm in Tzaneen were washed, dried, milled and sieved with subsequent use of powder particles within the 90–425 μm diameter range. Alkali treated mango seed shell powder (MSSP-AT) was then prepared by treatment with 5 M sodium hydroxide solution at room temperature under stirring for 3 h. The residue was filtered off and washed once with 1% (v/v) acetic acid solution and then repeatedly with distilled water until the rinse water was approximately pH 7. Thereafter, the MSSP-AT was dried in an oven set at 90 °C for 24 h and left to cool in a desiccator before storage in a stoppered glass bottle.

Carboxyl functionalized mango seed shell powder (MSSP-CF) was prepared by treating 10.0 g of MSSP-AT with EDTA dianhydride in 400 mL DMF under stirring and reflux at 75 °C for 20 h. The suspension was then filtered and washed with DMF followed by distilled water, then saturated sodium hydrogen carbonate solution, then once more by distilled water and finally 95% ethanol. The MSSP-CF was then dried in an oven at 90 °C for 24 h, cooled and stored in a stoppered glass bottle. Schematic representation of the MSSP-CF preparation by carboxyl functionalization is shown in Fig. 8.1.

Elemental, thermal degradation and functional group analysis of the mango seed shell powders were carried out using a CHNS-O analyser (Flash 2000, Thermo Scientific, USA), a thermogravimetric analyser (TGA 400, PerkinElmer, USA) and a Fourier transform infra-red (FTIR) spectrometer (Spectrum 400, PerkinElmer, USA), respectively.

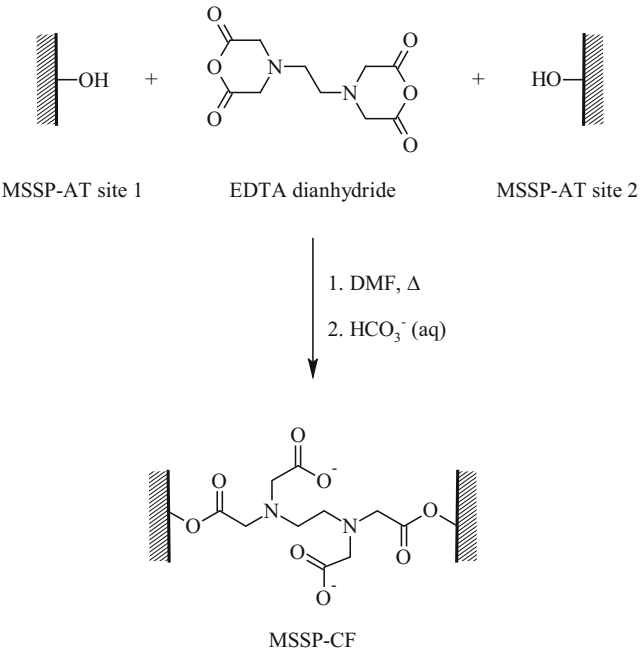

Fig. 8.1 MSSP-CF synthetic scheme

8.2.2 Composite Sorbent Preparation

Two percent (w/v) alginate solution was prepared by dissolving sodium alginate in distilled water warmed to between 60 and 70 °C. Thereafter, a 2% (w/v) suspension was prepared by adding MSSP-CF to the alginate solution and stirring overnight to ensure homogeneity. The suspension was then pumped through a micropipette tip and dropped into a 0.1 M aqueous solution of calcium chloride. The beads formed on contact were left in the calcium chloride solution for 20 h to allow hardening. Afterwards the solution was filtered off and the hydrogel beads were thoroughly washed with distilled water. The beads were frozen at −4 °C and then freeze dried for 48 h. Thus prepared, the calcium alginate-carboxyl functionalized *M. indica* seed shell composite sorbent was designated CA-MS.

8.2.3 Sorption Experiments

Two biosorption columns were prepared by packing 4.1 and 4.2 g of CA-MS in polythene tubes of 100 mm length and 15.5 mm internal diameter stoppered on either end using caps fitted with ceramic frits. Electroplating wastewater was obtained from an electroplating plant in Cape Town. The wastewater was split

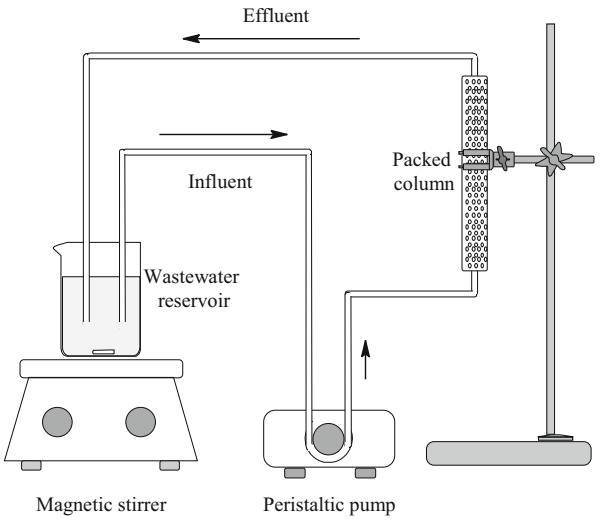

Fig. 8.2 Schematic of sorption experimental set-up

into two sets of 1 L aliquots. The first set was acidified to pH 1.8 by addition of concentrated sulfuric acid whilst the second was used in its natural state at pH 3.4.

In an individual sorption experiment, an aliquot of wastewater was pumped from a reservoir and fed upward through a column at a constant flow rate of 30 mL min^{-1}. The effluent was channeled back to the reservoir and the sorption cycle was run for 24 h (see Fig. 8.2). A sample was collected from the reservoir at the beginning and end of each sorption cycle and analyzed for copper, chromium, nickel and iron content on an inductively coupled plasma optical emission spectrophotometric (ICP-OES) analyzer (iCAP 7000, Thermo Scientific, USA). The column was then rinsed with distilled water prior to desorption cycle commencement to complete each experiment.

Desorption was carried out analogous to sorption with only 500 mL of 0.2 M hydrochloric acid solution as an eluent in place of the wastewater. After desorption, a sample of the spent eluent was collected from the reservoir and taken for metal content determination using ICP-OES. The column was flushed with 0.01 M sodium carbonate solution and then rinsed with distilled water prior to reuse in repeated sorption and desorption cycles. Percentage metal removal was calculated using Eq. (8.1):

$$\%\text{Removal} = \frac{(C_i - C_f)}{C_i} \times 100\% \tag{8.1}$$

where C_i (mg L^{-1}) and C_f (mg L^{-1}) represent metal concentration in the wastewater before and after sorption, respectively. Metal recovery (mg g^{-1}) was calculated using Eq. (8.2):

$$\text{Recovery} = \frac{C_{eluent} V_{eluent}}{M} \tag{8.2}$$

where C_{eluent} (mg L^{-1}) and V_{eluent} (L) represent metal concentration in the spent eluent and eluent volume, respectively. M (g) is the dry mass of immobilized sorbent packed in the column.

8.3 Results and Discussion

8.3.1 Carboxyl Functionalization

Evidence of surface modification was provided by elemental analysis data summarized in Table 8.1. Nitrogen composition rose from 0.25% in MSSP-AT to 2.84% for MSSP-CF, which translated to introduction of 0.925 mmol of EDTA per gram of MSSP-CF. Additionally, MSSP-CF had the highest oxygen content of 49.37%, up from 46.17% for MSSP-AT thus substantiating the introduction of the oxygen rich EDTA chains.

The FTIR spectra of MSSP-AT and MSSP-CF are illustrated in Fig. 8.3. Presence of the ester C=O stretch vibration peak at 1733 cm^{-1} on the MSSP-CF spectrum signaled grafting through esterification [4]. Occurrence of the esterification reaction was corroborated by signal attenuation at 1027 cm^{-1} indicating

Table 8.1 Elemental composition of MSSP-AT and MSSP-CF

	Composition (%)				
Material	C	H	N	O[a]	C_{EDTA} (mmol g^{-1})
MSSP-AT	46.79	6.79	0.25	46.17	–
MSSP-CF	42.64	5.15	2.84	49.37	0.925

[a]Computed by difference

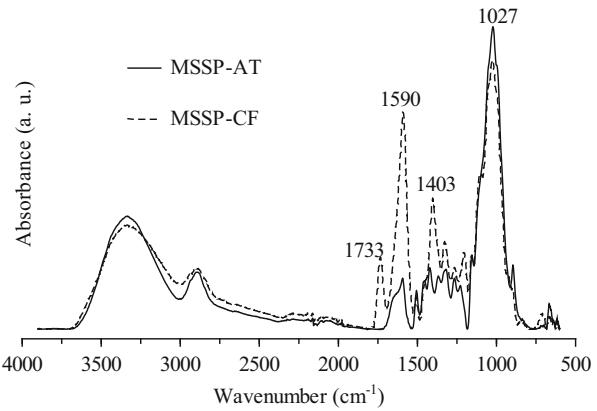

Fig. 8.3 FTIR spectra of MSSP-AT and MSSP-CF

conversion of primary alcoholic groups to ester links while EDTA ligand grafting was confirmed by signal strengthening at 1403 cm^{-1} and 1590 cm^{-1} attributed to carboxylate symmetric and asymmetric C–O stretching, respectively [5, 6].

Introduction of nitrogen, suggested earlier by the results of elemental analysis, was evidenced by appearance of the peak at 1203 cm^{-1} assigned to C–N stretch vibrations of the tertiary amine groups of the grafted ligand. Amplification of the band at 1328 cm^{-1} attributable to CH_2 wagging supported grafting of EDTA substituents, each comprising six methylene groups.

The thermogravimetric mass loss curves of the mango seed shell powders presented in Fig. 8.4 showed initial mass loss in the 40–150 °C range corresponding to loss of physically bound water accounting for 6.94% and 9.87% mass loss from MSSP-AT and MSSP-CF, respectively. Higher moisture content in MSSP-CF was due to widespread hydrogen bonding between water molecules and more accessible hydroxyls in the amorphous cellulose regions that resulted from modification [7] as well as ion-dipole interactions with carboxyl groups of the grafted ligand species. Thereafter, in the 220–340 °C range for MSSP-CF and 240–400 °C for MSSP-AT, mass loss was largely due to thermolysis of cellulose and hemicelluloses as well as, to a lesser extent, lignin [8, 9]. Above 400 °C thermal degradation was characterized by sustained, less rapid thermolysis of lignin and residual tar.

Mass loss during carbohydrate thermolysis was higher for MSSP-AT (66.94%) than MSSP-CF (47.54%). This can be explained by occurrence of competing dehydration and depolymerization pathways of the mechanism of carbohydrate thermolysis in disproportionate extents. Dehydration involved cross-linking of the cellulose chains together with evolution of water to form dehydrocellulose, which was then decomposed to char and volatile products. In the depolymerization pathway, cellulose chains were unzipped with scission of glucosidic bonds to produce laevoglucosan, which was further decomposed to volatile tars and gas [10]. The results therefore suggest that depolymerization was dominant in MSSP-AT carbohydrate degradation whereas for MSSP-CF the extent of dehydration was higher.

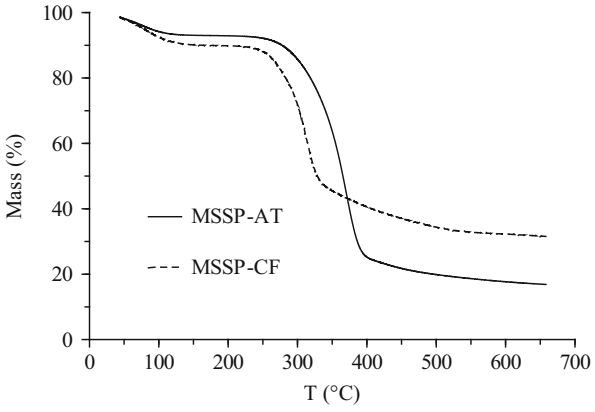

Fig. 8.4 Thermogravimetric mass loss curves of MSSP-AT and MSSP-CF

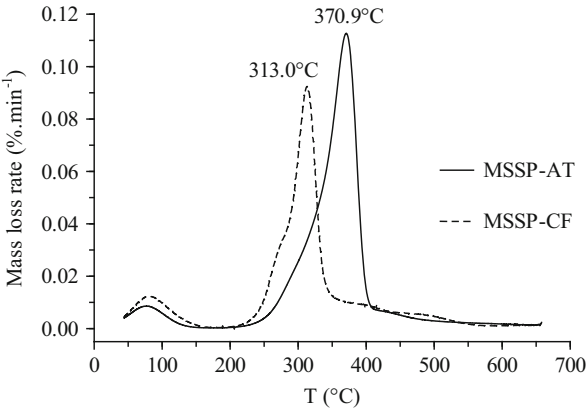

Fig. 8.5 Thermogravimetric mass loss rate curves of MSSP-AT and MSSP-CF

The temperatures corresponding to maximum degradation rate are clearly depicted in Fig. 8.5.

Maximum rate of degradation occurred at a lower temperature for MSSP-CF (313.0 °C) than MSSP-AT (370.9 °C). Since dehydration precedes depolymerization, this observation corroborated dominance of the former in MSSP-CF degradation as well as the latter during that of MSSP-AT. Suppression of depolymerization in MSSP-CF thermolysis can be explained by blockage of $–CH_2OH$ groups required for laevoglucosan formation [11] through reaction with the modifying agent resulting in a stable network of amorphous crosslinked cellulose as depicted in Fig. 8.1 [12].

8.3.2 Sorption of Cu, Cr, Ni and Fe from Electroplating Wastewater

Four consecutive column experimental runs using acidified (pH 1.8) as well as raw (pH 3.4) wastewater were carried out. Acidification was deemed desirable in order to boost chromium uptake on the basis of several works in the literature [13, 14].

8.3.2.1 Sorption from Acidified Wastewater (pH 1.8)

Fig. 8.6 illustrates observed copper, chromium, nickel and iron removal from raw electroplating wastewater with initial pH 1.8. Generally, removal of all four metals increased successively throughout the four experimental runs.

Progressive increase in metal removal was attributed to widespread oxidation of secondary hydroxyl to carboxyl groups. At initial pH of 1.8, it can be envisaged that binding of cationic metallic species would be greatly suppressed by competing H^+ ions. This apparent lack of adverse competitive effect of high initial H^+

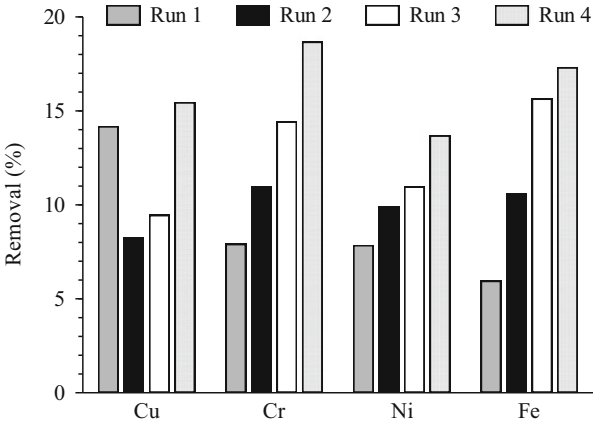

Fig. 8.6 Copper, chromium, nickel and iron removal from acidified electroplating wastewater (Room temperature, CA-MS mass: 4.0 g, Flow rate: 30 mL min^{-1}, Initial pH: 1.8, Contact time: 24 h, Initial metal concentration: Cu 904 mg L^{-1}; Cr 769 mg L^{-1}; Ni 5326 mg L^{-1}; Fe 755 mg L^{-1})

concentration on metal cation removal can be explained by consumption of large amounts of H^+ ions via a series of redox reactions as initiated by chromate ester formation as shown in Fig. 8.7.

Most of the H^+ ions in acidified solution were used in the protonation of $HCrO_4^-$ and $H_2Cr_2O_7^{2-}$ to form chromic and dichromic acid, respectively. Thereafter, chromate esters were formed on both alginate and MSSP-CF surfaces (reaction I) followed by reduction of Cr(VI) to Cr(V) with subsequent esterification of the product with a vicinal hydroxyl (reaction II). Subsequently, the bound chromium was reduced to the +4 and +3 oxidation states as depicted by reactions III and IV, respectively. Occurring simultaneously with reactions II, III and IV was oxidation of primary and secondary hydroxyls to carboxyl and keto groups, respectively [15, 16]. The overall reaction involving oxidation of hydroxyls at C6 of cellulose chains of MSSP-CF is given in Fig. 8.8.

Higher affinity of carboxyl and ketone groups in comparison to their parent hydroxyls therefore accounted for enhanced successive irreversible binding capabilities of the calcium alginate immobilized ATMS-CF.

Metal recovery from the acidified wastewater treatment column is presented in Fig. 8.9.

The amount recovered per unit mass of CA-MS packed in the column decreased from experimental runs 1–3. This suggested growing extent of irreversible binding on carboxyl groups as well as diminishing extent of reversible binding on hydroxyl groups thus corroborating occurrence of the redox reaction alluded to earlier. Moving on to run 4 there was an increase in recovery in all instances. This indicated possible saturation of the irreversible binding sites.

8.3.2.2 Sorption from Raw Wastewater (pH 3.4)

Figure 8.10 illustrates observed copper, chromium, nickel and iron removal from raw electroplating wastewater. For copper, chromium and iron highest removal,

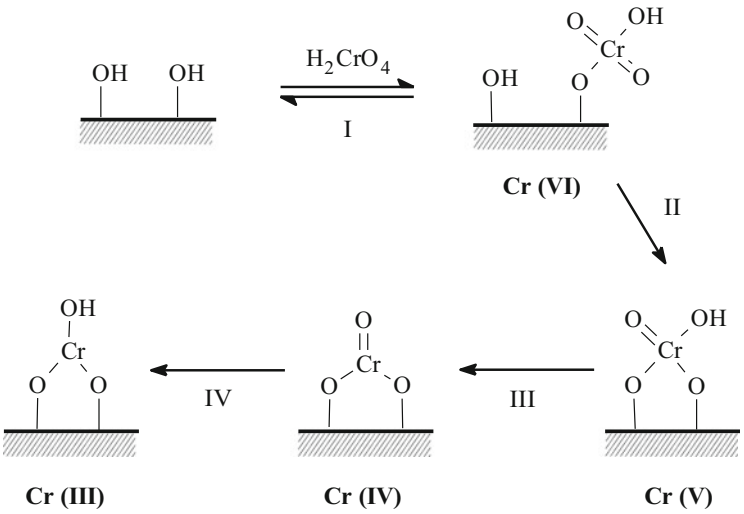

Fig. 8.7 Chromate ester formation and chromium reduction pathway

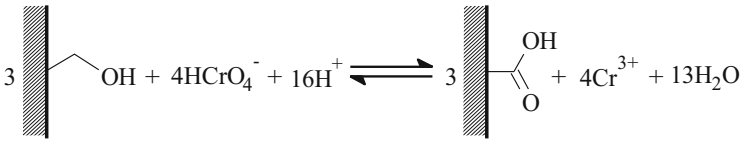

Fig. 8.8 Overall reaction for secondary hydroxyl oxidation and Cr(VI) reduction

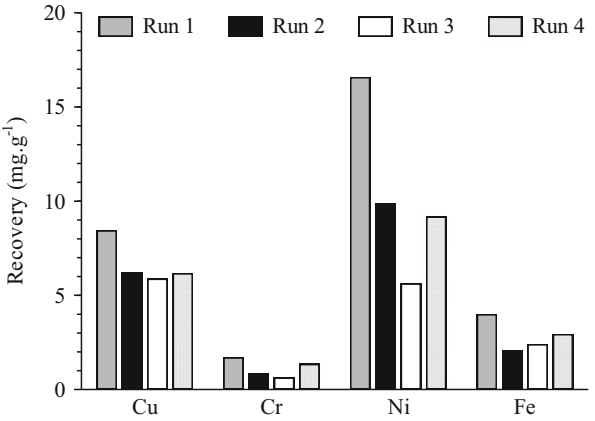

Fig. 8.9 Copper, chromium, nickel and iron recovery from acidified wastewater treatment column

noted as 12.3, 14.8 and 13.8%, respectively, occurred in the first experimental run. Thereafter, there was progressive decrease in removal which was ascribed to decrease in the number of unoccupied irreversible binding sites. Lowest removal

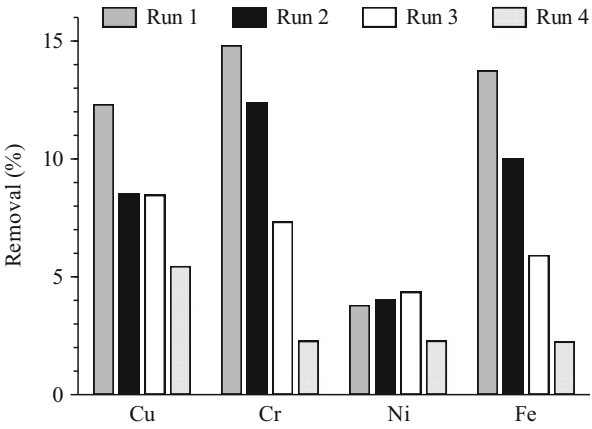

Fig. 8.10 Copper, chromium, nickel and iron removal from raw electroplating wastewater (Room temperature, CA-MS mass: 4.0 g, Flow rate: 30 mL min^{-1}, Initial pH: 3.4, Contact time: 24 h, Initial metal concentration: Cu 889 mg L^{-1}; Cr 689 mg L^{-1}; Ni 5404 mg L^{-1}; Fe 581 mg L^{-1})

for all metals was observed in the fourth experimental run and was attributed to binding on reversible binding sites, which, throughout all the desorption components of the experiments, were amenable to regeneration by hydrochloric acid scrubbing [17].

Nickel removal was lower in comparison to that of the three other metals largely due to significantly higher initial concentration in the wastewater. In contrast, however, nickel removal gradually increased from 3.8% in run 1 through 4.0% in run 2 and to a peak value of 4.4% in run 3. This suggested progressive increase in the proportion for irreversible binding sites, which was attributed to oxidation of hydroxyls to ketones and carboxyls, the oxidation products having the ability to form strong ionic interactions with metal cations. Mild oxidation was facilitated by prevailing slightly acidic conditions at pH 3.4.

Figure 8.11 presents the amounts of metal recovered from the loaded raw wastewater treatment column.

The amount of desorbed copper, chromium and iron varied slightly in the first three experimental runs. These results reflected the fraction metallic species bound reversibly on the sorbent surface, which were amenable to elution by dilute hydrochloric acid. Reduction in recovery observed in run 4 therefore confirmed conversion of reversibly binding secondary hydroxyls to irreversibly binding carboxyl groups by oxidation. Nickel recovery, however, progressively decreased from run 1 to run 3 thus corroborating the suggested change in nature of the binding functional groups. The change was only noticeable with nickel primarily because of its high initial concentration, which, owing to much higher driving force for sorption, resulted in preferential binding by freshly produced carboxyl groups. No significant change in nickel recovery was noted in run 4 signaling cessation of the oxidation process.

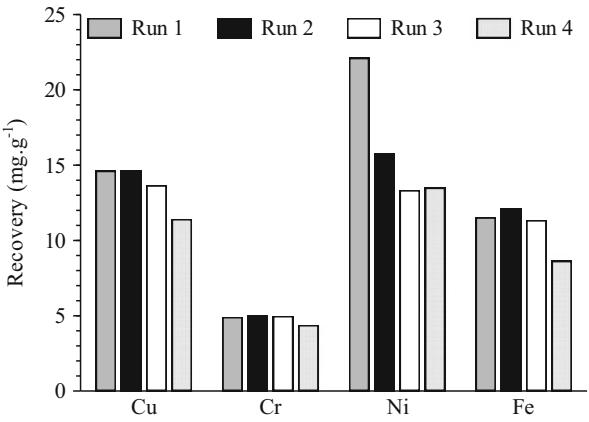

Fig. 8.11 Copper, chromium, nickel and iron recovery from raw wastewater treatment column

8.4 Conclusions

EDTA functional groups were grafted on the surfaces of mango seed shell powder. After carboxyl functionalization, the nitrogen content of the mango material increased from 0.25 % to 2.84%. Emergence of an FTIR peak corresponding to C–N bond vibration together with attenuation of carboxylate stretch vibration peaks confirmed grafting. The carboxyl functionalized mango seed shell powder was encapsulated in alginate, packed in a column and used for removal of copper, chromium, nickel and iron from electroplating wastewater. Experimental results for sorption from raw wastewater with initial pH 3.4 revealed diminished metal removal in successive sorption experimental runs. Conversely, sorption from wastewater that was acidified to pH 1.8 featured consecutively higher metal removal demonstrating conversion of surface secondary hydroxyl groups to carboxylate groups simultaneously with reduction of Cr(VI) to Cr(III).

References

1. Fivaz J (2008) South African mango growers association chairman's report 2007/08. S Af Mango Grow Assoc Res J 28:6–7
2. Henrique MA, Silverio HA, Neto WPF, Pasquini D (2013) Valorization of an agro-industrial waste, mango seed, by the extraction and characterization of its cellulose nanocrystals. J Environ Manage 121:202–209
3. Yang F, Liu H, Qu J, Chen JP (2011) Preparation and characterization of chitosan encapsulated *Sargassum* sp. biosorbent for nickel ions sorption. Bioresour Technol 102:2821–2828
4. Sun Z, Liu Y, Huang Y, Tan X, Zeng G, Hu X, Yang Z (2014) Fast adsorption of Cd^{2+} and Pb^{2+} by EGTA dianhydride (EGTAD) modified ramie fiber. J Colloid Interface Sci 434:152–158
5. Pereira FV, Gurgel LVA, Gil LF (2010) Removal of Zn^{2+} from aqueous single metal solutions and electroplating wastewater with wood sawdust and sugarcane bagasse modified with EDTA dianhydride (EDTAD). J Hazard Mater 176:856–863

6. Gusmao KAG, Gurgel LVA, Melo TMS, Gil LF (2013) Adsorption studies of methylene blue and gentian violet on sugarcane bagasse modified with EDTA dianhydride (EDTAD) in aqueous solutions: kinetic and equilibrium aspects. J Environ Manage 118:135–143
7. Jiang G-B, Lin Z-T, Huang X-Y, Zheng Y-Q, Ren C-C, Huang C-K, Huang Z-J (2012) Potential biosorbent based on sugarcane bagasse modified with tetraethylenepentamine for removal of eosin Y. Int J Biol Macromol 50:707–712
8. Roy A, Chakraborty S, Kundu SP, Majumder SB, Adhikari B (2013) Surface grafting of *Corchorus olitorius* fibre: a green approach for the development of activated bioadsorbent. Carbohydr Polym 92:2118–2127
9. Hajiha H, Sain M, Mei LH (2014) Modification and characterization of hemp and sisal fibers. J Nat Fibers 11:144–168
10. Draman SFS, Daik R, Latif FA, El-Sheikh SM (2014) Characterization and thermal decomposition kinetics of kapok (*Ceiba pentandra* L.)-based cellulose. BioResources 9:8–23
11. Lomakin SM, Rogovina SZ, Grachev AV, Prut EV, Alexanyan CV (2011) Thermal degradation of biodegradable blends of polyethylene with cellulose and ethylcellulose. Thermochim Acta 521:66–73
12. Medronho B, Andrade R, Vivod V, Ostlund A, Miguel MG, Lindman B, Voncina B, Valente AJM (2013) Cyclodextrin-grafted cellulose: physico-chemical characterization. Carbohydr Polym 93:324–330
13. Saha R, Saha B (2014) Removal of hexavalent chromium from contaminated water by adsorption using mango leaves (*Mangifera indica*). Desalin Water Treat 52:1928–1936
14. Kumari AR, Sobha K (2016) Removal of lead by adsorption with the renewable biopolymer composite of feather (*Dromaius novaehollandiae*) and chitosan (*Agaricus bisporus*). Environ Technol Innov 6:11–26
15. Nakano Y, Takeshita K, Tsutsumi T (2001) Adsorption mechanism of hexavalent chromium by redox within condensed-tannin gel. Water Res 35:496–500
16. Solomon GTW, Fryhle CB, Snyder SA (2014) Organic chemistry. Wiley, New Jersey
17. Zhou JL, Kiff RJ (1991) The uptake of copper from aqueous solution by immobilized fungal biomass. J Chem Technol Biotechnol 52:317–330

Chapter 9
Nitrogen Absorption and Immobilization Patterns as Cataysed by the Roots of *Acacia* Plants

Nancy Nyamai and Phanuel Oballa

Abstract Large tracts of soil in sub-Saharan Africa are nutrients deficient while inorganic fertilizers are unaffordable for most subsistence farmers. Rotations and/or intercropping of nitrogen fixing trees like *Acacia* species with crops may alleviate the nitrogen deficiency through biological nitrogen (N_2) fixation and redistribution of subsoil nitrogen to the surface. The study was conducted on an N-deficient, sandy loam (Alfisol) under bimodal rainfall conditions at Kendu Bay, Nyanza Province in Kenya to compare the effectiveness of *A. nilotica, A. senegal* and *A. xanthophloea*. This was carried out in order to improve degraded lands by fixing nitrogen from the air, extracting water and nutrients from the soil and investigating the resulting effects on maize yields. Optimal spacing for the *Acacia* trees for the nitrogen fixation was also evaluated in two seasons to enhance maize yields and nutrients extractions from the soil. Assessment of the relationship between the amount of phosphorus in the soil and nitrogen fixation/availability by the *Acacias* were also carried out simultaneously. There was poor response in the first season but there was significant increase ($P < 0.05$) in maize yield due to planting *A. nilotica*, *A. senegal* and *A. xanthophloea* in the second season. The planting of *A. nilotica* at different spacing in the second season also contributed to the significant increase in the maize yield. In the first season, the *Acacias* intercropping reduced maize yields. The yield reduction in the first season might be attributed to competition with maize plants when the trees had not grown long enough roots for effective nodulation, and nitrogen fixation while in the second season the *Acacia* trees had grown long roots that were effective in the nitrogen fixation. Again in the first season close planting

N. Nyamai (✉)
Department of Chemical and Physical Sciences, Walter Sisulu University, Private Bag XI WSU, Nelson Mandela Drive, Mthatha 5117, Eastern Cape, South Africa

Department of Research, Kenya Forestry Research Institute, KEFRI, P.O. Box 20412, Nairobi, Kenya
e-mail: nanyamai@yahoo.com

P. Oballa
Department of Research, Kenya Forestry Research Institute, KEFRI, P.O. Box 20412, Nairobi, Kenya
e-mail: poballa@kefri.org

P. Ramasami et al. (eds.), *Emerging Trends in Chemical Sciences*,
DOI 10.1007/978-3-319-60408-4_9

spacing of the *Acacia* reduced yields of the maize. In the second season there was significant ($P < 0.05$) maize yield increase under closely spaced *Acacia* trees. These results demonstrate that the benefits of *Acacia* intercropping in increasing maize yields are more effective after the *Acacias* have grown and the close spacing of *Acacia* may be more beneficial in effective nitrogen fixation and supply in the long run. There was increase in phosphorus concentration in maize plants in season two whereby *A. nilotica* had an increase in phosphorus from 0.183% in season one to 0.363% in season two. The close spacing of the trees was important in phosphorus build up and nitrogen fixation as shown by higher amounts of nitrogen in the soil and maize plants in season two. Soil pH did not vary and remained almost neutral with soil moisture content increasing due to added organic matter from the trees. The findings of this study can be used to intensify agroforestry at the farm level to increase food security in the Lake Victoria Basin and the work should involve all the stakeholders (farmers, extension officers, researchers, non-governmental organizations, leaders, and community based organizations) in decision making and implementation.

Keywords *Acacia nilotica* • *Acacia senegal* • *Acacia xanthophloea* • Nitrogen fixation • Soil rehabilitation • Wood • Maize

9.1 Introduction

All over Africa, *Acacias* have been grown traditionally as farm trees within and adjacent to arable crops. The main reason for this agroforestry system is that some *Acacia* species, such as *A. nilotica, A. senegal, A. xanthophloea* are rich in nitrogen because of their association with rhizobia bacteria which helps the *Acacias* to fix nitrogen and therefore provide long-term benefits to neighbouring plants [1].

In addition, the use of acacia leaves from alley cropping systems, biomass transfer systems, and improved tree fallows in the tropics have been shown to significantly contribute N to crops, and hence improve crop yields [2]. One of the consideration for selecting leguminous trees (acacia) for such systems is the net rate of N mineralization from the leaves, and hence the N benefit obtained by the crop.

However, the nitrogen nutrition of higher plants is dominated by two paradoxes. The reserve of molecular nitrogen in the atmosphere *ca.* 4×10^{15} tonnes (about 40,000,000 times what is involved in the biological cycle of the element) cannot be used by higher plants except when they are associated in symbiosis with nitrogen fixing bacteria. This is due to the high energy bond of the diatomic molecule N_2 ($\Delta H = +945$ kJ mol^{-1}) [3]. The only forms of mineral nitrogen that higher plants can use are NO_3^-, nitrate ion and NH_4^+, ammonium ion (Diagrams 9.1 and 9.2). The assimilation pathways of these two ions are represented in Fig. 9.1. In this biochemical reaction sequence, the first two stages, in which the nitrogen atom proceeds from its state of maximum reduction, require eight reduction equivalents, that is, the energy equivalent of 15–16 moles of adenosine triphosphate, ATP [3, 4].

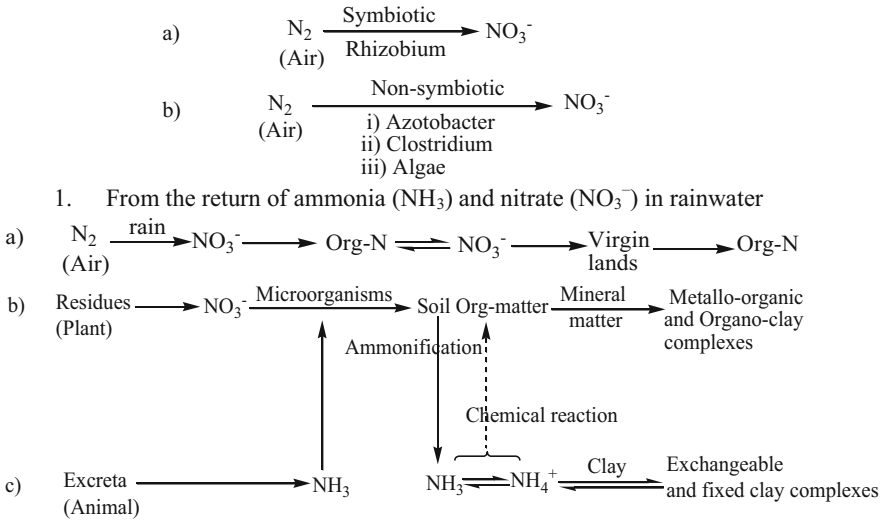

Diagram 9.1 Fixation of molecular N_2 by micro-organisms [3–5]

In comparison, the incorporation of ammonia in a carbon molecule by the GS-GOGAT pathway only consumes 5 ATP (Fig. 9.1) [4, 6]. This is the second paradox of nitrogen nutrition: in spite of the cost of this reduction all higher plants that are autotrophic for nitrogen possess the two enzymes nitrate and nitrite reductase necessary for the reduction of nitrate into ammonia, and nitrate appears to be the predominant form of their nitrogen supply.

9.2 The Nitrogen Cycle

The nitrogen cycle in soil is an integral part of the overall cycle of nitrogen in nature [6]. The source of the soil N is the atmosphere, where the strongly bonded gaseous molecule (N_2) is the predominant gas (79.08% by volume of the gases). The significance of N varies from the fact that after carbon, hydrogen, and oxygen, no other element is so intimately associated with the reactions carried out by living organisms [7]. The cycling of other nutrients notably phosphorus and sulphur is closely associated with biochemical nitrogen transformations [8].

The breakdown of biological nitrogen molecules causes the liberation of ammonia which is then oxidized to nitrate (Diagram 9.1). The last two stages of this mineralization form the process of nitrification, which has a particular biological and agronomical importance.

Bacteria of the Nitrosomonas type oxidize ammonia into nitrite, and bacteria of the Nitrobacter type oxidize nitrite into nitrate [3, 4, 6–8]. Both are chemosynthetic bacteria, using the energy produced by these oxidations to synthesize the ATP they

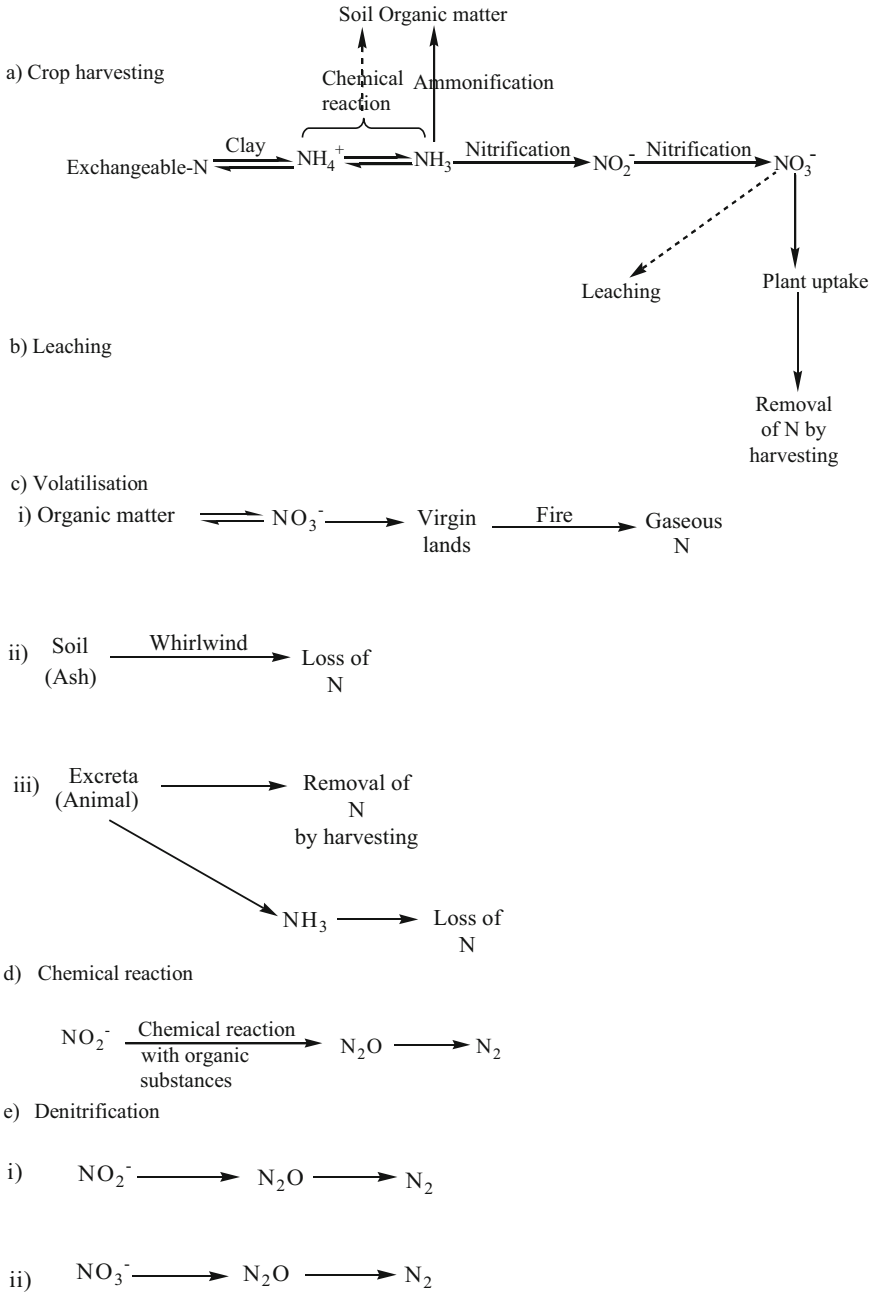

Diagram 9.2 Occurrence of nitrogen losses [3–5]

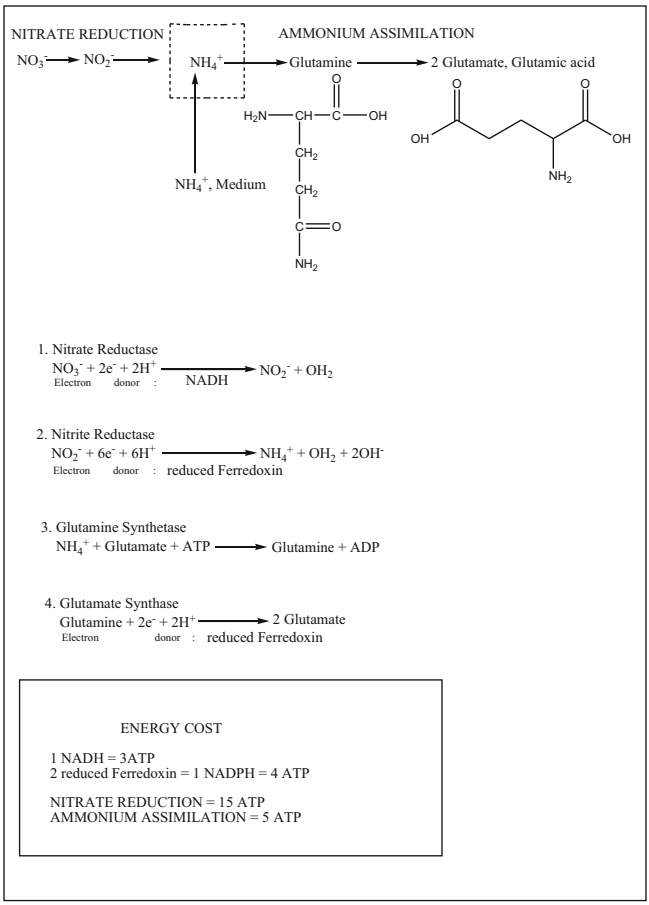

Fig. 9.1 Energy requirement for nitrate reduction and ammonium assimilation [3, 4, 6]. *NADH* nicotinamide adenine dinucleotide, *ATP* adenosine triphosphate, *GS* glutamine synthetase, *ADP* adenosine diphosphate, *GS-GOGAT* glutamine synthetase-glutamate synthase

require for the CO_2 reduction. These two oxidations are highly exergonic [8] and can be represented by the general reactions:

$$NH_4^+ + 3/2O_2 \rightarrow NO_2^- + H_2O + 2H^+ \quad \Delta G_o = -272 \text{ kJ mol}^{-1}$$
$$NO_2^- + ½O_2 \rightarrow NO_3^- \quad \Delta G_o = -71 \text{ kJ mol}^{-1}$$

These equations only express part of the reality. Molecular oxygen acts mainly as a terminal acceptor of electrons from the oxidation of nitrogen atom [6–9] and in the nitrite oxidation, the oxygen atom of the nitrate anion comes from water.

In soils, good aeration and good water availability are indispensable ecological factors for nitrification. The activity of nitrifying bacteria is also favoured by pH

close to neutrality and by fairly medium temperatures. These are the characteristics of fertile soils.

The free enthalpies of the two above reactions are high. The systems of electron carriers involved in these oxidations should make possible the recuperation of 2 ATP molecules per atom of oxygen consumed by Nitrosomonas, and 1 ATP for Nitrobacter, which would correspond to P/O ratios of 2 and 1 respectively.

9.3 Effect of Land Degradation in Lake Victoria Basin

Land degradation in the lake basin is of a major concern, not only for the health of the lake, but also for livelihood and food security of its rapidly expanding population. Soils around Lake Victoria are widely degraded and infertile due to continuous cropping with little or no fertilizers. This leads to poor crop production and requires use of high amounts of inorganic fertilizers to improve crop yields. Most residents around the Lake basin are poor and cannot afford the inorganic fertilizers. It is necessary that cheap methods, which reduce soil degradation and improve soil fertility be sought to improve the livelihood of residents around the basin. In some regions, lack of protective tree cover or removal of protective tree cover may lead to uncontrolled water runoff that erodes the soil and washes away nutrients. This can effectively shorten the growing season, again reducing crop yields.

9.4 Justification

In recent years, the most urgent problems around Lake Victoria region are directly or indirectly due to the invasion by water hyacinth on fishery, water transport and health. Fishermen are forced to engage in increasingly desperate and unsustainable use of natural resources on the land. These include exploitation of fragile areas such as wetlands, and clearing of vital forests to open up new arable lands and to gather firewood, thereby intensifying erosion. The destruction of the basins wetlands to create space for cultivation and grazing of cattle has in turn led to loss of biodiversity and to decreased agricultural returns and filtering effect on the water entering the lake via watercourses. By introducing multipurpose plant species like *Acacias*, these problems can be overcome.

9.5 Soil Fertility

Declining soil fertility as a result of continuous cropping without adequate input of fertilizers has been identified as one of the major biophysical problems facing smallholder farmers in sub-Saharan Africa. The result of which, is the perpetual

low per-capita food availability experienced in this region [7–9]. The problem of low crop yields is aggravated by the pressure on agricultural lands due to the ever-increasing human population. Shifting cultivation, a familiar practice that introduces a period in sequence referred as fallow, the resting state of an agricultural field, used to be a remedial measure for degraded farmlands [10]. During fallow periods, the naturally regenerating secondary vegetation is expected to restore soil fertility by building up nutrient stocks through biological processes, retrievals from subsoil, and through nutrient capture from subsurface lateral flow.

Shifting cultivation practice can effectively restore soil nutrient status provided the natural fallow periods are long enough; this may take 3–15 years for most nutrients, except for nitrogen which may be shorter [11]. After long periods of fallowing, burning vegetation and woody biomass may add additional nutrient reserves to the soil through ash, as well as help clear agricultural lands of weeds [12]. The nutrients accumulated in the topsoil through litter fall and in the vegetation during fallow period represent a capital gain for farmers. However, natural fallow periods have become shorter because of agricultural demands that the vegetation no longer impact sound ecological effects on degraded farmlands [13, 14]. Consequently, restoring soil fertility of degraded farms through natural fallowing has become unattainable in densely populated regions like the Lake Victoria basin, particularly Kendu bay, where land size per household is small and land is continuously under cultivation [15].

An obvious strategy to improve crop yields would be to apply inorganic nitrogen and phosphorus based fertilizers, since these two mineral nutrients have been diagnosed as most limiting for tropical soils. Significant yield responses are often observed in trials involving inorganic fertilizer applications [15, 16]. The major and most serious constraints to inorganic fertilizer use by resource-poor farmers in sub-Saharan Africa are associated with their high costs and low market availability [16]. Consequently, efforts to improve crop yields in nutrient depleted soils like Lake Victoria basin and other parts of Sub-Saharan Africa by low cost and sustainable agroforestry practices such as alley cropping and improved fallows have been proposed [17].

Alley cropping where crops are grown in alleys simultaneously with trees was the best-known agroforestry technology [18]. However, the soil ameliorating effect of trees in alleys varies according to the tree species [18], age of plantation [19], soil type and climate [19]. Improved fallow systems involve planting of selected fast growing trees/shrubs like *Acacias* during the fallow period that are expected to not only provide readily available nutrients for the subsequent crop, but also increase soil organic matter and hence improve soil physical conditions. The strategy of the system is to plant leguminous trees like *Acacia* that (1) accumulate nutrients in their biomass and subsequently recycle them through litter fall and green manure or mulch applications; (2) improve soil physical and chemical properties; and (3) act as a break crop to smother weeds [18, 19]. Such agroforestry interventions to meet the growing need for productive and environmentally friendly agricultural systems for resource-poor farmers have stimulated renewed interest in the mechanisms by which fallows restore ecosystem fertility [19].

Generally, *Acacia* alleys or fallows are established to overcome constraints to crop production by enhancing soil fertility during the cropping period. *Acacia* trees are successful pioneers in alley or fallow systems partly because, like many other members of the legume plant family, they have associations with two types of microorganism: rhizobia and mycorrhizae [20]. Rhizobia are defined as a group of small, soil-dwelling bacteria that produce nodules on the roots of leguminous plants. Within these nodules, rhizobia fix nitrogen from the soil environment, thereby supplying the legume with an essential element. The relationship between rhizobia and legumes is symbiotic, that is mutually beneficial. The bacteria obtain food (in the form of sugars) and amino acids from the plant and are provided with a beneficial environment in which to form their protective nodules. In return, the plant obtains nitrogen from rhizobial activity [20]. Since nitrogen is often lacking in depleted soils, rhizobia allow many legumes, including *Acacias*, to thrive in conditions that other plants cannot tolerate [18–20]. Mycorrhizae are specialised soil fungi that attach to the roots of many plants, including *Acacias* [19, 20]. These fungi form an elaborate network of fine threads, or hyphae, through which they are able to absorb phosphorus and other relatively immobile nutrients. These nutrients are passed on to the plant via its roots and, in return, the mycorrhizal fungi obtain sugars and amino acids. Phosphorus is a vital nutrient for plants as it facilitates the absorption of water and other nutrients, encourages root growth, improves disease resistance and thereby increases plant growth and yield [21]. Therefore, trees in fallow or alley systems improve soil fertility through the supply of N, P and cations; adjustment of soil pH and building up of soil organic matter; and improving soil physical structure [21].

9.6 Contributions of N through Biological N_2-Fixation

The contribution of nitrogen by leguminous trees through biological N_2 fixation (BNF) is well recognized for replenishing soil N [22, 23] although it is important to note that not all legumes fix atmospheric nitrogen. There are non-nodulating legumes such as *Acacia erioloba*, and *Senna siamea* that have been widely tested in some agroforestry systems and found to extract more soil N that they accumulate in their biomass [24]. Quantification of N_2-fixation, particularly for older trees, has proven difficult due to constraints in methodologies for measuring N_2-fixed [25]. Nonetheless, high variability is sometimes observed among provenances or isolines of tree species in percentages of total plant N derived from the atmosphere-%Ndfa [26]. The ranking of provenances for %Ndfa is also dependent on growth stage, and differences observed in short duration studies may not reflect long-term N_2-fixation in the field. Therefore, estimates of N_2-fixation by legume tree species are, to a large extent, site specific. For instance deficiency of available phosphorus, P, which is a characteristic of many tropical soils, can limit N_2-fixation and growth of legume [24–26]. So how well a species is adapted to a given site/environmental conditions may determine the quantity of atmospheric

N_2-fixed. Efficient absorption and utilization of P can be a critical factor for legumes growing in low P soils, lest their productivity and BNF potentials are adversely affected. Thus, increases in N_2-fixation by trees can be achieved through correct selection of tree germplasm and proper fertilization, particularly with phosphorus [26].

High phosphorus requirement for nodulation is considered to be responsible, at least in part, for the interactions between mycorrhizae and many legume species, including *Acacias*. Mycorrhizal infection of roots increases the acquisition of phosphorus in plants grown in low phosphorus soils [25, 26] and, thus increased root nodulation is realized.

9.7 Nutrients and Plants Growth

Nitrogen occupies a unique position among the elements essential for plant growth because of the rather large amounts required by most agricultural crops. A deficiency of N is shown by yellowing of the leaves and by slow and stunted growth. Other factors being favourable, an adequate supply of N in the soil promotes rapid plant growth and the development of dark-green colour in the leaves. Major roles of N in plant nutrition include: (1) component of chlorophyll, (2) component of amino acids, the building blocks of protein, (3) essential for carbohydrate utilization, (4) component of enzymes, vitamins, and hormones, (5) stimulates root development and activity, and (6) supports uptake of other nutrients [27].

Phosphorus is an essential constituent of all living organisms [27]. Plants deficient in P are stunted in growth and maturity is delayed. The lower leaves are typically yellow and tend to wither and drop off. Leaf tissue is usually abnormally dark green, often shading to red and purple hues because of excess anthocyanin accumulation. Phosphorus is needed for seed formation, root development, strength of straw in cereal crops, and crop maturity [28].

Potassium is essential for the healthy growth of the plants and cannot be replaced even by closely related elements such as sodium and lithium [29]. In plants it occurs as part of the cation of organic acids or as a soluble inorganic salt in the tissues. The formation and movement of carbohydrates in plants is contributed by potassium and its deficiency quickly reduces the carbohydrate content [30]. However, potassium determination was not carried out in this study since soil types around Kendu Bay are high P-sorbing Alfisols and oxisols, originally quite fertile but now widely depleted of N and P [30, 31].

9.7.1 Gains in Soil Nitrogen

Gains in soil N occur through fixation of molecular N_2 by microorganisms and from the return of ammonia (NH_3) and nitrate (NO_3^-) in rainwater; while losses occur

through crop removal, leaching, and volatilization [30, 31]. The conversion of molecular N_2 to combined forms occurs through biological N_2 fixation. Organic forms of nitrogen, in turn, are converted to NH_3 and NO_3^- through mineralization [31]. The conversion to NH_3 is termed ammonification; the oxidation of this compound to NO_3^- is termed nitrification [32]. The utilization of NH_3 and NO_3^- by plants and soil organisms constitutes assimilation and immobilization, respectively [30–32]. Combined N is ultimately returned to the atmosphere as molecular N_2, such as through biological denitrification, thereby completing the cycle [32].

Transformations of N in the soil are not solely mediated by microorganisms. Ammonia and nitrite (NO_2^-), produced as products of the microbial decomposition of nitrogenous organic materials, are capable of undergoing chemical reactions with organic substances, in some cases leading to the evolution of N gases [31, 32]. Through the association of humic materials with mineral matter, organo-clay complexes are formed whereby the N compounds are protected against attack by microorganisms. The positively charged ammonium ion (NH_4^+) undergoes substitution reactions with other cations of the exchange complex, and it can be fixed by clay minerals [5].

The basic feature of biological N transformations centres on oxidation and reduction reactions. Typical oxidation states are –3 for NH_3, +3 for NO_2^-, and +5 for NO_3^-. Other compounds have intermediate values (N = 0) [5].

9.8 Chemical Properties of Soil Phosphorus

In the pedosphere, P is found largely in its oxidized state as orthophosphate, ($H_2PO_4^-$) mostly as complexes with Ca, Fe, Al, and silicate minerals. Some secondary minerals of phosphate are wavellite [$Al_3(PO_4)_2(OH)_3{\cdot}5H_2O$], vivianite [$Fe_3(PO_4)_2{\cdot}8H_2O$], dufrenite [$FePO_4Fe(OH)_3$], strengite [$Fe(PO_4){\cdot}H_2O$], and variscite [$Al(PO_4){\cdot}2H_2O$]. Small amounts of phosphine gas, PH_3, often occur in lakes or marshes under highly reducing conditions [5].

9.9 Description of *A. nilotica*, *A. senegal* and *A. xanthophloea*

A. nilotica is a medium to large tree that can reach a height of 10 m, with an average of 4–7 m in height [33]. The crown is somewhat flattened or rounded, with a moderate density and the branches have a tendency to drop downwards if the crown is roundish [34]. The bark is blackish grey or dark brown in mature trees and deeply grooved, with longitudinal fissures while young branches are smooth and grey to brown in colour [34, 35]. The young twigs are covered with short paired hairs; slender, straight spines grow from a single base and sometimes curve

backwards, are up to 80 mm long and whitish but often reddish brown in colour. The leaves are twice compound, elliptical leaflets that can be bottle to bright green in colour [36]. The leaf stalks are very heavy. Very small glands, almost not noticeable with naked eye, are found at the base of most of the upper pinnae pairs [36, 37].

A. xanthophloea is a tree up to 25 m high with straight white thorns arranged in pairs and its bark is yellow [34–37]. Leaves are compound with 8–17 pairs of leaflets, while the flowers are in heads, and white [38]. Mature pods are yellow–brown, 4–12 cm long and slightly constricted between seeds, always in drooping position, never opening but breaking into segments, each with 5–10 pale dark green seeds [38].

A. senegal has a very variable growth form from a multi-stemmed shrub about 2 m high to a single-stemmed tree up to 12 m tall with hooked prickles arranged in threes, the central one hooked downwards, the two laterals curved upwards [39]. The bark is yellowish brown or grey-brown, peeling and papery and the leaves are compound with 8–18 pairs of tiny leaflets. Flowers are in spikes, white or cream, mature pods are grey-brown or red-brown, straight and tapering at both ends, up to 10 cm long, splitting open on the tree with 3–5 greenish brown seeds [39].

9.10 Ecology of *Acacias*

A. nilotica is a tropical species, growing where average annual temperatures range from 15 to 28 °C, being frost sensitive when young and withstanding daily maximum temperatures of 50 °C and it grows from sea level to over 2000 m altitude [38, 39]. *A. nilotica* prefers dry conditions, with an annual rainfall of 100–2300 mm, however the extremes are only found under irrigation or where planted outside its natural range, for instance in south-east Asia [39]. It occurs in both unimodal and bimodal rainfall regions with summer or winter regimes [37–39]. Depending on the subspecies, it will tolerate both drought and flooded conditions for several months. The sub-species *nilotica* and *tomentosa* are restricted to riverine habitats and seasonally flooded areas on alluvial clay soils. In the Indian subcontinent, sub sp. *indica* occurs in dry forests at low altitudes, usually on alluvial soils subject to flooding or on black cotton soils [39]. It is now widely planted on farms throughout the plains and will also grow on saline, sodic or alkaline soils and on soils with calcareous pans [40].

All over Africa, *Acacias* have been grown traditionally as farm trees within and adjacent to arable crops and livestock. The main reason for this agroforestry system is that some acacia species, such as *Faidherbia albida*, produce green leaves, which are in full growth during the wet season, providing shade to cattle and farm workers when the sun is hottest and does not obstruct the light needed by many field crops during the wettest part of the year [41].

Acacias also provide more long-term benefits to neighbouring plants [41]. Because of their association with rhizobia bacteria, acacias are rich in nitrogen

and, when parts of the trees die and decay, they fertilize the surrounding soil [39–41]. On the poor sandy soils of arid areas in sub-Saharan Africa, this cycle can help improve the growth and yield of field crops [41].

9.11 Experimental Site

This study was carried out on degraded soils in Kendu Bay location of Rachuonyo District, Nyanza Province of Western Kenya (0°06′N, 34°34′E, 1120 m above mean sea level). The rainfall distribution of the site is bimodal with the long (March–June) and short rains (September–December). This is due to the daily westerly wind from Lake Victoria which converges with the south-east wind (or trade wind), causing the air to rise, thus producing heavy showers, especially in the afternoon [42]. In western Kenya these relatively wet agro-ecological zones dominate except near the lake, where the air masses fall again (mean annual rainfall of 430 mm). The soil has been described as fine kaolinitic, isohyperthermic Kandiudalfic Eutrudox. The soil here is well-drained, sandy clay to clay with acid humic topsoil [43].

9.12 Experimental Design and Sampling Methods

Two experiments were set up in a randomized complete block design replicated three times. In the first trial, three species were evaluated: *A. nilotica*, *A. senegal* and *A. xanthophloea*. Unfertilized continuous maize (maize monoculture) was included as control and each plot was 6 m × 6 m in area. The *Acacia* species were planted at spacing of 2 m × 2 m.

In the second trial, effects of planting spacing were assessed using *A. nilotica* at different spacing of 2 m × 2 m, 3 m × 3 m, and 4 m × 4 m with maize monoculture as control. Maize in all plots was planted at spacing of 70 cm × 30 cm. In season one, the maize and *Acacia* seedlings were planted at the same time. In the second season, the maize was planted on the previous plots with Acacia.

Four months old *Acacia* seedlings were planted together with maize in the first trial that was followed by weeding to control weed growth while soil sampling was done two times per season at 0–15 cm depth to monitor nitrogen fixing capacity of various trees. Maize was planted at 70 cm by 30 cm in rows between the trees and on control plots twice a year at the beginning of the long and short rains. Total destructive samplings of the maize leaves were done at 10 weeks after planting. The harvested parts were chopped into small pieces of about 2 mm and put into sampling paper bags for analyses. The plant and soil samples were analyzed for nitrogen, phosphorus, and pH. The maize yields from the experimental sites were recorded.

9.13 Sources of Seeds and Seed Scarification

Acacia seeds were obtained from Kenya Forestry Research Institute, (KEFRI), Seed Centre in Muguga. The seeds were pre-treated by boiling in water for 10–15 s and then soaked for 24 h in cold water before sowing in a seed-bed. After germination, the seedlings were transplanted in polytubes where they were maintained until the plants were 25–30 cm. The type of maize that is grown in the region is PH 1 and its seed was sourced from Western seed distribution store at Kendu Bay.

9.14 Soil and Plant Sample Preparation

Soil samples were collected at 0–15 cm depth and placed in plastic bags, whereas plant samples were taken from blades opposite and below cob and placed in paper bags to reduce decomposition prior to preparation for analysis. The soil samples were dried in an oven at 40 °C until a constant dry weight was obtained. The soil lumps were crushed to separate gravel, roots and large organic residues. Smashing of any gravel was avoided to prevent getting unwanted results as the gravels could contain unwanted nutrients.

The soils were sieved through a 2 mm sieve, gently rubbing the crumbs through the mesh leaving the gravels and roots in the sieve. Coning and quartering retained a representative sample of approximately 250 g. Soils were further ground in a mortar in order to pass through a 60 mesh screen for total N and P analysis.

Plant samples were dried at 70 °C in an oven until a constant dry weight was obtained. The dried plant material was then chopped and ground using a Wiley mill and passed through a 2 mm sieve. The dried sample was further ground using a stainless steel cyclotec mill and the sample passed through 1.0 mm sieve. Representative samples of 25 g were retained by coning and quartering [44].

9.15 Soil pH in Water

This standard method used a soil: water ratio of 1:2.5. Analyses were conducted in batches of 33 with 30 soil samples, two repeated samples and 1 standard soil sample to monitor any contamination during analyses. Addition of 50 ml deionized water to 20 g soil followed before stirring the mixture for 10 min. The mixture was allowed to stand for 30 min, stirred again for 2 min then the pH of the soil suspension measured using a Rinna pH meter [44].

9.16 Analysis of Total Nitrogen and Phosphorus in Plants and Soils

Analysis of total nutrients required complete oxidation of organic matter. This was accomplished through acid/alkaline digestion of the plant and soil samples. Wet acid oxidation was based on Kjeldahl oxidation method [44, 45]. Hydrogen peroxide was added as an additional oxidizing agent, selenium was used as a catalyst while lithium sulphate was added to raise the boiling point of the mixture. The main advantages of this method are that single digestion was required (for either soil or plant) to bring all nutrients into solution; no volatilization of metals, N and P takes place. The procedure was fast, accurate and reproducible [44, 45].

9.16.1 Procedure Using a Block Digester

Digestions were carried out in batches of 20, with 17 samples, 1 standard soil sample and two blanks. The soil weight was 0.4 g while plant material weight was 0.2 g, ground to pass through 0.3 mm mesh and 0.1 mm mesh respectively and were weighed separately to the nearest 0.001 g, into labeled digestion tubes and the weight recorded. Addition of 1.8 g K_2SO_4 to each digestion tube for the soils followed, then 4.4 ml and 7.5 ml of digestion mixture were added to plant and soil in the digestion tubes respectively, swirled gently, and covered before allowing standing overnight. The next morning, the digestion tubes rack was placed into the block digester and the temperature was raised slowly from room temperature to about 330 °C for the plants and 360 °C for the soils. The plants were digested at 330 °C for 4 h after which the solution remained colourless and the remaining solid material was white.

The soils were digested by heating the samples at 100 °C for 1 h before removing the tube rack from the digestion block and allowing to cool. Three successive 1-ml aliquots of 30% H_2O_2 were added, mixing well after each addition, and making sure to allow the reaction to subside before the next addition. The rack was replaced in the digestion block and the temperature raised to 250 °C and heated for one hour, then the temperature was raised to 360 °C. Anti-bumping granules were added to reduce frothing and boiling over the tubes. The digestion took 5 h at 360 °C.

After digestion, the samples were allowed to cool before adding 70 ml of deionized water and mixed well, until there was no dissolution of more sediment. The tubes were stoppered immediately after cooling. Deionized water was added to the 75 ml mark and mixed well before allowing to settle overnight so that a clear solution could be taken from the top of the tube for analysis.

9.16.2 Determination of Total Nitrogen and Phosphorus in Soil

Acid digestion of the soil material was followed by colorimetric determination [45, 46].

9.16.3 Determination of Total Nitrogen and Phosphorus in Plant Tissue

The resultant solution from the digestion procedure was strongly acid. Colorimetric procedure for P estimates in such solutions was used while colorimetric analysis of nitrogen required the determination of ammonium which resulted from the Kjeldahl digestion of the plant tissue [45–47].

9.17 Data Analysis

The data generated were analyzed using SAS 8.2 (SAS Institute Inc. 1999) and MSTAT-C version 2 [48]. One-way and two-way analysis of variance (ANOVA) were performed on each data set and where there were significant differences means were separated by Tukey's range test at $P < 0.05$ in a randomized complete block design with three replicates.

9.18 Results

9.18.1 Nutrients Concentrations in Maize Leaves Intercropped with A. nilotica at Three Different Spacings

The level of nitrogen found in the leaves of maize plants intercropped with *A. nilotica* at different spacings in season one (March–May 2006) and in season two (Oct–Dec 2006) are presented respectively in Table 9.1 and Table 9.2. In season one, *A. nilotica* (4 m × 4 m spacing) + maize and maize monoculture had significantly ($P < 0.05$) low nitrogen content in the maize leaves compared to *A. nilotica* (2 m × 2 m spacing) + maize which had twice the percent nitrogen levels in *A. nilotica* (4 m × 4 m spacing) + maize and maize monoculture. The concentration of nitrogen in *A. nilotica* (2 m × 2 m spacing) + maize was also significantly ($P < 0.05$) higher than *A. nilotica* (3 m × 3 m spacing) + maize.

Table 9.1 Concentrations of nitrogen and phosphorus nutrients in maize leaves and maize grain yields from maize plants intercropped with *A. nilotica* at different spacings in season 1 and season 2

Season 1				Season 2		
Treatment	%N	%P	Maize grain (Mg ha^{-1})	%N	%P	Maize grain (Mg ha^{-1})
2 m × 2 m	0.67a	0.183a	8.33c	2.10a	0.363a	20.33a
3 m × 3 m	0.54b	0.127b	11.33b	1.83b	0.310a	13.33b
4 m × 4 m	0.31c	0.113b	15.33a	1.39c	0.250b	12.00b
Maize monoculture	0.31c	0.107b	16.00a	0.95d	0.317a	6.33c
$LSD_{0.05}$	0.04	0.03	2.38	0.15	0.06	3.21

Within the columns, values with the same letters are not significantly different at the 0.05 level of probability. $LSD_{0.05}$ = Least significant difference at the 0.05 level of probability

Table 9.2 Percent nitrogen in maize leaves as affected by *A. nilotica* spacing in the two seasons

Item	Season	Spacing				Mean season
		2 m × 2m	3 m × 3 m	4 m × 4 m	Maize monoculture	
% N conc in maize leaves	Season 1	0.67	0.54	0.31	0.31	0.46
	Season 2	2.10	1.83	1.39	0.95	1.57
	Mean	1.38	1.19	0.85	0.63	
	CV %			6.02		
	LSD ≤ 0.05			0.11		S
	Interactions			S		

S = Significant at P < 0.05 level of probability

In season two, nitrogen concentration in maize leaves was significantly ($P < 0.05$) different, *A. nilotica* (2 m × 2 m spacing) + maize being the highest, 2.10% followed closely by *A. nilotica* (3 m × 3 m spacing) + maize while maize monoculture was slightly lower than *A. nilotica* (4 m × 4 m spacing) + maize. However, it was observed that the nitrogen content in the maize leaves was much higher in season 2 than in season 1 (Fig. 9.2) and there was significant difference ($P < 0.05$) in the two seasons.

Phosphorus uptake by the maize significantly ($P < 0.05$) varied with the spacing of *A. nilotica* during season one (Table 9.1), *A. nilotica* (3 m × 3 m spacing) + maize, *A. nilotica* (4 m × 4 m spacing) + maize and maize monoculture were more or less the same but differed significantly with *A. nilotica* (2 m × 2 m spacing) + maize. In season two, A. *nilotica* (2 m × 2 m spacing) + maize, *A. nilotica* (3 m × 3 m spacing) + maize and maize monoculture were about the same in P concentration in maize leaves while *A. nilotica* (4 m × 4 m spacing) + maize was the lowest (Table 9.1). And there was significant ($P < 0.05$) difference in the two seasons (Table 9.3 and Fig. 9.3).

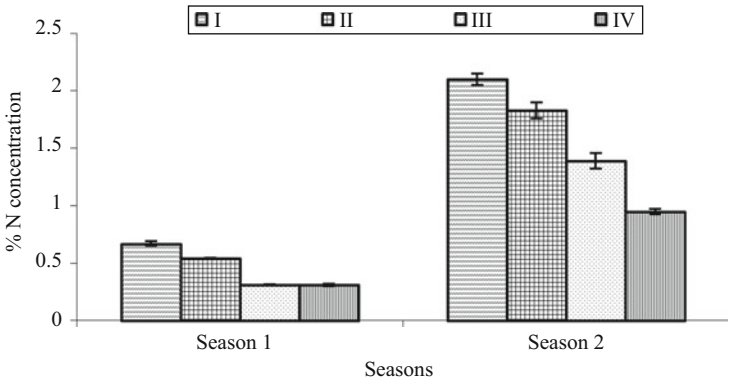

Fig. 9.2 Percent nitrogen levels in maize leaves as affected by *A. nilotica* spacing in the two seasons. (I) *A. nilotica* 2 m × 2 m, (II) *A. nilotica* 3 m × 3 m, (III) *A. nilotica* 4 m × 4 m and (IV) maize monoculture

Table 9.3 Percent phosphorus, P in maize leaves as affected by *A. nilotica* spacing in the two seasons

Item	Season	Spacing				Mean season
		2 m × 2 m	3 m × 3 m	4 m × 4 m	Maize monoculture	
%P conc in maize leaves	Season 1	0.18	0.13	0.11	0.10	0.13
	Season 2	0.36	0.31	0.25	0.32	0.31
	Mean spacing	0.27	0.21	0.18	0.21	
	CV %			9.34		
	LSD ≤ 0.05			0.04		S
	Interactions			S		

S= Significant at $P < 0.05$ level of probability

9.18.2 *Nutrient Levels in Soils Derived from Plots of Different* A. nilotica *Spacings*

Nitrogen levels in the soil did not differ significantly in season one (Table 9.4). However, significant ($P < 0.05$) differences in nitrogen levels occurred in season two where *A. nilotica* (2 m × 2 m spacing) + maize had the highest concentration followed by *A. nilotica* (3 m × 3 m spacing). Concentration of nitrogen in soils derived from plots with *A. nilotica* (4 m × 4 m spacing) and maize monoculture were about half the concentration of nitrogen in *A. nilotica* (2 m × 2 m spacing). However there was no significant ($P < 0.05$) difference when the N content of the soil was compared between the seasons, as shown in Table 9.5.

In season one, there was significant ($P < 0.05$) difference in phosphorus levels in the soil with *A. nilotica* (2 m × 2 m spacing) and maize monoculture being the

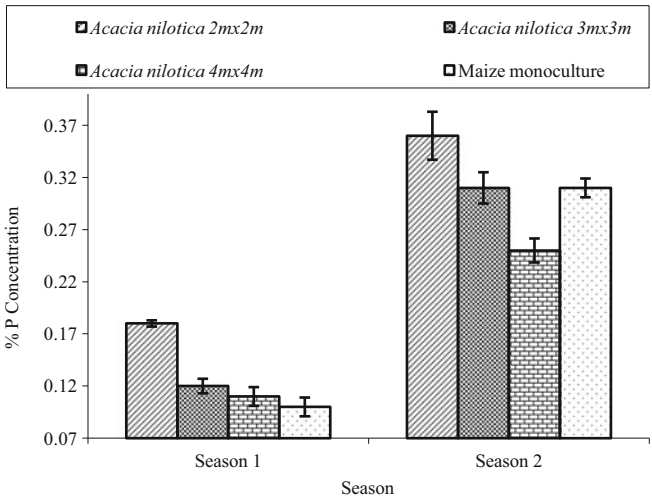

Fig. 9.3 Percent phosphorus levels in maize leaves as affected by *A. nilotica* spacing in the two seasons

highest, followed by *A. nilotica* (3 m × 3 m spacing) and lastly by *A. nilotica* (4 m × 4 m spacing) as shown in Table 9.4. In season two, there was significant difference among the treatments even though *A. nilotica* (2 m × 2 m spacing) and *A. nilotica* (3 m × 3 m spacing) both recorded high levels of phosphorus which were higher than the *A. nilotica* (4 m × 4 m spacing) and maize monoculture. When the %P level of the soils in the two seasons were compared statistically (Table 9.6), there was no significant ($P < 0.05$) difference.

There were no significant ($P < 0.05$) differences in soil moisture content in the two seasons (Table 9.7). During season one, *A. nilotica* (2 m × 2 m spacing) + maize plot had the highest moisture retention followed by *A. nilotica* (3 m × 3 m spacing) + maize plot, *A. nilotica* (4 m × 4 m spacing) + maize plot and finally by maize monoculture plot. In season two, *A. nilotica* (2 m × 2 m spacing) was highest, followed by *A. nilotica* (3 m × 3 m spacing), *A. nilotica* (4 m × 4 m spacing) and maize monoculture.

There was no significant ($P < 0.05$) difference in soil pH in the two seasons (Table 9.8). When *A. nilotica* of different spacing were compared in season one (Table 9.4), there was no significant ($P < 0.05$) difference in soil pH. In season two, there was significant ($P < 0.05$) difference in soil pH. *A. nilotica* (3 m × 3 m spacing) and *A. nilotica* (4 m × 4 m spacing) were not different from one another while *A. nilotica* (2 m × 2 m spacing) and maize monoculture were different from each other and from *A. nilotica* (3 m × 3 m spacing) and 4 m × 4 m spacing.

Table 9.4 Soil characteristics in *A. nilotica* plots of different spacing when intercropped with maize in the two seasons

Season 1					Season 2			
Treatment	%N	%P	Moisture content (%)	pH	%N	%P	Moisture content (%)	pH
2 m × 2 m	0.220a	0.227a	10.46a	7.040a	0.343a	0.270a	11.23a	6.983ab
3 m × 3 m	0.197a	0.187ab	8.66ab	7.077a	0.217b	0.213a	9.32b	7.023a
4 m × 4 m	0.193a	0.153b	8.39ab	7.093a	0.160c	0.147b	8.66b	7.020a
Maize monoculture	0.207a	0.217a	7.71b	7.043a	0.140c	0.127b	7.74b	6.977b
$LSD_{0.05}$	0.040	0.044	2.13	0.069	0.03	0.057	1.78	0.042

Within the columns, values with the same letters are not significantly different at the 0.05 level of probability

Table 9.5 Soil nitrogen levels as affected by *A. nilotica* spacing in the two seasons

Item	Season	Spacing				Mean season
		2 m × 2m	3 m × 3 m	4 m × 4 m	Maize monoculture	
% N conc in soil	Season 1	0.22	0.20	0.19	0.21	0.20
	Season 2	0.34	0.22	0.16	0.14	0.21
	Mean spacing	0.28	0.21	0.18	0.17	
	CV %			9.17		
	LSD ≤ 0.05			0.03		NS
	Interactions			0.05		

NS = Not significant at P < 0.05 level of probability

Table 9.6 Soil phosphorus levels as affected by *A. nilotica* spacing in the two seasons

Item	Season	Spacing				Mean season
		2 m × 2 m	3 m × 3m	4 m × 4 m	Maize monoculture	
% P conc in soil	Season 1	0.23	0.19	0.15	0.21	0.20
	Season 2	0.27	0.21	0.15	0.13	0.19
	Mean spacing	0.25	0.20	0.15	0.17	
	CV%			12.29		
	LSD ≤ 0.05			0.04		NS
	Interactions			NS		

NS = Not significant at P < 0.05 level of probability

Table 9.7 Moisture content (%) of the soil in the two seasons as affected by *A. nilotica* spacing when intercropped with maize

Item	Season	Spacing				Mean season
		2 m × 2m	3 m × 3 m	4 m × 4 m	Maize monoculture	
% Moisture content	Season 1	10.46	8.66	8.39	7.71	8.81
	Season 2	11.23	9.32	8.66	7.74	9.54
	Mean spacing	10.84	9.59	8.53	7.73	
	CV %			10.80		
	LSD ≤ 0.05			1.82		NS
	Interactions			NS		

NS = Not significant at P < 0.05 level of probability

Table 9.8 Soil pH in the two seasons as affected by *A. nilotica* spacing when intercropped with maize

Item	Season	Spacing				Mean season
		2 m × 2 m	3 m × 3 m	4 m × 4 m	Maize monoculture	
Soil pH	Season 1	7.04	7.08	7.09	7.04	7.06
	Season 2	6.98	7.00	7.02	6.98	6.99
	Mean spacing	7.01	7.06	7.03	7.01	
	CV %			0.42		
	LSD ≤0.05			0.05		NS
	Interactions			NS		

NS = Not significant at $P < 0.05$ level of probability

9.18.3 *Influence of* A. nilotica *Spacing on Maize Grain Yield*

Maize grain yields differed significantly ($P < 0.05$) in season one (Table 9.1). Maize monoculture and *A. nilotica* (4 m × 4 m spacing) were the highest followed by *A. nilotica* (3 m × 3 m spacing) and *A. nilotica* (2 m × 2 m spacing). Maize grain yield for season two also differed significantly ($P < 0.05$) among spacing. *A. nilotica* (2 m × 2 m spacing) grain yield was about three times higher than the grain yield obtained in maize monoculture treatment while *A. nilotica* (3 m × 3 m spacing) and *A. nilotica* (4 m × 4 m spacing) grain yield were almost doubled. When the two seasons were compared statistically, there was no significant ($P < 0.05$) difference, as shown in Table 9.9 and Fig. 9.4.

9.18.4 *Concentration of Nutrients in Leaves of Maize Plants Intercropped with Various Acacia Species*

There was significant ($P < 0.05$) variation in the maize leaf nitrogen content with seasons when the *Acacia* species were interplanted with maize. Table 9.10 and Fig. 9.5 show the concentration of nitrogen in leaves of maize plants when intercropped with three *Acacia* species. In the first season, there was significant ($P < 0.05$) difference (Table 9.11). Maize monoculture had about half the concentration as *A. nilotica* (2 m × 2 m spacing) + maize while *A. senegal* (2 m × 2 m spacing) + maize and *A. xanthophloea* (2 m × 2 m spacing) + maize were also higher than maize monoculture but did not differ significantly from one another.

In season 2 the maize N content in the *Acacia* plots did not significantly ($P < 0.05$) vary from one another (Table 9.11). Maize monoculture had the lowest N concentration in the maize leaves but there were no differences in *A. nilotica* (2 m × 2 m spacing) + maize, *A. senegal* (2 m × 2 m spacing) + maize and *A. xanthophloea*

Table 9.9 Maize grain yields as affected by *A. nilotica* spacing in the two seasons when intercropped with maize

Item	Season	Spacing				Mean season
		2 m × 2 m	3 m × 3 m	4 m × 4 m	Maize monoculture	
Yield (Grain) in Mg/ha	Season 1	8.33	11.33	15.33	16.00	12.75
	Season 2	20.33	13.33	12.00	6.17	12.96
	Mean spacing	14.33	12.33	13.67	11.08	
	CV %			13.21		
	LSD ≤0.05			3.12		NS
	Interactions			NS		

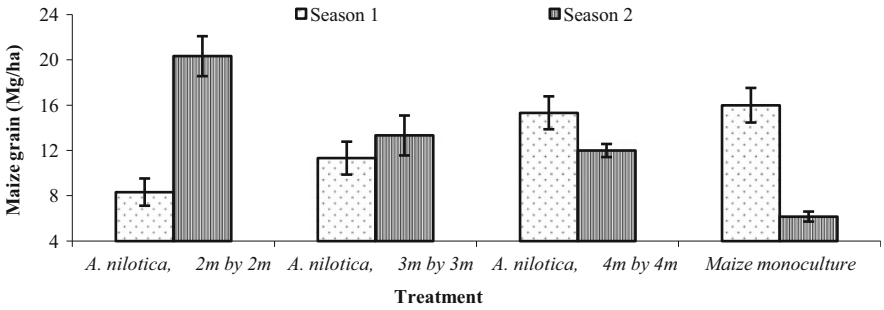

Fig. 9.4 Maize grain yield as affected by *A. nilotica* spacing in the two seasons

Table 9.10 Nitrogen uptake in maize leaves as influenced by different *Acacia* species in the two seasons

Item	Season	Species				Mean season
		A. nilotica	*A. senegal*	*A. xanthophloea*	Maize monoculture	
% N in maize leaves	Season 1	0.67	0.52	0.47	0.31	0.49
	Season 2	2.10	1.81	1.74	0.95	1.65
	Mean	1.39	1.17	1.10	0.63	
	CV %			16.37		
	LSD ≤0.05			0.32		S
	Interactions			S		

(2 m × 2 m spacing) + maize although *A. nilotica* (2 m × 2 m spacing) + maize was the highest.

Phosphorus uptake in maize as influenced by different *Acacia* species in the two seasons varied ($P < 0.05$) significantly (Table 9.12). When the *Acacia* species were compared per season, phosphorus concentration in maize leaves did not vary ($P < 0.05$) significantly in the three *Acacia* species but was significantly different from maize monoculture for season one (Table 9.11).

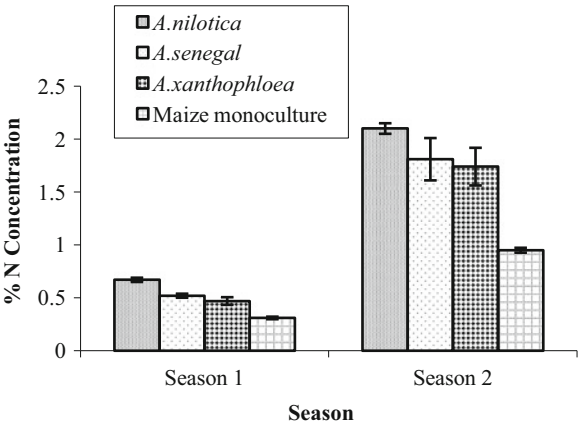

Fig. 9.5 Percent nitrogen concentration in maize leaves as affected by *A. nilotica*, *A. senegal*, and *A. xanthophloea*

Table 9.11 Nutrients concentrations in maize leaves and maize grain yields for *Acacia* species of 2 m × 2 m spacing when intercropped with maize in the two seasons

Season 1				Season 2		
Treatment	%N	%P	Maize grain (Mg ha^{-1})	%N	%P	Maize grain (Mg ha^{-1})
A. nilotica	0.67a	0.183a	8.33b	2.10a	0.363a	20.33a
A. senegal	0.52b	0.180a	7.33b	1.81a	0.330a	18.33a
A. xanthophloea	0.47b	0.170a	8.33b	1.74a	0.333a	13.67ab
Maize monoculture	0.31c	0.107b	16.00a	0.95b	0.317a	6.33b
$LSD_{0.05}$	0.08	0.022	2.64	0.52	0.060	7.41

Within the columns, values with the same letters are not significantly different at the 0.05 level of probability

Table 9.12 Phosphorus uptake in maize as influenced by different *Acacia* species in the two seasons

Item	Season	Species				Mean season
		A. nilotica	*A. senegal*	*A. xanthophloea*	Maize monoculture	
% P in maize leaves	Season 1	0.18	0.18	0.17	0.11	0.16
	Season 2	0.36	0.33	0.33	0.32	0.34
	Mean	0.27	0.25	0.25	0.21	
	CV %			9.26		
	LSD ≤0.05			0.04		S
	Interactions			S		

S = Significant at P < 0.05 level of probability

9.18.5 Soil Characteristics in Acacia Species Experiments

Comparison of *A. nilotica*, *A. senegal*, and *A. xanthophloea* in nitrogen availability and fixation in the soil (Table 9.13 and Fig. 9.6) shows that there was significant ($P < 0.05$) difference in the two seasons. And when each season was compared separately, there was still significant ($P < 0.05$) difference (Table 9.14). In season one, there was significant difference between species, and *A. xanthophloea* (2 m × 2 m spacing) had lower soil N than maize monoculture. Differences occurred also in season two. *A. nilotica* (2 m × 2 m spacing) was high in nitrogen concentration as compared to the rest of the *Acacia* species and maize monoculture. *A. senegal* and *A. xanthophloea* did not differ from each other but had higher soil N compared to maize monoculture.

There was no significant ($P < 0.05$) difference in soil phosphorus when season one and season two were compared, as illustrated in Table 9.15 and Fig. 9.7. In season two, there was significant ($P < 0.05$) difference (Table 9.14). *A. nilotica* (2 m × 2 m spacing), *A. senegal* (2 m × 2 m spacing) and *A. xanthophloea* (2 m × 2 m spacing) were higher in phosphorus levels than maize monoculture which was half the concentration of *A. nilotica* (2 m × 2 m spacing). On the other hand, there was no significant ($P < 0.05$) difference in soil phosphorus in season one.

In both seasons, when treatments were analysed according to *Acacia* species, *A. nilotica* (2 m × 2 m spacing), *A. senegal* (2 m × 2 m spacing) and *A. xanthophloea* (2 m × 2 m spacing) showed high moisture retention but there was no significant ($P < 0.05$) difference among the three treatments but when the above *Acacias* were compared to maize monoculture treatment, there was significant ($P < 0.05$) difference, as shown in Table 9.14. However, there were no significant ($P < 0.05$) differences when comparing season one and season two as given in Table 9.16.

Acacia species treatments showed no significant difference in soil pH in both seasons (Tables 9.14 and 9.17). *A. nilotica*, spacing 2 m × 2 m, *A. senegal*, spacing 2 m × 2 m, *A. xanthophloea*, spacing 2 m × 2 m, and maize monoculture treatments had an average soil pH of about 7.04 and 6.98 respectively in seasons 1 and 2.

Table 9.13 Soil nitrogen as affected by *A. nilotica, A. senegal* and *A. xanthophloea* in the two seasons

Item	Season	Species				Mean season
		A. nilotica	*A. senegal*	*A. xanthophloea*	Maize monoculture	
% N in soil	Season 1	0.22	0.23	0.19	0.21	0.21
	Season 2	0.34	0.23	0.27	0.14	0.25
	Mean	0.28	0.23	0.23	0.17	
	CV %			8.39		
	LSD ≤0.05			0.03		S
	Interactions			S		

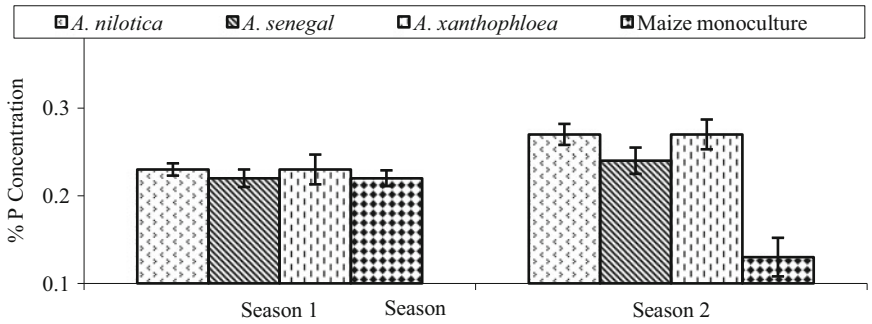

Fig. 9.6 Soil nitrogen levels as affected by *A. nilotica, A. senegal* and *A. xanthophloea* in the two seasons

9.18.6 Influence of Intercropping with Various Acacia Species on Maize Yield

In season one (Table 9.11), maize monoculture produced the highest maize grain yield while the remaining treatments, *A. xanthophloea* (2 m × 2 m spacing), *A. nilotica* (2 m × 2 m spacing), and *A. senegal* (2 m × 2 m spacing) were not statistically different. In season two maize yield intercropped with *A. nilotica* (2 m × 2 m spacing) was the highest followed closely by *A. senegal* (2 m × 2 m spacing). Yield obtained from maize monoculture was about half that obtained in *A. xanthophloea* (2 m × 2 m spacing) and about a third of that in either *A. nilotica* or *A. senegal*. When the two seasons were compared, there was significant ($P < 0.05$) difference (Table 9.18 and Fig. 9.8).

9.19 Discussion

9.19.1 Nutrients Concentrations in Maize Leaves in A. nilotica *of Three Different Spacings*

The results show that time of *A. nilotica* planting, relative to maize planting, and tree spacing are important factors that affect nutrients uptake. The time of planting and tree spacing affected N uptake of maize. Planting of *A. nilotica* at the beginning of season one showed higher N uptake by maize when the trees were spaced at 2 m × 2 m as compared to 3 m × 3 m and 4 m × 4 m (Table 9.1). This occurred as a result of the age and proximity of the *A. nilotica* trees to the maize plants. In season one, the *A. nilotica* trees had not developed extensive root system and could not provide much nitrogen as compared to season two. However, in season two, the root system of the trees had been developed extensively to distribute the captured nitrogen to reach the maize that were intercropped by *A. nilotica* at 2 m × 2 m

Table 9.14 Soil characteristics in *Acacia* species of 2 m × 2 m spacing when intercropped with maize in the two seasons

Season 1					Season 2			
Treatment	%N	%P	Moisture content (%)	pH	%N	%P	Moisture content (%)	pH
A. nilotica	0.220ab	0.227a	10.46a	7.040a	0.343a	0.270a	11.23a	6.983a
A. senegal	0.227a	0.220a	10.16a	7.050a	0.233b	0.243a	10.62a	6.983a
A. xanthophloea	0.193b	0.233a	10.33a	7.033a	0.270b	0.270a	10.96a	6.970a
Maize monoculture	0.207ab	0.217a	7.71b	7.043a	0.140c	0.127b	7.74b	6.977a
$LSD_{0.05}$	0.028	0.021	2.15	0.093	0.043	0.06	1.90	0.095

Table 9.15 Soil phosphorus as affected by *A. nilotica*, *A. senegal* and *A. xanthophloea* in the two seasons

Item	Season	Species				Mean season
		A. nilotica	*A. senegal*	*A. xanthophloea*	Maize monoculture	
% P in soil	Season 1	0.23	0.22	0.23	0.22	0.22
	Season 2	0.27	0.24	0.27	0.13	0.23
	Mean	0.25	0.23	0.25	0.17	
	CV %			8.76		
	LSD ≤ 0.05			0.04		NS
	Interactions			0.05		

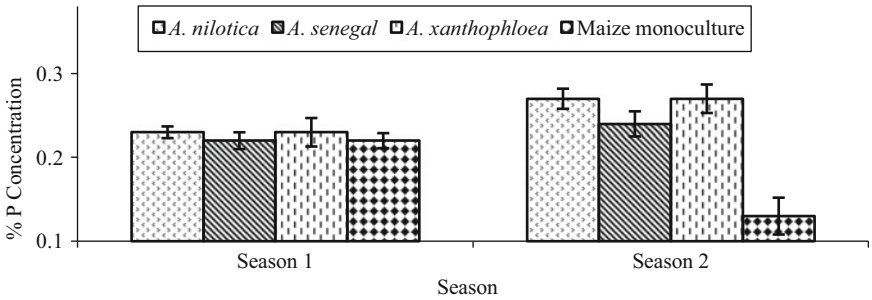

Fig. 9.7 Soil phosphorus levels as affected by *A. nilotica*, *A. senegal* and *A. xanthophloea* in the two seasons

Table 9.16 Moisture content (%) of the soil in the two seasons as affected by *A. nilotica*, *A. senegal* and *A. xanthophloea* when intercropped with maize

Item	Season	Species				Mean season
		A. nilotica	*A. senegal*	*A. xanthophloea*	Maize monoculture	
% Moisture content	Season 1	10.46	10.16	10.33	7.71	9.66
	Season 2	11.23	10.62	10.96	7.74	10.14
	Mean	10.84	10.39	10.64	7.73	
	CV %			9.59		
	LSD ≤0.05			1.74		NS
	Interactions			NS		

but the nitrogen distribution was lower in 3 m × 3 m and 4 m × 4 m. This trend indicates that there was not much dilution effect on the nitrogen availed to the maize by the roots of the *A. nilotica* trees at 2 m × 2 m as compared to 3 m × 3 m and 4 m × 4 m. The results in this study clearly indicate that the root systems of trees in arid lands can scavenge water and nutrients by being extensive, extending up to 50 m from the trees in some species [48, 49] or by rooting deeply.

Table 9.17 Soil pH in the two seasons as affected by *A. nilotica*, *A. senegal* and *A. xanthophloea* when intercropped with maize

Item	Season	Species				Mean season
		A. nilotica	*A. senegal*	*A. xanthophloea*	Maize monoculture	
Soil pH	Season 1	7.04	7.05	7.03	7.04	7.04
	Season 2	6.98	6.98	6.97	6.98	6.98
	Mean	7.01	7.03	7.00	7.01	
	CV %			0.62		
	LSD ≤0.05			0.76		NS
	Interactions			NS		

Table 9.18 Influence of intercropping with various *Acacia* species on maize yield

Item	Season	Species				Mean season
		A. nilotica	*A. senegal*	*A. xanthophloea*	Maize monoculture	
Yield (Grain) Mg/ha	Season 1	8.33	7.33	8.33	16.00	10.00
	Season 2	20.33	18.33	13.67	6.16	14.62
	Mean	14.33	12.83	11.00	11.08	
	CV %			21.33		
	LSD ≤0.05			55.5		S
	Interactions			S		

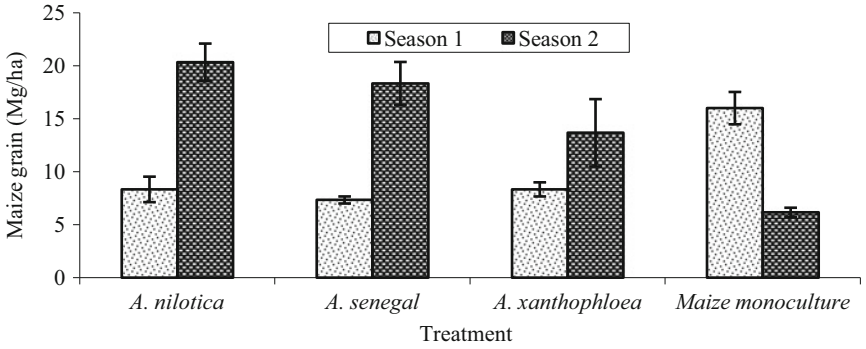

Fig. 9.8 Maize grain yield as affected by *A. nilotica*, *A. senegal*, and *A. xanthophloea* in the two seasons

The increase in P concentration in the maize leaves in season 2 (Tables 9.1 and 9.3) for the *A. nilotica* of different spacing shows that 2 m × 2 m increased P and that spacing of the trees is an important factor in P build up and its subsequent uptake by the intercropped plants. These results confirm that mycorrhizal associations formed by the *A. nilotica* facilitated the capture of phosphate ions by effectively enhancing the volume of soil exploited by the roots and the efficiency with

which P is extracted. Lajtha and Harrison [50] and Tinker [51] similarly reported that mycorrhizae are key facilitators for P capture by plants in P-depleted soils and that *Acacia* trees are successful pioneers partly because, like many other members of the legume plant family, they have associations with two types of microorganism: rhizobia and mycorrhizae.

The other contributions to the above results could have been through P cycling processes whereby plants convert inorganic P absorbed from the soil solution into organic forms in their tissues. The addition of plant material grown *in situ* to the soil as litter-fall, root decay, green manure incorporation, crop-residue returns and its subsequent decomposition results in the formation of organic forms of soil P.

9.19.2 Soil Nitrogen and Soil Phosphorus in A. nilotica *of Different Spacings*

The amounts of N reported in this study are within the range reported by Okalebo et al. [44, 51]. The difference in N amount in *A. nilotica* spacing can be partly explained by the low and erratic rainfall received during the cropping period, March 2006 to December 2006. Therefore, the growth and survival of the *A. nilotica* trees could have been hindered. As a result of such constraint, arable cropping becomes risky resulting in unstable crop yields since water is an important limiting factor in these arid and semi-arid ecosystems. The N response under 2m by 2m spacing during March-May 2006 rainy season (Tables 9.4 and 9.5) was that the seedlings competed with the maize for growth resources, such as water and nutrients, thereby reducing the residual effect, N fixation/availability of *A. nilotica* trees on maize.

In Oct–Dec 2006 rainy season, the *A. nilotica* trees had grown and the biomass produced was incorporated into the soil before planting of the second maize crop. As a result, the incorporated biomass and long roots of the *A. nilotica* trees resulting in effective N fixation was a source of N to maize as shown by increase in N concentrations (Tables 9.4 and 9.5). Maize monoculture and 4 m × 4 m recorded a decrease in N concentration in season two as there was no replacement of N taken up by the maize crop and amount of N fixed or made available to the maize was minimal as the *A. nilotica* trees were far apart thereby reducing the amount of N available to maize. The above results agree with other studies where the levels of N in the plant-available NH_4^+ and NO_3^- forms fluctuate during the cropping season and are dependent on factors such as soil moisture (rainfall pattern), cropping history, litter inputs and microbial activity [51].

According to this study, it is less clear what factors favoured higher N levels in *A. nilotica*, 2 m × 2 m as compared to *A. nilotica*, 3 m × 3 m spacing (Table 9.4). Becky [1, 51] reported that N levels decrease with distance from, or depth beneath each *Acacia* tree. Soil pH did not vary much in the two seasons and therefore had little or no effect on N and P availability.

The difference in P level in the soil in *A. nilotica* of different spacing did not vary greatly (Tables 9.4 and 9.6). However, this could have been as a result of the pH of the soil and the effect of organic matter. These findings are consistent with other studies where the greatest degree of P fixation occurs at very low and very high soil pH. As pH increases from below 5.0 to about 6.0 the Fe and Al–P become more soluble. Also as pH drops from greater than 8.0 to below 6.0, Ca–P compounds increase in solubility. Therefore, as a general rule in most mineral soils, P fixation is at its lowest (and plant availability is highest) when soil pH is maintained in the 6.0–7.0 range [52]. Organic matter (OM) generally has little capacity to strongly fix P ions. Soils high in OM especially active fractions of organic matter generally exhibit relatively low levels of P fixation. Several mechanisms are responsible for the reduced P fixation associated with high soil OM. First large humic molecules can adhere to the surfaces of clay and metal hydrous oxides particles, masking the P fixation sites and preventing them from interacting with P ions in solution. Second, organic acids produced by plant roots and microbial decay can serve as organic anions, which are attracted to positive charges and hydroxyls on the surface of clays and hydrous oxides. The organic anions may compete with P ions for fixation. Third, certain organic acids and similar compounds can entrap the reactive Al and Fe in stable organic complexes called chelates. Once chelated these metals are unavailable for reaction with P ions in solution.

When organic residues are added to soils, organic acids may be added directly to the soils with the residue or be produced as by-products during decomposition of the residues by microbial activity. The main acids are usually oxalic, malic, maleic, malonic, succinic, formic and acetic acids [51, 52]. These acids tend to be significantly lower in cultivated soils than uncultivated soils [53]. Organic acids in soil tend to form complexes with such metals as Al or Fe, which readily react with orthophosphate thus reducing P sorption and hence increasing orthophosphate availability to plants [54].

9.19.3 Maize Grain Yield

The plots used in this trial were continuously cultivated for several years with minimal inorganic fertilizer input. Therefore, the low yields observed were due to low soil fertility. The increase in yields recorded in season two in the *A. nilotica*, 2 m × 2 m spacing system as compared to *A. nilotica*, 3 m × 3 m, *A. nilotica*, 4 m × 4 m and maize monoculture (Table 9.1 and Fig. 9.4) was as a result of maximum N availability and fixation and lack of dilution effect in the available N or fixed N from the trees thereby enhancing nutrients uptake by the maize plants. *A. nilotica* trees resulted in the export of nitrogen through the thinned branches, harvested wood (Table 9.1). Although a sizeable proportion of nitrogen in *A. nilotica* could be due to a net input of nitrogen to the soil-plant system through biological N_2 fixation, the capture of nitrate from below the rooting depth of crops could have been higher in *A. nilotica* of close spacing as compared to other *Acacia* spacings and maize

monoculture. Becky [1, 54] similarly reported this interaction. Thus, *A. nilotica* trees and their respective spacing collectively served towards effective nitrogen availability for maize.

9.19.4 Concentration of Nutrients in Leaves of Maize Plants Intercropped with Various Acacia Species

According to the results of this study, the time of *Acacia* planting, relative to maize planting, and tree species are important factors that affect nutrients uptake.

A. nilotica exhibited a higher N uptake in the maize as compared to *A. senegal* and *A. xanthophloea* (Fig. 9.5). There was more direct benefit to the non-legume (maize) as the result of the nitrogen excretion by the legume (*A. nilotica*) as compared to *A. senegal* and *A. xanthophloea*. These results indicate that the potential for intensification of tree planting with species such as *A. nilotica* to enhance the soil N status will depend on the relative importance of N_2 fixation or N acquisition from a wide area in the enhancement of soil fertility and subsequent nutrient uptake by the intercropped non-legume plant [49, 52, 54]. In this study, the results show that *A. nilotica* can potentially absorb leached nutrients accumulated in subsoil below the rooting depth of the annual crop and that nutrients taken up by the trees from below the rooting zone of annual crops like maize become an input when transferred to surface soil in the form of leaves, litters, roots and prunings of the tree leaves and branches. The quality and quantity of the biomass produced by the trees which tend to be relatively higher for *A. nilotica* as compared to *A. senegal* and *A. xanthophloea* may be due to the fact that *A. nilotica* biomass degrades more rapidly than those of *A. senegal* and *A. xanthophloea*. The implications of this are that fast-decomposing biomass such as those of *A. nilotica* applied at planting, beginning of season two as compared to planting of the trees with maize together at the beginning of season one, would release some N to meet the maize N requirements. Similar results were found in the alfisols of sub humid tropics of Nigeria [4, 7, 48, 54]. *A. senegal* and *A. xanthophloea* biomass could have had a higher protein-binding capacity than *A. nilotica*; therefore, they released N more slowly.

The increase in P concentration in the maize leaves in season 2 (Tables 9.11 and 9.12) in the presence of the *Acacia* trees shows that *A. nilotica* increased P from 0.183 to 0.363%, indicating that *Acacia* species is an important factor in P build up and its subsequent uptake by the intercropped plants. These results clearly suggest that mycorrhizal associations formed by the *Acacias* facilitated the capture of phosphate ions by effectively enhancing the volume of soil exploited by the roots and the efficiency with which P is extracted [50, 54]. Mycorrhizae are key facilitators for P capture by plants in P-depleted soils [51–54].

9.19.5 Nitrogen and Phosphorus in Soils Derived from Plots with Acacia Species Intercropping

The amounts of N reported in this study are in the range reported in the literature [44, 52, 54]. The difference in N amount in *Acacia* species (Tables 9.14, 9.13 and Fig. 9.6) can be partly explained by the low and erratic rainfall received during the cropping period, March 2006 to December 2006 (c.f. Sect. 9.19.2).

The difference in P level in the soil in the three *Acacia* species did not vary greatly (Table 9.14 and Fig. 9.7). However, this could have been as a result of the pH of the soil and the effect of organic matter (c.f. Sect. 9.19.2).

9.19.6 Maize Grain Yield with Acacia Species

The plots used in this trial were continuously cultivated for several years with minimal inorganic fertilizer input. Therefore, the low yields observed were due to low soil fertility. The increase in yields recorded in season two in the *Acacia* species variation can presumably be attributed to the supply of plant-available N from decomposing litter and biomass (Table 9.11 and Fig. 9.8). Although a sizeable proportion of nitrogen in *A. nilotica* was due to a net input of nitrogen to the soil-plant system through biological N_2 fixation, the capture of nitrate from below the rooting depth of crops was higher in *A. nilotica* as compared to *A. senegal* and *A. xanthophloea*. Sheikh [35–37, 54] similarly reported this interaction. Thus, all *Acacias* collectively served towards effective nitrogen availability for maize.

Acacia trees, as compared to maize monoculture, increased grain yield of intercropped maize (Table 9.11 and Fig. 9.8) in season 2. The trend in yield increase was *A. nilotica* > *A. senegal* > *A. xanthophloea*. The species effect on maize grain yield can be explained in terms of the amount of nutrients captured by the *Acacia* trees, the ability of the trees to fix nitrogen, and the rainfall received in the growing season.

A. nilotica could have produced high-quality biomass with low contents of lignin and polyphenols, and high N content. The polyphenols of *A. nilotica* could be having low protein binding capacity as compared to *A. xanthophloea*, hence they can release N rapidly [48, 50, 54]. *A. xanthophloea* presumably had high contents of polyphenols with high protein binding capacity relative to *A. nilotica* and *A. senegal* [7, 16, 48, 54]. In terms of biomass quality produced, the species can be ranked in the order *A. nilotica* > *A. senegal* > *A. xanthophloea*. Sanginga et al. [26, 54] showed that high-quality biomass of legumes led to more N in the light fractions of soil organic matter, high pre-season soil inorganic N, and high aerobic N mineralization. Pre-season soil inorganic N at planting has been shown to be directly correlated with maize grain yield following legume-maize intercropping [26, 48, 51, 54]. The relatively lower biomass quality of *A. xanthophloea* and

A. senegal, as compared to *A. nilotica*, could result in greater duration of residual benefits to maize.

The low maize yield in the first season in *Acacias* as compared to maize monoculture was as a result of competition between the trees and the intercropped maize. Graham and Vanice [23, 52–54], in which it was observed that any increase in nutrient availability in the soil was used by the plant to produce more biomass rather than to increase nutrient concentrations, similarly observed this relationship.

9.20 Summary and Conclusions

The results suggest that the inclusion of *Acacia* trees into the maize cultivation by small scale farmers in western Kenya has potential to increase maize production by simultaneously improving soil fertility through N fixation, preventing losses of soil organic matter and increasing internal nutrient cycling. The system is more effective with closer spacing of the *Acacia* trees. Although all the acacia species improved maize yields, *A. nilotica* was more effective than *A. senegal* and *A. xanthophloea*.

The capability of *A. nilotica* to produce enough quantity of biomass and accumulate more nutrients was tested in a given area. *A. nilotica* is preferred as a suitable tree in Africa because of its ability to grow fast and produce nutrient-rich biomass. Production of more biomass that is of high quality, readily decomposable, is a key factor considered in the selection of desirable *Acacia* species. The process of symbiotic N_2-fixation is also affected by other environmental factors such as soil nutrient availability, especially P [1, 50, 54]. Nonetheless, all over Africa, *Acacias* have been grown traditionally as farm trees within and adjacent to arable crops and livestock. The main reason for this agroforestry system is that *Acacia* species like *A. nilotica* pods and seeds are themselves an important source of protein-rich fodder for both livestock and humans in times of food scarcity. In addition, the thorny armament of *Acacia* trees can provide brushwood fencing to protect crops, gardens and livestock. The trees also provide shade to cattle and farm workers when the sun is hottest and do not obstruct the light needed by many field crops during the wettest part of the year.

Acacias also provide more long-term benefits to the neighbouring plants. This is because of their association with rhizobia bacteria; when parts of the trees die and decay, they fertilize the surrounding soil. On the poor sandy soils of semiarid areas like Kendu Bay [42, 51, 54] and other areas in sub-Saharan Africa, this cycle can help improve the growth and yield of field crops.

9.21 Future Research

Since this study was carried out in one area, results might be different when carried out in other areas with varied field conditions within the Lake Basin. It is recommended that additional field studies be carried out in other areas within the region to confirm these results. Correlation studies between the amount of nitrogen fixed and biomass produced in the three *Acacias* were not carried out in this study but are important aspects that will help in understanding the already obtained results.

The economic importance of *A. nilotica*, *A. senegal* and *A. xanthophloea* needs to be explored since these trees have multipurpose applications and if put to use, the small scale farmers can get more income thereby improving their livelihood. There is need to collect more data so that some of the variations occurring can be authenticated, especially root study of the three *Acacia* species in taping nutrients below and making those nutrients available to other crops.

The age and canopy of the trees will affect the nitrogen levels in the soil. More data should be collected to determine the optimum level of the trees in fixing nitrogen and the effect of tree canopy on the other plants.

Acknowledgements This work was supported by the Kenya Forestry Research Institute, KEFRI and my mentor Prophet T.B. Joshua. The authors are grateful for the support.

References

1. Becky H (2004) The Acacia tree: a sustainable resource for Africa. FRP/DFID, Oxford, pp 9–24
2. Palm CA (1995) Contribution of agroforestry trees to nutrient requirements of intercropped plants. Agroforest Syst 30:105–124
3. Wagner SC (2011) Biological nitrogen fixation. Nat Educ Knowl 3:15
4. Keiko K, Richard LW, John DR (1987) Role of glutamate dehydrogenase in ammonia assimilation in nitrogen-fixing *Bacillus macerans*. J Bacteriol 169:4692–4695
5. Stevenson FJ (1986) Cycles of soil. Carbon, nitrogen, phosphorous, sulphur micronutrients. Wiley, New York, pp 106–108
6. Jansson SL, Persson J (1982) Mineralization and immobilization of soil nitrogen. In: Stevenson FJ (ed) Nitrogen in agricultural soils. Wiley, New York, pp 229–252
7. Buresh RJ, Tian G (1998) Soil improvement by trees in sub-Saharan Africa. Agroforest Syst 38:51–76
8. Palm CA, Myers RJK, Nandwa SN (1997) Combined use of organic and inorganic nutrient sources for soil fertility maintenance and replenishment. In: Buresh RJ, Sanchez PA, Calhoun F (eds) Replenishing soil fertility in Africa. Soil Society of America, Wisconsin, pp 193–217
9. Garrity DP (2004) Agroforestry and the achievement of the millennium development goals. Agroforest Syst 61:5–17
10. Sanchez PA (1999) Improved-fallows come of age in the tropics. Agroforest Syst 47:3–12
11. Szott LT, Palm CA, Buresh RJ (1999) Ecosystem fertility and fallow function in the humid and subhumid tropics. Agroforest Syst 47:163–196

12. Gallagher RS, Fernandes ECM, McCallie EL (1999) Weed management through short-term improved-fallows in tropical agro-ecosystems. Agroforest Syst 47:197–221
13. Franzel S (1998) Socio-economic factors affecting the adoption of potential improved tree fallows in Africa. Agroforest Syst 47:305–321
14. Jaiyeoba IA (2003) Changes in soil properties due to continuous cultivation in Nigerian semiarid savannah. Soil Till Res 70:91–98
15. Rao MR, Mathuva MN, Gacheru E, Radersma SPC, Jama B (2002) Duration of *Sesbania* fallow effect for nitrogen requirement of maize in planted fallow-maize rotation in western Kenya. Expl Agric 38:223–236
16. Sanchez PA (2002) Soil fertility and hunger in Africa. Sci Compass 295:2019–2020
17. Mafongoya PL, Dzowela BH (1999) Biomass production of tree fallows and their residual effect on maize in Zimbabwe. Agroforest Syst 47:139–151
18. Kang BT, Akinnifesi FK, Ladipo DO (1994) Performance of selected woody agroforestry species grown on an Alfisol and Ultisol in the humid lowland of west Africa and their effects on soil properties. J Trop For Sci 7:303–312
19. Tian G, Salako FK, Ishida F (2001) Replenishment of C, N, and P in a degraded Alfisol under humid tropical conditions: effect of fallow species and litter polyphenols. Soil Sci 166:614–621
20. Odee D (1990) Some characteristics of the *Rhizobium* symbiosis of *Sesbania sesban* and its potential for biological nitrogen fixation in Kenya. In: Macklin B, Evans DO (eds) Perennial *Sesbania* species in agroforestry systems. ICRAF and Nitrogen Fixing Tree Association, Wimanal, pp 203–209
21. Rajendran K, Devaraj P (2004) Biomass and nutrient distribution and their return of *Casuarina equisetifolia* inoculated with biofertilizers in farmland. Biomass Bioenerg 26:235–249
22. Sanginga N, Vanlauwe B, Danso SKA (1995) Management of biological N_2-fixation in alley cropping systems: estimation and contribution to N balance. Plant Soil 174:119–141
23. Graham PH, Vance CP (2000) Nitrogen fixation in perspective: an overview of research and extension needs. Field Crop Res 65:93–106
24. Young A (1997) Agroforestry for Soil Management, 2nd edn. CAB International, Wallingford, p 320
25. Chalk PM, Ladha JK (1999) Estimation of legume symbiotic dependence: an evaluation of techniques based on ^{15}N dilution. Soil Biol Biochem 31:1901–1917
26. Sanginga N, Bowen GD, Danso SKA (1990) Assessment of genetic variability for N_2-fixation between and within provenances of *Leucaena leucocephala* and *Acacia albida* estimated by ^{15}N labelling techniques. Plant Soil 127:169–178
27. Olson RA, Kurtz LT (1982) Crop nitrogen requirements, utilization and fertilization. In: Stevenson FJ (ed) Nitrogen in agricultural Soils. American Society of Agronomy, Wisconsin, pp 567–604
28. Mengel K, Kirkby EA (1982) Principles of plant nutrition, 2nd edn. International Potash Institute, Bern, pp 153–169
29. Giller KE (2001) Nitrogen fixation in tropical cropping systems, 2nd edn. CAB International, Wallingford, p 423
30. Hoekstra D, Corbett JD (1995) Sustainable agricultural growth for the highlands of East and Central Africa: prospects to 2020. International Food Policy Res Inst, Washington, pp 187–219
31. Ong C (2000) The link between land management and the lake in the Lake Victoria basin. In: Mugo F, Nyantika D, Nyasimi M (eds) Agroforestry seminar proceedings on improved land management in the Lake Victoria Basin, Kisumu, pp 7–12
32. Peeters T, Aleem MIH (1970) Oxidation of sulfur compounds and electron transport in *Thiobacillus denitrificans*. Archiv Mikrobiol 71:319
33. Armitage FB, Joustra PA, Ben Salem B (1980) Genetic resources of tree species in arid and semi-arid areas. FAO/IBPGR, Rome, Italy, p 11
34. Omondi W, Maua JO, Gachathi FN (2004) Tree seed handbook of Kenya, vol 1, 2nd edn. GTZ Forestry Seed Centre Muguga, Nairobi, pp 23–52

35. Sheikh MI (1989) *Acacia nilotica* (L.) Wild ex Del. Its production, management, and utilization. FAO/Regional Wood Energy Development Program in Asia (GCP/RAS/111/NET), Bangkok, Thailand, pp 23–45
36. Singh SP (1982) Growth studies of *Acacia nilotica*. Indian Forest 108:283–288
37. Thomas V, Grant R (2004) SAPPI tree spotting: Kwazulu–Natal and Eastern Cape. Jacana, Johannesburg, pp 22–27
38. Mandal AK, Ennos RA, Fagg CW (1994) Mating system analysis in a natural population of *Acacia nilotica* subspecies leiocarpa. Theor Appl Genet 89:931–935
39. Brenan JPM (1983) Manual on taxonomy of *Acacia* species: present taxonomy of four species of Acacia (*A. albida, A. senegal, A. nilotica, A. tortilis*). Food and Agriculture Organization of the United Nations, Rome, Italy, pp 27–31
40. Fagg CW, Barnes RD, Marunda CT (1997) African Acacia trials network: a seed collection of six species for provenance/progeny tests held at the Oxford Forestry Institute. Forest Genet Resour 25:39–50
41. Smestad BT, Tiessen H, Buresh RJ (2002) Short fallows of *Tithonia diversifolia* and *Crotalaria grahamiana* for soil fertility improvement in western Kenya. Agroforest Syst 55:181–194
42. Jaetzold R, Schmidt H (1982) Farm management handbook of Kenya. Typo-drunk, Rossdorf, W-Germany, pp 81–84
43. Ferralsol (2006). Encyclopaedia Britannica. https://global.britannica.com/science/Ferralsol
44. Okalebo JR, Kenneth WG, Paul LW (1993) Laboratory methods of soil and plant analyses. Soil Science Society of East Africa Technical Publication, Nairobi, pp 22–29
45. Parkinson JA, Allen SE (1975) A wet oxidation procedure suitable for determination of nitrogen and mineral nutrients in biological materials. Commun Soil Sci Plant Anal 6:1–11
46. Anderson JM, Ingram JSI (1989) A handbook of methods of analysis. C.A.B. International, Oxon, pp 11–39
47. Okalebo JR (1985) A simple wet ashing technique of P, K, Ca and Mg analysis of plant tissue in a single digest. Kenya J Sci Technol B6:129–133
48. Mafongoya PL, Giller KE, Palm CA (1998) Decomposition and nitrogen release patterns of tree prunings and litter. Agroforest Syst 35:77–97
49. Giller KE, Cadisch G (1995) Future benefits from biological nitrogen fixation: an ecological approach to agriculture. Plant Soil 174:255–277
50. Lajtha K, Harrison AF (1995) Strategies of phosphorus acquisition and conservation by plant species and communities. In: Tiessen H (ed) Phosphorus in the global environment: transfers, cycles and management, Scope 54. Wiley, New York, pp 139–147
51. Tinker PB (1975) Soil chemistry of phosphorus and mycorrhizal effects on plant growth. In: Sanders FE et al (ed) Endomycorrhizas. Academic, London, pp 353-371
52. Iyamuremye F, Dick RP (1996) Organic amendments and phosphorus sorption by soils. Adv Agron 56:139–185
53. Fox TR, Comerford NB (1990) Lower molecular weight and organic acids in selected soils of south eastern U.S.A. Soil Sci Soc Am J 54:1139–1144
54. Nziguheba G, Palm CA, Buresh RJ, Smithson PC (1998) Soil phosphorus fractions and adsorption as affected by organic and inorganic sources. Plant Soil 198:159–168

Chapter 10
Ultrasonic-Assisted Dispersive Solid Phase Microextraction (UA-DSPME) Using Silica@Multiwalled Carbon Nanotubes Hybrid Nanostructures Sorbent for Preconcentration of Trace Aflatoxin B_1 in Liquid Milk Samples

Geaneth P. Mashile, Anele Mpupa, and Philiswa N. Nomngongo

Abstract A reliable, simple, rapid and cost-effective extraction method based on ultrasonic-assisted dispersive solid phase microextraction (UA-DSPME) method using silica@multiwalled carbon nanotubes hybrid nanostructures combined with spectrophotometric detection was developed for the first time for preconcentration and determination of aflatoxin B_1 (AFB1) in liquid milk samples. Two level factorial design and central composite design in combination with response surface methodology were used to evaluate the factors affecting extraction and preconcentration procedure. The influence of different variables including mass of adsorbent, extraction time, eluent volume and sample volume was investigated in the optimization study. Under the optimal conditions, a dynamic linear range of 0.3–250 μg L^{-1} with detection limit of 0.1 μg L^{-1} was obtained. The intraday and interday precisions expressed as relative standard deviations were 3.2% and 4.3% respectively. The developed UA-DSPME/UV-Vis method was applied for extraction and preconcentration of AFB1 in real milk samples. As a result of relatively high enrichment factor (108), satisfactory extraction recoveries (96.8–99.2%) using only 62 mg of an adsorbent were achieved.

Keywords Aflatoxin B_1 • Ultrasonic-assisted dispersive solid phase microextraction • Silica multiwalled carbon nanotubes • Secondary metabolites • Liquid milk • UV-Vis spectrophotometry

G.P. Mashile • A. Mpupa • P.N. Nomngongo (✉)
Department of Applied Chemistry, University of Johannesburg, Doornfontein Campus, P.O. Box 17011, Johannesburg 2028, South Africa
e-mail: pnnomngongo@uj.ac.za; nomngongo@yahoo.com

P. Ramasami et al. (eds.), *Emerging Trends in Chemical Sciences*,
DOI 10.1007/978-3-319-60408-4_10

10.1 Introduction

The most basic human right is access to safe food and drinking water. However this basic right can be affected by natural contaminants such as mycotoxins [1]. The agricultural and food industries are already threatened by mycotoxins, as these toxins produce carcinogenic secondary metabolites called aflatoxins (AFs) [2]. The AFs contaminate mostly dietary staple food such as maize, groundnuts, rice, cassava and sorghum [3]. As a result, this creates a great loss in agriculture and the economy for developed and developing countries particularly African nations where food is already scarce. Six out of 18 AFs have been designated as important. These include aflatoxin B_1, B_2, G_1, G_2, M_1 and M_2 [4]. Among these six, the most significant is AFB1which accounts for 75% of all aflatoxin contaminations of crops and animal feeds [3]. Aflatoxin B_1 is widely spread in food crops such as grain, nuts, corn, cotton seeds, figs, spices as well as milk and other dairy products [3]. The presence of aflatoxins especially AFB1 in food poses a health risk as AFB1 has been classified by the International Agency for Research on Cancer (IARC) as a group 1 human carcinogen while aflatoxins G_1, G_2 and B_2 are categorised as group 2 human carcinogens [5–7].

In view of the above, many researchers have developed analytical methods for the determination of AFs. These methods include liquid chromatography with fluorescence detector (HPLC−FLD) or mass spectrometry (LC−MS/MS) which have been regarded as standard analytical methods for AFs due to their good accuracy and their capability to simultaneously detect total AFs in a single test [8]. However these methods are relatively expensive, time-consuming, and laborious, and require sophisticated equipment and highly skilled personnel. Currently, SPE with OASIS HLB, C18, ion exchange cartridges, and automated size-exclusion cartridge have been used for extraction of AFM1 from milk. Wang and Li [6] evaluated the effects of matrix interference in the analysis of 4 mycotoxins (OTA, ZEN, AFB1 & AFM1) in 21 liquid and powder milk samples using an automated size-exclusion SPE-UPLC-MS/MS method. The results demonstrated that the method was an appropriate approach for preventing problems associated with matrix effects. The recoveries of the four mycotoxins in fortified milk ranged between 98–120% and RSDs between 2–9%. The method LOD for the liquid and powder milk were 0.05–2 ng L^{-1} and 0.25–10 ng kg^{-1} respectively, while the LOQ for both liquid and powder milk were between 0.1–5 ng L^{-1} and 0.5–25 ng kg^{-1} respectively. Another concern is the lack of studies in the detection of toxins like AFB1 from milk residues other than AFM1.

The AFs are compounds that are pentaheterocyclic (Fig. 10.1) and highly conjugated, with natural fluorescence [9]. Thus, analytical methods developed for their analysis are either based on native fluorescence or acquired fluorescence properties. These fluorescence properties are known to be sensitive in the AFs natural environment and can be controlled by solvents, pH and water quenching. As a result this has enabled the development of more sensitive and selective methods based on the materials used [10]. Generally, the determination of AFs in real

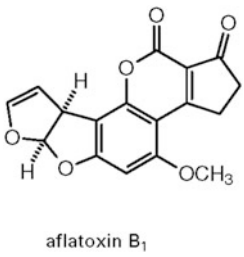

Fig. 10.1 Chemical structure of AFB1

samples requires an enrichment or pre-treatment procedure. Thus, pre-treatment procedures include dispersion-solid phase extraction (DSPE) [11], microwave assisted extraction-SPE [12], magnetic solid phase extraction (MSPE) [9, 13] and solid phase extraction [14]. These methods are known to have an ability to eliminate matrix interferences in milk and preconcentrate the AFs.

This study aimed at developing a simple, accurate and rapid method based on dispersive solid phase microextraction procedure combined with UV-Vis spectrophotometry for the extraction, preconcentration and determination of AFB1 in liquid milk samples. This was achieved by synthesizing the silica/multiwalled carbon nanotubes (SiO_2@MWCNT) hybrid nanostructures via sol-gel method but firstly functionalizing MWCNTs with mild acids methods. This study focused on AFB1 in milk because it is the most prevalent and toxic of all aflatoxins contaminating a wide range of agricultural products [1]. The motivation behind the study is that most of the studies investigated the amount of AFM1 in milk and neglected the trace amount of AFB1 that might remain when the AFB1 is metabolized into its hydroxylated metabolite AFM1. In addition, studies on the determination of AFB1 in other milk products such as rice milk and soymilk which might contain traces are limited.

10.2 Experimental

10.2.1 Materials and Reagents

All chemicals and reagents were of analytical grade except unless otherwise stated. Chromatographic grade acetone (MeCO), acetonitrile (MeCN), ethanol (EtOH) and methanol (MeOH) were obtained from Sigma-Aldrich (St Louis, MO, USA). Aflatoxin B_1 standard was purchased from Sigma-Aldrich (St Louis, MO, USA). Triton-X 114, tetraethyl orthosilicate (TEOS), sulphuric acid, nitric acid, multiwalled carbon nanotubes (D × L 110–170 nm × 5–9 μm) and ammonia solution (25% w/w) were also purchased from Sigma-Aldrich (St Louis, MO, USA).

10.2.2 Samples

Three different milk products (soymilk, rice milk and cow milk) were purchased in a local supermarket (Johannesburg, South Africa). All samples were stored at room temperature before analysis.

10.2.3 Cautions and Safety Considerations

Aflatoxins are carcinogenic compounds, thus when handling their solutions and extracts, precautions must be warranted. Gloves and other protective gear were worn as safety measure during the handling of the compounds. To guarantee the safety of research workers and avoid risk the stock solutions were prepared under a laminar flow and fume hood. Glassware and any material used during preparation of standards and samples were soaked in dilute sulphuric acid for several hours to remove any active absorption sites. Thereafter the glasswares were thoroughly rinsed with distilled water to remove all traces of acid [15]. Upon completion of all analysis all materials used for standards or sample preparation were decontaminated with sodium hypochlorite solution. Since aflatoxins are subject to light degradation, all analytical work was protected from daylight by keeping them in amber vials and standard solutions were stored at −20 °C.

10.2.4 Instrumentation

UV-Vis absorption spectra were acquired on a UV-2450 spectrophotometer (Shimadzu, Japan). The excitation and emission slits were both 5 nm and all measurements were performed in a quartz microcell at 25 ± 0.1 °C. A TESCAN VEGA 3 XMU LMH instrument (Czech Republic) scanning electron microscope (SEM) was used to characterize the size and morphology of adsorbent coupled with energy dispersive X-ray spectroscopy (EDS) for elemental composition analysis at an accelerated voltage of 20 kV. Chemical interactions were studied using a Perkin Elmer Spectrum 100 FT-IR spectrometer in the range of 400–4000 cm^{-1} with KBr pellets (Waltham, MA, USA). All pH measurements were done using an H1 9811-5 (HANNA instruments, Smithfield, Rhode Island, USA) pH meter supplied with a combined electrode.

10.2.5 Preparation of SiO_2@MWCNTs Adsorbent

The functionalization of MWCNTs by mild acid sonication was based on the procedure described by Fatin and colleagues [16]. Diluted acids (6 mol L^{-1} nitric acid and 6 mol L^{-1} sulphuric acid) were mixed in the ratio of 1:3. A mass of 500 mg MWCNTs was added to 100 ml of acid mixture in a conical flask. The mixture was then sonicated for 4 h in an ultrasonic bath and the temperature was maintained at 40 °C. Thereafter the sonicated mixtures were filtered through a filter paper and rinsed with distilled water until the filtrate was neutral. The yields on the filter paper were dried in a vacuum oven overnight at 80 °C. The synthesis strategy of the adsorbent was based on a reported method [17]. The modified MWCNTs were again added to the deionised water and sonicated for 10 min in an ultrasonic bath. This was then stirred vigorously for 20 min. Briefly, a solution of TEOS (0.0225 mol) and ethanol 1:1 (v/v) was prepared and left to mix for 20 min, after which 2 ml of H_2O was added and the solution was stirred for a further 5 min. The prepared TEOS solution was slowly added in the above mentioned solution using a dropping funnel. The pH value of the solution was adjusted to 9 with ammonia. The reaction was conducted at 80 °C for 6 h before allowing to rest for 24 h, and then filtered. The hybrid material was calcined at 500 °C in a chamber-type electric resistance furnace.

10.2.6 UA-DSPME Procedure

Liquid milk (10.00 ml) was measured accurately into 50 ml centrifuge tubes and centrifuged (4000 rpm) for 15 min. After centrifuging the fat layer was removed. The supernatant was then spiked with appropriate amounts of AFB1 and diluted with 30 ml phosphate buffer saline solution in a capped container with intensive shaking. The diluted aqueous solution phase was then transferred to a 50 ml sample tube that contains SiO_2@MWCNTs. The mixture was sonicated for 5 min to facilitate adsorption of AFB1 to the SiO_2@MWCNTs. The sample was then transferred and separated into centrifugation tubes which were centrifuged at max rpm for 10 min after which the supernatant was decanted. The eluent (MeCN: MeCO) 1:1 (v/v) was added to the centrifuge tube which was stirred for another 10 min. After desorption, the eluent was separated into amber vials and evaporated to dryness under nitrogen gas flow at room temperature. The dried residue was then dissolved in a mixture of 2 ml of 0.5mM Triton X-114 in 15% (v/v) acetonitrile: water and stirred for 5 min. The final solution was then taken for UV-Vis spectrophotometric and HPLC analysis.

The factors affecting the extraction and preconcentration of AFB1 were optimized using experimental design approaches. The screening process was achieved by a two-level fractional factorial (2^{4-1}) design. The factors investigated included mass of adsorbent, extraction time, eluent and sample volume (Table 10.1). In the

Table 10.1 Factors and levels of experimental designs

Variable	Low level (−)	Center point (0)	High level (+)
Mass of adsorbent (mg)	25	62.5	100
Extraction time (min)	5	17.5	30
Eluent volume (ml)	1	2	3
Sample volume (ml)	1	3	5

second step, the central composite design was used to optimize the most influential factors such as mass of adsorbent, extraction time and eluent volume. Minitab 17 software was used for processing the experimental data.

10.3 Results and Discussion

10.3.1 Characteristics of SiO_2@MWCNTs

MWCNTs were functionalised by sonication treatment in order to increase the interaction between MWCNTs and acids. Moreover, the sonication treatment was applied at 40 °C as functionalization by acid alone would take longer. Therefore the sonication caused the excitation of electrons in the acid solution in which electrophilic reactions would take place. As a result oxygenated species were formed due to opening of the aromatic ring on the carbon atom of the MWCNTs surface attracted by the electrophiles generated from acid attack.

The FT-IR spectra of MWCNTs and SiO_2@MWCNTs are shown in Fig. 10.2. As can be seen, the adsorbent spectrum (Fig.10.2b) showed characteristic absorption bands at 1086 and 801 cm^{-1} for Si-O-H and Si-O-Si respectively. They both have absorption peak around 1658 cm^{-1} for C=O because acidification generates carboxyl groups on the surface of CNTs. The large adsorbent peak around 3500 cm^{-1} was attributed to the O-H stretching vibration.

The morphology of the SiO_2@MWCNT adsorbent and functionalised MWCNTs was examined TEM as shown in Fig. 10.3. It can be seen in Fig. 10.3a that MWCNTs are intertwined into a complex network. In addition, the TEM image shows the one-dimensional hollow tubular structure of several MWCNTs. Figure 10.3b show the TEM images of the composite. It can be seen from this the MWCNTs were coated with spherical structure which are due to the incorporation of SiO_2.

10.3.2 Optimization of UA-DSPME

10.3.2.1 Factorial Design

A 2^{4-1} factorial design was used to determine the best extraction conditions for the UA-DSPME/UV-Vis method. The factors investigated included mass of adsorbent

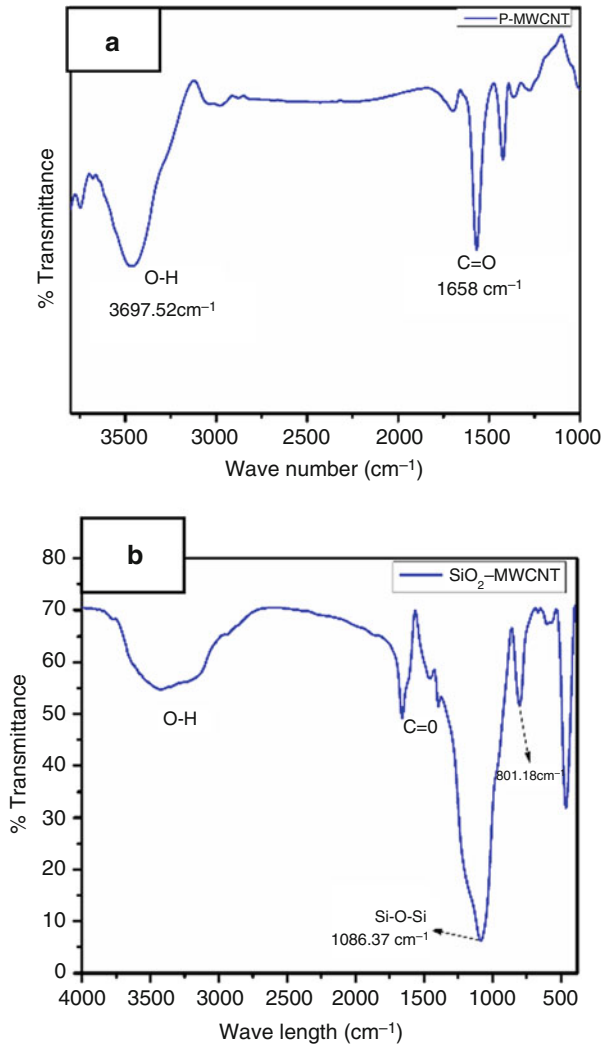

Fig. 10.2 (**a**) and (**b**) FT-IR spectra for MWCNTs and SiO_2@MWCNTs

(MA), extraction time (ET), eluent volume (EV) and sample volume (SV). The effect of factors in the UA-DSPME procedure was investigated by using analysis of variance (ANOVA) and the percentage recovery (%R) was considered as the analytical response. The typical design matrix and the analytical response (%R) are presented in Table 10.2.

The ANOVA results presented in terms of Pareto charts (Fig. 10.4) showed that the investigated factors were significant at 95% confidence level. However, looking at the bar length of the Pareto chart, sample volume was found to have little effect on the analytical response. Therefore, MA, ET and EV required a final optimization and the sample volume was fixed at 5.0 ml.

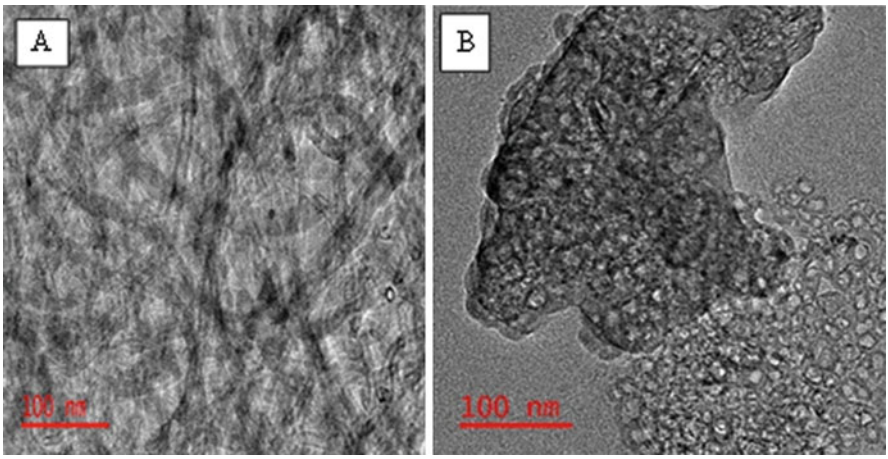

Fig. 10.3 TEM images for (**a**) functionalized MWCNTs, (**b**) SiO_2@MWCNTs

Table 10.2 List of experiments in the factorial design (actual values) for UA-DSPME optimization and the response values

Experiment	MA (mg)	ET (min)	EV (ml)	SV (ml)	%R
1	25	5	1	1	73.6
2	100	5	1	5	90.9
3	25	30	1	5	69.7
4	100	30	1	1	65.7
5	25	5	1	5	90.3
6	100	5	1	1	94.3
7	25	30	1	1	91.5
8	100	30	1	5	89.7
9	62.5	17.5	2	3	93.7
10	62.5	17.5	2	3	93.9
11	62.5	17.5	2	3	94.1

10.3.2.2 Further Optimization

A central composite design (CCD) matrix containing a total of 15 experiments and analytical response based on each of the experimental runs (Table 10.3), was used for further optimization of mass of adsorbent, eluent volume and extraction time. The CCD was chosen in order to provide a statistical model that is used to identify variables that lead to quantitative retention of AFB1. Percentage recoveries of the target analyte were investigated as the response function of CCD model in order to optimize the aforementioned variables. The experimental runs were randomized in order to minimize the effect of uncontrolled factors.

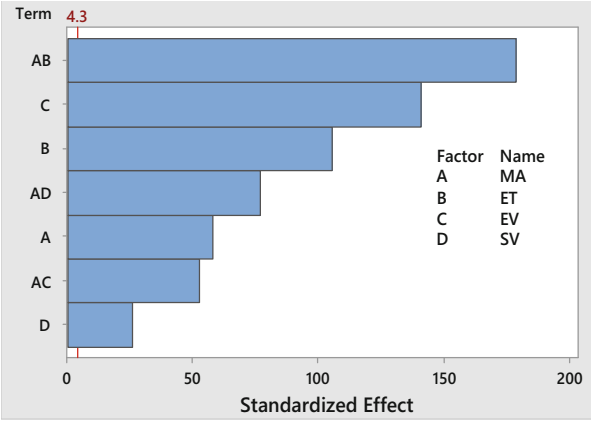

Fig. 10.4 Pareto charts of standardized effects for variables in the AFB1 preconcentration

Table 10.3 Experimental design using CCD and analytical response values

Run	MA (mg)	ET (min)	EV (ml)	% Recovery
1	25.0	5.0	1.25	73.7
2	100.0	5.0	1.25	78.1
3	25.0	30.0	1.25	43.3
4	100.0	30.0	1.25	96.0
5	25.0	17.5	0.50	53.9
6	100.0	17.5	0.50	33.1
7	25.0	17.5	2.00	98.8
8	100.0	17.5	2.00	97.8
9	62.5	5.0	0.50	76.2
10	62.5	30.0	0.50	54.5
11	62.5	5.0	2.00	82.8
12	62.5	30.0	2.00	98.9
13	62.5	17.5	12.5	99.7
14	62.5	17.5	1.25	99.3
15	62.5	17.5	1.25	99.9

The ANOVA results for the predicted response surface quadratic model for the recoveries of AFB1 were obtained (equation not shown). The quadratic equation for the model illustrated the dependence of the analytical response (% recovery) with respect to the evaluated variables [18]. In addition, the obtained 3D response surface plots (Fig. 10.5) were used to evaluate the interactive relationship between the independent variables and the analytical response [18]. It was observed that the maximum percentage recovery of AFB1 was obtained when MA = 62 mg, ET = 10 min and EV = 1.3 ml. Based on results obtained from FFD and CCD the optimum conditions for quantitative preconcentration of AFB1 were selected to be: MA = 62 mg, ET = 10 min, EV = 1.3 ml and SV = 5 ml.

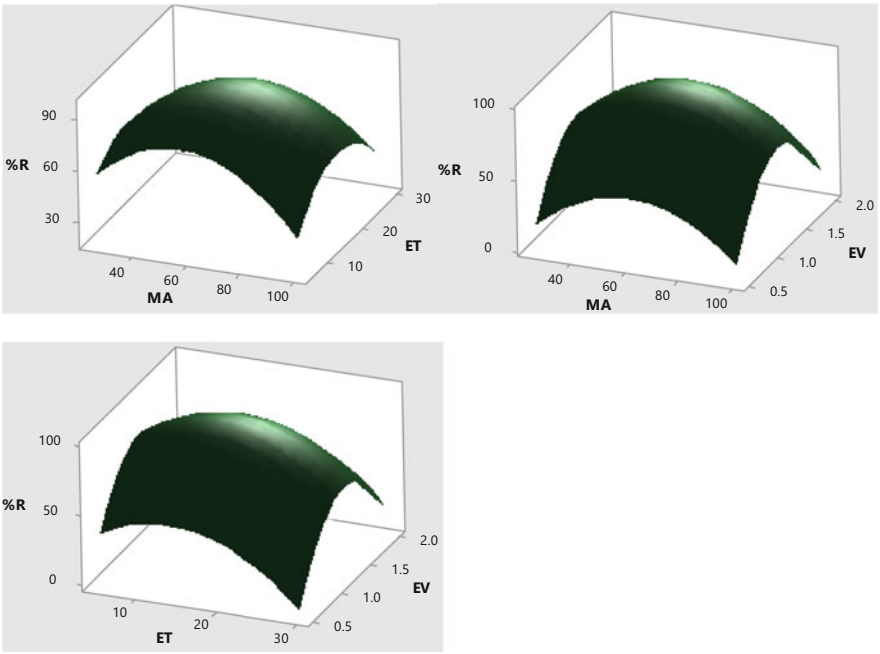

Fig. 10.5 Response surfaces obtained for AFB1 after extraction and preconcentration by UA-DSPME

10.3.3 Analytical Figures of Merit

Under optimum experimental conditions, a linear calibration graph for AFB1 was obtained over the range of LOQ to 250 μg L^{-1} with a correlation coefficient of 0.9997. The limits of detection and quantification calculated using these formulae: LOD = $\frac{3\times Sd}{b}$ and LOQ = $\frac{10\times Sd}{b}$, where *Sd* is the standard deviation of 10 replicate of 10 blank measurements and *b* is the slope of the calibration curve, were 0.1 and 0.3 μg L^{-1}. The possible matrix effect on the extraction and determination of AFB1 in milk samples, matrix-matched limit of detection (LOD) was evaluated from matrix-matched calibration [19]. The matrix-matched calibration was prepared by spiking appropriate amounts of AFB1 working solutions to the milk samples. The spiked solutions were then processed using the experimental procedure described above. The obtained matrix-matched LOD was 0.12 μg L^{-1}. This suggested that the sample matrix did not significantly affect the preconcentration and determination of AFB1. The precision of the developed method expressed as relative standard deviation (RSD%) was assessed through the investigation of repeatability (intraday, n = 10) and reproducibility (interday, n = 5). The intraday and interday precisions were found to be 3.2 and 4.3%, respectively. The enrichment (preconcentration)

Table 10.4 Determination of AFB1 in spiked soy milk sample using UA-DSPME/UV-Vis

Spiked (μg L^{-1})	Found (μg L^{-1})	Recovery (%)	HPLC-PDA	Recovery (%)
0	0.52 ± 0.08	–	0.49 ± 0.12	
5	5.36 ± 0.95	96.8	5.40 ± 0.87	98.2
10	10.49 ± 0.53	99.7	10.51 ± 0.78	100.2
25	25.32 ± 1.23	99.2	25.29 ± 1.53	99.2

factor (EF or PF) defined as the ratio of sensitivity of UA-DSPME/UV-Vis procedure to sensitivity of direct UV-Vis analysis of liquid sample was found to be 108.

10.3.4 Validation and Application

To evaluate the validity and the accuracy of the developed UA-DSPME/UV-Vis method, it was employed for the determination of AFB1 in liquid milk samples spiked with the aflatoxin B_1 at three different concentrations. It can be seen in Table 10.4 that AFB1 was found in soy milk liquid samples at concentration level of $\geq$0.50 μg L^{-1}. This implied that the raw material which is soy bean was contaminated by AFB1 and the decontamination method was not effective.

In addition, the accuracy and precision of the method were validated by comparative analysis of the spiked samples with HPLC-PDA analysis. It can be seen from Table 10.4 that the average recoveries of AFB1 from the liquid milk samples ranged from 96.8 to 99.7% and 98.2 to 100.2% for the developed and reference methods, respectively. The results demonstrated that there was no significant difference between the developed and reference method at 95% confidence level. These observations confirmed that the silica@multiwalled carbon nanotubes nanoadsorbent was suitable for the effective preconcentration of trace level of AFB1 in real milk samples. The developed method was further applied to determination of AFB1 in three different commercial milk samples (cow, soy and rice milk) that are widely consumed in South Africa. The concentration of AFB1 was found to be below the detection limit in cow milk while trace amounts ranging from 0.10 to 0.52 μg L^{-1} were detected in rice and soy milk samples. These observations suggested that in the cow-based milk, AFB1 is converted to AFM1 while in grain-based milk, traces of AFB1 are present.

10.4 Conclusions

In this study, a dispersive solid phase microextraction method employing silica@multiwalled carbon nanotubes as an adsorbent and UV-vis spectrophotometer were successfully applied to preconcentration and determination of AFB1 in liquid milk samples. The developed UA-DSPME method improved the LODs of

the UV-Vis spectrophotometer for quantification of AFB1, thus allowing its determination at trace concentrations. In addition, the use of UA-DSPME provided an acceptable enrichment factor and relatively high precision and accuracy. The developed system was successfully applied for the determination of AFB1 in real milk samples.

Acknowledgements The authors are grateful to the University of Johannesburg, Applied Chemistry Department and National Nanoscience Postgraduate Teaching and Training Programme (NNPTTP) for the permission to do this work.

References

1. Guchi E (2015) Implication of aflatoxin contamination in agricultural products. Am J Food Nutr 3:12–20
2. Ketney O (2015) Food safety legislation regarding of aflatoxins contamination. AUCTS 67:149–154
3. Malhotra BD, Srivastava S, Ali MA, Singh C (2014) Nanomaterial-based biosensors for food toxin detection. Appl Biochem Biotech 174:880–896
4. Dors GC, Caldas SS, Feddern V, Bemvenuti RH, dos Santos Hackbart HC, Moraes de Souza M, dos Santos Oliveira M, Garda-Buffon J, Primel EG, Badiale-Furlong E (2011) Aflatoxins: contamination, analysis and control. In: Guevara-Gonzalez RG (ed) Aflatoxins—biochemistry and molecular biology. INTECH, Croatia, pp 415–438
5. Singh C, Srivastava S, Ali MA, Gupta TK, Sumana G, Srivastava A, Malhotra BD (2013) Carboxylated multiwalled carbon nanotubes based biosensor for aflatoxin detection. Sensor Actuat B Chem 185:258–264
6. Wang X, Li P (2015) Rapid screening of mycotoxins in liquid milk and milk powder by automated size-exclusion SPE-UPLC–MS/MS and quantification of matrix effects over the whole chromatographic run. Food Chem 173:897–904
7. Campone L, Piccinelli AL, Celano R, Pagano I, Russo M, Rastrelli L (2016) Rapid and automated analysis of aflatoxin M1 in milk and dairy products by online solid phase extraction coupled to ultra-high-pressure-liquid-chromatography tandem mass spectrometry. J Chromatogr A 1428:212–219
8. Hussain I (2011) Aflatoxin measurement and analysis. In: Torres-Pacheco I (ed) Aflatoxins: detection, measurement and control. INTECH, Croatia, pp 130–146
9. Manafi MH, Allahyari M, Pourghazi K, Amoli-Diva M, Taherimaslak Z (2015) Surfactant-enhanced spectrofluorimetric determination of total aflatoxins from wheat samples after magnetic solid-phase extraction using modified Fe_3O_4 nanoparticles. Spectrochim Acta A 146:43–49
10. Appell M, Bosma WB (2011) Effect of surfactants on the spectrofluorimetric properties of zearalenone. J Lumin 131:2330–2334
11. Nasz S, Debreczeni L, Rikker T, Eke Z (2012) Development and validation of a liquid chromatographic-tandem mass spectrometric method for determination of eleven coccidiostats in milk. Food Chem 133:536–543
12. Fang G, Lau HF, Law WS, Li SFY (2012) Systematic optimisation of coupled microwave-assisted extraction-solid phase extraction for the determination of pesticides in infant milk formula via LC–MS/MS. Food Chem 134:2473–2480
13. Tan L, He R, Chen K, Peng R, Huang C, Yang R, Tang Y (2016) Ultra-high performance liquid chromatography combined with mass spectrometry for determination of aflatoxins using dummy molecularly imprinted polymers deposited on silica-coated magnetic nanoparticles. Microchim Acta 183:1469–1477

14. Wang Y, Liu X, Xiao C, Wang Z, Wang J, Xiao H, Yue T (2012) HPLC determination of aflatoxin M1 in liquid milk and milk powder using solid phase extraction on OASIS HLB. Food Control 28:131–134
15. Dragacci S, Grosso F, Gilbert J (2001) Immunoaffinity column cleanup with liquid chromatography for determination of aflatoxin M1 in liquid milk: collaborative study. JAOAC Int 84:437–443
16. Fatin MF, Ruslinda AR, Norhafizah S, Farehanim MA, Arshad MM, Ayub RM, Hashim U (2014) Oxidation functionalization of multiwalled carbon nanotube by mild acid sonication. In: Biomedical Engineering and Sciences (IECBES). Proc IEEE conference, pp. 686–689
17. He Y, Chen C, Zhong F, Chen H (2014) Synthesis and characterization: silicon oxide-coated multiwalled carbon nanotubes and properties of composite coating research. High Perform Polym 27:352–361
18. Nomngongo PN, Ngila JC (2014) Determination of trace Cd, Cu, Fe, Pb and Zn in diesel and gasoline by inductively coupled plasma mass spectrometry after sample clean up with hollow fiber solid phase microextraction system. Spectrochim Acta B 98:54–59
19. Hashemi M, Taherimaslak Z, Rashidi S (2014) Enhanced spectrofluorimetric determination of aflatoxin M1 in liquid milk after magnetic solid phase extraction. Spectrochim Acta A 128:583–590

Chapter 11
Removal of Ni(II) and Co(II) from Aqueous Solution Using Pine Cone: A Mechanism Study

Agnes Pholosi, Eliazer B. Naidoo, and Augustine E. Ofomaja

Abstract This study examines the uptake mechanism of pine cone for the removal of nickel and cobalt from aqueous solution. Surface characteristics of pine cone powder were analysed by Fourier Transform Infrared (FTIR) spectroscopy and scanning electron microscopy (SEM). To explain the mechanism of adsorption, change in solution pH and adsorption isotherms were applied. Increasing solution pH led to increased Ni(II) and Co(II) uptake with Ni(II) being more adsorbed. Adsorption capacities correlated well with change in solution hydrogen ion concentration when solution pH was varied between 3 and 8 and metal ion concentrations were varied between 5 and 150 mg/dm^3. FTIR analysis before and after adsorption showed C=O, C–O and phenolic-OH peaks changed in intensity and shifted in position. Dubinin–Radushkevich isotherm better fitted the experimental data than the Temkin isotherm. The affinities of the metals for functional groups on pine cone depended on ionic radius, surface precipitation complexes and covalent bond strength. The equilibrium binding constants increased with temperature, while heat of biosorption decreased with temperature suggesting biosorbent–biosorbate interaction effect. Desorption studies confirmed the ion-exchange mechanism. It was observed that Ni(II) showed stronger ion-exchange properties than Co (II) biosorption.

Keywords Ion-exchange mechanism • Biosorption • Pine cone • Hydrogen ion concentration • Ni(II) and Co(II) ion

11.1 Introduction

Application of cobalt in the areas of pigment production, alloy manufacturing and as catalyst in the chemical industry have been recorded as far back as the nineteenth century [1]. Cobalt exists naturally in the earth's crust with a composition averaging

A. Pholosi (✉) • E.B. Naidoo • A.E. Ofomaja
Biosorption and Wastewater Treatment Research Laboratory, Faculty of Applied and Computer Sciences, Department of Chemistry, Vaal University of Technology, P. Bag X021, Vanderbijlpark 1900, South Africa
e-mail: agnesp@vut.ac.za

P. Ramasami et al. (eds.), *Emerging Trends in Chemical Sciences*,
DOI 10.1007/978-3-319-60408-4_11

about 17.3 mg/kg [2] but has higher concentration in mafic–ultramafic igneous rocks where it is closely associated with nickel [3]. Laterite ores containing cobalt are found in combinations of cobalt with other metals, for example, Cu–Co sulfide, Ni–Cu–Co sulfide or Ni–Co sulfide. On the average, the Ni–Co grade ore can range from 0.1 to 1% Co and 0.5–2% Ni [1].

Due to the increased demand for cobalt in various industries and manufacturing processes such as nuclear power plants, mining, metallurgical, electroplating, paints, pigments, and electro-engineering, the need to separate cobalt and nickel efficiently in hydrometallurgical process is desirable [4, 5]. Unfortunately, the separation of cobalt and nickel has traditionally presented problems due to their similar chemical and physical properties [6, 7]. Separation techniques such as membrane separation [8], oxidation/reduction and precipitation [9], reverse osmosis [10], electrodialysis [11] and electrocoagulation [12] have been applied for the removal of Co(II) and Ni(II) from industrial effluents.

There has been increased interest in the removal of Ni(II) and Co(II) by various types of biomass from aqueous solution in recent times. Some examples of these studies include the use of moss [13], natural hemp fibre [14] and sunflower biomass [15] for the removal of cobalt from aqueous solution while *Mucor hiemalis* [16], pine cone [17] and sugarcane bagasse [18] have been applied for nickel removal from waste water.

Uptake mechanism of some biomass has been studied but this has not been the case for pine cone. Even though pine cone has been shown to bind well with metal ions in our previous studies [19, 20], its uptake mechanism for Ni and Co is not well understood. The aim of this research is to compare the uptake of Ni(II) and Co (II) onto pine cone biomass and to evaluate the uptake mechanism of both metals so as to determine the possibility of the application of this adsorbent for selective removal of these metals from binary solutions. The mechanism of the adsorption process was determined by changes in solution pH during adsorption, evidence of interaction by FTIR and desorption test using different desorption agents. Equilibrium and thermodynamic data of Ni(II) and Co(II) adsorption onto pine cone biomass were modelled using near regression program of the KyPlot 2.0 software which uses Quasi-Newton algorithm for finding the parameter values which minimize the sum of the squares of the errors (ERRSQ).

11.2 Materials and Methods

11.2.1 Materials

Pine tree cones were collected from a plantation in Vanderbijlpark, South Africa. The cones were washed to remove impurities such as sand and leaves. The washed cones were then dried at 90 ^{o}C for 48 h in an oven. The scales on the cones were

removed and crushed using a pulveriser. The pine cone powder was then sieved and particles between 45 and 90 μm were collected and used for analysis.

11.2.2 Methods

11.2.2.1 Determination of Charge Properties of Pine Cone

The quantities of acidic and basic functional groups on the pine surface were determined by Boehm titration [21], while the point zero charge (pH_{pzc}) was determined using the salt addition method [22].

11.2.2.2 Effect of Initial Solution pH on Ni(II) and Co(II) Adsorption

Mass of 0.5 g pine cone samples was added to five beakers each containing 100 cm^3 solution of 100 mg/dm^3 of either Ni(II) or Co(II) set at pH ranging from 3.0 to 8.0 using 0.1 mol/dm^3 of either HCl or NaOH solution. The mixture was then agitated at 200 rpm for 2 h at room temperature. At the end of the agitation, the mixtures were separated by centrifugation at 1000 rpm and the clear liquid was analysed for Ni(II) or Co(II) using atomic absorption spectrophotometer (AAS) Shimadzu AA 700.

11.2.2.3 Fourier Transform Infrared (FTIR) Spectroscopy Analysis

The FTIR spectra of pine cone before and after Ni(II) and Co(II) biosorption were recorded on a Fourier Transform Infrared, Perkin Elmer (USA) 400 spectrometer to elucidate the functional groups present.

11.2.2.4 Scanning Electron Microscope (SEM)

SEM images were obtained on a LEO 1430 instrument that has a tungsten filament as electron source. Imaging was done at 3 kV to further alleviate charge build-up. On each sample about 10 images were obtained at 75× magnification and a further 5 images at 150× magnification in order to provide a representative overview of each sample.

11.2.2.5 Equilibrium Isotherm and Desorption Studies

100 cm^3 solutions of Ni(II) and Co(II) with concentration ranging from 2 to 40 mg/dm^3, set at pH 7.0 were placed in 250 cm^3 conical flasks. Accurately

weighed amount of 0.5 g of ground pine cone was then added to the solutions. The conical flasks were then agitated at a constant speed of 145 rpm in a water bath set at 298, 303, 308 and 313 K. After shaking the flasks for 2 h, the pine cone powder was separated by filtration. The filtrates were analysed for remaining Ni(II) and Co (II) concentration by AAS. Desorption studies were performed by shaking the spent adsorbent in contact with the 40 mg/dm^3 solution in different desorbing agents (sodium hydroxide, hydrochloric acid, acetic acid and water) and determining the amounts of the metal ions released into solution.

11.3 Results and Discussion

11.3.1 Acidic and Basic Functional Groups on Pine Cone

The amount of acidic and basic groups on pine cone surface determined by Boehm titration revealed that the prevalent acidic group is the hydroxylic group which amounted to 2.03 mmol/g accounting for 79% of the total acidic sites. The hydroxylic groups are made up of hydroxylic groups of cellulose and hydroxylic groups of phenol in lignin. The carboxylic groups on the other hand make up 12.5% of the total acidic groups and amount to 0.32 mmol/g. The lactonic group makes up the least amount (8.2%) on pine surface with the value of 0.21 mmol/g. The quantity of basic groups on the pine surface was quite low (0.02 mmol/g), and this result is typical of some biosorbents acquired from agricultural waste materials [23, 24]. Since pine cone incorporates a number of acidic functional groups on its surface, the net charge on the material will depend on solution pH.

11.3.2 pH at Point Zero Charge (pH_{pzc})

pH_{pzc} gives an idea of the charge characteristic of the biosorbent surface. The results of pH_{pzc} test performed on the pine cone (Fig. 11.1) show that at low solution pHs below pH 7, pine cone surface carries a net positive charge. This is due to the interaction of the acidic groups on the pine surface with hydrogen ions in solution at low pH. As solution pH increases towards pH 7, the net positive charge on the pine surface reduces while the net negative charge increases and at solution pH of 7.02 the net charge on the pine surface becomes zero. Several other authors have obtained similar pH_{pzc} values of known agricultural wastes used as adsorbent. Pirbazari et al. [25] obtained a pH_{pzc} value of 6.7 for Foumanat tea waste; Reddy et al. [26] obtained a pH_{pzc} value of 7.0 for Jujuba seeds while Rangabhashiyam and Selvaraju [27] obtained a pH_{pzc} value of 7.0 for *Caryota urens* inflorescence waste biomass.

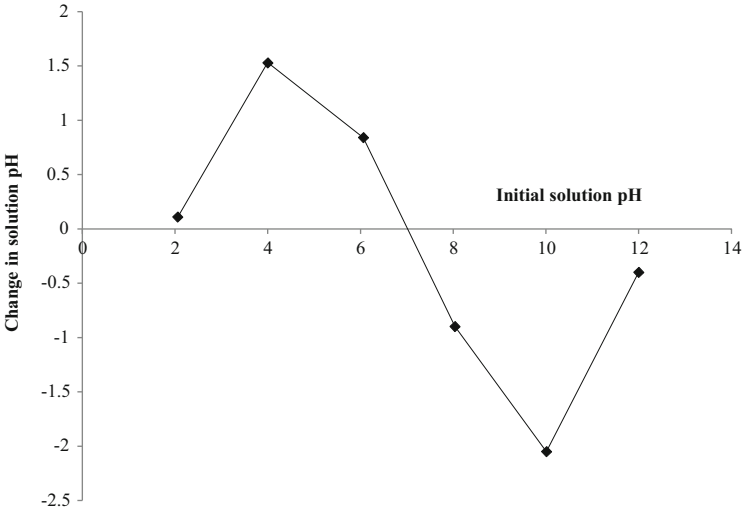

Fig. 11.1 pH_{pzc} for raw pine cone powder

11.3.3 Effect of Solution pH During Uptake of Ni(II) and Co (II) by Pine Cone

The solution pH does not only influence the surface charge of the biosorbent but also the speciation of the metal ions, and the degree of ionization of the biosorbate during the reaction [28]. The effect of solution pH on the Ni(II) and Co (II) adsorption capacity was studied at different solution pHs ranging from 1 to 8 and the results are shown in Fig. 11.2. Higher solution pHs above 8 were not used in this study since Ni(II) and Co(II) exist predominantly as Ni^{2+} and Co^{2+} until solution pH 8.

The pH profile shows that the Ni(II) and Co(II) biosorption capacities of pine cone increased rapidly as the solution pH increases from pH 1 to 6. Two reasons can be put forward to explain the low biosorption capacities which are: (1) the net surface charge on the pine cone is positive at this range of pH, and (2) competition between H^+ ions with Ni^{2+} and Co^{2+} for biosorption sites on the pine cone [29]. As solution pH is increased up to pH 7, the net negative charge on the surface increases until it equals the magnitude of positive charge at solution pH of 7. At solution pH 7, the biosorption capacities of Ni(II) and Co(II) are given as 3.15 and 2.52 mg/g respectively. Above pH 7, the net surface charge becomes negative and the biosorption capacities increase to 3.27 and 2.78 mg/g respectively.

Generally, for all solution pHs studied, the biosorption capacity of pine cone for Ni(II) was higher than Co(II) but the trend in the pH-adsorption profile was the same. This finding has two implications: (1) the mechanism for Ni(II) and Co (II) uptake by pine cone is the same due to the similarity in the pH profile; and (2) although both metals are divalent cations, certain characteristics of the metal

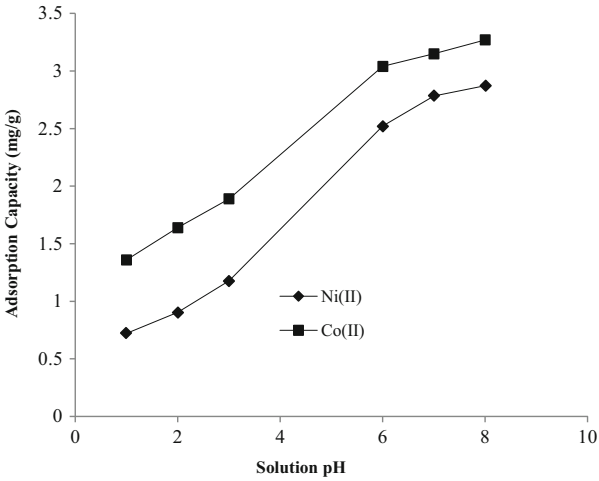

Fig. 11.2 Effect of initial solution pH on Ni(II) and Co(II) biosorption

ions give them different affinities for the functional groups on the biosorbent. The affinities of the metal ions to the functional groups on the pine cone surface are dependent on parameters such as ionic radius of the metal ion, surface precipitation complexes and covalent bond strength [30]. Some characteristics of Ni(II) and Co (II) are shown in Table 11.1.

Of the two metals, Ni(II) has a smaller ionic size of 0.72 Å, which implies that its charge density is higher than that of Co(II) with a larger ionic size of 0.74 Å**.** The higher charge density of Ni(II) gives it a greater coulombic attraction for the functional groups on the pine cone surface as compared with the Co(II) [30]. The small ionic size may also affect the migration rate of the metal ions into the matrix of the adsorbent, as the smaller size of Ni(II) allows it to penetrate and reach inner sites on the pine cone better than the Co(II) ion. The selectivity of metal ions for adsorption sites also depends on the ease with which metal ions form hydroxyl complexes as shown below:

$$M^{2+} + H_2O \Leftrightarrow MOH^{+} + H^{+}$$

This implies that the equilibrium constant, pK_a, value of the above reaction can be used to determine the adsorption behaviour of the metals [31]. The affinity of the metal for the functional groups increases with decrease in the pK_a value of the metal ion. Ni(II) ion has the lower pKa value as compared with Co(II), meaning that Ni (II) will have a lower degree of solvation. The implication is that Ni(II) ions remain longer in solution as Ni^{2+} and will more readily reach the solid-solution surface in this form for interaction [31].

Interaction between metal cations and electronegative atoms such as oxygen or nitrogen in acidic functional groups of biosorbents may involve the formation of a covalent bond, by sharing of lone pair of electrons with the metal cation. The preference for the formation of this covalent bond depends on the similarity

Table 11.1 Parameters characterizing the bonding strength of Ni(II) and Co(II)

Metal ion	Charge	Ionic radius (Å)	pK_a	Parameter for covalent binding, χ^2(Ionic radius + 0.85) (Å)
Ni(II)	2	0.72	9.4	5.73
Co(II)	2	0.74	9.6	5.62

between the electronegativity of the metal ion and the coordinating atom in the functional group. Therefore, the closer the electronegativity of the metal ion to the coordinating atom, the higher the covalent character [32]. Since selectivity or bonding strength increases with increasing polarizability of the metal ion, the parameter χ^2 ($r_{ionic\ crystal}$ + 0.85) was introduced to measure the strength of the covalent bond [33]. The constant 0.85 in the parameter represents the contribution of N or O donor atom radii to the distance, $r_{ionic\ radius}$ is the cationic radius and χ is the electronegativity of the metal ion [34]. The values of the parameter in Table 11.1 show that Ni(II) has a value of 5.73 while Co(II) has a value of 5.62. Therefore, Ni(II) has the higher tendency to form strong covalent bond with the oxygenated groups on pine cone due to the higher electronegativity and smaller ionic radius.

11.3.4 Changes in Equilibrium pH

If it is assumed that the uptake of Ni(II) and Co(II) onto pine cone was due to interaction between the metal ion and the lone pair of electrons on the O atom via covalent bonding, then two mechanisms are possible as shown below:

$$2B - OH + M^{2+} \Leftrightarrow 2B - O - M + 2H^{+} \quad \text{(Ion exchange reaction)}$$

$$2B - O^{-} + M^{2+} \rightarrow 2B - O^{-}M^{2+} \quad \text{(Complexation reaction)}$$

where B–OH is the functional group containing the electronegative atom (oxygen) on the pine (carboxylic –OH, phenolic –OH, etc), M^{2+} is the metal cation and H^{+} the displaced hydrogen ion in solution. Ion exchange mechanism usually predominates below pH_{pzc}, while complexation mechanism predominates above pH_{pzc} [35].

Ion exchange reactions are usually accompanied by changes in hydrogen ion concentration at the end of the biosorption process and the change in hydrogen ion concentration follows similar trends as the adsorption capacities at all solution pHs while for complexation reaction, the trend is absent at low pHs [36, 37].

Experimental data for initial and equilibrium solution pH, change in hydrogen ion concentration and adsorption capacity at constant initial concentration of 100 mg/dm^3 at varying pH and for varying initial concentrations between 5 and 150 mg/dm^3 at constant pH for Ni(II) and Co(II) are shown in Table 11.2.

Table 11.2 Change in solution pH at constant initial Ni(II) and Co(II) concentration (100 mg/dm^3) and at varying initial Ni(II) and Co(II) concentration (5–150 mg/dm^3)

Metal	Initial conc. (mg/dm^3)	pH_i	pH_f	ΔpH	$[H^+]_i$ mol/dm^3	$[H^+]_f$ mol/dm^3	Δ[H^+] mmol/dm^3	Adsorption capacity (mg/g)
Constant Conc.								
Ni(II)	100	3	2.71	0.29	0.001	0.00195	0.9498	1.36
	100	4	2.95	1.05	0.0001	0.00112	1.0220	1.64
	100	5	2.94	2.06	0.00001	0.00115	1.1315	1.89
	100	6	2.86	3.14	0.000001	0.00138	1.3794	3.04
	100	7	2.85	4.15	0.0000001	0.00141	1.4124	3.15
	100	8	2.89	5.11	0.00000001	0.00145	1.4454	3.27
Co (II)	100	3	2.79	0.21	0.001	0.00162	0.6218	0.20
	100	4	3.09	0.91	0.0001	0.00081	0.7128	0.90
	100	5	3.08	1.92	0.00001	0.00083	0.8218	1.18
	100	6	2.96	3.04	0.000001	0.00110	1.0955	2.52
	100	7	2.93	4.07	0.0000001	0.00117	1.1748	2.78
	100	8	2.91	5.09	0.00000001	0.00123	1.2303	2.87
Varying Conc.								
Ni(II)	5	7.91	2.90	5.01	1.23×10^{-8}	0.00126	1.2558	0.42
	20	7.97	2.89	5.08	1.07×10^{-8}	0.00129	1.2882	1.58
	50	7.96	2.87	5.09	1.10×10^{-8}	0.00135	1.3490	3.67
	100	7.95	2.85	5.10	1.12×10^{-8}	0.00141	1.4125	5.30
	150	7.93	2.83	5.10	1.17×10^{-8}	0.00148	1.4791	5.87
Co (II)	5	7.08	3.02	4.06	8.32×10^{-8}	0.00095	0.9549	0.38
	20	7.10	2.99	4.11	7.94×10^{-8}	0.00102	1.0232	1.48
	50	7.13	2.97	4.16	7.41×10^{-8}	0.00107	1.0714	3.39
	100	7.03	2.93	4.10	9.33×10^{-8}	0.00117	1.1748	4.98
	150	7.05	2.91	4.14	8.91×10^{-8}	0.00123	1.2302	5.36

The results show that the biosorption capacities of pine cone for Ni(II) and Co (II) increased with increasing initial solution pH and that the equilibrium pHs at the end of the biosorption process were all lower than the initial solution pHs. Table 11.2 also reveals that the adsorption capacity increased with increasing difference between the final and initial solution pH. This kind of trend is indicative of ion exchange process in which hydrogen ions are displaced from active sites and replaced by the metal ion [36, 37]. These trends imply that the fewer the H^+ ions in solution competing with metal ions for biosorption sites, the higher the adsorption capacity will be and that the amount of metal biosorbed is proportional to the amount of H^+ ions displaced. It was also observed that the change in solution pH and [H^+] in the reaction medium were higher for the Ni(II) biosorption system than for the Co(II) biosorption system. This result is also in line with the observed biosorption capacities (Ni(II) biosorption > Co(II) biosorption). A linear

relationship can therefore be drawn between the change in $[H^+]$ and the biosorption capacities of pine cone for Ni(II) and Co(II) as shown below:

$$\text{Ni(II) system:} \quad q_e = 3.948\Delta H^+ - 2.442 \qquad r^2 = 0.9911$$

$$\text{Co(II) system:} \quad q_e = 3.855\Delta H^+ - 1.807 \qquad r^2 = 0.9860$$

When the solution pH was fixed at pH 7 or 8 and the initial concentrations of Ni (II) and Co(II) varied between 5 and 150 mg/dm^3, the biosorption capacities and the change in $[H^+]$ of the reacting medium increased with increasing initial metal ion concentration. Therefore it can be concluded that as metal ion concentration increases in solution, the amount of exchange reaction increases and the hydrogen ions displaced into solution also increased [36]. Comparing the relationship between the initial metal ion concentrations, change in $[H^+]$ and biosorption capacities for Ni(II) and Co(II), it was observed that the change in $[H^+]$ and biosorption capacities for Ni(II) were higher than those of Co(II) and they both increased with increasing initial concentration. These results again indicate the active participation of ion exchange mechanism in the uptake of Ni(II) and Co (II) onto pine cone. Linear relationships were therefore drawn between the initial metal ion concentrations, change in $[H^+]$ and the biosorption capacities of pine cone for Ni(II) and Co(II) as shown below:

$$\begin{aligned}
&\text{For Ni(II) system:} && C_0 = 661.1\Delta H^+ - 832.5 && r^2 = 0.9904\\
&&& q_e = 25.36\Delta H^+ - 31.06 && r^2 = 0.9500\\
&\text{For Co(II) system:} && C_0 = 526.6\Delta H^+ - 509.5 && r^2 = 0.9675\\
&&& q_e = 18.97\Delta H^+ - 17.58 && r^2 = 0.9567
\end{aligned}$$

11.3.5 FTIR Spectra of Pine Cone Before and After Biosorption

The FTIR spectra of pine cone before and after biosorption of Ni(II) and Co(II) are shown in Fig. 11.3a–d. As expected it was observed that the spectrum for pine cone is composed of a variety of peaks associated with lignocellulosic materials (Fig. 11.3a). FTIR peaks characteristic of cellulose include the broad band at 3336.92 cm^{-1} representing hydrogen bond stretching vibration of α-cellulose [38]. The peaks at 2929.18 and 2880.95 cm^{-1} represent C-H stretching vibration from CH and CH_2 of the cellulose component [39]. The peak at 1371.20 cm^{-1} is assigned to C–H bending of methyl groups related to crystalline cellulose [39]. The shoulder at 1145.59 and peak at 898.14 cm^{-1} are indicative of C–O–C stretching at β-(1-4)-glycosidic linkage [40]. The peak at 1726.71 cm^{-1} represents the C=O

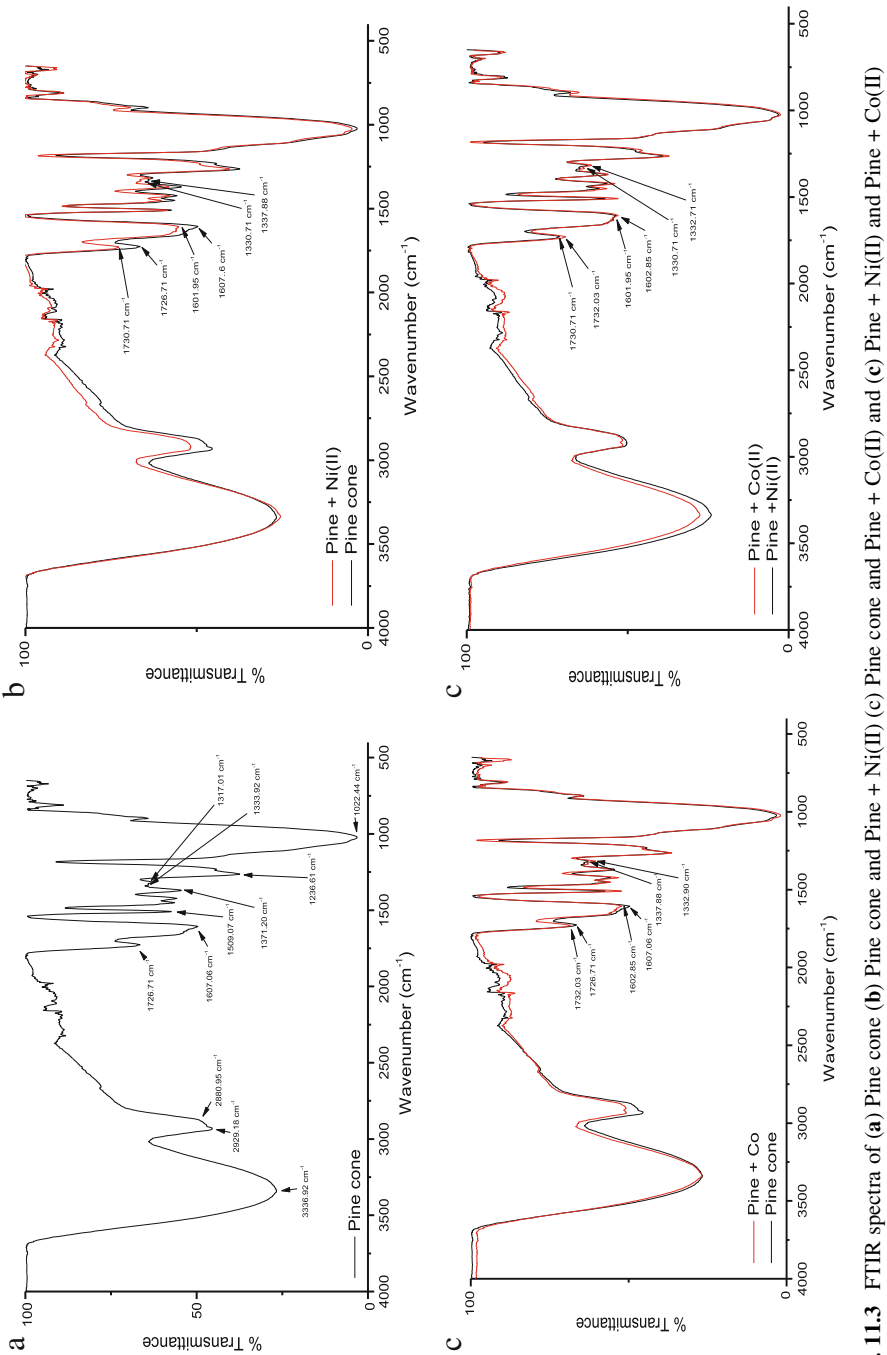

Fig. 11.3 FTIR spectra of (**a**) Pine cone (**b**) Pine cone and Pine + Ni(II) (c) Pine cone and Pine + Co(II) and (**c**) Pine + Ni(II) and Pine + Co(II)

Table 11.3 FTIR peaks for pine cone before and after Ni(II) and Co(II) adsorption

	Functional group					
Sample	OH (cm^{-1})	–CH (cm^{-1})	C=O (cm^{-1})	C–O (cm^{-1})	C–O–C (cm^{-1})	Phenolic-OH (cm^{-1})
Pine cone	3336.92	2929.18	1726.71	1607.06	1022.44	1337.88
Pine + Ni(II)			1730.71	1601.95		1330.71
Pine + Co(II)			1732.03	1602.85		1332.90

stretching vibration of lignin in the acetyl groups of hemicellulose [41] whereas the peak at 1022.44 cm^{-1} indicates C–O of secondary alcohol in cellulose.

Lignin in the biomaterial can be observed at characteristic peaks at 1607.06 cm^{-1} which is indicative of C–O stretching of lignin [38], while the peak at 1509.07 cm^{-1} represents C=C stretching vibrations of aromatic rings of lignin [42]. The peak at 1317.01 cm^{-1} is assigned to the asymmetric C–O–C stretching of lignin [43] while that at 1337.88 cm^{-1} denotes presence of phenolic hydroxyl group [44].

After the biosorption of Ni(II) onto the pine cone, the FTIR spectra are compared in Fig. 11.3b and Table 11.3.

The spectra show that there were few differences in the pine cone and Pine + Ni (II) spectra except in the intensities and peak positions of the groups at 1726.71 cm^{-1} representing the C=O, at 1607.06 cm^{-1} which is indicative of C–O stretching and at 1337.88 cm^{-1} due to phenolic hydroxyl group. This suggests that these three groups were responsible for adsorption of Ni(II). After Ni(II) adsorption, the C=O peak decreased in intensity and shifted from 1726.71 to 1730.71 cm^{-1}, the C–O stretching reduced and shifted from 1607.06 to 1601.95 cm^{-1}, while the phenol hydroxyl group peak shifted from 1337.88 to 1330.71 cm^{-1}. These results confirm the contribution of ion exchange mechanism between the acidic and phenolic sites on the pine cone with Ni(II) from aqueous solution.

After the adsorption of Co(II) onto the pine cone, the FTIR spectra are compared in Fig. 11.3c and Table 11.3. Observable differences can be seen in the intensities and peak positions of groups such as C=O, C–O and phenol–OH. After Co(II) adsorption, the C=O peak decreased in intensity and shifted from 1726.71 to 1732.03 cm^{-1}, the C-O stretching reduced and shifted from 1607.06 to 1602.85 cm^{-1}, while the phenol hydroxyl group peak shifted from 1337.88 to 1332.90 cm^{-1}.

Figure 11.3d shows a comparison between the FTIR spectra of pine + Ni(II) and pine + Co(II). The difference can be seen only in the intensity and peak position of the C=O peak. This peak is slightly more intense for pine + Co(II) than for the pine + Ni(II) and was respectively at position 1732.03 and 1730.71 cm^{-1}, the C–O peak was of equal intensity and at the same position and the phenol hydroxyl peak was at 1332.71 cm^{-1} for pine + Co(II) and 1330.71 cm^{-1} for pine + Ni(II) with the pine + Co(II) peak being slightly more intense.

Therefore it can be concluded that the C=O, C–O and phenolic –OH are the adsorption sites for Ni(II) and Co(II) and that Ni(II) were held more strongly on the C=O and phenol–OH than Co(II) probably leading to its higher uptake.

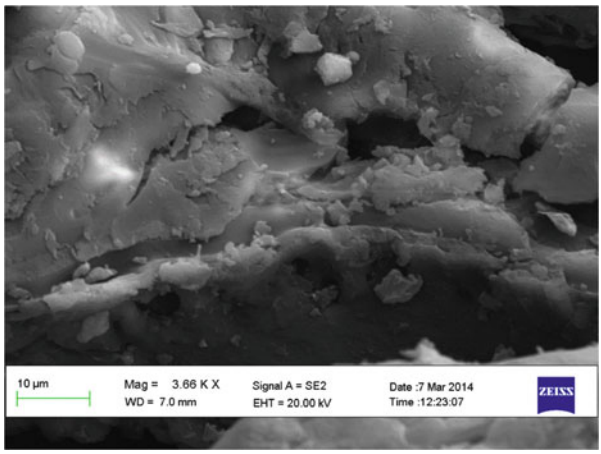

Fig. 11.4 SEM image of pine cone powder

11.3.6 Scanning Electron Microscope Analysis of Pine Cone

SEM image was used to observe the surface physical morphology of pine cone and it is shown in Fig. 11.4. From the image, the pine cone surface can be seen to be rough showing the presence of few large pores which provide access and large surface area for adsorption of nickel and cobalt ions [20].

11.3.7 Equilibrium Biosorption of Ni(II) and Co(II) onto Pine Cone

The relationship between pollutant molecules retained on the biosorbent surface and that remaining in solution at equilibrium at a fixed temperature can be described by a biosorption isotherm. From the curve plotted as solid phase concentration against liquid phase concentration, certain constants whose values express the surface properties and affinity or energy relationship between biosorbent and pollutant can be obtained [45].

The isotherm plots for the biosorption of Ni(II) and Co(II) onto pine cone from metal ion solutions of concentrations ranging from 5 to 40 mg/dm^3 and at temperatures 25, 30, 35 and 40 ^{o}C are shown in Fig. 11.5a, b.

The results reveal that the uptake of Ni(II) was higher than that of Co(II) at all temperatures and that uptake of the metals increased with increasing temperature. Metal ion uptake increased rapidly with initial concentration from 5 to 20 mg/dm^3 after which saturation of available surface for biosorption began to set in. With higher concentrations, uptake of metal ions increased only slightly leading to saturation of the surface. The phenomenon occurred at all temperatures for both Ni(II) and Co(II) biosorption.

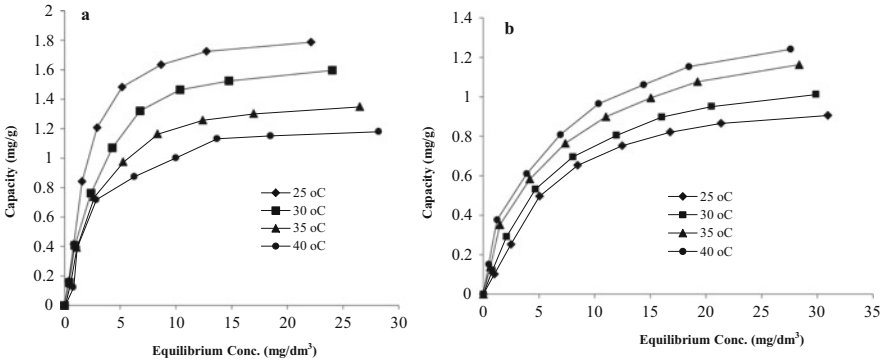

Fig. 11.5 Equilibrium biosorption of (**a**) Ni(II) and (**b**) Co(II) onto pine cone at different temperatures

11.3.7.1 Dubinin–Radushkevich (D–R) Isotherm

The Dubinin–Radushkevich (D–R) isotherm has the non-linear form

$$q_e = q_m \exp\left(-\beta\varepsilon^2\right)$$

where q_m is the Dubinin–Radushkevich monolayer biosorption capacity (mg/g), β is a constant related to biosorption energy (mol^2/kJ^2), and ε is the Polanyi potential which is related to the equilibrium concentration as follows:

$$\varepsilon = RT \ln\left(1 + \frac{1}{C_e}\right)$$

where R is the gas constant (8.314 J/mol K) and T is the absolute temperature. The constant E (kJ/mol) is the mean free energy change when 1 mol of the ion is transferred to the surface of the solid from infinity in the solution and can be computed using the relationship:

$$E = \frac{1}{\sqrt{2\beta}}$$

The magnitude of E can be related to the reaction mechanism. If E is in the range of 8–16 kJ/mol, sorption is governed by ion exchange [46]. In the case of $E <$ 8 kJ/mol, physical forces may affect the sorption mechanism.

Table 11.4 shows values of the Dubinin–Radushkevich isotherm constants along with two error estimation (variable error and coefficient of determination, r^2) for Ni (II) and Co(II) biosorption onto pine cone at temperatures ranging from 298 to 313 K.

Table 11.4 Dubinin–Radushkevich isotherm parameters for Ni(II) and Co(II) biosorbed onto pine cone

Metal ion	Temp (K)	β (mol^2/kJ^2)	q_m (mol/g)	E (kJ/mol)	r^2	Variable error
Ni(II)	313	-2.65×10^{-9}	2.46×10^{-4}	13.74	0.992	0.021
	308	-2.73×10^{-9}	1.99×10^{-4}	13.53	0.9925	0.028
	303	-3.03×10^{-9}	1.86×10^{-4}	12.77	0.9902	0.030
	298	-3.27×10^{-9}	1.69×10^{-4}	12.36	0.9949	0.040
Co(II)	313	-2.85×10^{-9}	2.17×10^{-4}	13.24	0.9904	0.025
	308	-3.10×10^{-9}	1.96×10^{-4}	12.69	0.9912	0.032
	303	-3.19×10^{-9}	1.67×10^{-4}	12.32	0.9903	0.048
	298	-3.26×10^{-9}	1.42×10^{-4}	12.38	0.9916	0.057

The results reveal that the Dubinin–Radushkevich monolayer biosorption capacity for Ni(II) biosorption were all higher than for Co(II) biosorption onto pine cone at all temperatures and the monolayer capacity increases with increasing temperature. The increasing monolayer capacity with increasing temperature suggests that the biosorption reaction is endothermic and is not physical in nature. The magnitude of increase in monolayer capacity with temperature is more pronounced with Ni (II) biosorption than for Co(II) biosorption suggesting stronger bonding of Ni(II) to pine cone than Co(II). The constant, β, is inversely related to the mean free energy change when 1 mol of the ion is transferred to the surface of the solid from infinity in the solution [47]. Table 11.4 shows that the values of β were higher for Ni (II) biosorption than for Co(II) biosorption except at 298 K and that the values increased with increasing temperature. This suggests that the transfer of Ni(II) ions from bulk solution to the biosorbent is more favoured than that of Co(II) and the spontaneity of the transfer reduces with temperature. The lower ease of transfer at higher temperatures may be due to higher surface coverage of the pine material leading to site saturation. Finally, the change in free energy values for Ni(II) and Co (II) biosorption were in the range of 8 to 16 kJ/mol, indicating that the biosorption mechanism is ion exchange [47]. The values of change in free energy were all higher for Ni(II) than for Co(II) biosorption except at 298 K.

11.3.7.2 Temkin Isotherm

The Temkin isotherm model assumes that the biosorption energy decreases linearly with the surface coverage due to biosorbent–biosorbate interactions and the biosorption is characterized by a uniform distribution of binding energies, up to some maximum binding energy. The non-linear form of Temkin isotherm model is given by the equation:

$$q_e = \frac{RT}{b} \ln (K_T C_e)$$

where b (J/mol) is the Temkin constant related to the heat of sorption and K_T (dm^3/g) is the equilibrium binding constant related to the maximum binding energy. The free energy change associated with the maximum binding energy is given as:

$$K_T = Exp(-\Delta G_{\max}/RT)$$

The corresponding enthalpy (ΔH) and entropy (ΔS) associated with the maximum binding energies can be obtained from the equation:

$$\Delta G_{max} = \Delta H_{max} - T\ \Delta S_{max}$$

The values of equilibrium binding constant, K_T, were found to be higher for Ni (II) biosorption than for Co(II) adsorption suggesting that stronger bonds are created for the pine cone-Ni(II) system than the pine cone-Co(II) system. The constant K_T increased with increasing temperature for the biosorption of both metal ions indicating that biosorption is favoured by temperature increase (endothermic). These results also revealed that the heat of biosorption reduced with increasing biosorption temperature indicating biosorbent–biosorbate interactions.

The values of change in free energy, enthalpy and entropy associated with the maximum binding energy are calculated and shown in Table 11.5.

The free energy changes associated with the maximum binding energies at each temperature were found to be negative indicating a spontaneous process for both metals at all temperatures. The free energy change became increasingly negative with increasing temperature indicating a chemical activated process and the magnitude of negative charge was higher for the pine cone-Ni(II) system than in the pine cone-Co(II) system. A positive enthalpy indicates that biosorption was endothermic and the endothermic nature was stronger for the Ni(II) than the Co (II) biosorption. The negative values of entropy show the preference of Ni(II) and Co(II) ions for the pine cone surface and suggest the possibility of some structural changes or readjustments in the Ni(II)/Co(II)–pine cone complex [48].

11.3.7.3 Comparison of Fit of Isotherm Model

The calculated values of the errors are shown in Tables 11.4 and 11.5 and plots of the predicted values of the isotherm models along with the experimental equilibrium values are displayed in Fig. 11.6a, b.

Generally, both isotherms fitted the equilibrium data to a reasonable extent considering the low values for the variable error and the correlation coefficient values above 0.94. The results for modelling of experimental data with the Dubinin–Radushkevich and Temkin isotherm show that the r^2 values for Ni (II) adsorption were generally higher than those of the Co(II) adsorption. The

Table 11.5 Temkin's isotherm parameters for Ni(II) and Co(II) biosorbed onto pine cone

Metal ion	Temp (K)	K_T (dm^3/mol)	B	b (kJ/mol)	r^2	Variable error	ΔG_{max} (kJ/mol)	ΔH (kJ/mol)	ΔS (J/molK)
Ni(II)	298	22.43	0.393	6.30	0.9643	0.025	−7.71		
	303	31.40	0.413	6.10	0.9691	0.032	−8.68	67.52	−0.2522
	308	58.02	0.425	6.03	0.9722	0.035	−10.40		
	313	78.16	0.466	5.58	0.9663	0.050	−11.34		
Co(II)	298	19.18	0.353	7.02	0.9710	0.027	−7.32		
	303	21.61	0.338	6.49	0.9588	0.034	−7.74	36.20	−0.1454
	308	25.14	0.417	6.14	0.9452	0.058	−8.26		
	313	39.59	0.449	5.80	0.9412	0.076	−9.57		

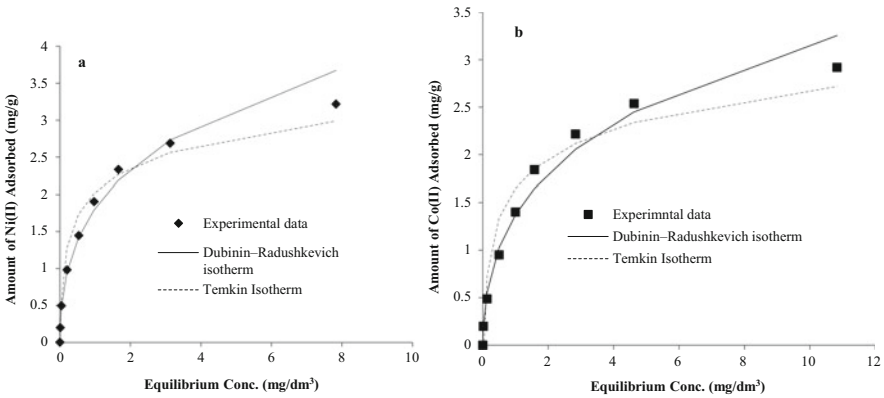

Fig. 11.6 Comparison of isotherm fit for (**a**) Ni(II) and (**b**) Co(II) onto pine cone at 298 K

results also indicate that the Dubinin–Radushkevich isotherm fitted the equilibrium isotherm data better than the Temkin isotherm as seen from the results of the correlation coefficient. The variable error values also follow similar trends as the correlation coefficient error method but they do not show the wide margin of difference reflected in the correlation coefficient values. When the experimental data were plotted against the Dubinin–Radushkevich and Temkin isotherm predicted values of the Ni(II) and Co(II) adsorption at 298 K (Fig. 11.6a, b), it was observed that Ni(II) adsorption shows better fit for Dubinin–Radushkevich than Temkin isotherm but at high concentration the fit reduced while the Temkin model seems to remain at constant difference over the range of concentrations used. For the Co(II) adsorption the difference between the model values and the experimental data was higher as compared with the Ni(II) adsorption. The Dubinin–Radushkevich model deviated more strongly from the experimental data at higher concentrations for the Co(II) biosorption while the Temkin model remained at an almost constant difference.

11.3.8 Desorption

The ability of pine cone biosorbents to adsorb and desorb Ni(II) and Co(II) ions was examined in an adsorption/desorption test in which 0.5 g of pine cone in contact with 50 cm^3 of 40 mg/dm^3 of Ni(II) and Co(II) solutions and the amount of Ni (II) and Co(II) ions adsorbed was determined. Figure 11.7 shows the results from the desorption studies carried out on the pine cone using sodium hydroxide, hydrochloric acid, acetic acid and water as desorbing agents.

The results show that HCl and NaOH desorbing agent gave the highest percentage desorption for Ni(II) and Co(II) and the percentage desorption of Ni(II) was

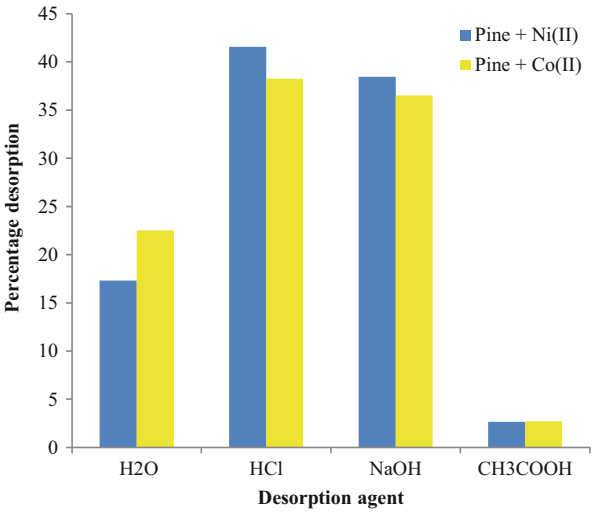

Fig. 11.7 Desorption studies of Ni(II) and Co (II) from pine cone using different desorbing agents

higher than that of Co(II). These results suggest that the biosorption is governed by a cation-exchange reaction of the type:

$$2\text{Pine-OH} + \text{Ni}^{2+}\left(\text{Co}^{2+}\right) \leftrightarrow 2\text{Pine-O}^{-}\text{Ni}^{2+}\left(\text{Co}^{2+}\right) + 2\text{H}^{+}$$

The percentage of Ni(II) and Co(II) displaced by HCl and NaOH were 41.56 and 38.47% and 38.25 and 36.57% respectively. When water was used as desorption agent on the other hand, only 17.32 and 22.53% of Ni(II) and Co(II) was desorbed indicating that the biosorption reaction was more chemical ion-exchange than physical biosorption. Finally, desorption by acetic acid which represents chemically non-reversible biosorption accounted for only 2.65 and 2.70%.

11.4 Conclusion

A comparative study on the uptake of pine cone for nickel and cobalt adsorption has been successfully studied. Ni(II) and Co(II) biosorption by pine cone were found to be dependent on the initial concentration and initial solution pH and were better under basic conditions. FTIR analysis have shown that hydroxylic and carboxylic groups play a major role in Ni(II) and Co(II) uptake by pine cone. Equilibrium analysis revealed that the monolayer coverage increased with temperature and the mean free energies were higher than 8 kJ/mol indicating ion-exchange mechanism which was also confirmed by the desorption studies.

References

1. Mudd GM, Weng Z, Jowitt SM, Turnbull ID, Graedel TE (2013) Quantifying the recoverable resources of by-product metals: The case of cobalt ore. Geol Rev 55:87–98
2. Rudnick RL, Gao S (2003) Composition of the continental crust. In: Holland HD, Turekian KK (eds) Treatise on geochemistry, vol 3.01. Elsevier, Pergamon, Oxford, pp 1–64
3. Donaldson JD, Beyersmann DB (2016) Cobalt and cobalt compounds. Ullmann's encyclopedia of industrial chemistry, 7th edn. Wiley (Chapter 7:38)
4. Repo E, Warchol JK, Kurniawan TA, Sillanpaa MET (2010) Adsorption of Co(II) and Ni (II) by EDTA- and/or DTPA-modified chitosan: kinetic and equilibrium modelling. Chem Eng J 161:73–82
5. Luo X, Guo B, Wang LF, Deng R, Qi S, Luo C (2014) Synthesis of magnetic ion-imprinted fluorescent Cd Te quantum dots by chemical etching and their visualization application for selective removal of Cd(II) from water. Colloids Surf A 462:186–193
6. Sadyrbaeva TZ (2015) Separation of cobalt(II) from nickel(II) by a hybrid liquid membrane electrodialysis process using anion exchange carriers. Desal 365:167–175
7. Olivier MC, Dorfling C, Eksteen JJ (2012) Evaluating a solvent extraction process route incorporating nickel preloading of Cyanex 272 for the removal of cobalt and iron from nickel sulphate solutions. Miner Eng 27:37–51
8. Nguyen NC, Chen SS, Hsu HT, Li SW (2013) Separation of three divalent cations (Cu^{2+}, Co^{2+} and Ni^{2+}) by NF membranes from pHs 3 to 5. Desal 328:51–57
9. Yadav AK, Kumar N, Sreekrishnac TR, Satya S, Bishnoi NR (2010) Removal of chromium and nickel from aqueous solution in constructed wetland: Mass balance, adsorption–desorption and FTIR study. Chem Eng J 160:122–128
10. Ipek U (2005) Removal of Ni(II) and Zn(II) from an aqueous solution by reverse osmosis. Desal 174:161–169
11. Benvenuti T, Krapf RS, Rodrigues MAS, Bernardes AM, Zoppas-Ferreira J (2014) Recovery of nickel and water from nickel electroplating wastewater by electrodialysis. Sep Purif Technol 129:106–112
12. Akbal F, Camcı S (2011) Copper, chromium and nickel removal from metal plating wastewater by electrocoagulation. Desal 269:214–222
13. Marešová J, Pipíška M, Rozložník M, Horník M, Remenárová L, Augustína J (2011) Cobalt and strontium sorption by moss biosorbent: Modeling of single and binary metal systems. Desal 266:134–141
14. Tofana L, Teodosiua C, Padurarua C, Wenker R (2013) Cobalt(II) removal from aqueous solutions by natural hemp fibers: Batch and fixed-bed column studies. Appl Surf Sci 285:33–39
15. Oguz E, Ersoy M (2014) Biosorption of cobalt(II) with sunflower biomass from aqueous solutions in a fixed bed column and neural networks modelling. Ecotox Environ Saf 99:54–60
16. Shroff KA, Vaidya VK (2011) Kinetics and equilibrium studies on biosorption of nickel from aqueous solution by dead fungal biomass of *Mucor hiemalis*. Chem Eng J 171:1234–1245
17. Malkoc E (2006) Ni(II) removal from aqueous solutions using cone biomass of *Thuja orientalis*. J Hazard Mater B137:899–908
18. Alomá I, Martín-Lara MA, Rodríguez IL, Blázquez G, Calero M (2012) Removal of nickel (II) ions from aqueous solutions by biosorption on sugarcane bagasse. J Taiwan Inst Chem Eng 43:275–281
19. Ofomaja AE, Pholosi A, Naidoo EB (2015) Application of raw and modified pine biomass material for cesium removal from aqueous solution. Eco Eng 82:258–266
20. Ofomaja AE, Naidoo EB (2010) Biosorption of lead(II) onto pine cone powder: studies on biosorption performance and process design to minimize biosorbent mass. Carbohydr Poly 82:1031–1042
21. Boehm HP (1994) Some aspects of the surface chemistry of carbon black and other carbons. Carbon 32:759–769

22. Ofomaja AE (2009) Removal of copper(II) from aqueous solution by pine and base modified pine cone powder as biosorbent. J Hazard Mater 168:909–917
23. Wing RE (1996) Corn fibre citrate: preparation and ion exchange properties. Ind Crops Prods 5:301–305
24. Leyva-Ramos R, Landin-Rodriguez LE, Leyva-Ramos S, Medellin-Castillo NA (2012) Modification of corncob with citric acid to enhance its capacity for adsorbing cadmium(II) from water solution. Chem Eng J 180:113–120
25. Pirbazari AE, Saberikhah E, Badrouh M, Emami MS (2014) Alkali treated Foumanat tea waste as an efficient adsorbent for methylene blue adsorption from aqueous solution. Wat Resour Indust 6:64–80
26. Reddy MCS, Sivaramakrishna L, Reddy AV (2012) The use of an agricultural waste material, Jujuba seeds for the removal of anionic dye (Congo red) from aqueous medium. J Hazard Mater 203:118–127
27. Rangabhashiyam S, Selvaraju N (2015) Evaluation of the biosorption potential of a novel *Caryota urens* inflorescence waste biomass for the removal of hexavalent chromium from aqueous solutions. J Taiwan Inst Chem Eng 47:59–70
28. Yu JX, Wang LY, Chi RA, Zhang YF, Xu ZG, Guo J (2013) Competitive adsorption of Pb^{2+} and Cd^{2+} on magnetic modified sugarcane bagasse prepared by two simple steps. Appl Surf Sci 268:163–170
29. Ofomaja AE, Unaubonah EI, Oladoja NA (2010) Competitive modeling for the biosorptive removal of copper and lead ions from aqueous solution by Mansonia wood sawdust. Bioresour Technol 10:3844–3852
30. Nazari MA, Cox PW, Waters KE (2014) Biosorption of copper, nickel and cobalt ions from dilute solutions using BSA-coated air bubbles. J Water Proc Eng 3:10–17
31. Hawari AH, Mulligan CN (2007) Effect of the presence of lead on the biosorption of copper, cadmium and nickel by anaerobic biomass. Proc Biochem 42:1546–1552
32. Dean JA (1985) Lang's handbook of chemistry. McGraw-Hill, New York
33. Marcus Y, Kertes AS (1969) Ion exchange and solvent extraction of metal complexes. Wiley, London
34. Nieboer E, McBryde WAE (1973) Free-energy relationships in coordination chemistry. III A comprehensive index to complex stability. Can J Chem 51:2512–2524
35. Zheng Y, Hua S, Wang A (2010) Adsorption behavior of Cu^{2+} from aqueous solutions onto starch-g-poly (acrylic acid)/sodium humate hydrogels. Desal 263:170–175
36. Ofomaja AE, Ho YS (2007) Effect of pH on cadmium biosorption by coconut copra meal. J Hazard Mater 139:356–362
37. Ho YS (2005) Effect of pH on lead removal from water using tree fern as the sorbent. Bioresour Technol 96:1292–1296
38. Ghali AE, Marzoug IB, Baouab HMV, Roudesli MS (2012) Separation and characterization of new cellulose fibres from the *Juncus acutus* plant. BioResources 7:2002–2018
39. Subramanian K, Kumar PS, Jayapal P, Venkatesh N (2005) Characterization of lingocellulosic seed fibre from *Wrightia Tinctoria* plant for textile applications—an exploratory investigation. Eur Poly J 41:853–866
40. Liu CF, Xu F, Sun JX, Ren JL, Curling S, Sun RC, Fowler P, Baird MS (2006) Physicochemical characteristics of cellulose from perennial ryegrass leaves (*Lolium perenne*). Carbohydr Res 341:2677–2687
41. Abraham E, Deepa B, Pothan LA, Jacob M, Thomas S, Cvelbar U, Anandjiwala RA (2011) Extraction of nanocellulose fibrils from lignocellulosic fibres: A novel approach. Carbohydr Poly 86:1468–1475
42. Sim SF, Ting W (2012) An automated approach for analysis of Fourier Transform infrared spectra (FTIR) of edible oils. Talanta 88:537–543
43. Jayaramudu J, Guduri BR, Varada RA (2010) Characterization of new natural cellulosic fabric *Grewia tilifolia*. Carbohydr Poly 79:847–855

44. El Mansouri N, Yuan Q, Huang E (2011) Synthesis and characterization of kraft lignin based expoxy resins. BioResources 6:2492–2503
45. Ofomaja AE, Ho YS (2007) Equilibrium sorption of anionic dye from aqueous solution by palm kernel fibre as sorbent. Dyes Pigm 74:60–66
46. El-Kamash AM, Zaki AA, El Geleel MA (2005) Modeling batch kinetics and thermodynamics of zinc and cadmium ions removal from waste solutions using synthetic zeolite A. J Hazard Mater B127:211–220
47. Karim AB, Mounir B, Hackar H, Bakasse M, Yaacoubi A (2009) Removal of Basic Red dye from aqueous solution by adsorption onto Moroccan clay. J Hazard Mater 168:304–309
48. Ghosh D, Bhattacharyya KG (2002) Adsorption of methylene blue on kaolinite. Appl Clay Sci 20:295–300

Chapter 12
Speciation Analysis of Inorganic Sb, Se and Te in Environmental Samples Using Modified TiO_2@MWCNTs Nanocomposite Packed Microcolumn prior to Hydride Generation-Inductively Coupled Plasma Optical Emission Spectrometry (HG-ICP-OES)

Philiswa N. Nomngongo

Abstract A simple, sensitive and selective method based on the combination of micro solid phase extraction and HG-ICP-OES for speciation analysis of Sb, Se and Te in environmental samples, has been developed. Titanium dioxide/multiwalled carbon nanotubes (TiO_2@MWCNTs) nanocomposite functionalized with Aliquat 336 was used as the sorbent material. Optimization of factors affecting the speciation of the target analytes was achieved using fractional factorial and Box-Behnken designs. Under optimum conditions, the limit of detection (n = 25) ranged from 1.0 to 1.6 ng L^{-1}. The repeatability and reproducibility (expressed in terms of relative standard deviation) ranged from 1.2–2.3% and 3.1–4.2%, respectively. The accuracy of the developed method was tested by the analysis of a certified reference material and spiked samples and the recovery percentages ranged from 96 to 109%. The proposed method was applied for the quantification of Sb, Se and Te species in real samples. The concentrations of total trace metals determined using the developed method were compared with those obtained using ICP-MS and the results obtained were in close agreement as statistically confirmed using Student paired t-test.

Keywords Speciation • Hydride generation • Trace elements Se/Sb/Te • Environmental samples • Nanocomposite adsorbent

P.N. Nomngongo (✉)
Faculty of Science, Department of Applied Chemistry, University of Johannesburg, Doornfontein Campus, P.O. Box 17011, Johannesburg 2028, South Africa
e-mail: pnnomngongo@uj.ac.za; nomngongo@yahoo.com

P. Ramasami et al. (eds.), *Emerging Trends in Chemical Sciences*,
DOI 10.1007/978-3-319-60408-4_12

12.1 Introduction

Selenium is an essential element for human beings and its major sources are from diet [1]. Selenium is a fundamental constituent of enzymes and plays a role as an antioxidant in the human body displaying redox activity through essential enzymes. The latter include thioredoxin reductase, iodothyronine deiodinase and glutathione peroxidase, among others [1–3]. Selenium is required in trace amounts, for this reason it becomes toxic when present in elevated concentrations (three to five times higher than the bio-essential dose). However, the toxicity of Se strongly depends on the chemical form or species of the element [2, 3]. Antimony on the other hand, is a cumulative toxic element with unknown biological function [2, 4]. The physico-chemical and toxic properties of this element depend on the binding form and oxidation state [4].

Antimony occurs in trace levels; however, due to the increase in modern applications, its concentration in the environment is increasing [2, 5–9]. In recent years Sb is used in a wide range of products, such as rubber and plastics, packaging materials, flame retardants, bactericides, and fungicides, among others [2, 4]. For this reason, the living organisms are subjected to an increasing antimony exposure [2, 5–9]. In view of the above, there is a need to identify and quantify the chemical forms of antimony to provide comprehensive information about its toxicity and human health relevance [4–9].

Tellurium (Te) has similar chemical and physical characteristics as Se and they are usually associated together in minerals and earth crust at trace to ultratrace levels. The most frequent inorganic species of this element in natural samples are tellurite and tellurate [5–10]. Tellurium is regarded as a rare, non-essential element and is known to be toxic to humans [11]. Similar to other elements, the toxicity of tellurium depends on the oxidation state, for example, the toxicity of Te(VI) is more serious than that of Te(IV) [10, 11]. Te tends to be accumulated in kidneys, heart, liver and spleen and it should not exceed 0.002 g kg^{-1}, as if exceeded it could lead to degeneracy of the liver and kidneys. Moreover, the emission of inorganic tellurium compounds in the environment may create serious problems due to the readily reactivity and chronic toxicity of this element [10].

In view of the above the determination of Sb, Se, Te in different sample matrices is of great importance due to their health effects [5–12]. However, compared to other trace elements, these elements are more difficult to detect by conventional techniques such as flame atomic absorption spectrometry (FAAS), graphite furnace atomic absorption spectrometry (GFAAS) and inductively coupled plasma-optical emission spectrometry (ICP-OES). This is because in ICP techniques, Sb, Se and Te suffer from low sensitivity due to their poor ionization efficiency in ICP, thus limiting their determination in real samples since they are present in ultra-trace low concentration [12–14]. In addition, FAAS and GFAAS are not suitable for determination of refractory metals such as Te and Sb. For this reason hydride generation (HG) coupled to spectrometric techniques have been widely used [5–9, 12, 13]. The advantages of using the HG include the elimination of matrix effects,

high sample introduction efficiency, improved sensitivity and selectivity, thus providing lower limits of detection [14]. In order to obtain the best performance using the HG system, parameters such as flow rate, concentration of reagents (HCl and $NaBH_4$), carrier gas and sample flow rate, among others need to be optimized. However, depending on the type of sample being analyzed, separation/pre-concentration technique coupled to spectrometric techniques such as ICP-OES, even if HG is being used, is required. For this reason, in the last decade, solid phase extraction (SPE) has been widely applied for trace element separation/pre-concentration [1, 15, 16]. This is because SPE displays excellent advantages such as high sensitivity, simultaneous enrichment and matrix elimination, reduced matrix interferences, easy automation, relatively high enrichment factors, and low cost [1, 15–17]. In addition, SPE has become more attractive due to the use of different adsorbent materials with high adsorption capacities [17]. In recent years, the use of nanometer sized adsorbents has received more attention; this is due to their superior properties. The latter include increased adsorbent reusability, stability and high adsorption capacity for metal ions in wide pH ranges [18, 19].

Therefore, this study reports the application of SPE-HG-ICP-OES procedure for pre-concentration and speciation of inorganic antimony, selenium and tellurium species in environmental samples. The separation/pre-concentration step was achieved using a microcolumn packed with Aliquat 336 coated-titanium dioxide/multiwalled carbon nanotubes nanocomposite. Two-level fractional factorial and Box-Behnken designs were used for the optimization of the experimental variables.

12.2 Experimental Section

12.2.1 Reagents and Materials

All reagents were of analytical grade unless otherwise stated and ultrapure water (specific conductance 0.05 μS cm^{-1}) from a Millipore Waters MilliQ purification unit (Merck Millipore, Bedford, MA, USA) was used throughout the experiments. Titanium butoxide, ammonia and ultrapure concentrated nitric acid (65%) were obtained from Sigma-Aldrich (St. Louis, MO, USA). Multi-walled carbon nanotubes (MWCNTs) with the outer diameter of 10 nm, core diameter of 4.5 nm, BET surface area of 280–350 m^2 g^{-1} and ≥98% purity were purchased from Sigma-Aldrich (St. Louis, MO, USA). The MWCNTs were further purified by stirring them in concentrated nitric acid at 70 °C for 12 h, followed by filtering and washing with distilled water, and then drying at 110 °C for 6 h [20]. Spectrascan single element standard (1000 mg L^{-1}) of Sb, Se and Te species (Teknolab, Norway) were used to prepare the working multi-element solutions. A Spectrascan multi-element standard solution at a concentration of 100 mg L^{-1} (Teknolab, Norway) was used to prepare the calibration standard solutions for quantification of analyte concentrations in model and real sample solutions.

12.2.2 Instrumentation

The quantification of the target analytes (Sb, Se and Te) was performed using an ICP-OES spectrometer (iCAP 6500 Duo, Thermo Scientific, UK) equipped with a charge injection device detector. In addition, the system was equipped with an integrated unit for HG. The samples were introduced via a concentric nebulizer and a cyclonic spray chamber.

An on-line pre-concentration system was performed using a MinipulsTM 3 peristaltic pump (Gilson, Villiers le Bel, France). Sample injection was achieved using a Rheodyne (Cotati, CA, USA) Model 50, four-way rotary valve. A self-made PTFE micro-column (2.85 mm i.d.), packed with nanoadsorbent was used in the manifold for extraction and pre-concentration of metals. PVC peristaltic pump tubing (Black/Black 0.76 mm i.d.) was employed to propel the sample, buffer and eluent, respectively. Minimum lengths of PTFE tubing were used for all connections. UV photoreduction was achieved with a 400 W mercury vapour lamp (15W G15T8 UV-C, Philips) that ignited with a suitable starter and choke, surrounded by 10 m PTFE tubing. The Sb 206.833, Se 196.026 and Te 214.281 nm spectral lines were used. The setup for the online solid phase extraction system was carried out according to Escudero et al. [1].

The morphological structure of the nanoadsorbent was observed using a scanning electron microscope (SEM) (JSM-6360LVSEM, JEOL Co., Japan) after gold coating. The specific surface area of the adsorbent was determined by Surface Area and Porosity Analyzer (ASAP2020 V3.00H, Micromeritics Instrument Corporation, Norcross, USA). All the gases used for analysis were instrument grade. X-ray powder diffraction (XRD) measurements were carried out with a Philips X-ray generator model PW 3710/31 diffractometer with automatic sample changer model PW 1775 (scintillation counter, Cu-target tube and Ni-filter at 40 kV and 30 mA).

12.2.3 Synthesis, Modification and Characterization of TiO_2@f-MWCNTs

The MWCNTs were first functionalized according to the method reported by Es'haghi et al. [19]. The preparation of TiO_2@f-MWCNTs composite was carried out according to the method reported by Gupta et al. [20] with some modification. Briefly, f-MWCNTs (500 mg) were dispersed into deionized water and magnetically agitated for 6 h at which acceptable level of dispersion was observed. Nanometer sized titania were synthesized by the sol-gel method. Appropriate amount (8.0 mL) of titanium butoxide was dissolved in ethanol, and the solution was then diluted with double distilled deionized water. The pH of the resulting solution was adjusted to 2 using 1.0 mol L^{-1} nitric acid. The titanium butoxide solution was carefully added (dropwise) into the dispersed f-MWCNTs. After that, the suspension was dried at 110 °C. The obtained material was heated up to 400 °C

for 90 min, where the pyrolysis process resulted in titania formation supported onto the f-MWCNTs' surface.

The resulting material was characterized by SEM, BET and XRD. The SEM images illustrate that the TiO_2 nanoparticles were well attached to the MWCNTs and the nanocomposites were well dispersed. The XRD patterns revealed that the synthesised TiO_2@MWCNTs nanocomposite material had crystalline peaks, which are attributed to anatase TiO_2. The nitrogen adsorption/desorption isotherms showed that the nanoadsorbent had a surface area of about 209 $m^2\ g^{-1}$. These observed characterization results were similar to those reported in the literature [21, 22].

The functionalization of the resulting nanocomposite material was performed according to Bahadir et al. [23], with some modifications. Briefly, 500 g of TiO_2@f-MWCNTs were mixed with 100 mL of 5% Aliquat 336 in methanol. The mixture was sonicated for 6 hours at room temperature and the suspension was separated by centrifugation at 5000 rpm. The resultant solid was washed with ultrapure water and dried in an oven at 110 °C.

12.2.4 Sample Preparation

The certified reference material NIST 1643e (fresh water) was obtained from the National Institute of Standards and Technology (NIST, Gaithersburg, MD, USA). Tap water and river water samples were collected from Soweto area (Johannesburg, South Africa) using pre-cleaned polypropylene sample bottles. For transportation from the sample site to the laboratory the samples were chilled in a cooler. All samples were filtered through 0.45 μm pore size membrane filters immediately after sampling without preservations. It should be noted that the acid was not added because it will alter the species of each metal present.

12.2.5 Multivariate Optimization of SPE-HG-ICP-OES System

The general pre-concentration procedure was adopted from previous studies [1]. The optimization of the parameters affecting the SPE-HG-ICP-OES system was performed using two level factorial and Box-Behnken designs. Five variables i.e. sample pH, eluent concentration (EC), eluent flow rate (EFR), reagent flow rate (RFR) and sample flow rate (SFR) were regarded as important factors. The concentration of $NaBH_4$, the Ar flow rate and the sample volume were 1.0 M and 0.8%, 0.65 L min^{-1} and 20 mL, respectively. These values have been optimized in previous studies [1, 13]. Maximum, central point and minimum levels in Table 12.1 for each factor were chosen according to the data from previous

Table 12.1 Factors and levels used for optimization strategy

Variables	Low (−)	Central point (0)	High (+)
Sample pH	2	6	10
Sample flow rate (SFR) (mL min^{-1})	5.0	7.5	10.0
Reagent flow rate (RFR) (mL min^{-1})	2.0	3.0	4.0
Eluent concentration (EC) (mol L^{-1})	1.0	1.5	2.0
Eluent flow rate (EFR) (mL min^{-1})	5.0	7.5	10.0

experiments. All the experiments were carried out in random order. The experimental data was processed by using the Statistica software program.

12.3 Results and Discussion

12.3.1 Multivariate Optimization of the SPE-HG-ICP-OES Method

Two level (2^{5-1}) fractional factorial design was used as a screening method for optimization of SPE-HG-ICP-OES method. Analysis of variance (ANOVA) was used to investigate the effect of the most influential factors and the percentage recoveries were used as the analytical response (Table 12.7). The ANOVA results produced in the form of Pareto charts (Figs. 12.1, 12.2 and 12.3) presented the main effects and their interactions. It was observed from the ANOVA results that sample pH, sample flow rate and eluent concentration were the most important variables for the determination of the studied analytes. Therefore, reagent and eluent flow rates were fixed at 3.0 and 5.0 mL min^{-1}, respectively. The most influential factors were further optimized using Box-Benhken design composed of a total of 14 experiments (Table 12.8). The response surface methodology 3D graphics (Fig. 12.4) of the quadratic models were used to evaluate the interactive relationships between the independent variables and the response [17]. The overall outcome revealed that as the sample pH, sample flow rate and eluent concentration increase the analytical response also increases. Therefore, based on the quadratic equations resulted from the 3D surface response plots, the optimum sample pH, sample flow rate and eluent concentration were found to be respectively 6, 8.5 mL min^{-1} and 2.0 mol L^{-1}. In view of the above, the results obtained from the screening analysis using 2^{5-1} fractional factorial and Box-Benhken designs revealed that optimum sample pH, reagent flow rate, sample flow rate, eluent concentration and eluent flow rate were 6, 3.0 mL min^{-1}, 8.5 mL min^{-1}, 2.0 mol L^{-1} and 5.0 mL min^{-1}, respectively.

12.3.2 Analytical Figures of Merit

The SPE-HG-ICP-OES system had a linear dynamic range of calibration from LOQs up to 350 μg L^{-1} for all the studied analytes ($R^2 = 0.9989–0.9991$). Under optimum conditions, the limits of detection (LOD) and quantification (LOQ) were calculated according to IUPAC recommendation from $C_{LOD} = 3 \times SDm^{-1}$ and $C_{LOQ} = 10 \times SDm^{-1}$, where SD is the standard deviation of the blank (n = 25) and m is the slope of the calibration curve. The LOD and LOQ were found to be 1.3, 1.6 and 1.0 ng L^{-1} and 4.3, 5.3 and 3.3 ng L^{-1} for Sb(V), Se(VI) and Te(VI), respectively. The repeatability and reproducibility in terms of standard deviation obtained for 15 repetitive analyses of 20 mL of multielement standard (10 μg L^{-1}) were evaluated. The RSDs for repeatability and reproducibility for Sb, Se and Te were 1.7, 2.3 and 1.2% and 3.1, 4.2 and 3.5%, respectively. The pre-concentration factor was found to be 22,500 (50 for pre-concentration system, and 450 for HG). The throughput sample was found to be 25 samples/h (2.4 min pre-concentration time and 20.0 mL sample volume).

The analytical figures of merit of the current method were compared with those recently reported in the literature by different researchers (Table 12.2). As it can be seen, the LOD, precision and enrichment factor of the proposed SPE-HG-ICP-OES method are comparable or better than the other procedures, and the enrichment factor is significantly higher than others. These findings demonstrated that the SPE-HG-ICP-OES method has some advantages over the reported methods. These advantages include lower detection limit, higher pre-concentration factor, simplicity and low cost. For this reason, it can be concluded that the developed method was suitable for the analysis of ultratrace species of Se, Sb and Te.

12.3.3 Reusability

The regenerability of an adsorbent is one of the key performance factors that needs to be evaluated. Generally, an ideal adsorbent should not only possess a high sorption capacity, but also exhibits a long-term stability [22]. The microcolumn was found to be reusable after regeneration with 5 mL of 2.0 mol L^{-1} HCl solution and 5 mL deionized water, respectively. It was observed that the column is stable up to 150 percolation and elution cycles. This phenomenon shows that the prepared nanocomposite had good stability under acidic conditions, which can significantly reduce the overall cost for the adsorbent [27].

Table 12.2 Comparison of analytical figures of merit of the current method with those recently reported in the literature by different researchers

Analyte	Analytical procedure	Sample matrices	Preconcentration factor	LOD (ng L^{-1})	RSD (%)	Ref.
Se(IV)	FI-HG-ICP-OES	Water and beverages	14875	30	0.17	[1]
Sb(V)	HG-ICP-OES	Bottled water	–	110	18	[14]
Sb, Se	HG-ICP-OES-slurry introduction	Water and soft drinks	18, 19	90, 100	3.0, 4.1	[13]
Te(VI)	DLLME-ETAAS	Water	125	4	3.7	[11]
Se(VI), Te(VI)	SPE/ICP-MS	Water	–	7, 3	5–13	[24]
Se(IV), Te(VI)	HG-AFS	Milk	–	12, 23	10, 12	[25]
Sb	FI-HG-DC-AFS	Water	26.6	2.5	4.8	[26]
Se	HG-HSSPME-ICP-OES	Water, beer, wort and yeast	–	800	3.4	[10]
Sb(V), Se (VI), Te (VI)	SPE-HG-ICP-OES	Water	22,500	1.3, 1.6, 1.0	1.7, 2.3, 1.2	This work

12.3.4 Validation and Application of the Developed Method

The accuracy of target element analysis was evaluated using spike recovery tests. This was done in order to control possible analyte matrix effect [1]. The recoveries of analytes from environmental matrices spiked at two concentration levels of 25 and 50 times the quantification limits for Sb (0.11 and 0.21 μg L^{-1}), Se (0.13 and 0.26 μg L^{-1}) and Te (0.08 and 0.17 μg L^{-1}) were determined. The analytical results are presented in Table 12.3. It can be seen from this table that quantitative recoveries of 96–109% for all the studied analytes were obtained.

In order to further validate the accuracy of the proposed method, the certified reference material (1643e) was analysed for elemental species and total content. It can be seen from Table 12.4 that the analytical results of the developed method are in agreement with certified values. In addition, the recoveries ranged from 97.2 to 100.1%, proving that the SPE-HG-ICP-OES method has a high accuracy.

The developed SPE-HG-ICP-OES procedure was successfully applied for the determination of trace amounts of Sb, Se and Te species in different water samples. It should be noted that the concentrations of Sb(III), Se(IV) and Te(IV) were mathematically calculated from the total content and the determined Sb(V), Se (VI) and Te(VI). The results are presented in Table 12.5. To verify the validity of the results obtained by the current method, the samples were also analyzed by ICP-MS (Table 12.6). The results were in good agreement and are not significantly

Table 12.3 Analytical results obtained in the analysis of spiked samples. The concentration values are expressed as the mean ± standard deviation of five replicates

Sample	Added ($\mu g\ L^{-1}$)	Sb(V) ($\mu g\ L^{-1}$)	Added ($\mu g\ L^{-1}$)	Se(VI) ($\mu g\ L^{-1}$)	Added ($\mu g\ L^{-1}$)	Te(VI) ($\mu g\ L^{-1}$)
Tap water 1	0	0.05 ± 0.01	0	186.3 ± 0.9	0	< LOD[a]
	0.11	0.16 ± 0.01	0.13	186.4 ± 0.04	0.08	0.08 ± 0.03
Recovery (%)		96.4		100		98.8
	0.21	0.26 ± 0.03	0.26	186.6 ± 0.3	0.17	0.17 ± 0.03
Recovery (%)		98.1		104		97.1
River water 1	0	0.32 ± 0.06	0	45.5 ± 1.0	0	3.10 ± 0.90
	0.11	0.44 ± 0.02	0.13	45.6 ± 0.2	0.08	3.18 ± 0.01
Recovery (%)		109		108		96.3
	0.21	0.52 ± 0.02	0.26	45.8 ± 1.2	0.17	3.28 ± 0.03
Recovery (%)		98.2		96.2		106

Total metal ion content Sb: 0.085 ± 0.005 $\mu g\ L^{-1}$ in tap water 1 and 0.91 ± 0.04 $\mu g\ L^{-1}$ in river water 1; Se: 188.7 ± 1.2 $\mu g\ L^{-1}$ in tap water 1 and 52.3 ± 0.7 $\mu g\ L^{-1}$ in river water 1; Te: 4.78 ± 0.15 $\mu g\ L^{-1}$ in river water 1

[a]< LOD: below the limits of detection

Table 12.4 Determination of Sb, Se and Te concentration (n = 6) in NIST 1643e (fresh water)

Analyte	Certified values ($\mu g\ L^{-1}$)	Obtained values ($\mu g\ L^{-1}$)	Recovery (%)
Sb	58.30 ± 0.11	58.33 ± 0.09	100.1
Se	11.97 ± 0.11	11.94 ± 0.12	99.7
Te	1.09 ± 0.14	1.05 ± 0.09	97.2

different at 95% confidence level. These findings proved that the developed method was suitable for the determination of trace Sb, Se and Te species.

12.4 Conclusion

This study reports the development of a SPE-HG-ICP-OES method for the determination of inorganic Sb, Se and Te species in water samples. The TiO_2@MWCNTs-Aliquat 336 was used as a solid phase material for selective pre-concentration of Sb(V), Se(VI) and Te(VI) species. The optimization of the experimental parameters affecting the speciation of analytes of interest was achieved using 2^{5-1} fractional factorial and Box-Benhken designs. Under optimized conditions, the SPE-HG-ICP-OES method proved to be suitable for the speciation of the target elements. In addition, the developed method was found to be simple, sensitive, selective, accurate and precise.

Acknowledgements The author wishes to thank the University of Johannesburg and National Research Foundation (South Africa, grant no. 99270) for financial assistance.

Table 12.5 Determination of antimony, selenium and tellurium concentration (μg L^{-1}, n = 4) in water samples

Sample	Sb(V)	Sb(total)	Sb(III)	Se(VI)	Se(total)	Se(IV)	Te(VI)	Te(total)	Te(IV)
River water 2	141.0 ± 1.2	166.4 ± 1.2	25.4 ± 0.8	19.4 ± 0.9	44.8 ± 1.0	< LOD	< LOD	< LOD	< LOD
River water 2	91.5 ± 1.7	120.2 ± 0.7	28.7 ± 0.6	45.5 ± 1.3	71.1 ± 1.2	25.6 ± 0.8	3.11 ± 0.19	5.01 ± 0.15	1.90 ± 0.13
Tap water 2	1.38 ± 0.15	1.50 ± 0.11	0.12 ± 0.09	53.8 ± 1.3	56.1 ± 1.2	2.31 ± 0.03	< LOD	< LOD	< LOD
Tap water 3	4.51 ± 0.12	5.93 ± 0.06	1.42 ± 0.11	23.9 ± 0.7	29.7 ± 0.8	5.80 ± 0.80	0.67 ± 0.01	1.07 ± 0.11	0.40 ± 0.02

Table 12.6 Determination of total antimony, selenium and tellurium concentration (μg L^{-1}) in water samples using ICP-MS

Sample	Sb(total)	Se(total)	Te(total)
River water 2	165.4 ± 2.3	45.1 ± 1.3	< LOD
River water 2	119.7 ± 1.6	69.8 ± 2.3	4.98 ± 0.23
Tap water 2	1.52 ± 0.32	55.9 ± 1.8	< LOD
Tap water 3	5.89 ± 0.12	30.1 ± 1.2	1.11 ± 0.13

Supplementary Data

Table 12.7 Matrix of 2^{5-1} full factorial design and the analytical response (% recovery) for each experiment

Column 1	SPH	SFR	EC	RFR	EFR	Sb(V)	Se(VI)	Te(VI)
1	2	5	1	2	10	49.45	57.97	53.32
2	10	5	1	2	5	50.23	56.96	57.10
3	2	10	1	2	5	63.55	69.93	70.10
4	10	10	1	2	10	64.12	70.98	72.60
5	2	5	3	2	5	69.63	72.92	63.01
6	10	5	3	2	10	70.57	74.83	70.89
7	2	10	3	2	10	78.96	84.40	83.01
8	10	10	3	2	5	79.87	90.59	89.99
9	2	5	1	4	5	75.32	66.55	70.75
10	10	5	1	4	10	76.32	68.76	73.08
11	2	10	1	4	10	83.69	98.05	79.07
12	10	10	1	4	5	84.65	100.97	80.89
13	2	5	3	4	10	95.32	84.54	82.43
14	10	5	3	4	5	96.01	86.11	84.20
15	2	10	3	4	5	94.36	93.32	94.96
16	10	10	3	4	10	95.15	94.89	95.67
17	6	7.5	2	3	7.5	80.69	82.72	81.20
18	6	7.5	2	3	7.5	80.52	82.56	81.20
19	6	7.5	2	3	7.5	80.45	82.79	81.27

Table 12.8 Experimental design using Box–Behnken design and analytical response values

Run	SPH	SFR	EC	Sb(V)	Se(VI)	Te(VI)
				Recovery (%)		
1	2	5	2	74.74	78.47	70.56
2	10	5	2	70.12	74.54	80.18
3	2	10	2	84.13	82.62	84.25
4	10	10	2	67.62	68.38	92.43
5	2	7.5	1	57.32	59.99	64.05
6	10	7.5	1	48.33	51.49	90.18
7	2	7.5	3	98.81	98.02	101.2
8	10	7.5	3	85.25	87.24	96.48
9	6	5	1	63.23	67.36	67.67
10	6	10	1	54.33	53.56	78.26
11	6	5	3	89.23	93.61	89.29
12	6	10	3	100.51	100.21	101.53
13	6	7.5	2	98.96	98.17	99.87
14	6	7.5	2	98.77	98.22	100.12
15	6	7.5	2	98.72	98.29	99.89

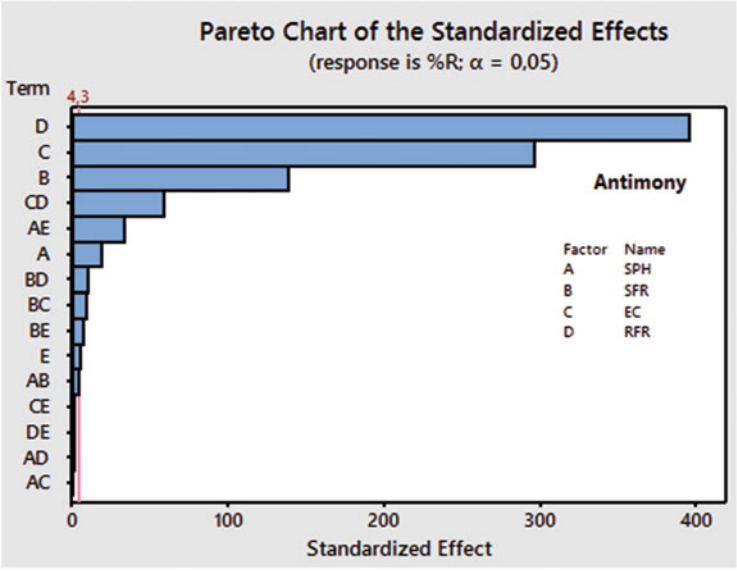

Fig. 12.1 Pareto chart of standardized effects for variables related to the preconcentration of Sb

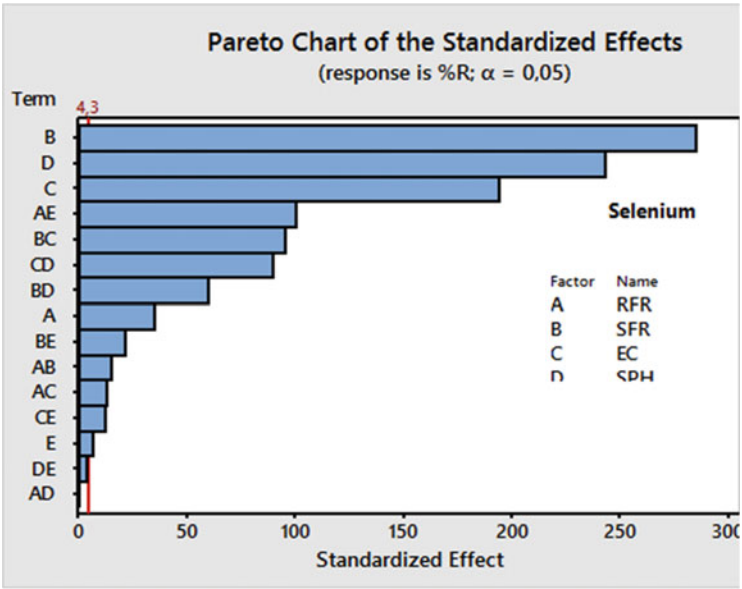

Fig. 12.2 Pareto chart of standardized effects for variables related to the preconcentration of Se

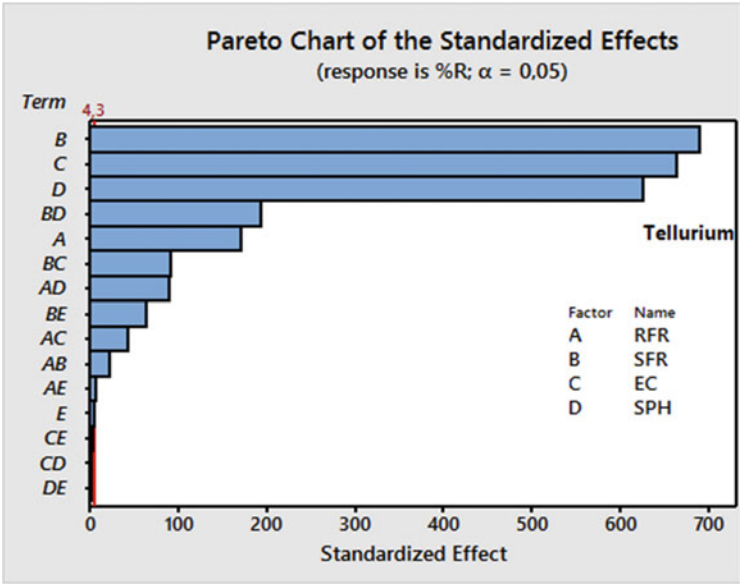

Fig. 12.3 Pareto chart of standardized effects for variables related to the preconcentration of Te

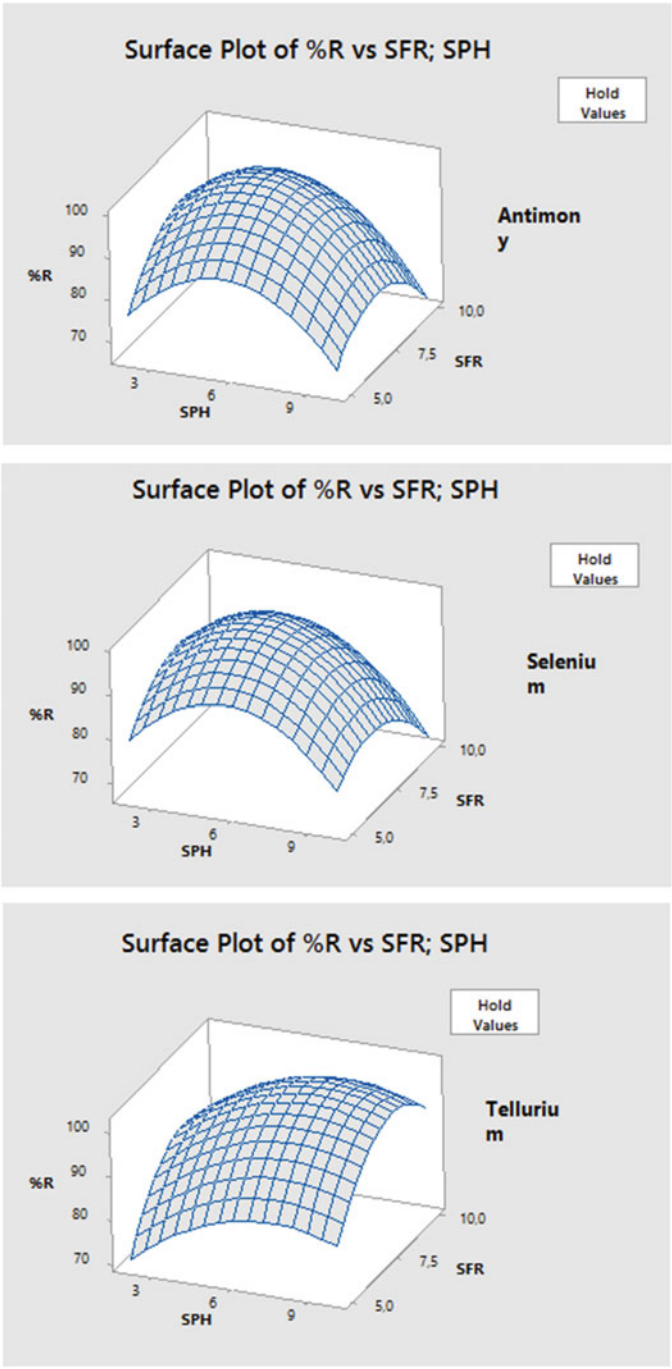

Fig. 12.4 Response surfaces obtained for Sb, Se and Te

References

1. Escudero LA, Pacheco PH, Gasquez JA, Salonia JA (2015) Development of a FI-HG-ICP-OES solid phase preconcentration system for inorganic selenium speciation in Argentinean beverages. Food Chem 169:73–79
2. Depoi FDS, Pozebon D (2012) The use of cloud point extraction and hydride generation for improving the Sb and Se limits of detection in ICP OES. J Braz Chem Soc 23:2211–2221
3. Latorre CH, García JB, Martín SG, Crecente RP (2013) Solid phase extraction for the speciation and preconcentration of inorganic selenium in water samples: a review. Anal Chim Acta 804:37–49
4. Jiang X, Wen S, Xiang G (2010) Cloud point extraction combined with electrothermal atomic absorption spectrometry for the speciation of antimony(III) and antimony(V) in food packaging materials. J Hazard Mater 175:146–150
5. Chen Y-W, Alizharani A, Deng T-L, Belzile N (2016) Valence properties of tellurium in different chemical systems and its determination in refractory environmental samples using hydride generation–atomic fluorescence spectroscopy. Anal Chim Acta 905:42–50
6. Belzile N, Chen Y-W (2015) Tellurium in the environment: a critical review focussing on natural waters, soils, sediments and airborne particles. Appl Geochem 63:83–92
7. Belzile N, Chen Y-W, Filella M (2011) Human exposure to antimony. I. Sources and intake. Crit Rev Environ Sci Technol 41:1309–1373
8. Chen Y-W, Belzile N (2010) High performance liquid chromatography coupled to atomic fluorescence spectrometry for the speciation of the hydride and chemical vapour-forming elements As, Se, Sb and Hg: a critical review. Anal Chim Acta 671:9–26
9. Filella M, Belzile N, Chen Y-W (2002) Antimony in the environment. A review focused on natural waters. I. Occurrence. Earth-Sci Rev 57:125–176
10. Ghasemi E, Najafi NM, Raofie F, Ghassempour A (2010) Simultaneous speciation and preconcentration of ultra traces of inorganic tellurium and selenium in environmental samples by hollow fiber liquid phase microextraction prior to electrothermal atomic absorption spectroscopy determination. J Hazard Mater 181:491–496
11. Najafi NM, Tavakoli H, Alizadeh R, Seidi S (2010) Speciation and determination of ultra trace amounts of inorganic tellurium in environmental water samples by dispersive liquid–liquid microextraction and electrothermal atomic absorption spectrometry. Anal Chim Acta 670:18–23
12. Tyburska A, Jankowski K, Rodzik A (2011) Determination of arsenic and selenium by hydride generation and headspace solid phase microextraction coupled with optical emission spectrometry. Spectrochim Acta B 66:517–521
13. Dados A, Kartsiouli E, Chatzimitakos T, Papastephanou C, Stalikas CD (2014) In situ trapping of As, Sb and Se hydrides on nanometer-sized ceria-coated iron oxide–silica and slurry suspension introduction to ICP-OES. Talanta 130:142–147
14. dos Santos VCG, Grassi MT, Abate G (2015) Speciation of antimony(III) and antimony(V) in bottled water by hydride generation-inductively coupled plasma optical emission spectrometry. Anal Lett 48:2921–2935
15. Nomngongo PN, Ngila JC, Kamau JN, Msagati TA, Moodley B (2013) Preconcentration of molybdenum, antimony and vanadium in gasoline samples using Dowex 1-x8 resin and their determination with inductively coupled plasma–optical emission spectrometry. Talanta 110:153–159
16. Xiong C, Qin Y, Hu B (2010) On-line separation/preconcentration of V(IV)/V(V) in environmental water samples with CTAB-modified alkyl silica microcolumn and their determination by inductively coupled plasma-optical emission spectrometry. J Hazard Mater 178:164–170
17. Nomngongo PN, Ngila JC (2014) Functionalized nanometer-sized alumina supported micro-solid phase extraction coupled to inductively coupled plasma mass spectrometry for preconcentration and determination of trace metal ions in gasoline samples. RSC Adv 4:46257–46264

18. Diniz KM, Tarley CRT (2015) Speciation analysis of chromium in water samples through sequential combination of dispersive magnetic solid phase extraction using mesoporous amino-functionalized Fe_3O_4/SiO_2 nanoparticles and cloud point extraction. Microchem J 123:185–195
19. Es'haghi Z, Khalili M, Khazaeifar A, Rounaghi GH (2011) Simultaneous extraction and determination of lead, cadmium and copper in rice samples by a new pre-concentration technique: hollow fiber solid phase microextraction combined with differential pulse anodic stripping voltammetry. Electrochim Acta 56:3139–3146
20. Gupta VK, Agarwal S, Saleh TA (2011) Synthesis and characterization of alumina-coated carbon nanotubes and their application for lead removal. J Hazard Mater 185:17–23
21. Alosfur FKM, Jumali MHH, Radiman S, Ridha NJ, Yarmo MA, Umar AA (2013) Modified microwave method for the synthesis of visible light-responsive TiO_2/MWCNTs nanocatalysts. Nanoscale Res Lett 8:1–3
22. Szőllősi G, Németh Z, Hernádi K, Bartók M (2009) Preparation and characterization of TiO_2 coated multi-walled carbon nanotube-supported Pd and its catalytic performance in the asymmetric hydrogenation of α,β-unsaturated carboxylic acids. Catal Lett 132:370-376
23. Bahadir Z, Bulut VN, Hidalgo M, Soylak M, Marguí E (2015) Determination of trace amounts of hexavalent chromium in drinking waters by dispersive microsolid-phase extraction using modified multiwalled carbon nanotubes combined with total reflection X-ray fluorescence spectrometry. Spectrochim Acta B 107:170–177
24. Yu C, Cai Q, Guo ZX, Yang Z, Khoo SB (2004) Simultaneous speciation of inorganic selenium and tellurium by inductively coupled plasma mass spectrometry following selective solid-phase extraction separation. J Anal Atom Spectrom 19:410–413
25. Cava-Montesinos P, de la Guardia A, Teutsch C, Cervera ML, de la Guardia M (2004) Speciation of selenium and tellurium in milk by hydride generation atomic fluorescence spectrometry. J Anal Atom Spectrom 19:696–699
26. Wu H, Wang X, Liu B, Liu Y, Li S, Lu J, Tian J, Zhao W, Yang Z (2011) Simultaneous speciation of inorganic arsenic and antimony in water samples by hydride generation-double channel atomic fluorescence spectrometry with on-line solid-phase extraction using single-walled carbon nanotubes micro-column. Spectrochim Acta B 66:74–80
27. Wang Y, Tian T, Wang L, Hu X (2013) Solid-phase preconcentration of cadmium(II) using amino-functionalized magnetic-core silica-shell nanoparticles, and its determination by hydride generation atomic fluorescence spectrometry. Microchim Acta 180:235–242

Chapter 13
Nano Transition Metal Alloy Functionalized Lithium Manganese Oxide Cathodes-System for Enhanced Lithium-Ion Battery Power Densities

Natasha Ross and Emmanuel Iwuoha

Abstract A new generation of battery technologies is necessary to address the challenges of the increasingly complex energy systems our society requires. A lithium-ion battery (LIB) is an advanced battery technology that uses lithium ions as a key component of its electrochemistry. Manganese oxide cathode material of rechargeable lithium-ion batteries offers a unique blend of lower cost and toxicity compared to the normally used cobalt, and has been demonstrated to be safer on overcharge. The common disadvantages affecting its performance are amendable through morphological and electrochemical properties changes. In this research work, alloy nanoparticles were synthesized and used as coating material with the objective to improve the microstructure and catalytic activities of pristine $LiMn_2O_4$. Co-precipitation and calcination methods were used to coat the $LiMn_2O_4$. The pristine $LiMn_2O_4$ and modified materials were examined using a combination of spectroscopic and microscopic techniques along with in detail galvanostatic charge–discharge tests. Microscopic results revealed that the novel composite cathode materials had high phase purity, well-crystallized particles and consistent morphological structures with narrow size distributions. The $LiPtAu_xMn_{2-x}O_4$ cathode effectively accommodated the structural transformations, which occur during Li^+ ion insertion with exchange current density i_0 (A cm^{-2}) of 1.83×10^{-4} and 3.18×10^{-4} for $LiMn_2O_4$. The enhancement of the capacity retention and higher electrode coulombic efficiency of the $LiPtAu_xMn_{2-x}O_4$ were significant, especially at high C rate. At enlarged cycling potential ranges the $LiM_xMn_{2-x}O_4$ ($x = 0.02$) sample delivered relevant discharge capacity of 90 mAh g^{-1} compared to $LiMn_2O_4$ (45 mAh g^{-1}).

Keywords Lithium-ion batteries • Lithium manganese oxide • Storage capacity • Energy density • Nanoparticles

N. Ross (✉) • E. Iwuoha
SensorLab, Department of Chemistry, University of Western Cape, Private Bag X17, Bellville, Cape Town 7535, South Africa
e-mail: nross@uwc.ac.za

P. Ramasami et al. (eds.), *Emerging Trends in Chemical Sciences*,
DOI 10.1007/978-3-319-60408-4_13

13.1 Introduction

The high specific energy and power available from lithium-ion batteries and the possibility to charge and discharge them hundreds of times are the reason for their key importance in electronic portable devices and future development of hybrid vehicles [1]. When a battery is operative, the redox reactions alter the electrode materials molecular/crystalline structure, affecting their stability, and hence require frequent replacement after several cycles. The high rate exchange of lithium ions requiring more power and faster charging generates significant stresses and strains in the electrodes that ultimately lead to performance degradation [2]. Therefore, improvement of the cathode materials is pivotal. The $LiMn_2O_4$ in LIB's performance remain inferior to other systems and consequently have a limited market, but are promising in industrial and electrical vehicles applications, as a result of their safety and cost/performance characteristics [3]. The need of a cathode catalyst to reversibly reduce oxygen and re-oxidize the oxide species back to oxygen largely stems from addressing the large overpotentials in the discharge–charge reactions. The challenges rise from the effort to increase the cycle life and stability of the cathode materials in standard commercial LIB's [4].

This work on AuPt alloy transition metal alloy-surface modified spinel $LiMn_2O_4$ cathode materials can provide a better connecting network for electron diffusion due to a shortened transportation path, i.e., highly crystalline nanostructures [5], enhanced phase transition kinetics of lithium ion intercalation/deintercalation and high rate discharge capabilities [6]. Lithium-ion batteries made using nanotechnology were found to demonstrate ultrahigh lithium storage [7].

13.2 Nanoalloys

Since their commercialization in the 1960s, bimetallic catalysts are widely utilized in many catalytic [8] and electrocatalytic applications [9]. Bimetallic nanoparticles are the combination of two metals in the nanoscale size range [10]. Alloying of metals is a way of developing new materials with better technological usefulness than their starting substances. The use of bimetallic nanoparticles may give rise to synergism with improvement of structural and physical properties [11]. Bimetallic nanoparticles often exhibit enhanced catalytic performances in terms of activity, selectivity, and stability, compared to the separate components [12]. Hence, bimetallic nano-catalysts provide a way to utilize smaller amounts of expensive catalyst material. This, together with the ability to make them in different sizes and shapes, makes them potentially useful for catalysis [13]. For example, the most favorable size for platinum-based electrocatalysis is in the range of 2–4 nm [14]. Therefore, synthesis of bimetallic nanoparticles that could exhibit well-controlled shapes, sizes, chemical composition, and structure has been explored in order to enhance their performances. Bimetallic nanoparticles have wide application in emerging technologies due to additional degrees of freedom as compared to monometallic nanoparticles [15].

13.3 Active Materials for the Positive Electrode of the Li-Ion Batteries

In general, the active materials for positive electrodes are compounds based on transition metals which can release lithium ions from the structure by oxidation of the transition metal cations. To obtain high rate capability and high reversibility, it is important that during intercalation the structure of the active material remains unaltered. Most of the active materials for the positive electrode of the lithium-ion batteries have a layered structure, with transitional metal ions ordered in a layer (slab) and lithium ions in the following layer (interslab). The disorder of the structure can be quantified from the amount of transition metals, which are in the interslab. Li^+ can diffuse rapidly in the structure only if the material is highly ordered [16]. Moreover, to obtain high enough specific energy density, it is necessary that at least one Li^+ per transition metal can be removed from (accommodated in) the structure. Also the electronic conductivity of the compounds is important. If it is too low, some conductive additives (mainly carbonaceous) have to be mixed in the electrode composition, thus lowering the specific energy. In this case, the reaction can occur only in the regions where the three phases (conductive additives, active material and electrolyte) meet together. $LiCoO_2$ was the first active material for positive electrode commercialized in large scale [17]. The $LiCoO_2$ has a layered structure. The complete removal of the lithium ions from the interslab results in structural changes leaving it electrochemically inactive with respect to Li^+ intercalation. $LiNiO_2$ has the same structure of the cobalt equivalent, but with the advantage of the lower cost. Studies suggest an excess of nickel in the structure, localized in the interslab and causes a reduction of the diffusion coefficient and consequently of the power capability. Moreover, the deintercalated compound seems to be unstable and therefore dangerous in contact with organic liquids [18]. $LiFePO_4$ is the first positive material, which is low cost, environmentally benign, and can be charged reversibly up to 1 Li^+ per Fe. The compound is an olivine and electrochemically active to Li^+ intercalation. However, its low electronic conductivity (10^{-9} S/cm) does not permit to use them "as they are", hence they have to be mixed with carbonaceous compounds [19]. Second-generation cathodes include modifications of the $LiNiO_2$, spinel cathodes $LiMn_2O_4$ and layered $LiMnO_2$. $LiMnO_2$ is a low cost compound and environmental friendly. The $LiMn_2O_4$ spinel compound has three equilibrium potentials for lithium ion intercalation, two are at 4.0 and 4.1 V (Li/Li^+), and one at 3.0 V (Li/Li^+). Often only the lithium intercalation at 4.0 and 4.1 V (Li/Li^+) is used, so that the cell is constructed in the discharged state [20]. The average oxidation state of the manganese is critical to obtain effective cycle life. When the oxidation state of the manganese is 3.58 or higher, the dissolution of the manganese is reduced and the spinel compound has a lengthier cycle life [21]. However, in the deintercalated state, the structure is not stable and changes to spinel [22]. To stabilize the structure, many transition metals have been used as substitutes of Mn [23].

13.4 Modification Techniques to Advance Cathode Performances

The challenges remaining for cathode materials include: stabilization during prolonged cycling, improving their rate capabilities, and demonstrating acceptable safety features. The best approaches appear to be addressing both their synthetic processes and exploit of the surface coating technique. One of the main strategies to improve the rate capability and safety of $LiMn_2O_4$ cathode materials is to develop powders with core–shell structures: active mass particles coated with protective layers that reduce detrimental reactions of the cathode material with solution species, yet allow fast migration of Li ions through them. If the surface reactivity of nanoparticles is properly attenuated, this can significantly increase the rate capabilities. Exchange of lithium ions with the electrolyte during charge and discharge process depends critically on the electrode microstructure, morphology as well as the inherent electrochemical properties.

13.5 Nanocoating

Electrochemical reactions start at the electrode-electrolyte interface, hence control of the interfaces via coating can decrease the interface side-reactions and improve the Li-ion diffusivity. The surface coating may also improve the electrochemical performance of the $Li_{1+x}Mn_{2-x}O_4$ spinel due to a decrease in the dissolution of Mn^{2+} and enhance the transportation of the Li^+ ions in the cathode material [4] and deliver enhanced capacity retention after cycling. After coating, M_x (M = AuPt) replaces the Mn^{3+} prone to disproportionation and forms $LiM_xMn_{2-x}O_4$, which obstructs the structural degradation of $LiMn_2O_4$. Among the cathode materials, spinel $LiMn_2O_4$ has the most destabilized structure at elevated temperatures. Hence, coating can lead to the decreased exothermic reactions on the delithiated cathode with electrolyte above 200 °C. Also capacity fade upon cycling largely depends on Mn dissolution: $Mn^{3+} \rightarrow Mn^{3+} + Mn^{2+}$ (with Mn^{2+} going into solution). The coating layer can also act as a resistance against Li^+ ion diffusion into the bulk. Therefore, the coating layer materials should have a dual contribution to both tolerance for Li-ion diffusion and hindrance of dissolution of transition metal ion during the lithiation [24].

13.6 Methodology

13.6.1 Synthesis of Spinel $LiMn_2O_4$

$LiMn_2O_4$ powders were prepared via a traditional solid state reaction method with minor modification. A stoichiometric amount of lithium and manganese acetate salts with a cationic ratio of (Li:Mn) 1:2 was dissolved in distilled water and completely mixed by gentle stirring. The resulting solution was evaporated at 80–100 °C for 10 h until a sol precursor was obtained. The precursor was further preheated at 400 °C for 1 h. To remove water further, the precursor was subjected to calcination at 880 °C for 10 h in a muffle furnace.

13.6.2 Synthesis of Nanoparticles in Microemulsion

The use of water-in-oil microemulsion for the synthesis of nanoparticles is one of the most promising methods. The application of this technology allows the preparation of the bimetallic nanoparticles with narrow size distribution. The particle size of the nanoparticles ranges between 1 to 50 nm but is strongly dependent of the surfactant employed. In principle, the process can be easily scaled up because of its straightforward synthetic strategy. This process was proven to be adaptable to the synthesis of a series of bimetallic nanoparticles with narrow size distribution. Scheme 13.1 shows the protocol for the fabrication of mono-dispersed bimetallic nanoparticles.

13.6.3 Synthesis of Bimetallic Pt/Au NPs

The synthesis employs $HAuCl_4$ and H_2PtCl_6 as precursors and oleylamine as the solvent, stabilizer, and reducing reagent. Since oleylamine is amphiphilic, it provides a polarized solvent environment and thus further allows the interaction of the two metal precursors to lower the thermal energy of Pt reduction. In a typical synthesis, $HAuCl_4$ and H_2PtCl_6 in a total amount of 0.02 M were dissolved in 5 mL of oleylamine and 5 mL oleic acid in ethylene glycol (EG) at 40 °C under Ar and then heated to 160 °C at a rate of 2 °C/min. The solution color changed from reddish yellow to pale yellow at 50–70 °C and then changed to dark purple at 80–90 °C. The reaction temperature was maintained at 160 °C for 2 h to give the final products.

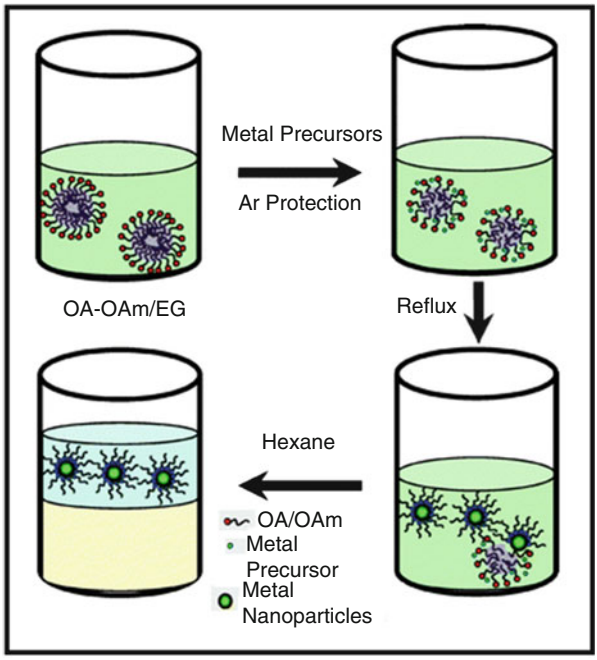

Scheme 13.1 Schematic representation of bimetallic nanoparticle synthesis in the emulsion-assisted multiphase system [25]

13.6.4 Synthesis of Alloy Functionalized $LiMn_2O_4$ and Coin-Cell Assembly

For the surface modification of $LiMn_2O_4$, the transition metal alloy nanoparticles were added to de-ionized water, dissolved completely and heated at 100 °C until the solvent evaporated. The product was annealed at 650 °C for 10 h in air. The electrodes were prepared by mixing 80 wt% of the $LiM_xMn_{2-x}O_4$ material with 15 wt% acetylene black (current collector) and 5 wt% polyvinylidene fluoride binder (PVDF, dissolved in *N*-methyl-2-pyrrolidone) to form a slurry. The slurry was cast on the aluminium foil with a thickness of about 66 μm. Rechargeable 2032 button cells (LR2032, 20d × 3.2 mm) were assembled and sealed in an argon-filled glove box with $LiM_xMn_{2-x}O_4$ as the working electrode, lithium foil as counter electrode, 1 M $LiPF_6$ dissolved in ethylene carbonate (EC, battery grade) and dimethyl carbonate (DMC, battery grade) (1:1 by volume) as the electrolyte.

13.7 Characterization

The shape and size of the microstructure of $LiM_xMn_{2-x}O_4$ nanopowders were determined using a Hitachi model X-650 scanning electron microanalyser (SEM) and a Tecnai G^2 F20 X-twin MAT 200 kV transmission electron microscope

(TEM). The materials were characterized by X-ray diffraction (XRD). The diffraction patterns were taken at room temperature in the range of $5 < 2\theta < 90^{\circ}$ using step scans. Test cells for electrochemical performance evaluation were cycled between 2.4 V and various preset charge cut-off potentials (vs. Li) galvanostatically with various current densities.

13.7.1 Charge/Discharge Profile at High and Low Current Densities

All charge/discharge rates were denoted using C-rate, where 1 C equals to 148 mA g^{-1} of the theoretical capacity of $LiMn_2O_4$. At such a current density of 148 mA g^{-1} the charge or discharge of $LiMn_2O_4$ from initial state requires 1 h. The actual charge/discharge process is not an equilibrium process unless the charge/discharge is carried out at low current density. Excellent cyclability at high C rates is advantageous in traction applications, where the ability of a battery to sustain fast (0.5–1 h) charging would solve the problem of the limited range in electric vehicles, and render superfluous the need for battery interchange. Therefore, all cathode materials were tested at charge and discharge rates of 0.1, 0.5, 1 and 10 C in a voltage range 2.4–4.8 V using a BST8-WA 220V 8 Channels Battery Analyzer.

Rate capability of all cathode materials synthesized was measured at discharge current densities from 0.1 to 10 C. Before each discharge, a full charge process was carried out at the same specific current rate of 29.4 mA g^{-1} (0.1 C). The discharge profiles at different rates were compared and analyzed. The capacitance of each sample was determined using Eq. (13.1), where C: capacitance (F), I: current (A), t: charge and discharge time (s), V: voltage difference between electrodes (V) and m: mass of anode and cathode respectively [26].

$$C = \frac{I \times t}{V}\left(\frac{1}{m_a} + \frac{1}{m_c}\right) \tag{13.1}$$

13.7.2 Effect of Heating

Thermogravimetric analysis (TGA) was employed to determine the preheating and minimum calcination temperature applying a heating rate of 10 °C/min from room temperature to 880 °C. The compositions of the calcined powders were analyzed with an inductively coupled plasma-atomic emission spectrometer (ICP-AES). Figure 13.1 showed that weight loss occurred in three temperature regions: 20–200 °C, 200–500 °C and 500–600 °C. The little weight loss of the first region was attributed to the superficial water loss due to the hygroscopic nature of the

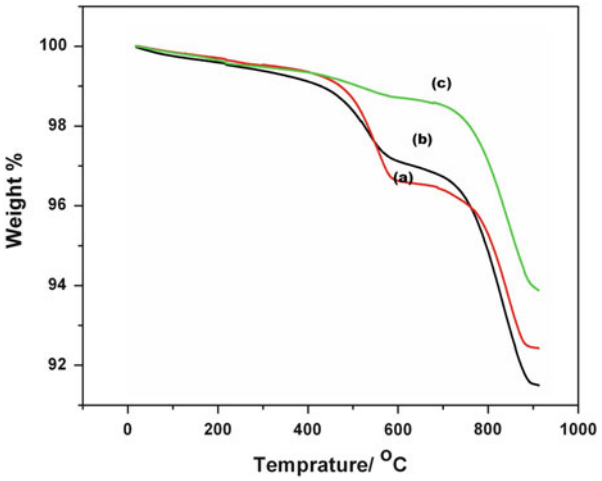

Fig. 13.1 TGA curves of synthesized $LiMn_2O_4$ calcined at 800 (**a**), 860 (**b**) and 880 °C (**c**), recorded at a heating rate of 10 °C min^{-1}

Table 13.1 Chemical composition by ICP (after sintering at 880 °C)

Content	Li	Mn
wt %	0.97	1.98

precursor complex. In the third region, the noticeable weight loss in the TG curve is due to the decomposition of the inorganic and the organic constituents of the precursor followed by crystallization of $LiMn_2O_4$ phase. In the last region the TGA curve became flat, indicating that no phase transformation occurred, and that any further heating only makes the structure of the samples more crystalline [27]. From the TGA trace, there is about 2.5% weight loss when the sample was heated up to 200 °C, which is due to the adsorbed water. Between 200 and 350 °C, about 5.5% weight loss is due to removal of acetates, which was followed by 2 wt% loss due to the removal of the surfactant.

13.7.3 Chemical Composition and Particle Morphology

The elemental ratio of $LiMn_2O_4$ was determined by ICP-AES measurements. The results are shown in Table 13.1.

The high resolution scanning electron micrograph (HRSEM) of the spinel $LiMn_2O_4$ is shown in Fig. 13.2a. The pure $LiMn_2O_4$ appears to have apparent primary particles around 50 nm and have the shape of spinel. The secondary particles of $LiMn_2O_4$ are about 100 nm, which are glomeration congregated tightly by primary particles, indicating that the crystals of the spinel $LiMn_2O_4$ grow very well and have inter-particle boundaries. Tapping mode AFM image is shown in

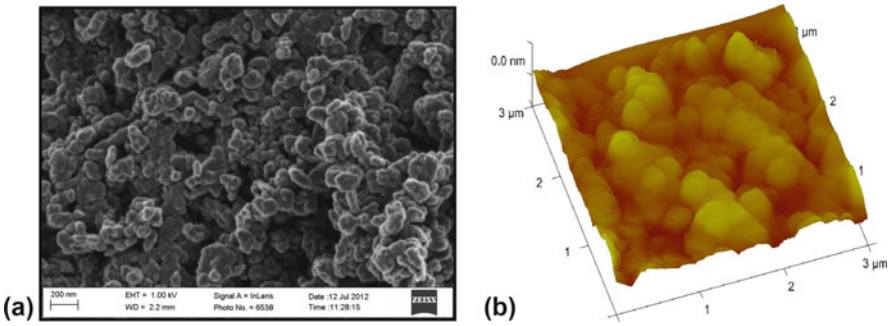

Fig. 13.2 HRSEM (**a**) and AFM (**b**) of $LiMn_2O_4$ sample consisting of round-bar-shaped spherical particles of <100 nm

Fig. 13.2b. Evidently, a rough structure with closely distributed micro-pores of less than 5 nm in diameter was observed with clear globular features and a large degree of surface roughness. HRTEM and EDX results of $LiMn_2O_4$ are displayed in Fig. 13.3a, b and c, respectively. Figure 13.3a shows the bright-field TEM micrographs of the $LiMn_2O_4$ nanoparticles corresponding to that of a single-crystal with a cubic structure with crystallite size distribution less than 100 nm. Figure 13.3b is an enlarged section of the areas shown in Fig. 13.3a. Figure 13.3c is a selected area diffraction (SAD) pattern corresponding to the (1 1 1) facet plane of the cubic lattice of $LiMn_2O_4$. The lattice fringes are clearly visible in the powder with a separation of 4.76 Å, indicating highly ordered crystallite. The fact that the (1 1 1) plane, the intercalated plane of the spinel structure, was well ordered from the inside to the surface reflects good cycling quality.

The TEM of $LiPtAu_{0.02}Mn_{1.98}O_4$ is displayed in Fig. 13.4. Despite having an asymmetrical coating layer, $LiPtAu_{0.02}Mn_{1.98}O_4$ nanoparticles consist of lattice fringes. The selected area diffraction pattern of $LiPtAu_{0.02}Mn_{1.98}O_4$ corresponds to a cubic lattice. Based on the diffraction spots from the super-lattice structure shown in Fig. 13.4c for the $LiPtAu_{0.02}Mn_{1.98}O_4$ SAED images, both $LiMn_2O_4$ and $LiPtAu_{0.02}Mn_{1.98}O_4$ adopt a typical spinel structure with *Fd3m* space group. This is well in agreement with the Rietveld refinement result that all transitional metal ions are randomly distributed at the octahedral sites. The formation of $LiPtAu_{0.02}Mn_{1.98}O_4$ nanoparticles is further validated by AFM. Tapping mode AFM are shown in Fig. 13.5. $LiPtAu_{0.02}Mn_{1.98}O_4$ nanoparticles are distributed evenly and confirm that PtAu alloy adhered well to the $LiMn_2O_4$ surface. The three-dimensional image in Fig. 13.5b shows surface globules with irregular islands and some smoother regions. The reduction in size may be due to the nanoparticles that carry a negative surface charge and strongly interact with the cationic $LiMn_2O_4$.

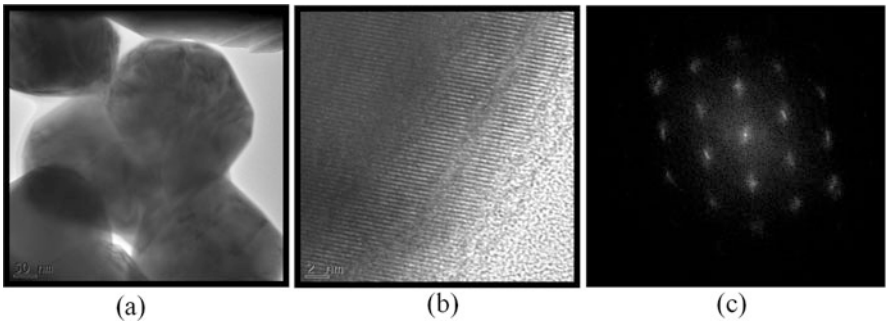

Fig. 13.3 TEM images of $LiMn_2O_4$ powders calcined at 880 °C (**a**) with lattice image (**b**) and electron diffraction patterns (**c**)

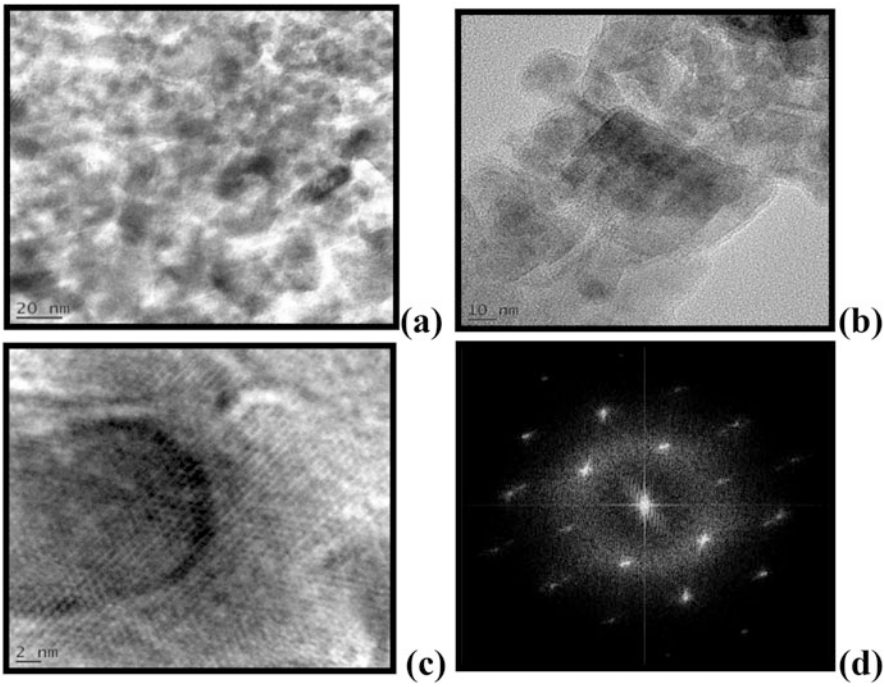

Fig. 13.4 HRTEM images of $LiPtAu_xMn_{2-x}O_4$ cathode (**a**) and (**b**) with lattice image (**c**) and electron diffraction pattern (**d**)

13.7.4 Crystal Structure and Phase Composition Analysis by X-ray Diffraction

The XRD patterns of PtAu coated-$LiMn_2O_4$ are shown in Fig. 13.6. Figure 13.6a shows that the lattice constant increases with temperature from 8.21 Å at 600 °C to

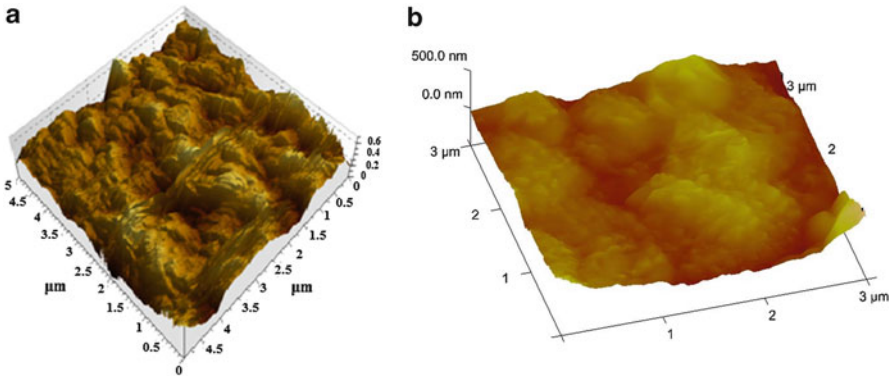

Fig. 13.5 AFM images of the $LiPtAu_{0.02}Mn_{1.98}O_4$ in tapping mode (**a**) and three-dimensional views (**b**)

8.26 Å at 880 °C. This behavior suggests the gradual formation of stoichiometric spinel. The XRD peak positions of $LiMn_2O_4$ at room temperature shifted towards lower diffraction angles. The shift of diffraction peaks towards higher diffraction angles means that the crystal lattice is compressed and if the peaks are shifted towards lower diffraction angle that means the lattice is expanded. This is synonymous with enhanced stability of the spinel. Figure 13.6b shows that the $LiPtAu_{0.02}Mn_{1.98}O_4$ composite crystallizes in a cubic spinel. Compared with that of pure $LiMn_2O_4$, the (1 1 1) peak of bimetallic nanoparticle modified material is intensified and shifted to a lower angle. The *d* spacing of (1 1 1) peak is 0.227 nm and 0.232 nm for $LiMn_2O_4$ and coated sample, respectively, which indicates that the $LiPtAu_{0.02}Mn_{1.98}O_4$ composite was formed. The $LiPtAu_{0.02}Mn_{1.98}O_4$ nanoparticles are highly crystalline and this could influence positively their electrochemical behavior in the lithium ion battery. The inset shows the PtAu alloy which exhibits a broad band at 38.35° (2θ) that matches with the (1 1 1) plane. The broad peak at 44.58° (2θ) is attributed to the (2 0 0) plane. Two additional bands are observed at 65° and 77.73° (2θ) corresponding to PtO_2. The particle size calculated on the base of (1 1 1) peak is 7 nm which is in close proximity to the value obtained from TEM measurements. The peak of the PtAu nanoparticles is between those of monometallic gold and platinum nanoparticles. Hence, the PtAu nanoparticles used to coat are not the mixtures of individual nanoparticles but bimetallic nanostructures [28]. The lattice constant of $LiPtAu_{0.02}Mn_{1.98}O_4$ increased slightly than that of $LiMn_2O_4$ from 8.2600 Å (7) to 8.2609 Å (5). This increase may be due to the lattice disparity between Pt and Au atoms [29] and the larger ionic radii compared to Mn^{3+}.

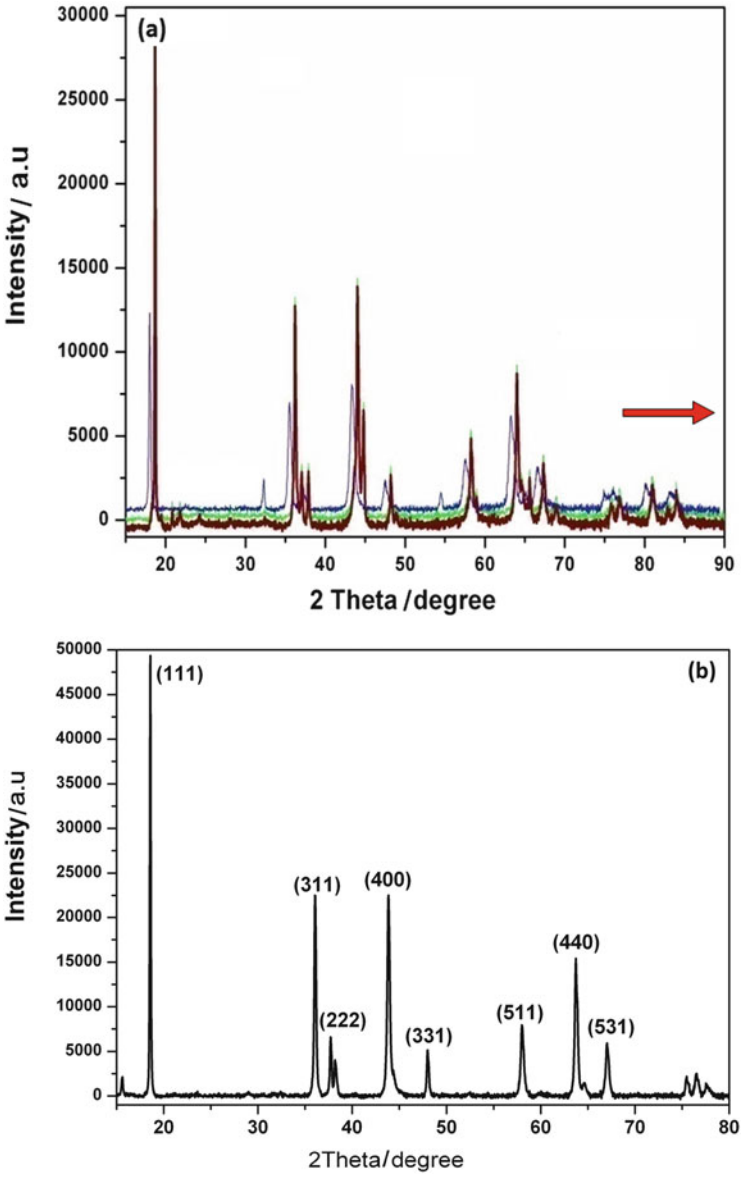

Fig. 13.6 XRD pattern of $LiMn_2O_4$ with peaks shifting towards higher diffraction angles after consecutive calcinations (**a**) and $LiPtAu_{0.02}Mn_{1.98}O_4$ cathode powder (**b**)

13.7.5 *Fourier-Transform Infrared and Raman Vibrational Spectroscopic Sample Analysis*

The FTIR spectra of pure $LiMn_2O_4$ and $LiPtAu_{0.02}Mn_{1.98}O_4$ nanoparticles are shown in Fig. 13.7a, b respectively. For $LiMn_2O_4$, the main distinct absorption peaks caused by the Mn–O vibration of the MnO_6 as shown in Fig. 13.7a, are in good agreement with previous reports. The high local symmetry of the parent cubic spinel $LiMn_2O_4$ is reflected in the observation of only two absorption bands centered at 602 and 515 cm^{-1} [30]. In Fig. 13.7b, major changes are observed in the region between 1600 and 3600 cm^{-1}; the peaks in the spectrum appear much smoother as those for $LiMn_2O_4$. This can be ascribed to the change in bending vibrations with formation of the $LiPtAu_{0.02}Mn_{1.98}O_4$ complex, which masks the absorption peaks of $LiMn_2O_4$. Other spectral changes were observed at 447, 596 and 817 cm^{-1}. It is evident that the peak at 596 cm^{-1} of $LiPtAu_{0.02}Mn_{1.98}O_4$ is more intensified than for $LiMn_2O_4$ at 602 cm^{-1}. However, the peak at 596 cm^{-1} exhibits similar behavior on the Li–Mn–O stretching vibration band but with a shoulder at 447 cm^{-1} due to the PtAu [30].

Figure 13.8 shows the Raman spectrum (RS) of $LiPtAu_{0.02}Mn_{1.98}O_4$. Comparing the RS features with those of $LiMn_2O_4$, the Raman band located at approximately 613 cm^{-1} can be viewed as the symmetric Mn–O stretching vibration of MnO_6

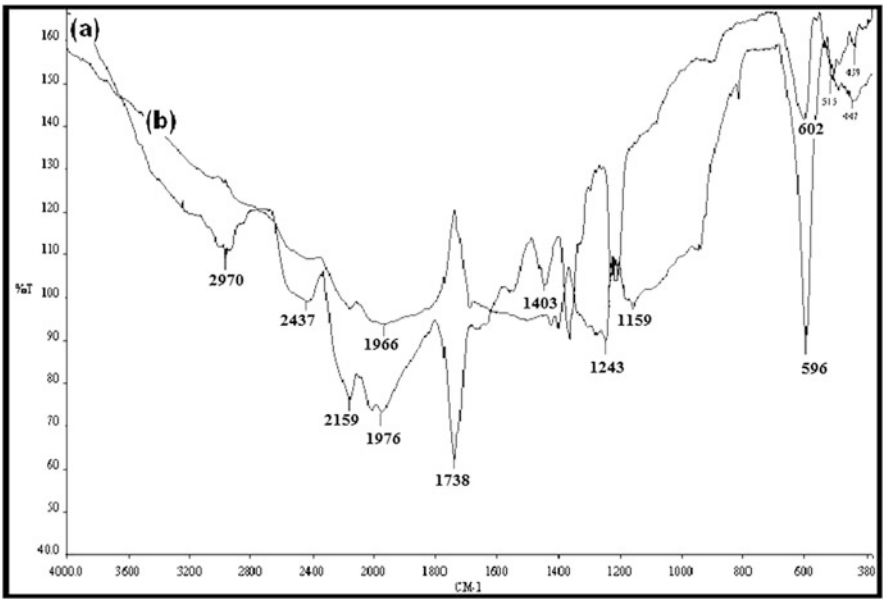

Fig. 13.7 FTIR spectra of $LiMn_2O_4$ (**a**) and $LiPtAu_{0.02}Mn_{1.98}O_4$ (**b**)

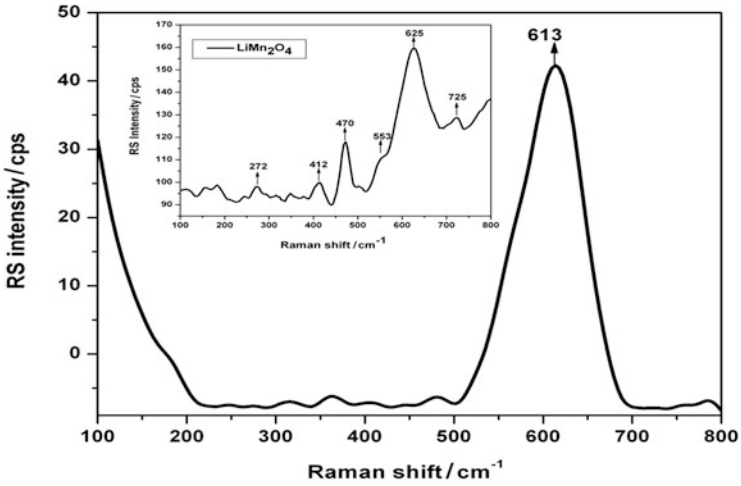

Fig. 13.8 Raman spectra of $LiPtAu_{0.02}Mn_{1.98}O_4$ and $LiMn_2O_4$ (*inset*)

units. RS peaks at lower frequencies are attributed to the deformation modes of the metal–oxygen chain of Mn–O–Mn in the MnO_6 lattice. However, the other vibrational signals in the low-frequency domain of the RS are much weaker than those obtained from $LiMn_2O_4$ due to the higher electronic conductivity of the PtAu coated-$LiMn_2O_4$ material for which the laser beams penetration depth is very low. In metals there are many energy levels near the Fermi level, i.e., many electrons available to move. Hence the high electronic conductivity is due to Pt–Au instead of the reduced carbon component. Carbon particles in the cathode provide electron pathways but can also obstruct pores that are the pathways for ions. Hence it is lessened as it can limit the overall cell functioning [31].

13.8 Electrochemical Performances

Figure 13.9 shows the cyclic voltammograms of $LiPtAu_xMn_{2-x}O_4$ at 0.01 (a) and 0.1 mV s^{-1} (b). The peaks with increasing voltage are ascribed to oxidation of the constituents in the cathode materials. The two-step lithium intercalation/deintercalation process in $LiPtAu_xMn_{2-x}O_4$, which is induced by lithium-ion ordering on the 8*a* tetrahedral sites, became less pronounced at 0.01 mV s^{-1}. The decrease in peak currents of the reversible reaction at higher voltage can be associated with the redox of $Mn^{3+/4+}$, which implies that the system is less prone to ion exchange with the $PtAu^{3+/4+}$ ions on the 16*d* octahedral sites in the spinel framework as it requires more energy. Figure 13.9c, d show the cyclic voltammograms for $LiMn_2O_4$ and $LiPtAu_{0.02}Mn_{1.98}O_4$ cycled at 0.1 mV s^{-1}. The peak separation at 4 V region (0.2 V) suggests an easier lithium intercalation and deintercalation process. Due to the expansion in the lattice parameter, the PtAu

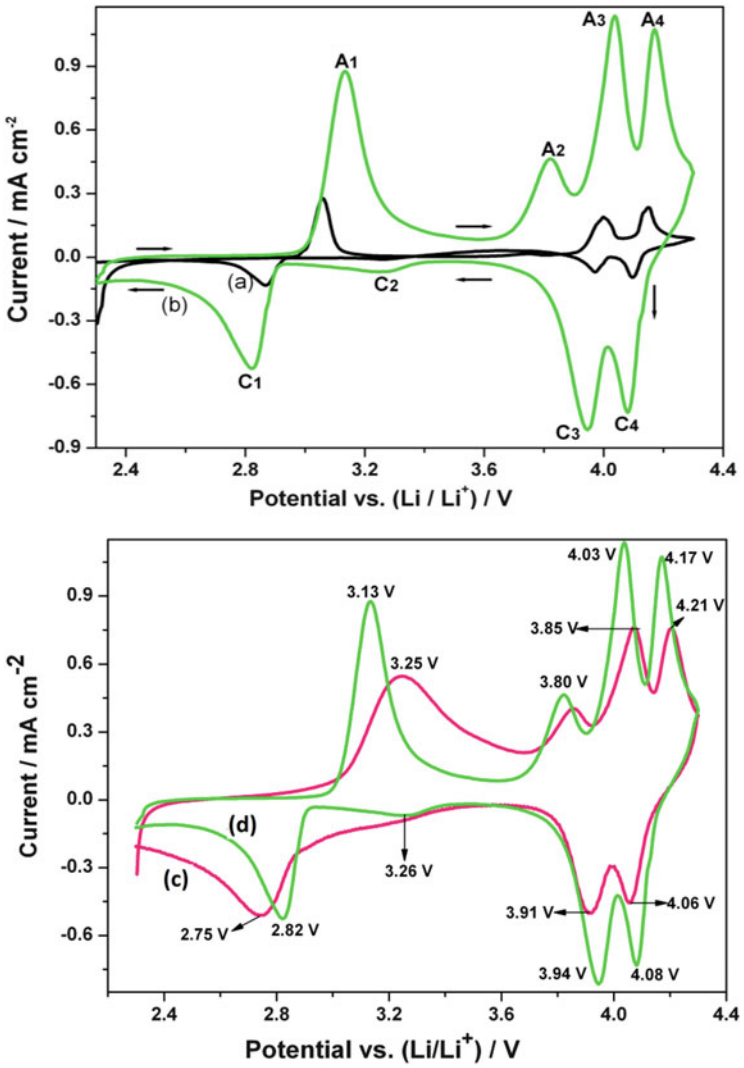

Fig. 13.9 Cyclic voltammograms of $LiPtAu_{0.02}Mn_{1.98}O_4$ at 0.01 (**a**) and 0.1 mV s^{-1} (**b**) and $LiMn_2O_4$ (**c**) and $LiPtAu_{0.02}Mn_{1.98}O_4$ (**d**) at 0.1 mV s^{-1} in EC: DMC, 1 M $LiPF_6$

coated spinel structure is able to provide larger diffusion channels and hence lower activation energy to facilitate faster transportation of Li^+ ions, i.e., better high rate performances including structural stability. The weak peak around 3 V indicates a small ratio of Mn^{3+} which fades out at extremely low scan rates [32]. At this rate, it is in the electrochemically inactive oxidation state of 4+ [33]. Concomitantly the $LiMn_2O_4$ has improved electrochemical activity and improved electrolyte accessibility.

13.8.1 Charge/Discharge Performance of $LiPtAu_{0.02}Mn_{1.98}O_4$ Cathode

Figure 13.10a shows the $LiPtAu_{0.02}Mn_{1.98}O_4$ cathode having a clear two-staged lithium intercalation behavior at a voltage of 3 V and 4.2 V, which is indicative of a single-phase spinel $LiMn_2O_4$ structure. The initial charge and discharge capacities were 139 mAh g^{-1} and 143 mAh g^{-1}, respectively. The initial charge/discharge capacity improved when compared to $LiMn_2O_4$ powder (119 mAh g^{-1}) because of the improved crystallinity and stability of the spinel structure. The discharge curve trend in the entire range from 2.4 to 4.5 V was comparable to a slightly oxygen-deficient spinel $LiMn_2O_4$ and about 70 mAh g^{-1} due to the lower ratio of Mn^{3+}/Mn^{4+} ions [34]. To evaluate the cycling behavior of $LiPtAu_{0.02}Mn_{1.98}O_4$, conditions up to 50 cycles were performed at 0.1 °C. The discharge capacity of $LiPtAu_{0.02}Mn_{1.98}O_4$ shows very good retention (Fig. 13.10b). After the first 10 cycles at 0.1 °C, the cell showed slight capacity loss with coulombic efficiency of 98%. The capacity retention after 50 cycles decreased to 78% with a coulombic efficiency of 98%.

13.8.2 Rate Capability

Figure 13.10b shows that the discharge capacity vs. number of cycles at different current rates of 14.8, 74, 148, 740 and 1480 mA g^{-1} are 140, 128.2, 116, 100 and 82 mAh g^{-1}, respectively. At the transition from 0.1 to 1 °C, the cell showed moderate capacity loss with a coulombic efficiency of about 92%. The $LiPtAu_{0.02}Mn_{1.98}O_4$ cell showed enhanced capacity retention at high current rate (10 C), with an average coulombic efficiency of 99%. The structure of $LiPtAu_{0.02}Mn_{1.98}O_4$ exhibits a more tolerable response to recurring charge-discharge processes at high C rates which is attributed to the alloy-induced reduction in the valency of Mn, as well as the favorable particle surface morphology. Furthermore, the decrease of discharge capacity for PtAu modified $LiMn_2O_4$ was much smaller than that of the pure $LiMn_2O_4$. The higher lithium storage capacity may be due to PtAu–Li intermetallic compound formation and catalytic effects of PtAu on the reaction of Li^+ with $LiMn_2O_4$.

13.8.3 Discharge Performance of $LiPtAu_{0.02}Mn_{1.98}O_4$

The charge/discharge rate affects the rated battery capacity. If the battery is being discharged very quickly (i.e., the discharge current is high), then the amount of energy that can be extracted from the battery is reduced and the battery capacity is lower. This is due to the necessary components for the reaction to occur do not necessarily have enough time to move to their necessary positions. Only a fraction

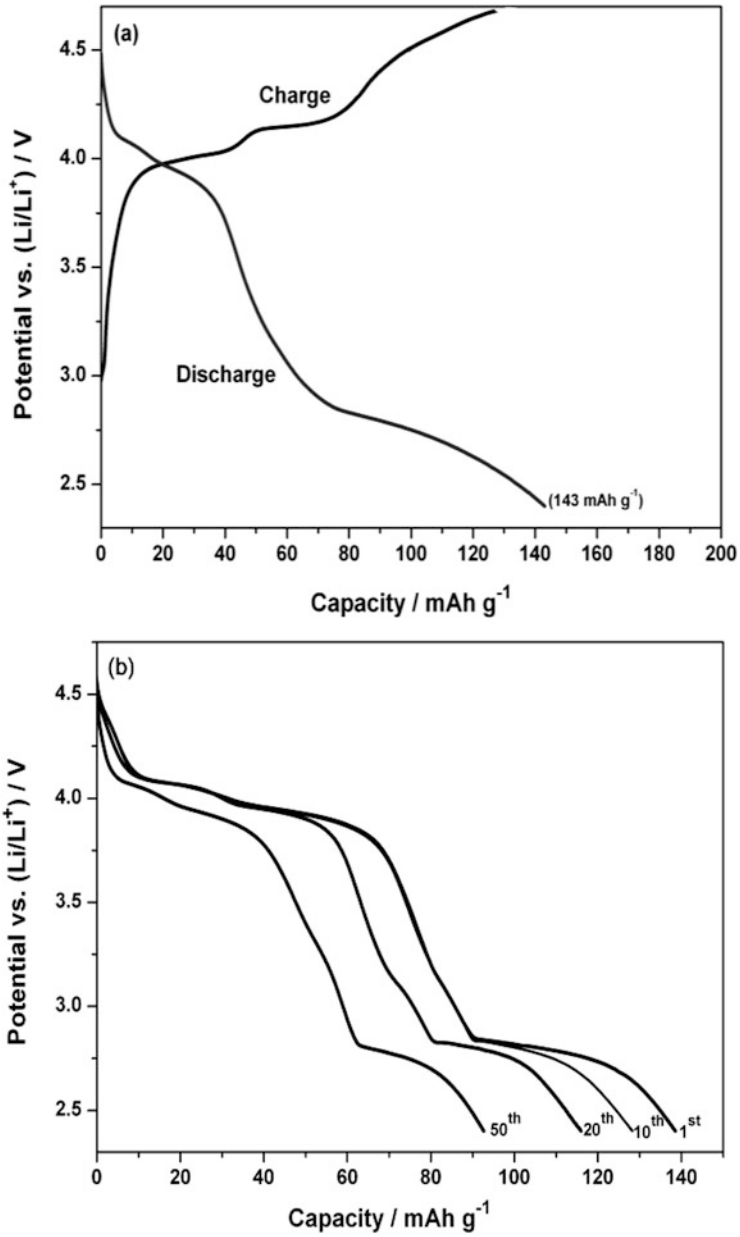

Fig. 13.10 $LiPtAu_{0.02}Mn_{1.98}O_4$ charge/discharge curve at 0.1 mA cm^{-2} cycled at 2.4–4.5 V (**a**) and discharge behaviour of the cell (**b**)

of the total reactants is converted and therefore the energy available is reduced. Alternately, when the battery is discharged at a very slow rate using a low current, more energy can be extracted from the battery and the battery capacity is higher.

The $LiPtAu_{0.02}Mn_{1.98}O_4$ material can release 90 mAh g^{-1} at the first cycles and maintain at 88.7 mAh g^{-1} at the 50th cycle (99% capacity retention). Evidently, even a small amount of the $alloy_x$ (0.02) species improved the kinetic properties of the parent compound due to the modification of both its microscopic and spectroscopic properties. These results indicate that the spinel phase is stabilized by the applied surface modification technique, and the large size of the coating species does not block the lithium pathway, instead it provides easier lithium ions diffusion [35]. The losses that reduce coulombic efficiency are primarily due to the loss in charge due to secondary reaction.

13.9 Conclusion

Novel transition metal alloy ($M_x = PtAu$) coated $LiMn_2O_4$ with improved high rate performances have been successfully designed and synthesized. The smaller potential differences of alloy functionalized-$LiM_xMn_{2-x}O_4$ cathodes suggest smaller polarization due to faster insertion/extraction of Li^+ ions in the spinel structure. The improvement in diffusivity of Li^+ ions may be attributed to three reasons. Firstly, the enhanced electronic conductivity in M_x coated-$LiMn_2O_4$ spinel structure is beneficial for more rapid Li^+ transportation. Secondly, the vacancies at the octahedral sites created by M_x coating provide additional diffusion paths for lithium ions. Thirdly, the increase in lattice parameter after M_x coating enabled faster lithium diffusion. Faster lithium mobility initiated better high rate performances including low polarization and better structural stability. The diameter of the nanoparticles is <100 nm, so the required Li^+ diffusion distance is effectively shortened. It can be concluded that the $LiPtAu_{0.02}Mn_{1.98}O_4$ has a lower energy barrier for Li^+ ions diffusion hence being more kinetically favorable. Since the metal alloy nanoparticles slightly penetrate the surface of the spinel $LiMn_2O_4$, the modified $LiM_xMn_2O_4$ suppressed the Jahn-Teller distortion. These improvements are due to enhanced electronic conductivity and lithium diffusivity resulting from transition metal alloy coating. The results suggest that the $PtAu_{0.02}$ coating particles act as a protective layer that prevents the oxygen from outgoing which led to major improvements and could be a new viable approach for producing advanced lithium ion battery cathodes with improved electrochemical properties. Further efforts are directed toward developing a coating to make the development of the 5-V batteries a reality.

Acknowledgment This work was financially supported by South Africa's National Research Foundation (NRF).

References

1. Stevenson KJ (2012) The origin, development, and future of the lithium-ion battery. J Solid State Electrochem 16:2017–2018
2. Tavassol H, Jones EMC, Sottos NR, Gewirth AA (2016) Electrochemical stiffness in lithium-ion batteries. Nat Mater 15:1182–1187
3. Nguyen VH, Gu H-B (2014) $LiFePO_4$ batteries with enhanced lithium-ion-diffusion ability due to graphene addition. J Appl Electrochem 44:1153–1163
4. Julien CM, Mauger A, Zaghib K, Groult H (2014) Comparative issues of cathode materials for Li-ion batteries. Inorganics 2:132–154
5. Nitta N, Wu F, Tae Lee J, Yushin G (2015) Li-ion battery materials: present and future. Mater Today 18:252–264
6. Arico AS, Scrosati B, Tarascon JM, Van Schalkwijk W (2005) Nanostructured materials for advanced energy conversion and storage devices. Nat Mater 4:366–377
7. Das B (2016) Smarter lithium-ion batteries, Scientists create "sandwich-like" nanoporous material to better lithium-ion batteries. doi:10.1038/nmiddleeast:136
8. Yu W, Porosoff MD, Chen JG (2012) Review of Pt-based bimetallic catalysis: from model surfaces to supported catalysts. Chem Rev 112:5780–5817
9. Stamenkovic VR, Fowler B, Mun BS, Wang GF, Ross PN, Lucas CA, Markovic NM (2007) Improved oxygen reduction activity on $Pt_3Ni(111)$ via increased surface site availability. Science 315:493–497
10. Jellinek J (2008) Nanoalloys: from theory to application. Faraday Discuss 138:1
11. Ceylan A, Jastrzembski K, Shah SI (2006) Enhanced solubility Ag-Cu nanoparticles and their thermal transport properties. Metal Mater Trans A 37:2033–2038
12. Redjala T, Remita H, Apostolescu G, Mostafavi M, Thomazeau C, Usio D (2006) Bimetallic Au-Pd and Ag-Pd clusters synthesised by γ or electron beam radiolysis and study of the reactivity/structure relationships in the selective hydrogenation of buta-1,3-diene. Gas Oil Sci Technol Rev 61:789–797
13. Burda C, Narayanan R, El-Sayed MA (2005) Chemistry and properties of nanocrystals of different shapes. Chem Rev 105:1025–1102
14. Zhao D, Xu B-Q (2006) Enhancement of Pt utilization in electrocatalysts by using gold nanoparticles. Angew Chem 45:4955–4959
15. Li Y, Yin F, Chen Y, Palmer RE, Johnston RL (2008) Structures and optical properties of 4–5 nm bimetallic AgAu nanoparticles. Faraday Discuss 138:363–373
16. Qian D, Xu B, Cho H-M, Hatsukade T, Carroll KJ, Meng YS (2012) Lithium lanthanum titanium oxides: a fast ionic conductive coating for lithium-ion battery cathodes. Chem Mater 24:2744–2751
17. Ozawa K (1994) Lithium-ion rechargeable batteries with $LiCoO_2$ and carbon electrodes: the $LiCoO_2$/C system. Solid State Ionics 69:212–221
18. Han DW, Ryu WH, Kim WK, Eom JY, Kwon HS (2013) Effects of Li and Cl codoping on the electrochemical performance and structural stability of $LiMn_2O_4$ cathode materials for hybrid electric vehicle applications. J Phys Chem C 117:4913–4919
19. Xu H, Zhang H, Mu Y, Feng Y, Wang Y (2015) General and green strategy toward high performance positive electrode materials for rechargeable Li ion batteries with crop stalks as the host carbon matrices. ACS Sustainable Chem Eng 3:1650–1657
20. Whittingham MS (2004) Lithium batteries and cathode materials. Chem Rev 104:4271–4301
21. Hao X, Gourdon O, Liddle BJ, Bartlett BM (2012) Improved electrode kinetics in lithium manganospinel nanoparticles synthesized by hydrothermal methods: identifying and eliminating oxygen vacancies. J Mater Chem 22:1578–1591
22. Hausbrand R, Cherkashinin G, Ehrenberg H, Gröting M, Albe K, Hess C, Jaegermann W (2015) Fundamental degradation mechanisms of layered oxide Li-ion battery cathode materials: Methodology, insights and novel approaches. Mat Sci Eng B 192:3–25

23. Ma S, Hou X, Lin Z, Huang Y, Gao Y, Hu S, Shen J (2016) One-pot facile co-precipitation synthesis of the layered $Li_{1+x}(Mn_{0.6}Ni_{0.2}Co_{0.2})_{1-x}O_2$ as cathode materials with outstanding performance for lithium-ion batteries. J Solid State Electrochem 20:95–103
24. Dhindsa K (2015) Enhancement in electrochemical performance of advanced battery electrodes using carbon-nanomaterial composites. Wayne State University Dissertations, Paper 1126
25. Xu Z, Carlton CE, Allard LF, Shao-Horn Y, Hamad-Schifferli K (2010) Direct colloidal route for Pt-covered AuPt bimetallic nanoparticles. J Phys Chem Lett 17:2514–2518
26. Jamnik J, Maier J (2001) Generalised equivalent circuits for mass and charge transport: chemical capacitance and its implications. Phys Chem Chem Phys 3:1668–1678
27. Luo J, Petkov V, Kariuki NN, Wang L, Njoki P, Mott D, Lin Y, Zhong C.J (2005) Article phase properties of carbon-supported gold−platinum nanoparticles with different bimetallic compositions. Chem Mater 17:3086–3091
28. Habas SE, Radmilovic V, Somorjai GA, Yang P (2007) Shaping binary metal nanocrystals through epitaxial seeded growth. Nat Mater 6:692–697
29. Zacharias NA, Nevers DR, Skelton C, Knackstedt K, Stephenson D. E, Wheeler DR (2013) Direct measurements of effective ionic transport in porous Li-ion electrodes. J Electrochem Soc 160:A306
30. Julien C, Pereira-Ramos JP, Momchilov A (2012) New trends in intercalation compounds for energy storage. Technology and engineering. Springer Science & Business Media, Heidelberg, p 654. ISBN 9401003890
31. Thirunakaran R, Gopukumar S, Rajalakshmi R (2009) Cerium and zinc: Dual-doped $LiMn_2O_4$ spinels as cathode material for use in lithium rechargeable batteries. J Power Sources 187:565–574
32. Liu W, Shi Q, Qu Q, Gao T, Zhu G, Shao J, Zheng H (2017) Improved Li-ion diffusion and stability of a $LiNi_{0.5}Mn_{1.5}O_4$ cathode through *in situ* co-doping with dual-metal cations and incorporation of a superionic conductor. J Mater Chem A 5:145–154
33. Zhang X, Zheng H, Battaglia V, Axelbaum RL (2011) Electrochemical performance of spinel $LiMn_2O_4$ cathode materials made by flame-assisted spray technology. J Power Sources 196:3640–3645
34. Kong J-Z, Ren C, Tai G, Zhou F (2014) Ultrathin ZnO coating for improved electrochemical performance of $LiNi_{0.5}Co_{0.2}Mn_{0.3}O_2$ cathode material. J Power Sources 266:433–439
35. Loftager S, García-Lastra JM, Vegge T (2017) A density functional theory study of the carbon-coating effects on lithium iron borate battery electrodes. Phys Chem Chem Phys 19:2087–2094

Chapter 14
Synthesis, Spectral Analysis and Biological Evaluation of 5-Substituted 1,3,4-Oxadiazole-2-yl-4-(Piperidin-1-ylsulfonyl)Benzyl Sulfide

Hira Khalid, Aziz-ur-Rehman, M. Athar Abbasi, Rashad Hussain, Abdul Malik, Muhammad Ashraf, and M. Qaiser Fatmi

Abstract 1,3,4-Oxadiazole bearing compounds are one of the most attractive class for researchers due to their biological activities. In the undertaken research, a new series of 5-substituted 1,3,4-oxadiazole-2-yl-4-(piperidin-1-ylsulfonyl) benzylsulfides (**6a–k**) were synthesized. The synthesis was carried out by converting different organic acids sequentially into corresponding esters, hydrazides and 5-substituted-1,3,4-oxadiazole-2-thiols **(4a–k)**. Finally, the target compounds, **6a–k** were prepared by stirring 5-substituted-1,3,4-oxadiazole-2-thiols with 1-(4-(bromomethyl)phenyl sulfonyl)piperidine **(5)** in the presence of *N*,*N*-dimethylformamide (DMF) and sodium hydride. All the structures were elucidated by modern spectroscopic techniques. The synthesized compounds were screened against butyrylcholinesterase (BChE) enzyme and also subjected for molecular docking studies to find ligand-BChE binding affinity and ligand orientation in active sites of human BChE protein. Amino acid residues such as Gly116, His438, Tyr332 and Ser198 are found to be important common residues for binding of highlighted compounds and are likely to be involved in the ligands' stabilization in the binding site.

H. Khalid (✉)
Department of Chemistry, Forman Christian College University, Ferozpur Road, Lahore, Pakistan
e-mail: dr.hknajmee@gmail.com

Aziz-ur-Rehman • M. Athar Abbasi
Department of Chemistry, Government College University, Lahore, Pakistan

R. Hussain • M. Qaiser Fatmi
Department of Biosciences, COMSATS Institute of Information Technology, Chak Shahzad, Islamabad, Pakistan

A. Malik
HEJ Research Institute of Chemistry, International Center for Chemical and Biological Sciences, University of Karachi, Karachi, Pakistan

M. Ashraf
Department of Biochemistry and Biotechnology, The Islamia University of Bahawalpur, Bahawalpur, Pakistan

P. Ramasami et al. (eds.), *Emerging Trends in Chemical Sciences*,
DOI 10.1007/978-3-319-60408-4_14

Keywords 1,3,4-Oxadiazole • Benzylsulfide • 1-(4-(Bromomethyl) phenylsulfonyl)piperidine • BChE • Molecular docking

14.1 Introduction

Organic chemists are interested to design and synthesize new and therapeutically active compounds, useful to alleviate different disorders and diseases. Scientists have to face a serious confront of increased resistance against the traditional antimicrobial drugs and so are in search to develop new biologically active compounds with excellent therapeutic activity. Oxadiazole is a class of heterocyclic organic compounds that is known because of its magnificent therapeutic potential. Thousands of oxadiazole and their derivatives have been synthesized and evaluated for different antimicrobial and enzyme inhibition activities. Oxadiazoles possess interesting anti-inflammatory [1, 2], fungicidal [3], insecticidal [4], herbicidal [5], antibacterial [6], antitumor [7], antitubercular [8], antiviral, anticonvulsant and analgesic activities [9]. Piperidine nucleus is famous for its therapeutic potential. A large number of compounds have been synthesized and studied to evaluate their pharmaceutical potentials [10]. Compounds containing piperidine moiety are useful to normalize the insulin level, level of plasma glucose and for the treatment of cocaine abuse, etc. Such compounds are also used as anesthetics [11].

The present work involves the poly-functional synthesis of compounds having both 1,3,4-oxadiazole sulfonamide and piperidine moiety in continuation of our previously reported works [12–15]. It was speculated that 2,5-disubstituted 1,3,4-oxadiazole ring along with the potential piperidine ring moiety will boost the activity of the molecule. The synthesis was carried out through the intermolecular cyclization of different phenyl/aryl/aralkyl/ heterocyclic organic acid hydrazides to the corresponding 5-substituted-1,3,4-oxadiazol-2-thiols and finally to 5-substituted-1,3,4-oxadiazole-2-yl 4-(piperidin-1-ylsulfonyl)benzyl sulfide products. Furthermore, the synthesized compounds were screened against butyrylcholinesterase (BChE) enzyme and it was observed that the different electrophilic substitutions influenced significantly the enzyme inhibition activity from moderate to excellent level. Molecular docking studies were carried out to rationalize these ligand-BChE interactions at molecular level by identifying the binding patterns and predicting the affinities of inhibitors in the binding pockets of BChE. Binding models of compounds **6a, 6d** and **6i** were found to be highly potent from the presented series of synthesized compounds.

14.2 Experimental Section

14.2.1 Measurements

All the chemicals (Merck & Alfa Aesar) and analytical grade solvents were purchased through local suppliers. Melting points were taken on a Griffin and George melting point apparatus by open capillary tube method. TLC plate F_{256} 20 × 20 cm coated with silica gel, developed by different ratios of *n*-hexane and EtOAc as solvent system, was used to detect the purity of the synthesized compounds. With the help of KBr pellet, IR spectra were recorded by using a Jasco-320-A spectrophotometer. ^{1}H-NMR spectra were recorded on Bruker spectrometers at two different frequencies *i.e*. 300 and 400 MHz, taken in deuterated chloroform and methanol, demonstrating chemical shifts value in ppm taking TMS as reference standard. ^{13}C-NMR spectra were recorded at 75 MHz. EIMS spectra were taken by a JMS-HX-110 spectrometer.

14.2.2 Synthesis

14.2.2.1 General Procedure for the Synthesis of Different Aralkyl/Aryl Substituted Ethyl Esters (2a–2k)

The aralkyl/aryl carboxylic acids (5g, **1a–1k**) were taken in 250 mL round bottom flasks and dissolved in 20 mL ethanol along with 2.5 mL *conc*. H_2SO_4. The mixture was refluxed for 3–4 h. Thin layer chromatography was used to monitor the reaction by using *n*-hexane and EtOAc as solvent system. On completion, the reaction contents were transferred to a separating funnel containing distilled water (30 mL). Na_2CO_3 solution was added to neutralize the contents till no effervescence. Diethyl ether was added to the separating funnel followed by vigorous shaking and the contents were left to set up two layers. All the unreacted organic acids and sulfuric acid (in the form of salts) and methanol were shifted to aqueous layer which was discarded. The ethyl esters **(2a–2k)** were afforded from the organic layer after distilling off the diethyl ether.

14.2.2.2 General Procedure for the Synthesis of Different Aralkyl/Aryl Substituted Hydrazides (3a–3k)

Aralkyl/aryl substituted ethyl esters (0.025 mol, **2a–2k**) were taken in 250 mL round bottom flasks and dissolved in methanol (50 mL). Hydrazine hydrate (80%, 0.05–0.07 mol) was introduced into the reaction flask along with stirring for 2–3 h at room temperature. Some of the hydrazides were formed at room temperature while some esters got transformed on refluxing with continuous stirring.

Completion of reaction was confirmed by TLC using *n*-hexane and EtOAc as solvent system. On completion, excess of methanol was distilled off and cold distilled water was added to obtain the precipitates. Precipitates were filtered, washed with water and dried. The purity of aralkyl/aryl substituted hydrazides **(3a–3k)** was cross-checked again by TLC.

14.2.2.3 General Procedure for the Synthesis of 5-Aralkyl/Aryl-1,3,4-Oxadiazole-2-Thiols (4a–4k)

Aralkyl/aryl substituted hydrazides (0.01 mol, **3a–3k**) were taken in 250 mL round bottom flasks, dissolved in ethanol followed by the addition of KOH (0.03 mol) to provide basic media and CS_2 (0.01 mol). The reaction mixture was set to reflux for 4–6 h and the reaction progress was monitored by TLC using different ratios of *n*-hexane and EtOAc as solvent system. On completion, the reaction mixture was acidified (pH = 2) to remove unreacted hydrazides in the form of salts and also to convert thiol group of oxadiazole into acidic form. Distilled water was added and the reaction mixture was vigorously shaken to get rid of unreacted contents and to afford the precipitates of products **(4a–4k)**. The precipitates were filtered, washed with water and dried. To get the pure product, the precipitates were re-crystallized from methanol.

14.2.2.4 Procedure for the Synthesis of 1-(4-(Bromomethyl) Phenylsulfonyl)Piperidine (5)

Piperidine (0.005 mol) was taken in a round bottom flask containing basic aqueous solution with pH maintained at 9.0 and set to stir. Equimolar amount of 4-(bromomethyl)benzenesulfonyl chloride was introduced into the reaction flask with continuous stirring under dynamic pH control. Reaction completion was monitored *via* TLC utilizing different ratios of *n*-hexane and EtOAc. On completion, reaction mixture was acidified (pH = 2) to remove the remaining piperidine in the form of salt and shaken well to obtain the product **(5)**. The precipitate was filtered, washed with water and dried. ^{1}H-NMR (CD_3OD, 400 MHz): δ (ppm) 7.71 (d, J = 8.4 Hz, 2H, H-3″ & H-5″), 7.63 (d, J = 8.4 Hz, 2H, H-2″ & H-6″), 4.62 (s, 2H, H-7″), 2.96 (t, J = 5.6 Hz, 2H, H_e-2‴ & H_e-6‴), 2.01 (br.t, J = 9.6 Hz, 2H, H_a-2‴ & H_a-6‴), 1.64-1.59 (m, 4H, H-3‴ & H-5‴), 1.56-1.52 (m, 2H, H-4‴).

14.2.2.5 General Procedure for the Synthesis of 5-Aralkyl/Aryl-1,3,4-Oxadiazole-2-yl 4-(Piperidin-1-ylsulfonyl)Benzyl Sulfide (6a–6k)

5-Aralkyl/aryl-1,3,4-oxadiazole-2-thiols (0.1 g, **4a–4k**) were taken in 100 mL round bottom flasks and dissolved in DMF used as reaction media. On complete

dissolution, 2 mg NaH was added and stirred for half an hour. Then equimolar amount of synthesized electrophile i.e. 1-(4-(bromomethyl)phenylsulfonyl)piperidine (**5**) was introduced into the reaction flask and stirring was continued for a further 1–2 h. TLC was used to follow the reaction completion using *n*-hexane and EtOAc solvent system. On completion, the contents were basified (pH = 9) to remove the unconverted oxadiazole by changing it to corresponding salt and cold distilled water was added to yield the precipitates. The precipitates were filtered, washed with water and dried. In cases where products did not transform into precipitates, the latter were obtained by solvent extraction.

14.2.2.6 5-(1-(Phenylsulfonyl)Piperidin-4-yl)-1,3,4-Oxadiazole-2-yl-4-(Piperidin-1-ylsulfonyl)Benzyl Sulfide (6a)

White powder; Yield: 87%; M.P. 138–139 °C; Mol. For.: $C_{25}H_{30}N_4O_5S_3$; Mol. Wt.: 562.7; IR (KBr, cm^{-1}): ν_{max}: 3021 (C–H stretching of aromatic ring), 1631 (C=N stretching of oxadiazole ring), 1519 (C=C aromatic stretching), 1339 (–SO_2 stretching), 1257 (C=S bond stretching), 1247 & 1065 (C–O–C bond stretching). ^{1}H-NMR ($CDCl_3$, 300 MHz): δ (ppm) 7.75 (d, J = 8.4 Hz, 2H, H-3″ & H-5″), 7.73 (d, J = 8.4 Hz, 2H, H-2″ & H-6″), 7.67 (d, J = 8.4 Hz, 2H, H-2‴ & H-6‴), 7.54-7.56 (m, 2H, H-3‴′ & H-5‴′), 7.62-7.58 (m, 1H, H-4‴′), 4.44 (s, 2H, H-7″), 3.69-3.72 (m, 2H, H_e-2′ & H_e-6′), 2.97-2.95 (m, 2H, H_e-2‴ & H_e-6‴), 2.85-2.80 (m, 1H, H-4'), 2.60-2.53 (m, 2H, H_a-2′ & H_a-6′), 2.12-2.07 (m, 2H, H_a-2‴ & H_a-6‴), 1.93-1.87 (m, 4H, H-3′ & H-5′), 1.62-1.59 (m, 4H, H-3‴ & H-5‴), 1.43-1.39 (m, 2H, H-4‴). ^{13}C-NMR ($CDCl_3$, 75 MHz): δ (ppm) 169.1 (C-5), 166.8 (C-2), 140.7 (C-1″), 137.9 (C-4″), 137.3 (C-1‴′), 132.9 (C-4‴′), 129.6 (C-3‴′ & C-5‴′), 129.1 (C-2″ & C-6″), 128.1 (C-3″ & C-5″), 127.6 (C-2‴′ & C-6‴′), 46.9 (C-2‴ & C-6‴), 45.1 (C-2′ & C-6′), 35.8 (C-4′), 32.5 (C-7″), 28.3 (C-3′ & C-5′), 25.1(C-3‴ & C-5‴), 23.5 (C-4‴). EI-MS (*m*/*z*): 562 (12%)[M^+], 252 (16%), 238 (53%), 224 (12%), 170 (5%), 156 (100%), 141 (12%), 82 (91%), 77 (35%).

14.2.2.7 5-(4-Methylphenyl)-1,3,4-Oxadiazole-2-yl-4-(Piperidin-1-ylsulfonyl) Benzyl Sulfide (6b)

White powder; Yield: 75%; M.P. 119–120 °C; Mol. For.: $C_{21}H_{23}N_3O_3S_2$; Mol. Wt.: 429.5. IR (KBr, cm^{-1}): ν_{max}: 3022 (C–H stretching of aromatic ring), 1635 (C=N stretching of oxadiazole ring), 1514 (C=C aromatic stretching), 1339 (–SO_2 stretching), 1273 (C=S bond stretching), 1242 & 1073 (C–O–C bond stretching). ^{1}H-NMR ($CDCl_3$, 400 MHz): δ (ppm) 7.83 (d, J = 8.0 Hz, 2H, H-2′ & H-6′), 7.69 (d, J = 8.0 Hz, 2H, H-3″ & H-5″), 7.60 (d, J = 8.0 Hz, 2H, H-2″ & H-6″), 7.29 (d, J = 8.0 Hz, 2H, H-3′ & H-5′), 4.52 (s, 2H, H-7″), 2.97 (t, J = 5.2 Hz, 2H, H_e-2‴ & H_e-6‴), 2.40 (s, 3H, CH_3-4′), 2.03 (br.t, J = 5.2 Hz, 2H, H_a-2‴ & H_a-6‴), 1.62-1.59 (m, 4H, H-3‴ & H-5‴), 1.40-1.38 (m, 2H, H-4‴). EI-MS (*m*/*z*): 429 (12%)[M^+],

345 (21%), 281 (32%), 238 (21%), 205 (35%), 191 (41%), 148 (81%), 119 (53%), 117 (100%), 91 (78%), 84 (73%), 77 (45%), 66 (42%), 51 (49%).

14.2.2.8 5-(4-Hydroxyphenyl)-1,3,4-Oxadiazole-2-yl-4,4-(Piperidin-1-ylsulfonyl)Benzyl Sulfide (6c)

Pale yellow powder; Yield: 81%; M.P. 123–125 °C; Mol. For.: $C_{20}H_{21}N_3O_4S_2$; Mol. Wt.: 431.5. IR (KBr, cm^{-1}): ν_{max}: 3027 (C–H stretching of aromatic ring), 1634 (C=N stretching of oxadiazole ring), 1516 (C=C aromatic stretching), 1338 (–SO_2 stretching), 1275 (C=S bond stretching), 1247 & 1074 (C–O–C bond stretching). ^{1}H-NMR ($CDCl_3$, 400 MHz): δ (ppm) 7.86 (d, $J = 8.8$ Hz, 2H, H-2′ & H-6′), 7.70 (d, $J = 8.0$ Hz, 2H, H-3″ & H-5″), 7.61 (d, $J = 8.0$ Hz, 2H, H-2″ & H-6″), 6.91 (d, $J = 8.8$ Hz, 2H, H-3′ & H-5′), 4.51 (s, 2H, H-7″), 2.98-2.94 (m, 2H, H_e-2‴ & H_e-6‴), 2.01 (br.t, $J = 9.6$ Hz, 2H, H_a-2‴ & H_a-6‴), 1.62-1.60 (m, 4H, H-3‴ & H-5‴), 1.40-1.39 (m, 2H, H-4‴). EI-MS (*m*/*z*): 431 (15%)[M^+], 347 (21%), 283 (32%), 238 (21%), 207 (35%), 193 (41%), 148 (81%), 121 (53%), 119 (100%), 91 (81%), 84 (73%), 77 (45%).

14.2.2.9 5-(4-Aminophenyl)-1,3,4-Oxadiazole-2-yl-4-(Piperidin-1-ylsulfonyl)Benzyl Sulfide (6d)

Shiny yellow powder; Yield: 79%; M.P. 110–112 °C; Mol. For.: $C_{20}H_{22}N_4O_3S_2$; Mol. Wt.: 430.5. IR (KBr, cm^{-1}): ν_{max}: 3037 (C–H stretching of aromatic ring), 1627 (C=N stretching of oxadiazole ring), 1523 (C=C aromatic stretching), 1343 (–SO_2 stretching), 1274 (C=S bond stretching), 1239 & 1076 (C–O–C bond stretching). ^{1}H-NMR ($CDCl_3$, 400 MHz): δ (ppm) 7.89 (d, $J = 8.0$ Hz, 2H, H-2′ & H-6′), 7.71 (d, $J = 8.0$ Hz, 2H, H-3″ & H-5″), 7.62 (d, $J = 7.6$ Hz, 2H, H-2″ & H-6″), 7.49 (d, $J = 7.6$ Hz, 2H, H-3′ & H-5′), 4.53 (s, 2H, H-7″), 2.99 (t, $J = 5.6$ Hz, 2H, H_e-2‴ & H_e-6‴), 2.03 (br.t, $J = 5.2$ Hz, 2H, H_a-2‴ & H_a-6‴), 1.62-1.60 (m, 4H, H-3‴ & H-5‴), 1.40-1.39 (m, 2H, H-4‴). EI-MS (*m*/*z*): 430 (15%)[M^+], 346 (21%), 282 (32%), 238 (21%), 206 (35%), 192 (41%), 148 (81%), 120 (53%), 118 (100%), 90 (81%), 84 (73%), 77 (45%).

14.2.2.10 5-(4-Nitrophenyl)-1,3,4-Oxadiazole-2-yl-4-(Piperidin-1-ylsulfonyl)Benzyl Sulfide (6e)

Turmeric powder; Yield: 75%; M.P. 122–123 °C; Mol. For.: $C_{20}H_{20}N_4O_5S_2$; Mol. Wt.: 460.5. IR (KBr, cm^{-1}): ν_{max}: 3037 (C–H stretching of aromatic ring), 1629 (C=N stretching of oxadiazole ring), 1524 (C=C aromatic stretching), 1331 (–SO_2 stretching), 1269 (C=S bond stretching), 1245 & 1071 (C–O–C bond stretching). ^{1}H-NMR ($CDCl_3$, 300 MHz): δ (ppm) 8.33 (d, $J = 9.0$ Hz, 2H, H-3′ & H-5′), 8.14 (d, $J = 8.7$ Hz, 2H, H-2′ & H-6′), 7.73 (d, $J = 8.1$ Hz, 2H, H-3″ & H-5″), 7.64

(d, $J = 8.1$ Hz, 2H, H-2″ & H-6″), 4.58 (s, 2H, H-7″), 3.10-2.95 (m, 4H, H-2‴ & H-6‴), 1.62-1.60 (m, 4H, H-3‴ & H-5‴), 1.40-1.39 (m, 2H, H-4‴). EI-MS (*m*/*z*): 460 (15%)[M^+], 376 (21%), 312 (32%), 238 (21%), 236 (35%), 223 (41%), 150 (53%), 148 (81%), 122 (100%).

14.2.2.11 5-(2-Chlorophenyl)-1,3,4-Oxadiazole-2-yl-4-(Piperidin-1-ylsulfonyl) Benzyl Sulfide (6f)

Buff colored shiny crystals; Yield: 78%; M.P. 90–91 °C; Mol. For.: $C_{20}H_{20}ClN_3O_3S_2$; Mol. Wt.: 449.9. IR (KBr, cm^{-1}): ν_{max}: 3033 (C–H stretching of aromatic ring), 1629 (C=N stretching of oxadiazole ring), 1524 (C=C aromatic stretching), 1331 (–SO_2 stretching), 1269 (C=S bond stretching), 1245 & 1071 (C–O–C bond stretching). ^{1}H-NMR (CD_3OD, 400 MHz): δ (ppm) 7.87 (dd, $J = 7.6$, 1.6 Hz, 1H, H-3′), 7.72 (d, $J = 8.0$ Hz, 2H, H-3″ & H-5″), 7.60 (dt, $J = 8.0$, 1.6 Hz, 1H, H-4′), 7.57 (dd, $J = 7.6$, 1.6 Hz, 1H, H-6′), 7.56 (d, $J = 8.0$ Hz, 2H, H-2″ & H-6″), 7.50 (dt, $J = 7.6$, 1.2 Hz, 1H, H-5′), 4.63 (s, 2H, H-7″), 2.93 (t, $J = 5.2$ Hz, 2H, H_e-2‴ & H_e-6‴), 2.03 (br.t, $J = 5.2$ Hz, 2H, H_a-2‴ & H_a-6‴), 1.61-1.57 (m, 4H, H-3‴ & H-5‴), 1.39-1.37 (m, 2H, H-4‴). EI-MS (*m*/*z*): 449 (15%)[M^+], 365 (21%), 301 (32%), 238 (21%), 225 (35%), 211 (41%), 148 (81%), 139 (100%), 137 (53%), 111 (81%), 84 (73%), 76 (45%).

14.2.2.12 5-(4-Chlorophenyl)-1,3,4-Oxadiazole-2-yl-4-(Piperidin-1-ylsulfonyl) Benzyl Sulfide (6g)

Mustard granular solid; Yield: 78%; M.P. 112–113 °C; Mol. For.: $C_{20}H_{20}ClN_3O_3S_2$; Mol. Wt.: 449.9. IR (KBr, cm^{-1}): ν_{max}: 3013 (C–H stretching of aromatic ring), 1617 (C=N stretching of oxadiazole ring), 1507 (C=C aromatic stretching), 1347 (−SO_2 stretching), 1243 (C=S bond stretching), 1237 & 1087 (C–O–C bond stretching). ^{1}H-NMR (CD_3OD, 400 MHz): δ (ppm) 7.91 (d, $J = 8.8$ Hz, 2H, H-2′ & H-6′), 7.71 (d, $J = 8.0$ Hz, 2H, H-3″ & H-5″), 7.58 (d, $J = 8.4$ Hz, 2H, H-3′ & H-5′), 7.57 (d, $J = 8.4$ Hz, 2H, H-2″ & H-6″), 4.62 (s, 2H, H-7″), 2.91-2.85 (m, 4H, H-2‴ & H-6‴), 1.84-1.81 (m, 4H, H-3‴ & H-5‴), 1.61-1.57 (m, 2H, H-4‴). EI-MS (*m*/*z*): 449 (15%)[M^+], 365 (21%), 301 (32%), 238 (21%), 225 (35%), 211 (41%), 148 (81%), 139 (100%), 137 (53%), 111 (81%), 84 (73%), 76 (45%).

14.2.2.13 5-Benzyl-1,3,4-Oxadiazole-2-yl-4-(Piperidin-1-ylsulfonyl) Benzyl Sulfide (6h)

Peach colored gummy solid; Yield: 86%; Mol. For.: $C_{21}H_{23}N_3O_3S_2$; Mol. Wt.: 429.5. IR (KBr, cm^{-1}): ν_{max}: 3019 (C–H stretching of aromatic ring), 1637 (C=N stretching of oxadiazole ring), 1521 (C=C aromatic stretching), 1329 (–SO_2 stretching), 1241 (C=S bond stretching), 1231 & 1083 (C–O–C bond stretching).

^{1}H-NMR ($CDCl_3$, 300 MHz): δ (ppm) 7.74 (d, $J = 8.4$ Hz, 2H, H-3″ & H-5″), 7.61 (d, $J = 8.4$ Hz, 2H, H-2″ & H-6″), 7.50 (dd, $J = 8.0$, 1.2 Hz, 2H, H-2′ & H-6′), 7.42-7.38 (m, 3H, H-3′ to H-5'), 7.38-7.34 (s, 2H, H-7′), 4.53 (s, 2H, H-7″), 2.98 (t, $J =$ 5.2 Hz, 2H, H_e-2‴ & H_e-6‴), 2.05 (br.t, $J = 5.2$ Hz, 2H, H_a-2‴ & H_a-6‴), 1.62-1.59 (m, 4H, H-3‴ & H-5‴), 1.40-1.39 (m, 2H, H-4‴). EI-MS (*m*/*z*): 429 (12%)[M^+], 345 (21%), 281 (32%), 238 (21%), 205 (35%), 191 (41%), 148 (81%), 119 (53%), 117 (100%), 91 (78%), 84 (73%), 77 (45%), 65 (42%).

14.2.2.14 5-(2-Phenylethenyl)-1,3,4-Oxadiazole-2-yl-4-(Piperidin-1-ylsulfonyl) Benzyl Sulfide (6i)

Light green powder; Yield: 84%; M.P. 156–158 °C; Mol. For.: $C_{22}H_{23}N_3O_3S_2$; Mol. Wt.: 441.5. IR (KBr, cm^{-1}): ν_{max}: 3019 (C–H stretching of aromatic ring), 1623 (C=N stretching of oxadiazole ring), 1515 (C=C aromatic stretching), 1341 (–SO_2 stretching), 1253 (C=S bond stretching), 1229 & 1073 (C–O–C bond stretching). ^{1}H-NMR ($CDCl_3$, 400 MHz): δ (ppm) 7.70 (d, $J = 8.4$ Hz, 2H, H-3″ & H-5″), 7.61 (d, $J = 8.4$ Hz, 2H, H-2″ & H-6″),7.50 (dd, $J = 8.0$, 1.2 Hz, 2H, H-2′ & H-6′), 7.42-7.38 (m, 3H, H-3′ to H-5′), 7.38 (d, $J = 16.4$ Hz, 1H, H-7′), 6.94 (d, $J = 16.4$ Hz, 1H, H-8′), 4.53 (s, 2H, H-7″), 2.98 (t, $J = 5.2$ Hz, 2H, H_e-2‴ & H_e-6‴), 2.05 (br.t, $J = 5.2$ Hz, 2H, H_a-2‴ & H_a-6‴), 1.62-1.59 (m, 4H, H-3‴ & H-5‴), 1.40-1.39 (m, 2H, H-4‴). EI-MS (*m*/*z*): 441 (12%)[M^+], 357 (21%), 293 (32%), 238 (21%), 217 (35%), 203 (41%), 171 (81%), 131 (53%), 129 (100%), 103 (78%), 84 (73%), 77 (45%).

14.2.2.15 5-(Naphthalen-1-ylmethyl)-1,3,4-Oxadiazole-2-yl-4-(Piperidin-1-ylsulfonyl)Benzyl Sulfide (6j)

Creamy white sticky solid; Yield: 80%; Mol. For.: $C_{25}H_{25}N_3O_3S_2$; Mol. Wt.: 479.6. IR (KBr, cm^{-1}): ν_{max}: 3021 (C–H stretching of aromatic ring), 1625 (C=N stretching of oxadiazole ring), 1519 (C=C aromatic stretching), 1353 (–SO_2 stretching), 1247 (C=S bond stretching), 1229 & 1075 (C–O–C bond stretching). ^{1}H-NMR ($CDCl_3$, 400 MHz): δ (ppm) 8.06 (d, $J = 8.0$ Hz, 1H, H-4′), 7.86 (dd, $J =$ 8.8, 1.6 Hz, 1H, H-8′), 7.82 (dd, $J = 6.8$, 2.8 Hz, 1H, H-5′), 7.57 (d, $J = 8.4$ Hz, 2H, H-3″ & H-5″), 7.51 (dt, $J = 8.0$, 1.2 Hz, 1H, H-7′) , 7.44-7.42 (m, 3H, H-2′, H-3′ & H-6′), 7.36 (d, $J = 8.4$ Hz, 2H, H-2″ & H-6″), 4.59 (s, 2H, H-11′), 4.34 (s, 2H, H-7″), 2.97 (t, $J = 5.2$ Hz, 2H, H_e-2‴ & H_e-6‴), 2.10-2.06 (m, 2H, H_a-2‴ & H_a-6"'), 1.63-1.57 (m, 4H, H-3‴ & H-5‴), 1.40-1.38 (m, 2H, H-4‴). EI-MS (*m*/*z*): 479 (12%)[M^+], 395 (21%), 331 (32%), 255 (35%), 241 (34%), 238 (21%), 169 (23%), 167 (45%), 141 (81%), 127 (53%), 84 (73%), 76 (45%).

14.2.2.16 5-Phenyl-1,3,4-Oxadiazole-2-yl-4-(Piperidin-1-ylsulfonyl) Benzyl Sulfide (6k)

Off-white powder; Yield: 76%; M.P. 71–72 °C; Mol. For.: $C_{20}H_{21}N_3O_3S_2$; Mol. Wt.: 415.5. IR (KBr, cm^{-1}): ν_{max}: 3020 (C–H stretching of aromatic ring), 1631 (C=N stretching of oxadiazole ring), 1511 (C=C aromatic stretching), 1335 ($–SO_2$ stretching), 1269 (C=S bond stretching), 1249 & 1079 (C–O–C bond stretching). ^{1}H-NMR (CD_3OD, 400 MHz): δ (ppm) 7.91 (dd, $J = 8.4$, 1.6 Hz, 2H, H-2′ & H-6′), 7.72 (d, $J = 8.0$ Hz, 2H, H-3″ & H-5″), 7.59 (d, $J = 8.0$ Hz, 2H, H-2″ & H-6″), 7.57-7.54 (m, 3H, H-3′ to H-5′), 4.62 (s, 2H, H-7″), 2.91 (t, $J = 5.6$ Hz, 2H, H_e-2‴ & H_e-6‴), 2.01 (br.t, $J = 9.6$ Hz, 2H, H_a-2‴ & H_a-6‴), 1.82-1.78 (m, 4H, H-3‴ & H-5‴), 1.56-1.53 (m, 2H, H-4‴). EI-MS (*m*/*z*): 415 (12%)[M^+], 331 (21%), 267 (32%), 191 (35%), 177 (41%), 105 (53%), 103 (100%), 77 (45%).

14.2.3 Butyrylcholinesterase Assay

The BChE inhibition activity was performed in accordance with the literature method [16] with small alterations. Total volume of the reaction mass was 100 µL containing 60 µL Na_2HPO_4 buffer, 50 mM and pH 7.7. 10 µL test compound, 0.5 mM $well^{-1}$, was added followed by the addition of 10 µL BChE (0.5 unit $well^{-1}$). The contents were mixed, pre-read at 405 nm and then pre-incubated for 10 min at 37 °C. 10 µL of substrate (butyrylthiocholine chloride, 0.5 mM $well^{-1}$) was used to initiate the reaction followed by the addition of 10 µL DTNB, 0.5 mM $well^{-1}$. After 15 min of incubation at 37 °C, absorbance was measured at 405 nm using a 96-well plate reader Synergy HT, Biotek, USA. All experiments were carried out with their respective controls in triplicate. Eserine (0.5 mM $well^{-1}$) was used as positive control. The percent inhibition was calculated using the following equation:

$$\text{Inhibition } (\%) = (\text{Abs of Control} - \text{Abs of Test comp}) \times 100/(\text{Abs of Control})$$

where,
Control = Total enzyme activity without inhibitor; Test = Activity in the presence of test compound.

IC_{50} values were calculated using EZ–Fit Enzyme kinetics software (Perrella Scientific Inc. Amherst, USA) and were the mean of three different independent values taken at different dilutions.

14.2.4 Molecular Docking

The 3D coordinate file of human BChE (PDB accession code, *2WID*) was retrieved from protein data bank, and the missing residues were constructed by aligning it to the other pdb file (PDB accession code, *1P0P*). All water molecules were removed from the retrieved crystal structure using Visual Molecular Dynamics, VMD 1.9 [17]. The 3D structures of all compounds were constructed in pdb format and subsequently optimized at semi-empirical RM1 level of theory using the program Gabedit [18] and MOPAC 2012 [19] respectively and were allowed to dock with human BChE, which was accomplished by the software, Auto Dock Vina [20]. A total of 20 runs were performed for each docking and the remaining parameters were set to default values.

The search space was restricted to a grid box size of 46 × 46 × 46 in x, y and z dimensions, respectively, centered on the binding site of protein with x, y, and z coordinates of 120.491, 106.059 and −136.443 Å, respectively. All the docking runs were performed on Intel(R) Core(TM) i5-2410M CPU @ 2.30 GHz of Sony origin, with 6.0 GB DDR RAM. Auto Dock Vina was compiled and run under Windows 7 Professional 64-bit operating system.

14.3 Results and Discussion

14.3.1 Chemistry

The 2,5-disubstituted 1,3,4-oxadiazoles, **6a–6k** were synthesized according to the protocol given in Scheme 14.1 and the different 5-substituted molecules are mentioned in Table 14.1. The general reaction conditions and the structure characterization are described in the experimental section.

Aim of presented research work was to synthesize therapeutically active compounds that can be considered in drug development program. We have synthesized some new 2,5-disubstituted 1,3,4-oxadiazole compounds and investigated the BChE enzyme activity of all the synthesized compounds. The synthesis was performed in different steps. First, the phenyl/aryl/aralkyl/heterocyclic organic acids **(1a–1k)** were converted into their corresponding ethyl esters **(2a–2k)** by refluxing in conc. H_2SO_4 and ethanol for 5–6 h. Second, the ethyl esters **(2a–2k)** were subsequently converted into hydrazides **(3a–3k)** by refluxing and stirring them with hydrazine hydrate (80%) using methanol as solvent for 3–4 h. Third, the synthesized hydrazides **(3a–3k)** were subjected to cyclization to prepare 5-substituted-1,3,4-oxadiazole-2-thiols **(4a–4k)** by refluxing for 4–6 h with CS_2 in the presence of KOH as base. The products were obtained by acidifying the mixture. The electrophile **5** was synthesized by stirring piperidine with 4-bromomethylbenzenesulfonyl chloride in basic aqueous media and the product was obtained by the addition of acid followed by filtration. Fourth,

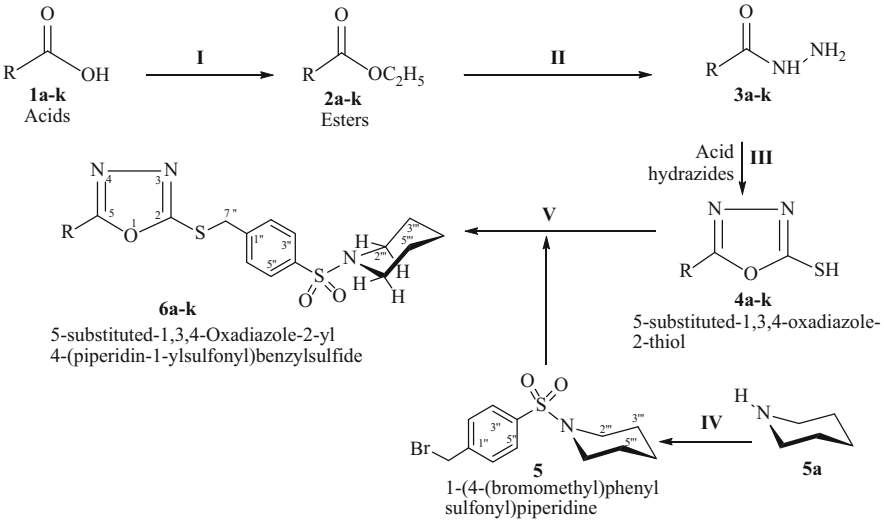

Scheme 14.1 Outline for the synthesis of 5-substituted-1,3,4-oxadiazole-2-yl 4-(piperidin-1-ylsulfonyl)benzyl sulfide. Reagents and conditions: (I) H_2SO_4/EtOH/refluxing for 3–4 h; (II) N_2H_4/MeOH/stirring for 4–6 h; (III) CS_2/KOH/EtOH/refluxing for 3–6 h; (IV) 4-bromomethylbenzene sulfonylchloride/H_2O/5% Na_2CO_3 soln/stirring for 1 h; (V) DMF/NaH/stirring for 2–3 h

Table 14.1 Different 5-substituted aralkyl groups

Compound	R	Compound	R	Compound	R
6a	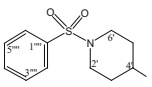	**6e**	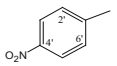	**6i**	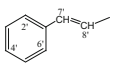
6b	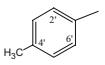	**6f**		**6j**	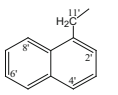
6c	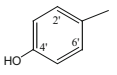	**6g**	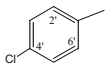	**6k**	
6d	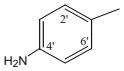	**6h**	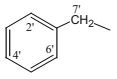		

these 5-substituted-1,3,4-oxadiazole-2-thiols **(4a–4k)** were treated with 1-(4-(bromomethyl)phenylsulfonyl)piperidine **(5)** in the presence of DMF as solvent and NaH as base. The final products **(6a–6k)** were collected by the addition of cold water and filtration or solvent extraction depending upon the conditions. The structures of the synthesized compounds were ascertained by ^{1}H-NMR, IR and mass spectral data as illustrated in the experimental section.

Compound **6a** was synthesized as a white powder having yield 87% and melting point 138–139 °C. In the IR spectrum, the characteristic peaks appeared at 3021, 1631, 1519 and 1339 cm^{-1} corresponding to C–H stretching, C=N stretching, C=C stretching and stretching of sulfonyl group respectively. The molecular formula $C_{25}H_{30}N_4O_5S_3$ was established by HR-MS showing $[M]^+$ at *m*/*z* 562.728 (calcd for $C_{25}H_{30}N_4O_5S_3$ 562.723). In the EI-MS spectrum the molecular ion peak appeared at 562 while base peak showed at *m*/*z* 156. One distinct peak appeared at *m*/*z* 224 which indicated the presence of 1-(phenylsulfonyl)piperidin-4-yl group in the molecule. In the ^{1}H-NMR spectrum, signals appeared at δ 7.75 ppm as doublet with coupling constant equal to 8.4 Hz having integration of two protons and a doublet at δ 7.73 ppm with coupling constant 8.4 Hz having integration of two protons which confirmed the presence of 1,4-disubstituted benzene ring in the molecule. The mono-substituted benzene ring is affirmed by a doublet appearing at δ 7.67 ppm with *J* value of 8.4 Hz corresponding to two protons while the remaining three protons of the ring appeared as multiplets at chemical shift 7.62-7.58 and 7.56-7.54 ppm. Signals for piperidine ring attached directly to oxadiazole ring appeared at δ (ppm) 3.69-3.72 (m, 2H, H_e-2′ & H_e-6′), 2.60-2.53 (m, 2H, H_a-2′ & H_a-6′), 1.93-1.87 (m, 4H, H-3′ & H-5′) and 2.80 (m, 1H, H-4′) and that for other piperidine ring appeared at 2.97-2.95 (m, 2H, H_e-2‴ & H_e-6‴), 2.12-2.07 (m, 2H, H_a-2‴ & H_a-6‴), 1.62-1.59 (m, 4H, H-3‴ & H-5‴) and 1.43-1.39 (m, 2H, H-4‴). In broad band (BB) and distortionless enhancement by polarization transfer (DEPT) ^{13}C-NMR spectra, 17 signals appeared disclosing the presence of 5 quaternary carbons, 6 methine carbons and 6 methylene carbons. Downfield signals appearing at δ (ppm) 169.1 and 166.8 were assigned to C-5 and C-2, quaternary oxygenated carbons of oxadiazole ring. Signals of methylene carbons of piperidine ring attached to oxadiazole ring at fourth position resonated at 45.1 ppm for C-2′ & C-6′, and 28.3 ppm for C-3′ & C-5′ with double intensity indicating two carbon atoms while methine carbon appeared at 35.8 ppm for C-4′ with single intensity. Three signals at 46.9, 25.1 and 23.5 ppm were assigned to the other piperidine ring attached to sulfonyl group; the first two for methylene carbons, C-2‴ & C-6‴ and C-3‴ & C-5‴ respectively with double intensity, and the third for methine carbon C-4‴. Aromatic methine carbons of *p*-disubstituted phenyl ring resonated at δ (ppm) 129.1 (C-2″ & C-6″) and 128.1 (C-3″ & C-5″) corresponding to two carbons each because of double intensity as compared to other signals while quaternary signals of this ring emerged at δ (ppm) 140.7 and 137.9 for C-1″ & C-4″. Other phenyl ring gave signals of methine at δ (ppm) 129.6 (for C-3⁗ & C-5⁗) and 127.6 (for C-2⁗ & C-6⁗) with large intensity revealing presence of two carbons while one methine signal was revealed at δ (ppm) 132.9 (for C-4⁗) and the quaternary carbon (C-1⁗) appeared at δ (ppm) 137.3. All these signals collectively confirmed the structure of compound **6a** and named as 5-(1-(phenylsulfonyl) piperidin-4-yl)-1,3,4-oxadiazole-2-yl-4-(piperidin-1-ylsulfonyl)benzyl sulfide. Similarly, the structures of all the other synthesized compounds were elucidated by the help of above mentioned analytical techniques. The mass fragmentation pattern of the compound **6a** is provided in Fig. 14.1.

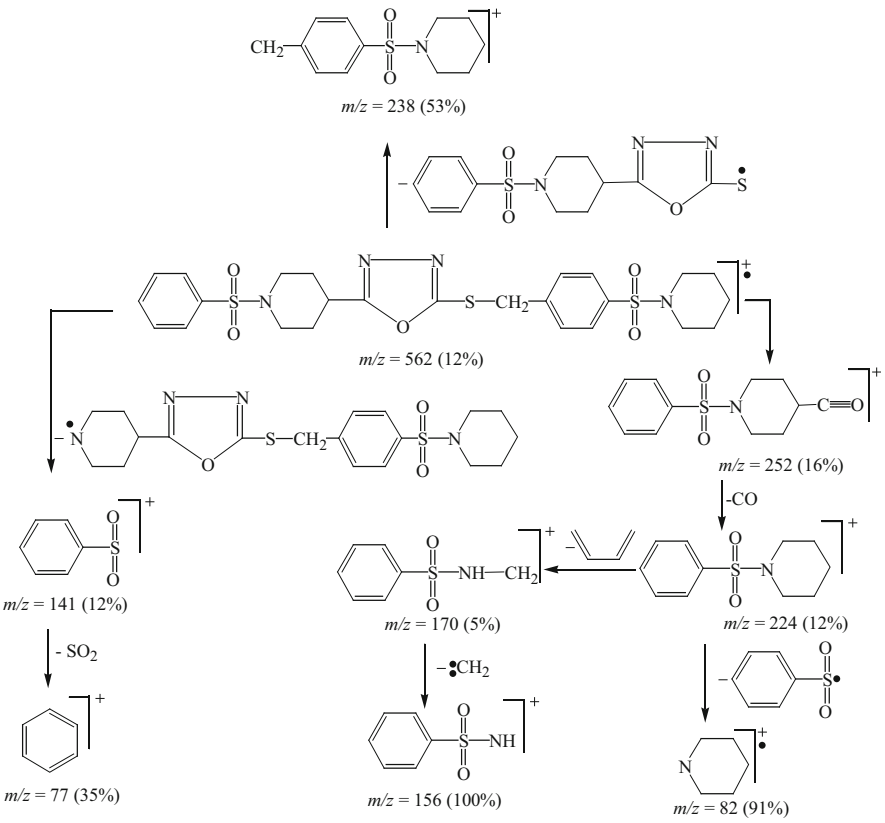

Fig. 14.1 Mass fragmentation pattern for 5-(1-(phenylsulfonyl)piperidin-4-yl)-1,3,4-oxadiazole-2-yl 4-(piperidin-1-ylsulfonyl)benzyl sulfide **(6a)**

*14.3.2 Enzyme Inhibition Activity (*In vitro*)*

The results of in vitro enzyme inhibition activity of the synthesized compounds against BChE are described in Table 14.2. The screening of the synthesized 5-substituted-1,3,4-oxadiazole-2-yl 4-(piperidin-1-ylsulfonyl)benzyl sulfide compounds revealed that almost all of them showed promising inhibitory potential against BChE except 5-(4-methylphenyl)-1,3,4-oxadiazole-2-yl-4-(piperidin-1-ylsulfonyl) benzyl sulfide (**6b**) and 5-phenyl-1,3,4-oxadiazole-2-yl 4-(piperidin-1-ylsulfonyl)benzyl sulfide (**6k**). The compound 5-(2-phenylethenyl)-1,3,4-oxadiazole-2-yl-4-(piperidin-1-ylsulfonyl)benzyl sulfide (**6i**) showed promising inhibitory potential having IC_{50} value 12.15 ± 0.17 μmol/L as compared to the reference standard, eserine having IC_{50} value 0.04 ± 0.001 μmol/L, probably due to the presence of 2-phenylethenyl group in the molecule. Another compound 5-(4-aminophenyl)-1,3,4-oxadiazole-2-yl-4-(piperidin-1-ylsulfonyl)benzyl sulfide (**6d**) also showed good inhibitory potential with an IC_{50} value of 22.13 ± 0.14

Table 14.2 Results for BChE enzyme inhibition of the synthesized compounds

	BChE		
Sample Code	Conc./well (mM)	Inhibition (%)	IC_{50} (μmol/L)
6a	0.5	95.81 ± 0.44	10.51 ± 0.21
6b	0.5	29.61 ± 0.68	–
6c	0.5	73.59 ± 0.17	129.71 ± 0.21
6d	0.5	83.47 ± 0.81	22.13 ± 0.14
6e	0.5	64.51 ± 0.31	189.61 ± 0.11
6f	0.5	71.25 ± 0.21	148.71 ± 0.19
6g	0.5	75.69 ± 0.71	116.31 ± 0.11
6h	0.5	61.63 ± 0.55	165.21 ± 0.14
6i	0.5	91.63 ± 0.45	12.15 ± 0.17
6j	0.5	69.25 ± 0.18	161.21 ± 0.14
6k	0.5	53.22 ± 0.47	–
Eserine	0.25	**91.29 ± 1.17**	**0.040 ± 0.001**

μmol/L, probably due to the attachment of the para-amino substituted phenyl group at the C-5 position of the 1,3,4-oxadiazole nucleus. The compound 5-(1-(phenylsulfonyl)piperidin-4-yl)-1,3,4-oxadiazole-2-yl-4-(piperidin-1-ylsulfonyl) benzyl sulfide (**6a**) exhibited the best potential, having IC_{50} value of 10.51 ± 0.21 μmol/L, presumably because of the presence of two sulfonamide linkages and an oxadiazole ring that collectively enhanced its bioactivity potential. The activity order of the synthesized compounds was **6a** > **6i** > **6d** > **6g** > **6c** > **6f** > **6j** > **6e** > **6h**. Such type of compounds can further be exploited and their derivatives could be synthesized to get closer to IC_{50} values of the standard, eserine. In this way, the compounds could be potential targets in the drug invention and drug development program.

14.3.3 Molecular Docking Analysis

In order to elucidate the probable mechanism by which the title compounds could enhance anti-BChE activity and to rationalize the ligand-protein interaction at molecular level for establishing structure activity relationship, molecular docking of the potent inhibitors from a series of compounds was executed into the receptor site of the crystal structure of BChE. The highly potent compounds from the series were selected on the basis of IC_{50} values which were determined experimentally. The enzyme inhibition data are provided for all the synthesized compounds in Table 14.2. Compounds **6a**, **6i** and **6d** were found to be the most active against BChE among the series of the compounds in respective order. Their candidacy of being highly potent was also supported by their docking score as these compounds possessed good binding affinity with the BChE protein. The binding energies of

compounds **6a, 6i** and **6d** are found to be −11.1, −10.2 and −9.9 kcal/mol, respectively, with BChE which are significantly lowered as compared to the reference inhibitor, eserine *i.e.*, −7.50 kcal/mol, indicating a strong binding affinity of these compounds with BChE. The binding energies and binding residues of the highlighted compounds are given in Table 14.3.

The compounds **6a, 6i** and **6d** were the most potent inhibitor of BChE with IC_{50} values of 10.51 ± 0.21, 12.15 ± 0.17 and 22.13 ± 0.14 μmol/L, respectively, with eserine, the reference standard having IC_{50} value of 0.040 ± 0.001 μmol/L. The binding models of compounds **6d, 6i** and **6a** in the active site of BChE are depicted respectively in Fig. 14.2a, b, and c. Compound **6d** was found to bind to the BChE through nitrogen of its amino group projecting toward the backbone amino group of Pro285 (bond distance= 3.22 Å) and Ser287 (2.82 Å) and the oxygen atoms of sulfonyl group and oxadiazole ring oriented toward the hydroxyl group of Tyr332 (3.03 and 3.04 Å) and backbone amino group of Gly116 (3.39 Å). Both nitrogen atoms of oxadiazole ring are involved in H-bonding with the amino group of His438 (2.87 and 3.20 Å) and hydroxyl group of Ser198 (2.85 and 2.88 Å). Tyr332 and Leu286 are involved in van der Waals interactions (VDW) with **6d** (Fig. 14.2c). Compound **6i** was bound to the BChE through its oxygen atoms of sulfonyl group with the amino groups of Gly116 (3.26 Å), Gly117 (2.80 Å), His438 (2.84 Å) and hydroxyl group of Ser198 (3.03 Å). There is one arene-H interaction between His438 and the inhibitor (Fig. 14.2b). A number of van der Waals interactions are involved in binding of **6i** with BChE including Trp231, Leu286, Val288, Trp82, Phe398, Phe329 and Gly439 amino acid residues. Compound **6a** being the most potent is not only ranked top in the list of IC_{50} values but also exhibited the highest docking score with a binding energy value of −11.1 kcal/mol, indicating a positive correlation between experiment and theory. The binding of **6a** is promising with the presence of two arene-arene interactions through benzenesulfonyl and oxadiazole ring with Trp82 and Tyr332 unlike **6d** and **6i.** The compound **6a** forms several VDW interactions with Trp82, Gly115, Gly116, Phe398, Trp231, Val288 and Leu286 residues of BChE protein which stabilize the compound in the binding site and possibly make it a strong BChE inhibitor. Oxygen atoms of sulfonyl group are found to form H-bonds with the backbone amino group of Gly116 (3.04 Å), Gly117 (3.01 Å), His438 (2.90 Å) and the hydroxyl group of Ser198 (3.13 Å). There are three weak H-bonds between sulfonyl and oxadiazole ring of inhibitor and backbone nitrogen of Ala199 (4.41 Å) and hydroxyl of Tyr332 (3.16 and 3.12 Å). Amino acid residues such as Gly116, His438, Tyr332, Trp82 and Ser198 are found to be important common residues for binding of highlighted compounds and most likely are involved in the potential activity of compounds as anti-BChE agents. The presence of residues Trp82, His438 and Gly116 have been reported in literature in binding models of potential BChE inhibitors [21, 22]. In the present study exclusive binding residues were observed in addition to the reported BChE binding residues making the compounds as potent moieties for the anti-BChE activity.

Table 14.3 Results obtained from the molecular docking of most active compounds from series

Cpd	B.E (kcal/mol)	H-bonding		Arene-arene interaction	Arene-H interaction	VDW
		Interacting residues	Distance (Å)			
6a	−11.10	Gly116:b NH---O:SO_2	3.04	Trp82 with C_6H_5:SO_2		Trp82 with C_5H_9N
		Gly117:b NH---O:SO_2	3.01	Tyr332 with C_2N_2O		Gly115 with C_5H_9N
		Ser198:OH---O:SO_2	3.13			Gly116 with C_5H_9N
		Ala199:b NH--- O:SO_2	4.41[a]		–	Phe398 with C_5H_9N
		HIs438:NH---O:SO_2	2.90			Trp231 with C_5H_9N
		HIs438:NH---O:SO_2	2.90			Val288 with C_5H_9N
		Tyr332:OH---N:C_2N_2O	3.16[a], 3.12[a]			Leu286 with C_5H_9N
6d	−9.9	His438:NH---N:C_2N_2O	2.87, 3.20			Tyr332 with C_5H_9N
		Ser198:OH---N:C_2N_2O	2.85, 2.88			Leu286 with C_6H_5-NH
		Gly116:b NH---O:C_2N_2O	3.39[a]			
		Tyr332:OH---O:SO_2	3.03, 3.04	–	–	
		Pro285:b NH---N:NH_2	3.22			
		Ser287:b NH---N:NH_2	2.82			
6i	−10.20	Gly116:b NH---O:SO_2	3.26	Gly 439	His438 with C_8H_7	Trp231 with C_5H_9N
		Gly117:b NH---O:SO_2	2.80			Leu286 with C_5H_9N
		Tyr332:OH---N:C_2N_2O	2.97, 3.34			Val288 with C_5H_9N
		Ser198:OH---O:SO_2	3.03	–		Trp82 with C_2N_2O and [a]C_8H_7
		His438:NH---O:SO_2	2.84			Phe398 with C_5H_9N
						Phe329 with C_5H_9N and SO_2-Ph

b backbone, *B.E* binding energy, *VDW* van-der Waals interactions
[a]Indicates weak H-bonding due to large distance or unfavorable angle

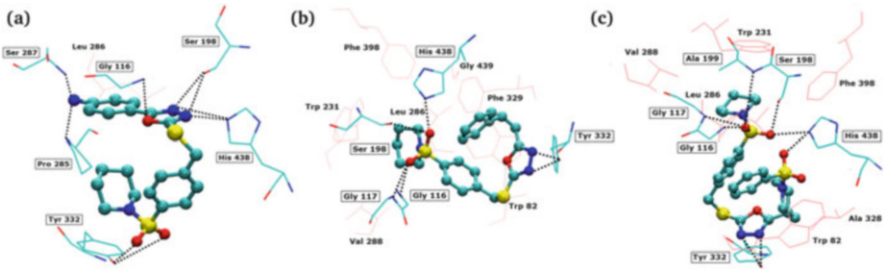

Fig. 14.2 Binding models of compounds **6d** (**a**), **6i** (**b**) and **6a** (**c**) in the active site of human BChE protein

14.4 Conclusion

Structure elucidation by spectroscopic analysis confirmed the proposed structures of synthesized moieties. Screening against BChE enzyme revealed that compounds **6a, 6d** and **6i** were the most potent inhibitors as indicated by their IC_{50} values as compared to eserine taken as reference standard. These compounds exhibit best binding models with promising hydrogen bonding, VDW and arene-arene interactions. In this study 1,3,4-oxadiazole bearing series were synthesized from a variety of esters and compounds were subjected to substitutions which bring diversity in their binding and activity. This study has provided a qualitative relationship between ligands' substitutions with their anti-BChE function. It can be speculated that the presence of para-amino, vinyl and piperidine sulfonyl group substitution is significant for the BChE active site binding and consequently the anti-BChE activity.

Acknowledgement The authors are thankful to the Higher Education Commission of Pakistan for the financial support regarding this research work and the spectroscopic analysis.

References

1. Omar FA, Mahfouz NM, Rahman MA (1996) Design, synthesis and anti-inflammatory activity of some 1,3,4-oxadiazole derivatives. Eur J Med Chem 131:819–825
2. Goswami BN, Kataky JCS, Baruah JN (1984) Synthesis and antibacterial activity of 1-(2,4-dichlorobenzoyl)-4-substituted thiosemicarbazides, 1,2,4-triazoles and their methyl derivatives. J Heterocyclic Chem 21:1225–1229
3. Holla BS, Poojary KN, Kalluraya B, Gowda PV (1996) 5-Substituted-1,3,4-oxadiazolin-2-thiones. Indian J Heterocyclic Chem 5:273–276
4. Hasan A, Thomas NF, Gapil S (2011) Synthesis, characterization and antifungal evaluation of 5-substituted-4-amino-1,2,4-triazole-3-thioesters. Molecules 16:1297–1309
5. Omar MT (1997) Synthesis of new xanthenone derivatives of expected antibilharzial activity. Arch Pharm Res 20:602–609

6. Matsumoto K, Kawamura Y, Yasuda Y, Tanimoto T, Matsumoto K, Yoshida T, Shoji JJ (1998) Isolation and characterization of Thioxamycin. Antibiot (Tokyo) 42:1465–1469
7. Shafi SS, Radhakrishnan TR (1995) Synthesis and antibacterial activity of some 2,5-di-substituted-1,3,4-oxadiazole 1,3,4-thiadiazole, 1,2,4-triazole and 4-thiazolidinone. Indian J Heterocyclic Chem 5:133–138
8. Tan TMC, Chen Y, Kong KH, Bai J, Li Y, Lim SG, Ang TH, Lam Y (2006) Synthesis and the biological evaluation of 2-benzenesulfonylalkyl-5-substituted-sulfanyl-[1,3,4]-oxadiazoles as potential anti-hepatitis B virus agents. Antiviral Res 71:7–14
9. Wagle S, Adhikari AV, Kumari NS (2008) Synthesis of some new 2-(3-methyl-7-substituted-2-oxoquinoxalinyl)-5-(aryl)-1,3,4-oxadiazoles as potential non-steroidal anti-inflammatory and analgesic agents. Indian J Chem 47B:439–448
10. Sanchez-Sancho F, Herrandon B (1998) Short syntheses of (S)-pipecolic acid,(R)-coniine, and (S)-δ-coniceine using biocatalytically-generated chiral building blocks. Tetrahedron-Asymmetry 9:1951–1965
11. Nithiya S, Karthik N, Jayabharathi J (2011) In vitro antioxidant activity of hindered piperidone derivatives. Int J Pharm Pharm Sci 3:254–256
12. Aziz-ur-Rehman FA, Abbas N, Abbasi MA, Khan KM, Ashraf M, Ahmad I, Ejaz SA (2013) Synthesis, characterization and biological screening of 5-substituted-1,3,4-oxadiazole-2yl-N-(2-methoxy-5-chlorophenyl)-2-sulfanyl acetamide. Pak J Pharm Sci 26:345–352
13. Aziz-ur-Rehman FA, Abbasi MA, Rasool S, Malik A, Ashraf M, Ahmad I, Ejaz SA (2013) Synthesis of new N-(5-chloro-2-methoxyphenyl)-4-(5-substituted-1,3,4-oxadiazol-2-ylthio) butanamide derivatives as suitable lipoxygenase inhibitors. J Saudi Chem Soc 20:S488–S494
14. Aziz-ur-Rehman NK, Abbasi MA, Khalid H, Khan KM, Ashraf M, Ahmad I, Ejaz SA (2012) Synthesis, spectral characterization and biological activity of S-substituted derivatives of 5-(4-nitrophenyl)-1,3,4-oxadiazole-2-thiol. Asian J Pharm Health Sci 3:370–376
15. Aziz-ur-Rehman SSZ, Abbasi MA, Abbas N, Khan KM, Shahid M, Mahmood Y, Akhtar MN, Lajis NH (2012) Synthesis, antibacterial screening and hemolytic activity of S-substituted derivatives of 5-benzyl-1,3,4-oxadiazole-2-thiol. Int J Pharm Pharm Sci 4:676–680
16. Ellman GL, Courtney KD, Andres V, Featherstone RM (1961) A new and rapid colorimetric determination of acetylcholinesterase activity. Biochem Pharmcol 7:88–95
17. Humphrey W, Dalke A, Schulten K (1996) VMD: visual molecular dynamics. J Mol Graph 14:33–38
18. Allouche AR (2010) Gabedit—A graphical user interface for computational chemistry softwares. J Comput Chem 32:174–182
19. Stewart JJ (2007) Optimization of parameters for semi-empirical methods. V: modification of NDDO approximations and application to 70 elements. J Mol Model 13:1173–1213
20. Trott O, Olson AJ (2010) AutoDock Vina: improving the speed and accuracy of docking with a new scoring function, efficient optimization, and multithreading. J Comput Chem 31:455–461
21. Primožič I, Hrenar T, Tomić S (2012) Binding modes of quinuclidinium esters to butyrylcholinesterase. Croat Chem Acta:8577–8583
22. Özturan Özer E, Tan OU, Ozadali K, Küçükkılınç T, Balkan A, Uçar G (2013) Synthesis, molecular modeling and evaluation of novel N′-2-(4-benzylpiperidin-/piperazin-1-yl) acylhydrazone derivatives as dual inhibitors for cholinesterases and Aβ aggregation. Bioorg Med Chem Lett 23:440–443

Chapter 15
Cation Influence on Zirconium/Hafnium Fluoride Coordination

Steven J. Lötter, Walter Purcell, Johann T. Nel, and Bernardus van Brecht

Abstract Interest in the Zr and Hf fluoride compounds stemmed from a need for water soluble reference materials (RM) for analytical method development and validation of Zr/Hf containing materials and minerals. Numerous mono-valent inorganic (alkali metals) and organic (ammonium type) cations were used to try and isolate the $(Zr/Hf)F_6^{2-}$ anions.

$$(Zr/Hf)F_4 + 2MF \xrightarrow{HF} M_2(Zr/Hf)F_6 \left(M = K^+, Rb^+, Cs^+, NH_4^+, N(C_2H_5)_4^+, PPh_4^+\right)$$

The structures that were isolated for some of these cations indicated the profound influence of the cation on the type and coordination of the metal-fluorido bonds in these compounds. The coordination number of the metal center changed from eight for K^+ (smallest of alkali metals) to six for Cs^+ (largest of alkali metals) while the type of metal-fluorido bonds ranged from a combination of mono-, di- and tri-bridged to no bridging at all, depending on the size and type of cations used during the crystallization.

Keywords Zirconium • Hafnium • Fluorido • Monovalent • Reference material

S.J. Lötter • W. Purcell (✉)
Department of Chemistry, University of the Free State, 205 Nelson Mandela Drive, Bloemfontein 9300, South Africa
e-mail: purcellw@ufs.ac.za

J.T. Nel
The South African Nuclear Energy Corporation SOC Ltd. (Necsa), P.O. Box 582, Pretoria 0001, South Africa

B. van Brecht
Department of Chemistry South Campus, Nelson Mandela Metropolitan University, Port Elizabeth 6001, South Africa

P. Ramasami et al. (eds.), *Emerging Trends in Chemical Sciences*,
DOI 10.1007/978-3-319-60408-4_15

15.1 Introduction

Fluorine is one of the most reactive elements on the periodic table and reacts with almost all the elements, metals and non-metals alike [1]. The fluoride anion with its Ne electron configuration has the ability to form strong σ-bonds with numerous metal ions in their higher oxidation states [2]. In coordination chemistry, the halogens normally act as monodentate ligands [3]. Fluoride ions, however, are also well-known to form bridging compounds with the fluoride ion acting as a bridge between different metal centers. The bridging compounds can progress from isolated multinuclear compounds to three-dimensional, totally bridged compounds [4].

Industrially, the most important fluoride compound is HF, which is extensively used in the production of herbicides, high octane fuels, plastics, fluorescent light bulbs and in uranium conversion. It is also used in the production of refrigerants (CFCs) and fluoro-polymers such as the well-known commercial product polytetrafluoroethylene (PTFE), otherwise known as Teflon™ [5]. NaF is widely used in wood preservative and toothpaste manufacturing [6]. A more recent application of fluoride salts is their use in combination as coolants in molten salt nuclear reactors (MSR), which use thorium as nuclear fuel where LiF-ThF_4 is the molten salt. A combination LiF-NaF-KF [7] was evaluated in the intermediate cooling loops of these reactors due to their relatively low thermal neutron capture cross-sections, low melting (500 °C) and boiling points (1200 °C) and high heat transfer capacities. More recent fluoride salt combinations investigated in these reactors, namely, NaF:ZrF_4 (50-50%), NaF-KF-ZrF_4 (10-48-42%) and LiF-NaF-ZrF_4 (42-29-29%) [8], have proved to be non-toxic with low tritium yields while NaF-ZrF_4-UF_4 was used as a coolant in the so-called 'Aircraft Reactor Experiment' [9].

Zirconium fluoride compounds are mainly used as a grain refiner in metal and alloy production of iron, magnesium, steel and non-ferrous alloys. They are also used in the optical industry as fluorozirconate glass as coatings on lenses or as optical fibers, also known as ZBLAN glasses [10]. They can be used as a precursor for nuclear and non-nuclear grade zirconium metal production [11–14]. It is also used in fireworks production, the fireproofing of materials used in electric vacuum techniques, as well as in glass, enamel and ceramic production [15]. Anhydrous ZrF_4 is hygroscopic and three different crystalline phases have been reported, namely, the monoclinic α-phase [16], the tetragonal β-phase (P42/m space group) and finally the γ-phase with an unknown structure. At 400 °C, both the β- and the γ-phases irreversibly transform to the α-phase [17]. The geometry around the zirconium in ZrF_4 was reported as a square antiprism with each F atom bridging a pair of zirconium atoms forming a three-dimensional totally bridged compound [18]. Hydrated ZrF_4 compounds (mono- and trihydrates) have also been reported and structurally characterized. The $ZrF_4 \cdot 3H_2O$ [19] compound is described as a 3D structure having discrete dimeric $Zr_2F_8(H_2O)_6$ groups with the Zr atoms sharing a common F···F edge and which also form O - H···F and O–H···O hydrogen bonds

with a decahedron arrangement round the Zr atom. The terminal Zr-F bond distances were determined as 1.996–1.999 Å and that of the bridging Zr-F as 2.118–2.214 Å. The $ZrF_4{\cdot}H_2O$ [20] compound on the other hand forms polymeric chains. The Zr-F bond distances have been reported as 2.013–2.033 Å for the terminal bonds and 2.106–2.166 Å for the bridging bond distances. Numerous other ZrF_6^{2-} compounds and even ZrF_7^{3-} [21, 22] have also been isolated and structurally reported [23, 24].

The chemistry and industrial applications of hafnium on the other hand are not as well developed as those of Zr, mainly due to the difficulty in separation and the similarity in their chemistry [25]. The most common binary compounds of hafnium are hafnium oxide, hafnium carbide and hafnium halides [26]. A small number of Hf–F have been structurally characterized and include H_2HfF_6 [27], $[N(CH_3)_4]_2[HfF_6]$ [28], $[N(CH_3)_4]_2[HfF_4(H_2O)_2]$ [29], $(N_2C_4H_{14})_2[HfF_6]$ [30] and $(N_2C_6H_{18})_2[HfF_6]$ [31]. The similarity between the Zr and Hf fluoride structures is also evident from these results and the Hf complexes also exhibit single and bridged fluoridos with single Hf–F bond distances between 1.98–2.02 Å and bridging Hf–F bond distances between 2.14 and 2.17 Å [28].

Our interest in the Zr and Hf fluoride compounds stemmed from a need for water soluble metal (Zr/Hf) reference materials (RM) for analytical method development and validation for different Zr/Hf containing materials and minerals. It is a well-known fact that the chemistry of these two elements are almost identical [32] and most of the applications of Zr and Hf are not separated due to the identical nature of their chemical and physical properties. It is only in the nuclear industry where ultra-pure Zr metal [32] (max Hf content = 100 ppm) is required mainly due to the unacceptable high thermal capture properties of Hf. The ultimate aim of this project was the development of new and alternative hydrometallurgical separation processes for natural zircon and plasma dissociated zircon (PDZ) [33, 34].

The hygroscopic nature as well as the poor water solubility of ZrF_4 made it unsuitable for use as a RM. In the process of synthesizing a water soluble "in-house" RM, numerous mono-valent inorganic (alkali metals) and organic (ammonium type) cations were used to try and isolate $(Zr/Hf)F_6^{2-}$ anions [Eq. (15.1)].

$$(Zr/Hf)F_4 + nM^+F^- \xrightarrow{HF} M_n(Zr/Hf)F_{(4+n)} \tag{15.1}$$

where M = different monovalent cations ($M = K^+$, Rb^+, Cs^+, NH_4^+, $N(C_2H_5)_4^+$, PPh_4^+). A number of these structures were structurally characterized in the 1950–1970s, most probably with powder diffraction [35] and it was decided to revisit the ones that were successfully isolated to (i) ensure their correct molar mass/empirical formula for method validation purposes and (ii) to verify the coordination mode around the center cation. A total of nine different inorganic salts were isolated and the crystal structures for the different cations indicated the profound influence of the cation on the type and coordination of the metal fluorido bonds in these compounds, ranging from a combination of mono-, di- and tri-bridged and no bridging at all, depending on the size and type of cations used during the crystallization.

15.2 Experimental

15.2.1 Reagents and Equipment

Reagent grade zirconium tetrafluoride, hafnium tetrafluoride, potassium fluoride, cesium fluoride, rubidium fluoride, tetramethylammonium chloride, tetraethylammonium (TEA) chloride, tetrabutylammonium chloride, tetraphenylphosphonium chloride, and analytical grade 48% hydrofluoric acid were obtained from Sigma Aldrich. Experimental densities were determined using a Micromeritics AccuPyc II 1340 helium gas pycnometer. Zirconium analyses ($\lambda = 343.823$ nm) were performed with a Shimadzu ICPS-7510 sequential spectrometer and a Spectro Arcos EOP ICP-OES spectrometer. Cesium analyses ($\lambda = 455.5$ nm) were performed with an Agilent 7700cx ICP-MS while the potassium ($\lambda = 766.5$ nm) and rubidium (794.8 nm) analyses were performed using a Varian AA140 atomic absorption spectrometer. Ultra-pure water (0.04 mS/cm) was used in all cases.

15.2.2 Syntheses and Characterization of Zirconium /Hafnium Fluoride Compounds

Samples of between 0.1 and 1.7 g $(Zr/Hf)F_4$ were accurately weighed off to 0.1 mg, placed in plastic beakers and dissolved with the addition of 20.0 mL distilled water and 0.5 mL of 48% hydrofluoric acid. To each of the dissolved $(Zr/Hf)F_4$ samples, 2 or 3 equivalents of different fluoride salts (K^+, Cs^+, Rb, NH_4^+, $N(C_2H_5)_4^+$ and PPh_4^+) were added. Colorless, translucent crystals were obtained after several weeks. A summary of the experimental conditions and product characterization is reported in Table 15.1.

15.2.3 Crystallography

In all cases where crystallization took place, at least one well-formed crystal was selected and sent for crystallographic analysis. Of all the fluoride salts investigated, only potassium, cesium, rubidium, ammonium, tetraethyl ammonium and tetraphenylphosphonium yielded crystals suitable for structure determination.

X-ray diffraction (XRD) analysis was performed at the University of the Free State and Nelson Mandela Metropolitan University. The radiation source was a fine-focus sealed tube emitting molybdenum Kα radiation at a wavelength of 0.71073 nm with ω- and φ-scans at 100 K. The radiation monochromator was composed of graphite. A Bruker Kappa Apex II X-ray Crystallography System was used to collect the reflection data using SHELXL-97 [36]. Refinement was carried

Table 15.1 Experimental conditions and metal quantification results of the different isolated Zr/Hf compounds

Expected complex[a]	Cation donor	Mass of cation donor (g)	Mass of $(Zr/Hf)F_4$ (g)	% Zr in complex (theoretical %)	% Cation in complex (theoretical %)
K_2ZrF_6	KF	0.7	1.0	32.5(32.2)	27.6(27.6)
Rb_2ZrF_6	RbF	–	–	23.8(24.5)	44.1(45.4)
Cs_2ZrF_6	CsF	0.1	0.1	54.2(56.4)	19.4(19.3)
$(NH_4)_2ZrF_6$	NH_4F	0.5	1.0	26.5(25.8)	–
(TEA) $ZrF_5 \cdot H_2O$	$(N(C_2H_5)_4)F$	0.2	0.1	24.9(27.9)	–
K_2HfF_6	KF	1.7	1.0	47.9(48.1)	21.0(21.1)
Rb_2HfF_6	RbF	0.2	0.1	37.7(38.5)	36.1(36.9)
Cs_2HfF_6	CsF	0.15	0.1	32.6(32.0)	48.6(47.6)
$(PPh_4)_2[HfF_6] \cdot 2H_2O$	$PPh_4Cl/NH_4F \cdot HF$	0.1	0.05	17.2(16.9)	–

[a]0.5 mL 48% HF added to all solutions

out using F^2 against all reflections while the weighted R-factor wR and goodness of fit S were based on F^2. Conventional R-factors were based on F, with F set to zero for negative F^2. The threshold expression of $F^2 > 2\sigma(F^2)$ was used only for calculating R-factors. All cell refinements were done using SAINT-Plus and data reduction with SAINT-Plus and XPREP [37]. To correct the absorption effects, the multi-scan technique and software package SADABS [38] was used. The crystal structure was solved by the direct method package SIR-97 [39] and refined with the aid of WinGX [40]. The graphical representation of the crystal structure was obtained with the program DIAMOND [41] and the structures were drawn at 50% probability level. The crystal structures were solved by direct methods using SHELXTL [38]. Non hydrogen atoms were refined anisotropically, while the methyl and aromatic hydrogen atoms were placed in geometrically idealized positions (C–H = 0.95–0.98 Å) and constrained to ride on their parent atoms ($U_{iso}(H) = 1.5U_{eq}(C)$ and $1.2U_{eq}(C)$). The most important crystallographic data are reported in Tables 15.2 and 15.3.

15.3 Discussion of Results

The crystallography of many of these inorganic salts was challenging due to the inherent symmetry and special positions possible for the atoms present in the structure and in some cases several space groups were evaluated for correctness. Eventually only two of the structures with carbon atoms present in the cation, namely $(PPh_4)_2[HfF_6] \cdot 2H_2O$ (CCDC 1443802) and $(N(C_2H_5)_4)[ZrF_5] \cdot H_2O$ (CCDC 1444148) were successfully deposited at the Cambridge data center. Little doubt

Table 15.2. Summary of crystallographic data and refinement parameters for five different zirconium compounds

Chemical formula		K_2ZrF_6	Rb_2ZrF_6	Cs_2ZrF_6	$C_{16}H_{44}N_2OZr_2F_{10}$	$N_2H_{10}OZrF_6$
Compound name		Potassium di-μ-fluorido-tetrafluoridozirconate (IV)	Rubidium hexafluorido zirconate(IV)	Cesium hexafluorido zirconate(IV)	Tetraethyl ammonium di-μ-fluorido-bis-(trifluoridozirconate(IV)) monohydrate	Ammonium mono-μ-fluorido-tris-μ-fluorido bis-tetrafluoridozirconate(IV) monohydrate
Formula weight		283.42	376.16	471.04	652.97	233.24
Temperature (K)		293(2)	293(2)	293(2)	200(2)	200(2)
Wavelength Mo K_α (nm)		0.71073	0.71073	0.71073	0.71073	0.71073
Crystal system		Monoclinic	Trigonal	Trigonal	Monoclinic	Orthorhombic
Space group		C2/c	P3-m1	P3-m1	C2/c	Pca21
Cell lengths (Å)	a	6.543(5)	6.1169(6)	6.3862(3)	15.8130(4)	13.3330(4)
	b	11.359(5)	6.1169(6)	6.3862(3)	12.3456(3)	7.6871(2)
	c	6.926(5)	4.7778(5)	4.9833(3)	13.4704(4)	11.6613(3)
Cell angles (°)	α	90.0	90.0	90.0	90.0	90.0
	β	90.774(5)	90.0	90.0	109.4660(10)	90.0
	γ	90.0	120.0	120.0	90.0	90.0
Cell volume ($Å^3$)		514.7(6)	154.82(3)	176.01	2479.39	1195.19(6)
Z		4	1	1	4	8
Theoretical density (g/cm^3)		3.657	4.035	4.444	1.749	2.592
Measured density (g/cm^3)		3.68(3)	3.998	4.226(3)	–	
Crystal size (nm^3)		0.445 × 0.192 × 0.137	0.200 × 0.135x0.122	0.217 × 0.127 × 0.106	0.312 × 0.115 × 0.089	0.354 × 0.192 × 0.137
Absorption coefficient		3.792	17.426	11.783	0.926	0.782
F(000)		528	168	1601	1328	864

Theta range for data collection (°)		3.59 to 27.97	3.846 to 28.337	3.684 to 28.200	2.39 to 28.31	2.650 to 28.322
Index ranges		$-8 \geq h \geq 7$	$-8 \geq h \geq 8$	$-8 \geq h \geq 7$	$-21 \geq h \geq 21$	$-17 \geq h \geq 17$
		$-14 \geq k \geq 12$	$-8 \geq k \geq 8$	$-8 \geq k \geq 8$	$-14 \geq k \geq 16$	$-10 \geq k \geq 10$
		$-9 \geq l \geq 9$	$-6 \geq l \geq 6$	$-6 \geq l \geq 6$	$-17 \geq l \geq 13$	$-15 \geq l \geq 15$
Reflections collected		1194	163	184	3090	2980
Independent reflections		1172[R(int) = 0.0209]	163[R (int) = 0.0227]	184[R (int) = 0.0227]	2774[R(int) = 0.0152]	2897
Refinement method		SHELXL-97	SHELXL-97	SHELXL-97	SHELXL-97	SHELXL-97
Data/Restraints/ Parameters		1172/2/66	163/0/13	169/0/13	2774/0/144	2897/1/164
Goodness of fit on F^2		1.125	1.166	1.266	1.042	1.227
Final R indices [$I \geq 2\sigma(I)$]		$R_1 = 0.0302$ $wR_2 = 0.0775$	$R_1 = 0.0502$ $wR_2 = 0.1239$	$R_1 = 0.0111$ $wR_2 = 0.0269$	$R_1 = 0.0162$ $wR_2 = 0.0454$	$R_1 = 0.0320$ $wR_2 = 0.0830$
R indices (all data)		$R_1 = 0.0306$ $wR_2 = 0.077$	$R_1 = 0.0502$ $wR_2 = 0.1239$	$R_1 = 0.0495$ $wR_2 = 0.1345$	$R_1 = 0.0197$ $wR_2 = 0.0475$	$R_1 = 0.0329$ $wR_2 = 0.0835$

Table 15.3 Summary of crystallographic data and refinement parameters for four different hafnium compounds

Chemical formula		K_2HfF_6	Rb_2HfF_6	Cs_2HfF_6	$(PPh_4)_2[HfF_6]\cdot 2H_2O$
Compound name		Potassium di-μ-fluorido-bis-tetrafluoridohafnatate(IV)	Rubidium di-μ-fluorido-bis-tetrafluoridohafnatate(IV)	Cesium hexafluorido hafnatate(IV)	Tetraphenylphosphonium hexafluoridohafnatate(IV). dihydrate
Formula weight		370.69	1762.25	558.31	1058.26
Temperature (K)		293(2)	293(2)	293(2)	293(2)
Wavelength Mo K_α		0.71073	0.71073	0.71073	0.71073
Crystal system		Orthorhombic	Monoclinic	Trigonal	Triclinic
Space group		Cmcm	C2/c	P3-m1	P-1
Cell lengths (Å)	a	6.5459(7)	21.4921(4)	6.3482(9)	10.0723(5)
	b	11.3836(12)	6.5616(1)	6.3482(9)	11.0591(6)
	c	6.8580(7)	16.0741(4)	4.9779(6)	21.1870(10)
Cell angles (°)	α	90.0	90.0	90.0	75.749(2)
	β	90.0	101.590(1)	90.0	77.842(2)
	γ	90.0	90.0	120.0	71.111(2)
Cell volume ($Å^3$)		511.03(9)	154.82(3)	173.75	2142.06(19)
Z		4	4	1	2
Theoretical density (g/cm^3)		4.818	4.668	5.336	1.641
Measured density (g/cm^3)		4.79	4.2	5.1	1.61
Crystal size (nm^3)		0.367 × 0.201 × 0.200	0.182 × 0.205 × 0.155	0.222 × 0.135 × 0.111	0.255 × 0225 × 0.187
Absorption coefficient		22.080	29.710	25.366	2.582
F(000)		656	2684	236	1054
Theta range for data collection (°)		3.58 to 28.23	2.587 to 28.326	3.706 to 25.242	2.48 to 28.30

Index ranges		$-8 \geq h \geq 8$	$-28 \geq h \geq 20$	$-8 \geq h \geq 7$	$-12 \geq h \geq 13$
		$-14 \geq k \geq 15$	$-8 \geq k \geq 8$	$-8 \geq k \geq 8$	$-13 \geq k \geq 14$
		$-8 \geq l \geq 9$	$-21 \geq l \geq 21$	$-6 \geq l \geq 6$	$-25 \geq l \geq 28$
Reflections collected			2756	236	38437
Independent reflections		1172 [R(int) = 0.0209]	2684 [R(int) = 0.0227]	184 [R(int) = 0.0227]	10553 [R(int) = 0.0152]
Refinement method		SHELXL-97	SHELXL-97	SHELXL-97	SHELXL-97
Data / Restraints / Parameters		370/0/30	2756/0/152	184/0/13	10553/6/548
Goodness of fit on F^2		1.265	1.082	1.295	1.075
Final R indices [$I \geq 2\sigma(I)$]		$R_1 = 0.0301$ $wR_2 = 0.0831$	$R_1 = 0.1817$ $wR_2 = 0.3964$	$R_1 = 0.0911$ $wR_2 = 0.2027$	$R_1 = 0.0152$ $wR_2 = 0.0401$
R indices (all data)		$R_1 = 0.0301$ $wR_2 = 0.0831$	$R_1 = 0.1914$ $wR_2 = 0.3997$	$R_1 = 0.0911$ $wR_2 = 0.2033$	$R_1 = 0.0165$ $wR_2 = 0.0401$

exists about the final structures and the coordination (chemistry) around the central metal in all the other inorganic structures and their inclusion and discussion in this paper is considered as be vital to demonstrate the influence of the different cations on the type and number of fluoride coordination in these complexes.

15.3.1 Syntheses of the Different Zirconium/Hafnium Fluorido Complexes

The zirconium/hafnium tetrafluoride salts were used as starting materials in the syntheses of all the different compounds according to the overall reaction as indicated in Eq. (15.1). The addition of HF not only assisted with the dissolution of the MF_4 compounds, but it also acted as an additional source of fluoride ions to ensure the formation of the highly soluble $(Zr/Hf)F_6^{2-}$ anions. The Li^+ and Na^+ salts only yielded white/colorless powders in this study; however, the Li^+ structure was reported in 1969 [42] and 1985 [43] while the Na^+ structure again in 2013 [44]. The analytical analysis of the metal content in the different salts are reported in Table 15.1. It is clear from these excellent metal recoveries that any of the isolated salts can be used as a primary RM in the analytical method development process. The metal recoveries, which ranged between 98 and 100%, indicated that the salts were pure, the correct empirical/molecular masses were used in the calculations (from the structure elucidations), the salts represented relatively simple elemental matrices, and all were very soluble in water or slightly acidic media.

15.3.2 Crystal Structures of the Different Zirconium Fluorido Complexes

15.3.2.1 Crystal Structure of Potassium di-μ-fluorido-tetrafluoridozirconate(IV), K_2ZrF_6

K_2ZrF_6 crystallized in the monoclinic space group C2/c with 4 molecules per unit cell, similar to the space group reported in 1976 [44, 45]. The most important bond lengths and angles of the ZrF_6^{2-} anion are listed in Table 15.4, while the numbering scheme is presented in Fig. 15.1. The anion consists of a long polymeric chain with four monodentate (terminal) and four bridged Zr-F surrounding the zirconium atom, totalling with a coordination number of eight. The results clearly show a difference between the monodentate and the bridging bond distances with the bond distances varying between 2.030(4) and 2.079(4) Å for the monodentate bonds while that for the bridging Zr-F bond varies between 2.140(4) and 2.194(4) Å. The K⋯⋯F interactions vary between 2.623(4) and 3.002(4)Å. The cis F-Zr-F bond angles vary between 66.7(2) and 79.0(1)° and the *trans* bond angles between 139.5(1) and 145.2(1)°. Coordination around the zirconium is a twisted

Table 15.4 Selected bond/contact distances and angles in the different zirconium compounds

Compound									
K_2ZrF_6		Rb_2ZrF_6		Cs_2ZrF_6		$(N(C_2H_5)_4)[ZrF_5]\cdot H_2O$		$(NH_4)_2[ZrF_6]\cdot H_2O$	
Bond	Distance (Å)	Bond	Distance (Å)	Bond	Distance (Å)	Bond	Distance (Å)	Bond	Distance (Å)
Zr1-F1	2.030(4)	Zr1-F1	1.997(3)	Zr1-F1	2.001(1)	Zr1-F11	1.9785(9)	Zr1-F14	2.025(4)
Zr1-F2	2.140(4)	Rb1---F1	2.883(3)	Cs1---F1	3.2275(2)	Zr1-F12	1.9632(8)	Zr1-F12	2.067(4)
Zr1-F3	2.079(4)	Rb1---F1′	3.0848(6)	Cs1---F1′	3.322(1)	Zr1-F13	2.1401(9)	Zr1-F13	2.037(4)
Zr1-F2	2.194(4)	Rb1---F1″	3.177(4)	Cs1---F1″	3.091(1)	Zr1-F15	1.9652(8)	Zr1-F15	2.030(4)
Zr1-F2	2.060(3)	Zr---Rb	3.8303(6)	Zr---Cs	3.995(3)	Zr1-F31	2.1564(9)	Zr1-F2	2.133(3)
Zr1-F4	2.154(4)					Zr1-F13′	2.1605(7)	Zr1-F11	2.136(3)
Zr1-F4	2.194(4)					Zr1-F31′	2.1351(8)	Zr1-F1	2.187(4)
Zr1-F6	2.078(4)					N1-C11	1.513(2)	Zr1-F3	2.325(4)
Zr1-F5	2.060(3)					N1-C13	1.516(2)	Zr2-F22	2.023(4)
K1---F1	2.712(4)					N1-C15	1.517(2)	Zr2-F21	2.029(4)
K1---F3	2.787(4)					N1-C17	1.517(2)	Zr2-F23	2.032(4)
K1---F1	2.924(4)					C11-C12	1.507(2)	Zr2-F24	2.063(4)
K1---F2	2.756(4)							Zr2-F3	2.114(4)
K2---F2	3.002(4)							Zr2-F11	2.139(3)
K2---F3	2.679(4)							Zr2-F1	2.218(4)
K4---F2	2.796(5)							Zr2-F2	2.303(3)
K2---F2	2.623(4)								
Zr1---K1	3.776(1)								

(continued)

Table 15.4 (continued)

Bond	Angle (°)	Bond	Angle (°)	Bond	Angle (°)	Bond	Angle (°)	Bond	Angle (°)
F1-Zr-F2	74.0(1)	F1-Zr-F1′	180.0	F1-Zr-F1′	180.0(2)	F11-Zr1-F12	95.29(4)	F14-Zr1-F15	88.6(2)
F1-Zr-F3	73.4(1)	F1-Zr-F1″	87.06(14)	F1-Zr-F1″	87.4(2)	F11-Zr1-F13	88.40(4)	F14-Zr1-F13	97.7(2)
F3-Zr-F2	78.6(1)	F1-Zr-F1‴	92.94(14)	F1-Zr-F1‴	92.5(2)	F11-Zr1-F15	173.47(4)	F15-Zr1-F13	152.7(2)
F1-Zr-F5	139.5(1)	Zr-F1-Rb(1)	163.33(17)	Zr-F1-Cs(1)	164.2(2)	F11-Zr1-F31	87.37(4)	F14-Zr1-F12	151.5(2)
F1-Zr-F6	145.2(1)	Zr-F1-Rb(2)	95.44(5)	Zr-F1-Cs(2)	93.8(1)	F12-Zr1-F13	77.35(3)	F13-Zr1-F12	84.3(2)
F2-Zr-F3	79.0(1)	Zr-F1-Rb(3)	92.68(13)	Zr-F1-Cs(3)	96.8(2)	F12-Zr1-F15	91.03(4)	F14-Zr1-F2	134.8(1)
F4-Zr-F2	66.7(2)					F12-Zr1-F31	77.79(3)	F15-Zr1-F2	109.1(2)
F5-Zr-F2	73.6(1)					F13-Zr1-F15	85.43(3)	F13-Zr1-F2	85.0(2)
F6-Zr-F2	76.1(1)					F13-Zr1-F31	72.97(3)	F14-Zr1-F11	75.2(2)
F3-Zr-F4	76.9(1)					F15-Zr1-F31	86.54(3)	F15-Zr1-F11	79.8(2)
F3-Zr-F2	145.1(1)					Zr1-F13-Zr2	113.93(4)	F13-Zr1-F11	76.3(2)
F3-Zr-F6	74.7(1)					Zr1-F31-Zr2	113.64(4)	F12-Zr1-F11	77.7(2)
F4-Zr-F5	73.3(1)					C11-N1-C13	110.7(1)	F2-Zr1-F11	147.1(2)
F4-Zr-F6	77.2(1)					C11-N1-C15	106.3(1)	F14-Zr1-F1	81.0(2)
F5-Zr-F6	75.0(1)					C11-N1-C17	111.5(1)	F15-Zr1-F1	72.4(2)
Zr-F1-K2	122.7(1)					C13-N1-C17	105.7(1)	F13-Zr1-F1	134.7(2)
						C15-N1-C17	111.2(1)	F12-Zr1-F1	117.4(2)
						N1-C11-C12	115.7(2)	F2-Zr1-F1	66.6(2)
						N1-C13-C14	114.8(1)	F14-Zr1-F3	72.4(2)
								F15-Zr1-F3	134.6(2)
								F13-Zr1-F3	72.2(2)
								F12-Zr1-F3	134.1(2)
								F2-Zr1-F3	65.7(2)
								F11-Zr1-F3	130.5(2)
								F1-Zr1-F3	64.3(1)
								Zr1-F11-Zr2	177.1(4)

								F23-Zr2-Zr1	105.4(1)
								F24-Zr2-Zr1	113.9(1)
								F11-Zr2-Zr1	168.3(2)
								F2-Zr2-Zr1	37.08(9)
								Zr1-F1-Zr2	103.4(2)

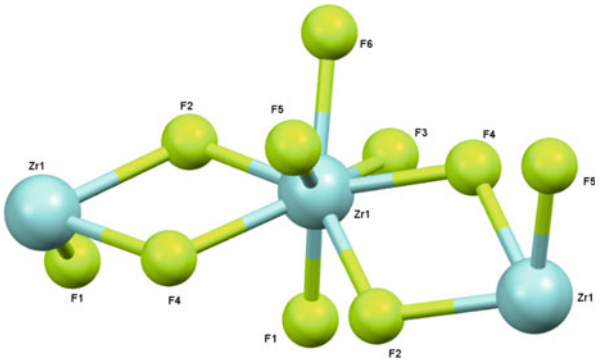

Fig. 15.1 Perspective view of the anion in potassium di-μ-fluorido-tetrafluoridozirconate (IV) with atomic labelling scheme

dodecahedron while that around the potassium is an irregular polyhedron. These results corroborate those obtained for the same structure, which was isolated using ZrO_2 [46] as starting material as well as in $K_2[Ni(H_2O)_6][ZrF_6]_2$ [47].

15.3.2.2 Crystal Structure of Rubidium Hexafluorido Zirconate(IV), Rb_2ZrF_6

This salt crystallizes in the trigonal space group P3-m1 with one molecule in the unit cell. The most important bond lengths and angles of the ZrF_6^{2-} anion are listed in Table 15.4 while the numbering scheme is presented in Fig. 15.2. The zirconium and the rubidium atoms are situated in special positions in the crystal lattice and the space group requires the placement of only one fluoride atom. The zirconium atom is octahedrally surrounded by six fluoride atoms with Zr-F bond length of 1.997 (3) Å while the *cis* F-Zr-F bond angles vary between 87 and 92° and the *trans* F-Zr-F bond angle is equal to 180°. Interestingly, the Zr fluoride complexes that are isolated from a combination of Rb^+ and NH_4^+ as cations [48] yield a polymeric Zr structure where the Zr atoms are connected via alternating mono- and tri-fluorido bridged bonds to produce the polyhedral, which has a dicapped trigonal prism around one Zr atom and an intermediate between a dicapped trigonal prism and a dodecahedron. The terminal Zr-F bond distances vary between 2.0208(7) and 2.3487(8) Å and bridging metal fluorido bonds vary between 2.0137(7) and 2.2172(7) Å.

15.3.2.3 Crystal Structure of Cesium Hexafluorido Zirconate(IV), Cs_2ZrF_6

The title compound also crystallizes in the trigonal space group P3-m1 (as for Rb_2ZrF_6 in the previous paragraph) with only one molecule in the unit cell. The most important bond lengths and angles of the ZrF_6^{2-} anion are listed in Table 15.4 while the numbering scheme is presented in Fig. 15.3. The zirconium lies at a

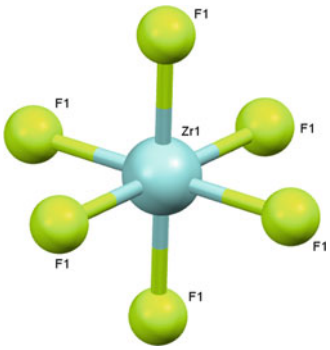

Fig. 15.2 Perspective view of the anion in rubidium hexafluorido zirconate (IV) with atomic labelling

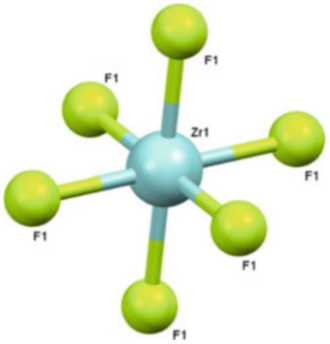

Fig. 15.3 Perspective view of the anion in cesium hexafluorido zirconate (IV) with atomic labelling

special position, which requires the placement of only one fluoride ion. The zirconium atom is octahedrally surrounded by six monodentate fluorido ligands with a Zr-F bond distance equal to 2.001(1) Å. All the *cis* F-Zr-F bond angles deviate slightly from 90°. The Cs·····F interactions range between 3.091(1) and 3.322(1) Å and the Cs atom is surrounded by eleven F atoms. The same Zr octahedral geometry was observed in $Ag_2ZrF_6{\cdot}8NH_3$ and $Ag_2HfF_6{\cdot}8NH_3$ [49].

15.3.2.4 Crystal Structure of Tetraethyl ammonium di-μ-fluorido-bis-(trifluoridozirconate(IV)) monohydrate, $(N(C_2H_5)_4)[ZrF_5]H_2O$

The title complex crystallizes in the monoclinic space group C2/c with 4 molecules in the unit cell. The most important bond lengths and angles of the ZrF_5^- anion are listed in Table 15.4 while the numbering scheme is presented in Fig. 15.4. The anion in this case also exists as a polymeric chain with the zirconium atom surrounded by three monodentate fluorido anions and four bridged fluoride ligands, with a coordination number of seven. The monodentate Zr-F bond distances vary between 1.9632(8) and 1.9785(9) Å and the Zr-F bridging bonds between 2.1351 (8) and 2.1605(7) Å. The monodentate bonds, situated *trans* to each other, have a

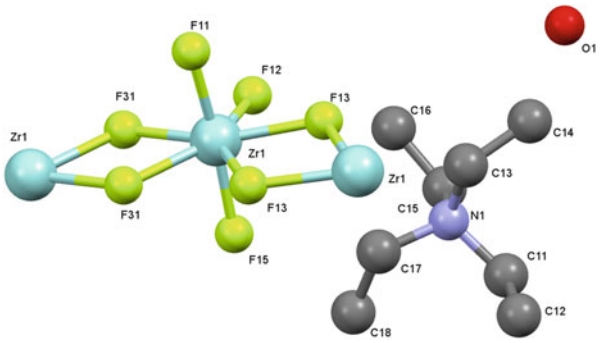

Fig. 15.4 Perspective view of the tetraethyl ammonium di-μ-fluorido-bis-(trifluoridozirconate(IV)) monohydrate indicating the polymeric chain structure

bond angle of 173.47(4)° while the *cis* bond angles vary between 85.43(3) and 95.29(4)°. The coordination polyhedron around the zirconium is pentagonal bipyramidal. Unexpectedly only one $N(C_2H_5)_4^+$ cation is associated with an anion unit, resulting in a 1:1 cation to anion ratio. The bond distances and angles in the $N(C_2H_5)_4^+$ cation are considered normal [50]. Hydrogen interactions exist between F13----H13A (2.667 Å), F15----H17B (2.497 Å), F12---H16A (2.911 Å) and O1---F11 (2.845 Å).

15.3.2.5 Crystal Structure of Ammonium mono-μ-fluorido-tris-μ-fluorido bis-tetrafluoridozirconate(IV) monohydrate, $(NH_4)_2[ZrF_6]\cdot H_2O$

The ammonium salt crystallizes in the orthorhombic space group Pca21 with eight molecules per unit cell. The most important bond lengths and angles of the ZrF_6^{2-} anion are listed in Table 15.4 while the numbering scheme is presented in Fig. 15.5. In this structure the Zr atom is surrounded by four monodentate fluorido ligands and four bridged fluorido ligands, with a coordination number of eight. Most interesting about this structure is the formation of a structure containing alternating single and triple bridged fluorido groups between the zirconium atoms. The monodentate Zr-F bond distances vary between 2.025(4) and 2.067(4) Å and 2.023(4) and 2.063(4) Å for the two different Zr atoms. The single bridged Zr-F bond distances are 2.136 (3) and 2.139(4) Å. The Zr-F bond distances on the side that contain the three bridged Zr-F bonds vary between 2.133(3) and 2.325(4) Å for the one Zr atom and between 2.114(4) and 2.303(2) Å for the other Zr atom. This Zr anion (ZrF_6^{2-}) configuration is identical to that obtained for the combination of Rb^+ and NH_4^+ as cations [51] and $(N_2H_6)_3M_2F_{13}$ [52]. Hydrogen interactions which exist between F15-----H11 equals to 2.179 Å, F21---H21 equals to 2.080 Å and finally, between F2----H31 equals to 2.326 Å.

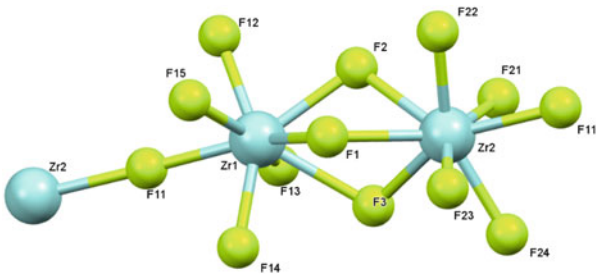

Fig. 15.5 Numbering scheme of the anion in mono-μ-fluorido-tris-μ-fluorido bis-(tetrafluoridozirconate (IV) monohydrate

15.3.3 Crystal Structures of the Different Hafnium Fluorido Complexes

15.3.3.1 Crystal Structure of Potassium di-μ-fluorido-bis-tetrafluoridohafnatate(IV), K_2HfF_6

The hafnium analogue of the potassium salt is identical to that of zirconium. K_2HfF_6 crystallizes in the orthorhombic space group Cmcm with 4 molecules per unit cell. The most important bond lengths and angles of the HfF_6^{2-} anion are listed in Table 15.5 while the numbering scheme is presented in Fig. 15.6. The anion also consists of long polymeric chains with four monodentate and four bridged Hf-F surrounding the hafnium atom, totaling a coordination number of eight. The bond distances between the monodentate and the bridging metal-fluorido ligands also vary with bond distances between 2.031(10) and 2.058(9) Å for the monodentate bonds while those for the bridging Hf-F bond vary between 2.108(9)and 2.184 (9) Å. The K⋯⋯F interactions vary between 2.708(8) and 3.351(2) Å. Coordination around the hafnium is a twisted dodecahedron while that around the potassium is an irregular polyhedron. The same Hf polyhedra were previously observed in K_2HfF_6 [27] and $(N(CH_3)_4)[HfF_5(H_2O)]$ [29], which also exhibited a 1:1 cation:anion ratio.

15.3.3.2 Crystal Structure of Rubidium Di-μ-fluorido-bis-tetrafluoridohafnatate(IV), Rb_2HfF_6

The similarity between the Zr and Hf structures is not continued with rubidium as cation. The rubidium salt crystallizes in the monoclinic space group C2/c with four molecules per unit cell. This structure is very similar to that of the potassium salt, except for the metal-F bridged bonds which are situated *cis* and *trans* in this structure, and not both *trans* as in the potassium salt. The most important bond lengths and angles of the HfF_6^{2-} anion are listed in Table 15.5 while the numbering scheme is presented in Fig. 15.7. The Hf-F terminal bond distances vary between 1.981(4) and 2.256(6) Å (*trans* to bridging metal-F bond) while the bridging Hf-F bond distances range between 2.112(4) and 2.201(4) Å. The bond angles between

Table 15.5 Selected bond/contact distances and angles in the different hafnium compounds

Compound							
K_2HfF_6		Rb_2HfF_6		Cs_2HfF_6		$(PPh_4)_2[HfF_6]\cdot 2H_2O$	
Bond	Distance (Å)	Bond	Distance (Å)	Bond	Distance (Å)	Bond	Distance (Å)
Hf - F1	2.058(9)	Hf-F1	2.112(4)	Hf1-F1	1.995(6)	Hf1-F1	1.9824(9)
Hf – F2	2.031(10)	Hf-F3	2.031(4)	Hf1-F1′	1.995(6)	Hf1-F4	1.9869(9)
Hf - F3	2.108(9)	Hf-F4	2.120(5)			Hf1-F6	1.9866(10)
Hf – F3	2.184(9)	Hf-F5	1.993(4)	Cs1---F1	3.079(6)	Hf1-F2	1.9938(9)
K1---F3	2.802(9)	Hf-F8	2.027(4)	Cs1---F1′	3.2085(10)	Hf1-F5	2.0036(9)
K1---F2	2.725(8)	Hf-F9	2.133(7)			Hf1-F3	2.0155(9)
K1---F1	2.708(8)	Hf-F10	1.990(4)			P1-C131	1.7936(15)
K1---F3	3.351(2)	Hf2-F1	2.201(4)			P1-C111	1.7933(15)
K2---K1	2.928(8)	Hf2-F2	2.111(5)			P1-C141	1.7956(16)
K1---F1	2.710(8)	Hf2-F4	2.184(5)			P1-C121	1.8047(15)
Hf1---K1	3.772(3)	Hf2-F6	1.989(5)			P2-C211	1.7905(15)
		Hf2-F7	1.977(4)			P2-C231	1.7915(16)
		Hf2-F11	2.256(6)			P2-C221	1.7950(15)
		Hf2-F12	1.981(4)			P2-C241	1.7975(15)
		Rb1---F1	2.891(4)				
Bond	Angle (°)	Bond	Angle (°)	Bond	Angle (°)	Bond	Angle (°)
F2-Hf-F1	73.5(4)	F1-Hf-F3	121.4(2)	F1-Hf-F1′	180.0(3)	F1-Hf1-F4	90.23(4)
F2′-Hf-F3	74.7(2)	F1-Hf-F4	68.2(2)	F1-Hf-F1″	87.5(3)	F1-Hf1-F6	90.59(4)
F2′-Hf-F1′	146.7(4)	F1-Hf-F5	119.1(2)	F1-Hf-F1‴	92.5(3)	F4-Hf1-F6	178.78(4)
F2′-Hf-F2	139.7(6)	F1-Hf-F8	76.7(2)	Hf-F1-Cs1	164.0(3)	F1-Hf1-F2	178.08(4)
F2-Hf-F3	95.44(11)	F1-Hf-F9	149.9(2)	Hf-F1′-Cs1	96.84(11)	F4-Hf1-F2	89.63(4)
F1-Hf-F3	77.2(2)	F1-Hf-F10	77.0(2)	Hf-F1″-Cs1	93.7(2)	F6-Hf1-F2	89.59(4)
F1-Hf-F3′	128.0(2)	F3-Hf-F4	75.8(2)			F1-Hf1-F5	91.41(3)

F3-Hf-F3′	66.0(4)	F3-Hf-F5	93.9(2)			F4-Hf1-F5	89.23(3)
Hf-F3-K3	109.1(3)	F3-Hf-F8	81.7(2)			F6-Hf1-F5	89.85(5)
		F3-Hf-F5	80.0(2)			F2-Hf1-F5	90.51(3)
		F3-Hf-F10	158.7(2)			F1-Hf1-F3	89.34(4)
		F4-Hf-F5	76.4(2)			F4-Hf1-F3	91.73(4)
		F4-Hf-F8	117.9(2)			F6-Hf1-F3	89.19(5)
		F4-Hf-F9	144.9(2)			F2-Hf1-F3	88.75(4)
		F4-Hf-F10	124.0(2)			F5-Hf1-F3	178.79(4)
		F5-Hf-F8	163.0(2)			C131-P1-C111	111.48(7)
		F5-Hf-F9	80.5(2)			C131-P1-C141	106.52(7)
		F5-Hf-F10	84.6(2)			C111-P1-C141	110.7(7)
		F8-Hf-F9	82.6(2)			C131-P1-C121	114.17(7)
		F8-Hf-F10	93.5(2)			C131-P1-C111	111.64(7)
		F9-Hf-F10	78.8(2)			C111-P1-C121	107.79(7)
		F1-Hf2-F2	72.7(2)			C141-P1-C121	109.24(7)
		F1-Hf2-F4	65.5(2)			C211-P2-C231	109.97(7)
		F1-Hf2-F6	138.4(2)			C211-P2-C221	110.83(7)
		F1-Hf2-F7	74.8(2)			C231-P2-C221	107.74(7)
		F1-Hf2-F11	136.6(2)			C211-P2-C241	109.88(7)
		F1-Hf2-F12	74.6(2)			C231-P1-C241	108.75(8)
						C221-P1-C241	109.62(7)

the two different sets of bridging metal-fluorido atoms range between 65.5(2) and 76.7(2)°.

15.3.3.3 Crystal Structure of Cesium Hexafluorido Hafnatate(IV), Cs_2HfF_6

In this structure, the similarity between the two metal ions is repeated with Cs_2HfF_6 also in the trigonal space group P3-m1 (as was Cs_2ZrF_6) with only one molecule in the unit cell. The most important bond lengths and angles of the HfF_6^{2-} anion are listed in Table 15.5 while the numbering scheme is presented in Fig. 15.8. The cesium and hafnium atoms lie on special positions, which again require the placement of only one fluoride ion. The hafnium is octahedrally surrounded by six monodentate fluorido ligands with a Hf-F bond distance equal to 1.995(6) Å, which is slightly shorter than the corresponding Zr-F bond distance. All the *cis* F-Hf-F bond angles deviate slightly from 90° while the *trans* F-Hf-F is 180.0(3)°. The Cs·····F interactions range between 3.079(6) and 3.2085(10) Å and the Cs atom is surrounded by eleven F atoms. The same octahedral orientation of fluorido ions around the Hf was observed in $[N(CH_3)_4]_2[HfF_6]$ and $(N_2C_6H_{18})_2[HfF_6]$ [31].

15.3.3.4 Crystal Structure of Tetraphenylphosphonium hexafluorido hafnatate(IV) dihydrate, $(PPh_4)_2HfF_6{\cdot}2H_2O$

This structure crystallizes in the triclinic space group P-1 with two moles per unit cell. The most important bond lengths and angles of the HfF_6^{2-} anion are listed in Table 15.5 while the numbering scheme is presented in Fig. 15.9. The hafnium atom is surrounded by six terminal bonded fluorido ligands (similar to the Cs structure) with Hf-F bond distances varying between 1.9824(9) and 2.0155(9) Å. The *cis* F-Hf-F bond angles vary between 88.75(4) and 91.73(4)° and the *trans* F-Hf-F bond angles between 178.08(4) and 178.79(4)°. The P-C bond distances as well as the C-P-C bond angles are considered normal [51, 53]. Hydrogen interactions exist between F2----H224 (2.751 Å), F6---H224 (2.607 Å), F5----H233 (2.461 Å) and F5---H12 (H_2O) (2.003 Å).

15.3.4 Comparison of Results

The beauty of the science in this study is not necessarily the individual structures themselves, but in a comparison of the different structures. The most important difference between this set of structures and those already reported in literature, is that all the current structures were synthesized according to the same reaction and isolated using different cations as per Eq. (15.1).

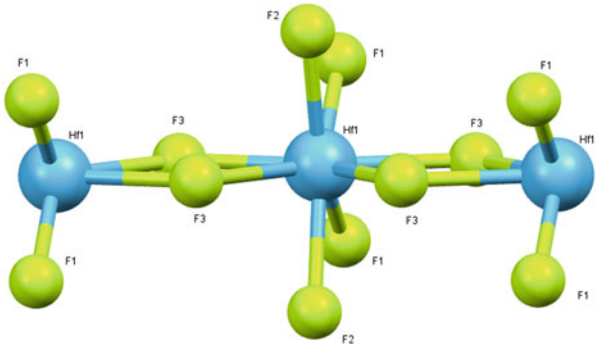

Fig. 15.6 Perspective view of the anion in potassium di-μ-fluorido-bis-tetrafluoridohafnatate (IV) with atomic labelling scheme

The metal tetrafluoride compounds were used as starting material in all cases and an excess of fluoride ions in the form of HF was added. The additional F^- ions reacted with the metal tetrafluoride compound and the metal expanded its coordination sphere to form the hexafluorido-metal anions. In theory it means that identical metal species are in solution prior to the addition of monovalent fluoride (M^+F^-) and therefore, one would expect to isolate only one type of anion from all the solutions, which is normally the case for transition metal complexes. And yet, a wide variety of metal-fluoride anions are isolated for the different cations, clearly suggesting that the cations play an important role in the final metal-fluorido coordination number and type. It is only the size and nature of the cation that differ in these structures with the alkali-metal cation radii ranging from 0.76 Å for Li to 1.67 Å for Cs^+ [54], 5 Å for $(N(C_2H_5)_4)^+$ [55], 1.43 Å for NH_4^+ [56] and 4.2 Å for PPh_4^+ [57]. The metal cations can be regarded as hard acids and the nitrogen or ammonium type cations as moderate acids. The results in Table 15.6 clearly highlight the differences and similarities of isolated structures [58].

Results obtained from the different structures suggest that polymerization between the different zirconium groups is more prevalent in the presence of the smaller cations, Na^+ [44] and K^+ (and most probably for Li^+) while the larger cations such as Rb^+ and Cs^+ prevent the formation of the fluorido bridged structures, which lead to the formation of the monomer structures. In this process, the smaller cations stimulate the formation of higher coordination numbers around the metal ion (eight in total) while the larger cations result in smaller coordination numbers (six in total). A possible explanation is that smaller cations do not prevent the formation of the polymer anions as the ZrF_6^{2-} concentration increases at the crystallization point and these smaller cations then fit in between the holes or layers that are formed by the long polymer chain. The larger cations can prevent the ZrF_6^{2-} ions from getting close enough to each other to form the polymer chains and hence resulting in the octahedral complexes. Another explanation is that the polymer structures are the main zirconium species that are formed when additional F^- ions are introduced into the solution. They remain unchanged during crystallization with the smaller cations filling the holes between the polymer chains. The

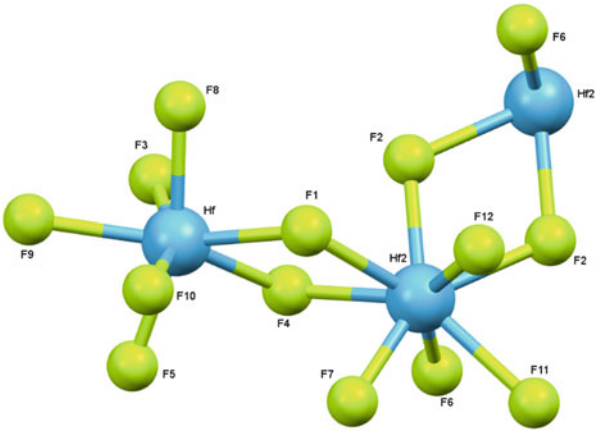

Fig. 15.7 Perspective view of the anion in rubidium di-μ-fluorido-bis-tetrafluoridohafnatate (IV) with atomic labelling scheme

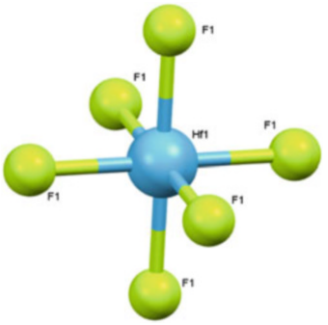

Fig. 15.8 Perspective view of the anion in cesium hexafluorido hafnatate (IV) with atomic labelling

larger cations, however, require larger spaces in the crystal lattice which force the polymer chains to break, resulting in the normal octahedral complex.

The ammonium-type of cations have a completely different influence on the type and coordination number in the zirconium structure. Ammonium as cation results in a change from a four *trans* fluorido-bridged molecule (2:2 orientation), observed in the K_2ZrF_6 structure, to four *trans* orientated bridged molecule with a 1:3 orientation. The tetraethyl ammonium cation results in the formation of the four *trans* fluorido-bridged molecule (2:2 orientation), but the cation:complex ratio changes to 1:1 cation:complex as compared to the 2:1 ratio observed for all the other isolated complexes, resulting in a coordination number of seven for the zirconium metal center. Interestingly, even the ZrF_6^{2-} anions associated with a combination of K^+ and NH_4^+ as cations ($K_{2-x}(NH_4)_xZrF_6$) [46] or double salts such as the $K_2[Ni(H_2O)_6][ZrF_6]$ result [47] in the formation of the 2:2 fluorido-bridged anion.

The same tendency is observed for the hafnium structures. The smaller alkali metal cations result in the 2:2 fluorido-bridged anion while the larger Cs^+ and PPh_4^+ cations lead to the isolation of the 6 coordinated octahedral HfF_6^{2-} anion. Interestingly the anion in $Ag_2Hf_6{\cdot}8NH_3$ [49] with an Ag^+ ionic radius of 1.02Å [59] also results in the 6-coordinated octahedral anion, suggesting the influence of the

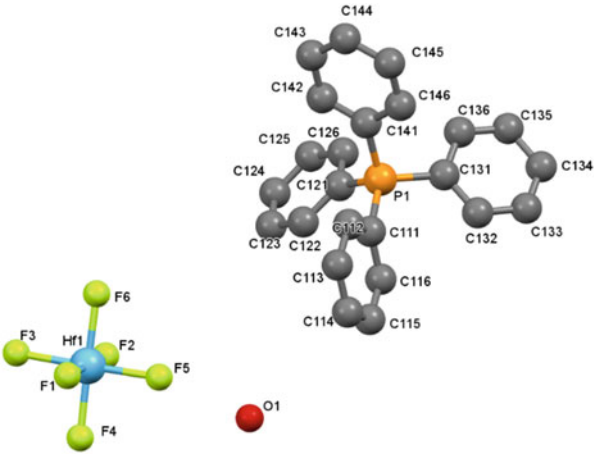

Fig. 15.9 Perspective view of tetraphenylphosphonium hexafluorido hafnatate (IV) compound with atomic labelling (showing only one cation and one crystal water)

additional molecules in the crystal lattice. However, the anion in the Rb^+ structure differs from the zirconium analogue, and in fact from the rest of the structures. The anion in this structure forms a 2:2 fluorido-bridged anion, contrary to the octahedral ZrF_6^{2-} anion, but interestingly the arrangement of the four bridging metal-fluorido bonds are now in 1:2 *trans* and 1:3 *cis* arrangement. The 1:3 *trans* fluorido-bridged anion is also observed for Hf in $(N_2H_6)_3[Hf_2F_{13}]$ [52] and $Rb_{2-x}(NH_4)_xZrF_6$ [48]. Research also indicates that divalent nitrogen containing ligands result in the formation of either 2:2 bridged or six coordinated monomers for Hf.

The chemical and physical properties of the F^- anion are the main reasons for these interesting results. The relatively small size of the F^- anion as well as its hard basic nature [60] allow the ligand to act as a monodentate ligand to metal centers. In the right chemical environment it can also bond via its other lone pair of electrons to metal centers, which are in close proximity and have vacant orbitals for chemical bonding to form bridged bonds between different metal centers, unless prevented or hindered by steric or electronic factors. The results obtained in this study clearly suggest that the cations (size and type) used to crystallize the Zr/Hf anion play a very important role in the type and the number of Zr/Hf-F bonds observed (CN 6, 7 and 8) in the solid state. Factors which may also play an important role are experimental conditions such as fluoride concentration and potentially temperature.

15.4 Conclusion

The reaction between $(Zr/Hf)F_4$ and different monovalent metal fluoride salts yielded unexpected and interesting results. Not only did the different cations influenced the coordination number, but also the number of single metal-F bonds as well as the number and type of bridged metal-F bonds in the different fluorido structures.

Table 15.6. Comparison of the different metal fluorido complexes

Compound	K/Zr	Rb/Zr	Cs/Zr	TEA/Zr	NH_4^+/Zr	K/Hf	Rb/Hf	Cs/Hf	PPh_4/Hf
Cation radius/Å	1.38	1.52	1.67	5	1.43	1.38	1.52	1.67	4.2
Cation:metal ratio	2:1	2:1	2:1	1:1	2:1	2:1	2:1	2:1	2:1
Terminal (Zr/Hf)-F bonds	4	6	6	3	4	4	4	6	6
Total number of (Zr/Hf)-F bonds[a]	8	6	6	7	7	8	8	6	8
Number of trans di-μ (Zr/Hf)-F-(Zr/Hf) bridging bonds	4	0	0	4	3	4	3	0	0
Number of cis di-μ (Zr/Hf)-F-(Zr/Hf) bridging bonds	0	0	0	0	3	0	3	0	0
Number of mono-μ (Zr/Hf)-F-(Zr/Hf) bridging bonds	0	0	0	0	0	0	0	0	0
Number of tri-μ (Zr/Hf)-F-(Zr/Hf) bridging bonds	0	0	0	0	0	3	0	0	0

[a]Include both terminal and bridging bonds

Acknowledgements The authors thank the Research Fund of this University, the NMMU and the National Research Foundation of the Republic of South Africa for financial support.

References

1. Chemistry Explained (2014) Fluorine. http://www.chemistryexplained.com/elements/C-K/Fluorine.html. Accessed 10 Nov 2014
2. Cotton FA, Wilkinson G (1976) Advanced inorganic chemistry, 3rd edn. Interscience Publishers, New York
3. Davis MF, Levason W, Reid G, Webster M (2006) Synthesis and characterisation of tin (IV) fluoride complexes of phosphine and arsine oxide ligands. Polyhedron 25:930–936
4. Wilkinson G, Gillard RD, McCleverty JA (1987) Comprehensive coordination chemistry: ligands, vol 2. Pergamon Press, Oxford
5. Standard Fluoromers PVT. Ltd (2014) Production process of PTFE polymer. http://www.standard-ptfe.com/production-process-of-ptfe.php. Accessed 8 Nov 2014
6. Chandler S (2014) Common uses of sodium fluoride. http://www.livestrong.com/article/344745-common-uses-of-sodium-fluoride/. Accessed 7 Nov 2014
7. World Nuclear Association (2016) Molten salt reactors. http://www.world-nuclear.org/information-library/current-and-future-generation/molten-salt-reactors.aspx. Accessed 16 July 2016
8. Forsberg CW (2004) Reactors with molten salts: options and missions. Oak Ridge National Laboratory, Oak Ridge
9. Bettis ES, Cottrell WB, Mann ER, Meem JL, Whitman GD (1957) The aircraft reactor experiment—operation. Nucl Sci Eng 2:841–853

10. MRS Research Group (2015) Global and Chinese zirconium fluoride (CAS 7783-64-4) market 2015 industry trends, analysis, overview, & forecasts 2020. http://www.mrsresearchgroup.com/market-analysis/global-and-chinese-zirconium-fluoride-cas-7783-64.html. Accessed 16 Mar 2016
11. Havenga JL, Nel JT (2010) The manufacturing of zirconium metal powder by means of a high temperature plasma process. 2010 I.E. International Conference on Plasma Sciences (ICOPS), 21-24 June 2010, Virginia
12. Retief WL, Nel JT, du Plessis W, Crouse PL, le Roux, JP (2010) Treatment of minerals. Patent application, PCT/IB2010/054067, 18 July 2012
13. Baroch CJ, Beyer GH (1956) Preparation of zirconium from zirconium tetrafluoride. Ames Laboratory ISC Technical Reports. Paper 127
14. American Elements (2014) Zirconium fluoride. http://www.americanelements.com/zrf.html. Accessed 5 Nov 2014
15. Amirthalingam V, Muralidharan KV (1964) X-ray crystallographic studies on β-ZrF_4. J Inorg Nucl Chem 26:2038–2039
16. Brown PL, Curti E, Grambow B, Ekberg C (2005) Chemical thermodynamics of zirconium. In: Mompean FJ, Perrone J, Illemassène M (eds) Chemical thermodynamics. Elsevier, Amsterdam
17. Burbank RD, Bensey FN (1956) The crystal structure of zirconium tetrafluoride. U.S. At. Energy Commission. Rep., K-1280. Union Carbide Nuclear Company, Oak Ridge
18. Voit EI, Didenko NA, Gayvoronskaya KA, Gerasimenko AV (2016) Structure of $ZnZrF_6 \cdot nH_2O$ (n = 6–2) and $ZnZrF_6$ crystallohydrates according to vibrational spectroscopy data. Opt Spectrosc. doi:10.1134/S0030400X16080233
19. Davidovich RL, Pushilin MA, Logvinova VB, Gerasimenko AV (2013) Crystal structure of monoclinic modifications of zirconium and hafnium tetrafluoride trihydrates. J Struct Chem 54:541–546
20. Kojić-Prodić B, Gabela F, Ružić-Toroš Ž, Šljukić M (1981) Structure of aquatetrafluorozirconium(IV). Acta Cryst B37:1963–1965
21. Hampson GC, Pauling L (1938) The structure of ammonium heptafluorozirconate and potassium heptafluorozirconate and the configuration of the heptafluorozirconate group. J Am Chem Soc 60:2702–2707
22. Meddar L, El-Ghozzi M, Avignant D (2008) New heptafluorozirconates and -hafnates $A^IB^{II}Zr(Hf)F_7$ (A^I = Rb, Tl; B^{II} = Ca, Cd)—synthesis, structures, and structural relationships. Z Anorg Allg Chem 634:565–570
23. Fischer J, Elchinger R, Weiss R (1967) Crystal structure of dicopper octafluorozirconate dodecahydrate, $Cu_2ZrF_8.12H_2O$. Chem Commun:329–330
24. Godneva MM, Motov DL, Boroznovskaya NN, Klimkin VM (2007) Synthesis of zirconium (hafnium) fluoride compounds and their X-ray luminescence properties. Russ J Inorg Chem 52:661–666
25. Blumenthal WB (1958) The chemical behavior of zirconium. D. van Nostrand Company, Inc., Princeton
26. Kirk-Othmer (1980) Encyclopedia of chemical technology, vol 12, 3rd edn. Wiley-Interscience Publication, Wiley, New York
27. Neumann C, Saalfeld H, Gerdau E, Guse W (2010) Crystal structure refinement of K_2HfF_6. Z Kristalogr Cryst Mater 175:159–164
28. Gerasimenko AV, Davidovich RL, Logvinova VB, Gaivoronskaya KA, Voit EI, Merkulov EB (2013) Synthesis and study of tetramethylammonium hexafluoridozirconate and hexafluoridohafnate solvated by $H_2O{\cdot}HF$ adducts and $[N(CH_3)_4]_2ZrF_6$. J Fluor Chem 149:42–52
29. Gerasimenko AV, Davidovich RL, Tkachev VV, Ng SW (2006) Bis(tetramethylammonium) di-μ-fluoro-bis[aquatetrafluorohafnate(IV)]. Acta Cryst E62:m196–m197

30. Tkachev VV, Atovmyan LO, Logvinova VB, Davidovich RL (1996) Hexamethylene-1,6-diammonium bis(μ_2-fluoro)-diaqua-octafluoro-dihafnium(IV) dehydrate. Koord Khim 22:831–834
31. Marsh RE, Spek AL (2001) Use of software to search for higher symmetry: space group C2. Acta Cryst B 57:800–805
32. ASTM B349/B349M—16 Standard specification for zirconium. https://www.astm.org/Standards/B349.htm. Accessed 5 Nov 2013
33. McPherson R, Rao R, Shafer BV (1985) The reassociation of plasma dissociated zircon. J Mater Sci 20:2597–2602
34. Havenga JL, Nel JT (2012) The manufacture of plasma-dissociated zircon (PDZ) via a non-transferred arc process utilizing three 150 kW DC plasma torches. J S Afr Inst Min Metall 112:497–500
35. ICSD. https://icsd.fiz-karlsruhe.de/search. Accessed 28 Jan 2016
36. Sheldrick GM (1997) SHELXL97 Program for the refinement of crystal structures. Germany
37. Bruker (2004) SAINT-Plus Version 7.12 (including XPREP). Bruker AXS Inc., Madison
38. Bruker (1998) SADABS Version 2004/1 Bruker AXS Inc Madison, Wisconsin
39. Altomare A, Burla MC, Camalli M, Cascarano GL, Giacovazzo C, Guagliardi A, Moliterni AGG, Polidori G, Spagna R (1999) SIR97: a new tool for crystal structure determination and refinement. J Appl Cryst 32:115–119
40. Farrugia LJ (1999) WinGX suite for small-molecule single-crystal crystallography. J Appl Cryst 32:837–838
41. Brandenburg K, Putz H (2006) Diamond, Release 3.Oe, Crystal Impact GbR, Bonn, Germany
42. Bode H, Teufer G (1956) Über strukturen von hexafluorozirkonaten und hexafluorohafnaten. Z Anorg Allg Chem 283:18–25
43. Almeida R, MacKenzie J (1985) Short range structures of fluoride glasses. J Phys Colloq 46:75–79
44. Brik MG, Srivastava AM (2013) First-principles calculations of the structural, electronic, optical and elastic properties of the new phosphors, Na_2ZrF_6 and K_2ZrF_6. Solid State Sci 24:30–35
45. Hoppe R, Mehlhorn B (1976) Die kristallstruktur von K_2ZrF_6. Z Anorg Allg Chem 425:200–208
46. Gerasimenko AV, Tkachenko IA, Kavun VY, Didenko NA, Sergienko VI (2006) Synthesis and complex investigation of potassium ammonium hexafluorozirconates: I. Synthesis and X-ray diffraction study of $K_{2-x}(NH_4)_xZrF_6$ ($0 < x < 2$) crystals. Russ J Inorg Chem 51:9–22
47. Oudahmane A, Mnaouer N, El-Ghozzi M, Avignant D (2011) Dipotassium hexaaquanickel (II) bis[hexafluoridozirconate(IV)]. Acta Cryst E 67:i6–i7
48. Gerasimenko AV, Kavun VY, Didenko NA, Slobodyuk AB, Uvarov NF, Sergienko VI (2007) Synthesis, structure, ion mobility, phase transitions and ion transport in rubidium ammonium hexafluorozirconates. Russ J Inorg Chem 52:713–726
49. Meng W, Kraus F (2008) Crystal structures of $Ag_2ZrF_6{\cdot}8NH_3$ and $Ag_2HfF_6{\cdot}8NH_3$ and their synthesis by the "reactive fluoride route" in liquid ammonia. Eur J Inorg Chem:3068–3074
50. Purcell W, Roodt A, Basson SS, Leipoldt JG (1990) The crystal structure of tetraethylammonium aquatetracyanooxorhenate(V). Trans Met Chem 15:239–241
51. Purcell W, Visser HG (2016) Evidence of unusually long metal–aqua interaction: the crystal structure of tetraphenylphosphonium rhenium(V) aquatetracyanonitrido monohydrate tri-terpyridine. J Chem Crystallogr 46:15–20
52. Rahten A, Leban I, Milićev S, Ëmva B (1990) Crystal structure and vibrational spectra of hydrazinium (2+) tri-μ-fluoro bis[pentafluorozirconate(IV)] fluoride and vibrational spectra of its hafnium analogue. J Crystallogr Spectr Res 20:9–15
53. Purcell W, Visser HG (2015) Rhenium(V)-nitrido complexes with different nitrogen donor bidentate ligands. Trans Met Chem 40:899–906
54. Chellan P, Sadler PJ (2015) The elements of life and medicines. Philos Trans A Math Phys Eng Sci 373:20140182

55. Buurman ET, Pennock J, Tempest DW, Teixeira de Mattos MJ, Neijssel OM (1989) Replacement of potassium ions by ammonium ions in different micro-organisms grown in potassium-limited chemostat culture. Arch Microbiol 152:58–63
56. Hoyles M, Krishnamurthy V, Siksik M, Chung S-H (2008) Brownian dynamics theory for predicting internal and external blockages of tetraethylammonium in the KcsA potassium channel. Biophys J 94:366–378
57. Schamberger J, Clarke RJ (2002) Hydrophobic ion hydration and the magnitude of the dipole potential. Biophys J 82:3081–3088
58. Ritter S (2003) Hard and soft acids and bases. Chem Eng News 81:50
59. HSAB Concept (2016) http://www.cyclopaedia.info/wiki/HSAB-concept. Accessed 18 Aug 2016
60. Marcus Y (1988) Ionic radii in aqueous solutions. Chem Rev 88:1475–1498

Chapter 16
Beneficiation of Niobium and Tantalum from Tantalite Ore Using Physical and Chemical Processes

M. Nete and W. Purcell

Abstract The extraction of niobium and tantalum from two tantalum-niobium ore materials obtained from Mozambique, using a combination of magnetic separation, acid leaching, solvent extraction and ion exchange methods was investigated. One sample consisted mainly of manganotantalite while the other of ferrotantalite. The magnetic separation procedure removed 61.8(2)% Fe_2O_3 and 46.4(4)% TiO_2 from the ferrotantalite and 8.9(3)% Fe_2O_3 and 8.8(7)% TiO_2 from manganotantalite. H_2SO_4 leaching removed 62.3(6)% U_3O_8 and 61.1(3)% ThO_2 from manganotantalite and 73.6(2)% U_3O_8 from ferrotantalite. Ammonium bifluoride dissolution and subsequent H_2SO_4 5-methyl-2-hexanone (MIAK) extraction proved to be the most efficient procedure for separation and isolation of a high purity tantalum oxide. The optimal conditions for Ta separation were 4.0 M H_2SO_4 aqueous solution and organic: aqueous ratio (O/A) = 1:1. Stripping was accomplished using double distilled water. Recoveries of 100.8(3)% Ta_2O_5 and 0.20(3)% Nb_2O_5 for manganotantalite, and 100.50(9)% Ta_2O_5 and 0.67(6)% Nb_2O_5 for ferrotantalite were obtained in the strip solutions. Nb was isolated from the mineral matrices using Dowex Marathon anion exchange resin. Recoveries of 100.2(4)% and 94.5(4)% Nb_2O_5 for manganotantalite and ferrotantalite samples respectively were obtained in the 6.0 M HCl elution, while the other elements were eluted with 4.0 M HCl. The entire process resulted in a total loss of approximately 13% for both Nb_2O_5 and Ta_2O_5 with approximately 96% purity for both metal oxides. Average recoveries of 97.8(7)% Ta_2O_5 and 1.4(6)% Nb_2O_5 were obtained in the Ta rich product while 0.8(4)% Ta_2O_5 and 94.4(5)% Nb_2O_5 were obtained in the Nb rich product.

Keywords Tantalite • Tantalum • Niobium • Separation • Analysis

M. Nete (✉)
Department of Chemistry, University of the Free State, Bloemfontein 9300, South Africa

The South African Nuclear Energy Corporation SOC Ltd. (Necsa), P.O. Box 582, Pretoria 0001, South Africa
e-mail: netem@ufs.ac.za

W. Purcell
Department of Chemistry, University of the Free State, Bloemfontein 9300, South Africa

P. Ramasami et al. (eds.), *Emerging Trends in Chemical Sciences*,
DOI 10.1007/978-3-319-60408-4_16

16.1 Introduction

Tantalum and niobium are extracted from a variety of minerals and concentrates. The major source of niobium and tantalum is columbite-tantalite, also called coltan, with a general chemical formula $(Fe,Mn)(Nb,Ta)_2O_6$. The two elements also exist in more than 150 other minerals and are usually present as complex metal oxides and hydroxides with the exception of behierite, where the elements are associated with borates $(Ta,Nb)(BO_4)$ [1]. These tantalum/niobium containing mineral deposits are widespread across the earth [2, 3], but many of the deposits contain small amounts of niobium and tantalum. Brazil and Australia have the largest high-grade niobium and tantalum resources and are therefore the major world producers of these metals, followed by Canada, Mozambique and Ethiopia.

The demand for Nb and Ta in various applications has increased steadily over the past two decades due to their importance in the production of modern industrial materials and high tech consumer products, ranging from super alloys to electronic devices such as cell phones [4]. About 75% of Nb is used in the ferro-niobium alloy by high-strength low-alloy steel manufacturers. Niobium improves the strength and reduces grain boundary deformation of the high-strength low-alloy steel, which is used for the manufacturing of vehicle bodies, railway tracks, ship hulls, and oil and gas pipelines. Niobium's low thermal neutron capture cross section makes it an attractive metal for nuclear power application where it is used with zirconium to produce zirconium alloys for nuclear reactors. Over 60% of the total global tantalum consumption is in electronic industry. Tantalum metal and Ta_2O_5, in relatively small amounts, are used in the manufacturing of cell phone capacitors [5]. Tantalum capacitors offer the highest capacitance density in the smallest possible size.

All Ta and Nb applications in industry are highly dependent on the purity of the final product [6]. Mineral beneficiation processes to separate and purify different metals from complex mineral matrices such as tantalite, are normally dictated by elemental composition, physical and chemical properties of the impurities as well as those of the target analyte(s) [7].

The first step in treating raw minerals includes the physical concentration of the minerals by means of gravity (high specific gravity/density of the minerals), electrostatic, and/or magnetic separation near the site of origin [8]. The initial chemical treatment step for the subsequent hydrometallurgical beneficiation process of many of the industrial extraction and refining processes uses a combination of HF and H_2SO_4 at elevated temperatures as dissolution step [9]. This process usually affords the complete dissolution of the mineral, which converts metal oxides to the Ta/Nb fluoride complexes with all the other elements (impurities) present in the mineral. One of the first processes that successfully separated and isolated Ta and Nb involved fractional crystallization of the K_2TaF_6 after HF dissolution of the minerals [10].

The second step involves filtration of the slurry, followed by separation processes involving solvent extraction using methyl isobutyl ketone (MIBK) [11–13], or ion exchange using an amine extractant in kerosene as solvent [14]. These processes produce Ta and Nb in high purity. Another method that is mainly used for the treatment of Ta/Nb/Ti/ rare earth elements (REE) concentrates, involves the mixing of the concentrate with coke, which is then passed through a chlorination process whereby most of the rare earths and Th are precipitated and the other main elements are converted to a mixture of Ta-Nb-Ti oxychloride gas. Temperature reduction of the gas results in the precipitation of Fe, the alkali metals and the rest of the Th [9]. Further cooling of the purified Ta/Nb oxychloride/chloride gas mixture leads to liquid formation and the two metal chloride complexes ($TaCl_5$/$NbCl_5$) are separated by fractional distillation. In the final step, the $NbCl_5$ reacts with steam to produce the hydroxides, which are then calcined to produce the metal oxide while the $TaCl_5$ reacts with NH_4OH to produce Ta_2O_5. A more elaborate beneficiation process was also proposed by Amuda et al. [15] for the treatment of Nigerian tantalum/niobium multi-ore mineral concentrations. Gupta and Suri [16] summarized different chemical processes for the treatment of pyrochlore using nitric acid, hydrochloric and hydrofluoric acid. Additionally Gupta and Suri [16] showed that columbite-tantalites can be fused with sodium carbonate, sodium hydroxide, potassium hydroxide, combinations of these alkaline fluxes, with the addition of sodium nitrate or sodium peroxide. Acid fluxes such as potassium hydrogen phosphate, sodium thiosulphate and potassium hydrogen bifluoride are mentioned.

Recent studies by Nete et al. [17] analytically followed the stepwise or individual separation process for different ferrotantalite minerals. The methodology behind the development and the monitoring of this process was to remove large amounts of impurities prior to the complete dissolution and beneficiation process. The effectiveness of each process or step was followed by a detailed chemical analysis of each fraction obtained in the process. The first step in the beneficiation process involved the magnetic removal of some of the impurities associated with minerals. Results obtained from this study revealed that more than 60% of each of Fe_2O_3 and TiO_2 were removed from a mineral sample with only 2% loss of Ta and Nb by magnetic separation [17]. The second step in the process involved the removal of radioactive compounds by acid leaching. This study indicated that more than 60% U_3O_8 and ThO_2 were leached from the tantalite using concentrated H_2SO_4 (3 h at 50 °C) with less than 5% loss of Nb_2O_5 and Ta_2O_5 [17]. The third step in the process explored the effectiveness of ammonium bifluoride as flux for the dissolution of a manganotantalite sample. Fourthly, the resulting solution was treated with MIAK as extractant at different acid concentrations and Ta was successfully separated (99%) from the Nb and rest of the impurities in solution [11]. The same study revealed that both Ta and Nb could be separated from the rest of the impurities using a weak anion exchange resin (Dowex Marathon).

The aim of the current study is to combine all the steps mentioned above as a total beneficiation process (magnetic separation, acid treatment, dissolution, solvent extraction and ion exchange) and to evaluate the total mineral beneficiation process on a step-by-step basis after the application of all the physical and chemical processes for the tantalite mineral samples (Fig. 16.1). Finally, the Ta and Nb

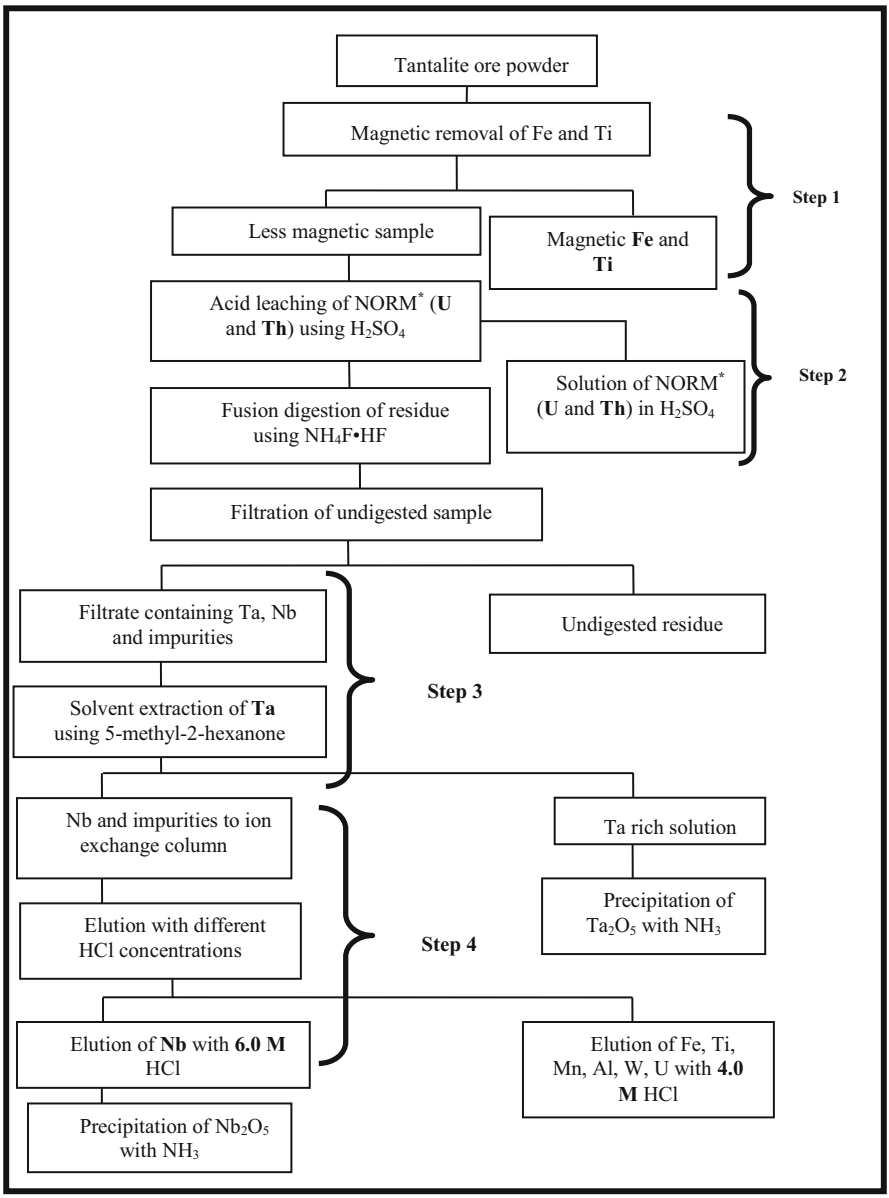

*NORM = Naturally Occurring Radioactive Materials

Fig. 16.1 Tantalite ore treatment scheme for the separation and purification of Nb and Ta

products are converted to the metal oxides and the purity of each product obtained during the process is evaluated.

16.2 Experimental

16.2.1 Reagents and Equipment

Two tantalite samples (manganotantalite and ferrotantalite) from Mozambique were supplied by the South African Nuclear Energy Corporation Limited (Necsa). The elemental compositions (as the oxides) of the two mineral ores were previously reported [18, 19] and are included in some of the tables to facilitate comparisons. Standard solutions containing 1000 mg/L Ta, Nb, Ti, Sn, W, Si as well as multi-element standard No. XXVI containing 1000 mg/L each of Mn, Al and Fe were bought from Merck. Standard solutions of 1000 mg/L Th and U were bought from De Bruyn Spectroscopic. High purity ammonium bifluoride ($NH_4F{\cdot}HF$) and MIAK were procured from Merck and used as received. A weakly basic anion exchanger Dowex Marathon (350–450 μm), was purchased from Sigma Aldrich. Analytical grade 32% HCl and 97% H_2SO_4 were bought from Associated Chemical Enterprises. Double distilled water was used in all experiments.

The mineral samples were received as coarse samples with particle sizes ranging from 0.1 mm to 5 mm. The samples were ground into a fine powder (maximum 250 μm particle size) using a vibratory disc mill in a closed steel milling vessel. Magnetic separations were accomplished using a weak magnetic field (variable electromagnet). Acid leaching experiments were performed on a Heidolph hot plate stirrer supplied by Labotec. Flux fusions were performed in a Thermo Scientific Thermolyne Compact Benchtop muffle furnace using a Pt crucible. Grade B glass and PTFE volumetric flasks purchased from Merck and Boeco SP series adjustable volume pipettes were used for sample preparations. Merck glass columns with an internal diameter of 1.2 cm were used for ion exchange separations. Centrifugation was performed in a centrifuge supplied by MSE. A Shimadzu ICPS-7510 ICP-OES (inductively coupled plasma optical emission) sequential plasma spectrometer was used for the elemental analysis of the sample solutions. Results are reported as the percentage metal oxides of the most stable oxidation state of the elements for comparison purposes. The average results for triplicate analyses are reported with standard deviations to indicate the uncertainty in the last digit of the value.

16.2.2 Separation and Analytical Procedures

16.2.2.1 Preparation of ICP-OES Calibration Solutions and Measurements

Appropriate volumes of the 1000 ppm metal stock and acid solutions were added in 100.0 mL volumetric flasks. A flux salt was melted and dissolved in double distilled water. A 5.0 mL melted flux solution was added to each standard solution and diluted to the mark with double distilled water to ensure matrix matching. Standard solutions with concentrations 1.0, 3.0, 5.0, 7.0, and 10.0 ppm were prepared. The blank solution was prepared by diluting 5.0 mL solution of fused flux and 10.0 mL 97% H_2SO_4 with double distilled water in a 100.0 mL volumetric flask. Quantitative analyses of the elements were performed at predetermined [18] spectral emission lines.

A set of calibration solutions of Nb and Ta ranging from 1.0 to 10.0 ppb as well as a blank solution were prepared in 10.0 mL 97% H_2SO_4 in 100.0 mL volumetric flasks for analysis of these elements by inductively coupled plasma-mass spectroscopy (ICP-MS). The operating ICP-OES and ICP-MS conditions in Table 16.1 were maintained throughout the study.

16.2.2.2 Magnetic Separation of Impurities from Tantalite (Step 1 in Fig. 16.1) [11]

Portions of 1.0 g of both ore samples were accurately weighed and spread over a smooth glass surface. The magnetic and non-magnetic particles were manually separated using an in-house electromagnetic device set at the magnetic field intensity of 43.8(6) mT. The separated magnetic and non-magnetic portions were

Table 16.1 Experimental operating conditions for ICP-OES and ICP-MS

	Value	
Parameter	ICP-OES	ICP-MS
RF power	1.2 kW	1.2 kW
Coolant gas flow	14.0 L/min	7.0 L/min
Plasma gas flow	1.2 L/min	1.50 L/min
Carrier gas flow	1.0 L/min	0.60 L/min
Sample uptake method	Peristaltic pump	Peristaltic pump
Sampling depth	–	5.0 mm
Spray chamber	Glass cyclonic spray chamber with concentric nebulizer	Glass cyclonic spray chamber with concentric nebulizer

weighed to determine the amount of mass lost during the separation process. The magnetic sample was digested by flux fusion using $NH_4F{\cdot}HF$ and dissolved with double distilled water [11, 20].

16.2.2.3 Acid Leaching of Radioactive Materials (Step 2 in Fig. 16.1)

The non-magnetic portions of the ore samples were quantitatively transferred to a 100 mL beaker and mixed with 10 mL volume of 97% H_2SO_4. The acid/ore mixture was stirred on a hot plate maintained at 50 °C for 3 h. The obtained ore slurry was centrifuged to separate the solids from the liquid. The supernatant liquid was separated from the residue by decantation and quantitatively transferred to a 100.0 mL volumetric flask, which was subsequently filled to the mark with double distilled water. The residual sample was washed with water and dried at 110 °C for 2 h.

16.2.2.4 Dissolution of Residual Ore Samples

The dried ore residues obtained in Step 2 of Fig. 16.1 of both samples were accurately weighed (to 0.1 mg) and quantitatively transferred to a platinum crucible for further digestion using $NH_4F{\cdot}HF$. The sample was homogeneously mixed with $NH_4F{\cdot}HF$ in a 1:20 sample:flux mass ratio and subsequently fused at 250 °C for 30 min. The melt was cooled to room temperature and dissolved in double distilled water. Visual inspection indicated that about 0.1% of the sample had remained undissolved. The undigested residue was filtered and washed with double distilled water. The filtrate was quantitatively transferred into a 100.0 mL PTFE volumetric flask and diluted to the mark with distilled water and was used for the solvent extraction and ion exchange separation processes in the following steps.

16.2.2.5 Solvent Extraction Separation of Nb and Ta in Mineral Samples (Step 3 in Fig. 16.1)

A 5.0 mL aliquot of the filtrate solutions obtained in the dissolution of residual ore samples was transferred to a glass-separating funnel and 5 mL of 8.0 M H_2SO_4 solution was added to this solution. The solution was extracted with two successive portions of 10.0 mL of MIAK. The niobium rich aqueous solution was collected in a 100 mL beaker for column separation in the following step. The organic phase was back extracted with two portions of 20 mL water. The water solutions were combined and quantitatively transferred to a 100.0 mL volumetric flask. The acidity of the solution was adjusted with H_2SO_4 to match the blank and the standard solutions matrices for ICP-OES analysis.

16.2.2.6 Ion Exchange Separation (Step 4 in Fig. 16.1)

The niobium containing aqueous solutions obtained in Step 3 were quantitatively transferred to a glass column of 1.2 cm internal diameter filled to 15 cm height with Dowex Marathon wba anion exchanger. Sequential elution of the metal ions in the mineral solution was carried out using 4.0 M and 6.0 M HCl at a flow rate of 1.7 mL/min. Fractions (60.0 mL) were collected and quantitatively transferred to 100.0 mL volumetric flasks.

16.2.2.7 Characterization of Ta and Nb Products

The Ta and Nb rich solutions of both mineral ore samples were divided into two portions each. Tantalum and niobium oxides were precipitated from their enriched solutions by addition of an excess of 25% ammonium hydroxide [10]. The precipitates were air dried and subsequently calcined to 900 °C to remove ammonium fluoride and any residual extractant, and to convert the formed hydrated tantalum oxide to the pentoxide. The identities of the tantalum products were evaluated by spectroscopy and comparing the obtained spectra to that of commercially pure pentoxide.

An excess of the KF solution was also added to the other portions of the Ta and Nb rich solutions for the possible crystallization of potassium fluorotantalate and fluoroniobate compounds such as K_2TaF_7 [10]. Solutions were allowed to stand for two days for the crystallization to occur. Crystals were successfully isolated in Ta solution and were separated from the mother solution by decantation. No precipitate was observed in Nb rich solution.

The concentrations of Ta and Nb in KF/Ta and the NH_3/(Ta, Nb) precipitates were determined by ICP-OES and ICP-MS. The white solid (Ta and Nb products) obtained after calcination, was accurately weighed (to 0.1 mg) and dissolved using $NH_4F{\cdot}HF$ flux fusion procedure [19, 21]. A visual inspection of the solution indicated that the entire sample had dissolved for both Nb and Ta products. The sample solutions were quantitatively transferred to 100.0 mL volumetric flasks and their acidity was adjusted accordingly with H_2SO_4 to match that of the blank and the standard solutions. Approximately 0.02 g of KF/Ta precipitate was accurately weighed (to 0.1 mg), dissolved in 10 mL of concentrated H_2SO_4 in a beaker and quantitatively transferred to a 100.0 mL volumetric flask. The solutions were allowed to cool down to ambient temperature and filled to the mark with double distilled water.

16.3 Results and Discussion

16.3.1 Removal of Impurities by Magnetic Separation and Acid Leaching (Steps 1 and 2)

Advantage was taken of the fact that the mineral ore samples displayed some degree of magnetic properties. Results (Tables 16.2 and 16.3 and Figs. 16.2 and 16.3) indicated that large amounts of Fe and Ti were successfully removed from the strongly magnetic portion of the finely powdered (maximum 250 μm particle size) ferrotantalite sample. Recoveries of 9.0(2)% Nb_2O_5, 8.6(3)% Ta_2O_5, 61.8(2)% Fe_2O_3 and 46.4(4)% TiO_2 were recorded in the magnetic portion of the ferrotantalite sample. Similar recoveries were obtained in the magnetic portion of manganotantalite with 8.2(3)% Nb_2O_5 and 9.2(5)% Ta_2O_5 (compared to ferrotantalite), but unexpectedly lower Fe and Ti (8.9(3)% Fe_2O_3, and 8.8(7)% TiO_2) recoveries. Metallic iron and many of its compounds are magnetic. However, magnetic properties are also affected by the chemical constituents in that particular

Table 16.2 Chemical composition of ferrotantalite after magnetic separation and acid leaching treatment

Analyte	% Expected [18, 19]	Magnetic portion	Acid leached	
			Filtrate	Residue
Ta_2O_5	29.2(2)	2.5(3)	0.08(1)	26.06(4)
Nb_2O_5	13.2(5)	1.2(2)	0.15(4)	10.5(4)
TiO_2	10.1(7)	4.7(8)	0.08(4)	6(1)
Mn_3O_4	3.9(3)	0.4(1)	0.13(4)	3.53(3)
Fe_2O_3	19.7(1)	12.2(2)	0.37(1)	9(1)
ThO_2	0.08(5)	0.01(2)	0.04(1)	0.06(1)
U_3O_8	0.20(3)	0.003(2)	0.15(2)	0.15(4)
WO_3	0.4(2)	0.01(1)	0.030(1)	0.30(6)

Table 16.3 Chemical composition of manganotantalite after magnetic separation and acid leaching treatment

Analyte	% Expected [18, 19]	Magnetic portion	Acid leached	
			Filtrate	Residue
Ta_2O_5	27.8(9)	2.6(5)	0.3(1)	24.5(1)
Nb_2O_5	27.1(5)	2.4(3)	1.2(2)	24.6(4)
TiO_2	2.6(1)	0.24(7)	0.12(2)	2.04(2)
Mn_3O_4	7.9(9)	0.7(4)	0.40(3)	6.85(1)
Fe_2O_3	7.7(9)	0.8(3)	0.74(9)	6.1(2)
ThO_2	0.40(8)	0.06(2)	0.33(1)	0.26(1)
U_3O_8	3.0(3)	0.3(2)	1.8(1)	0.97(2)
WO_3	1.9(2)	0.13(5)	0.10(1)	1.20(6)
SnO_2	1.5(3)	0.12(3)	0.040(9)	0.70(4)

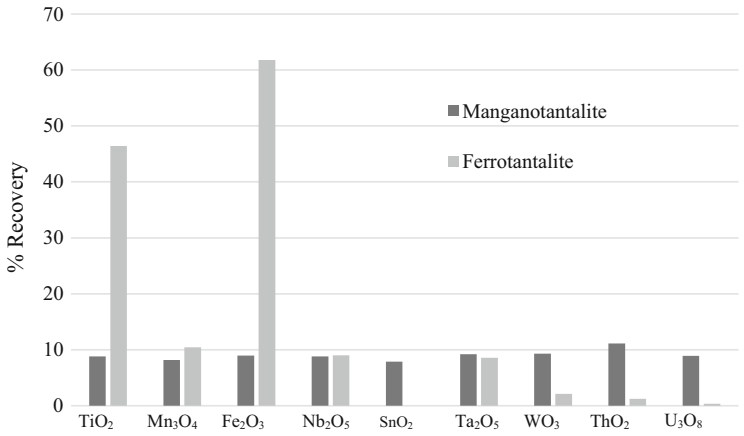

Fig. 16.2 Comparison of percentage recoveries of the elements in the magnetic portion of the tantalite minerals

material. Heck [20] indicated that manganese(II) oxide (MnO) and iron(II) oxide (FeO) are among the antiferromagnetic compounds. Interestingly, the Mn_3O_4 and Fe_2O_3 content (~8% in Table 16.3) in manganotantalite (Mn^{2+}, Fe^{2+}) (Ta, Nb)$_2O_6$ [22] are comparable while the same ratio differs with a factor of 5 (Table 16.2) in favor of Fe_2O_3 in the more magnetically inclined ferrotantalite. Additionally the magnetic separation indicates that the magnetism decreases as the ratio between the elements decreases. A possible explanation for this observation is that the Mn atoms (with the opposite electron spin orientation) cancel the magnetic moment of Fe atoms resulting in an overall antiferromagnetic or low magnetic state for the manganotantalite sample, while the same is not true for the ferrotantalite (less Mn and thus more magnetic properties). Another possible reason for the low Fe concentration in the magnetic portion of manganotantalite could be as a result of Fe originating from a different mineral host such as hematite non-magnetic iron mineral [23]. As previously proposed by Nete et al. [17] it is possible that removal of Ti by magnetic separation could be due to an insufficient liberation procedure. The possible existence of Ti in magnetic Fe-Ti minerals such as ilmenite is attributed to the combined removal of the two elements.

The radioactive elements were leached from the tantalite ore materials by treating a finely ground sample with concentrated sulfuric acid at 50 °C for 3 h. Tables 16.2 and 16.3 and Fig. 16.3 show that reasonable concentrations of uranium and thorium are leached into the H_2SO_4 solution with 62.3(6)% U_3O_8 and 61.1(3)% ThO_2 (in manganotantalite) and 73.6(2)% U_3O_8 (in ferrotantalite) recoveries. Habash and Smith [24] found that thorium forms a soluble sulfate salt, Th$(SO_4)_2$, at temperatures as low as 40 °C and sulfuric acid concentrations down to 0.5 M. The successful leaching of uranium on the other hand has been reported [25] to be a function of the presence and concentration of sulfate ion as a driving force rather than the H^+ concentration. Leaching of U and Th from mineral ores is well

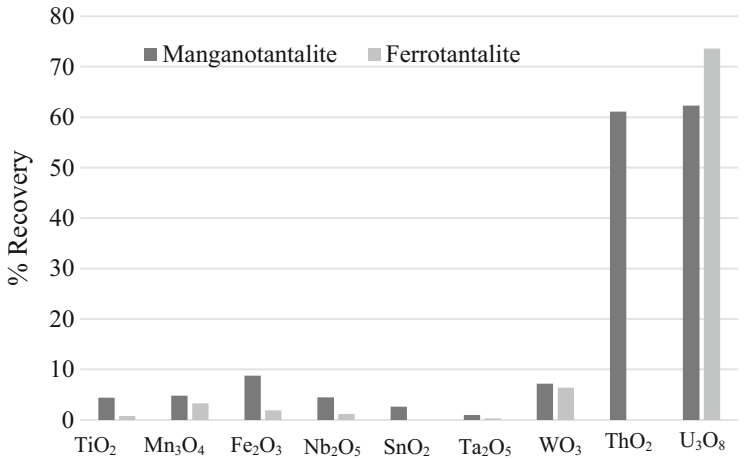

Fig. 16.3 Comparison of percentage recoveries of the elements in the acid leached solution of the tantalite minerals

understood. However, the selection of the experimental conditions for leaching of the elements [11] has not been expanded to include isolating pure Ta or Nb compounds from tantalite minerals.

16.3.2 Solvent Extraction of Tantalum from Tantalite Matrices (Step 3)

In the solvent extraction step it is clear that Ta can also successfully be extracted from $H_2SO_4/NH_4F{\cdot}HF$ solution using MIAK compared to MIBK, which is commonly used for these extraction purposes. Average recoveries, calculated on residual composition, of 100.8(3)% and 100.5(9)% Ta_2O_5 were obtained in manganotantalite and ferrotantalite, respectively (Table 16.4). The results also showed relatively low concentrations of other elements in the Ta rich solution in both the manganotantalite and ferrotantalite. These results are in good agreement with the previous results, which were obtained with the same procedure [11], but without prior magnetic separation and acid leaching processes. The results indicate the successful separation of Ta from the majority of impurities, including niobium, and its purification or enrichment in this step. MIAK was selected as extractant instead of the more commonly used MIBK, because of the more favorable extraction coefficient, which was previously obtained for tantalum(V) in the same mineral using the different organic solvents [11]. The results obtained in this part of the study indicated that Ta was selectively extracted at the selected experimental conditions into the MIAK, while leaving Nb and other metal impurities in the acidic aqueous solution (Table 16.4).

Table 16.4 Element quantification after solvent extraction using MIAK (% recoveries are based on residue composition)

Analyte	%Recovery	
	Manganotantalite	Ferrotantalite
Ta_2O_5	100.8(3)	100.5(9)
Nb_2O_5	0.20(3)	0.67(6)
Fe_2O_3	0.98(2)	1.01(8)
Mn_3O_4	0.29(1)	0.28(7)
TiO_2	0.1(1)	0.99(1)
WO_3	0.15(8)	0.06(7)
SnO_2	0.01(1)	<0.01
U_3O_8	0.34(9)	0.20(5)
ThO_2	0.05(4)	0.04(8)

Table 16.5 Concentrations of elements in eluent solutions of different acid concentrations (% recoveries are based on residue composition)

Metal oxide	%Recovery			
	Manganotantalite		Ferrotantalite	
	4.0 M fractions	6.0 M fractions	4.0 M fractions	6.0 M fractions
Ta_2O_5	0.49(2)	0.5(1)	0.540(7)	1.3(8)
Nb_2O_5	<0.01	100.2(4)	0.48(3)	94.5(4)
ThO_2	92.31(4)	7.69(4)	<0.00	<0.01
U_3O_8	14.43(4)	<0.01	86.7(2)	<0.01
WO_3	75.83(5)	0.50(8)	60.0(8)	0.67(1)
TiO_2	82.84(6)	<0.01	64.2(1)	<0.01
Mn_3O_4	81.9(2)	<0.01	58.9(1)	<0.01
Fe_2O_3	84.4(2)	<0.01	49.6(8)	<0.01
SnO_2	<0.01	<0.01	0.01(1)	<0.01

16.3.3 Ion Exchange Separation of Nb from Tantalite Matrices (Step 4)

The results (Table 16.5) indicated that the Nb compound was successfully isolated from tantalite mineral ore. Average recoveries of 100.2(4)% and 94.5(4)% Nb_2O_5 were obtained from manganotantalite and ferrotantalite, respectively. Recovery values of 0.50(8)% WO_3 and 7.69(4)% ThO_2 were also found in the Nb rich manganotantalite solution (Table 16.5). The quantitative results for Th and W in these analyses may be less accurate since the total recoveries of these elements in all the separation steps are much higher than 100%. For example, 135.41% ThO_2 was obtained by adding all the Th recovery values in the beneficiation process (magnetic separation, acid leaching, solvent extraction, 4.0 M HCl elution and 6.0 M HCl elution). These unsatisfactory recovery results for Th do not eliminate the possibility of contamination (small amounts) in the isolated Nb compound by these elements. The inaccuracy in the Th, U and W analyses can also be attributed to their low concentrations in these mineral samples since the quantification of Th

and U in the different steps in the beneficiation process were done in close proximity to their limits of detection and quantification by the ICP-OES, e.g., 0.002 to 0.05 mg/L for Th and 0.01 to 0.5 mg/L for U [26–28].

The retention and separation of Nb on an anion exchange column at 4.0 M acid can be attributed to the different compounds, which were formed during the dissolution step. Nete et al. [17] indicated that the impurities in tantalite (Fe, Ti, Mn, W, etc.) are easily eluted from the column. It is anticipated that these impurities form compounds, which hydrolyse (less stable fluoride complexes) easily in water to produce positively charged complexes and which allow for separation of impurity elements from the negatively charged Ta and Nb complexes. Anhydrous manganese fluoro complexes with the formulae MnF_4^-, MnF_5^{2-} and MnF_6^{3-} have been reported [29]. However, manganese(III) fluoride is said to instantaneously hydrolyse in water to form either the manganese aqua ions $Mn(OH)^{2+}$, $[Mn(OH)(H_2O)_x]^{2+}$ or hydrated $[Mn(H_2O)_6]^{3+}$. The iron halogen complexes such as K_3FeF_6 and $CsFeF_4$ have also been isolated. Cotton and Wilkinson [29] have also indicated that iron(III) in particular has a very high tendency to hydrolyse in aqueous solutions to form complexes such as $[Fe(H_2O)_6]^{3+}$ and $[Fe(OH)(H_2O)_5]^{2+}$.

16.3.4 Determination of the Quality of Ta and Nb Purification Products

The elemental content of the KF/Ta crystals and the Nb and Ta oxides (obtained from all the previous extraction and subsequent isolation steps) were determined by ICP-OES and ICP-MS. Results of chemical analysis of both metal oxides and KF/Ta crystals are presented in Table 16.6. The percentage metal recoveries in the formed product from the precipitation of the tantalum and niobium by NH_3 were calculated as $\%M_2O_5$ (M = Nb/Ta) while solid (crystals) obtained after the addition of KF salt to the tantalum enriched solution was calculated as %Ta in K_2TaF_7 and $KTaF_6$.

Good mean recoveries were obtained in the Nb and Ta enriched samples with 95.8(5) to 97.2(7)% Nb_2O_5 and 96.3(8) to 101.6(7)% Ta_2O_5 in manganotantalite, as well as 94.9(5) to 96.5(9)% Nb_2O_5 and 96.8(2) to 98.0(8)% Ta_2O_5 in ferrotantalite.

Table 16.6 Quantification of Ta and Nb in final product after separation (n.d. = not detected)

	% Recovery							
	ICP-MS				ICP-OES			
	Manganotantalite		Ferrotantalite		Manganotantalite		Ferrotantalite	
Sample	Nb	Ta	Nb	Ta	Nb	Ta	Nb	Ta
Nb_2O_5	97.2(7)	1.8(1)	96.5(9)	3(2)	95.8(5)	3(1)	94.9(5)	1.3(7)
Ta_2O_5	2.8(9)	96.3(8)	1.2(6)	96.8(2)	1.0(1)	101.6(7)	0.99(6)	98.0(8)
K_2TaF_7	n.d.	43.8(2)	n.d.	47.6(7)	5(3)	49.0(3)	3(2)	48.1(7)
$KTaF_6$	n.d.	36.3(6)	n.d.	35.1(1)	5.1(4)	43.6(3)	4(3)	42.4(2)

Table 16.7 Quantitative determination of the impurities in the purified Nb and Ta products (metal oxides) using ICP-OES (n.d. not detected)

	Tantalum rich product		Niobium rich product	
Analyte	Manganotantalite	Ferrotantalite	Manganotantalite	Ferrotantalite
Ta_2O_5	97.8(7)	96.8(2)	0.8(4)	0.7(2)
Nb_2O_5	1.4(6)	1.0(4)	94.4(5)	93.6(1)
Fe_2O_3	0.8(6)	0.5(2)	0.02(1)	0.7(3)
Mn_3O_4	0.3(5)	0.2(1)	0.17(8)	0.05(2)
TiO_2	0.6(2)	0.4(2)	0.4(3)	0.5(3)
Al_2O_3	n.d.	n.d.	1.0(9)	n.d.
U_3O_8	0.02(2)	n.d.	0.04(2)	0.01(1)
ThO_2	0.5(7)	0.03(2)	n.d.	n.d.
WO_3	0.6(6)	n.d.	0.2(2)	n.d.
SnO_2	0.4(9)	n.d.	n.d.	n.d.

According to Agulyansky and Eckert et al. [10, 30] the potassium fluorotantalate (K_2TaF_7) is expected to form when the potassium salt such as KF is added to the Ta rich fluoride solution. However, the quantitative results obtained by both ICP-OES and ICP-MS indicated that Ta recovery from the crystalline product was less than 50% (Table 16.6). The IR spectrum of this product (KF/Ta) indicates the possible presence of water peaks (3325–2960 cm^{-1}) and thereby suggests that a hydrated product is obtained. The addition of the crystal water to the proposed formula of K_2TaF_7 indicated some increase in the %recovery of Ta (e.g. 1, 2, 3 water molecules lead to %recovery increase from 49.0 to 52.2, 54.5 and 56.8% respectively). The low Ta recovery in this product could also be due to an incomplete reaction (not exceeding the Ksp for total crystal formation), or the formed product was contaminated with the unreacted starting material, or the formation of other K–Ta products other than the expected hexa or heptafluorotantalate.

The Nb and Ta oxides (calcined samples) were also analysed for other metal impurities using ICP-OES and the results are given in Table 16.7. It is important to note that the concentrations of most of the other elements (all the elements except Ta and Nb) were extremely low (due to small initial amounts of mineral ores used as starting material and the subsequent decrease in amounts with each separation step), to the extent that the ppm concentrations observed were below the lowest point of the calibration range in both the Ta rich and the Nb rich samples, and therefore are considered unreliable.

16.4 Conclusion

The extraction of niobium and tantalum from tantalite mineral using a combination of magnetic separation, acid leaching, solvent extraction and ion exchange methods was investigated for the separation of Ta and Nb from each other and from the coexisting elements. Magnetic separation removed most of Fe and Ti from the

ferrotantalite while acid leaching significantly reduced the concentrations of radioactive Th and U from the two samples. The results obtained from acid leaching of radioactive tantalite indicated that there was some loss of the two main metals (especially Nb, 4.02% Nb_2O_5 due to its solubility in H_2SO_4) while the radioactive materials, which remained in the residue may still be at unacceptable levels. Solvent extraction of Ta and Nb from the $NH_4F{\cdot}HF/H_2SO_4$ feed solution allowed the separation of Ta from Nb and the rest of the mineral matrix. The observed differences in the extraction efficiencies between Ta and Nb can be explained by the differences in the formation constants of the fluoro-tantalum complexes in acidic solutions as compared to the fluoro-niobium complexes [14], or the differences in the stability of the complexes once formed.

A column packed with an anion exchange Dowex Marathon resin achieved effective separation of Nb from the impurity elements. All the impurity elements were eluted by a 4.0 M HCl solution. The adsorbed Nb was successively and quantitatively eluted by a 6.0 M HCl solution. The entire beneficiation process resulted in a total loss of approximately 13% of both Nb_2O_5 and Ta_2O_5. The quantitative analysis indicated convincingly low levels of metal impurities in the obtained pentoxides and Nb_2O_5 and Ta_2O_5 of 96% purity were obtained.

The proposed hydrometallurgical beneficiation process for the separation and purification of Ta and Nb in this study has several advantages and includes the use of a magnetic separation technique, which requires less sample preparation while substantially decreasing the major impurities in the downstream products. The removal of major amounts of the radioactive elements in the leaching step does not only decrease their contribution to downstream contamination, but also renders the material safer and more acceptable for handling or transport. The use of $NH_4F{\cdot}HF$ as a fluoride source for the dissolution of samples is also an added advantage. The $NH_4F{\cdot}HF$ has a low melting point (125 °C) which encourages low fusion temperature. Furthermore, $NH_4F{\cdot}HF$ melts dissolve in water and as such, low overall acidity solutions are produced, which make them safer to handle for further processing. High purity Nb oxide was produced from four successive steps while Ta oxide was obtained from only three processing steps using MIAK with more favourable extraction coefficients ($D_{MIAK} = 6.210$, $\alpha_{MIAK} = 327.47$ compared to $D_{MIBK} = 3.658$, $\alpha_{MIBK} = 299.93$ [17]).

Acknowledgements The authors thank the Research Fund of the University of the Free State, the National Research Foundation of South Africa, Necsa and the New Metals Development Network (NMDN) of the Advanced Metals Initiative (AMI) of the Department of Science and Technology of South Africa (DST) for financial support.

References

1. Demartin F, Diella V, Gramaccioli CM, Pezzotta F (2001) Schiavinatoite, (Nb, Ta) BO_4, the Nb analogue of behierite. Eur J Miner 13:159–165
2. Roskill Information (2005) The economics of Niobium, 10th edn. Roskill Information Services, London

3. Roskill Information (2005) The economics of Tantalum, 9th edn. Roskill Information Services, London
4. Hayes K, Burge R (2003) Coltan mining in the democratic republic of Congo: how tantalum-using industries can commit to the reconstruction of the DRC. Fauna & Flora International, Cambridge
5. Engineers Edge (2015) Tantalum capacitors review. Available from: http://www.engineersedge.com/instrumentation/tantalum_capacitors.htm
6. Park KS, Kim NB, Woo HJ, Lee KY, Yoon YY, Hong W (1994) Determination of impurities in niobium metal by a radiochemical neutron activation analysis. J Radioanal Nucl Chem 179:81–86
7. Grewal I (2013) Mineral processing introduction [homepage on the Internet]. Available from: http://met-solvelabs.com/library/articles/mineral-processing-introduction/. Cited 24 Nov 2014
8. Falconer A (n.d.) Tin, tungsten and tantalum. Available from: http://ttms999.com/ttt.html
9. Tantalum-Niobium International Study Center (n.d.) Tantalum—raw materials and processing. Available from: http://www.tanb.org/tantalum
10. Agulyansky A (2004) The chemistry of tantalum and niobium fluoride compounds. Elsevier B. V., Amsterdam
11. Nete M, Koko F, Theron T, Purcell W, Nel JT (2014) Primary beneficiation of tantalite using magnetic separation and acid leaching. Int J Miner Metall Mater 21:1153–1159
12. Kabangu MJ, Crouse PL (2012) Separation of niobium and tantalum from Mozambican tantalite by ammonium bifluoride digestion and octanol solvent extraction. Hydrometallurgy 129–130:151–155
13. Maiorov VG, Nikolaev AI, Sklokin LI, Baklanova IV (2001) Extractive recovery of tantalum (V) and niobium(V) with octanol from hydrofluoric acid solutions containing large amounts of titanium(IV). Russ J Appl Chem 74:945–949
14. El Hussaini OM, Rice NM (2004) Liquid-liquid extraction of niobium and tantalum from aqueous sulphate/fluoride solutions by a tertiary amine. Hydrometallurgy 72:259–267
15. Amuda MOH, Esezobor DE, Lawal GI (2007) Adaptable technologies for life-cycle processing of tantalum bearing minerals. J Miner Mater Charact Eng 6:69–77
16. Gupta CK, Suri AK (1994) Extractive metallurgy of niobium. CRC Press, Boca Raton
17. Nete M, Purcell W, Nel JT (2014) Separation and isolation of tantalum and niobium from tantalite using solvent extraction and ion exchange. Hydrometallurgy 149:31–40
18. Nete M, Purcell W, Snyders E, Nel JT, Beukes G (2012) Characterization and alternative dissolution of tantalite mineral samples from Mozambique. J South Afr Inst Min Metall 112:1079–1086
19. Nete M, Purcell W, Nel JT (2014) Comparative study of tantalite dissolution using different fluoride salts as fluxes. J Fluor Chem 165:20–26
20. Heck C (1974) Magnetic materials and their applications. Butterworths, London
21. Nete M, Purcell W, Nel JT (2013) Evaluation of ammonium bifluoride dissolution on different tantalum and niobium mineral samples. In: Precious metals 2013 conference. Advanced Metals Initiative, Cape Town, 14–16 October 2013
22. Sahama TG (1980) Minerals of the tantalite-niobite series from Mozambique. Bull Miner 103:190–197
23. Geoscience Australia (2012) Australian atlas of mineral resources, mines, and processing centres. Iron Ore, Department of Resources, Energy and Tourism, Minerals Council of Australia. Available from: http://www.australianminesatlas.gov.au/aimr/commodity/iron_ore.html
24. Habash J, Smith AJ (1983) Structure of thorium sulphate octahydrate, $Th(SO_4)_2 \cdot 8H_2O$. Acta Cryst C 39:413–415
25. Multi-Agency Radiological Laboratory Analytical Protocols Manual (2004) http://www.epa.gov/rpdweb00/docs/marlap/402-b-04-001a-title_etc.pdf
26. Evans Analytical Group (2007) ICP-OES and ICP-MS detection limit guidance. Available from: http://www.eaglabs.com/documents/icp-oes-ms-detection-limit-guidance-BR023.pdf

27. PerkinElmer (2008-2011) Atomic spectroscopy: a guide to selecting the appropriate technique and system. Available from http://www.perkinelmer.com/PDFs/Downloads/BRO_WorldLeaderAAICPMSICPMS.pdf
28. Schibler J, Moore D, De Borba B (2007) Setting meaningful detection and quantitation limits for chromatography methods. Dionex Corporation, Sunnyvale, CA, USA. Available from: http://www.dionex.com/en-us/webdocs/52823-LPN-1926 Chromeleon.pdf
29. Cotton FA, Wilkinson G (1988) Advanced inorganic chemistry, 5th edn. Wiley, New York
30. Eckert J, Reichert K, Schnitter C, Seyeda H (2001) Processing of columbite-tantalite ores and concentrates for niobium and niobium compounds in electronic applications. In: Proceedings of the international symposium niobium, science and technology. Minerals, Metals and Materials Society, Orlando Florida, 2–5 December 2001

Chapter 17
Recent Applications of Laccase Modified Membranes in the Removal of Bisphenol A and Other Organic Pollutants

Lebohang E. Koloti, Nonjabulo P. Gule, Omotayo A. Arotiba, and Soraya P. Malinga

Abstract Bisphenol A (BPA) has been found to be the most rapidly generated endocrine disrupting compound (EDC) with an annual production of over 10 million tons. This synthetic compound has been used extensively in the production of polycarbonate plastics, epoxy resins and thermal papers. It has been detected at elevated levels in industrial wastewater effluents, natural waters and drinking water. Recent studies have shown that BPA affects the proper functioning of the endocrine system in human beings and animals. Exposure to BPA has been associated with immunotoxic, mutagenic and carcinogenic effects at very low levels (ng/L to μg/L). It has also been proven that BPA increases chances of having diabetes, obesity and cancer. Thus, the removal of BPA from water has become a major concern in water research. Enzymatic degradation of BPA has proven to be an efficient and environmentally friendly approach and the use of laccase modified membranes has been reported in many studies. This article provides an in-depth review on the removal of BPA and other toxic organic micro-contaminants from water by laccase modified membrane systems.

L.E. Koloti • S.P. Malinga (✉)
Department of Applied Chemistry, University of Johannesburg, Doornfontein Campus, P.O. Box 17011, Doornfontein, 2028 Johannesburg, South Africa
e-mail: smalinga@uj.ac.za

N.P. Gule
Department of Polymer Science, Stellenbosch University, P/B X1 Matieland, Stellenbosch 7602, South Africa

O.A. Arotiba
Department of Applied Chemistry, University of Johannesburg, Doornfontein Campus, P.O. Box 17011, Doornfontein, 2028 Johannesburg, South Africa

Centre for Nanomaterials Science Research, University of Johannesburg, Johannesburg, South Africa

P. Ramasami et al. (eds.), *Emerging Trends in Chemical Sciences*,
DOI 10.1007/978-3-319-60408-4_17

17.1 Introduction

A wide range of organic pollutants originating from various chemical classes with diverse physico-chemical properties are detected in the environment, especially in most water systems [1]. However, there is limited information on "emerging" micro-pollutants which are a potential risk to human health and the environment. Endocrine disrupting compounds (EDCs) are a group of these newly emerging pollutants. EDCs alter the normal functions of the endocrine system even at very low levels (nano-levels), thus threatening both human and animal health [2]. Among these EDCs, BPA has been found to be the most rapidly generated compound by industrial production [3]. BPA is toxic in nature and has compelled researchers to devise more efficient methods for its removal from water [4]. Oxidative biotransformation of BPA using enzymes has proven to be an environmentally friendly and effective approach for the removal of BPA from water [5]. Numerous researchers have investigated the use of laccase immobilized on membranes for the removal of BPA [6]. To the best of our knowledge, no study has provided a comprehensive review on the various factors that facilitate the removal efficiency of BPA from water through the use of laccase modified membranes. Thus, this review provides an overview on removal of BPA and other toxic emerging micro-pollutants from water using laccase modified membranes.

17.2 Bisphenol A

17.2.1 Origin and Prevalence

BPA was first synthesised by a Russian chemist, A.P. Dianin in 1891 through condensation of phenol with acetone (Fig. 17.1) [1]. The estrogenic effects of BPA were reported in the 1930s, but its use as a synthetic oestrogen did not become popular [7]. Later, it was discovered that BPA can be used in the production of plastics (such as polycarbonate plastics), epoxy resins and thermal papers [5, 8, 9]. This led to intense preparation of this monomer which was then used in various consumer products such as plastic toys, dental sealants, food packaging, plastic bottles, and electronic devices [10, 11]. In 2011, the increased demand on BPA resulted in its global consumption being over 5.5 million metric tons which led to the ubiquity of this micro-pollutant in the environment [12].

BPA has found its way into humans, animals and plants through food and drinking water due to the intense use of BPA-containing food packaging and plastic bottles. Scientific studies have shown that residual BPA can either diffuse out of polycarbonate packaging materials or during hydrolysis of the polymer due to alkaline conditions and temperature of packaged food. For decades, there has been a great concern towards BPA exposure in infants since BPA was detected in their feeding bottles [13]. A survey conducted by Pouokam et al. revealed that

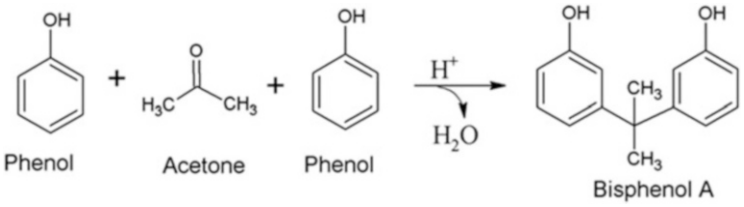

Fig. 17.1 Synthetic route of BPA by condensation of phenol and acetone

feeding bottles containing BPA are being sold in countries such as Cameroon and Nigeria [14]. The study showed that almost all the plastic bottles in Cameroonian shops did not carry the "BPA-free" sign and over 80% feeding bottles in Nigerian shops were also not BPA free [14]. South Africa is the first developing country to take safety measures against BPA containing commodities. In 2011, the South African health ministry banned the production, importation, exportation and selling of BPA containing bottles used by infants [14].

BPA has been detected in most water systems which increases the chances of its exposure to human beings and animals [15]. Traceable amounts of BPA are discharged directly into water bodies (such as marine and fresh waters) and some traces are found in nearby surroundings of plastic manufacturing industries [11]. BPA leaches out into surface waters through the hydrolysis of most polycarbonate plastics and epoxy resins [1]. In Japan, BPA has been detected in landfill leachates (up to 17.2 mg/L) and in drinking tap water (up to 0.1 μg/L). In China, BPA has been found at concentration of 27.3 μg/L in natural surface water [12]. These high levels of BPA are detrimental to human health.

Traces of BPA have also been detected in developing countries in Africa. Maduka et al. reported the presence of BPA in water at the Enugu municipality in South East Nigeria [16]. The study revealed BPA concentrations in tap water (0.20 ± 0.07 μg/L), well water (0.21 ± 0.07 μg/L), river water (0.18 ± 0.04 μg/L) and rain water (0.40 ± 0.16 μg/L) [16]. The high levels of BPA were ascribed to the poor disposal of sewage that contain BPA. The highest levels of BPA were found in rain water because of environmental contamination by industrial activities [16]. A study conducted by Omoruyi et al. further revealed BPA concentrations ranging from 124.2 ng/L to 1.0008 μg/L in 31% of bottled water samples in Nigeria [17].

Olujimi et al. detected the concentration of BPA and nonylphenol using ultra-performance liquid chromatography tandem mass spectrometry (UPLC/MS) from samples collected in Cape Town Flats waste treatment works (in Strandfontein) [18]. The wastewater treatment plant in Strandfontein uses activated sludge for treating domestic, agricultural and industrial effluents. This study reported a high concentration of BPA of up to 384.3 ± 131.7 μg/L in the wastewater treatment plant. Nonylphenol (another endocrine disruptive compound) was also found to reach concentrations ranging from 0.53 ± 0.15 to 9.83 ± 3.47 mg/L. BPA in the landfill leachates was found at concentrations of 0.022 ± 0.002 to 9.59 ± 1.48 mg/L and nonylphenol concentration ranged from 1.04 ± 0.43 to 137.41 ± 4.73 mg/L. In

the sewage sludge, BPA concentrations ranged from 0.17 ± 0.01 to 2.28 ± 0.13 μg/g, while nonylphenol levels ranged from 0.42 ± 0.02 to 8.76 ± 0.72 μg/g. The detected levels of these endocrine disrupting phenols in the wastewater treatment plant and the landfill leachates exceed the allowable limit of phenols (10 μg/L) in water as stated by the South African National Standards (SANS) [19]. This high concentration of endocrine disruptors, BPA and nonylphenol, can be a threat to nearby residents and about 30,000 migrant birds that are found around these areas.

Another study conducted by De Jager et al. in South Africa revealed a detectable amount of BPA ranging from 0.0478 ng/L to 0.06798 ng/L in selected drinking water distribution points in Pretoria and Cape Town [20]. The water samples were collected from 20 distribution points and were analysed using gas chromatography-mass spectrometry (GC-MS). The BPA levels were found to be less than those reported in developed countries like China where BPA concentrations ranging from 38.9 to 55.8 ng/L in water have been reported [20]. Even though most developing countries are becoming aware of the detrimental effects of BPA on human health and wildlife, the major challenge is in linking detectable concentrations of urinary BPA to its exposure route [21]. Recently, a study conducted by Nahar et al. reported BPA urinary concentrations of 0.6 ng/L (in rural areas) and 1 μg/L (in urban areas) in young girls living in Egypt [21]. It was concluded that the main source of BPA exposure to these girls was the consumption of canned food and storing food in plastic packages. The cans and plastics used for storing food contain high levels of BPA and this was the only study in Africa that attempts to link detected urinary BPA to the sources of exposure [21].

17.2.2 Health Effects of BPA

Recent studies have shown that BPA affects the proper functioning of several hormones such as sex hormones, insulin, leptin and thyroxin which impact negatively on human and animal health [7, 22, 23]. Exposure to BPA has been associated with immunotoxic, mutagenic and carcinogenic effects [2, 9, 24]. It has also been proven that high levels of BPA in the human system can result in diabetes and obesity [2, 3, 12]. Lang et al. established a direct relationship between BPA dosage and type-2 diabetes using data obtained from a National Health and Nutrition Examination Survey (NHANES) 2003–2004 from individual American participants [7]. The researchers found that higher total urinary BPA was linked to diagnosis of type-2 diabetes [7]. Carwile and Michels also found that increased urinary BPA can be associated to higher chances of body mass index and obesity [9]. BPA has shown estrogenic activity at very low doses of 0.23 pg/mL and has been found to increase the rate of proliferation of breast cancer cells [25]. BPA binds to oestrogen nuclear receptors responsible for regulating transcription and cell membrane receptors associated with calcium mobilization and intracellular signalling in the endocrine system [25]. Cell membrane receptors have proven to be

more sensitive towards BPA resulting in observable effects even at extremely low BPA concentrations (ppt levels) [26].

Owing to its toxic nature and adverse effects to human health, the removal of BPA from water has become a major concern world-wide. Various conventional wastewater treatment methods have been employed in efforts to remove BPA from water, but this recalcitrant pollutant still persists in most wastewater treatment plants due to its complex aromatic structure and low biodegradability [27, 28].

17.3 Conventional Wastewater Treatment Methods for the Removal of BPA

Various studies have demonstrated the removal of BPA by numerous methods which may be physical, chemical and biological processes.

17.3.1 Physical Methods

The most common physical techniques that have been used in the removal of BPA from water are adsorption and membrane filtration separation processes.

17.3.1.1 Adsorption

Several studies have reported adsorption as the most cost-effective, easiest and fastest technique for the removal of BPA in aqueous medium [8, 29]. Moreover, this method does not produce any harmful secondary product [30]. Therefore, adsorption, as a well-known equilibrium separation method, has become the most widely used process for the removal of most phenolic pollutants such as BPA from contaminated water. A myriad of adsorbent nanomaterials have been explored for the removal of BPA from water. These include activated carbon, natural materials such as clay, and biosorbents such as chitosan [9, 31–33]. However, the main disadvantage of the use of adsorbents for water remediation is that adsorbents only transfer BPA from the aqueous phase into their matrix without transformation into non-harmful products. The accumulation of BPA in the absorbents renders them as secondary pollutants which may also be difficult to dispose [34]. Moreover, BPA has high solubility in water, thus reducing its chances of adsorption on the surface of adsorbent, especially at low concentrations [35].

17.3.1.2 Membrane Separation

Membrane filtration has also proven to be an effective approach in the removal of small molecules and trace-level contaminants such as BPA [36, 37]. Thus, the use of membranes in the removal of most organic pollutants has captured the attention of most researchers in the field of water remediation. Membranes can be classified into microfiltration (MF), ultrafiltration (UF), nanofiltration (NF) and reverse osmosis (RO) depending on their pore size and separating force. Due to their relatively high porosity, UF membranes have shown great potential for the removal of most EDCs. Moreover, these types of membranes require lesser amount of operating pressure when compared with NF and RO membranes, making the use of UF membranes economically viable [38]. However, the performance of the membrane towards the removal of most organic pollutants such as BPA deteriorates with time due mainly to irreversible membrane fouling [39].

17.3.2 Chemical Methods

Several studies have also been reported on the removal of BPA from wastewater by chemical methods which mainly involve the use of photochemical methods.

17.3.2.1 Advanced Oxidation Processes

Advanced oxidation processes (AOPs) have been used to completely disrupt BPA from water [40–42]. Complete mineralization of most organic pollutants is achieved due to the generation of very reactive oxygen intermediates such as hydroxyl radicals which are capable of degrading organic pollutants such as BPA to water, carbon dioxide and some mineral acids [42]. AOPs include the use of ozone, hydrogen peroxide, Fenton's reagent, and various nanoparticles (e.g. TiO_2) [39, 41, 43]. The use of AOPs in the degradation of most organic contaminants require electrical energy as a source of radiation, which renders this approach considerably costly. There is also a possibility of nanocatalyst such as TiO_2 leaching into water systems and its aggregation may impact negatively on the aquatic life.

17.3.3 Biological Methods

Researchers have also taken advantage of the metabolic properties of micro-organisms to effectively degrade organic pollutants from water [44].

17.3.3.1 Use of Activated Sludge

Orozco and co-workers illustrated the aerobic biodegradation of BPA using activated sludge [45]. In a study conducted by Zhao et al., sorption and biodegradations of BPA were investigated in a lab-scale aerobic activated sludge system [44]. After 5 h, BPA removal reached almost 100%, of which 98% removal was due to degradation by the activated sludge [44]. However, the hazardous nature of BPA normally results in a drop in bacterial count during acclimatization resulting in the reduced performance in this approach in BPA degradation.

17.3.3.2 Use of Algal-Bacterial System

Researchers have taken advantage of the symbiotic relationship between bacteria and algae to biodegrade BPA in water. In this system, algae provide bacteria with the oxygen required in the bacterial degradation of BPA, while the carbon dioxide produced during degradation is used by the algae in photosynthesis. The synergistic effect of degradation by algae and bacteria also enhanced the biotransformation of BPA in water. However, generation of toxic by-products may inhibit the activity of the bacteria responsible for the biodegradation of BPA [44]. Enzymatic degradation has proven to be an alternative method that can overcome these limitations while still maintaining high biodegradation efficiency of BPA.

17.4 Enzymatic Degradation

Though various conventional methods have been employed in the removal of BPA from water, the persistence of BPA in most wastewater treatment plants shows the limitations of such methods. Removal of endocrine disruptors such as BPA from wastewater using oxidizing enzymes has proven to be an environmentally friendly and effective approach [12, 46]. A number of ligninolytic oxidative enzymes such as manganese peroxidase, horseradish peroxide and laccase have been used in the biodegradation of BPA [5, 47, 48]. Among these oxidative enzymes, laccase has been widely used because of its high selectivity and reactivity [5]. Laccase is an oxidoreductase which has copper atoms in its catalytic centres [49, 50]. Laccase is known for its capability to catalyse the oxidation of ortho- and para-diphenols, aminophenols, chlorophenols, polyamines, polyphenols, lignin and aryl diamines [51]. This process involves four-electron reduction of dioxygen to water [52]. Low molecular weight mediators can be used for improved bio-catalytic degradation by acting as electron shuttles between the enzyme and the substrate [52].

Daassi et al. studied the possible degradation of BPA by laccase from white rot fungi using GC-MS [48]. The results obtained confirmed the formation of β-hydroxybutyric acid upon oxidative biotransformation of BPA using laccase

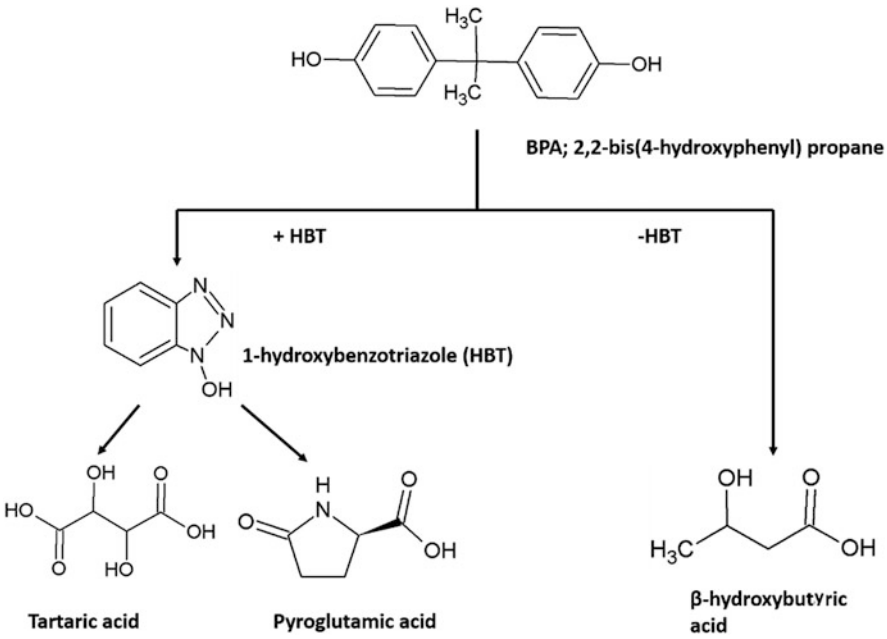

Fig. 17.2 Biodegradation pathways of BPA using laccase from *Coriolopsis gallica* [48]

from white rot fungi [48]. Tartaric acid (a carboxylic acid derivative) was formed when BPA was degraded in the presence of 1-hydroxybenzotriazole (HBT) as a laccase-mediator. Pyroglutamic acid was also formed as a supplementary oxidative product when HBT mediator was used. The proposed biodegradation pathways are illustrated in Fig. 17.2 [48].

Application of free enzymes in water treatment has high operation costs because they are difficult to recover for reuse, and they have a shorter life-time as they are less stable [53–56]. Free enzymes activity is inhibited by the harsh microenvironment properties such as very high or low pH, extreme temperature and high ionic strength in effluent streams [57, 58]. Therefore, enzyme immobilization on various support systems has been considered as a promising technique in wastewater remediation because of its several advantages over the use of free enzymes.

17.4.1 Membranes as Suitable Supports for Enzyme Immobilization

Immobilization of enzymes on nanostructured materials has shown great advantages in preserving enzyme properties. Firstly, it allows better handling of the biodegradation system whilst retaining enzyme activity at extreme environmental conditions such as high temperature and pH [59]. Secondly, immobilized enzymes

are confined in specific regions on the nanostructured supports and their stability is enhanced by the remarkable properties of these supports. Therefore, immobilized enzymes have increased half-lives which enable their repeated use in various applications such as in water treatment [60].

The catalytic performance of immobilized enzyme strongly depends on the properties of these supports, such as its material type, composition, structure and mechanical properties [61]. Improved stability and reusability of the immobilized enzyme are attributed to good biocompatibility, thermal and mechanical properties exhibited by the carrier or support [58]. Different nanostructured materials such as mesoporous silica, nanotubes, nanoparticles and nanofibers have been used as enzyme carriers because of their advantageous properties towards enzyme immobilization [62, 63]. These nanostructured supports have extremely high surface area-volume ratios which give rise to a large specific area for maximum enzyme loading and enzyme stability [57, 64].

However, some of these carriers have some shortcomings which result in reduced enzyme performance. For instance, mesoporous silica usually confines enzyme molecules on its inner surface, which limits the diffusion of substrate and product in/from the active centre of the immobilized enzyme [58]. Nanoparticles and nanotubes are capable of overcoming mass transfer limitations; however, their dispersion and recycling is difficult [58]. The use of nanofibers can overcome these limitations, while providing the advantageous features of nanosized materials. Thus, nanofibrous membranes have proven to be suitable supports for enzyme immobilization in enzymatic degradation of most emerging water contaminants such as BPA.

Recently, the major challenge has been on enhancing the stability of the immobilized enzymes on the membrane, without any compromise in the activity of the immobilized enzymes. Laccase enzymes have been immobilized on membranes (of different chemical and morphological nature) for improved degradation of BPA from water. This enzyme has been immobilised on various polymeric membranes for the degradation of most phenolic pollutants like BPA due to its improved stability and catalytic performance [65]. Laccase enzymes have been immobilized on membranes through adsorption, entrapment and covalent attachment. It is worth noting that the reduction in the activity of an immobilized enzyme cannot be completely avoided due to denaturation of enzyme. However, the level of enzyme inactivation depends on the method of immobilization [58].

17.4.2 Methods for the Immobilisation of Enzymes

17.4.2.1 Adsorption

Adsorption is a reversible method of enzyme immobilization in which the enzymes are attached to the matrix of the nanostructured support through physical forces such as hydrogen bonding, van der Waals forces, and hydrophilic interactions [66] (Fig. 17.3). The advantage of this simple method is the weak binding forces

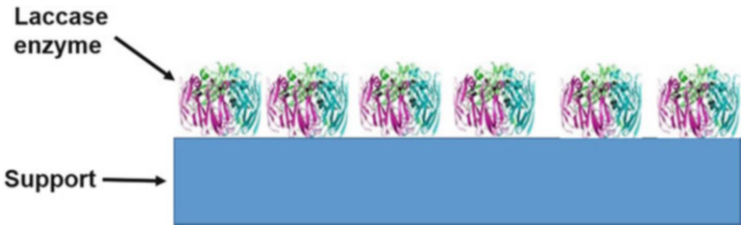

Fig. 17.3 Immobilization of enzymes by adsorption

between the enzyme and the support which allow the free change in conformation of the enzyme, leading to the retained catalytic activity of the enzyme [67, 68]. However, the enzymes can leak from the matrix due to relatively weak interactions. The choice of the carrier or support depends on the presence of the specific active groups which in turn enable effective carrier-enzyme interactions [53].

17.4.2.2 Entrapment

This method involves the inclusion of the enzyme within a polymeric network which allows the substrates and the products to pass through, but retains the enzyme inside the network [66] (Fig. 17.4). Biocompatible matrices have been used to protect the immobilized enzymes from inactivation due to the by-products by covering the catalytic sites [5]. Enzymes can be entrapped through gel or fibre entrapping and micro-encapsulation. Several authors have used this method for the immobilization of laccase on polymeric membranes. Generally, the application of entrapped enzymes is limited by inhibited mass transfer which makes it difficult for the substrate to reach the active sites of the enzyme. This method also requires high concentration of the enzyme and occasional inactivation of enzymes is usually experienced [69].

17.4.2.3 Covalent Binding

Covalent binding involves the use of a chemical coupling reagent which introduces certain functional groups that will link the nanostructured support functional groups to the amino acid residue of the enzyme [70]. Covalent binding forms the most stable interactions between the enzyme molecule and the support (Fig. 17.5). Therefore, enzyme leakage from the support into the reaction medium is limited [58]. The greater stability associated with covalent enzyme immobilization has been found to increase resistance to high temperatures and pH. Multiple-point binding of enzymes has been found as one of the underlying factors resulting in the enhanced stability of the immobilized enzymes [71]. However, this multiple-point attachment may sometimes distort the bio-active conformation of the enzyme thus resulting in its inactivation. Non-biospecific binding of immobilized enzymes on support have also been reported to cause inactivation of immobilized enzyme. Spacer arms with flexible chains have been used to allow enough space for the

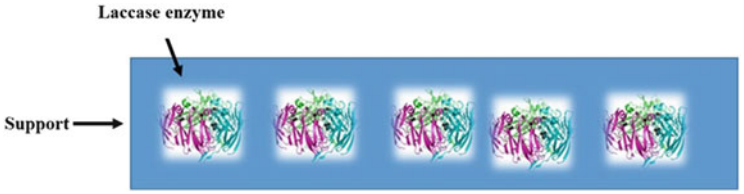

Fig. 17.4 Immobilization of enzymes by entrapment

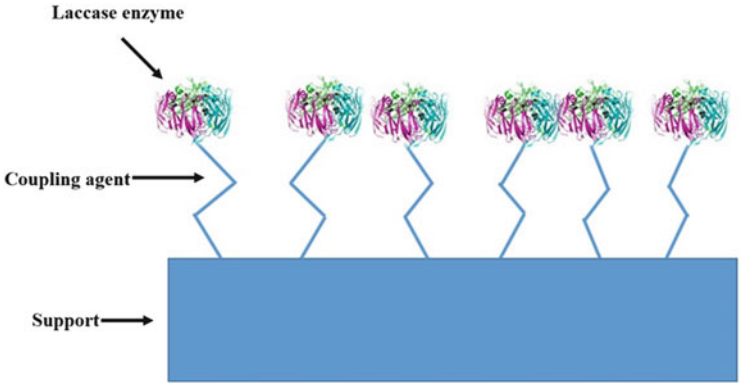

Fig. 17.5 Immobilization of enzymes by covalent bonding

necessary enzyme conformational changes to maximize the exposure of the catalytic sites to the substrate. Spacer arms such as polyethyleneimine (PEI), hexamethylenediamine (HMDI) and bovine serum albumin (BSA) have been used [72–74]. The covalent reactions commonly used result in binding through amide, ether, thio-ether, or carbamate bonds [75, 76].

The improved stability and retained catalytic activity of enzymes immobilized on membranes have led into extensive application of the laccase modified membranes towards removal of most emerging pollutants in water.

17.5 Removal of BPA and Other Pollutants by Laccase Modified Membranes

17.5.1 Laccase Modified Chitosan Based Nanofibrous Membranes

Laccase has been attached covalently to a wide range of polymeric nanofibrous membranes for the removal of emerging organic pollutants. A study conducted by Xu and co-workers presented the preparation of laccase immobilized chitosan/poly (vinyl alcohol) nanofibrous membrane for removal of 2,4-dichlorophenol from

water [65]. In the synthesis of this bio-catalytic membrane, a homogeneous solution of chitosan/poly(vinyl alcohol) was electrospun on an aluminium foil and then activated with glutaraldehyde as a cross-linker prior to laccase immobilization. The laccase modified membrane had a removal efficiency of 87.6% for 2,4-dichlorophenol, which was much higher than that of free enzymes (82.7%) [65]. Biocompatible polymers such as chitosan are capable of retaining the catalytic activity of the immobilized enzymes which in turn results in improved degradation efficiency [77]. The abundant amino functional groups present in the chitosan/poly (vinyl alcohol) composite membrane resulted in high laccase loading efficiency of 853 mg/g fibers and 69.1% retained activity for the immobilized laccase. The carboxyl groups in the laccase reacted with amino groups on the fiber surface to form stable peptide bonds. The immobilized enzymes were able to retain their ideal conformation due to the stable covalent bonds between the immobilized laccase and the nanofibrous membrane support. Moreover, the chitosan/poly(vinyl alcohol) nanofibrous carrier also showed significant adsorption efficiency which contributed to improved removal of 2,4-dichlorophenol.

Maryskova et al. further immobilized laccase from the white rot fungus *Trametes versicolor* on polyamide 6/chitosan nanofibers [78]. Chitosan is a bio-polymer that offers a biocompatible matrix for enzyme immobilizations. It has improved hydrophilic properties and abundant groups that can be used to attach enzymes such as laccase [78]. The enzyme was covalently bound on the electrospun nanofibers by the use of two spacer arms, bovine serum albumin (BSA) and HMDI using glutaraldehyde as a cross-linker. The degradation ability of the laccase modified nanofibers was tested in a mixture of BPA and 17α-ethinylestradiol (EE2) in water. The laccase modified nanofiber mat with HMDI as a spacer arm, exhibited about 100% removal efficiency for both BPA and 17 α-ethinylestradiol in 6 h. The use of BSA as a spacer resulted in 92% and 96% removal efficiency of BPA and 17α-ethinylestradiol, respectively. The laccase modified nanofibrous mat prepared using HMDI spacer was found to maintain removal efficiency of 60% for BPA and 47% for 17α-ethinylestradiol after 3 cycles. When BSA was used as a spacer, the removal efficiencies were 33% for BPA and 77% for 17-α-ethinylestradiol after 3 cycles. The HMDI-modified bio-catalytic nanofibers retained about 81% of their initial activity, and the BSA-modified biocatalytic nanofibers only retained around 55% of its initial activity over 14 days. The improved storage stability of the HMDI-modified enzyme active nanofibers confirmed the use of HMDI as suitable spacer for enhanced stability of laccase enzymes [76].

17.5.2 Poly(Methyl Methacrylate-co-Ethyl Acrylate) Microfibrous Membrane

Xu et al. immobilized horseradish peroxidase (HRP) on poly(methyl methacrylate-co-ethyl acrylate) (PMMA CEA) microfibrous membrane for the degradation of

BPA [75]. Prior to enzyme immobilization, the microfibrous membrane was activated with PEI as a coupling agent and glutaraldehyde as a cross-linker. HRP loading of 285 mg/g was achieved with BPA removal efficiency of 93% in 3 h which was much higher than that of free laccase (61%) [75]. The excellent catalytic performance of the enzyme modified membrane could be due to the use of spacer arm which improves mobility of immobilized enzyme in order to attain suitable conformation [73]. The ultrathin highly porous poly(methyl methacrylate-co-ethyl acrylate) nanofibers also provide sufficient surface area for improved adsorption of BPA. Therefore, the remarkable removal efficiency of BPA can be ascribed to the combined degradation and adsorption effects of the catalytic membrane.

17.5.3 Laccase Immobilized Poly(Styrene-alt-Maleic Anhydride)/Poly(Styrene-co-Maleic Anhydride) Support

Ignatova et al. covalently immobilized laccase from *Trametes versicolor* on poly (styrene-alt-maleic anhydride)/poly(styrene-co-maleic anhydride) nanofibrous mats through diazotization process [79]. The electrospun microfibrous mat was first functionalized with *p*-phenylenediamine as a spacer to introduce the amine groups on the reactive maleic anhydride moieties found on the neat microfibrous mats. The amino-functionalized microfibrous mat was diazotized prior to covalent binding of laccase. The nanofibrous mat loaded with 40 ± 0.7 mg/g of laccase achieved 60% BPA removal efficiency in 90 min. The catalytic activity of the laccase modified mat was maintained over 30 cycles of reuse. A continuous bioreactor system was used to determine the effect of feed flow rate on BPA removal. The optimum flow rate for effective BPA degradation was found to be 1.3 mL/s. There was no significant change in BPA removal when the flow rate was increased; instead the integrity of the mat was destroyed [79]. The high BPA removal rate was attributed to the enhanced enzyme loading capacity due to the presence of numerous maleic anhydride functional groups on the electrospun microfibrous mat. Cloete et al. also qualitatively confirmed the covalent attachment of horseradish peroxidase and glucose oxidase on poly(styrene-alt-maleic anhydride) through direct binding of the enzymes on the maleic anhydride moieties [80]. The average activity of the immobilized horseradish peroxidase was found to be 21% greater than that of free enzymes [80]. The high loading efficiency due to abundant anchoring sites on the support results in enhanced catalytic activity of the immobilized enzyme which in turn increases its biodegradation efficiency.

17.5.4 Laccase Carrying Polyamide 6/Chitosan Nanofibers

Laccase has also been immobilized on various polyamide matrices. Silva et al. immobilized laccase on a woven polyamide 6,6 [81]. The woven polyamide 6,6 was first treated with protease for enzymatic hydrolysis to produce reactive amino groups that could be used as anchoring sites for the covalent attachment of laccase. HMDI was used as a spacer arm. The immobilized laccase achieved 78 h half-life, which was 18% higher than that of free enzymes. This study therefore demonstrated the use of polyamide supports for improved stability of laccase enzymes [81]. The use of HMDI as spacer arm provides enough distance for improved mobility of the immobilized enzymes which allows them to attain the ideal conformation changes for enhanced catalytic activity.

17.5.5 Laccase Immobilized on Poly(D,L-Lactide), Poly(D,L-Lactide-co-Glycolide) and Methoxypolyethylene Glycol-Poly(Lactide-co-Glycolide) Nanofibrous Membrane

Dai et al. encapsulated laccase enzymes within a core-shell structure of electrospun poly(D,L-lactide), poly(D,L-lactide-co-glycolide) and methoxypolyethylene glycol-poly(lactide-co-glycolide) for bioremediation of polycyclic aromatic hydrocarbons (phenanthrene, fluoranthene, benz[a]anthracene and benz[a]pyrene) from soil in aqueous medium [82]. Laccase was embedded in the core and the pores shell of the nanofibers and thus promoted the mass transfer of the substrate to the embedded laccase enzymes. Poly(D,L-lactide) laccase carrying electrospun nanofibrous membrane exhibited low activity recovery which was mainly attributed to the hydrophobic nature of poly(D,L-lactide). The hydrophobic surface may lead to undesirable non-specific binding which impacts on the native conformation of the immobilized enzyme [57, 82]. In contrast, methoxypolyethylene-poly(lactide-co-glycolide) showed retained activity, but very low stability due to its hydrophilicity. The hydrophilic nanofibers of methoxypolyethylene glycol-poly(lactide-co-glycolide) swelled and disintegrated in aqueous medium resulting in leaching out of the entrapped laccase enzymes and loss in activity [83]. The degradation efficiency for the laccase modified nanofibrous membrane was over 90% for phenanthrene and fluoranthene and 80% for benz[a]anthracene and benz[a]pyrene. These enhanced degradation efficiencies were ascribed to the strong affinity of the hydrophobic polycyclic hydrocarbons to adsorb and pre-concentrate on the pores of the fibers that provide accessible route to encapsulated laccase enzymes. The overall removal of the polycyclic hydrocarbons was attributed to the enhanced adsorption and enzymatic degradation.

17.5.6 *Laccase-Poly(D,L-Lactic-co-Glycolic Acid) Nanofibrous Membrane*

Sathishkumar et al. immobilized laccase on poly(lactic-co-glycolic acid) nanofibrous membrane for the biodegradation of diclofenac from water [84]. Laccase was covalently bound on the poly(lactic-co-glycolic acid) nanofibers using glutaraldehyde cross-linker. The laccase carrying nanofibrous membrane exhibited 100% diclofenac transformation over three recycle use and complete diclofenac over six reuse cycles. These applications were carried out in the presence of syringaldehyde as a redox mediator. The immobilized laccase had a relative activity of 82% compared to that of free laccase enzyme. The improved activity of the immobilized laccase was ascribed to the suitable enzyme microenvironment provided by the biocompatible synthetic poly(lactic-co-glycolic acid) which is often used in biomedical applications [84].

17.5.7 *Laccase-Multiwalled Carbon Nanotubes/Poly(D,L-Lactide-co-Glycolide)*

Recently, carbon nanotubes have been used to improve the adsorption capacity and degradation performance of laccase carrying nanofibrous membranes. Dai et al. in 2016 improved the adsorption and degradation efficiency of a laccase carrying poly (D,L-lactide-co-glycolide) nanofibrous membrane towards the removal of BPA from water by the incorporation of multi-walled carbon nanotubes in the biocatalytic membrane [69]. The multi-walled carbon nanotubes modified membrane was prepared by emulsion electrospinning, the active laccase and multi-walled carbon nanotubes were encapsulated inside the fibers. The multi-walled carbon nanotubes laccase carrying membrane had an improved activity recovery of 85.3% (compared to free enzymes) which was higher than that of laccase modified membrane without the addition of the multi-walled carbon nanotubes (71.2%). Addition of the multi-walled carbon nanotubes in the laccase modified nanofibrous membrane improved the removal efficiency of BPA by up to 90% accompanied by a degradation efficiency of 80% and increase in adsorption efficiency of 45% compared to the laccase carrying nanofibrous membrane without the multi-walled carbon nanotubes. The enhanced degradation efficiency was mainly attributed to the presence of multi-walled carbon nanotubes which promoted direct electron transfer laccase-catalytic reaction [69].

17.5.8 Laccase-Multiwalled Carbon Nanotubes/Poly(D,L-Lactide) Nanofibrous Membrane

Dai and co-workers further enhanced the adsorption and degradation of BPA, triclosan and 2,4-dichlorophenol by modifying laccase carrying poly(D,L-lactide) nanofibrous membrane with multi-walled carbon nanotubes [35]. The removal efficiencies of the multi-walled carbon nanotubes biocatalytic membranes reached up to 95.5%, 92.6% and 99.7% for BPA, 2,4-dichlorophenol and triclosan, respectively. The laccase carrying multi-walled carbon nanotubes nanofibrous membrane exhibited high reactivity recovery (88.9% greater than free laccase), and improved operational and storage stability compared to the laccase modified membrane (without the multi-walled carbon nanotubes). The enhanced catalytic properties of the multi-walled carbon nanotubes modified membranes were ascribed to the improved adsorption efficiency and promoted electron transfer between laccase and the pollutant [35]. The inclusion of multi-walled carbon nanotubes in the nanofibrous membrane results in an increase in specific surface area, which therefore provided more sorption sites for the pollutant in aqueous medium. The improved adsorption efficiency due to the presence of multi-walled carbon nanotubes may also result in the pre-concentration of the pollutant around the active sites of laccase enzymes which in turn results in improved degradation efficiency. The remarkable electrical conductivity of the multi-walled carbon nanotubes promotes the direct electron transfer in laccase catalytic reactions.

Multi-walled carbon nanotubes were used to improve the catalytic performance of laccase immobilized on poly(vinyl alcohol)/chitosan nanofibrous membrane for the degradation of diclofenac [85]. The laccase modified membrane with incorporation of multi-walled carbon nanotubes attained a high activity retention (76.7% of free enzymes) than the laccase modified membrane without the nanotubes (63.5%). The removal efficiency of diclofenac for multi-walled nanotubes modified membrane was 100% in 6 h and was higher than that of laccase carrying membranes without the nanotubes (84.9%). Cyclic voltammetry measurements further confirmed the electrochemical capacitance of the multi-walled nanotubes modified membrane. Thus, the enhanced catalytic activity of the immobilized laccase on the multi-walled carbon nanotubes laccase carrying nanofibrous membrane was due to a synergistic effect of high specific surface area and promoted electron transfer between the laccase and the substrate [85]. Figure 17.6 illustrates the preparation of the multi-walled carbon nanotubes laccase immobilized on poly(vinyl alcohol)/chitosan nanofibrous membrane for biotransformation of diclofenac in water.

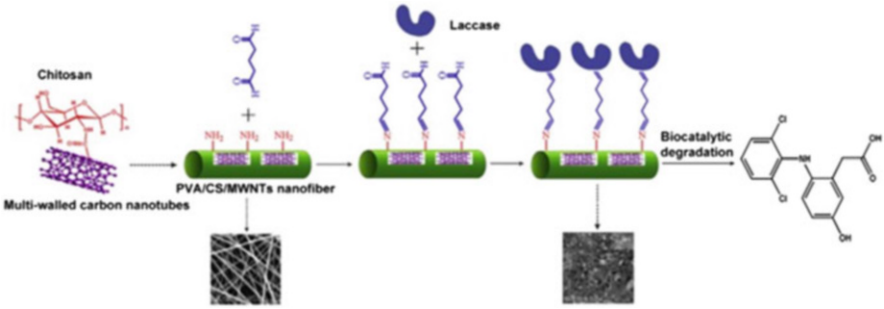

Fig. 17.6 Biocatalytic degradation of multi-walled carbon nanotubes-laccase immobilized on poly(vinyl alcohol)/chitosan nanofibrous membrane [85]

17.5.9 Cross-linked Carbon Nanotubes-Based Biocatalytic Membranes

Ji et al. prepared a biocatalytic membrane through cross-linking of the carbon nanotubes to form a stable coating on the hydrophilic polyvinylidene fluoride (PVDF) membrane with subsequent immobilization of laccase by physical adsorption and covalent bonding [86]. The carbon nanotubes were deposited on the PVDF membrane and further cross-linked with glutaraldehyde (Fig. 17.7a). A solution of laccase enzyme was passed through the carbon nanotubes modified membrane in the dead end filtration cell for immobilization of laccase through adsorption. Adsorption of enzymes on the carbon nanotubes could be by: (i) van der Waal forces and Π–Π stacking between the aromatic residues in the enzymes and the surface of carbon nanotubes; (ii) hydrophobic interactions between amino acids with hydrophobic side chains and the nanotubes surface; (iii) amphiphilic interactions resembling surfactant-like interactions; (iv) electrostatic interactions; and (v) hydrogen bonding between the amine terminal groups in the enzymes and the hydroxyl and carboxyl functional groups in the carbon nanotubes [67].

Laccase was also covalently bound on the carbon nanotubes modified membrane using *N*-(3-dimethylaminopropyl) *N*-ethylcarbodiimide chloride (EDC) and *N*-hydroxysuccinimide (NHS) as coupling agents (Fig. 17.7b). High laccase loading was achieved through covalent attachment of the laccase molecules ascribed to EDC-mediated stable covalent binding of carboxylated carbon nanotubes and laccase molecules. However, the laccase enzymes attached covalently exhibited lower apparent activity and activity recovering than for enzymes immobilized through adsorption. Covalent attachment of enzymes on supports may mitigate leaching out of enzymes, but the covalent bonds (especially multiple binding or non-biospecific attachment) may distort the natural conformation of the enzymes which leads to enzyme denaturation [57]. Moreover, the possibility of undesired lateral interactions between over-crowded enzymes may result in reduced activity of the immobilized enzymes [87].

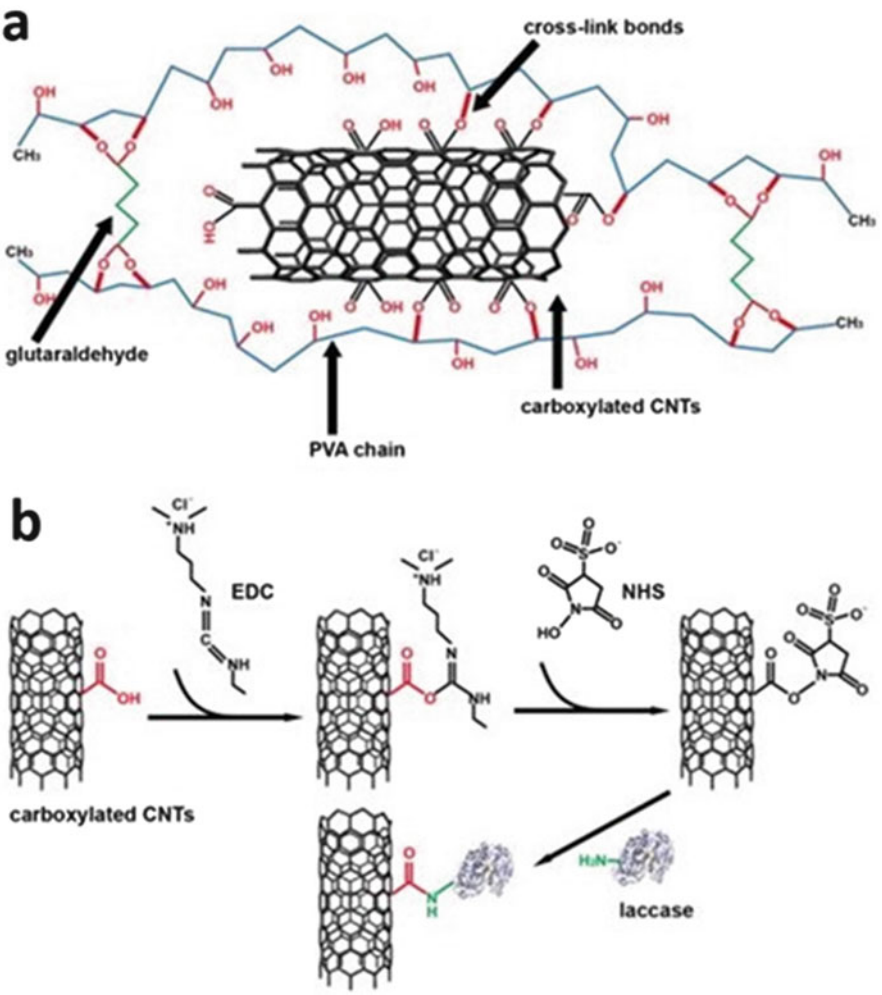

Fig. 17.7 Schematic diagram of the cross-linking mechanism of carbon nanotubes (CNTs), polyvinyl alcohol (PVA) and glutaraldehyde (GLU) (**a**) and laccase immobilization on CNTs coating layer via covalent bonding (**b**) [86]

The carbon nanotubes-based biocatalytic membrane was tested for the removal of various recalcitrant pollutants (BPA, diclofenac, ibuprofen, carbamazepine and clofibric acid) in a cocktail mixture under a dead end filtration cell. The carbon nanotubes modified membrane removed BPA (97%) and diclofenac (94%) at an operating flux of 15 L/m^{2}h. Ibuprofen (85%), carbamazepine (60%) and clofibric acid (55%) were removed at operating flux of 10 L/m^{2}h. The high removal efficiency of the prepared biocatalytic membrane was attributed to the improved mass diffusion of the micro-pollutants into the immobilized enzymes which resulted in accelerated biotransformation of the pollutants [57]. The improved

laccase loading upon modification of the membranes with carbon nanotubes was also a probable explanation to the enhanced removal performance of the biocatalytic membrane. The enhanced removal of the recalcitrant pollutants (ibuprofen, carbamazepine and clofibric acid) was ascribed to the generation of radicals (formed through oxidation of BPA) that could react with other non-phenol pollutants either as a mediator or via cross-coupling reactions [57].

17.5.10 Laccase Supported on TiO_2 Nanoparticles

Nanoparticles have also been used extensively for the immobilization of laccase for water purification purposes [50]. The intrinsic high surface area, tuneable surface and good stability have rendered nanoparticles as better supports for enzyme immobilization [88]. Most importantly, the highly curved nanoparticles, having the same size as the enzyme molecules, allow a high degree of freedom for the active sites of the enzymes thus preventing lateral interactions between the immobilized enzymes [87]. Hou et al. immobilized laccase on TiO_2 nanoparticles and TiO_2 blended polyethersulfone membrane using different surface functionalization techniques and immobilization approaches [87]. Laccase was immobilized on the nanoparticles and titania-modified membrane by physical adsorption, sequential and glutaraldehyde post-treatment techniques.

Physical adsorption technique exhibited lower activity recovery (up to $48 \pm 6\%$) than expected. This was attributed to the use of speed centrifugation for the removal of loosely attached laccase enzymes. The high shear forces might have distorted the native conformation of the attached enzymes which led to their inactivation [87]. In the sequential approach, the TiO_2 nanoparticles were first functionalized with 3-aminopropyltriethoxysilane (APTES) prior to covalent attachment of laccase (Fig. 17.8a). The glutaraldehyde post-treatment involved the binding of laccase on the 3-aminopropyltriethoxysilane modified TiO_2 nanoparticles in the absence of glutaraldehyde and subsequent cross-linking of the laccase immobilized nanoparticles with glutaraldehyde (Fig. 17.8b). Sequential procedure proved to be the best approach for laccase immobilization on the TiO_2 nanoparticles and the TiO_2 modified membrane. The results revealed an improved apparent activity (0.135 ± 0.015 U/mg support) and activity recovery ($79 \pm 6\%$) for the sequential approach of immobilization despite the low laccase loading (5.1 ± 0.5 μg/mg support). The glutaraldehyde used as a coupling agent allowed enough distance of immobilized laccase from support which resulted in improved mobility of the immobilized laccase, thus higher catalytic performance [87]. These results were in good agreement with a study conducted by Cabana et al. where laccase was immobilized on a Celite R-633 support using different immobilization techniques such as physical adsorption, sequential and glutaraldehyde post-treatment technique [89]. The immobilized laccase was tested for the removal of BPA, nonylphenol, and triclosan in a continuous packed bed reactor. Total elimination of the three endocrine

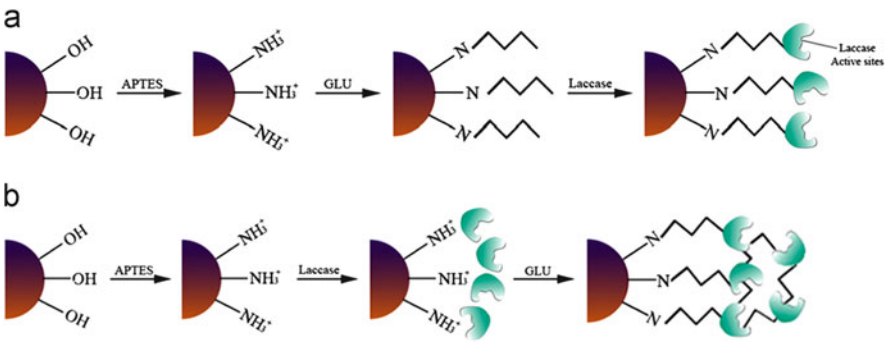

Fig. 17.8 Schematic representation of sequential laccase immobilization procedure (**a**) and glutaraldehyde post treatment (**b**) [87]

disrupting micro-pollutants (5 mg/L) was achieved over a 200 min contact time over five cycles [89].

17.5.11 Laccase Supported on Magnetic Fe_3O_4/SiO_2 Nanoparticles

A covalent attachment of laccase on magnetic Fe_3O_4/SiO_2 nanoparticles for improved biotransformation of azo dye from water has also been reported [90]. Almost 100% procion red MX-5B dye was decolourized in 20 min when the laccase carrying magnetic nanoparticles were used. The remarkable degradation rate was ascribed to the possible conformational changes of the laccase upon immobilization which promoted faster and direct electron transfer between laccase and the substrate as was confirmed by high responsive current at the glassy carbon electrode modified with immobilized laccase [90]. However, enzymes immobilized on nanoparticles may be difficult to recover and reuse and these are drawbacks for their application in wastewater treatment [25].

Enzymes immobilized on nanoparticles have been embedded on membranes for ease of recovery and reusability of immobilized enzymes. These hybrid systems also allow the applicability of the immobilized enzymes in a continuous configuration such as in enzyme membrane reactors for large scale applications [54, 87]. The continuous membrane separation configurations also enhance mass transfer for improved catalytic performance of the biocatalytic membranes.

17.5.12 Laccase Immobilized on Nanoparticles Functionalized Membranes

Hou et al. immobilized laccase on a TiO_2 functionalized PVDF membrane for the biodegradation of BPA [91]. The PVDF membrane was coated with TiO_2 nanoparticles using a sol-gel coating technique [92]. Laccase was covalently immobilized on the TiO_2 composite membrane via sequential immobilization using 3-aminopropyltriethoxysilane and glutaraldehyde. BPA removal efficiency of over 80% was achieved when PVDF parent membrane with pore sizes of 0.1 μm and 0.45 μm were used in the preparation of the biocatalytic composite membrane. The improved removal efficiency was ascribed to the enhanced mass transfer (at a flux of 20–30 L/m^2h) in a dead end filtration set up. Moreover, nano-sized structures such as nanoparticles have high surface area which may result in high enzyme loading and retained catalytic activity of immobilized enzymes for improved degradation efficiency. However, a decrease in removal efficiency was observed when the flux was further increased. This was ascribed to the limited retention time of BPA with immobilized laccase at higher flow rate [92].

17.5.13 Laccase Based-Enzyme Membrane Reactors

Immobilization of laccase enzymes on biocompatible polymeric membranes have proven to be an advantageous approach for the removal of trace organic pollutants [84, 91, 93]. However, large scale applications such as wastewater treatment plants favour the use of enzyme membrane reactors for the removal of most emerging micro-contaminants such as BPA. This approach involves the use of membranes with pore sizes that are smaller than the enzyme molecule to prevent leaching of the enzymes. The semi-permeable membrane creates a barrier that separates the enzymes from degradation products and the pollutant [92, 94, 95]. This technique involves use of free enzymes in a continuous process which offsets the mass transfer limitations and the undesirable inactivation of enzymes which is almost unavoidable during enzyme immobilization [49, 96].

Nguyen et al. reported on the use of an enzyme membrane reactor (EMR) for the continuous removal of BPA and diclofenac using a commercially available laccase [97]. A polyacrylonitrile hollow fiber ultrafiltration (UF) membrane was submerged in a reactor to prevent the wash out of laccase enzymes. The EMR degraded about 96% BPA in 4 h at neutral pH using syringaldehyde as a redox mediator. An overall BPA removal of 80% was achieved irrespective of pH after 22 h. The high removal efficiency of BPA was ascribed to the –OH group found in BPA which is a strong electron donating group thus rendering BPA a vulnerable substrate to laccase [97].

In a study conducted by Escalona et al., BPA was removed from water through catalytic oxidation of laccase and horseradish peroxidase in a membrane-reactor integrated system [25]. A BPA removal rate of about 95% was achieved in 180 min

for both enzymes under optimum conditions (pH 6 and 7 and laccase concentration of 0.2 U/mL). Coupling reaction system with nanofiltration membrane resulted in combined BPA removal by biotransformation and rejection. However, there was a significant decline in normalized flux during operation mainly due to concentration polarization and fouling [25].

Another study on the use of an enzymatic reactor was reported by Diano et al. [52]. Laccase was attached on a porous nylon hydrophobic membrane that was grafted with glycidyl methacrylate and phenylenediamine was used as a spacer [52]. Non-isothermal conditions have proven to be desirable for improved mass transfer in hydrophobic biocatalytic membranes. The temperature gradient normally results in improved substrate diffusion which in turn increases the frequency of enzyme and substrate contact time. Georgiva et al. covalently immobilized laccase on polypropylene membrane for the catalytic biotransformation of phenol and its derivatives in water [51]. The catalytic oxidation of 2-chlorophenol, 3-chlorophenol, 4-chlorophenol, nonylphenol and chloroxyphene were found to be at the same rate to that of phenol (21 μmol/min), while that of paracetamol, 3-methoxyphenol and chloroxyphenol was relatively smaller (17 μmol/min). High conversion rates for 2,4-dichlorophenol and BPA (34 μmol/min and 26 μmol/min, respectively) were reported [51].

17.6 Conclusion

The detrimental health effects caused by BPA have prompted researchers all over the world to come up with environmentally friendly and effective techniques that can completely eliminate BPA from various water systems. Enzymatic degradation of BPA has become a reliable method for effectively removing this pollutant in water. Enzymes, referred to as “green catalysts” are environmentally friendly and have high selectivity and reaction rates as compared to their chemical catalysts counterparts. However, the application of enzymes for water treatment on a large scale is normally hampered by their low tolerance to harsh micro environmental conditions found in most wastewater which may include extreme pH, temperature and ionic strength. Enzyme immobilization has gained much popularity in the field of biotechnology for improving the stability and catalytic activity of the immobilized enzymes. Most importantly, immobilized enzymes could be easily recovered and used repeatedly thus improving the economic feasibility of this approach. However, there is an inevitable change in native enzyme conformation upon immobilization which normally results in slight loss in enzyme activity. This negligible loss in catalytic performance of the immobilized enzymes depends heavily on the type of immobilization technique, the chemical and physical properties of the support and the physicochemical parameters during immobilization.

Laccase has been used extensively in the bioremediation of most phenolic pollutants such as BPA. Immobilization of laccase on membranes with different morphologies has been successfully employed for the removal of BPA from water. The

high specific surface area acquired through proper tailoring of the membranes increases the adsorption and degradation of BPA. Numerous nanostructured materials have been used to fabricate biocatalytic membranes with ideal properties for remarkable degradation efficiency of BPA.

The degradation efficiency of laccase modified membranes may be hampered by mass transfer limitations and product inhibition in batch systems. Therefore, continuous enzyme membrane reactor systems have been used to overcome such limitations. The transport rate and contact time of the substrate and the immobilized laccase can be easily controlled by adjusting the feed flow rate. The degradation efficiency of BPA has been found to be dependent on the substrate-enzyme contact time and frequency influenced by the feed flow. However, at flow rates or flux higher than the optimum rate, BPA degradation efficiency has been found to decrease primarily due to insufficient contact time between the substrate and immobilized enzyme and the possible denaturation of the enzymes under intense shear forces. Fouling and concentration polymerization of membranes may also result which impact negatively on the economic viability of this approach. Therefore, modification of these existing approaches or postulation of more effective techniques are still of great need for removal of BPA and other highly toxic pollutants from water.

Acknowledgements The authors are grateful to the Water Research Commission (Project No: K52488//3), Thuthuka National Research Foundation (TTK150608118953), Centre for Nanomaterials Science Research, University of Johannesburg (Faculty of Science), for funding.

References

1. Michalowicz J (2014) Bisphenol A—sources, toxicity and biotransformation. Environ Toxicol Pharmacol 37:738–758
2. Annamalai J, Namasivayam V (2015) Endocrine disrupting chemicals in the atmosphere: their effects on humans and wildlife. Environ Int 76:78–97
3. Giulivo M, Lopez De Alda M, Capri E, Barceló D (2016) Human exposure to endocrine disrupting compounds: their role in reproductive systems, metabolic syndrome and breast cancer. A review. Environ Res 151:251–264
4. Umar M, Roddick F, Fan L, Aziz AZ (2013) Application of ozone for the removal of bisphenol A from water and wastewater—a review. Chemosphere 90:2197–2207
5. Gassara F, Brar SK, Verma M, Tyagi RD (2013) Bisphenol A degradation in water by ligninolytic enzymes. Chemosphere 92:1356–1360
6. Lin J, Liu Y, Chen S, Le X, Zhou X, Zhao Z, Ou Y, Yang J (2016) Reversible immobilization of laccase onto metal-ion-chelated magnetic microspheres for bisphenol A removal. Int J Biol Macromol 84:189–199
7. Rochester JR (2013) Bisphenol A and human health: a review of the literature. Reprod Toxicol 42:132–155
8. Yang Q, Gao M, Luo Z, Yang S (2016) Enhanced removal of bisphenol A from aqueous solution by organo-montmorillonites modified with novel Gemini pyridinium surfactants containing long alkyl chain. Chem Eng J 285:27–38

9. Dehghani MH, Ghadermazi M, Bhatnagar A, Sadighara P, Jahed-Khaniki G, Heibati B, McKay G (2016) Adsorptive removal of endocrine disrupting bisphenol A from aqueous solution using chitosan. J Environ Chem Eng 4:2647–2655
10. Huang Q, Weber WJ (2005) Transformation and removal of bisphenol A from aqueous phase via peroxidase-mediated oxidative coupling reactions: efficacy, products, and pathways. Environ Sci Technol 39:6029–6036
11. Huang YQ, Wong CK, Zheng JS, Bouwman H, Barra R, Wahlstrom B, Neretin L, Wong MH (2012) Bisphenol A (BPA) in China: a review of sources, environmental levels, and potential human health impacts. Environ Int 42:91–99
12. Flint S, Markle T, Thompson S, Wallace E (2012) Bisphenol A exposure, effects, and policy: a wildlife perspective. J Environ Manage 104:19–34
13. Hoekstra EJ, Simoneau C (2013) Release of bisphenol A from polycarbonate: a review. Crit Rev Food Sci Nutr 53:386–402
14. Pouokam GB, Ajaezi GC, Mantovani A, Orisakwe OE, Frazzoli C (2014) Use of bisphenol A-containing baby bottles in Cameroon and Nigeria and possible risk management and mitigation measures: Community as milestone for prevention. Sci Total Environ 481:296–302
15. Zhou Y, Chen L, Lu P, Tang X, Lu J (2011) Removal of bisphenol A from aqueous solution using modified fibric peat as a novel biosorbent. Sep Purif Technol 81:184–190
16. Maduka IC, Ezeonu FE, Neboh EE, Shu EN, Ikekpeazu EJ (2010) BPA and environmental estrogen in potable water sources in Enugu municipality, south-east, Nigeria. Bull Environ Contam Toxicol 85:534–537
17. Omoruyi MI, Ahamioje D, Pohjanvirta R (2014) Dietary exposure of Nigerians to mutagens and estrogen-like chemicals. Int J Environ Res Public Health 11:8347–8367
18. Olujimi OO, Fatoki OS, Daso AP, Akinsoji OS, Oputu OU, Oluwafemi OS, Songca SP (2013) Levels of nonylphenol and bisphenol A in wastewater treatment plant effluent, sewage sludge and leachates around Cape Town, South Africa. In: Valdez CJ, Maradona EM (eds) Handbook of wastewater treatment. CRC Press, Boca Raton, pp 305–316
19. SANS 214 (2006) (Ed. 6). www.alabbott.co.za/docs/2985_SANS-241_spec.pdf. Accessed 6 Feb 2017
20. De Jager C, Swart P, Truebody B (2013) Estrogenic activity and endocrine disrupting chemical (EDC) status in water obtained from selected distribution points in Pretoria and Cape Town. WRC report no. KV 317/13
21. Baluka SA, Rumbeiha WK (2016) Bisphenol A and food safety: lessons from developed to developing countries. Food Chem Toxicol 92:58–63
22. Wetherill YB, Akingbemi BT, Kanno J, McLachlan JA, Nadal A, Sonnenschein C, Watson CS, Zoeller RT, Belcher SM (2007) In vitro molecular mechanisms of bisphenol A action. Reprod Toxicol 24:178–198
23. Meeker JD, Calafat AM, Hauser R (2010) Urinary bisphenol A concentrations in relation to serum thyroid and reproductive hormone levels in men from an infertility clinic. Environ Sci Technol 44:1458–1463
24. Doherty LF, Bromer JB, Zhou Y, Aldad TS, Taylor HS (2010) In utero exposure to diethylstilbestrol (DES) or bisphenol-A (BPA) increases EZH2 expression in the mammary gland: an epigenetic mechanism linking endocrine disruptors to breast cancer. Horm Cancer 1:146–155
25. Escalona I, de Grooth J, Font J, Nijmeijer K (2014) Removal of BPA by enzyme polymerization using NF membranes. J Memb Sci 468:192–201
26. Vom Saal FS et al (2007) Chapel Hill bisphenol A expert panel consensus statement: integration of mechanisms, effects in animals and potential to impact human health at current levels of exposure. Reprod Toxicol 24:131–138
27. Park Y, Sun Z, Ayoko GA, Frost RL (2014) Bisphenol A sorption by organo-montmorillonite: implications for the removal of organic contaminants from water. Chemosphere 107:249–256
28. Erjavec B, Hudoklin P, Perc K, Tisler T, Dolenc MS, Pintar A (2016) Glass fiber-supported TiO_2 photocatalyst: efficient mineralization and removal of toxicity/estrogenicity of bisphenol A and its analogs. Appl Catal B Environ 183:149–158

29. Tsai WT, Hsu HC, Su TY, Lin KY, Lin CM (2006) Adsorption characteristics of bisphenol-A in aqueous solutions onto hydrophobic zeolite. J Colloid Interface Sci 299:513–519
30. Rathnayake SI, Xi Y, Frost RL, Ayoko GA (2016) Environmental applications of inorganic-organic clays for recalcitrant organic pollutants removal: bisphenol A. J Colloid Interface Sci 470:183–195
31. Katsigiannis A, Noutsopoulos C, Mantziaras J, Gioldasi M (2015) Removal of emerging pollutants through granular activated carbon. Chem Eng J 280:49–57
32. Gong S, Li S, Ma J, Zhang X (2016) Synthesis of recyclable powdered activated carbon with temperature responsive polymer for bisphenol A removal. Sep Purif Technol 157:131–140
33. Park Y, Ayoko GA, Frost RL (2011) Application of organoclays for the adsorption of recalcitrant organic molecules from aqueous media. J Colloid Interface Sci 354:92–305
34. Jiuhui QU (2008) Research progress of novel adsorption processes in water purification: a review. J Environ Sci 20:1–13
35. Dai Y, Yao J, Song Y, Wang S, Yuan Y (2016) Enhanced adsorption and degradation of phenolic pollutants in water by carbon nanotube modified laccase-carrying electrospun fibrous membranes. Environ Sci Nano 3:857–868
36. Yuksel S, Kabay N, Yuksel M (2013) Removal of bisphenol A (BPA) from water by various nanofiltration (NF) and reverse osmosis (RO) membranes. J Hazard Mater 263:307–310
37. Wu H, Niu X, Yang J, Wang C, Lu M (2016) Retentions of bisphenol A and norfloxacin by three different ultrafiltration membranes in regard to drinking water treatment. Chem Eng J 294:410–416
38. Heo J, Flora JR, Her N, Park YG, Cho J, Son A, Yoon Y (2012) Removal of bisphenol A and 17β-estradiol in single walled carbon nanotubes-ultrafiltration (SWNTs-UF) membrane systems. Sep Purif Technol 90:39–45
39. Escalona I, Fortuny A, Stuber F, Bengoa C, Fabregat A, Font J (2014) Fenton coupled with nanofiltration for elimination of bisphenol A. Desalination 345:77–84
40. Gmurek M, Olak-Kucharczyk M, Ledakowicz S (2016) Photochemical decomposition of endocrine disrupting compounds—a review. Chem Eng J 310:437–456
41. Keykavoos R, Mankidy R, Ma H, Jones H, Soltan J (2013) Mineralization of bisphenol A by catalytic ozonation over alumina. Sep Purif Technol 107:310–317
42. Sharma J, Mishra IM, Kumar V (2015) Degradation and mineralization of bisphenol A (BPA) in aqueous solution using advanced oxidation processes: UV/H_2O_2 and UV/$S_2O_8^{2-}$ oxidation systems. J Environ Manage 156:266–275
43. Wu W, Shan G, Wang S, Zhu L, Yue L, Xiang Q (2016) Environmentally relevant impacts of nano-TiO_2 on abiotic degradation of bisphenol A under sunlight irradiation. Environ Pollut 216:166–172
44. Zhao J, Li Y, Zhang C, Zeng Q, Zhou Q (2008) Sorption and degradation of bisphenol A by aerobic activated sludge. J Hazard Mater 155:305–311
45. Ferro Orozco AM, Lobo CC, Contreras EM, Zaritzky NE (2013) Biodegradation of bisphenol-A (BPA) in activated sludge batch reactors: Analysis of the acclimation process. Int Biodeterior Biodegrad 85:392–399
46. Hirano T, Honda Y, Watanabe T, Kuwahara M (2000) Degradation of bisphenol A by the lignin-degrading enzyme, manganese peroxidase, produced by the white-rot basidiomycete, *Pleurotus ostreatus*. Biosci Biotechnol Biochem 64:1958–1962
47. Taboada-Puig R, Eibes G, Lloret L, Lu-Chau TA, Feijoo G, Moreira MT, Lema JM (2016) Fostering the action of versatile peroxidase as a highly efficient biocatalyst for the removal of endocrine disrupting compounds. N Biotechnol 33:187–195
48. Daâssi D, Prieto A, Zouari-Mechichi H, Martínez MJ, Nasri M, Mechichi T (2016) Degradation of bisphenol A by different fungal laccases and identification of its degradation products. Int Biodeterior Biodegrad 110:181–188
49. Lloret L, Eibes G, Feijoo G, Moreira MT, Lema JM (2012) Degradation of estrogens by laccase from *Myceliophthora thermophila* in fed-batch and enzymatic membrane reactors. J Hazard Mater 213–214:175–183

50. Wang H, Zhang W, Zhao J, Xu L, Zhou C, Chang L, Wang L (2013) Rapid decolorization of phenolic azo dyes by immobilized laccase with Fe_3O_4/SiO_2 nanoparticles as support. Ind Eng Chem Res 52:4401–4407
51. Georgieva S, Godjevargova T, Mita DG, Diano N, Menale C, Nicolucci C (2010) Enzymatic Non-isothermal bioremediation of waters polluted by phenol and some of its derivatives by laccase covalently immobilized on polypropylene membranes. J Mol Catal B Enzym 91: 210–218
52. Diano N, Grano V, Fraconte L, Caputo P, Ricupito A (2007) Non-isothermal bioreactors in enzymatic remediation of waters polluted by endocrine disruptors: BPA as a model of pollutant. Appl Catal B Environ 69:52–261
53. Zhu W, Zhang Y, Hou C, Pan D, He J, Zhu H (2016) Covalent immobilization of lipases on monodisperse magnetic microspheres modified with PAMAM-dendrimer. J Nanoparticle Res 18:1–13
54. Jochems P, Satyawali Y, Dejonghe W (2011) Green chemistry enzyme immobilization on/in polymeric membranes: status, challenges and perspectives in biocatalytic membrane reactors (BMRs). Green Chem 13:1609–1623
55. Srbová J, Slováková M, Křípalová Z, Žárská M, Špačková M, Stránská D, Bílková Z (2016) Covalent biofunctionalization of chitosan nanofibers with trypsin for high enzyme stability. React Funct Polym 104:38–44
56. Jolivalt C, Brenon S, Caminade E, Mougin C, Pontié M (2000) Immobilization of laccase from *Trametes versicolor* on a modified PVDF microfiltration membrane: Characterization of the grafted support and application in removing a phenylurea pesticide in wastewater. J Memb Sci 180:103–113
57. Wang ZG, Wan LS, Liu ZM, Huang XJ, Xu ZK (2009) Enzyme immobilization on electrospun polymer nanofibers: an overview. J Mol Catal B Enzym 56:189–195
58. Sulaiman S, Mokhtar MNA (2015) Review: potential usage of cellulose nanofibers (CNF) for enzyme immobilization via covalent interactions. Appl Biochem Biotechnol 175:1817–1842
59. Gao Y, Truong Y, Cacioli Y, Butler P, Kyratzis L (2014) Bioremediation of pesticide contaminated water using an organophosphate degrading enzyme immobilized on nonwoven polyester textiles. Enzyme Microb Technol 54:38–44
60. Mugdha A, Usha M (2012) Enzymatic treatment of wastewater containing dyestuffs using different delivery systems. Sci Rev Chem Commun 2:31–40
61. Fernando Bautista L, Morales G, Sanz R (2010) Immobilization strategies for laccase from *Trametes versicolor* on mesostructured silica materials and the application to the degradation of naphthalene. Bioresour Technol 101:8541–8548
62. Khoobi M, Motevalizadeh SF, Asadgol Z, Forootanfar H, Shafiee A, Faramarzi MA (2015) Polyethyleneimine-modified superparamagnetic Fe_3O_4 nanoparticles for lipase immobilization: characterization and application. Mater Chem Phys 150:77–86
63. Saleem M, Rafiq M, Seo SY, Lee KH (2016) Acetylcholinesterase immobilization and characterization, and comparison of the activity of the porous silicon-immobilized enzyme with its free counterpart. Biosci Rep 36:1–9
64. Zhu J, Sun G (2012) Lipase immobilization on glutaraldehyde-activated nanofibrous membranes for improved enzyme stabilities and activities. React Funct Polym 72:839–845
65. Xu R, Zhou Q, Li F, Zhang B (2013) Laccase immobilization on chitosan/poly(vinyl alcohol) composite nanofibrous membranes for 2,4-dichlorophenol removal. Chem Eng J 222:321–329
66. Brena B, Gonzalez-Pombo P, Batista-Viera F (2013) Immobilization of enzymes: a literature survey. In: Guisan JM (ed) Immobilization of enzymes and cells: third edition, Methods in molecular biology, vol 1051. Springer, New York, pp 15–31
67. Tavares AP, Silva CG, Dražić G, Silva AMT, Loureiro JM, Faria JL (2015) Laccase immobilization over multi-walled carbon nanotubes: kinetic, thermodynamic and stability studies. J Colloid Interface Sci 454:52–60
68. Krajewska B (2014) Enzyme immobilization by adsorption: a review modifier enzyme. Adsorption 20:801–821

69. Dai Y, Yao J, Song Y, Liu X, Wang S, Yuan Y (2016) Enhanced performance of immobilized laccase in electrospun fibrous membranes by carbon nanotubes modification and its application for bisphenol A removal from water. J Hazard Mater 317:485–493
70. Kim J, Grate J, Wang P (2006) Nanostructures for enzyme stabilization. Chem Eng Sci 61: 1017–1026
71. Jindong A (2010) Enzyme immobilised on woolen cloth. PhD Thesis, University of Auckland, New Zealand
72. Fatarella E, Spinelli D, Ruzzante M, Pogni R (2014) Nylon 6 film and nanofiber carriers: preparation and laccase immobilization performance. J Mol Catal B Enzym 102:41–47
73. Isgrove FH, Williams RJ, Niven GW, Andrews AT (2001) Enzyme immobilization on nylon-optimization and the steps used to prevent enzyme leakage from the support. Enzyme Microb Technol 28:225–232
74. Hamidi A, Rashidi M, Asgari D, Aghanejad A, Davaran S (2012) Covalent immobilization of trypsin on a novel aldehyde-terminated pamam dendrimer. Bull Korean Chem Soc 33: 2181–2186
75. Xu R, Chi C, Li F, Zhang B (2013) Immobilization of horseradish peroxidase on electrospun microfibrous membranes for biodegradation and adsorption of bisphenol A. Bioresour Technol 149:111–116
76. Maryšková M, Ardao I, García-González CA, Martinová L, Rotková J, Ševců A (2016) Polyamide 6/chitosan nanofibers as support for the immobilization of *Trametes versicolor* laccase for the elimination of endocrine disrupting chemicals. Enzyme Microb Technol 89: 31–38
77. Quan J, Liu Z, Branford-White C, Nie H, Zhu L (2014) Fabrication of glycopolymer/MWCNTs composite nanofibers and its enzyme immobilization applications. Colloids Surf B Biointerf 121:417–424
78. Cabana H, Ahamed A, Leduc R (2011) Conjugation of laccase from the white rot fungus *Trametes versicolor* to chitosan and its utilization for the elimination of triclosan. Bioresour Technol 102:1656–1662
79. Ignatova M, Stoilova O, Manolova N, Mita D, Diano N, Nicolucci C, Rashkov I (2009) Electrospun microfibrous poly(styrene-alt-maleic anhydride)/poly(styrene-co-maleic anhydride) mats tailored for enzymatic remediation of waters polluted by endocrine disruptors. Eur Polym J 45:2494–2504
80. Cloete W, Adriaanse C, Swart P, Klumperman B (2011) Facile immobilization of enzymes on electrospun poly(styrene-alt-maleic anhydride) nanofibres. Polym Chem 2:1479–1481
81. Silva C, Silva CJ, Zille A, Guebitz GM, Cavaco-Paulo A (2007) Laccase immobilization on enzymatically functionalized polyamide 6,6 fibres. Enzyme Microb Technol 41:867–875
82. Sirisha VL, Jain A, Jain A (2016) Enzyme immobilization: an overview on methods, support material and applications of immobilized enzymes, 1st edn. Elsevier, Amsterdam
83. Dai Y, Yin L, Niu J (2011) Laccase-carrying electrospun fibrous membranes for adsorption and degradation of PAHs in shoal soils. Environ Sci Technol 45:10611–10618
84. Sathishkumar P, Chae J, Unnithan AR, Palvannan T, Yong H, Lee K, Cho M, Kamala-Kannan S, Oh B (2012) Enzyme and microbial technology laccase-poly(lactic-co-glycolic acid) (PLGA) nanofiber: Highly stable, reusable, and efficacious for the transformation of diclofenac. Enzyme Microb Technol 51:113–118
85. Xu R, Tang R, Zhou Q, Li F, Zhang B (2015) Enhancement of catalytic activity of immobilized laccase for diclofenac biodegradation by carbon nanotubes. Chem Eng J 262:88–95
86. Ji C, Hou J, Chen V (2016) Cross-linked carbon nanotubes based biocatalytic membranes for micro-pollutants degradation: performance, stability, and regeneration. J Memb Sci 520: 869–880
87. Hou J, Dong G, Ye Y, Chen V (2014) Laccase immobilization on titania nanoparticles and titania-functionalized membranes. J Memb Sci 452:229–240
88. Zimmermann YS, Shahgaldian P, Corvini PF, Hommes G (2011) Sorption-assisted surface conjugation: A way to stabilize laccase enzyme. Appl Microbiol Biotechnol 92:169–178

89. Cabana H, Alexandre C, Agathos SN, Jones JP (2009) Immobilization of laccase from the white rot fungus *Coriolopsis polyzona* and use of the immobilized biocatalyst for the continuous elimination of endocrine disrupting chemicals. Bioresour Technol 100:3447–3458
90. Dai J, Wang H, Chi H, Wang Y, Zhao J (2016) Immobilization of laccase from *Pleurotus ostreatus* on magnetic separable SiO_2 support and excellent activity towards azo dye decolorization. J Environ Chem Eng 4:2585–2591
91. Sathishkumar P, Kamala-Kannan S, Cho M, Kim JS, Hadibarata T, Salim MR, Oh BT (2014) Laccase immobilization on cellulose nanofiber: The catalytic efficiency and recyclic application for simulated dye effluent treatment. J Mol Catal B Enzym 100:111–120
92. Hou J, Dong G, Ye Y, Chen V (2014) Enzymatic degradation of bisphenol-A with immobilized laccase on TiO_2 sol-gel coated PVDF membrane. J Memb Sci 469:19–30
93. Lante A, Crapisi A, Krastanov A, Spettoli P (2000) Biodegradation of phenols by laccase immobilised in a membrane reactor. Process Biochem 36:51–58
94. López C, Mielgo I, Moreira MT, Feijoo G, Lema JM (2002) Enzymatic membrane reactors for biodegradation of recalcitrant compounds. Application to dye decolourisation. J Biotechnol 99:249–225
95. Nady E, Lepossa A, Prettl Z (2012) Mass transfer through a biocatalytic membrane reactor. Ind Eng Chem Res 51:1635–1646
96. Nady N, Charles M, Franssen R, Zuilhof H, Boom RM, Schroën K (2012) Enzymatic modification of polyethersulfone membranes. Water 4:932–943
97. Nguyen LN, Hai FI, Price WE, Leusch FD, Roddick F, McAdam EJ, Magram SF, Nghiem ID (2014) Continuous biotransformation of bisphenol A and diclofenac by laccase in an enzymatic membrane reactor. Int Biodeterior Biodegrad 95:25–32

Chapter 18
Synthesis and Characterization of a Novel Bio Nanosponge Filter (pMWCNT-CD/TiO_2-Ag) as Potential Adsorbent for Water Purification

Anny Leudjo Taka, Kriveshini Pillay, and Xavier Yangkou Mbianda

Abstract This study reports the synthesis and characterization of a novel bio nanosponge filter for applications in water treatment. Firstly the oxidized multiwalled carbon nanotubes (MWCNTs) were chlorinated using oxalyl chloride and then phosphorylated via an amidation reaction. The phosphorylated carbon nanotube (pMWCNT) obtained was polymerized with β-cyclodextrin (βCD) using hexamethylene diisocyanate (HMDI) as a linker. The resulting polymer (pMWCNT-βCD) was decorated by a sol-gel method with TiO_2 and Ag nanoparticles to obtain a biopolymer nanocomposite, pMWCNT-βCD/TiO_2-Ag. For a better evaluation of the target material, CD polymer and pMWCNT-CD polymer were also synthesized for comparison purposes. Fourier-transform infrared (FTIR) spectroscopy was used to confirm the presence of functional groups on the surface of modified MWCNTs and the polymerization reaction. Laser Raman spectroscopy analysis showed the presence of MWCNT, CD and the anatase crystalline form of TiO_2 in the nanocomposite. Preliminary adsorption studies were also conducted in order to test the capability of the new bio nanosponge filter to remove metal ions pollutants from synthetic wastewater solutions.

Keywords Cyclodextrin • Bio nanosponge filter • Nanocomposite • Amidation reaction • Phosphorylated multiwalled carbon nanotubes • TiO_2 nanoparticle and adsorption

18.1 Introduction

Access to clean and potable water is currently a worldwide challenge due to the pollution of water by human activities, sewage, industrial effluents, etc. [1, 2]. In this regard, the increased demand for new adsorbent nanocomposite materials with

A. Leudjo Taka (✉) • K. Pillay • X.Y. Mbianda (✉)
Department of Applied Chemistry, University of Johannesburg, Doornfontein, Johannesburg 2028, South Africa
e-mail: lytany04@yahoo.fr; kriveshinip@uj.ac.za; mbianday@uj.ac.za

P. Ramasami et al. (eds.), *Emerging Trends in Chemical Sciences*,
DOI 10.1007/978-3-319-60408-4_18

good properties and high efficiency for pollutant removal, has attracted a lot of research attentions [1, 2]. For this reason, this study reports an investigation on the synthesis and characterization of a novel bio nanosponge filter or biopolymer nanocomposite capable to remove the organic, inorganic and pathogenic microorganism pollutants from waste water. The new adsorbent nanocomposite is made up of a combination of cyclodextrin nanosponge polymer, phosphorylated multiwalled carbon nanotube, titania (TiO_2) and silver nanoparticles.

Cyclodextrins (CDs) are cyclic oligosaccharides and they are produced as a result of enzymatic reactions (intramolecular transglycosylation) on starch with the amylase of *Bacillus macerans* [3–5]. There exists three types of natural cyclodextrins (α-CD, β-CD and γ-CD) with 6, 7, 8 glucose units respectively, attached by α-(1,4) glucosidic bonds forming a ring. Of these three natural CDs which also differ in ring size and solubility, β-CDs are the most widely used due to their good reactivity and lower cost [3–5]. The use of cyclodextrins has attracted a lot of research attention because they possess extraordinary properties such as their capacity to form inclusion complexes with a guest molecule and their ability to be modified using for example a cross-linking agent (e.g. isocyanate linker) to form nanosponge polyurethanes exhibiting even more attractive properties [3, 6, 7].

In this regard, extensive research has been done in our group and elsewhere on the synthesis of nanosponge cyclodextrin polyurethanes and on how to improve their properties by modifying them with either nanoparticles, functionalized MWCNTs (oxidized or phosphorylated MWCNTs) or dendrimers [3, 7–12]. Hence, by modifying the nanosponge cyclodextrin polyurethanes, polymer-based nanocomposite materials with high potential in many applications especially in water purification are formed.

Nanocomposites can be defined as materials with multiphases where one of the phases has nanoscale additives [13]. They are likely to present extraordinary properties arising from the combination of each component [13]. Depending on the type of matrix used, the nanocomposites can be classified as polymer matrix nanocomposites (PMNC), ceramic matrix nanocomposites (CMNC) and metal matrix nanocomposites (MMNC) [13]. In this study the CD polymer was the matrix because polymers are considered to be good hosting matrices for composite materials. This is due to the fact that they can easily be tailored to yield a variety of bulk physical properties [13]. In addition polymers, especially the organic ones such as CD polymers, have been reported to have long term stability and good processability [13]. For this reason, β-CD polymer in this study was modified with phosphorylated carbon nanotubes as reported by Mamba and co-workers [2] in order to obtain the polymer pMWCNT-CD. This was further modified in this work by decorating it with TiO_2 and Ag nanoparticles in order to get a novel bio nanosponge filter (pMWCNT-CD/TiO_2-Ag) with organic, inorganic and antimicrobial properties. To the best of our knowledge, the synthesis of this type of material has never been reported elsewhere.

This paper reports the synthesis of a novel bio nanosponge filter (phosphorylated carbon nanotubes-cyclodextrin/Ag-doped titania) and its characterization using a variety of thermal, spectroscopic and electron microscopic techniques. The results

obtained from the characterization of the novel phosphorylated carbon nanotubes-cyclodextrin/Ag-doped titania are also discussed and compared with the control samples (native CD polymer and pMWCNT-CD polymer). In addition, the preliminary test results for the removal of lead and cobalt ions from the synthetic waste water using the novel bio nanosponge filter are also presented.

18.2 Experimental Methodology

18.2.1 Chemicals and Materials

All the chemicals and materials purchased were used as received. MWCNTs (purity > 90%, diam. × L 110–170 mm × 5–9 μm), β-CDs (97%), titanium tetraisopropoxide (TTIP), 2-propanol, oxalyl chloride, diethyl(alpha-aminobenzyl)-phosphonate (97%), 6-amino-hexanol (97%), *N*,*N*-dimethylformamide (DMF, 99.9%), hexamethylene diisocyanate (HMDI, 98.0%) and cobalt(II) nitrate hexahydrate (ACS reagent 98%) were obtained from Sigma-Aldrich, South Africa. Lead(II) nitrate (98%) was purchased from Saarchem, Merck Chemicals, South Africa and silver nitrate (99.8%) was obtained from Rochelle Chemicals, South Africa.

18.2.2 Purification and Oxidation of Multi-walled Carbon Nanotubes

As received MWCNTs (pristine MWCNTs) were purified by Soxhlet extraction with toluene for 24 h. Thereafter the product was dried at 80 °C to obtain purified MWCNTs.

The oxidation of MWCNTs was done by acid treatment as described by previous studies [2, 9] using a mixture of 3:1 H_2SO_4:HNO_3. After the acid treatment reaction, the mixture was diluted with distilled water (about 500 ml) and allowed to cool down to room temperature. The MWCNTs were filtered using a membrane microfiltration apparatus and then extensively rinsed with distilled water until the wash water reached a neutral pH. The resulting product was dried in an oven at 80 °C overnight.

18.2.3 Synthesis of the Biopolymer Nanocomposites: pMWCNT-CD/Ag-TiO_2

18.2.3.1 Phosphorylation of Oxidized MWCNTs

It was carried out following the methodology reported by Mamba and co-workers [2]. In summary, 0.1 g of oxidized MWCNTs dispersed in 50 ml of DMF were chlorinated using 3.35 ml of oxalyl chloride at 0 °C. The mixture was stirred for 2 h at 0 °C for an additional 2 h at room temperature. Then the reaction temperature was increased to 70 °C and the mixture stirred overnight to get rid of the excess of oxalyl chloride. The following day, 1 g of diethyl(alpha-aminobenzyl)-phosphonate hydrochloride (dissolved in DMF) and 6-amino-hexanol (0.25 g in DMF) were added simultaneously to the reaction mixture using dropping funnels. Then the temperature was raised to 100 °C and the mixture stirred for 5 days. Afterwards the reaction mixture was filtered, washed with a small amount of ethanol and DMF and dried in the oven at 80 °C for 24 h to yield 0.411 g of pMWCNT.

18.2.3.2 Polymerisation of Phosphorylated MWCNTs (pMWCNTs) with β-CDs

It was performed as described by Mamba et al. [2] using HMDI as a linker. In summary, 0.05 g of pMWCNT (5%) sonicated in 5 ml DMF was mixed with 1 g of β-CD (also dispersed in 25 ml DMF). The reaction mixture was stirred under nitrogen atmosphere at room temperature while adding dropwise 6 ml of HMDI. Then the temperature was increased to 75 °C and stirring was continued for 24 h. Afterwards the reaction was cooled down and the product obtained, that is phosphorylated MWCNTs-CD (pMWCNTs-CD), was precipitated in acetone, filtered, washed and dried in oven at 80 °C (Yield = 3.965 g).

18.2.3.3 Sol-Gel Method to Obtain pMWCNTs-CD/Ag-TiO_2 Biopolymer

This final step of the synthesis was done following a procedure reported by Perumal and co-workers [14] with some modifications. In short, 2.5 ml of titanium tetraisopropoxide (TTIP) was added to 0.607 g of pMWCNTs-CD polymer previously dispersed in 12.5 ml of 2-propanol (ratio pMWCNTs-CD polymer:TiO_2 was 90%). The mixture was then stirred for 10 min followed by a hydrolysis reaction where 2.5 ml of an aqueous solution (pH 2) containing an appropriate weighed amount of $AgNO_3$ to give a Ag:Ti ratio of 7%, was added dropwise to the mixture solution while stirring. The resulting sol was stirred vigorously and continuously for 24 h at room temperature. Then the suspension was dried at 80 °C for 2 h to yield 1.758 g of pMWCNT-CD/TiO_2-Ag. During the reaction and drying process, the

beaker was covered with aluminium foil paper. After 2 h of drying, the product obtained was calcined at 150 °C for 15, 60 and 120 min in an electric furnace.

18.2.3.4 Synthesis of Native CD Polymer

Native CD polymer was prepared as reported in previous studies [3, 7, 9, 10] by reacting a dimethylformamide (DMF) solution of β-CDs with HMDI (bifunctional linker). The product was obtained in good yield (3.718 g).

18.2.4 Characterization Techniques

Fourier-transform infrared (FTIR) spectroscopy was used to confirm the functionalization of the MWCNTs and polymerisation reaction. For the analysis a transparent pellet for respective samples was prepared using a mechanical press by mixing 99 parts of potassium bromide (KBr) with 1 part of the sample to be analysed. The spectra obtained were recorded on a Perkin Elmer (FTIR, spectrum 100) spectrophotometer with 16 scans per spectrum, at a resolution of 4 cm^{-1}, over the range of 4000–400 cm^{-1}.

Thermogravimetric analysis (TGA) was done for the thermal stability studies of the polymer synthesized. The analysis was done using a Pyris Series-TGA 4000 analyser under nitrogen atmosphere (20 ml/min) at a rate of 10 °C/min and temperature programmed from 30 to 900 °C. About 10 mg of each sample was used for analysis.

The curves of the differential scanning calorimetry (DSC) were recorded using a Mettler Toledo DSC 822^e. The analysis was done under nitrogen atmosphere at a flow rate of 25 ml/min, heating rate 10 °C/min and about 5 mg of each sample was heated from 25 to 500 °C, then cooling back to 25 °C. In this work, the DSC curves reported are only the heating part (from 25 to 500 °C) of the DSC analysis.

Raman spectra were obtained using a Bruker Senterra Infinity 1 Raman microscope with the beam path set at 10× magnification. This analysis was employed to evaluate the quality of the samples prepared and for phase identification of TiO_2 present in the new biopolymer nanocomposite synthesized.

X-ray diffraction spectroscopy analyses were performed using a Rigaku Ultima IV X-Ray (40 kV, 30 mA) diffractometer with cobalt Kα radiation (wavelength = 0.179 nm). The data were processed using PDXL software loaded with ICDD card (database). The conditions for analysis were as follows: scan speed 2 deg/min, step width 0.02 degree, scan range 3–90 degrees.

The surface area, pore volume and pore size of the synthesized polymers were determined by the Brunauer-Emmett-Teller (BET) method on a Micromeritics Tristar 3000 surface area and porosity analyser. To analyze the samples, about 0.25 g of each sample was degassed for 4 h under nitrogen at 100 °C.

Scanning electron microscopy (SEM) (Vega 3 Tescan) coupled with energy dispersive spectroscopy (EDS) was employed to determine the surface morphologies and the elemental compositions of the materials synthesized. For analysis, a few mg of each sample was placed on a carbon tape. All the polymer samples were then gold coated in order to make their surfaces conductive whereas the carbon tapes with oxidized MWCNT and phosphorylated MWCNT were not coated.

18.2.5 Preliminary Adsorption Experiments

The adsorption experiments (Fig. 18.1) were performed as described by Mamba and co-workers [2]; pMWCNT-CD/Ag-TiO_2 bio nanosponge filter prepared was tested for its ability to remove each of the metal ions (Pb^{2+} and Co^{2+}) from the pollutant solutions (2–20 ppm) prepared. These preliminary tests were done at room temperature with the pH of the test solutions adjusted between 5 and 7.8. This was because the average pH range of the tap drinking water is between 5 and 6 and the pH range of water from reservoirs and rivers varied from 5.8 to 7.8. These preliminary tests were also conducted using CD polymer and pMWCNT-CD polymer, just for comparative purposes.

18.3 Results and Discussion

18.3.1 Purification and Oxidation of MWCNTs

Multi-walled carbon nanotubes (MWCNTs) was used as the type of CNTs because of their high surface area, superior mechanical, electrical, chemical and many other

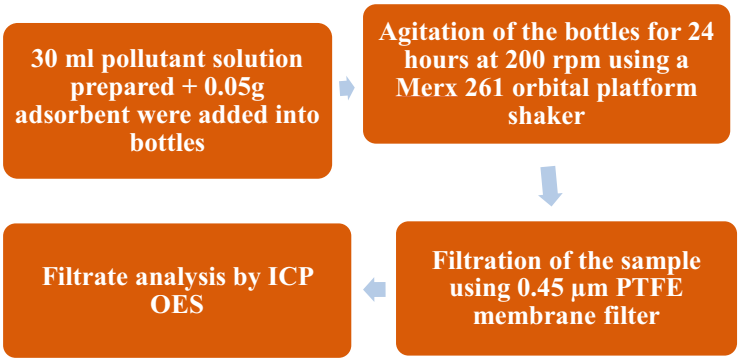

Fig. 18.1 Flow diagram for batch adsorption studies

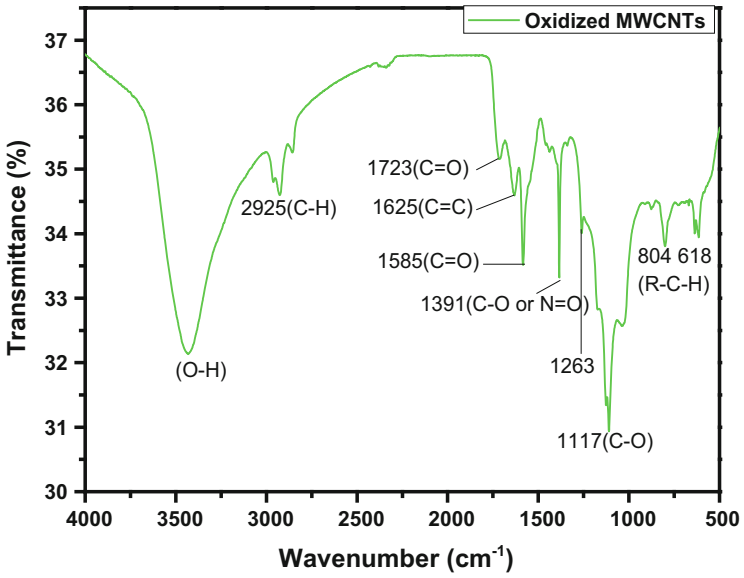

Fig. 18.2 FTIR spectrum of the oxidized MWCNTs

properties compared to single-walled carbon nanotubes (SWCNTs) and double-walled carbon nanotubes (DWCNTS) [15, 16].

The first step in the synthesis of the new bio nanosponge filter was the Soxhlet purification of MWCNTs. The aim was to remove soluble impurities such as amorphous carbon and fullerenes. Then the purified MWCNTs were oxidized by acid treatment to introduce functional groups on their surface which are initiation points for further chemical reactions [16]. The presence of these functional groups was confirmed by FTIR analysis (Fig. 18.2). After the acid treatment of the MWCNTs, one can clearly notice the presence of functional groups such as C=O (1723 and 1585 cm^{-1}) and C–O (1263 cm^{-1}) indicating that the oxidation of MWCNTs was achieved.

18.3.2 Synthesis of Phosphorylated MWCNTs

The oxidized MWCNT obtained after acid treatment was further modified by an amino-phosphonate along with an amino-alcohol, to produce phosphorylated MWCNTs (pMWCNTs) [2, 17]. This is because the phosphorylated MWCNTs obtained were proved to have good properties to be used in combination with CD [2, 9]. Moreover, phosphonate groups present on the surface of phosphorylated MWCNTs were shown to be effective complexing agents for di and trivalent cations from water [2, 17].

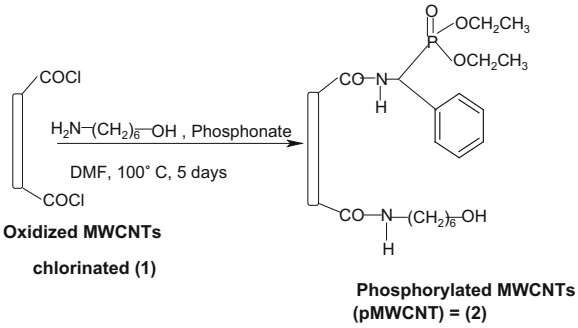

Phosphonate=Diethyl(α-aminobenzyl)-phosphonate

Fig. 18.3 Phosphorylation of MWCNTs

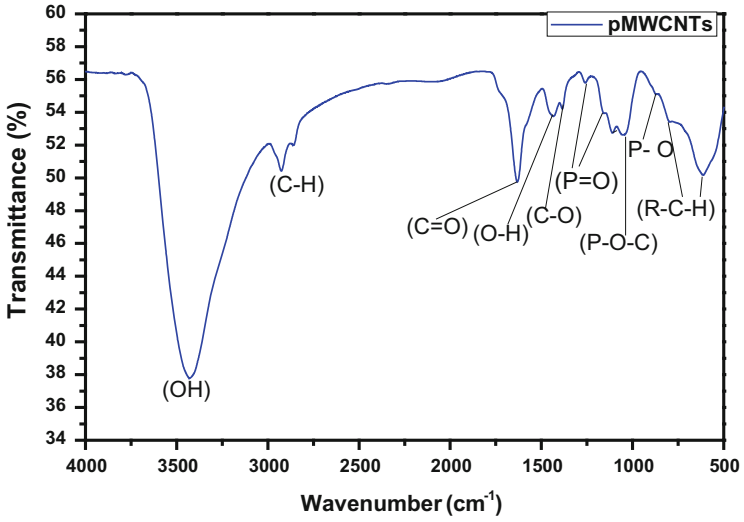

Fig. 18.4 FTIR spectrum of the phosphorylated MWCNTs (pMWCNTs)

Figure 18.3 illustrates the reaction scheme for the phosphorylation of MWCNTs. The amino alcohol (6-amino-hexanol) was added during the phosphorylation of MWCNTs in order to provide possible sites for the polymerisation of phosphorylated MWCNT with cyclodextrin [2]. The product was obtained in good yield (0.411g) >100% (mass/mass) and characterized by FTIR, Raman and SEM-EDS.

The appearance of the functional groups such as O–H (1439 cm^{-1}), P=O (1253 and 1165 cm^{-1}), P–O–C (1038 cm^{-1}) and P–O (873 cm^{-1}) [2, 18] in the spectrum of the phosphorylated MWCNTs (Fig. 18.4) confirmed that the phosphorylation of the oxidized MWCNTs was successful.

Figure 18.5 depicts the Raman spectra of oxidized and phosphorylated MWCNTs. The Raman spectrum of oxidized MWCNTs was plotted just for comparison purpose. From these spectra, three distinctive Raman bands which

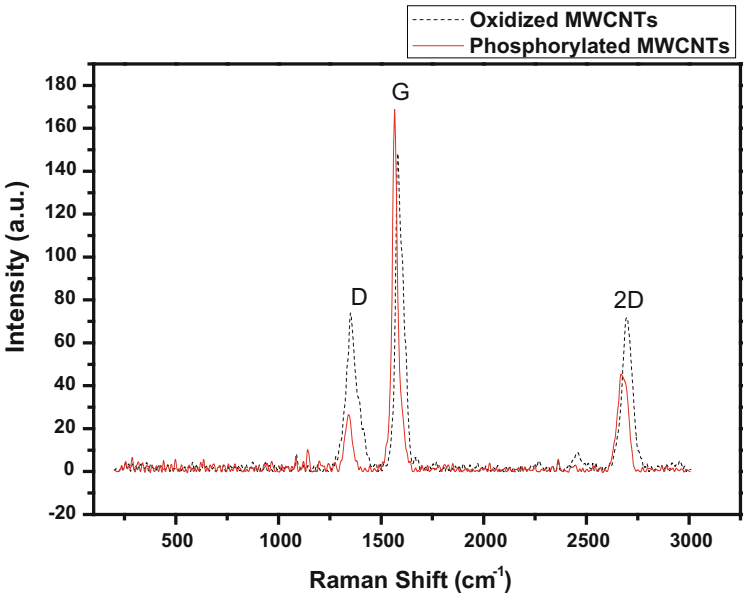

Fig. 18.5 Raman spectra of oxidized and phosphorylated MWCNTs

are: the D, G, and 2D, characteristic of MWCNT can be observed. The 2D band also called G′ was observed approximately around 2700 cm^{-1} for all MWCNT samples. According to the literature, the G band usually refers to the ordered or crystalline graphitic structures in MWCNTs while the D band indicates the presence of some disorder or defects within the graphitic structures in MWCNTs [16, 19, 20]. These disorders have been assigned to either the amorphous carbons trapped, tubes edges or the sp^3 hybridized carbons at the defect sites.

Moreover to evaluate the quality of MWCNT, the intensities ratio of the D band relative to the G band (I_D/I_G) were also calculated [16]. The values obtained are summarized in Table 18.1 as well as the observed values for the D, G and 2D bands for each MWCNT sample. It was reported that there is an increase of the I_D/I_G ratio due to the increase in functionalization time [16]. This is because, during the functionalization of MWCNT, the sp^2 hybridized carbon gets converted to the sp^3 hybridized carbon [19, 20]. In this work from the values of the ratio obtained it can be concluded that the conditions used for the functionalization of MWCNTs did not damage the tubes.

The intensity ratios (I_D/I_G) of oxidized and phosphorylated MWCNTs were calculated and found to be 0.85 and 0.86, respectively. From the values obtained there was a slight increase in the ratio of the I_D/I_G after phosphorylation of MWCNTs. This was due to the phosphorylation taking place via the acyl chloride bond attached on the defect site of the MWCNTs [17]. However an increase in the G band from some graphitic oxidation of the surface of phosphorylated MWCNTs was noted. Similar observations were also reported by Mpendulo [17]. Hence, from

Table 18.1 Raman spectral data

Sample name	D band (cm^{-1})	G band (cm^{-1})	2D band (cm^{-1})	I_D/I_G
Oxidized MWCNTs	1349	1586	2695	0.85
pMWCNTs	1340	1560	2677	0.86

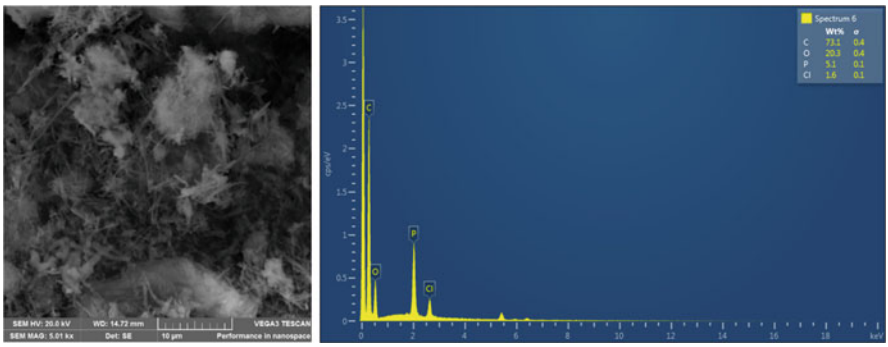

Fig. 18.6 SEM image and EDS scan of phosphorylated MWCNT

this evaluation, the graphitic structure of MWCNT after phosphorylation was still maintained. It can be confirmed that MWCNTs have not been damaged after the phosphorylation reaction.

The SEM micrographs in Fig. 18.6 showed that the surface morphology of phosphorylated MWCNT is like some entangled mesh. Mpendulo [17] had also similar SEM observation for the phosphorylated CNT. In addition, the EDS spectrum of phosphorylated MWCNT (pMWCNT) (Fig. 18.6) showed the presence of the elements C, O, P and Cl. Chlorine was detected because of its residual on the surface of MWCNTs (which remained as an impurity) resulting from the oxalyl chloride used.

18.3.3 Synthesis of the Bio Nanosponge Filter: pMWCNT-CD/Ag-TiO_2

18.3.3.1 Synthesis of pMWCNT-CD Polymer

Figure 18.7 illustrates the synthetic pathway for polymerization of pMWCNTs with β-CDs. The linker HMDI was used in order to reduce the solubility of CDs in water since the CDs are soluble in water. In addition, to be able to use the synthesized polymers for water treatment, it is very important to make them water insoluble by using an excess of diisocyanate linker to ensure maximum polymer cross-linking [2, 3, 7].

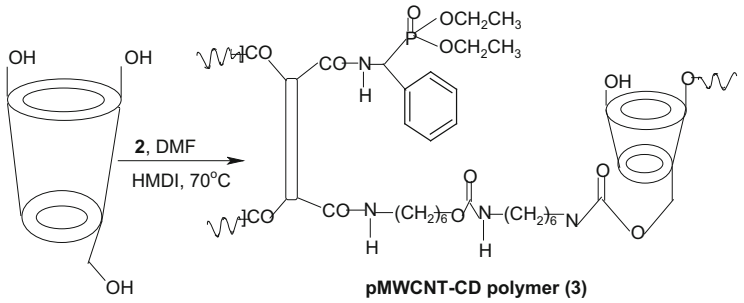

Fig. 18.7 Synthetic pathway for polymerization of pMWCNTs with β-CDs

18.3.3.2 Sol-Gel Method to Obtain pMWCNT-CD/Ag-TiO_2

The synthesis of TiO_2 nanoparticles and TiO_2 based nanocomposite can be achieved using a variety of methods including: electro-spinning, chemical vapour deposition, sol-gel, electrophoretic deposition, and hydrothermal method [21–23]. Among these methods, sol-gel process is the most preferred since it has been shown to be a simple and effective method for the synthesis of inorganic and organic-inorganic nanomaterials [14, 23, 24]. Woan and co-workers [22] have reported on the different ways of coating CNTs with TiO_2. In this work, the TiO_2 and Ag nanoparticles were attached to the surface of the pMWCNT-CD polymer composite or embedded in the pMWCNT-CD polymer matrix. This was achieved by coating the polymer with TiO_2 and Ag nanoparticles following the same concept of a sol-gel process.

In this process the precursors, metal alkoxides (e.g. titanium isopropoxide) are usually used for the nucleation and the growing of titania on dispersed nanomaterials (e.g. CNTs, pMWCNTs-CD polymer) in a liquid medium (e.g. 2-propanol) at temperatures lower than 100 °C followed by hydrolysis and polycondensation reactions [21, 22, 24]. Then the addition of the metal salts (e.g. $AgNO_3$), if applicable, is usually done during the hydrolysis step. After the sol-gel process, the sample must be dried and thermally treated (calcined) to prevent further poly-condensation from taking place as well as to transform the material into its crystalline form [21, 24]. It is worth mentioning that in the hydrolysis process, water is added in the form of an acidic or basic solution in order to change the rate of the reaction by affecting the growth of the nanoparticles [22].

Moreover, among the various metal alkoxides (e.g. titanium ethoxide, titanium butoxide, etc.), the titanium isopropoxide was used as a TiO_2 precursor in this study because it is less sensitive to humidity and dissolves easily in alcohols (e.g. isopropanol) [22]. Titanium butoxide is even less sensitive to humidity but it cannot readily dissolve in alcohol due to its high viscosity [22].

It is also important to note that beside the metal alkoxide precursors for TiO_2 in sol gel method, the precursors such as titanium oxysulfate ($TiOSO_4$) and titanium

tetrachloride ($TiCl_4$) were also previously used [22, 25–27]. However they were found inefficient especially when the nanomaterials used are insoluble in water [22, 25–27].

The synthesized pMWCNT-CD/Ag–TiO_2 polymers were characterized by FTIR, TGA, DSC, Raman, XRD, SEM and BET. pMWCNT-CD and CD polymers were also synthesized, calcined and their characterization results were presented for comparison purposes.

FTIR Analysis

Figure 18.8a, b illustrate the FTIR spectra of the uncalcined and calcined synthesized polymers respectively. From these spectra, the peak at 2273 cm^{-1} corresponding to the isocyanate peak was not observed. This serves as proof that the polymerisation reaction was completed and the linker was successfully incorporated by the appearance of the NH(CO) peak of carbamate linkage at around 1645 and 1527 cm^{-1}. Additional functional groups can also be observed such as: the O–H group, N–H of amide groups at 3424 cm^{-1}; the C=O stretch of the amide group at around 1712 cm^{-1}; the benzyl group (C=C) at around 1634 cm^{-1}; the symmetric and the asymmetric C–H in CH_2 bonded to oxygen [2] at 2856 and 2935 cm^{-1}. The FTIR spectrum of pMWCNT-CD/TiO_2-Ag polymer also shows a strong peak at around 1391 cm^{-1} which is related to the Ti–O–C group [28] present in the new bio nanosponge polymer.

Moreover, it can be observed that all the polymers synthesized (uncalcined and calcined) have the same FTIR pattern. However the only differences are the phosphonate functional groups (P=O and P–O) present in the polymer samples containing pMWCNT. In Fig. 18.9, the band at around 1391 cm^{-1} is related to the Ti–O–C group [28] present in the pMWCNT-CD/TiO_2-Ag polymer which disappears slowly as the calcination time increases.

TGA Analysis

TGA coupled with the derivative thermogravimetric (DTG) curve is a good technique used to study the thermal stability of carbon or nanocomposites materials as well as to evaluate the purity and the composition of the material under study.

TGA analysis was used to investigate the thermal stability of the nanosponge polymers synthesized (CD, pMWCNT-CD and pMWCNT-CD/TiO_2-Ag). The TGA and DTG profiles of the calcined polymers were all similar. Figures 18.10a, b and 18.11a, b show the results of the analyses. From these figures, it can be observed that in general three different parts of thermal decomposition are involved in the thermal behavior of the polymers synthesized. The first part (50–200 °C) was assigned to the loss of water or moisture and solvents present in the polymer, the second part, from 250 to below 400 °C, was ascribed to the loss of carbamate groups and cyclodextrin and the third part above 400 °C, was attributed to the

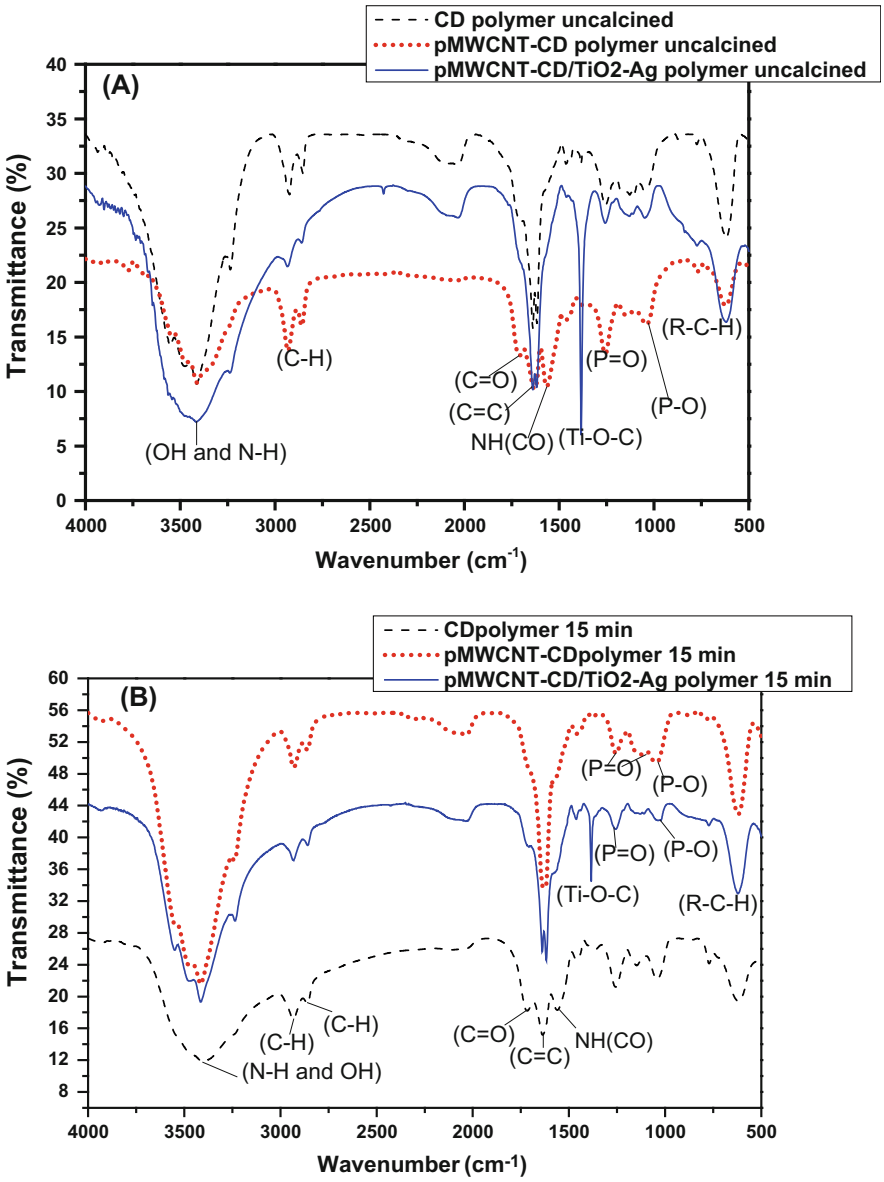

Fig. 18.8 FTIR spectra of the polymers synthesized: (**a**) uncalcined and (**b**) calcined for 15 min

complete decomposition of cyclodextrin skeleton [2, 29]. In addition it can also be noticed that for the polymer containing CNTs (pMWCNT-CD and pMWCNT-CD/TiO_2-Ag), at temperature above 400 °C, the complete decomposition of CNTs skeleton also occurs. Thus, for the polymer composites, the peak corresponding

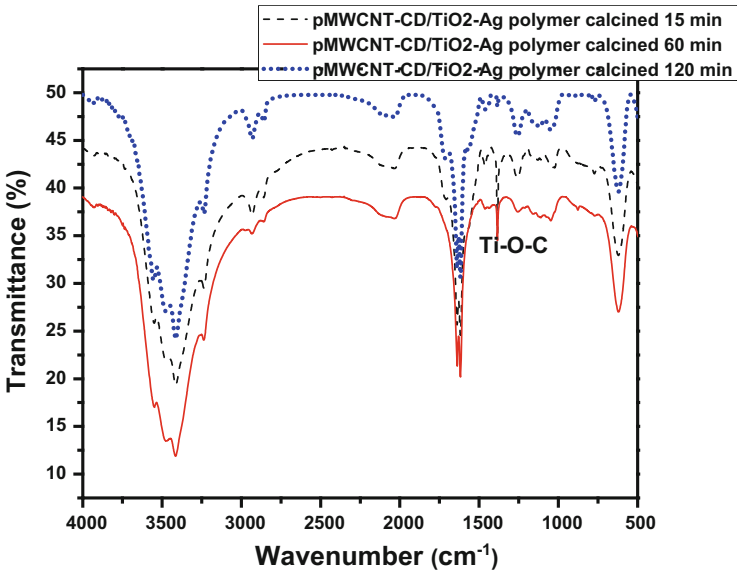

Fig. 18.9 FTIR spectra of pMWCNT-CD/TiO_2-Ag polymer synthesized and calcined at different times

to the complete decomposition of CNTs skeleton overlaps with the peak related to the complete decomposition of CD skeleton.

One can also notice from Figs. 18.10 and 18.11, that there is a minimal difference between the TGA and DTG profiles of uncalcined and calcined polymers. This means that the thermal stability of the polymers was not really affected by the calcination process. However, it was observed from the TGA and the DTG profiles of the nanosponge polymers (uncalcined and calcined) that the thermal stability is affected by the modification of the polymer. This is because it can be clearly observed that the stability of the native CD polymer has improved after its modification with either pMWCNT alone or with both pMWCNT and TiO_2 and Ag nanoparticles.

DSC Analysis

DSC analysis is usually used to measure the energy absorbed or liberated by a sample subjected to a temperature program (heating from 25 to 500 °C). In this study, it was also used to obtain more information regarding the thermal stability and purity of the polymers synthesized.

Figure 18.12a depicts the DSC curves of the uncalcined polymers and these curves correlate well with a typical DSC curve of a semicrystalline polymer.

The sharp curves or peaks observed indicate the purity of the samples. This means that all the polymers were successfully synthesized and pure. It can be

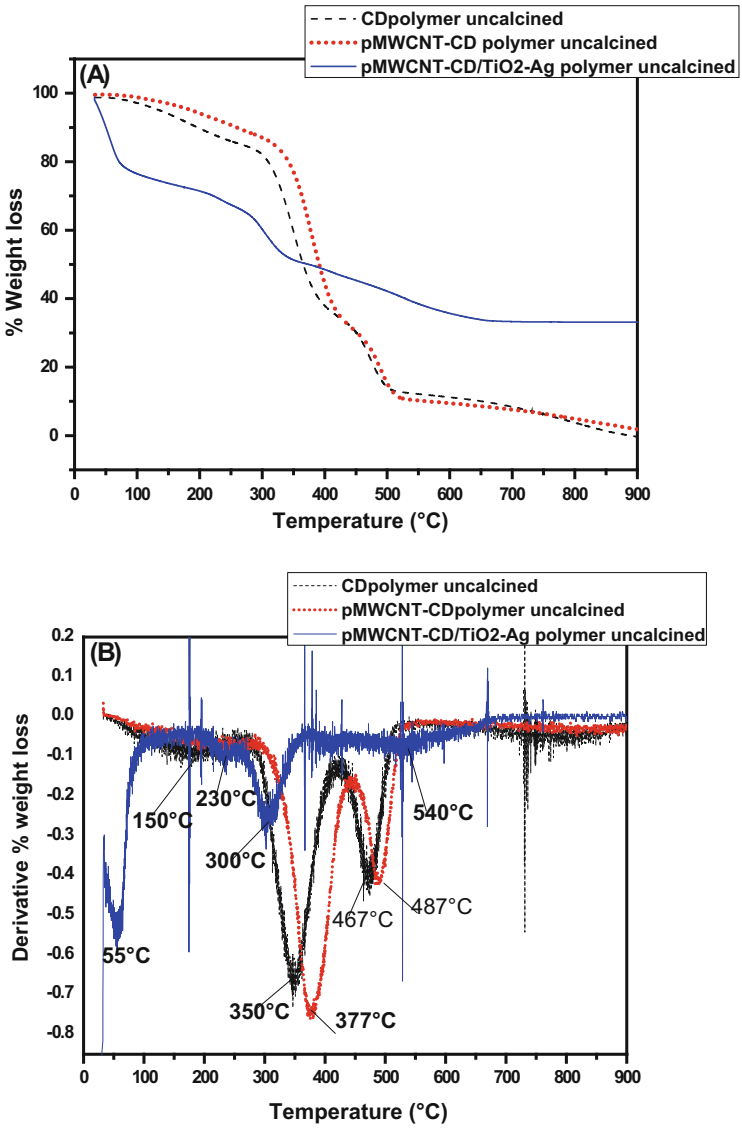

Fig. 18.10 TGA (**a**) and derivative TGA (**b**) spectra of the uncalcined polymers

noticed in Fig. 18.12a, that the pMWCNT-CD/TiO_2-Ag polymer has two endothermic peaks (99 °C, 298 °C) and two exothermic peaks (229 °C, 444 °C) whereas the native CD and pMWCNT-CD polymers have three endothermic peaks (73 °C, 367 °C, 465 °C and 90 °C, 372 °C, 470 °C respectively) and one exothermic peak (308 °C and 311 °C respectively). For all the samples the first endothermic peak corresponds to the loss of water from the polymers, the second endothermic peak in

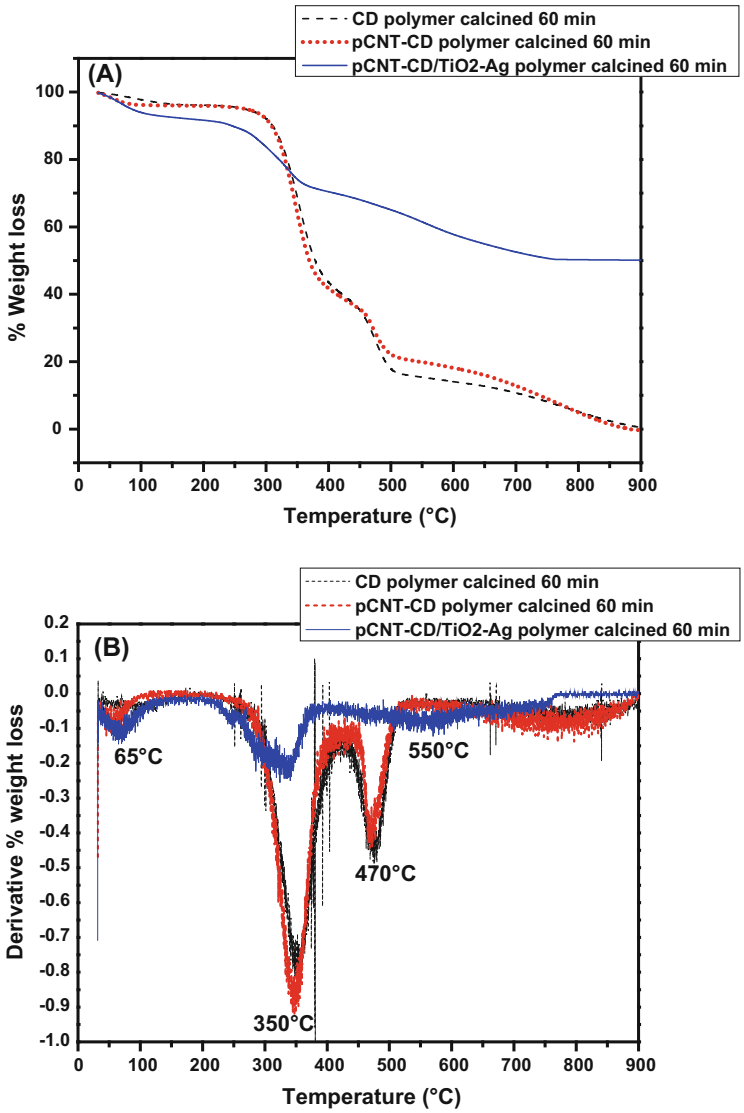

Fig. 18.11 TGA spectra (**a**) and derivative TGA spectra (**b**) of the calcined polymers for 60 min

all the samples can be ascribed to the melting of the polymers which, in TGA spectra (uncalcined polymers) corresponds also to the region for maximum rate of pyrolysis [30]. The third endothermic peak (in native CD and pMWCNT-CD polymers) can be assigned to the complete melting with decomposition of the polymers.

The exothermic peaks observed can be associated with the thermal degradation temperatures of the polymers. The second exothermic peak at 444 °C in pMWCNT-

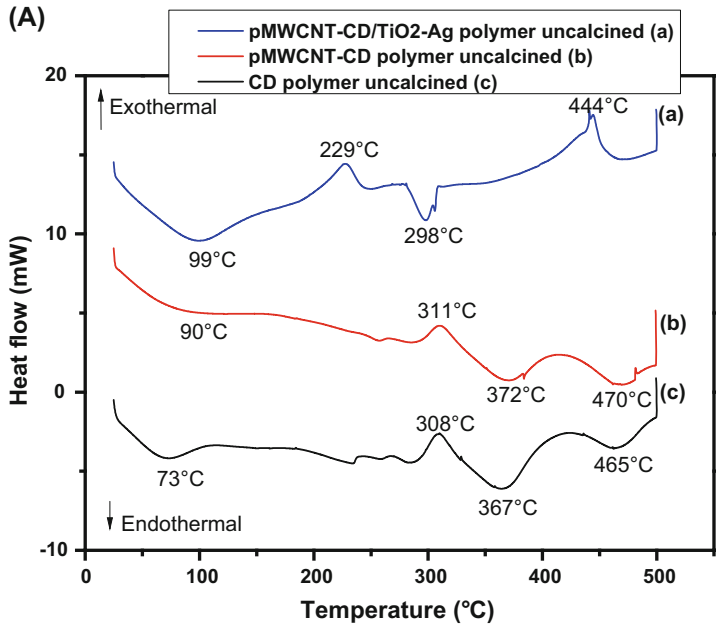

Fig. 18.12a DSC curves of the uncalcined polymers

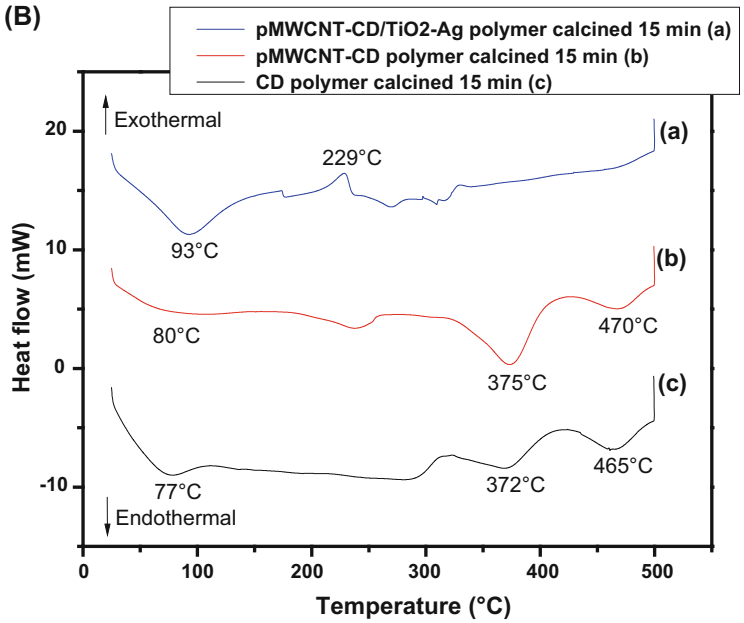

Fig. 18.12b DSC curves of the calcined polymers for 15 min

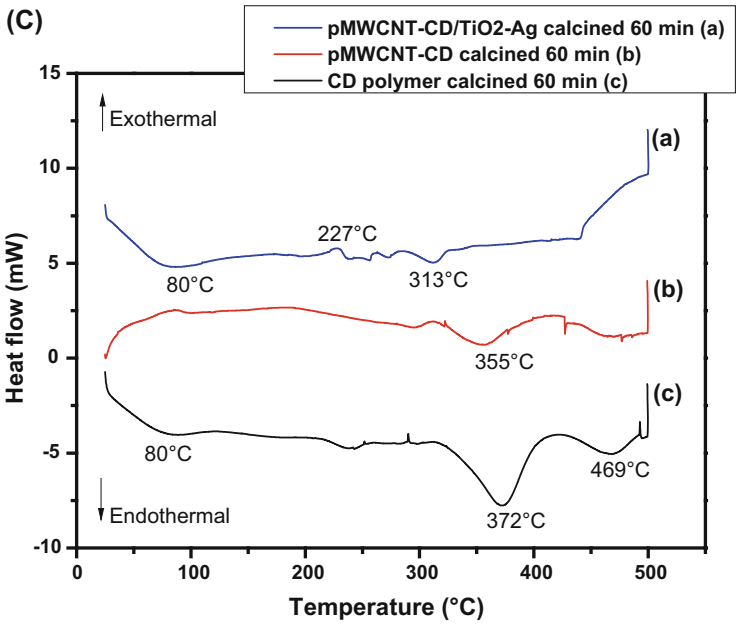

Fig. 18.12c DSC curves of the calcined polymers for 60 min

CD/TiO_2-Ag polymer corresponds to its complete thermal degradation and beginning of oxidative degradation in air. In addition, it can also be noted that the pMWCNT-CD/TiO_2-Ag biopolymer is more stable than the native CD polymer and pMWCNT-CD polymer, since its complete degradation temperature (444 °C) was higher than the degradation temperatures of native CD polymer (308 °C) and pMWCNT-CD polymer (311 °C).

From the results obtained from Fig. 18.12a, one can also say that the nanosponge polymers synthesized are polymorph materials which means that they exist in more than one crystal structure or they have more than one morphology. This assumption will be confirmed by Raman, XRD and SEM analyses.

Figures 18.12b and 18.12c show the DSC curves of the calcined polymers. It can be observed that the DSC curves of the calcined polymers present different trends compared to the uncalcined polymers which could be due to the calcination process. Therefore, the stability of the polymers is affected by the calcination. Hence the polymers should not be calcined after their synthesis.

Raman Spectroscopy Analysis

Raman analysis was also performed to confirm the presence of MWCNT, CD and TiO_2 in the polymer nanocomposite synthesized.

Figure 18.13a, b show the Raman spectra of the new bio nanosponge polymer (pMWCNT-CD/TiO_2-Ag) uncalcined and calcined respectively. The Raman bands observed at 147, 262, 426, 599 and 811 cm^{-1} (Fig. 18.13a) can be assigned to a mixture of the anatase and brookite phase of TiO_2 [24, 31]. Gotic et al. [32] have also obtained a mixture of anatase and brookite for their uncalcined TiO_2 and TiO_2 calcined at 150 °C. In the literature [32], Raman bands for anatase were reported to

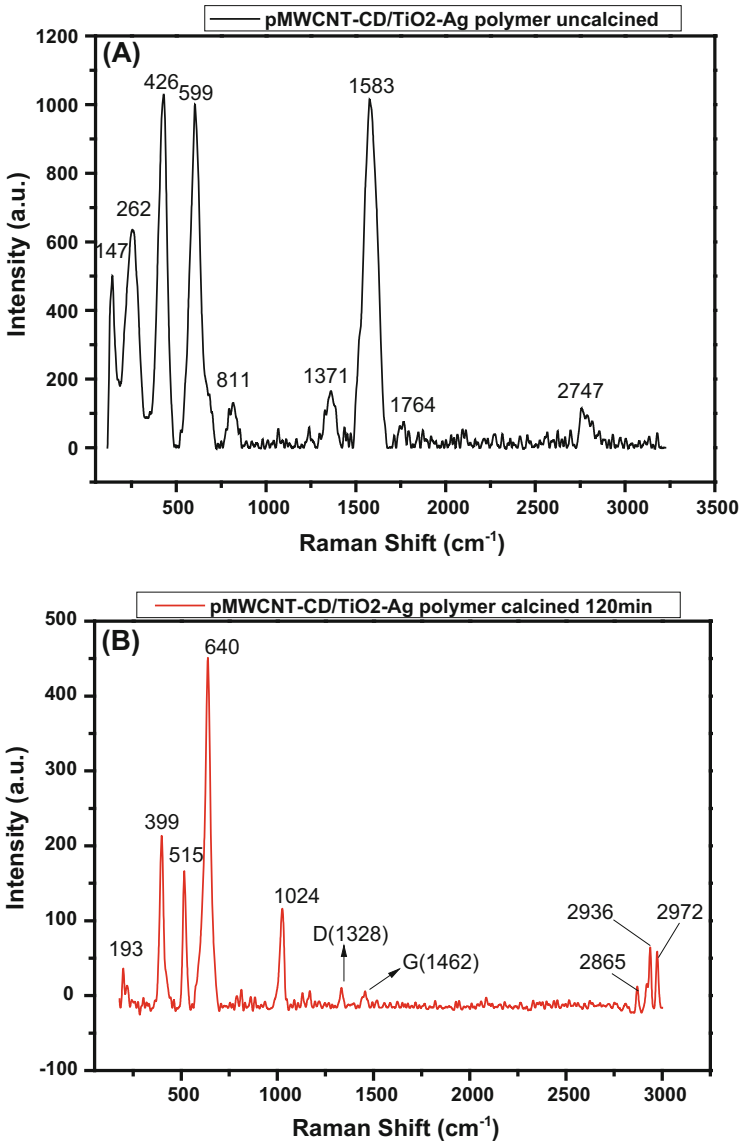

Fig. 18.13 Raman spectra of pMWCNT-CD/TiO_2-Ag polymer: (**a**) uncalcined and (**b**) calcined

be around 143, 395, 512, and 645 cm^{-1} corresponding to the $E_{g(1)}$, $B_{1g(1)}$, A_{1g}+$B_{1g(2)}$ and $E_{g(2)}$ modes of anatase, respectively, in TiO_2 [24, 31]. Raman active photons of rutile TiO_2, B_{1g}, E_g, A_{1g} and B_{2g}, were reported to be at approximately 232, 447, 612 and 826 cm^{-1} respectively [32, 33] whereas the Raman bands for brookite were reported to be at 128, 153, 247, and 636 cm^{-1} [32, 34]. Hence, from these reported values, it can be concluded that the new polymer nanocomposite (pMWCNT-CD/TiO_2-Ag) is a bicrystalline structure (polymorph), containing anatase and brookite phases. This assertion will be further confirmed by XRD analysis (Fig. 18.14). The formation of a band at around 262 cm^{-1}, due to the second order scattering and disorder effects, is observed. This band at 262 cm^{-1} was found to have also a complex nature which at high resolution, shows a significant structure [32, 34–36].

In addition, the Raman bands of MWCNTs in the polymer nanocomposite were also observed at 1371 cm^{-1} (D band) and 1583 cm^{-1} (G band). The G band was noted to be very intense and overlap with NH–CO of carbamate group from polymerisation. C=O peak at 1764 cm^{-1} related to polymerisation, was also observed. The Raman shifts around 2747 cm^{-1} (C–H peak) could be related to cyclodextrin polymer structural cavity.

In Fig. 18.13b, the bands observed at 193, 399, 515 and 640 cm^{-1} are characteristic of the anatase phase of TiO_2 [24, 31, 32]. According to the literature these bands correspond to the $E_{g(1)}$, $B_{1g(1)}$, A_{1g}+$B_{1g(2)}$ and $E_{g(2)}$ modes of anatase, respectively, in TiO_2 [24, 31, 32]. Moreover, the Raman bands of MWCNTs were observed at 1328 cm^{-1} (D band) and 1462 cm^{-1} (G band) with a decrease in intensity of these D and G bands. Raman shifts around 2865, 2936 and 2972 cm^{-1} (C–H peaks) could be related to cyclodextrin polymer structural cavity. Moreover, it was also noticed that after calcinations for a maximum of 120 min, the NH–CO and C=O peaks related to polymerisation were not observed on Raman whereas they were found in IR.

XRD Spectroscopy Analysis

XRD patterns were obtained in order to further confirm the purity and the crystallinity of the sample synthesized. The XRD patterns of the calcined polymers (15, 60 and 120 min) were all similar. From the results obtained (Fig. 18.14a, b), a broad amorphous peak was observed for CD polymer and pMWCNT-CD polymer before and after calcination. Whereas good crystalline peaks were observed before calcination for the polymer composite of interest (pMWCNT-CD/TiO_2-Ag), after calcination up to 120 min, no peaks were observed. Therefore, from these observations, it can be confirmed that both pMWCNT-CD and CD polymers are amorphous. However by modifying pMWCNT-CD polymer composite with TiO_2 and Ag, the new biopolymer composite obtained just after the drying process, is a crystalline material. However after calcination, the new bio nanosponge polymer composite loses its crystallinity to become amorphous.

Raoov et al. [29] have reported that the amorphous nature of CD polymer was because the polymeric chains throughout have lost their regularity due to the

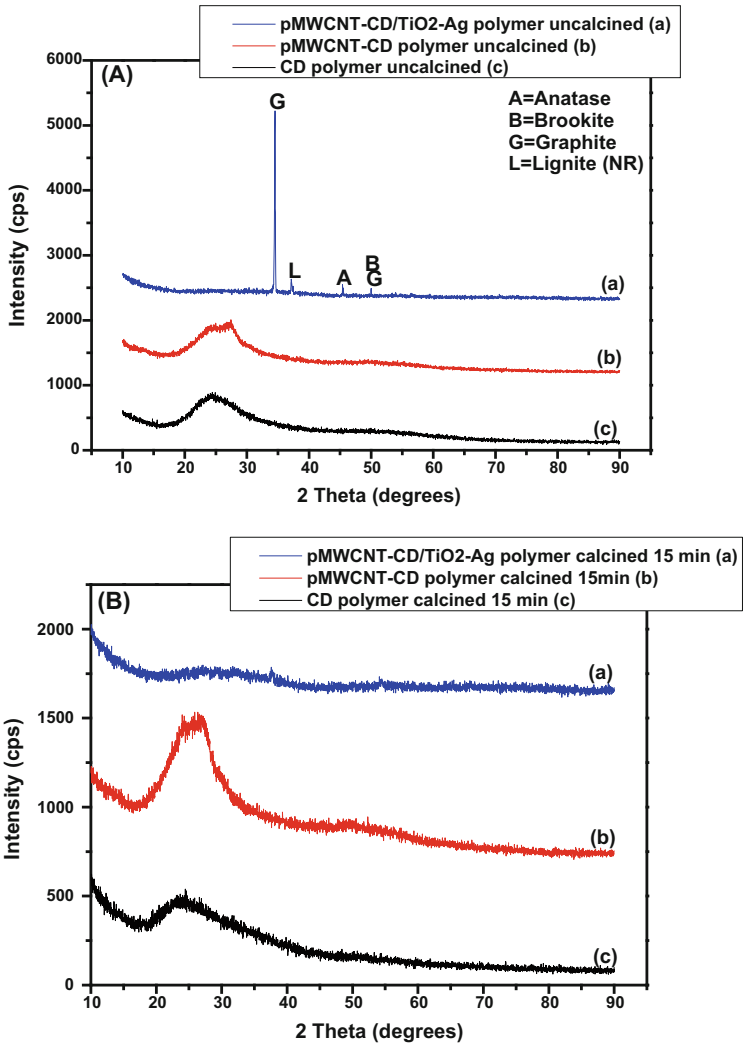

Fig. 18.14 XRD patterns of the nanosponge polymers: (**a**) uncalcined and (**b**) calcined

introduction of the bulky linker molecule. In this study, the introduction of pMWCNT to the CD polymer still did not help whereas by incorporating TiO_2 and Ag nanoparticles to the pMWCNT-CD polymer, this helps to improve the regularity of the polymeric chains by enhancing the crystallinity of the polymer. Moreover it can also be said that the calcination process perhaps also affects the regularity of pMWCNT-CD/TiO_2-Ag polymeric chains by causing the loss of crystallinity. Hence, the new polymer nanocomposite obtained pMWCNT-CD/TiO_2-Ag should not be subjected to the calcination process to avoid the loss of crystallinity. In addition, the peaks obtained in the XRD pattern of pMWCNT-CD/

TiO_2-Ag polymer nanocomposite (uncalcined), could be a result of a mixture of pure crystallite phases which are anatase and brookite TiO_2, graphite and lignite (NR) at two theta of about 45.6, 49.9, 34.5 and 37.2 respectively. Hence the novel bio nanosponge filter prepared exists in more than one crystal structure (polymorph material).

The average crystallite size of the most intense XRD peak (the dominant phase, graphite) was calculated using the Scherrer equation (18.1) [31] below and it was found to be 92.72 nm.

$$D = \frac{k\lambda}{\beta \text{Cos } \theta} \tag{18.1}$$

D is the average crystallite size, **k** is a constant equal to 0.9; **λ** is the wavelength (nm) of cobalt Kα radiation and its value is 0.179 nm; **β**, the FWHW of the peak of interest obtained by XRD; **Theta** (θ) is the Bragg angle.

BET Surface Area Analysis

Table 18.2 presents the summary of the results after the BET surface area analysis. From the results obtained, it can be noted that amongst all the nanosponge polymers synthesized, the novel bio nanosponge polymer composite (pMWCNT-CD/TiO_2-Ag) has the highest surface area and pore volume (352.546 m^2/g and 0.408 cm^3/g respectively) with the lowest pore size (4.633 nm). It can also be noticed that the surface area of all the nanosponge polymers calcined is lower than the surface area of uncalcined nanosponge polymers. Hence, the calcination process affects the surface area of the nanosponge polymers. The nanosponge polyurethanes in general should not be calcined after their synthesis. In addition, one can also observe from Table 18.2 that the higher the surface area, the bigger the pore volume and smaller the pore size.

Table 18.2 Results summary of the BET surface area analysis

Nanosponge polymer	Surface area (m^2/g)	Pore volume (cm^3/g)	Pore size (nm)
pMWCNT-CD/TiO_2-Ag (uncalcined)	352.546	0.408	4.633
pMWCNT-CD/TiO_2-Ag (calcined 60 min)	273.353	0.289	4.224
pMWCNT-CD (uncalcined)	0.985	0.00833	27.899
pMWCNT-CD (calcined 60 min)	0.908	0.00633	33.830
CD (uncalcined)	2.091	0.0223	42.595
CD (calcined 60 min)	0.0151	0.00311	826.033

Electron Microscopy Analysis

The new bio nanosponge filter synthesized (pMWCNT-CD/TiO_2-Ag) physically appears to be a light grey powder whereas the CD polymer was a white granular solid and pMWCNT-CD was pale black to grey granular solid. From the SEM images obtained, it was observed that the nanosponge polymers synthesized have more than one morphology. The polymer nanocomposite, pMWCNT-CD/TiO_2-Ag (Fig. 18.15a–c), looks like a cluster, slab or an aggregation of granular particles with a rough surface. pMWCNT-CD (Fig. 18.16a, b) and CD polymers (Fig. 18.17a, b), appear like a sponge, woven or an aggregation of granular particles with a rough surface.

However for all the polymers calcined, it was also noticed that the granular particles were agglomerated onto a rod-like structure (Figs. 18.15d, 18.16c, d, 18.17c, d).

The EDS spectrum of pMWCNT-CD/TiO_2-Ag (Fig. 18.15) clearly confirmed that the polymer nanocomposite pMWCNT-CD/TiO_2-Ag was successfully prepared due to the presence of the elements C, O, Ag and Ti. The EDS scans of pMWCNT-CD polymer (Fig. 18.16) and CD polymer (Fig. 18.17) confirmed the presence of C and O as major elements. The presence of gold element in the polymer samples results from the gold coating of the materials before analysis.

18.3.4 Preliminary Adsorption Studies

The preliminary adsorption results obtained for Pb^{2+} and Co^{2+} are presented in Fig. 18.18. The percent removal of each pollutant (amount of pollutant adsorbed) [2] and adsorption [9] capacity were calculated using the equation below (18.2) and (18.3) respectively:

$$\%\text{Removal} = [(\text{Co} - \text{Ct})/\text{Co}] \times 100 \tag{18.2}$$

$$\text{q} = [(\text{Co} - \text{Ct})/\text{m}] \times \text{V} \tag{18.3}$$

where Co is the initial concentration of pollutant, Ct is the final concentration obtained after adsorption at specific time, m is the mass of the adsorbent used and V is the volume of the pollutant solution (lead or cobalt). The synthesized nanosponge polymers were tested as adsorbent material to evaluate their ability to actually act as filters, able to remove the selected pollutant (lead and cobalt) metal ions from the synthetic waste water prepared at different concentrations (2–20 ppm).

From the results obtained, the adsorption capacity of the bio nanosponge filter (pMWCNT-CD/TiO_2-Ag) was the highest for both Pb^{2+} and Co^{2+} removal compared to the CD polymer and pMWCNT-CD polymer. The maximum percentage of removal of lead was found to be 99.67% with adsorption capacity (q) of 11.96 mg/g at 10 ppm using pMWCNT-CD/TiO_2-Ag whereas it was found to be 69%

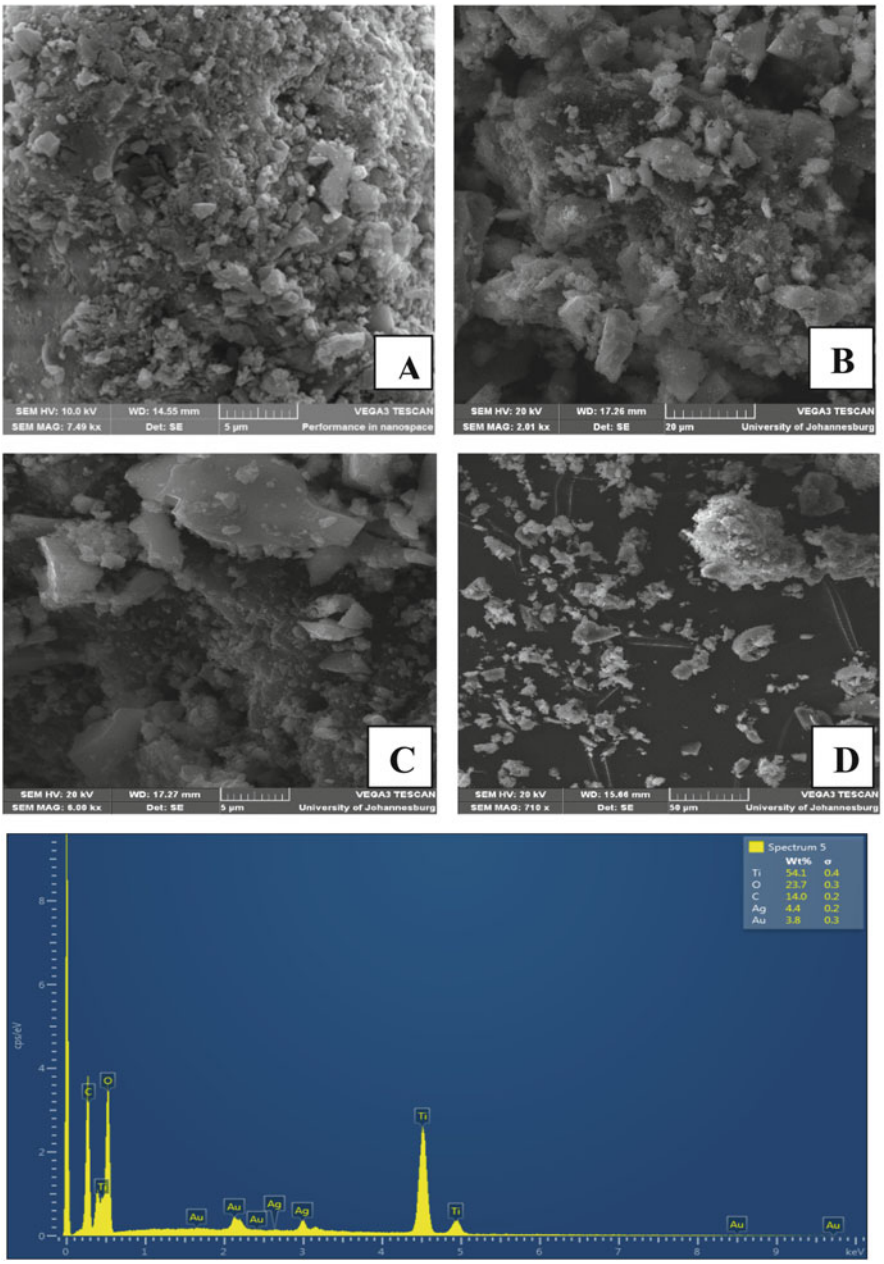

Fig. 18.15 SEM images [(**a**) uncalcined; (**b**, **c** & **d**) calcined] and EDS scan of pMWCNT-CD/TiO_2-Ag

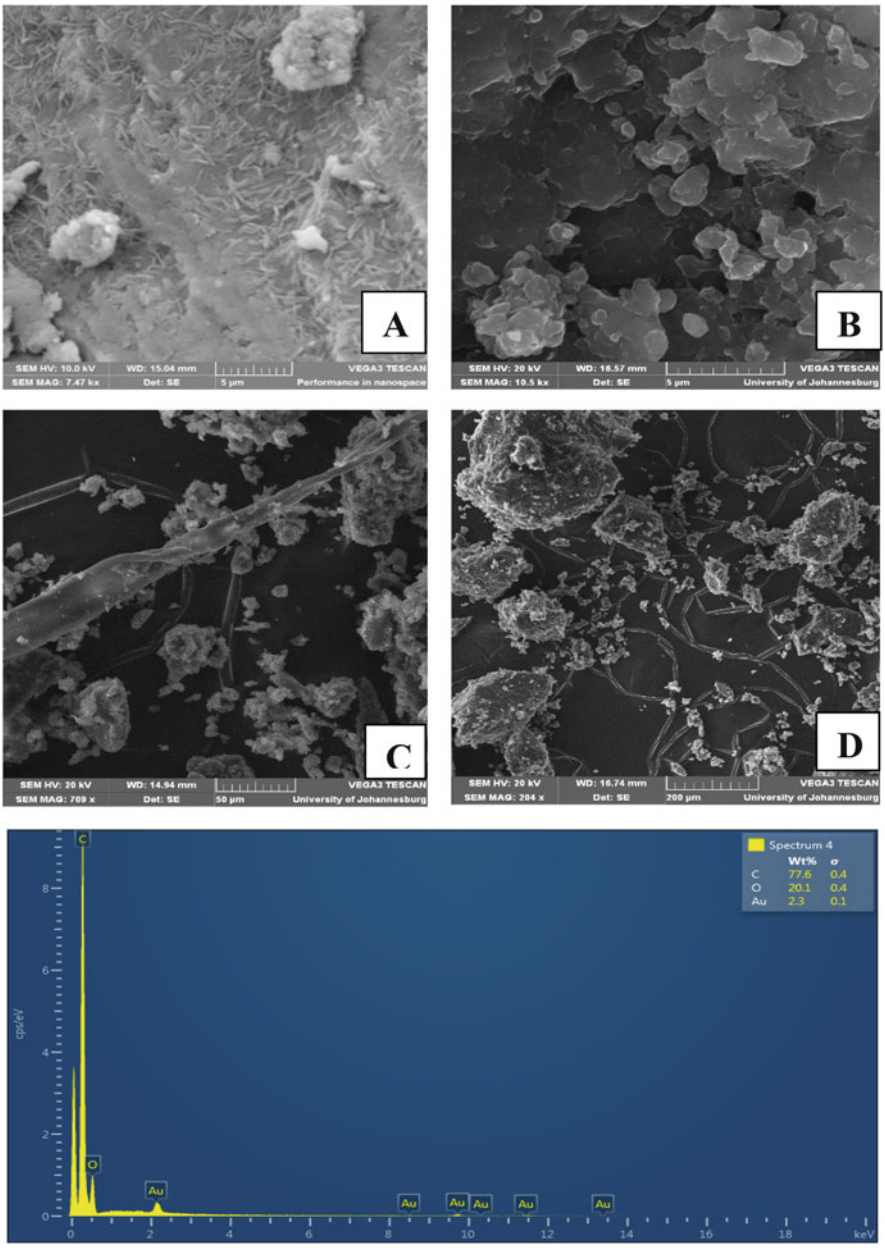

Fig. 18.16 SEM images [(**a**) uncalcined; (**b**, **c** & **d**) calcined] and EDS of pMWCNT-CD nanosponge polymer

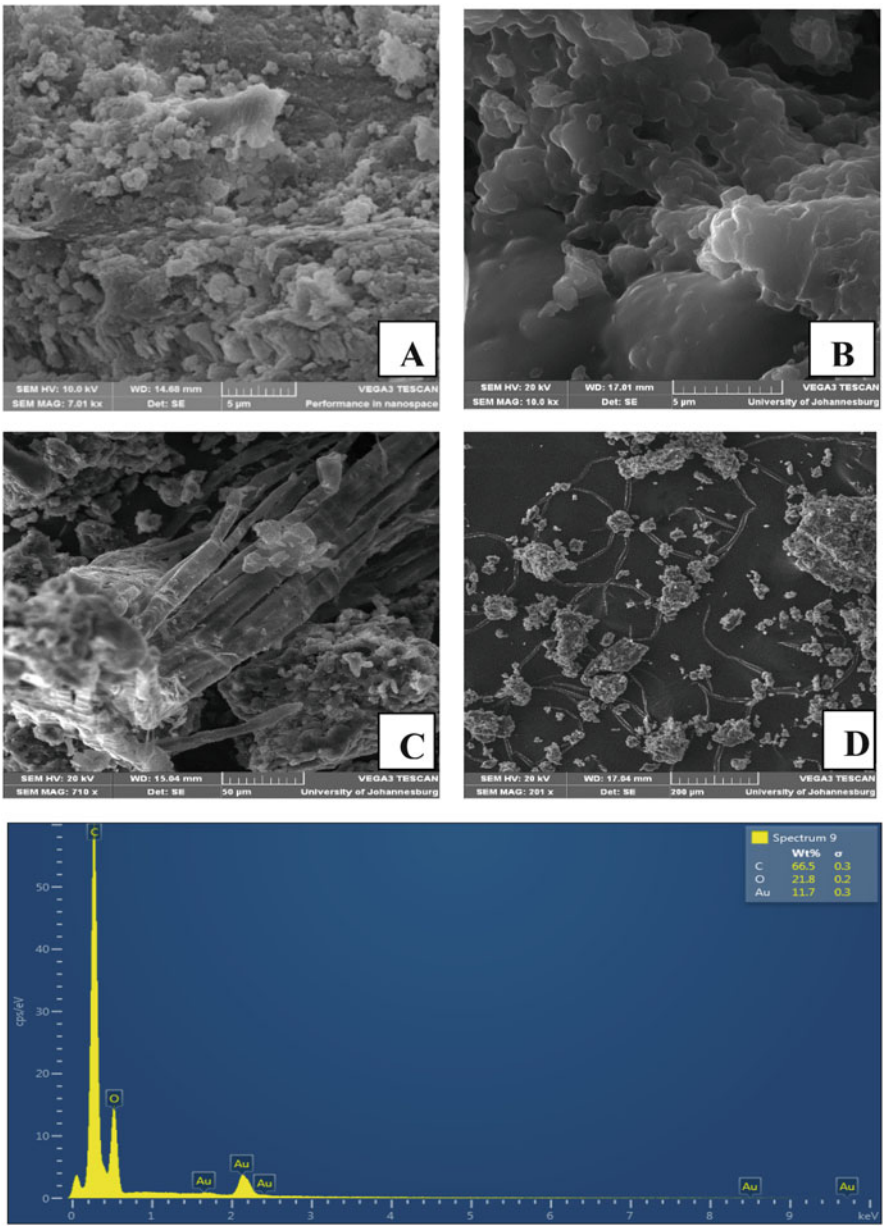

Fig. 18.17 SEM images [(**a**) uncalcined; (**b**, **c** & **d**) calcined] and EDS scan of CD nanosponge polymer

(q = 0.77 mg/g) and 64% (q = 0.83 mg/g) at 2 ppm using pMWCNT-CD and CD polymer respectively (Fig. 18.18). In the case of cobalt adsorption, the percentage of removal reached its maximum with 99.18% and a capacity of 10.71 mg/g at

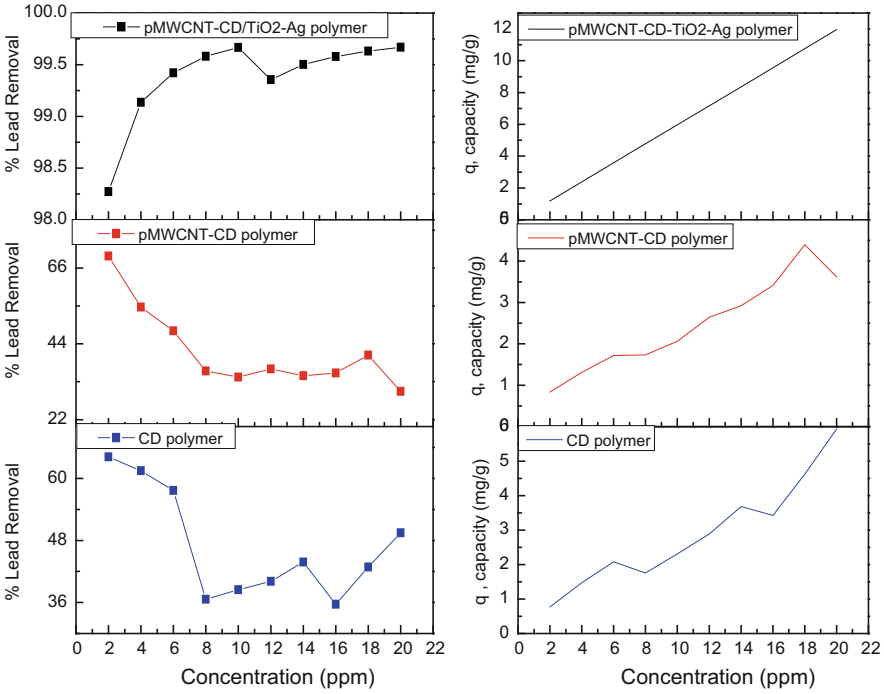

Fig. 18.18 Preliminary adsorption study of lead at different initial concentrations using the nanosponge polymer synthesized (conditions: pH 5–7.8; 0.05g of adsorbent used and adsorption for 24 h at 25 °C)

18 ppm using pMWCNT-CD/TiO_2-Ag. However the maximum removal of cobalt was reached at 6 ppm using pMWCNT-CD and CD polymer with 63.2% (q = 2.28 mg/g) and 62.97% (q = 2.27 mg/g) respectively (Fig. 18.19).

In addition it can be observed that the adsorption behavior of pMWCNT-CD/TiO_2-Ag bio nanosponge polymer composite is different from that of pMWCNT-CD and CD polymers. This can be explained by the incorporation of TiO_2 and Ag nanoparticles into pMWCNT-CD polymer and also the difference in their surface area. For example when pMWCNT-CD/TiO_2-Ag polymer was used as an adsorbent, there were more adsorption sites (very large surface area) available. For this reason, the percentage removal and the adsorption capacity, q, of lead increased as the concentration increased (Fig. 18.18). On the other hand, pMWCNT-CD or CD polymers have less adsorption sites (small surface area) available for the pollutant. Hence, the percentage removal of lead decreased while the removal capacity, q, increased as the concentration increased (Fig. 18.18).

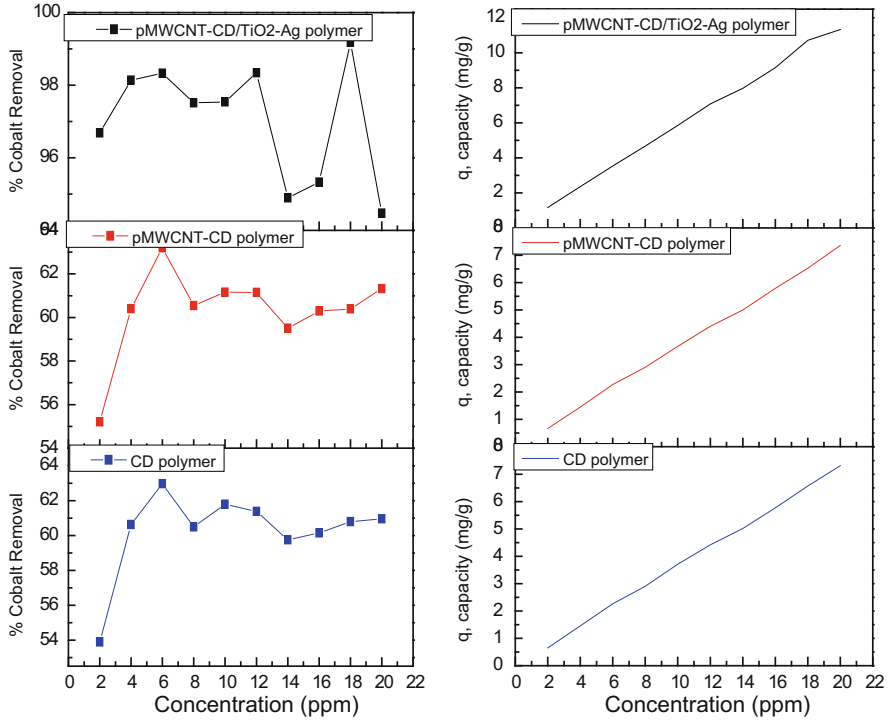

Fig. 18.19 Preliminary adsorption study of cobalt at different initial concentrations using the nanosponge polymer synthesized (conditions: pH 5–7.8; 0.05 g of adsorbent used and adsorption for 24 h at 25 °C)

18.4 Conclusion

The bio nanosponge filter or biopolymer nanocomposite (pMWCNT-CD/TiO_2–Ag) was successfully synthesized and characterized. It physically appears as a light grey powder.

From the SEM pictures obtained, the new biopolymer nanocomposite looks like a cluster or an aggregation of granular particles with rough surface whereas pMWCNT-CD and CD polymers appear like a sponge or woven. EDS scan obtained confirm the successful incorporation of the TiO_2 and Ag nanoparticles to pMWCNT-CD polymer. FTIR and Raman results of the nanosponge polymers synthesized also correlate very well since the peaks related to C=O and NH(CO) of carbamate groups from polymerisation were well identified. Moreover, it was also noticed that the Raman band of NH(CO) of carbamate group from polymerisation at 1581 cm^{-1} overlapped with the G (graphitic) peak of MWCNT.

The thermal treatment process (calcination) affects the BET surface area, the crystallinity and also slightly affects the thermal stability of the biopolymer

composite (pMWCNT-CD/TiO_2-Ag). Hence the biopolymer nanocomposite should not be calcined after synthesis to avoid the loss of the regularity throughout the polymeric chain of pMWCNT-CD/TiO_2-Ag perhaps caused by the calcination process.

The novel biopolymer nanocomposite (pMWCNT-CD/TiO_2-Ag) synthesized has effectively demonstrated the ability to act as a filter with a maximum of 99.67% and 99.18% removal for lead and cobalt respectively. Therefore further adsorption studies will be performed in the future work to investigate in depth on the removal of inorganic, organic and microorganism pollutants using the new bio nanosponge filter (pMWCNT-CD/TiO_2-Ag).

Acknowledgements The authors would like to acknowledge the National Research Foundation (NRF), the University of Johannesburg and Water Research Commission (WRC) for the financial supports and the facilities offered. DST/NRF Centre of Excellence in Strong Materials at the University of the Witwatersrand is also appreciated for the Raman & BET surface area analyses, and above all the God Almighty.

References

1. Amin MT, Alazba AA, Manzoor U (2014) A review of removal of pollutants from water/wastewater using different types of nanomaterials. Adv Mater Sci Eng 2014:1–25
2. Mamba G, Mbianda XY, Govender PP (2013) Phosphorylated multiwalled carbon nanotube-cyclodextrin polymer: synthesis, characterisation and potential application in water purification. Carbohydr Polym 98:470–476
3. Mhlanga SD, Mamba BB, Krause RW, Malefetse TJ (2007) Removal of organic contaminants from water using nanosponge cyclodextrin polyurethanes. J Chem Technol Biotechnol 82:382–388
4. Nitalikar MM, Sakarkar DM, Jain PV (2012) The cyclodextrins: a review. J Curr Pharm Res 10:1–6
5. Del Valle EMM (2004) Cyclodextrins and their uses: a review. Process Biochem 39:1033–1046
6. Krause RW, Mamba BB, Bambo FM, Malefetse TJ (2010) Cyclodextrin polymers: synthesis and application in water treatment. In: Hu J (ed) Cyclodextrins chemistry and physics. Transworld Research Network, Trivandrum, pp 1–25
7. Salipira KL, Krause RW, Mamba BB et al (2008) Cyclodextrin polyurethanes polymerized with multi-walled carbon nanotubes: synthesis and characterization. Mater Chem Phys 111:218–224
8. Salipira KL, Mamba BB, Krause RW et al (2008) Cyclodextrin polyurethanes polymerised with carbon nanotubes for the removal of organic pollutants in water. Water SA 34:113–118
9. Mamba G, Mbianda XY, Govender PP et al (2010) Application of multiwalled carbon nanotube-cyclodextrin polymers in the removal of heavy metals from water. J Appl Sci 10:940–949
10. Mamba BB, Krause RW, Malefetse TJ, Nxumalo EN (2007) Monofunctionalized cyclodextrin polymers for the removal of organic pollutants from water. Environ Chem Lett 5:79–84
11. Sithole SP, Mamba BB, Krause RW, Mapolie SW Cyclodextrin dendrimers containing nanocatalysts for the removal of natural organic matter (nom) and other micropollutants from water: a short review. Water Inst SA:1–9

12. Mamba BB, Krause RW, Dlamini N The synthesis and application of cyclodextrin polyurethanes containing nanoparticles in water treatment. http://www.waternetonline.ihe.nl/downloads/uploads/symposium/zambia-2007/Water for People/Krause.pdf. Accessed 9 Aug 2014
13. Jeon IY, Baek JB (2010) Nanocomposites derived from polymers and inorganic nanoparticles. Materials (Basel) 3:3654–3674
14. Perumal S, Sambandam GC, Prabu MK, Ananthakumar S (2014) Synthesis and characterization studies of nano TiO_2 prepared via sol-gel method. Int J Res Eng Technol 3:651–657
15. Burghard M, Balasubramanian K (2005) Chemically functionalized carbon nanotubes. Small 1:180–192
16. Motchelaho MAM, Xiong H, Moyo M et al (2011) Effect of acid treatment on the surface of multiwalled carbon nanotubes prepared from Fe-Co supported on $CaCO_3$: correlation with Fischer-Tropsch catalyst activity. J Mol Catal A Chem 335:189–198
17. Mpendulo NT (2006) Phosphorylation of multiwalled carbon nanotubes. University of Johannesburg
18. Danilich MJ, Burton DJ, Marchant RE (1995) Infrared study of perfluorovinylphosphoric acid, perfluoroallylphosphonic acid, and pentafluoroallyldiethylphosphonate. Vib Spectrosc 9:229–234
19. Shrestha S, Choi WS, Song W et al (2010) Preparation and field emission properties of Er-decorated multi-walled carbon nanotubes. Carbon N Y 48:54–59
20. Ramesh BP, Blau WJ, Tyagi PK et al (2006) Thermogravimetric analysis of cobalt-filled carbon nanotubes deposited by chemical vapour deposition. Thin Solid Films 494:128–132
21. Nyamukamba P, Greyling C, Tichagwa L (2011) Preparation of photocatalytic TiO_2 nanoparticles immobilized on carbon nanofibres for water purification. University of Fort Hare
22. Woan K, Pyrgiotakis G, Sigmund W (2009) Photocatalytic carbon-nanotube-TiO_2 composites. Adv Mater 21:2233–2239
23. Leudjo A, Pillay K, Yangkou X (2017) Nanosponge cyclodextrin polyurethanes and their modification with nanomaterials for the removal of pollutants from waste water: a review. Carbohydr Polym 159:94–107
24. Leudjo Taka A (2014) Metal-decorated carbon nanostructures for photocatalytic reduction of CO_2. University of Johannesburg
25. Xia XH, Jiia ZH, Yu Y et al (2007) Preparation of multiwalled carbon nanotube supported TiO_2 and its photocatalytic activity in the reduction of CO_2 with H_2O. Carbon 45:717–721
26. Wu YC, Liu XL, Ye M, Xie T (2008) Preparation and properties of carbon nanotube-TiO2 nanocomposites. Acta Physico-Chimica Sin 24:97–102
27. Yen CY, Lin YF, Hung CH, et al (2008) The effects of synthesis procedures on the morphology and photocatalytic activity of multiwalled carbon nanotubes/TiO(2) nanocomposites. Nanotechnology 19:45604
28. Zhu J, Zhang J, Chen F, et al (2005) High activity TiO2 photocatalysts prepared by a modified sol-gel method: characterization and their photocatalytic activity for the degradation of XRG and X-GL. Top Catal 35:261–268
29. Raoov M, Mohamad S, Abas MR (2014) Synthesis and characterization of β-cyclodextrin functionalized ionic liquid polymer as a macroporous material for the removal of phenols and As(V). Int J Mol Sci 15:100–119
30. Simelane S (2011) Phosphorylated nanoporous β-cyclodextrin polymers: synthesis, characterization and their application in water purification. University of Johannesburg
31. Kuvarega AT, Krause RWM, Mamba BB (2014) Multiwalled carbon nanotubes decorated with nitrogen, palladium co-doped TiO2 (MWCNT/n, Pd co-doped TiO2) for visible light photocatalytic degradation of eosin yellow in water. Nanotechnol Sustain Dev First Ed 2:73–88
32. Gotić M, Ivanda M, Popović S, et al (1997) Raman investigation of nanosized TiO2. J Raman Spectrosc 28:555–558
33. Felske A, Plieth WJ (1989) Raman spectroscopy of titanium dioxide layers. Electrochim Acta 34:75–77

34. Tompsett GA, Bowmaker GA, Cooney RP, et al (1995) The Raman spectrum of brookite, TiO2 (Pbca, Z=8). J Raman Spectrosc 26:57–62
35. Porto SPS, Fleury PA, Damen TC (1967) Raman spectra of TiO2, MgF2 ZnF2, FeF2 and MnF2. Phys Rev 154:522
36. Hara Y, Nicol M (1979) Raman spectra and the structure of rutile at high pressures. Phys status solidi 94:317–322

Chapter 19
Novel Approaches to Environmental Monitoring

Patricia B.C. Forbes

Abstract The monitoring of environmental pollutants is vital to ensure environmental management is effective and potential negative impacts to the environment and human health are understood and mitigated. The sampling and analysis of environmental matrices is often challenging and costly, which invariably curtails the extent of monitoring performed. Researchers are therefore constantly investigating novel alternatives to existing analytical methods, which may offer advantages in terms of parameters such as: cost, speed, selectivity, sensitivity, portability, and accuracy. Herein we review a number of such novel methods for organic pollutants, which we have developed primarily for application in the monitoring of air pollutants. Semi-volatile organic air pollutants, such as polycyclic aromatic hydrocarbons (PAHs), may be present in both the gas and particle phases. Novel denuders which can simultaneously sample both phases have numerous benefits over traditional sampling approaches, including reduced sampling artifact formation and portability. Biomonitors are a cost effective means of sampling over wide geographical areas. The use of lichens as biomonitors for atmospheric PAHs as well as airborne metals can provide useful environmental monitoring information. In addition, nanomaterials, such as quantum dots, show promise in fluorescence sensor applications for the detection of organic pollutants (including PAHs) in water.

Keywords Environmental monitoring • Environmental pollutant • Denuder • Biomonitor • Lichen • Fluorescence sensor

19.1 Introduction

Environmental monitoring is a vital component in the protection of human health and the environment. In addition to the need for environmental compliance monitoring related to local legislative pollutant limits, environmental monitoring is typically required by international treaties dealing with the protection of the environment such as the Stockholm Convention on Persistent Organic Pollutants,

P.B.C. Forbes (✉)
Department of Chemistry, University of Pretoria, Pretoria 0002, South Africa
e-mail: patricia.forbes@up.ac.za

P. Ramasami et al. (eds.), *Emerging Trends in Chemical Sciences*,
DOI 10.1007/978-3-319-60408-4_19

to which many countries are signatories. There are numerous sources of pollution in modern communities, which results in a complex mixture of compounds.

Pollutants may have negative effects on human health and the environment, such as degradation of ecosystems, even at trace levels. Human health effects may arise after exposure to environmental pollutants, which could be either via acute or chronic exposure. The potential human health effects which may be incurred upon exposure to air pollutants, for example, include respiratory illness, heart disease and carcinogenicity. Evidence of these effects are illustrated by the fact that diesel engine exhaust emissions were declared carcinogenic to humans as exposure to these emissions has been linked to an increased risk for lung cancer [1]. Exposure to airborne particulate matter has also been associated with numerous health effects including heart disease [2, 3] and respiratory illness [3].

The need for the development of analytical methods which are robust, sensitive and selective is thus clearly evident [4, 5], which includes sampling techniques for environmental pollutants which are efficient and effective [6].

Traditional, standard analytical approaches often utilize specialized equipment and are of high cost, which limit their application and thereby the extent of environmental monitoring conducted in countries with limited resources [7]. Unique local conditions in terms of resource availability, environmental pollution sources and vulnerable communities, may therefore call for unique monitoring solutions. Here the development of a number of novel approaches to environmental monitoring is discussed, which aim to improve analytical speed, simplicity, cost, portability, sensitivity and/or selectivity. Non-destructive and screening approaches are valuable in this context, where they may provide a first tier of qualitative or semi-quantitative information for the selection of samples which may then be analyzed more comprehensively by traditional methods.

As environmental pollutants vary widely in terms of chemical composition (both inorganic and organic) as well as the sample matrix in which they may be present (air, water, soil, biota, etc.), therefore a range of analytical methods are required. It also needs to be remembered that pollutants may cycle between the environmental compartments, as illustrated in Fig. 19.1, and thereby between matrices due to their physico-chemical properties and ambient environmental conditions (such as seasonal changes in temperature) [8].

19.2 Denuders for Monitoring Semi-volatile Organic Air Pollutants

Semi-volatile organic compounds (SVOCs) have a vapour pressure range of 10^{-8}–10^{-2} Torr and can exist in the atmosphere in both gas and particle associated phases [9]. Polycyclic aromatic hydrocarbons (PAHs) are a class of SVOCs which are generated upon the combustion of organic fuels, including diesel, coal and biomass and are therefore widely present in the environment. The partitioning of SVOCs

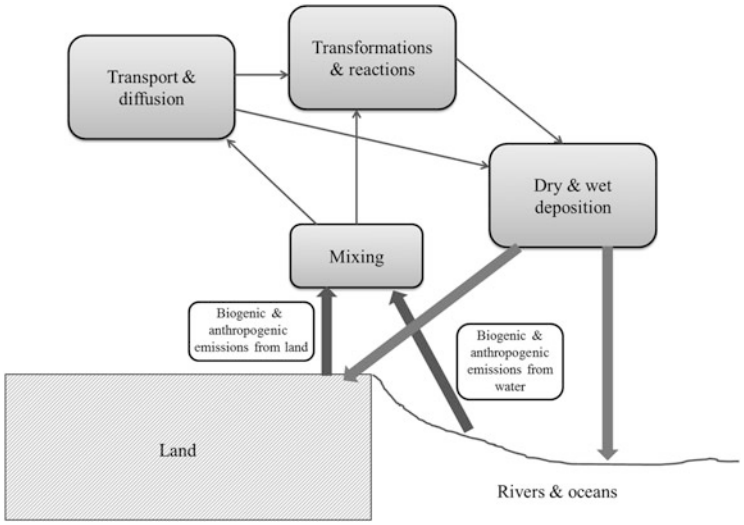

Fig. 19.1 Environmental cycling of emitted air pollutants, showing the major environmental processes (adapted from [2])

between the gas and particle phases affects the environmental cycling of these pollutants, including the relative importance of wet and dry deposition as atmospheric removal processes (refer to Fig. 19.1) [10]. In addition, human health effects of these compounds are dependent on their physical state in the atmosphere due to variations in lung deposition patterns, for example [11].

High volume samplers which are traditionally used for sampling gas and particle phase SVOCs consist of an upstream filter followed by an adsorbent such as polyurethane foam or XAD-2 [12]. These systems have inherent limitations which lead to sampling inaccuracies as a consequence of blow-off (volatilization) and adsorption effects [13]. We have thus developed a portable, low cost denuder, which allows for the efficient simultaneous sampling of gas and particle phase SVOCs [14]. This denuder consists of two multi-channel silicone rubber traps in series [each glass tube is 178 mm long and contains 22 parallel 55 mm long polydimethylsiloxane (PDMS) tubes of 0.3 mm i.d.]. The traps, which collect gas phase analytes, are separated by a quartz fibre filter for particle phase collection. The first trap samples gas phase SVOCs via diffusion into the PDMS, whilst any SVOCs which blow-off particles collected on the filter during sampling are sorbed into the PDMS of the second trap downstream of the filter [14].

Each component of the denuder (two traps and the filter) is analyzed separately via thermal desorption (TD) into a gas chromatograph with mass spectrometric detection (GC-MS) to allow for phase specific information to be obtained. The gas phase collection and particle phase transmission efficiencies through the PDMS traps have been determined to be suitable using both theoretical and experimental approaches. It was found using the experimental setup shown in Fig. 19.2 that the

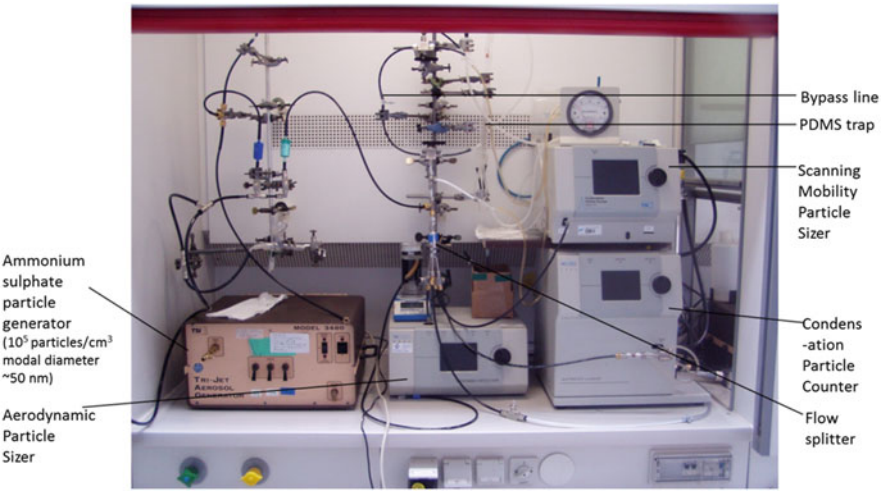

Fig. 19.2 Experimental setup to determine the particle transmission efficiency through a multi-channel silicone rubber trap as compared to a bypass line

overall transmission efficiency of ammonium sulphate particles with a modal diameter of 50 nm was 92% [14].

This denuder has been successfully applied to the simultaneous monitoring of gas and particle phase atmospheric SVOCs which were emitted from a range of sources, such as sugar cane combustion [14], diesel engine emissions in underground mining environments [15], household fires (shown in Fig. 19.3) [16, 17] and pesticide applications [18].

The fact that the components of this denuder can be directly thermally desorbed using commercial TD equipment avoids contamination issues and minimizes environmental impact. In addition, the entire sample is transferred to the GC column, therefore short sampling times at low sampling flow rates (~500 mL min^{-1}) may be used, allowing for good temporal profiles and excellent portability, as battery operated personal sampling pumps can be employed.

The denuders allow for a better understanding of the partitioning of atmospheric SVOCs between the gas and particle phases and thereby their potential impacts to human health and the environment. They can also assist in the elucidation of the mechanisms of human health effects upon exposure to these pollutants.

19.3 Lichens as Biomonitors of Air Pollution

Lichens (Fig. 19.4) are symbiotic organisms consisting of an algae and a fungus [19]. They have a slow growth rate and it has been shown that the concentrations of pollutants in lichens are representative of a time integrated exposure to ambient air pollutants [20]. Lichens therefore provide a simple, convenient and cost effective

Fig. 19.3 Sampling of domestic fire SVOC emissions by means of the multi-channel silicone rubber trap denuder, utilizing a portable sampling pump

Fig. 19.4 A foliose lichen

means of sampling air pollution. They have thus been employed in the biomonitoring of a range of inorganic (such as metals) and organic (including PAHs and polychlorinated dibenzo[*p*]dioxins) air pollutants [20, 21].

Sample preparation is a critical step in the utilisation of lichens as biomonitors [20–22]. We have recently developed a new application of the QueCHERS (Quick, Easy, Cheap, Effective, Rugged, Safe) sample extraction method for the determination of PAHs in *Parotrema austrosinense (Zalhbr.)* Hale lichens [23]. This

method is affordable, uses minimum solvent volumes, is quick and simple and it delivers superior extraction efficiencies to traditional extraction methods, such as soxhlet and ultrasonic assisted extraction. The method was successfully employed in determining the PAH profile differences between lichens growing at a non-impacted reference site and an industrial site in South Africa, as shown in Fig. 19.5. The results showed that the background site contained significantly more of the more volatile (and less toxic) PAHs with lower numbers of fused benzene rings, whilst the lichens from the industrial area contained predominantly 5- and 6-ring PAHs, which are more toxic [24]. The potential value of lichens as biomonitors in source apportionment studies is thus clearly evident.

There is a variety of sample preparation methods which are employed in biomonitoring studies which can significantly impact the results obtained. This needs to be borne in mind when comparing results from different studies [20, 21].

19.4 Fluorescence Sensors for Pollutants

Quantum dots (QDs) are nanomaterials which have a number of optical properties which make them ideal fluorescence sensors, including high quantum yields, high molar extinction coefficients, broad absorption with narrow, symmetric

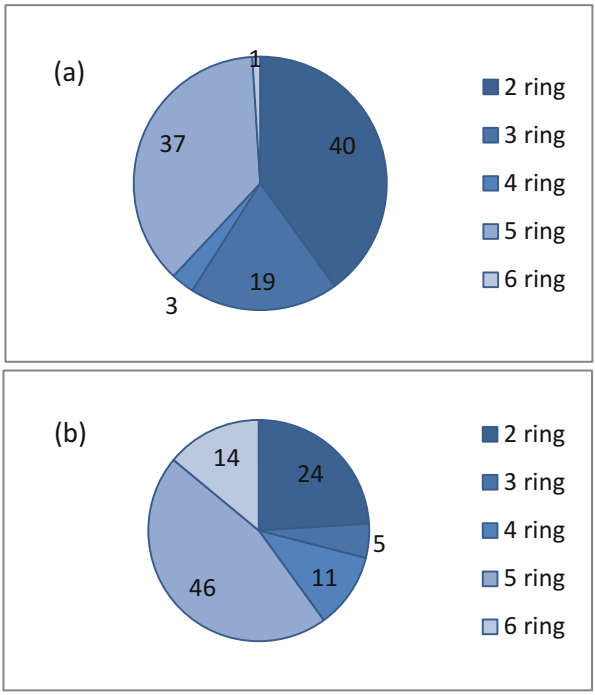

Fig. 19.5 Relative % contributions of different size PAHs to the total PAH content of a lichen sampled at a background (reference) site (**a**) and an industrial area (**b**) [24]

photoluminescence spectra spanning the UV to the near-infrared region of the electromagnetic spectrum, as well as good resistance to photobleaching due to their photostability. The fluorescence emission wavelength of QDs is size-tunable and their broad excitation spectra allow for excitation at a wavelength far removed from that of their emission [25].

Fluorescence sensors which utilize QDs have been employed in the analysis of numerous pollutants, including emerging chemical pollutants (ECPs), defined as chemicals which do not have a regulatory status, but which may have an adverse effect on human health and the environment [26]. The ECPs of current concern include a wide range of compounds including phthalates, polychlorinated biphenyls (PCBs), PAHs and Bisphenol A, in addition to disinfectants, pharmaceuticals and hormones [27]. The chemical structures of some of these compounds are shown in Fig. 19.6.

Fluorescence sensing has thus been applied to personal care products [28], pesticides [29] and PAHs [30], for example. In the latter case, we have developed a novel nanocomposite of L-Cys-CdSeTe/ZnSe/ZnS QDs coupled to graphene for sensing PAHs in water [30]. A limit of detection of 0.19 μg L^{-1} was obtained for phenanthrene under optimum conditions, whilst the limit of detection of anthracene, pyrene and naphthalene were estimated to be ~0.26 μg L^{-1} [30].

Means to enhance the selectivity of QD-based fluorescence sensors is an area of ongoing intensive research, which will facilitate the widespread, commercial application of these devices.

19.5 Concluding Comments

The novel monitoring methods for environmental pollutants reported here are being developed to improve the speed, simplicity, portability, sensitivity and/or selectivity of traditional, standard analytical methods at a reasonable cost. They may also be viewed as screening analyses in some applications, which are complementary to the traditional methods.

Additional areas receiving research focus in the field of environmental analysis include developments in sampling techniques, such as passive sampling utilizing devices which are cost effective and portable [31] as well as miniaturized sampling and analyte pre-concentration techniques, such as solid phase microextraction [6, 32]. These are often combined with enhanced instrumental analytical methods with high selectivity and sensitivity.

There are pros and cons with every analytical procedure. It is therefore necessary for the specific aims and requirements of an environmental monitoring campaign to be considered in deciding which method is most appropriate and fit for purpose. Here a number of options for environmental monitoring of organic pollutants have been presented, which may guide the reader in evaluating the less standardised approaches available in this regard. It must be remembered that much research is

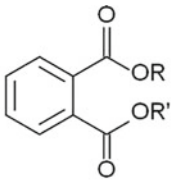

General structure of a phthalate molecule

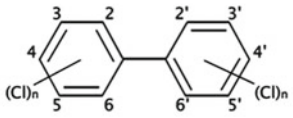

General structure of a PCB molecule

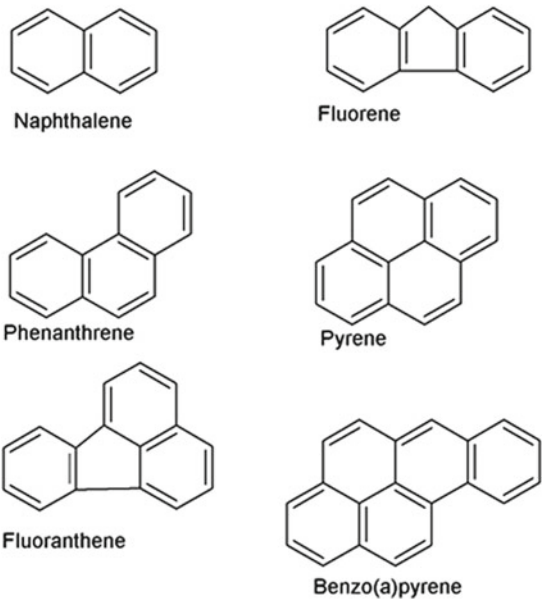

Selected PAHs

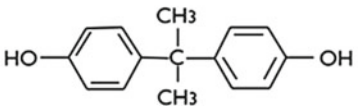

Bisphenol A

Fig. 19.6 Examples of chemical compounds considered to be emerging chemical pollutants

still required to ensure sufficient and efficient environmental monitoring is conducted to protect both the environment and human health.

Acknowledgements The extensive contribution of postgraduate students and collaborators to the work discussed here is gratefully acknowledged. Funders of this research are thanked, including the University of Pretoria, the South African National Research Foundation (NRF), the Water Research Commission (WRC) and the Photonics Initiative of South Africa (PISA). Contributions by PerkinElmer, Restek, Wirsam, Leco, ThermoFisher Scientific and Waters are also acknowledged.

References

1. IARC (International Agency for Research on Cancer) (2012) Diesel engine exhaust carcinogenic. Press release no. 213
2. Peters A (2005) Particulate matter and heart disease: evidence from epidemiological studies. Toxicol Appl Pharmacol 207:S477–S482
3. Kappos AD, Bruckmann P, Eikmann T, Englert N, Heinrich U, Höppe P, Koch E, Krause GHM, Kreyling WG, Rauchfuss K, Rombout P, Schultz-Klemp V, Thiel WR, Wichmann H-E (2004) Health effects of particles in ambient air. Int J Hyg Environ Health 207:399–407
4. Forbes PBC (2015) Perspectives on the monitoring of air pollutants (Chap 1). In: Forbes P (ed) Comprehensive analytical chemistry vol. 70: monitoring of air pollutants: sampling, sample preparation and analytical techniques. Elsevier, Netherlands, pp 3–9
5. Pérez-Bendito D, Rubio S (1998) Environmental analytical chemistry. Elsevier, Netherlands
6. Pawliszyn J (2002) Sampling and sample preparation in field and laboratory—fundamentals and new directions in sample preparation. Elsevier, Netherlands
7. Forbes PBC, Rohwer ER (2008) Monitoring of trace organic air pollutants—a developing country perspective. WIT Trans Ecol Envir 116:345–355
8. Forbes PBC, Garland RM (2016) Outdoor air pollution (Chap 4). In: de la Guardia M, Armenta S (eds) Comprehensive analytical chemistry vol. 73: the quality of air. Elsevier, Netherlands, pp 73–96
9. Hart KM, Pankow JF (1994) High-volume air sampler for particle and gas sampling. II: use of backup filters to correct for the adsorption of gas-phase polycyclic aromatic hydrocarbons to the front filter. Environ Sci Technol 28:655–661
10. Finizio A, Mackay D, Bidleman T, Harner T (1997) Octanol-air partition coefficient as a predictor of partitioning of semi-volatile organic chemicals to aerosols. Atmos Environ 31:2289–2296
11. Temime-Roussel B, Monod A, Massiani C, Wortham H (2004) Evaluation of an annular denuder tube for atmospheric PAH partitioning studies – 1: evaluation of the trapping efficiency of gaseous PAHs. Atmos Environ 38:1913–1924
12. US EPA (1999) Compendium of methods for the determination of toxic organic compounds in ambient air, 2nd ed., EPA/625/R-96/010b. United States Environmental Protection Agency, Cincinnati, OH
13. Forbes PBC, Rohwer ER (2015) Denuders (Chap 5). In: Forbes P (ed) Comprehensive analytical chemistry vol. 70: monitoring of air pollutants: sampling, sample preparation and analytical techniques. Elsevier, Netherlands, pp 153–181
14. Forbes PBC, Karg EW, Zimmermann R, Rohwer ER (2012) The use of multi-channel silicone rubber traps as denuders for polycyclic aromatic hydrocarbons. Anal Chim Acta 730:71–79
15. Geldenhuys G, Rohwer ER, Naudé Y, Forbes PBC (2015) Monitoring of atmospheric gaseous and particulate polycyclic aromatic hydrocarbons in South African platinum mines utilising

portable denuder sampling with analysis by thermal desorption–comprehensive gas chromatography–mass spectrometry. J Chrom A 1380:17–28
16. Forbes PBC (2012) Particle emissions from household fires in South Africa. WIT Trans Ecol Environ 157:445–456
17. Forbes PBC, Karg EW, Geldenhuys G, Nsibande SA, Zimmermann R, Rohwer ER (2013) Characterisation of atmospheric semi-volatile organic compounds. Clean Air J 23:3–6
18. Naudé Y, Rohwer ER (2012) Novel method for determining DDT in vapour and particulate phases within contaminated indoor air in a malaria area of South Africa. Anal Chim Acta 730:112–119
19. Forbes PBC, Thanjekwayo M, Okonkwo JO, Sekhula M, Zvinowanda C (2009) Lichens as biomonitors for manganese and lead in Pretoria, South Africa. Fresenius Environ Bull 18:609–614
20. Forbes PBC, van der Wat L, Kroukamp EM (2015) Biomonitors (Chap 3). In: Forbes P (ed) Comprehensive analytical chemistry vol. 70: monitoring of air pollutants: sampling, sample preparation and analytical techniques. Elsevier, Netherlands, pp 53–108
21. Van der Wat L, Forbes PBC (2015) Lichens as biomonitors for organic air pollutants. TrAC 64:165–172
22. Kroukamp EM, Wondimu T, Forbes PBC (2016) Metal and metalloid speciation in plants: overview, instrumentation, approaches and commonly assessed elements. TrAC 77:87–99
23. Van der Wat L (2015) Lichens as biomonitors of atmospheric polycyclic aromatic hydrocarbons. MSc dissertation, University of Pretoria, South Africa
24. Van der Wat L, Forbes P (2016) Lichen biomonitors for atmospheric polycyclic aromatic hydrocarbons. National Association for Clean Air Conference Mbombela (Nelspruit), South Africa. ISBN: 978-0-620-70646-9
25. Ruedas-Rama MJ, Walters JD, Orte A, Hall EAH (2012) Fluorescent nanoparticles for intracellular sensing: a review. Anal Chim Acta 751:1–23
26. Liu Q, Zhou Q, Jiang G (2014) Nanomaterials for analysis and monitoring of emerging chemical pollutants. TrAC 58:10–22
27. Gavrilescu M, Demnerová K, Aamand J, Agathos S, Fava F (2014) Emerging pollutants in the environment: present and future challenges in biomonitoring, ecological risks and bioremediation. New Biotechnol 32:147–156
28. Montaseri H, Forbes PBC (2016) A review of monitoring methods for triclosan and its occurrence in aquatic environments. TrAC 85:221–231
29. Nsibande SA, Forbes PBC (2016) Fluorescence detection of pesticides using quantum dot materials—a review. Anal Chim Acta 945:9–22
30. Adegoke O, Forbes PBC (2016) L-cysteine-capped core/shell/shell quantum dot-graphene oxide nanocomposite fluorescence probe for polycyclic aromatic hydrocarbon detection. Talanta 146:780–788
31. Greenwood R, Mills G, Vrana B (2007) Passive sampling techniques in environmental monitoring. Elsevier, Netherlands
32. Pawliszyn J (2000) Theory of solid-phase microextraction. J Chromatogr Sci 38:270–278

Chapter 20
Endosymbiotic Bacteria Isolated from Algoa and Kalk Bay, South Africa, as Source of Antimicrobial Compounds

J.K. Mhlongo, D.R. Beukes, and M. Trindade

Abstract Microbial marine endosymbionts are considered a rich source of secondary metabolites with pharmaceutical, industrial, and agricultural value. This comes after research has shown that the microorganisms harbored by marine invertebrates are likely to be responsible for the production of a significant number of compounds isolated from marine invertebrates. In this study a number of isolated marine bacteria were cultured on different media in order to explore and activate secondary metabolite genes encoded in their genome. The antimicrobial properties were assessed using eight test strains (*E. coli* 1699 [Cubist Pharmaceuticals], *B. cereus* ATCC10702, *P. putida* ATCC27853, *M. aurum*, *S. epidermidis* ATCC14990, multi-resistant *S. aureus*-MRSA-MB5393, *A. fumigatus* ATCC 46645 and *C. albicans* MY1055) utilizing well diffusion, agar overlay and high throughput screening (HTS). The strains with interesting antimicrobial profiles were identified by sequencing the 16S rRNA gene. Production of secondary metabolites, activation and deactivation were observed under different laboratory culturing conditions. Several strains showed multiple antimicrobial activity either on solid or liquid media. These results indicate the presence and expression of different secondary metabolite pathways under different media composition and confirm the notion that microorganisms associated with marine sponges are a great source of bioactive secondary metabolites.

Keywords Marine bacteria • Secondary metabolite • Endosymbiont • Marine sponge • Antimicrobial

J.K. Mhlongo • M. Trindade (✉)
Institute for Microbial Biotechnology and Metagenomics, Department of Biotechnology, University of the Western Cape, Cape Town, South Africa
e-mail: 3278602@myuwc.ac.za; ituffin@uwc.ac.za

D.R. Beukes
School of Pharmacy, University of the Western Cape, Cape Town, South Africa
e-mail: dbeukes@uwc.ac.za

P. Ramasami et al. (eds.), *Emerging Trends in Chemical Sciences*,
DOI 10.1007/978-3-319-60408-4_20

20.1 Introduction

Bacteria associated with marine sponges are very important producers of valuable and unique chemicals, useful in pharmaceutical, agricultural and cosmetic industries [1]. Marine sponges have for decades been thought to be solely responsible for the production of active bio-compounds extracted from them, however new evidence suggests that the microorganisms associated with the sponges are the producers of the compounds [2–5]. Compounds such as Jaspamide produced by *Jaspis sp*. are supporting this as it shows structural similarity to Chondramide which was isolated from *Chondromyces crocatus* [4].

In the past research has focused on isolation of active secondary metabolites from terrestrial sources despite the oceans harboring a huge diversity of microorganisms with many of them unknown or uncharacterized. As such, marine bacteria serve as a potential source of unique chemistry as it is an understudied group [6, 7]. This together with the fact that little is known about the South African marine biota and chemical diversity [8], motivated the search for bacteria associated with marine sponge in the South African coastal line. South Africa's coastal line is about 3000 km and it is characterized with three different temperature zones with the west coast being the coldest, followed by the east coast with subtropical temperatures and the south being the warmest [8]. These currents influence the diversity of organisms greatly and therefore the South African coast offers a rich source of unique adaptation characteristics [9].

Both macro- and micro-organisms produce a wide range of natural products (NPs) which are grouped into different classes based on how they are biosynthesized. The common NPs are polyketides, non-ribosomal peptides, bacteriocins, ribosomal peptides, siderophores, terpenes and hybrids of these classes [10, 11]. The production of these compounds can be triggered by a number of environmental stimulators. The stimulator can be biotic (bacteria, archaea, invertebrate and fungi) and abiotic (salinity, high or low temperature, drought, and light availability). These stimulators trigger the transcription of the genes responsible for the proteins needed for the biosynthesis of the NPs [12]. The precursors for the synthesis of secondary metabolites are obtained from primary metabolite intermediates [1].

To our knowledge there are limited/no studies on the antimicrobial potential of microorganisms found in the South African marine environment despite the known high diversity of marine sponges recorded. Currently only one published study showcases the potential of South African marine environment as a source of bioactive bacterial compounds, however this study was focusing only on Actinomycetes [13].

In this study the antimicrobial potential of 23 microorganisms isolated from marine invertebrates sampled from the Algoa and Kalk bays (South Africa) was assessed against gram positive and gram negative bacteria and fungal indicator strains, including multidrug resistant strains, under different culturing conditions.

20.2 Materials and Methods

20.2.1 Materials

All chemicals used during the study were either purchased from Sigma Aldrich, Merck, New England Biolab, Kappa Biotech and Life Technologies. Strains used for antimicrobial testing included *E. coli* 1699 (Cubist Pharmaceuticals), *B. cereus* ATCC10702, *P. putida* ATCC27853, *M. aurum, S. epidermidis* ATCC14990, multi-resistant *S. aureus*-MRSA-MB5393, *A. fumigatus* ATCC 46645 and *C. albicans* MY1055.

20.2.2 Methods

20.2.2.1 Cultivation of the Isolated Strains

A total of 23 marine isolates were cultured and screened for their ability to produce active secondary metabolites under standard laboratory conditions. The strains were tested using both solid and liquid culture. The selected strains were also tested with the use of high throughput screening (HTS) platforms for anti-inflammatory activity [14], antimicrobial activity against multi-resistant *S. aureus*-MRSA-MB5393, *A. fumigatus* ATCC 46645 and *C. albicans* MY1055 [15, 16]. All test strains were cultured in Luria broth/agar ([LB/A], g/l: 10 g tryptone, 5 g yeast extract, 10 g NaCl) at 37 °C for 24 h. Fermentation was carried out using glucose yeast and malt extract ([GYM], g/l: 4 g glucose, 4 g yeast extract, 10 g malt extract, 24 g sodium chloride, 2 g calcium carbonate, 5.3 g magnesium chloride, 0.7 g potassium chloride and 0.1 g calcium chloride), tryptic soya broth ([TSB], g/l: 3 g tryptic soya broth, 18 g sodium chloride, 2 g magnesium chloride, 0.075 g calcium chloride), activated charcoal medium ([ACM], g/l: 2.38 g Hepes, 3 g sodium pyruvate, 0.1 g yeast extract, 3 g soya bean peptone, 0.3 g sodium nitrate, 0.1 g monopotassium phosphate, 0.15 g magnesium sulfate heptahydrate and 3 g activated charcoal) and Zobell broth ([ZBB], g/l: 1.25 g yeast extract, 3.75 g peptone, 18 g sodium chloride, 2 g magnesium chloride, 0.525 g potassium chloride and 0.075 g calcium chloride) medium for liquid fermentation and 15 g/l agar was added for solid fermentation.

20.2.2.2 Antimicrobial Activity Screening

Methods employed for screening bioactivity include: i) well diffusion, ii) soft agar overlay, and iii) HTS for antifungal, anti-yeast, and anti-inflammatory. Inoculum cultures (10 ml) were prepared in GYM media in 50 ml MacConkey bottles at room temperature with shaking at 150 rpm for 2 days. The culture was then used to

inoculate 10 ml of four types of media, ZBB, TSB, ACM and GYM, in 50 ml MacConkey bottles and fermented for 14 days under the same incubation conditions as for the inoculum cultures. The antimicrobial activity of the fermentation broths was determined using the well diffusion technique [17]. After 14 days, the cultures were centrifuged at 6000 rpm for 10 minutes to remove the cell debris. The supernatant was collected and stored at 4 °C until use.

The bacterial test strains used to assess antimicrobial activity were *E. coli* 1699 (Cubist Pharmaceuticals), *B. cereus* ATCC10702, *P. putida* ATCC27853, *M. aurum,* and *S. epidermidis* ATCC14990 and were cultured for 24 h in 10 ml media, and diluted to achieve a cell suspension of approximately 1.5×10^8 cells per ml. Eighty microliters of the test strain were spread on a Luria agar-containing petri dish (100 cm diameter). Wells were made on the agar and ±100 µl of the supernatant was added. The plates were left under the laminar flow to allow for pre-diffusion of the supernatant into the agar for about 2 h. The plates were then incubated at 37 °C for 24 h. Zones of inhibitions were observed and results were recorded.

An agar overlay assay was also employed as one technique for the antimicrobial assay screening. The marine isolates were spotted on an agar plate and incubated for 14 days at room temperature to allow production of natural products. The agar plates were then overlaid with 6 ml of soft Luria agar inoculated with a test strain and incubated for 24 h at 37 °C. Clear zones were observed the following day and the results were recorded in a table format.

For anti-fungal, anti-yeast and anti-inflammatory activity screening, semi-fractionated extracts were used. The marine isolates were cultured in 10 ml TSA, ZBA, GYM and ACM media for 14 days as described above. Extracts were prepared by acetone extraction where an equal volume of acetone was added to the culture and incubated on an orbital shaker for 1 h. The acetone was evaporated in a fume hood before the crude extract was applied to fractionation columns. Fractionation columns were prepared by first puncturing holes into the bottom of a 15 ml falcon tube and then covering it with glass wool. The tube was filled with 10 ml of SP207ss resin (Sigma-Aldrich). The columns were then equilibrated by washing with 50 ml of acetone, followed by a wash of 50 ml methanol and a final wash with 100 ml MilliQ water. After crude extracts were added to the columns, the columns were washed with 50 ml MilliQ water. The organic extract was eluted with 50 ml of acetone. The eluate was collected and the acetone was evaporated in a CentriVap centrifugal vacuum concentrator (Labconco). The dried extract was resuspended in dH_2O and screened against *Aspergillus fumigatus* ATCC 46645 [15], *S. aureus*-mrsa MB5393 and *Candida albicans* MY155 [16]. The extracts were also assessed for anti-inflammatory activity against Tumor necrosis factor-α (TNF-α) [14].

20.2.2.3 Genetic Characterization

Genomic DNA of the most interesting strains was extracted using the CTAB method and the 16S rRNA gene amplified using E9F (GAGTTTGATCCTGGCT CAG) [18] and Ur1510R (GGTTACCTTGTTGTTACACTT) [19] primers with polymerase chain reaction under the following conditions: 95 °C for 3 min, 95 °C for 30 s, 55 °C for 35 s, 72 °C for 1 min and 15 min at 72 °C for final extensions using DreamTaq polymerase (Thermo Scientific™) in a total of 50 µl. The expected 1.5 kb amplicon was visualised and excised after agarose gel electrophoresis and purified with a NucleoSpin® Gel and PCR Clean-up kit. The purified DNA products were sequenced by the Central Analytical Facility at Stellenbosch University using an ABI PRISM 377 automated sequencer. The sequenced data were processed using Chromas Pro software (version 1.5a) for alignment and manual editing of sequences and compared with those available on Genbank database using the NCBI BLASTn tool (www.blast.ncbi.nlm.gov).

20.3 Results and Discussion

20.3.1 Antimicrobial Screening

A total of 23 marine bacteria were screened against eight test strains using the overlay assay, HTS and well diffusion assay (Table 20.1). Only three strains (PE12-126, PE08-33(3).1 and KB18-15) did not show any activity for both liquid and solid fermentation experiments. From the extracts prepared from liquid cultures and screened using HTS, three showed no activity (PE06-56, PE12-116 and PE08-149B). All isolates showed some biological activity using at least one of the screening processes. Although not representative of the total biodiversity, this indicates that the South African coastline is a rich source of bioactive secondary metabolite (SM) producers.

Some of the isolates showed broad or narrow or species-specific activities (Table 20.1). For example, PE14-07 showed antibacterial activity against both gram negative and positive strains, KB11-25 showed activity against gram positive bacteria while KB18-15 showed activity against *S. aureus-mrsa*-MB5393 only respectively. This was also observed by Anand and co-workers [20] when working with bacteria isolated from marine sponges. A significant number of the isolates produced activity against the two multi-drug resistant test strains; four strains (KB07-58, PE06-34, KB18-15 and PE06-105) showed activity against *Staphylococcus aureus* (MRSA) while PE06-34, PE06-56, PE06-117, PE08-149B, PE12-116, PE12-107, PE13-172, PE14-07, PE14-63, PE14-104, and KB08-48 inhibited the growth of the *E. coli* 1699. Twelve strains displayed anti-fungal activity, and

Table 20.1 Antimicrobial properties of all isolates screened using the well diffusion, HTS and agar overlay technique

Organism	*E. coli* 1699	*P. putida*	*S. epidermis*	*B. cereus*	*M. aurum*	*S. aureus*-mrsa-	*C. albicans*	*A. fumigatus*	Anti-inflammatory
PE06-56	GYM, ACM*	GYM/ACM*	GYM, ACM*	ACM*	GYM				
PE12-116	GYM*-	GYM	GYM		GYM				
PE08-149B	GYM*, ZBB	GYM*	GYM	GYM*	GYM				
PE14-07	GYM, ZBB	GYM	GYM, ZBB	GYM*, ZBB*	GYM		ZBB, TSB	ZBB, TSB	GYM
PE14-104	GYM, ZBB	GYM	GYM, ZBB				ZBB, TSB	ZBB	
PE12-126								ZBB	
PE14-63	GYM		GYM, ZBA*-	GYM			ZBB, TSB	ZBB, TSB	
KB07-58		ZBB*-				ZBB			
PE06-34	ZBB, TSB, GYM*-	ZBB		TSB		ACM			
KB18-15						ACM			
PE14-115							ZBB	ZBB	
KB08-21.1			GYM*-	GYM*					TSB
KB08-22.1			GYM*-	GYM*-					GYM
KB08-48	TSB*-		GYM*-				ZBB, TSB	ZBB, TSB	ZBB
KB11-25			GYM*-	GYM*-				ZBB, GYM	ACM
PE06-117	ZBA*-								GYM
PE08-33(3).1									ACM
PE12-107	GYM*-							ACM	ACM
PE13-172	ZBA*-			ZBA*-					ZBB, TSB
PE13-161			GYM				ZBB	ZBB	
KB11-44					GYM		ZBB	ZBB	
PE08-149A		GYM					TSB	TSB	
PE06-105				GYM, TSA*		ACM		TSB, ZBB	

Blank space indicates no observed activity; absence of * indicates activity observed only in liquid, * indicates activity observed in liquid and solid media, and *- means activity only observed in solid media and not liquid

eight showed anti-yeast activity, with six of them showing activity against both. Nine strains out of twenty-three gave anti-inflammatory activity.

A change in the antimicrobial profile of cultured strains was observed with some strains showing highest bioactivity on solid media while others showing greater bioactivity when cultured in liquid (Table 20.1). This phenomenon was observed in the production of pyrrocidines A and B by a *Cylindrocarpon* sp. LL-Cyan426 strain [21]. Most literature available highlighting the effect in the change of this condition dealt mainly with fungal activity, with bacterial studies being limited. *Penicillium commune* QSD-17 was cultured on solid rice media and resulted in the production of two new compounds which were not observed in liquid culture namely isophomenone and 3-deacetylcitreohybridonol [22]. In this study, it can be seen that the state of the medium, whether solid or liquid, also influences bacteria which results in differential expressing of certain biosynthetic pathways.

The effect of media also plays a very critical role in the production of secondary metabolites with simple changes such as the carbon or nitrogen source [23]. This is clearly demonstrated by our strains where GYM, ZBA and TSA resulted in the most antimicrobial activity hits compared to when cultured in ACM. This is well known and referred to as OSMAC (One Strain Many Active Compounds). Such media-dependent expression of bioactivity could suggest that multiple biosynthetic pathways are involved in the production of diverse bioactive secondary metabolites [24].

20.3.2 Genetic Identification

Six selected strains with impressive antimicrobial profiles were identified by 16S rRNA sequence analysis (Table 20.2). Five showed high sequence identity to species which have previously been associated with the marine environment, and specifically with marine invertebrates and belonging to the phyla Proteobacteria [25]. Three of the strains belong to the *Bacillus* genus, well known for their secondary metabolite production [26–28].

PE14-07 could represent a novel *Pseudovibrio* species due to only 95% sequence similarity. *Pseudovibrio ascidiaceicola* was first proposed as a novel species relatively recently, when it was isolated from a sea squirt in 2006, with

Table 20.2 16S rRNA gene sequencing results

Strain ID	Similar organism	Similarity %
PE14-07	*Pseudovibrio ascidiaceicola* strain F423	95
PE06-34	*Bacillus anthracis* str. Ames	100
PE14-63	*Vibrio tasmaniensis* strain Carson D39	99
PE08-149B	*Bacillus weihenstephanensis* strain DSM 11821	99
KB08-48	*Bacillus anthracis* str. Ames	99
PE14-104	*Vibrio pomeroyi* strain CAIM 578	100

the genus being only established in 2004 after isolation of *P. denitrificans* from coastal sea water [29]. This indicates that *Pseudovibrio* are abundantly distributed in the marine environment worldwide as they have been isolated from a number of marine invertebrates.

A *Pseudovibrio* sp. isolated from a marine sponge *Haliclona simulans* showed bioactivity with a similar profile to what we observed for the *Pseudovibrio sp.* PE14-07 strain, with the only difference being that activity against MRSA was not observed for PE14-07. This could be due to the fact that they used a starch yeast extract-peptone–seawater (SYP-SW) media to activate a pathway responsible for the MRSA activity [30]. This observation strengthens the importance of media composition as it plays a critical role in the production of secondary metabolites.

20.4 Conclusion

Marine sponge-associated bacteria are a good source of bioactive secondary metabolites with broad activity spectrum. This study demonstrates that South African marine sponges are also richly endowed with a wide range of bioactivities. The number of activities against multi-drug resistant bacteria could represent novel sources of much needed antibiotics, especially where resistance is already being observed against the last line of defense antibiotics. Based on the superiority of GYM in the induction of secondary metabolites, it should be included in the primary screening of all bacterial isolates for their ability to produce bioactive compounds. *Pseudovibrio* sp. PE14-07, *Vibrio pomeroyi* sp. P14-104 and *Bacillus* sp. KB08-48 are good candidates for further studies which could result in isolation of new compounds due to the broad bioactivity shown by these strains.

Acknowledgments The authors would like to acknowledge the University of the Western Cape, the National Research Foundation of South Africa, the Medical Research Council of South Africa and PharmaSea for funding this work.

References

1. Zhao XQ (2011) Genome-based studies of marine microorganisms to maximize the diversity of natural products discovery for medical treatments. Evid Based Complement Alternat Med 2011:1–11
2. Harvey A (2008) Natural products in drug discovery. Drug Discov Today 13:894–901
3. Piel J (2006) Bacterial symbionts: prospects for the sustainable production of invertebrate-derived pharmaceuticals. Curr Med Chem 13:39–50
4. Sabdono A, Radjasa OK (2011) Microbial symbionts in marine sponges: marine natural product factory. J Coast Dev 11:57–61

5. Zarins-Tutt JS, Barberi TT, Gao H, Mearns-Spragg A, Zhang L, Newman DJ, Miriam Goss RJ (2016) Prospecting for new bacterial metabolites: a glossary of approaches for inducing, activating and upregulating the biosynthesis of bacterial cryptic or silent natural products. Nat Prod Rep 33:54–72
6. Prieto ML, O'Sullivan L, Tan SP, McLoughlin P, Hughes H, O'Connor PM, Cotter PD, Lawlor PG, Gardiner GE (2012) Assessment of the bacteriocinogenic potential of marine bacteria reveals Lichenicidin production by seaweed-derived Bacillus spp. Mar Drugs 10:2280–2299
7. Debbab A, Aly AH, Lin WH, Proksch P (2010) Bioactive compounds from marine bacteria and fungi: marine bioactive compounds. J Microbial Biotechnol 3:544–563
8. Davies-Coleman MT, Beukes DR (2004) Ten years of marine natural products research at Rhodes University. S Afr J Sci 100(11–12):539–544
9. Demain AL, Fang A (2000) The natural functions of secondary metabolites. Adv Biochem Eng Biotechnol 69:1–39
10. Weber T, Blin K, Duddela S, Krug D, Kim HU, Bruccoleri R, Lee SY, Fischbach MA, Müller R, Wohlleben W, Breitling R, Takano E, Medema MH (2015) antiSMASH 3.0—a comprehensive resource for the genome mining of biosynthetic gene clusters. Nucleic Acids Res 43:W237–W243
11. Ziemert N, Podell S, Penn K, Badger JH, Allen E, Jensen PR (2012) The natural product domain seeker NaPDoS: a phylogeny based bioinformatic tool to classify secondary metabolite gene diversity. PLoS One 7:e34064
12. Hanssen KØ (2014) Isolation and characterisation of bioactive secondary metabolites from Arctic marine organisms. http://hdl.handle.net/10037/7017
13. Cwala Z, Igbinosa EO, Okoh AI (2011) Assessment of antibiotics production potentials in four actinomycetes isolated from aquatic environments of the Eastern Cape Province of South Africa. Afr J Pharm Pharmacol 5:118–124
14. Svenson J (2013) MabCent: arctic marine bioprospecting in Norway. Phytochem Rev 12:567–578
15. Monteiro MC, de la Cruz M, Cantizani J, Moreno C, Tormo JR, Mellado E, De Lucas JR, Asensio F, Valiante V, Brakhage AA, Latgé JP, Genilloud O, Vicente F (2012) A new approach to drug discovery: high-throughput screening of microbial natural extracts against *Aspergillus fumigatus* using resazurin. J Biomol Screen 17:542–549
16. Martín J, da Sousa T, Crespo G, Palomo S, González I, Tormo JR, de la Cruz M, Anderson M, Hill RT, Vicente F, Genilloud O, Reyes F (2013) Kocurin, the true structure of PM181104, an anti-methicillin-resistant *Staphylococcus aureus* (MRSA) thiazolyl peptide from the marine-derived bacterium *Kocuria palustris*. Mar Drugs 11:387–398
17. Scorzoni L, Benaducci T, Almeida AMF, Silva DHS, Bolzani VS, Mendes-Giannini MJS (2009) Comparative study of disk diffusion and microdilution methods for evaluation of antifungal activity of natural compounds against medical yeasts *Candida* spp and *Cryptococcus* sp. Rev Ciênc Farm Básica E Apl 28:25–34
18. Farrelly V, Rainey FA, Stackebrandt E (1995) Effect of genome size and rrn gene copy number on PCR amplification of 16S rRNA genes from a mixture of bacterial species. Appl Environ Microbiol 61:2798–2801
19. Reysenbach AL, Giver LJ, Wickham GS, Pace NR (1992) Differential amplification of rRNA genes by polymerase chain reaction. Appl Environ Microbiol 58:3417–3418
20. Anand TP, Bhat AW, Shouche YS, Roy U, Siddharth J, Sarma SP (2006) Antimicrobial activity of marine bacteria associated with sponges from the waters off the coast of South East India. Microbiol Res 161:252–262
21. Bigelis R, He H, Yang HY, Chang LP, Greenstein M (2006) Production of fungal antibiotics using polymeric solid supports in solid-state and liquid fermentation. J Ind Microbiol Biotechnol 33:815–826
22. Gao SS, Shang Z, Li XM, Li CS, Cui CM, Wang BG (2012) Secondary metabolites produced by solid fermentation of the marine-derived fungus *Penicillium commune* QSD-17. Biosci Biotechnol Biochem 76:358–360

23. VanderMolen KM, Raja HA, El-Elimat T, Oberlies NH (2013) Evaluation of culture media for the production of secondary metabolites in a natural products screening program. AMB Express 3:1–7
24. Devi P, Wahidullah S, Rodrigues C, Souza LD (2010) The sponge-associated bacterium *Bacillus licheniformis* SAB1: a source of antimicrobial compounds. Mar Drugs 8:1203–1212
25. Dupont S, Carre-Mlouka A, Descarrega F, Ereskovsky A, Longeon A, Mouray E, Florent I, Bourguet-Kondrack ML (2014) Diversity and biological activities of the bacterial community associated with the marine sponge *Phorbas tenacior* (Porifera, Demospongiae). Lett Appl Microbiol 58:42–52
26. Lee YK, Lee JH, Lee HK (2001) Microbial symbiosis in marine sponges. J Microbiol Seoul Korea 39:254–264
27. Bastos J, Kohn LK, Fantinatti-Garboggini F, Padilla MA, Flores EF, da Silva BP, de Menezes CB, Arns CW (2013) Antiviral activity of *Bacillus* sp. isolated from the marine sponge *Petromica citrina* against bovine viral diarrhea virus, a surrogate model of the hepatitis C virus. Viruses 5:1219–1230
28. Phelan RW, O'Halloran JA, Kennedy J, Morrissey JP, Dobson AD, O'Gara F, Barbosa TM (2012) Diversity and bioactive potential of endospore-forming bacteria cultured from the marine sponge *Haliclona simulans* Sporeformers from the marine sponge *H. simulans*. J Appl Microbiol 112:65–78
29. Crowley S, O'Gara F, O'Sullivan O, Cotter P, Dobson A (2014) Marine *Pseudovibrio* sp. as a novel source of antimicrobials. Mar Drugs 12:5916–5929
30. Kennedy J, Baker P, Piper C, Cotter PD, Walsh M, Mooij MJ, Bourke MB, Rea MC, O'Connor PM, Ross RP, Hill C, O'Gara F, Marchesi JR, Dobson AD (2009) Isolation and analysis of bacteria with antimicrobial activities from the marine sponge *Haliclona simulans* collected from Irish waters. Mar Biotechnol 11:384–396

Chapter 21
Pd-MCM-41 and Ni–Boride–Silica Catalyst Synthesis, Characterization and Its Application for Reduction of Substituted Aromatics: An Environmentally Benevolent Approach

Ateeq Rahman, Daniel Likius, and Veikko Uahengo

Abstract Microporous and mesoporous silica catalysts, MCM-41, derived from zeolite type catalysts, are easily synthesized in laboratory scale and commercially available SiO_2 have applications in reduction reactions. Nickel boride (Ni B) silica catalysts denoted as Cat A were characterized by XRD, IR, SEM, BET surface area and chemisorption studies. Nickel boride generated in situ on silica were found to be super active catalysts for reduction of nitro aromatics, aldehydes, ketones, alkenes, phenols and in reductive amination of aldehydes and ketones at low temperatures, whereas Pd(II)-MCM-41 denoted as Cat B exhibited catalytic activity for reduction of nitro aromatics, aldehydes, and hydrodehalogenation reactions. Efficient catalytic activity for reduction reactions was exhibited by the Ni and Pd catalysts which were found to be reusable, atom economy, reproducible and environmentally friendly. A comparative study of these catalysts is presented.

Keywords Ni–SiO_2 • Pd(II) MCM-41 • Reduction • Hydrodehalogenation

21.1 Introduction

Many traditional organic reactions use stoichiometric reagents because they provide excellent activity, selectivity and specificity at low temperatures. However, the necessity to regenerate these materials after reaction leads to the production of large quantities of waste. Due to growing environmental concerns, the laws and regulations governing the disposal of industrial effluents are becoming increasingly tighter. The foremost challenge for the fine chemical manufacturing industries is therefore to seek cleaner processes in order to minimize the production of waste [1].

A. Rahman • D. Likius (✉) • V. Uahengo
Department of Chemistry and Biochemistry, Faculty of Science, University of Namibia, Private Bag, 13301 Windhoek, Namibia
e-mail: arahman@unam.na; daniels@unam.na; vuahengo@unam.na; vuahengo@gmail.com

P. Ramasami et al. (eds.), *Emerging Trends in Chemical Sciences*,
DOI 10.1007/978-3-319-60408-4_21

There are many methods of effecting reduction which may or may not lead to hydrogenation, but in this article only processes leading to the addition of hydrogen or replacement of a functional group by hydrogen will be considered. Reduction of organic functional groups can be categorized into (i) addition of hydrogen to unsaturated groups in the reduction of ketones to alcohols, and (ii) addition of hydrogen across single bonds leading to cleavage of functional groups (hydrogenolysis). The early pioneering work was largely ignored because of poor yields and long reaction times, but the situation has changed considerably following the appearance of stimulating heterogeneous catalysts and the introduction of greater catalyst loadings and different hydrogen donors. A new family of mesoporous molecular sieves was discovered by the researchers at Mobil Oil Corporation, and scientists have shown considerable and continuously growing interest since its discovery at the beginning of the 1990s [2, 3]. This fact led to extend the application of redox molecular sieves for oxidation of organic molecules. One member of mesoporous family MCM-41 with hexagonal arrangement and narrow pore size distribution varying between 3 and 10 nm, according to the surfactant used in the synthesis, high specific surface area (ffi1000 m^2/g) and structural thermal stability, but with low hydrothermal stability and adjustable heteroatom compositions enable these materials to be widely used as adsorbents, catalytic supports, and heterogeneous catalysts [4]. The incorporation of active metals into the framework of MCM-41 molecular sieves makes them particularly valuable for catalytic applications, some of which are mentioned in the text. Since the first account of the synthesis of mesoporous molecular sieves in alkaline medium appeared, a large number of publications on the synthesis of mesoporous materials, mainly MCM-41 have been reported. The synthesis of mesoporous materials has also been carried out in acidic and neutral medium. Pinnavaia [5] proposed a neutral template synthesis mechanism based on hydrogen bonding between primary amines and neutral inorganic species. Such mesoporous molecular sieves are called hexagonal mesoporous silica (HMS).

The recently discovered family of mesoporous materials, MCM-41, have potential for industrial application due to their being ‘tunable’, having a large pore size. However, our work is to develop a suitable catalyst to promote the conversion of reactants while maintaining well-dispersed active sites and exhibiting good structural stability, which still remains a challenge.

21.2 Valuable Catalytic Applications

Supported nickel catalysts find widespread applications in many important industrial hydrogenation and hydrogenolysis processes such as steam reforming of methane and higher paraffins, or methanation of synthetic gas. In view of good results obtained, the authors explored the use of Pd(II)-MCM41 (Cat B) prepared by functionalizing MCM-41 with 3-triethoxysilylpropylamine and subsequent complexation with dichlorobis(benzylcyano) palladium(II) for reduction of nitro-

aromatics and hydrodehalgenation reactions [5]. On the other hand the supported Ni silica catalysts were tested for catalytic reactions such as reduction of functional groups such as nitro, aldehydes, ketones, phenols, alkenes, and bromo benzene. Hydrogenation of aqueous glucose has also been carried out using supported nickel and ruthenium catalysts. Catalysts were prepared by precipitation, impregnation, sol-gel and template synthesis using SiO_2, TiO_2, Al_2O_3 and carbon as support materials. Industrially nickel catalysts were used for the polymerization of cyclo-olefins, and conversion of ethene to propene which is used as an intermediate for the production of polypropylene. Conversion of CO_2 to CO with CH_4 over Ni–SiO_2 catalyst [1, 4–7] has also been investigated.

The manuscript details a comparison of Cat A (Ni–SiO_2) and Cat B (Pd(II)-MCM-41) for reduction reactions at moderate conditions (Scheme 21.1), avoiding high temperature and high hydrogen pressure to minimize the thermal risks during industrial production [8–10]. It addresses also the achievement of high conversion and selectivity using mild reducing agents, to produce the desired chemical compound in the required quality. Additional features looked into are the operational simplicity, safety, energy efficient procedure and scope to recover the investment and developmental costs in a reasonable time.

Thus, the objective of this work is to study the capability of Ni loaded support catalysts on silica for selective reduction reactions of substituted aromatic compounds to their corresponding products. Table 21.1 illustrates the effect of the Ni loading on the process and the catalytic aptitude of the system for a potential use in industrial processes. Aromatic amines and aromatic alcohols are generally prepared by the reduction of nitro aromatics and aromatic aldehydes usually by the use of Pd, Ni, Rh, Pt, Ru or calcined Ni-hydrotalcite [11]. The main limitations of the earlier reports are the high temperature, pressure, and sophisticated autoclaves required for the catalytic activity of metals such as Ni, Pt and Pd [4].

The authors studied the oxidation of *p*-nitro benzyl alcohol using nickel supported silica catalytic system at 65 °C into *p*-nitrobenzaldehyde, and the reduction of nitro aromatics, aldehydes, ketones, alkenes, phenols and reductive amination of aldehydes and ketones at low temperatures. Also reduction of nitroaromatics and hydrodehalogenation reactions were also performed using Pd (II)-MCM-41 (Cat B). Both catalysts showed successful completion of these reactions with excellent conversion and selectivity (Table 21.1).

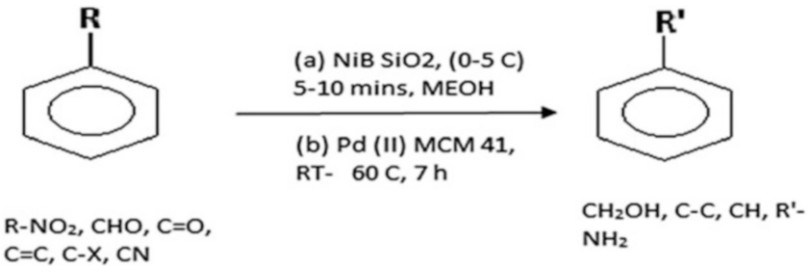

Scheme 21.1

Table 21.1 Reduction of aromatic functional groups to their corresponding products

S.No	Starting material (S)[a]	Catalyst	Product	Conversion (%)	Selectivity (%)
1.	C_6H_5–NO_2	A	C_6H_5–NH_2	100	100
2.	C_6H_5–NO_2	B	C_6H_5–NH_2	100	100
3.	HO–C_6H_4–NO_2	A	HO–C_6H_4–NH_2	75	100
4.	HO–C_6H_4–NO_2	B	HO–C_6H_4–NH_2	20	100
5.	CHO–C_6H_4–NO_2	A	CH_2OH–C_6H_4–NH_2	95	100
6.	CHO–C_6H_4–NO_2	B	CH_2OH–C_6H_4–NH_2	45	100
7.	C_6H_5–Br	A	C_6H_6	75	100
8.	C_6H_5–Br	B	C_6H_6	65	100
9.	NO_2–C_6H_4–CH_3	A	NH_2–C_6H_4–CH_3	65	100
10.	NO_2–C_6H_4–CH_3	B	NH_2–C_6H_4–CH_3	45	100
11.	C_6H_5–OH	A	C_6H_{11}–OH	20	100
12.	C_6H_5–CHO	A	C_6H_5–CH_2OH	100	100
13.	4Br–C_6H_4–CHO	A	4Br–C_6H_4–CH_2OH	100	100
14.	4Br–C_6H_4–CHO	B	4Br–C_6H_4–CH_2OH	45	100
15.	C_6H_5–CHO + Bu^nNH_2	A	$PhCH_2NHBu^n$	100	100
16.	C_6H_5–CHO + Ph–NH_2	A	$PhCH_2NHPh$	100	100
17.	4Br–C_6H_4–CHO + Ph–NH_2	A	4Br–$_6H_4CH_2NHPh$	75	100
18.	4Br–C_6H_4–CHO + $PhCH_2NH$	A	4Br–$C_6H_4CH_2$ $NHCH_2Ph$	70	100

[a]Substrate 2.00 mmol, Cat A-(NiB–SiO_2) 200 mg, $NaBH_4$ 200 mg, MeOH 10 ml, (0–5 °C), 10–15 min, Cat B-(Pd-MCM-41) 25 mg, THF 10 ml, RT, H_2 3–5 h

21.3 Experimental Section

21.3.1 Materials and Methods

All chemicals, dichlorobis(benzylcyano)palladium(II), tetraethyl orthosilicate (TEOS), hexadodecyl amine, 2-propanol, nickel nitrate and silica gel particle size 63–200 μm, 70–230 mesh, pore size 100 Å, were obtained from Fluka.

21.3.2 Preparation of Ni–SiO_2 (Cat A)

The catalyst was prepared by impregnation method by dissolving nickel nitrate nonahydrate (2.5 g) in distilled water (20.0 ml) and adding to it silica gel (5.0 g), stirring for 2 h using a magnetic stirrer at room temperature (20–22 °C) and ageing at room temperature overnight. The excess water is removed by heating the mixture on a water bath and using a rotavapor under mild vacuum to evaporate the water. The catalyst material is dried in an oven at 100 °C for 12 h [11].

21.3.3 Typical Reduction Procedure Using Cat A

To a solution of nitrobenzene (2.0 mmol) in 10 ml methanol, catalyst (200 mg) was added followed by slow addition of sodium borohydride (200 mg) at 0 °C for 5 min. The reaction mixture was magnetically stirred continuously for 10 min during which all starting material was consumed. The reaction progress was monitored by TLC. The reaction mixture was quenched with deionized water and extracted with ethyl acetate. The organic layer was dried with sodium sulfate and the solvent was evaporated on a rotavapor to give crude aniline which was then subjected to column chromatography to afford pure aniline product. The final product was characterized by ^{1}H and ^{13}C NMR spectroscopy using a 400 MHz Bruker instrument. GC–MS samples were run on an Agilent 6890 GC/5973, MS column: J & W HP5-MS. GC results were obtained on a GC System 6820, Agilent Technologies equipped with flame ionization detection (FID) and a carbowax OVI capillary column and compared with standard sample.

21.3.4 Preparation of Pd(II)-MCM-41 (Cat B)

The mesoporous material MCM-41 (pure silica) was synthesized as described below using a reported procedure [17]. First a solution was prepared by mixing 1 mmol of TEOS with 6 mol of ethanol and 1 mol of isopropanol. At the same time a second solution was obtained by mixing hexadecylamine (0.3 mol) in water (36 mol). The two solutions were then mixed under stirring at room temperature for about 1 h. The product obtained was aged at 25 °C for 12 h under static conditions. The resulting solid was recovered by centrifugation, washed with distilled water 8–10 times and filtered. Finally, the synthesized sample was air dried at room temperature for 24 h. One gram of MCM-41 was calcined at 550 °C overnight and refluxed with 0.686 mmol of 3-triethoxypropylamine in dry toluene in inert atmosphere for 48 h. This was then complexed with dichlorobis (benzylcyano) palladium(II) in dry benzene under stirring at room temperature. The bright yellow coloured complex obtained was then filtered, soxhlet extracted with benzene for 8 h, filtered, washed with benzene and dried under vacuum to afford the final required catalyst.

21.3.5 Typical Reduction Procedure Using Cat B

Pd(II)-MCM-41 catalyst (25 mg) was added to a solution of nitrobenzene (2.0 mmol) in 10 ml THF. The resulting solution was magnetically stirred in the presence of a hydrogen balloon attached to the round bottom flask at room temperature and monitored by TLC, till the starting material was consumed. Then the

reaction mixture was filtered and the solvent was evaporated on a rotavapor to give crude product aniline which was then subjected to column chromatography to afford pure aniline product. The final product was characterized by ^{1}H and ^{13}C NMR spectroscopy using a JEOL Eclipse 270 NMR spectrometer ($\delta C = 146.6$, 129.3, 118.4 and 115.1 ppm and $\delta H = 7.1$, 6.7, 6.6 and 3.6 ppm). GC–MS samples were run on an Agilent 6890 GC/5973, MS column: J&W HP5-MS and compared with standard sample.

21.3.6 Characterization of Catalysts

Ni silica catalysts were characterized by the following techniques: XRD, BET, IR spectroscopy, SEM, UV DRS, and chemisorption.

21.4 Results and Discussion

Aromatic compounds with functional groups are key intermediates for the manufacture of dye stuff, pharmaceutical, agricultural, photographic chemicals, additives, surfactants, textiles auxiliaries, chelating agents and polymers [1–3] in chemical industries. The benefits of simple preparation, low cost, ease of handling and the efficiency of anchored palladium complexes in selective organic transformations, prompted us to explore the possibility of their use in the reduction of nitro aromatics, azides and in hydrodehalogenation reactions. Pd(II)-MCM-41 (Cat B) exhibited encouraging results for the reduction of nitro aromatics, aldehydes, ketones, azides and for hydrodehalogenation reactions of chlorobenzene, bromobenzene, 3-chlorotoluene at room temperature with excellent conversions and selectivity. The catalyst showed 3 cycles of reusability and no leaching of catalysts was observed. Nickel silicates with layered structure are well known as phyllosilicates, hydro silicates, or surface silicates. The authors prepared the catalysts Ni–SiO_2 (Cat A) by simple impregnation method. Fine amorphous powders of Ni–SiO_2 (Cat A) were obtained showing that Ni particles are well distributed over the silica surface which is confirmed by XRD characterization technique. Selective oxidation of alcohols is an important transformation from industry point of view [1, 2]. The authors reported previously the use of 10% Ni–SiO_2 (Cat A) for the oxidation of *p*-nitrobenzyl alcohol to *p*-nitrobenzaldehyde in the presence of hydrogen peroxide and the controlled oxidation of benzhydrol to benzophenone with excellent conversion and selectivity [9, 12, 13]. When $NaBH_4$ is added to nickel silica catalysts at 0–5 °C, a black precipitate is formed with the spontaneous evolution of hydrogen which indicates that NiB species are generated in situ and behave as superactive catalysts for reduction reaction of bromobenzene, benzaldehyde, phenol, styrene, toluene, and for reductive amination of aldehydes and ketones as shown in Table 21.1 for some of the reactions.

The authors have reported the use of catalyst Ni–SiO_2 (Cat A) in a number of reactions including Knoevenagel condensation in liquid phase. All the Knoevenagel reactions resulted in 100% selectivity but the conversions differed with varying amounts of catalysts, with 10% Ni–SiO_2 (Cat A) proving to be the superior catalyst. The catalytic activity of 10% Ni–SiO_2 (Cat A) towards Knoevenagel reaction of 4-hydroxy benzaldehyde and malononitrile and ethyl cyanoacetate with substituted benzaldehydes were investigated and were found to be effective. All the Ni-supported catalysts were characterized by XRD, IR, BET, SEM instruments, and chemisorption studies. Ni silica catalysts of all samples showed particle size in the range of 20–250 Å and the moisture content observed was 7% [12].

The characterized catalysts showed better results compared with the literature reported catalysts [8, 9]. Extension of this work is being carried out with different borohydrides in order to evaluate the best catalytic system. A model reaction was tested for leaching of Ni metal from Ni–SiO_2 (Cat A). The filtrate was subjected to reduction reactions with model substrate under the same conditions and it was observed that the reaction did not occur. This indicates that the Ni metal was intact on the surface of the silica support which is confirmed by IR studies showing that nickel silica are heterogeneous catalysts [14].

21.4.1 X-Ray Diffraction

The XRD studies on the Ni silica (Cat A) were carried out on a Phillips-PW 1830 powder X-ray diffraction instrument. The XRD spectra (Fig. 21.1) showed the characteristic bands of the nickel phase and support, but no mixed nickel oxide support phases were identified. The pattern for the supports was that of crystallized

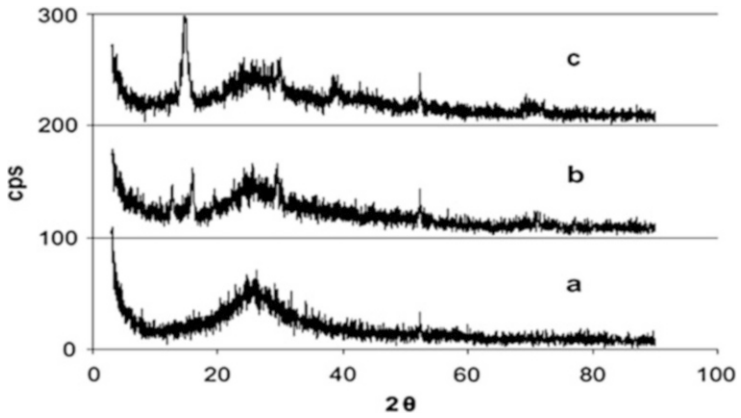

Fig. 21.1 XRD pattern of (**a**) 5% Ni–SiO_2 (**b**) 10% Ni–SiO_2 (**c**) 15% Ni–SiO_2

materials with well-defined bands except for the amorphous structure, as only one broad peak around $2\theta = 25^{\circ}$ appeared, which is characteristic of silica [8, 9, 11].

21.4.2 UV Visible Spectroscopy

Spectra of the supported materials, after initial drying, but before calcination and reduction, were measured by diffuse reflectance uv spectroscopy and their absorption maxima and assignments are recorded. Ni–SiO_2 of all percentages showed a band in the range of 740 nm^{-1} while nickel nitrate aqueous solution and nickel nitrate showed respectively UV bands in the range of 728 and 707 nm^{-1}.

21.4.3 BET Surface Area

BET surface area analysis of 10% Ni-silica (Cat A) was carried out using the Brunauer–Emmett–Teller equation. As a higher catalytic activity was observed with 10% Ni–SiO_2 (Cat A) the surface area of only 10% Ni–SiO_2 was estimated and was found to be 180 m^2g^{-1}.

21.4.4 Dispersion of Ni on Silica Surface

The gels with macropores have micro- and mesopores and show a high specific surface area. Thus, Ni–SiO_2 with a distinct aggregated structure was prepared in this work. Incidentally, the wet gel contains nickel as a cation dissolved in the solvent phase. The solvent phase can move relatively fast in the wet silica gel, and aggregation of the nickel salt easily occurs during drying even in the gel without macropores [8]. In the gel with hierarchical pores, therefore, inhomogeneous aggregation probably occurs in the macropores during drying. In order to prepare a catalyst with high activity, it is necessary to disperse the nickel species only in the silica gel skeleton. For the sample prepared by impregnation on silica gel, diffraction peaks of NiO were observed. The SEM-EDX result clearly shows that the aggregation of large NiO particles occurs in the macropores. Because of sintering, the NiO aggregates grow in the large spaces during calcination at 500 °C especially for the sample with high NiO loading. The NiO aggregates in the macropores are easily reduced to large Ni particles. Despite the inhomogeneity of the Ni dispersion in the samples, they show relatively high Ni surface areas. As suggested from the XRD results, a part of the Ni in the samples is trapped in the mesopore of the gel skeleton, which cannot grow during heating and reduction due to the pore walls of the silica. The small Ni particles probably contribute to the high Ni surface area. Dispersion of the Ni species in both CG and SE samples without macropores can be

regarded as standard in the nickel/silica prepared by the usual sol-gel process. In the samples, aggregation of Ni occurs during drying to become a crystal of nickel nitrate salt [15]. A wet silica gel prepared under acidic conditions consists of a polymeric network rather than particle aggregates. Therefore, the aggregation of the nickel nitrate salt can proceed even in the mesoscale space during drying. The NiO particle size agrees well with the correlation length of the wet silica gel, typically of the order of 10 nm [11, 12, 16].

21.4.5 SEM Characterization

The morphology and location of metallic species on the surface of the catalyst were examined by scanning electron microscopy (SEM) using a JEOL JSM-6100 microscope equipped with an energy-dispersive X-ray analyzer (EDX). Images were taken with an emission current of 100 μA by a tungsten filament and an accelerator voltage of 12 kV. The SEM figures of 5 and 10% Ni loaded silica and morphology (Fig. 21.2) depicted that crystalline Ni of 2–4 μm are well distributed over the silica surface and Fig. 21.2d showed the scans of 15% Ni loaded silica, which indicates that the distribution of Ni on support is either in conglomerates or in layers, thus hindering the participation of both Ni and silica at active sites in the reaction. SiO_2 or Ni^{2+} individually had no catalytic effect on the reaction. The observed reactivity

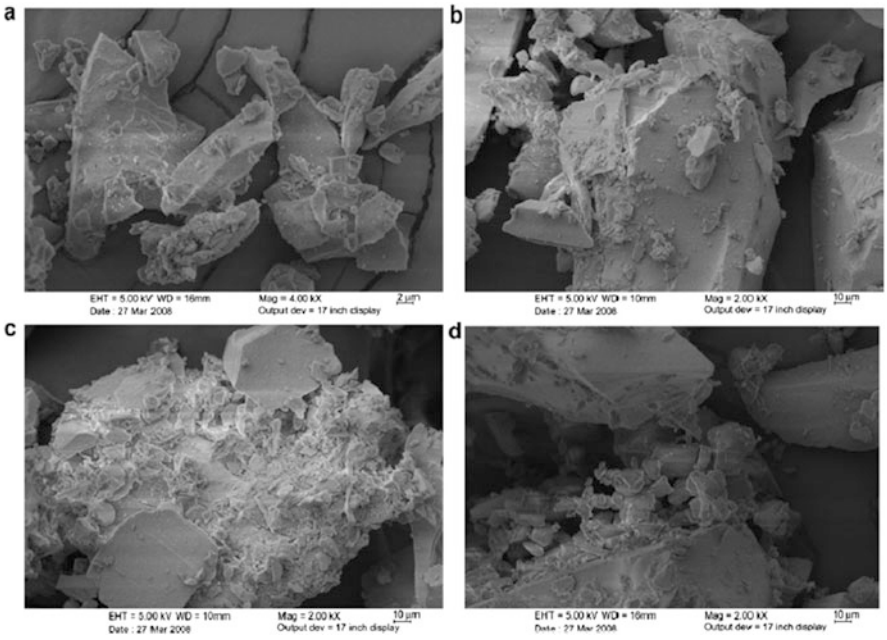

Fig. 21.2 SEM images of (**a**) 5% Ni–SiO_2 (**b**) 10% Ni–SiO_2 (**c**) and (**d**) 15% Ni–SiO_2

of Ni supported on silica material can be possibly attributed to the metal and support interactions, and the resultant changes in surface properties of the reactive sites. Earlier studies by Urbano et al. [15] have revealed that supported Ni catalysts prepared with $Ni(NO_3)_2$ by impregnation exhibit wide size distribution in contrast to those prepared by more controlled deposition and precipitation method route which generate low metallic Ni particles. The low metallic surface of nickel on the silica support encourages the formation of nickel oxide crystals. The presence of weak interaction between the metal and support, due to little distribution of Ni entailing the formation of the layer of impregnated Ni, probably contributed to the increase of catalytic activity [16–18]. The observed non-reactivity with 15% Ni loaded material, could be possibly due to the multilayer of Ni loading on the support resulting in loss of activity as suggested by Blanco et al. [14]. This is also supported by the SEM analysis of the different amounts of Ni loaded silica in the current study. An examination of SEM results (Fig. 21.2) suggest that the Ni particles are well distributed in 5 and 10% Ni loaded material with fine particles but the 15% loaded material shows Ni multilayers and conglomeration of Ni particles on the silica surface.

21.4.6 FT-IR Spectroscopy of Ni–SiO_2 (Cat A)

As the results of both 10 and 5% Ni–SiO_2 were similar, only the 10% Ni–SiO_2 (Cat A) results are discussed. The examination of IR spectra of 5 and 10% Ni loaded SiO_2 showed band at 1100 cm^{-1} (asymmetrical Si–O–Si) due to formation of silicates [12]. The vibrational stretching frequency of the hydrogen atom in the hydroxide catalysts, 5 and 10% Ni–SiO_2 (Cat A) appears at 3422 cm^{-1} indicating it has ordered cation distribution [14–16]. In the IR results of 10% Ni–SiO_2, the strong and intense absorption band between 1078 and 1050 cm^{-1} showed the presence of Si–O–Ni bonds. This Ni active species in association with silica is responsible for the activation of sodium borohydride with the evolution of hydrogen with immediate formation of nickel boride species. These results conclusively demonstrate that 10% Ni-silica catalyst is ideally suited for selective nickel boride silica initiated reduction of nitro aromatics to aromatic amines with good conversion and high selectivity [11, 12].

21.4.7 FT-IR Spectroscopy of Pd(II)-MCM-41 (Cat B)

The IR spectra of the ligand and the complex showed silylpropyl amine bands. The complex showed an additional band at 356 cm^{-1} indicating the presence of terminal Pd-Cl [12]. Pd content of the catalysts was determined by plasma analysis (1.99%).

21.4.8 Chemisorption of Ni Silica Catalysts

The absence of carbon monoxide adsorption when helium was used as the carrier was amazing in the light of the TPR experiments and a range of other physical techniques which indicated the presence of nickel metal. Catalysts were reduced in dihydrogen/dinitrogen conditions. The samples were heated to 723 K well above the maximum rate of hydrogen abstraction observed and the catalysts were held at this temperature until no further hydrogen uptake was observed. The reason for the absence of carbon monoxide adsorptive capacity was confirmed as the carbon dioxide chemisorption was due to the presence of surface oxygen [11, 12]. These results suggest that the removal of monolayer and sub-monolayer levels of oxygen from nickel catalysts is kinetically slow and that in the absence of a reducing atmosphere will block the surface to carbon monoxide adsorption. Interestingly the use of di-hydrogen as a carrier gas was sufficient to allow adsorption of carbon monoxide. No evidence was obtained to suggest that the di-hydrogen removed the surface oxygen at 298 K. Two explanations can be advanced although neither is entirely acceptable. If the oxygen was randomly distributed over the surface under helium and the action of di-hydrogen was to cause agglomeration into islands then a significant proportion of the adsorptive capacity could be reclaimed. Alternatively if the surface oxygen was to diffuse into the bulk or be re-dispersed throughout the crystallite, then adsorptive capacity would also be regained.

21.5 Conclusions

Ni–B–SiO_2 (Cat A) are found to be super active catalysts compared to Pd(II)-MCM-41 (Cat B) for reduction reactions. Various functional groups attached to aromatic substrates were reduced with Ni B silica (Cat A) where nickel boride species are formed *in situ* when Ni is reacted with $NaBH_4$ for reduction of aromatic substrates at low temperature with high conversion, and 100% selectivity. Characterization of Ni–SiO_2 catalyst by XRD, FT-IR, UV diffusion, SEM, chemisorption studies, particle size and moisture content, confirms the crystallinity of nickel incorporated on silica. 15% nickel on silica is found to be inactive for reduction reactions from XRD and SEM studies which confirm that excess nickel reduces the activity of the catalysts. A variety of functional groups attached to aromatics such as *p*-nitrophenol, nitrobenzene, benzaldehyde, benzene, bromobenzene, phenol, 4-bromobenzaldehyde are reduced at 0–5 °C by 5 and 10% Ni–SiO_2 to their respective products with maximum conversion and 100% selectivity while Pd(II)-MCM-41 (Cat B) reduces nitro aromatics at room temperature and aromatic alkyl halides, 4-bromobenzaldehyde, aromatic substituted azides such as benzyl azide to corresponding amines. The characterization of 5 and 10% Ni–SiO_2 (Cat A) and the results demonstrate that they are super active catalysts compared to Pd(II)-MCM-41 (Cat B) for reduction reactions, in terms of reusability, atom economy,

environmentally friendly and applicability for large scale reactions which excludes harsh reaction conditions and use of additives.

Acknowledgement This study was supported by the Environmental Investment Fund (EIF) of Namibia: Matching fund subsidy from National Commission on Research Science and Technology (NCRST) for strengthening capacity at universities and research institution in Namibia.

References

1. Sheldon RA (1996) Selective catalytic synthesis of fine chemicals: opportunities and trends. J Mol Catal A 107:75–83
2. Kresge CT, Leonowicz ME, Roth JW, Vartuli JC, Beck JS (1992) Ordered mesoporous molecular sieves synthesized by a liquid crystal template mechanism. Nature 359:710–712
3. Beck JS, Vartuli JC, Roth WJ, Leonowicz ME, Kresge CT, Schmitt KD, Chu CT-W, Olson DH, Sheppard EW, McCullen SB, Higgins JB, Schlenker JL (1992) A new family of mesoporous molecular sieves prepared with liquid crystal templates. J Am Chem Soc 114:10834–10843
4. Vartuli JC, Degnan TF Jr (2007) Applications of mesoporous molecular sieves in catalysis and separations. Stud Surf Sci Catal 168:837–854
5. Pinnavaia TJ (1983) Intercalated clay catalysts. Science 220:365–371
6. Arnold H, Dobert F, Gaube J, Ertl G, Knozinger H, Weitkempl J (eds) (1997) Handbook of heterogeneous catalysis, vol 5. Wiley, New York, pp 2165–2184
7. Blaser HU, Siegrist U, Steiner H, Studer M, Sheldon RA, van Bekkum H (eds) (2001) Fine chemicals through heterogeneous catalysis. Wiley, New York, pp 389–394
8. Saadi A, Merabti R, Rassoul Z, Bettahar MM (2006) Benzaldehyde hydrogenation over supported nickel catalysts. J Mol Catal A 253:79–85
9. Kockritz A, Sebek M, Dittmar A, Radnik J, Bruckner A, Bentrup U, Pohl M, Hugl H, Magerlein W (2006) Ru catalyzed oxidation of primary alcohols. J Mol Cat A 246:85–99
10. Bonelli B, Cozzolino M, Tesser R, Serio Di M, Piumrtti M, Garrone E, Santacesaria E (2007) Study of the surface acidity of TiO_2/SiO_2 catalysts by means of FTIR measurements of CO and NH_3 adsorption. J Catal 246:293–300
11. Ferreira-Aparicio P, Rodriguez-Ramos I, Anderson JA, Guerrero-Ruiz A (2000) Mechanistic aspects of the dry reforming of methane over ruthenium catalysts. Appl Catal 202:183–196
12. Khodadadi B (2016) Nickel doping effect on the photo catalytic activity of TiO_2/SiO_2 nanocomposite. Bulg Chem Commun 48:238–243
13. Mobley JK, Crocker M (2015) Catalytic oxidation of alcohols to carbonyl compounds over hydrotalcite and hydrotalcite-supported catalysts. RSC Adv 5:65780–65797
14. Blanco PH, Wu C, Williams PT (2014) Influence of Ni/SiO_2 catalyst preparation methods on hydrogen production from the pyrolysis/reforming of refuse derived fuel. Int J Hydrogen Energy 39:5723–5732
15. Urbano FJ, Marinas JM (2001) Hydrogenolysis of organohalogen compounds over palladium supported catalysts. J Mol Catal A 173:329–345
16. Ermakova MA, Ermakov DY (2002) Ni/SiO_2 and Fe/SiO_2 catalysts for production of hydrogen and filamentous carbon via methane decomposition. Catal Today 77:225–235
17. Komiya S, Sone T, Usui Y, Hirano M, Fukuoka A (1996) Condensation reactions of benzaldehyde catalysed by gold alkoxides. Gold Bull 29:131–136
18. Solymosi F (1991) The bonding, structure and reactions of CO_2 adsorbed on clean and promoted metal surfaces. J Mol Catal 65:337–358

Chapter 22
Antidiabetic Potential of *Erythrina abyssinica* via Protein Tyrosine Phosphate 1B Inhibitory Activity

Derek Tantoh Ndinteh

Abstract *Erythrina abyssinica* is one of over 100 species that belongs to the genus *Erythrina* and that is widely used in traditional medicine. It is used in the treatment of various ailments, one of which is the management and treatment of type 2 diabetes. The increasing prevalence of diabetes worldwide and especially in Africa has become a serious public health concern. The need to develop novel therapies with mechanisms of action that are mimetic of the insulin-signaling pathway is necessary in face of the high rates of secondary failure and side effects of existing therapies. One of these potential targets that has emerged is protein tyrosine phosphate 1B, which recently was identified as a major negative regulator in the insulin-signaling pathway. Cohort studies showed reduced risk of type 2 diabetes associated with high intakes of dietary flavonoids. In this study, we described the isolation and protein tyrosine phosphate inhibitory activity of various flavonoids from *Erythrina abyssinica*. Sixty-eight flavonoids were identified and 43 were found to inhibit protein tyrosine phosphate 1B in a dose dependent manner, with inhibition values ranging from 4.2 to 40 μM.

Keywords *Erythrina abyssinica* • Flavonoids • PTP1B • Diabetes

22.1 Introduction

There is an increasing prevalence of diabetes in the world and it has become a serious public health challenge worldwide and even more so in Africa [1]. It is possibly one of the fastest growing diseases in the world today which is characterized mainly by cellular resistance to insulin mediated disposal of glucose or impaired insulin production [2]. The reduction in mortality from infectious condi-

D.T. Ndinteh (✉)
Drug Discovery, Complementary and Alternative Medicine Group, Department of Applied Chemistry, Faculty of Sciences, University of Johannesburg, P.O. Box 17011, Johannesburg 2028, South Africa
e-mail: dndinteh@uj.ac.za

P. Ramasami et al. (eds.), *Emerging Trends in Chemical Sciences*,
DOI 10.1007/978-3-319-60408-4_22

tions coupled to changes in lifestyle are some of the main contributors to making type 2 diabetes a considerable public health priority. From a global perspective, statistics from 2013 indicate that over 382 million people had this disease worldwide with type 2 diabetes making up most of the cases [3]. Predictions say that by the year 2035 about 592 million people will die of diabetes. The economic costs (direct medical costs, labor days lost, short term morbidity, etc.) of diabetes seem to be on the increase worldwide [4]. Added to this is the plethora of severe secondary conditions that arise from diabetes like diabetic retinopathy, severe renal malfunction and/or failure and of course ocular effects. Scientific evaluation of traditional herbal remedies for diabetes is becoming important in current strategies to manage and control the pathological aspects of diabetes. This is made necessary by the concomitant high costs and poor availability of current therapies for many rural populations. More so, significant sections of world populations rely either partially or entirely on herbal medicine to address their healthcare needs due to a number of factors, like cost, availability of treatment, etc. Alternative and complementary strategies for the management, prevention and treatment of diabetes are a necessity especially in Africa. The African traditional pharmacopeia has many plants that are used in the treatment of symptoms associated with the occurrence of diabetes. Plants of the genus Erythrina are heavily used in traditional pharmacopeia around the world [5].

Erythrina abyssinica is one of the 100 and more species that belongs to the genus Erythrina. It is widely distributed in tropical and subtropical regions worldwide [6]. It is used in traditional East African medicine for the management and treatment of type 2 diabetes [7]. It is also used in various traditional medicine systems for the treatment of malaria, syphilis [8–10], microbial infections [10, 11], pneumonia, prostate cancer, sexually transmitted diseases [12], trachoma and elephantiasis [13], anthrax [14], ear, nose and throat infections [15], diarrhea [16], eye inflammation and general body swelling [14]. The bark and roots are a source in local communities for useful dyes. The seeds are used to decorate trinkets, bracelets and necklaces and the tree is a popular option to counteract soil loss, erosion and for soil conservation terraces. More so, its leaf fall in the dry season is a rich source of mulch [14]. Erythrina species have been shown to be very rich in flavonoids. Numerous studies have exemplified novel bioactive flavonoids from various Erythrina species [17–20]. Flavonoids have been shown to have a wide variety of bioactive properties and have been useful in the management of a number of various health conditions [21, 22].

Flavonoids are a group of naturally occurring polyphenol heterocycles, which are found to occur widely in the plant kingdom across different genera. They are classified into about 13 groups, some of which are flavanols, flavanones, chalcones, isoflavanols, pterocarpans, coumestans, aurones, bioflavonoids, etc. Cohort studies carried out showed a trend that indicates that the consumption of dietary flavonoids was associated with reduced risk of type 2 diabetes [21]. *Erythrina abyssinica* has been shown in many studies to be very rich in flavonoid content [10, 23].

At present in the management of type 2 diabetes there are about eight hypoglycaemic drugs in use administered via oral routes and these can be classified based on their mechanisms of action [24]. These can either be amylin analogues, insulin secretagogues, glucan-like peptide 1 receptor antagonists, thiazolidinediones, α-glucosidase inhibitors, dipeptyl peptidase-4 inhibitors, biguanidines and sodium-glucose cotransporter-2 inhibitors. In spite of the relative availability of hypoglycaemic entities for the management of diabetes, there are still a number of severe limitations that are associated with the management of type 2 diabetes. Some of these are high rates of secondary failure, adverse side effects such as peripheral oedema, hypotension, etc. One of the major causes of the failure is due to the fact that most of these mechanisms of action are not mimetic of the insulin signaling pathway. Thus it is necessary to focus effort on investigating drugs that mimic insulin signaling preferentially. Of the various potential drug targets for the treatment of type 2 diabetes, protein tyrosine phosphate-1B (PTP1B) has recently emerged as a major negative regulator in the insulin signaling pathway [24–27]. This implies that finding novel entities that are PTP1B inhibitors might provide an efficient means of reducing blood sugar levels while mitigating side effects associated with present therapies. Plants extracts are rich sources of novel active and safer drugs for the treatment of diabetes [28]. Previous reports indicate that there are more than 1000 plants species being used to treat type 2 diabetes all over the world [29] and various natural compounds display PTP1B inhibitory activity [30].

On screening extracts from *Erythrina abyssinica*, we found that various organic extracts of the stem bark inhibited PTP1B activity up to 80% at concentrations as low as 30 μg/mL. This prompted further investigation on *Erythrina abyssinica* in the search for potential PTP1B inhibitors. We isolated a number of flavonoids out of this plant, some of which displayed inhibitory activity against PTP1B [31, 32]. This article is a summary of the flavonoids isolated and characterized from *Erythrina abyssinica* and which were found to have PTP1B inhibiting activity. This article discusses the PTP1B inhibitory effects of these compounds and the possible structure activity relationship.

22.2 Isolation

E. abyssinica stem bark was harvested in June 2005 in Mukono, Uganda. Voucher specimen (No. 0001) was deposited at the Department of Botany, Makerere University, Uganda after being authenticated by Prof. John Silike-Muruumu. The dried stem bark (5 kg) was extracted with methanol (MeOH). After removal of the solvent under reduced pressure, the crude extract was suspended in water and partitioned with n-hexane, ethyl acetate (EtOAc) and n-butanol (nBuOH) consecutively. The EtOAc-soluble fraction was found to be the most active (50% inhibition at 30 μg/mL) among the solvent fractions. The EtOAc extract of *E. abyssinica* was then subjected to a succession of chromatographic procedures such as silica gel

chromatography and high-pressure liquid chromatography (HPLC). In the course of this study, 68 compounds were extracted from *Erythrina abyssinica*. They belonged to the flavonoid class of compounds and consisted of flavanones, chalcones, pterocarpans and deoxyflavanones.

22.2.1 Flavanones

The dietary intake of flavanones in various studies has been shown to have significant effect in reducing the risk of developing diabetes or mitigating the severity of the disease in various patients. The anti-diabetic activity of flavonoids in general and flavanones seems to occur via a series of mechanisms. The hypothesized link between inflammation and diabetes, the demonstrated anti-oxidant properties of flavanones coupled to cohort studies and dietary surveys have shown the anti-diabetic potency of flavanones [33]. Thirty four flavanones were isolated and identified from the stem bark of *Erythrina abyssinica* [31, 32, 34] and are depicted in Fig. 22.1. They were tested for their inhibitory activity against PTP1B using a repeat assay and the results are presented in Table 22.1.

Except for compounds **1, 8**, **12**, **14**, **17**, **20–24**, **30** and **31**, all the other compounds inhibited PTP1B dose-dependently. The recorded IC_{50} values ranged between 13.9 $\pm$ 2.1 and 26.7 $\pm$ 1.2 μM where **11** was the most active compound and **9** was the least active. The controls used were ursolic acid and RK-682 (a potent, selective and competitive inhibitor of PTP). Most of the compounds had the 5,7-dihydroflavanone skeleton and the major differences came from the substitution patterns in the B ring. All of the compounds which inhibited PTP1B in a non-dose dependent manner have a fused 2,2-dimethylpyran moiety on the B ring and do not possess a free prenyl group in their structure. Comparing structurally close compounds, **11** showed a higher activity than that of **8** and **12**. Compounds **15** and **18** showed higher activity than **17** and **20–22**, and compounds **27**, **28** and **32** showed a better activity than **30** and **31**. The significant structural difference seems to be the presence or absence of a free prenyl (not fused) indicating that the presence of a prenyl group into the B ring may be responsible for better biological activity. Compounds **10**, **13**, **16** and **29** where the prenyl group is absent, have relatively good activity, suggesting that the presence of a methoxy group at the 5′ or 3′ position may be also important for PTP1B inhibitory activity. The presence of hydrophobic moieties (methoxy or prenyl residues) on the B ring seems to increase the inhibitory effects of the flavanones against PTP1B, while the presence of hydrophilic moieties (hydroxyl groups) does not seem to affect this particular biological activity.

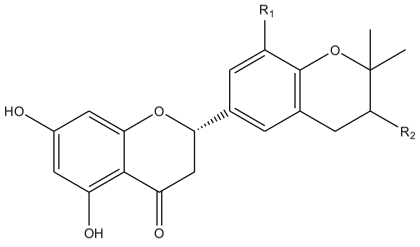

1 R_1 = H, R_2 = H
Abyssinoflavanone V
8 R_1 = OH, R_2 = H
Sigmoidin C
10 R_1 = OCH_3, R_2 = H
Abyssinin I
23 R_1 = OH, R_2 = OH
Sigmoidin D

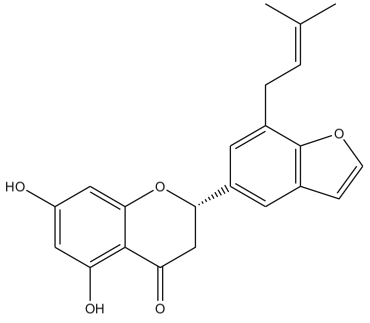

2 Abyssinoflavanone VI

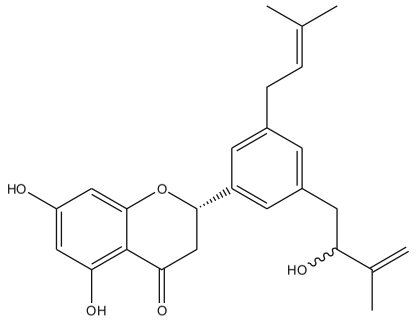

3 Abyssinoflavanone VII

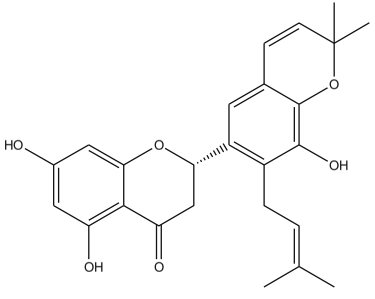

4 Sigmoidin F

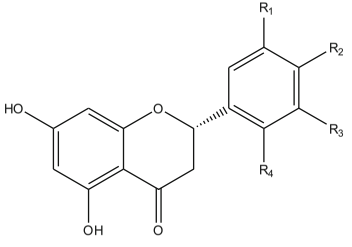

5 R_1 = prenyl, R_2 = R_3 = OH, R_4 = H
Sigmoidin B
6 R_1 = OCH_3, R_2 = OH, R_3 = prenyl, R_4 = H
Abyssinin II
7 R_1 = R_4 =1"-prenyl, R_2 = R_3= OH
Sigmoidin A
9 R_1= prenyl, R_2 = OH, R_3 = R_4 = H
3'-prenylnarringenin

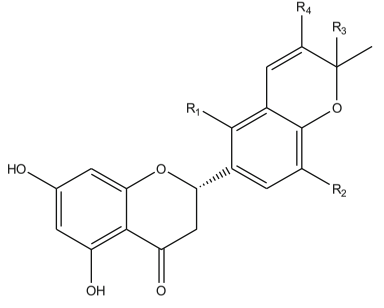

11 R_1 = prenyl, R_2 = OH, R_3 = CH_3, R_4 = H
12 R_1 = H, R_2 = OH, R_3 = CH_2OH, R_4 = H
13 R_1 = H, R_2 = OCH_3, R_3 = CH_2OH, R_4 = OH
24 R_1 = H, R_2 = OH, R_3 = CH_3, R_4 = OH
Sigmoidin G

Fig. 22.1 Structures of flavanones from *E. abyssinica*

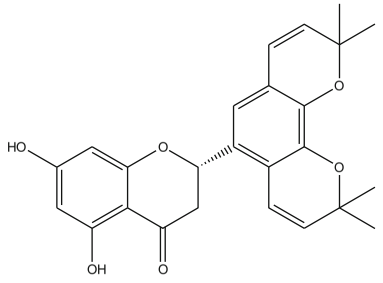

14

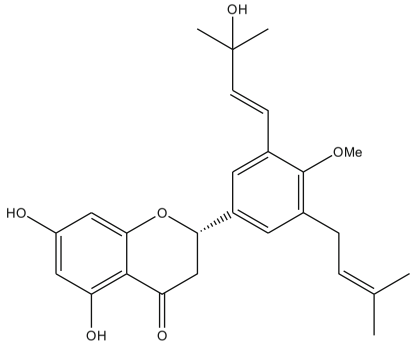

25 Burtinone hydrate

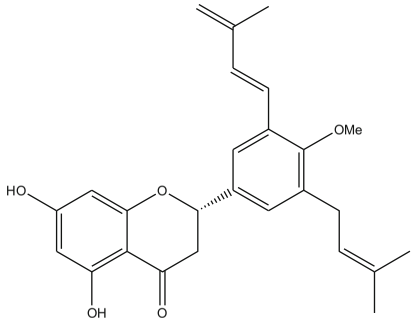

26 Burtinone

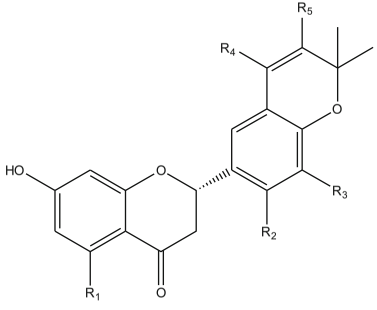

15 $R_1 = R_5 = OH$, $R_2 = R_4 = H$, $R_3 =$ prenyl
16 $R_1 = R_5 = OH$, $R_2 = R_4 = H$, $R_3 = OCH_3$
17 $R_1 = R_4 = R_5 = OH$, $R_2 = R_3 = H$
18 $R_1 = R_4 = R_5 = OH$, $R_2 = H$, $R_3 =$ prenyl
19 $R_1 = R_4 = R_5 = OH$, $R_2 =$ prenyl, $R_3 = OH$
20 $R_1 = R_3 = OH$, $R_2 = R_5 = H$, $R_4 = (=O)$
21 $R_1 = R_2 = R_4 = H$, $R_3 = R_5 = OH$
22 $R_1 = R_2 = H$, $R_3 = R_4 = R_5 = OH$

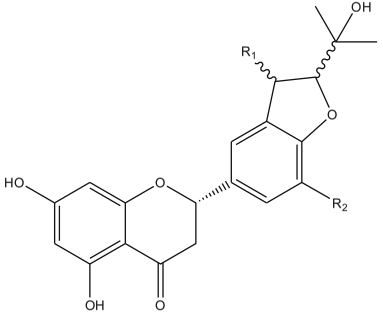

27 $R_1 = H$, $R_2 =$ prenyl
28 $R_2 = OH$, $R_2 =$ prenyl
29 $R_1 = H$, $R_2 = OCH_3$
30 $R_1 = H$, $R_2 = OH$
31 $R_1 = OH$, $R_2 = OH$
32 $R_1 = OH$, $R_2 =$ prenyl

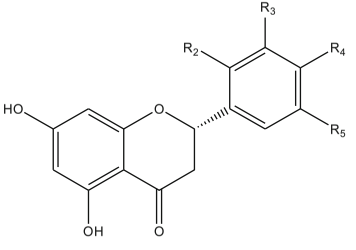

33 $R_1 = R_2 = H$, $R_3 = OH$, $R_4 = OCH_3$, $R_5 =$ prenyl
34 $R_1 = R_4 = R_5 = OH$, $R_2 = R_3 =$p renyl

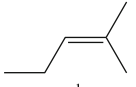

prenyl group

Fig. 22.1 (continued)

Table 22.1 PTP1B inhibitory activity of flavanones from *E. abyssinica*

Compound	PTP1B inhibitory activity (μM)
1[a]	>40
8[a]	>40
12[a]	>40
14[a]	>40
17[a]	>40
20[a]	>40
21[a]	>40
22[a]	>40
23[a]	>40
24[a]	>40
30[a]	>40
31[a]	>40
11	13.9 ± 2.1
4	14.2 ± 1.7
7	14.4 ± 0.8
15	14.9 ± 1.6
27	15.2 ± 1.2
3	15.7 ± 0.4
29	16.1 ± 1.1
33	16.2 ± 1.1
6	17.3 ± 1.4
13	17.9 ± 1.7
28	17.9 ± 2.6
19	18.2 ± 1.2
10	18.2 ± 1.4
16	18.2 ± 2.1
32	18.3 ± 1.6
25	18.9 ± 1.3
2	18.9 ± 1.9
18	19.0 ± 1.8
5	19.4 ± 2.3
34	19.6 ± 2.3
26	21.6 ± 2.1
9	26.7 ± 1.2
Ursolic acid	3.6 ± 0.2
RK-682	4.7 ± 0.5

[a]Insignificant activity

22.2.2 Chalcones

Chalcones have been shown to have some biological activities, including anti-cancer, anti-malarial, anti-microbial, anti-inflammatory, anti-protozoal [35].

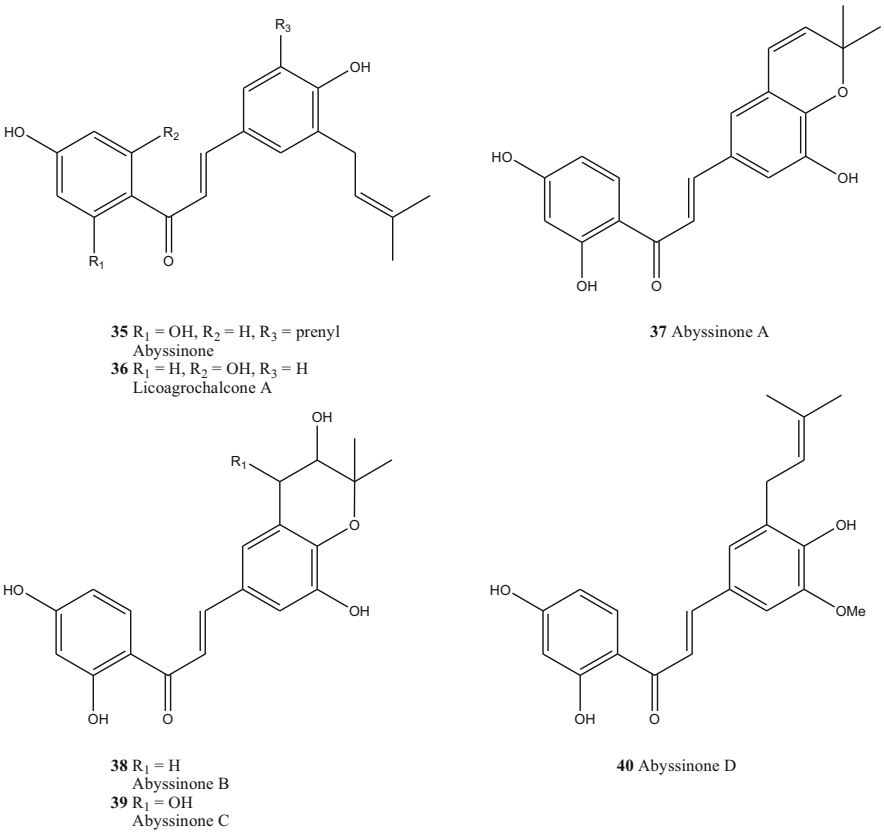

35 R_1 = OH, R_2 = H, R_3 = prenyl
Abyssinone
36 R_1 = H, R_2 = OH, R_3 = H
Licoagrochalcone A

37 Abyssinone A

38 R_1 = H
Abyssinone B
39 R_1 = OH
Abyssinone C

40 Abyssinone D

Fig. 22.2 Structures of chalcones from *E. abyssinica*

Table 22.2 Inhibitory effects of chalcones from *E. abyssinica*

Compound	Inhibitory activity(μM)
35	20.6 ± 2.1
36	16.9 ± 0.7

Six chalcones (**35**–**40**) shown in Fig. 22.2 were isolated from the stem bark of *Erythrina abyssinica*. All were assayed for their inhibitory activity against PTP1B using RK-682 and ursolic acid as positive controls [36]. Only two prenylated chalcones, namely **35** and **36** were found to be active (Table 22.2). The activity seems again to be associated with the presence of a free prenyl on the ring B of the chalcone. Based on the activity profiles, compound **40** (Abyssinone D) should have shown activity. The absence of activity observed was attributed to human error at this stage and not to any significant scientific factor. Although we observe the presence of two prenyl groups in structure **35**, it is less inhibitory than compound **36**, which suggests that the presence of one prenyl group is favored.

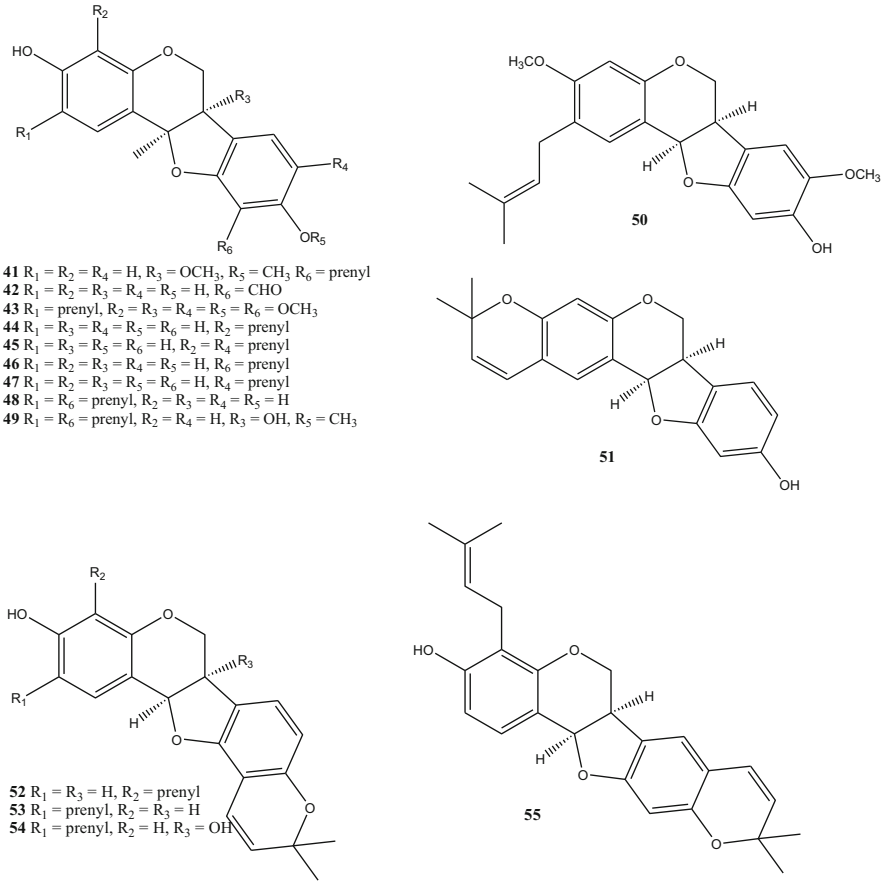

Fig. 22.3 Structures of pterocarpans isolated from *E. abyssinica*

22.2.3 Pterocarpans

Fifteen pterocarpans were isolated and characterised from the EtOAc extract of the stem bark of *Erythrina abyssinica* [37]. The isolated compounds **41–55** (Fig. 22.3) were evaluated for their inhibitory activity on PTP1B (Table 22.3). Among the isolates, **45**, **52**, **53**, **55** and compound **41** significantly inhibited PTP1B activity with values ranging from 4.2 ± 0.2 to 19.3 ± 0.3 μM. Compound **52** showed more potent inhibitory activity compared to the reference compound RK-682 although less potent than ursolic acid. The compounds where there was a free prenyl group showed inhibitory activity against PTP1B. Compounds **52**, **53**, **54** and **55** which have a 2,2-dimethylpyran ring fused to the C-9 or C-10 position showed considerably stronger inhibitory activity compared to the other active compounds with just the free prenyl group. This indicates that the fused ring on the B ring significantly enhances the inhibitory activity against PTP1B.

Table 22.3 PTP1B inhibitory effects of pterocarpans isolated from *E. abyssinica*

Compound	Inhibitory activity (μM)
50	>40
48	>40
47	>40
46	>40
43	>40
42	>40
49	20.8 ± 1.5
44	19.5 ± 1.5
41	19.3 ± 0.3
54	8.8 ± 0.5
53	7.8 ± 0.5
51	7.6 ± 0.9
45	7.3 ± 0.1
55	6.4 ± 0.6
52	4.2 ± 0.2
RK-682	4.5 ± 0.5
Ursolic acid	3.6 ± 0.2

22.2.4 Deoxyflavonoids

Deoxyflavonoids were also isolated and characterised from *Erythrina abyssinica*. Among the 13 deoxyflavonoids isolated (Fig. 22.4), five displayed a strong inhibitory activity against PTP1B [38]. All the isolates, except for **61**, **63, 64**, **65** and **68**, inhibited PTP1B activity in a dose-dependent manner with IC_{50} values ranging from 14.9 ± 1.6 to 35.8 μM (Table 22.4). Although compounds **65** and **68** have similar structures to compounds **66** and **67** (the former have a proton at position 5′ and the latter have a prenyl at this position in the B ring), there was a considerable improvement in the inhibitory activity against PTP1B in the latter.

22.3 Conclusion

Sixty-eight flavonoids were isolated from the stem bark of *Erythrina abyssinica*: 34 flavanones, 6 chalcones, 15 pterocarpans and 13 deoxyflavonoids and were tested for their ability to inhibit the PTP1B activity among which 41 were found to inhibit PTP1B activity in a dose-dependent manner. The presence of lipophilic substituents such as a prenyl group and a methoxy group were found to promote activity in all the different classes of flavonoids. Compounds with better activity belong to the pterocarpans family.

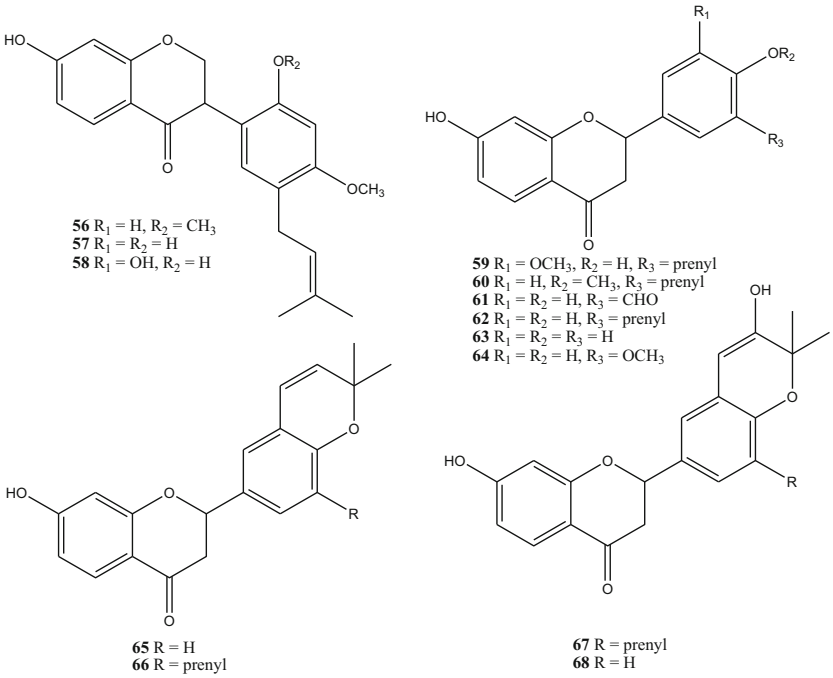

Fig. 22.4 Structures of deoxyflavonoids isolated from *E. abyssinica*

Table 22.4 Inhibitory effects of isolated deoxyflavonoids on PTP1B enzyme

Compound	Inhibitory activity (μM)
61	>40
63	>40
68	>40
64	>40
65	>40
67	35.8
62	29.2
66	22.6
59	19.2
57	17.2
60	16.5
56	15.2
58	14.9
Ursolic acid	3.6
RK-682	4.7

Acknowledgements The author wishes to acknowledge the Fomum foundation for support in this work.

References

1. Mattei J, Malik V, Wedic NMK, Hu FB, Spiegelman D, Willett WC, Campos H (2015) Reducing the global burden of type 2 diabetes by improving the quality of staple foods: the global nutrition and epidemiologic transition initiative. Glob Health 11:1–20
2. Devendra D, Liu E, Eisenbarth GS, Davis B (2004) Clinical review type 1 diabetes: recent developments. BMJ 328:750–754
3. Shi Y, FB H (2016) The global implications of diabetes and cancer. Lancet 383:1947–1948
4. Tao Z, Shi A, Zhao J (2015) Epidemiological perspectives of diabetes. Cell Biochem Biophys 73:181–185
5. De Araújo-Júnior JX, De Oliveira MSG, Aquino PGV, Alexandre-Moreira MS, Sant'Ana AEG (2012) A phytochemical and ethnopharmacological review of the genus Erythrina. In: Rao V (ed) Phytochemicals – a global perspective of their role in nutrition and health. InTech, Rijeka
6. Oliver-Bever B (1981) Medicinal plants in Tropical West Africa. Cambridge University Press, New York
7. Mohammed A, Ibrahim MA, Islam MS (2014) African medicinal plants with antidiabetic potentials: a review. Planta Med 80:354–377
8. Kokwaro JO (1976) Medicinal plants of East Africa. Literature Bureau, Nairobi
9. Mitscher LA, Drake S, Gollapudi SR, Okwute SK (1987) A modern look at folkloric use of anti-infective agents. J Nat Prod 50:1025–1040
10. Yenesew A, Induli M, Derese S, Midiwo JO, Heydenreich M, Peter MG, Akala H, Wangui J, Liyala P, Waters NC (2004) Anti-plasmodial flavonoids from the stem bark of *Erythrina abyssinica*. Phytochemistry 65:3029–3032
11. Kamat VS, Chuo FY, Kubo I, Nakanishi K (1981) Anti-microbial agents from an East African plant *Erythrina abyssinica*. Heterocycles 15:1163–1170
12. Wagate JM, Mbaria CG, Gakuya DW, Nanyingi MO, Kareru PG, Njuguna A, Nduhiu G, Macharia JK, Njonge FK (2010) Review of pharmacological effects of *Glycyrrhiza radix* and its bioactive compounds. Phytother Res 24:150–153
13. Ichimaru M, Moriyasu M, Nishiyama Y, Kato A, Mathenge SG, Juma FD, Nganga JN (1996) Structural elucidation of new flavanones isolated from *Erythrina abyssinica*. J Nat Prod 59:1113–1116
14. Orwa C, Mutua A, Kindt R, Jamnadass R, Anthony S (2009) *Erythrina abyssinica*. Agroforestry Database 4.0, pp 1–5
15. Njoroge GN, Bussmann RW (2006) Traditional management of ear, nose and throat (ENT) diseases in Central Kenya. J Ethnobiol Ethnomed 2:1–9
16. Njoroge GN, Kibunga JW (2007) Herbal medicine acceptance, sources and utilization for diarrhoea management in a cosmopolitan urban area (Thika, Kenya). Afr J Ecol 45:65–70
17. Nkengfack AE, Sanson DR, Fomum ZT, Tempesta MS (1989) 8-prenylluteone, a prenylated isoflavone from *Erythrina eriotriocha*. Phytochemistry 28:2522–2526
18. Fomum ZT, Ayafor JF, Mbafor JT, Mbi CM (1986) Erythrina studies. Part 2. Structures of three novel prenylated antibacterial flavanones, sigmoidins A-C, from *Erythrina sigmoidea* Hua. J Chem Soc Perkin Trans 1:33–37
19. Njamen D, Mbafor JT, Fomum ZT, Kamanyi A, Mbanya J-C, Recio MC, Giner RM, Manez S, Rios JL (2004) Anti-inflammatory activities of two flavanones, sigmoidin A and sigmoidin B, from *Erythrina sigmoidea*. Planta Med 70:104–107

20. Nkengfack AE, Kouam J, Vouffo TW, Meyer M, Tempesta MS, Fomum ZT (1994) An isoflavanone and a coumestan from *Erythrina sigmoidea*. Phytochemistry 35:521–526
21. Oh JS, Kim H, Vijayakumar A, Kwon O, Choi YJ, Huh KB, Chang N (2016) Association between dietary flavanones intake and lipid profiles according to the presence of metabolic syndrome in Korean women with type 2 diabetes mellitus. Nutr Res Pract 10:67–73
22. Rahman MZ, Rahman MS, Kaisar A, Hossain A, Rashid MA (2010) Bioactive isoflavones from *Erythrina variegata* L. Turk J Pharm Sci 7:21–28
23. Muthaura CN, Keriko JM, Derese S, Yenesew A, Rukunga GM (2011) Investigation of some medicinal plants traditionally used for treatment of malaria in Kenya as potential sources of antimalarial drugs. Exp Parasitol 127:609–626
24. Johnson TO, Ermolieff J, Jirousek MR (2002) Protein tyrosine phosphatase 1B inhibitors for diabetes. Nat Rev Drug Discov 1:696–709
25. Xue B, Kim YB, Lee A, Toschi E, Bonner-Weir S, Kahn CR (2007) Protein-tyrosine phosphatase 1B deficiency reduces insulin resistance and the diabetic phenotype in mice with polygenic insulin resistance. J Biol Chem 282:23829–23840
26. Elchebly M, Normandin D, Cheng A, Himms-Hagen J, Chan CC, Ramachandran C, Gresser MJ, Tremblay ML, Kennedy BP (1999) Increased insulin sensitivity and obesity resistance in mice lacking the protein tyrosine phosphatase-1B gene. Science 283:1544–1548
27. Ahmad F, Azevedo JL, Cortright R, Dohm GL, Goldstein BJ (1997) Alterations in skeletal muscle protein-tyrosine phosphatase activity and expression in insulin-resistant human obesity and diabetes. J Clin Invest 100:449–458
28. Newman DJ, Cragg GM (2007) Natural products as sources of new drugs over the last 25 years. J Nat Prod 70:461
29. Coman C, Rugină OD, Socaciu C (2012) Plants and natural compounds with antidiabetic action. Not Bot Hortic Agrobot Cluj-Napoca 40:314–325
30. Jiang C, Liang L, Guo Y (2012) Natural products possessing protein tyrosine phosphatase 1B (PTP1B) inhibitory activity found in the last decades. Acta Pharmacol Sin 33:1217–1245
31. Cui L, Lee HS, Ndinteh DT, Mbafor JT, Kim YH, Le TVT, Nguyen PH, Oh WK (2010) New prenylated flavanones from *Erythrina abyssinica* with protein tyrosine phosphatase 1B (PTP1B) inhibitory activity. Planta Med 76:713–718
32. Cui L, Thuong PT, Lee HS, Ndinteh DT, Mbafor JT, Fomum ZT, WK O (2008) Flavanones from the stem bark of *Erythrina abyssinica*. Bioorg Med Chem 16:10356–10362
33. Vinayagam R, Xu B (2015) Antidiabetic properties of dietary flavonoids: a cellular mechanism review. Nutr Metab (Lond):1–20
34. Cui L, Thuong PT, Lee HS, Ndinteh DT, Mbafor JT, Fomum ZT, Oh WK (2008) Flavanones from the stem bark of *Erythrina abyssinica*. Bioorg Med Chem 16:10356–10362
35. Singh R, Bharti N (2010) Characterization of cyclodextrin inclusion complexes – a review. J Pharm Sci Technol 2:171–183
36. Cui L, Phuong TT, Hyun SL, Njamen D, Mbafor JT, Fomum ZT, Lee J, Young HK, Won KO (2008) Four new chalcones from *Erythrina abyssinica*. Planta Med 74:422–426
37. Nguyen PH, Van Le TT, Thuong PT, Dao TT, Ndinteh DT, Mbafor JT, Kang WK, WK O (2009) Cytotoxic and PTP1B inhibitory activities from *Erythrina abyssinica*. Bioorg Med Chem Lett 19:6745–6749
38. Nguyen PH, Dao TT, Kim J, Phong DT, Ndinteh DT, Mbafor JT, Oh WK (2011) New 5-deoxyflavonoids and their inhibitory effects on protein tyrosine phosphatase 1B (PTP1B) activity. Bioorg Med Chem 19:3378–3383

Chapter 23
2-Amino-5-Bromo-3-Iodoacetophenone and 2-Amino-5-Bromo-3-Iodobenzamide as Synthons for Novel Polycarbo-Substituted Indoles and Their Annulated Derivatives

Mmakwena M. Mmonwa and Malose J. Mphahlele

Abstract 2-Amino-5-bromo-3-iodoacetophenone and 2-amino-5-bromo-3-iodobenzamide represent important synthons for the design and synthesis of various nitrogen-containing heterocyclic compounds and their annulated derivatives. We have demonstrated that these halogenated aniline derivatives undergo palladium catalyzed Sonogashira cross-coupling with terminal acetylenes to afford the corresponding 2-amino-3-(arylalkynyl)acetophenones and 2-amino-3-(arylalkynyl) benzamides. These alkynylated aniline derivatives in which the alkynyl moiety is adjacent to the nucleophilic nitrogen atom were, in turn, subjected to palladium chloride-mediated heteroannulation to yield novel 1-(2-aryl-1*H*-indol-7-yl) ethanones and 2-aryl-1*H*-indole-7-carboxamides, respectively. Molecular hybridization to append an indole moiety to a chalcone framework was achieved via initial Claisen-Schmidt aldol condensation of 2-amino-5-bromo-3-iodoacetophenone with benzaldehyde derivatives followed by sequential palladium catalyzed Sonogashira cross-coupling and heteroannulation. Likewise, boric acid-mediated cyclocondensation of the 3-alkynyl-5-bromoanthranilamides with benzaldehyde derivatives followed by palladium chloride-mediated cyclization afforded the corresponding 2,3-dihydro-1*H*-pyrrolo[3,2,1-*ij*]quinazolin-1-ones.

Keywords 2-Amino-5-bromo-3-iodoacetophenone • 2-Amino-5-bromo-3-iodobenzamide • Indoles • Indole-chalcones • 1*H*-Pyrrolo[3,2,1-*ij*]quinazolin-1-ones

M.M. Mmonwa • M.J. Mphahlele (✉)
Department of Chemistry, College of Science, Engineering and Technology, University of South Africa, P.O. Box 392, Pretoria 0003, South Africa
e-mail: mphahmj@unisa.ac.za

P. Ramasami et al. (eds.), *Emerging Trends in Chemical Sciences*,
DOI 10.1007/978-3-319-60408-4_23

23.1 Introduction

The structural diversity and biological importance of nitrogen-containing heterocyclic compounds such as indoles have made them important targets for synthesis over the years. Indole moiety constitutes the most common unit prevalent in the framework of most alkaloids with biological activity [1]. Indole-3-carbinol **1** (Fig. 23.1), for example, was first isolated from cruciferous vegetables and was found to exhibit various biological properties such as anticarcinogenic, antioxidant, and antiatherogenic properties [1]. Phidianidines **2a** and **2b** (Fig. 23.1), on the other hand, were isolated from the shell-less marine opisthobranch mollusk *Phidiana militaris* and these compounds were found to exhibit antitumor activity against the HeLa and C6 cells with the IC_{50} values within nanomolar range [2]. Lin and Snider later prepared compounds **2a** and **2b** (Fig. 23.1) by coupling the corresponding 2-(1*H*-indol-3-yl)acetyl chloride with (5-azidopentyl)-2-hydroxyguanidine in the presence of triethylamine in dichloromethane [3]. The analogous 3-[2-(5-chloro-2-phenyl-1*H*-indol-3-yl)-1-(dimethylamino)ethyl]naphthalen-2-ol, **3** (Fig. 23.1), which was synthesized via a multicomponent reaction of 2,5-disubstituted indole-3-carboxaldehyde, secondary amine and 2-naphthol was found to exhibit significant antifungal activity [4].

Indole derivatives have also been found to exhibit interesting photophysical (electronic absorption and emission) properties and some of them are components of dyes or organic light emitting diodes (OLEDs) [5–8]. For example, a 4-[(3a,7a-dihydro-1*H*-indol-3-yl)(1*H*-indol-3-yl)methyl]-2,6-dimethylphenol dye, **4** (Fig. 23.2) prepared from the reaction of 1*H*-indole with 4-hydroxy-3,5-dimethylbenzaldehyde in methanol was used as a probe for the determination of water content in water miscible organic solvents such as acetone, acetonitrile, tetrahydrofuran and dioxane [7]. The electronic absorption spectra of indole derivative **4** acquired in pure organic solvents (e.g. acetone, acetonitrile, tetrahydrofuran, and dioxane) revealed that this compound absorbs in the yellow region at λ_{ab} *ca.* 450 nm. Significant red shift of the absorption band to the pink region (λ_{ab} *ca.* 530 nm) was observed when the electronic

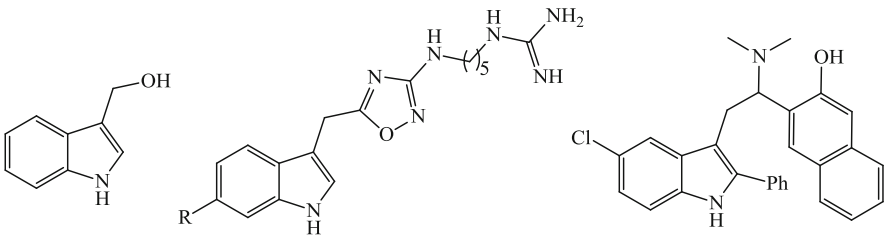

1 **2**: R = H **(a)**, Br **(b)** **3**

Fig. 23.1 Examples of biologically active indole derivatives

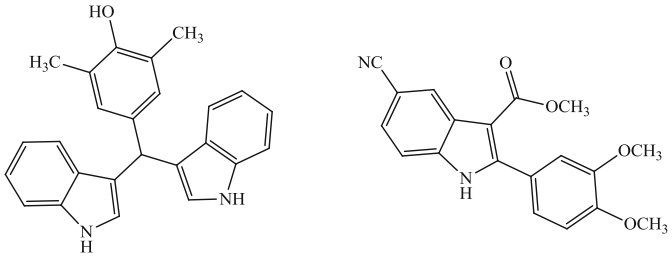

4 **5**

Fig. 23.2 Examples of indole-based dye **4** and **5** employed in light emitting materials

absorption spectra of indole derivative **4** were acquired in these solvents in the presence of 10% of water [7]. A blue electroluminescent device, ITO/NPB/**5**/TPBI/Alq_3/Mg–Ag, comprising of indium tin oxide (ITO) as a substrate, 4,4′-bis[*N*-(1-naphthyl)-*N*-phenylamino]biphenyl (NPB) as a hole, methyl 5-cyano-2-(3,4-dimethoxyphenyl)-1*H*-indole-3-carboxylate **5**, 1,3,5-tris(*N*-phenylbenzimidazol-2-yl)benzene as a hole blocking material, tris(8-hydroxyquinoline)aluminium (Alq_3) as electron transporting material and magnesium-silver (Mg-Ag) as electrode has been developed [8]. Indole **5** (Fig. 23.2) was, in turn, prepared via the Larock heteroannulation of 4-amino-3-iodobenzonitrile and methyl 3-(3,4-dimethoxyphenyl)propiolate in DMF.

Carbon-based substituents are predominant components of many indole derivatives with interesting biological [1] and photophysical properties [5–8]. Several conventional methods for the construction of indole framework have been reported in the literature and these include the Fischer indole synthesis from aryl hydrazones [9–11], the Madelung cyclization of *N*-acyl-*o*-toluidines [12–15] and the Batcho–Leimgruber synthesis from *o*-nitrotoluenes and dimethylformamide acetals [16]. Non-conventional methods which involve the use of transition metal as catalysts to promote the C–C or C–N bond formation in the construction of the indole skeleton have also been developed [17, 18]. Our research interest is on the use of *ortho*-halogenated aniline derivatives as precursors for the metal-mediated alkynylation and subsequent heteroannulation to construct the indole moiety. We have employed symmetrical and mixed dihalogenated 2-aminoacetophenones and 2-aminobenzamides (anthranilamides) to effect a site-selective palladium catalyzed cross-coupling to incorporate an arylalkynyl moiety *ortho* to the nucleophilic amine group. These 2-alkynylaniline derivatives were found to undergo metal-mediated *endo-dig* cyclization to afford polycarbo-substituted indole-based compounds and their polynuclear derivatives as described below.

23.2 Sequential Halogenation of 2-Aminoacetophenone and 2-Aminobenzamide

The halogenated 2-aminoacetophenones and the analogous 2-aminobenzamides were prepared as depicted in Scheme 23.1. Commercially available 2-aminoacetophenone **6a** (R = $-CH_3$), for example, was transformed into 2-amino-5-bromoacetophenone **7a** using pyridinium tribromide (PTB) in dichloromethane at 0 °C to room temperature (RT) for 3 h following the literature method [19]. 2-Amino-5-bromobenzamide **7b**, on the other hand, was prepared by reacting the commercially available 2-aminobenzamide **6b** (R = $-NH_2$) with *N*-bromosuccinimide (NBS, 1 equivalent) in acetonitrile at RT for 0.5 h [20]. Further halogenation of the 2-amino-5-bromoacetophenone **7a** and 2-amino-5-bromobenzamide **7b** with *N*-iodosuccinimide (NIS, 1.2 equiv.) in acetic acid at RT afforded 2-amino-5-bromo-3-iodoacetophenone **8a** and 2-amino-5-bromo-3-iodobenzamide **8b**, respectively [20, 21]. The use of 2 mol equiv. of NBS in acetic acid on **6a** and **6b** at RT for 2 h afforded the 3,5-dibromoaminoacetophenone **9a** and 3,5-dibromoaminobenzamide **9b** [22, 23].

We employed the mixed dihalogenated benzoic acid derivatives **8a** and **8b** as substrates for the site-selective palladium mediated cross-coupling reactions as described below.

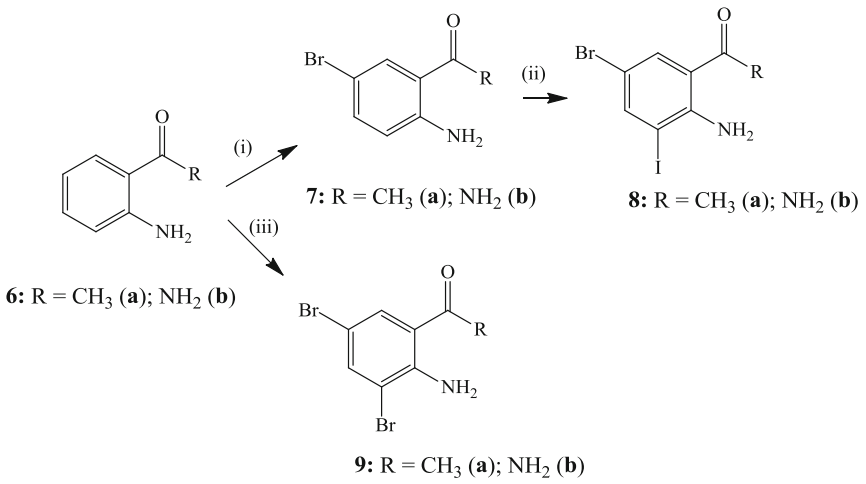

Scheme 23.1 Sequential halogenation of aniline derivatives **6**. *Reagents and conditions*: (i) PTB, CH_2Cl_2, 0 °C to RT, 3 h (**7a**) or NBS, CH_3CN, RT, 0.5 h (**7b**); (ii) NIS, AcOH, RT, 1 h; (iii) NBS (2 equiv.), AcOH, RT, 2 h

23.3 Palladium Catalyzed Cross-Coupling of the Dihalogenated Aniline Derivatives 8a and 8b

We have taken advantage of the difference in reactivity of the Csp^2-halogen bonds (I > Br > Cl > F) to effect a site-selective carbon-carbon bond formation of the mixed halogenated aniline derivatives **8**. 2-Amino-5-bromo-3-iodoacetophenone **8a** (R = CH_3) and 2-amino-5-bromo-3-iodobenzamide **8b** (R = NH_2) were each subjected to the Sonogashira cross-coupling with terminal alkynes (1.2 equiv.) in the presence of $PdCl_2(PPh_3)_2$–CuI catalyst mixture and potassium carbonate as a base in aqueous DMF at RT for 5 h (Scheme 23.2). Aqueous work-up and purification with silica gel column chromatography afforded in sequence traces of the homo-coupled dimer and the expected 3-alkynylated 2-amino-5-bromoacetophenones **10a–c** [21] and the analogous 3-alkynylated 2-amino-5-bromobenzamides **10d–f** [24], respectively.

The 3-alkynylated 2-amino-5-bromoacetophenones **10a–c** were further subjected to the Suzuki-Miyaura cross-coupling with arylboronic or styrylboronic acids in the presence of $PdCl_2(PPh_3)_2$ as PdL_2 source, tricyclohexylphosphine (PCy_3) as a ligand and K_2CO_3 as a base in dioxane (aq) at 80 °C to afford the corresponding polysubstituted aniline derivatives **11a–n** (Scheme 23.3) [21]. The ^{1}H NMR spectra of the 5-styryl–substituted derivatives (Ar^2 = –CH=CHAr) revealed the presence of two sets of doublets with coupling constant values (J_{trans}) of about 16.0 Hz, which confirmed the *E* orientation around the C–C double bond.

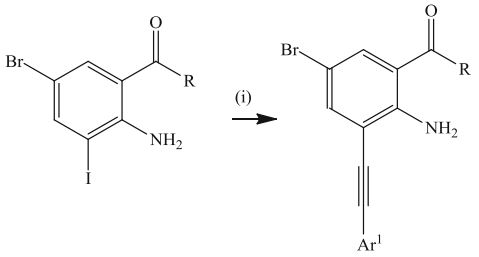

8: R = CH_3 (**a**); NH_2 (**b**) **10a–c** (R = CH_3); **10d–f** (NH_2)

Compound	R	Ar^1	%Yield
10a	-CH_3	C_6H_5-	91
10b	-CH_3	4-FC_6H_4-	89
10c	-CH_3	4-$MeOC_6H_4$-	75
10d	-NH_2	C_6H_5-	85
10e	-NH_2	4-FC_6H_4-	84
10f	-NH_2	3-ClC_6H_4-	87

Scheme 23.2 Site-selective Sonogashira cross-coupling of **8a** and **8b**. *Reagents and conditions*: (i) HC≡CAr^1, $PdCl_2(PPh_3)_2$, CuI, K_2CO_3, DMF (aq), RT, 5 h

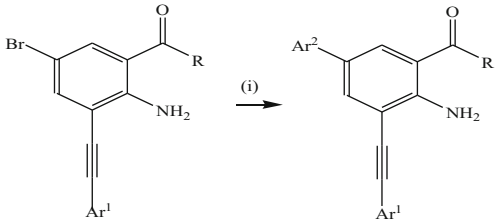

10a–c **11a–n**

Compound	Ar^1	Ar^2	%Yield
11a	C_6H_5-	C_6H_5-	79
11b	C_6H_5-	4-FC_6H_4-	66
11c	C_6H_5-	4-$MeOC_6H_4$-	75
11d	4-FC_6H_4-	C_6H_5-	69
11e	4-FC_6H_4-	4-FC_6H_4-	63
11f	4-FC_6H_4-	4-$MeOC_6H_4$-	70
11g	4-$MeOC_6H_4$-	C_6H_5-	73
11h	4-$MeOC_6H_4$-	4-FC_6H_4-	61
11i	4-$MeOC_6H_4$-	4-$MeOC_6H_4$-	66
11j	C_6H_5-	C_6H_5CH=CH-	75
11k	C_6H_5-	4-FC_6H_4CH=CH-	62
11l	4-FC_6H_4-	C_6H_5CH=CH-	73
11m	4-FC_6H_4-	4-FC_6H_4CH=CH-	60
11n	4-$MeOC_6H_4$-	4-FC_6H_4CH=CH-	65

Scheme 23.3 Suzuki-Miyaura cross coupling of **10a–c**. *Reagents and conditions*: (i) $Ar^2B(OH)_2$, $PdCl_2(PPh_3)_2$, PCy_3, K_2CO_3, dioxane (aq), 80 °C, 2 h

23.4 Palladium Catalyzed Route to Indole Derivatives

The remarkable bioactivity along with the unique structural assortment displayed by polysubstituted indoles influenced us to design and synthesize unsymmetrical polycarbo-substituted NH-free indole derivatives bearing an acetyl group on the benzo ring for further studies of biological properties. To our knowledge, the only examples of indole derivatives bearing an acetyl group on the fused benzo ring were those prepared via a modified Vilsmeir-Haack acetylation or Friedel-Crafts acylation of the 5,6-dimethoxy-2,3-diphenyl-1*H*-indole, respectively [25]. The analogous 2,5,7-trisubstituted indoles have also been recently synthesized by Cacchi et al. based on alkynylation-heteroannulation and the Suzuki-Miyaura cross-coupling reactions of the 2-bromo-4-(chloro/methyl)-6-iodoanilines [18]. The 3-alkynylated 2-aminoacetophenones **11a–n** were subjected to palladium chloride ($PdCl_2$) in acetonitrile at 90 °C under argon atmosphere for 3 h to afford

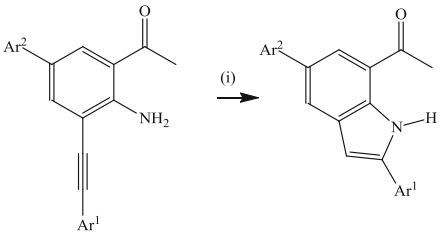

11a–n **12a–n**

Compound	Ar^1	Ar^2	%Yield of 12
12a	C_6H_5-	C_6H_5-	70
12b	C_6H_5-	4-FC_6H_4-	75
12c	C_6H_5-	4-$MeOC_6H_4$-	70
12d	4-FC_6H_4-	C_6H_5-	70
12e	4-FC_6H_4-	4-FC_6H_4-	70
12f	4-FC_6H_4-	4-$MeOC_6H_4$-	72
12g	4-$MeOC_6H_4$-	C_6H_5-	67
12h	4-$MeOC_6H_4$-	4-FC_6H_4-	80
12i	4-$MeOC_6H_4$-	4-$MeOC_6H_4$-	70
12j	C_6H_5-	C_6H_5CH=CH-	62
12k	C_6H_5-	4-FC_6H_4CH=CH-	68
12l	4-FC_6H_4-	C_6H_5CH=CH-	63
12m	4-FC_6H_4-	4-FC_6H_4CH=CH-	62
12n	4-$MeOC_6H_4$-	4-FC_6H_4CH=CH-	68

Scheme 23.4 $PdCl_2$-mediated heteroannulation of **11**. *Reagents and conditions*: (i) $PdCl_2$, CH_3CN, reflux, 3 h

the corresponding polycarbo-substituted indoles **12a–n**, exclusively (Scheme 23.4) [21].

Literature reports revealed that the indole derivatives substituted with a nitrogen-containing group on the fused benzo ring exhibit significant antitumor properties [26, 27]. This prompted us to prepare the analogous *N*-(2,5-diarylindol-7-yl)acetamides **14** via Beckmann rearrangement reaction of the oximes derived from the known 1-(2,5-diarylindol-7-yl)ethanones **12a–g** [21]. The latter were first reacted with hydroxylamine hydrochloride in the presence of pyridine in ethanol under reflux to afford the corresponding oximes **13a–g** (Scheme 23.5). Beckmann rearrangement of compounds **13a–g** with trifluoroacetic acid (TFA) in acetonitrile under reflux for 2 h afforded the corresponding *N*-(2,5-diarylindol-7-yl)acetamides **14a–g**, which were formed through aryl migration. The methodology described in this investigation for the synthesis of C-7 aminated NH-free indoles is complementary to the method previously developed by Cacchi et al. [18]. These authors made

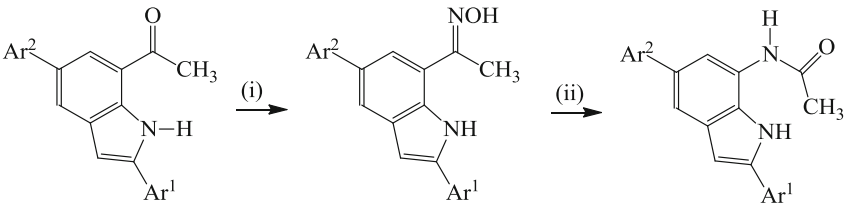

12a–g		13a–g		14a–g
Compound	**Ar^1**	**Ar^2**	**%Yield of 13**	**%Yield of 14**
a	4-FC_6H_4-	4-FC_6H_4-	94	80
b	4-$MeOC_6H_4$-	4-FC_6H_4-	87	75
c	4-FC_6H_4-	4-$MeOC_6H_4$-	88	73
d	4-$MeOC_6H_4$-	4-$MeOC_6H_4$-	88	70
e	C_6H_5-	4-$FC_6H_4CH{=}CH$-	76	78
f	4-FC_6H_4-	4-$FC_6H_4CH{=}CH$-	75	77
g	4-$MeOC_6H_4$-	4-$FC_6H_4CH{=}CH$-	76	69

Scheme 23.5 Beckmann rearrangement of the 1-(2,5-diaryl-1*H*-indol-7-yl)ethanone oximes **13a–g**. *Reagents and conditions*: (i) $NH_2OH.HCl$, pyridine, EtOH, reflux, 12 h; (ii) TFA, CH_3CN, reflux, 2 h

use of the Buchwald-Hartwig C–N bond formation of the incipient 7-bromoindoles with primary and secondary amines to afford the amino-substituted indole derivatives. Series of 2,5- and 3,5-disubstituted 7-aminoindoles, on the other hand, have also been prepared before via a three component Wittig reaction of pyrrole-3-carboxaldehydes with fumaronitrile and PEt_3 followed by chemoselective C-6 alkylation of the intermediate *cis*-allylic nitriles followed by cyclization through an intramolecular Houben−Hoesch reaction [28].

23.5 Molecular Hybridization of Indole and Chalcone on the Same Molecular Framework

From the molecular design point of view, the combination of two pharmacophores into a single molecule has been found to enhance the biological properties of the resultant hybrid molecules. When indole and chalcone moieties are linked together on the same molecular framework, for example, they tend to enhance the overall electronic absorption and emission properties [6, 29] and the biological efficacy of the resultant molecular hybrids [30–33]. The most common framework of indole-

chalcones synthesized to-date has the α,β-unsaturated carbonyl moiety attached to the C-3 position of the indole ring either through the carbonyl carbon **15** or through the β-carbon **16** (Fig. 23.3). Such indole-chalcone hybrids are generally accessible via the Claisen-Schmidt aldol condensation of the corresponding 3-acetylindoles or indole-3-carbaldehydes [32]. These 3-substitituted indoles are themselves, in turn, prepared via the Friedel-Crafts acylation [34], acylation of 3-indolylzinc chlorides or indole Grignard reagents [35] or Vilsmeier-Haack reaction with $POCl_3$ and DMF [36].

Claisen-Schmidt aldol condensation of 2-amino-5-bromo-3-iodoacetophenone **8a** (R = CH_3) with benzaldehyde derivatives in the presence of potassium hydroxide in ethanol at RT for 12 h afforded the corresponding 2-amino-5-bromo-3-iodochalcones **17a–d** in high yield and purity (Scheme 23.6). The *E*-geometry around the olefinic framework of the 2-aminochalcones **17a–d** was confirmed by two sets of doublets at about δ 7.40 and 7.74 ppm with coupling constant values J_{trans} = 15.5–16.0 Hz corresponding to the vinylic protons.

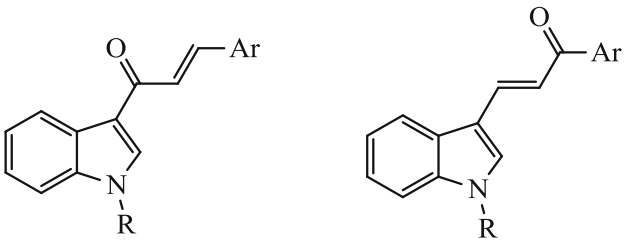

15 **16**

Fig. 23.3 Generalized structures of the commonly known indole-chalcones

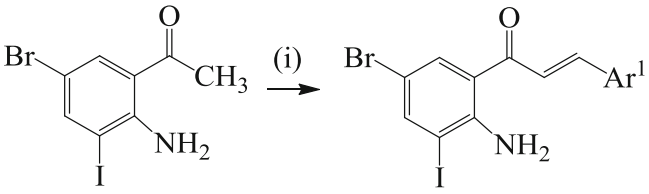

8a **17a–d**

Compound	Ar^1	%Yield
17a	C_6H_5-	81
17b	4-FC_6H_4-	84
17c	4-ClC_6H_4-	91
17d	4-$MeOC_6H_4$-	93

Scheme 23.6 Claisen-Schmidt aldol condensation of **8a**. *Reagents and conditions*: (i) ArCHO, KOH, EtOH, RT, 12 h

Treatment of compounds **17a–d** with aryl acetylenes (1.2 equiv.) in the presence of $PdCl_2(PPh_3)_2$–CuI catalyst mixture and cesium carbonate as a base in ethanol under reflux for 2 h afforded after aqueous work-up and purification by column chromatography on silica gel the corresponding 3-alkynylated 2-amino-5-bromochalcones **18a–f**, exclusively (Scheme 23.7). The 3-alkynylated 2-aminochalcones **18a–f** were, in turn, subjected to $PdCl_2$-mediated heteroannulation in acetonitrile at 90 °C for 3 h to afford the corresponding indole-appended chalcone derivatives **19a–f**.

We decided to incorporate a trifluoroacetyl group at the 3-position of the ambident indole moiety of compounds **19a–f** with possible retention of the N-H group, which has been found to be essential for the anti-proliferative activity of indole derivatives [37]. Compounds **19a–f** were subjected to trifluoroacetic anhydride (1.2 equiv.) in THF under reflux for 5 h and isolated by aqueous work-up and recrystallization the corresponding 3-trifluoroacetylindole-chalcones **20a–f**, exclusively (Scheme 23.8) [38].

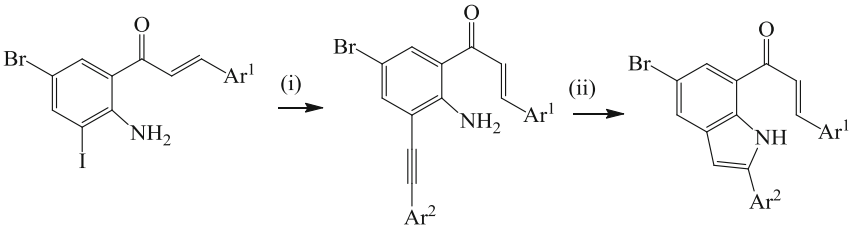

17a–d		18a–f		19a–f
Compound	**Ar^1**	**Ar^2**	**%Yield of 18**	**%Yield of 19**
a	C_6H_5-	C_6H_5-	76	75
b	4-FC_6H_4-	C_6H_5-	81	63
c	4-ClC_6H_4-	C_6H_5-	71	71
d	4-$MeOC_6H_4$-	C_6H_5-	62	53
e	4-ClC_6H_4-	4-$CF_3OC_6H_4$-	78	70
f	4-$MeOC_6H_4$-	4-$CF_3OC_6H_4$-	82	54

Scheme 23.7 Sonogashira cross-coupling of **17a–d** and subsequent $PdCl_2$-mediated cyclization. *Reagents and conditions*: (i) HC≡CAr^2, $PdCl_2(PPh_3)_2$, CuI, Cs_2CO_3, EtOH, reflux, 2 h; (ii) $PdCl_2$, CH_3CN, 90 °C, 3 h

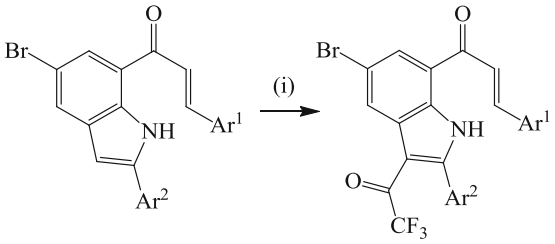

19a–f **20a–f**

Compound	Ar^1	Ar^2	%Yield of 20
20a	C_6H_5-	C_6H_5-	88
20b	4-FC_6H_4-	C_6H_5-	76
20c	4-ClC_6H_4-	C_6H_5-	91
20d	4-$MeOC_6H_4$-	C_6H_5-	62
20e	4-ClC_6H_4-	4-$CF_3OC_6H_4$-	90
20f	4-$MeOC_6H_4$-	4-$CF_3OC_6H_4$-	88

Scheme 23.8 Trifluoroacetylation of **19a–f**. *Reagents and conditions*: (i) $(CF_3CO)_2O$, THF, reflux, 5 h

23.6 Synthesis of 2,3-Dihydro-1*H*-pyrrolo[3,2,1-*ij*] quinazolin-1-ones

We envisaged that molecular hybridization framework to construct a pyrrole ring onto a dihydroquinazolinone framework through the standard indole synthesis would lead to the 2,3-dihydro-1*H*-pyrrolo[3,2,1-*ij*]quinazolin-1-ones. Consequently, we subjected the 2-amino-3-(arylethynyl)-5-bromobenzamides **10a–c** to boric acid-mediated cyclocondensation with benzaldehyde derivatives to afford the corresponding 2-aryl-8-(arylethynyl)-6-bromo-2,3-dihydroquinazolin-4(1*H*)-ones **21a–l** (Scheme 23.9). The latter were, in turn, subjected to $PdCl_2$-mediated *endo-dig* cyclization in dioxane under reflux to afford the corresponding 2,3-dihydro-1*H*-pyrrolo[3,2,1-*ij*]quinazolin-1-ones **22a–l** (Scheme 23.9) [24].

23.7 Conclusions and Perspectives

We have demonstrated that a halogen atom *ortho* to the amine group on an aromatic ring facilitates palladium catalyzed Sonogashira cross-coupling with terminal acetylenes followed by heteroannulation to incorporate an indole moiety.

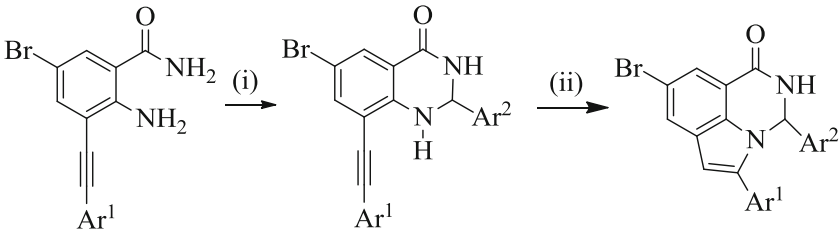

10a–c **21a–l** **22a–l**

Compound	Ar^1	Ar^2	%Yield of 21	%Yield of 22
a	C_6H_5-	C_6H_5-	86	58
b	C_6H_5-	4-FC_6H_4-	88	53
c	C_6H_5-	4-ClC_6H_4-	86	62
d	C_6H_5-	4-$MeOC_6H_4$-	93	60
e	4-FC_6H_4-	C_6H_5-	91	57
f	4-FC_6H_4-	4-FC_6H_4-	92	56
g	4-FC_6H_4-	4-ClC_6H_4-	83	58
h	4-FC_6H_4-	4-$MeOC_6H_4$-	92	60
i	3-ClC_6H_4-	C_6H_5-	80	68
j	3-ClC_6H_4-	4-FC_6H_4-	95	62
k	3-ClC_6H_4-	4-ClC_6H_4-	96	76
l	3-ClC_6H_4-	4-$MeOC_6H_4$-	97	72

Scheme 23.9 Cyclocondensation of **10a–c** with benzaldehyde derivatives followed by $PdCl_2$-mediated heteroannulation of **21a–l**. *Reagents and conditions*: (i) Ar^2CHO, boric acid, 120 °C, 5 min.; (ii) $PdCl_2$, dioxane, 90 °C

Indoles derived from 2-amino-5-bromo-3-iodoacetophenone contain several reactive centres which enable further elaboration via C-3 trifluoroacetylation and Beckmann rearrangement of the corresponding oximes to afford nitrogen-containing derivatives. Molecular hybridization via initial Claisen-Schmidt aldol condensation of 2-amino-5-bromo-5-iodoacetophenone with benzaldehyde derivatives followed by Sonogashira cross-coupling and heteroannulation afforded indole-appended chalcones. Likewise, molecular hybridization to incorporate a pyrrole ring onto a quinazolinone framework was achieved via palladium chloride-mediated *endo-dig* C*sp*–N cyclization of the corresponding 8-alkynylated 2,3-dihydroquinazolin-4(1*H*)-ones to afford angular 2,3-dihydro-1*H*-pyrrolo[3,2,1-*ij*]quinazolin-1-ones. The ambident electrophilic 1,3-diaryl-2-propen-1-one (chalcone) moiety has established itself as an important scaffold for one-pot nucleophilic addition reactions via attack on the carbonyl group (1,2-addition) and subsequent conjugate addition reaction with 1,2-binucleophiles to afford biologically-relevant 5- and 6-membered nitrogen-containing

heterocycles such as pyrroles, pyrazoles, indoles, isoxazoles, imidazoles, pyrazoles, indazoles, tetrazoles, pyrimidines and pyridines. This makes the indole-chalcones prepared in our laboratory suitable candidates for further transformation to afford novel molecular hybrids with potential biologically properties.

Acknowledgements The authors are grateful to the University of South Africa and the National Research Foundation (SA) for financial assistance.

References

1. Zhang M-Z, Chen Q, Yang G-F (2015) A review on recent developments of indole-containing antiviral agents. Eur J Med Chem 89:421–441
2. Carbone M, Li Y, Irace C, Mollo E, Castelluccio F, Pascale AD, Cimino G, Santamaria R, Guo Y-W, Gavagnin M (2011) Structure and cytotoxicity of phidianidines A and B: first finding of 1,2,4-oxadiazole system in a marine natural product. Org Lett 13:2516–2519
3. Lin H-Y, Snider BB (2012) Total synthesis and biological evaluation of phidianidines A and B uncovers unique pharmacological profiles at CNS targets. J Org Chem 77:4832–4836
4. Raghunath SA, Mathada KN (2014) Synthesis and biological evaluation of aminonaphthols incorporated indole derivatives. Int J Med Chem:1–12
5. Shigemitsu Y, Wang B-C, Nishimura Y, Tominaga Y (2011) Photophysical properties of arylcarbonitrile derivatives: synthesis, absorption and emission spectra, and quantum chemical studies. Dyes Pigments 92:580–587
6. Pannipara M, Asiri AM, Alamry KA, Arshad MN, El-Daly SA (2015) Synthesis, spectral behaviour and photophysics of donor-acceptor kind of chalcones: excited state intramolecular charge transfer and fluorescence quenching studies. Spectrochim Acta A 136:1893–1902
7. Kim KN, Song KC, Noh JH, Chang S-K (2009) A simple phenol-indole dye as a chromogenic probe for the ratiometric determination of water content in organic solvents. Bull Kor Chem Soc 30:197–200
8. Hwu JR, Hsu YC, Josephrajan T, Tsay S-C (2009) Fine tuning of blue photoluminescence from indoles for device fabrication. J Mater Chem 19:3084–3090
9. Chandrasekhar S, Mukherjee S (2015) A convenient modification of the Fischer indole synthesis with a solid acid. Synth Commun 45:1018–1022
10. Bobko MA, Evans KA, Kaura AC, Shuster LE, Su D-S (2012) Synthesis of 2,5-disubstituted-3-cyanoindoles. Tetrahedron Lett 53:200–202
11. Matcha K, Antonchick AP (2014) Cascade multicomponent synthesis of indoles, pyrazoles, and pyridazinones by functionalization of alkenes. Angew Chem Int Ed 53:11960–11964
12. Köhling P, Schmidt AM, Eilbracht P (2003) Tandem hydroformylation/Fischer indole synthesis: a novel and convenient approach to indoles from olefins. Org Lett 5:213–216
13. Eduque RM, Creenia EC (2015) Microwave-assisted Fischer indole synthesis of 1,2,3,4-tetrahydrocarbazole using pyridinium-based ionic liquids. Procedia Chem 16:413–419
14. Hu Y-L, Fang D, Li D-S (2016) Novel and efficient heterogeneous 4-methylbenzenesulfonic acid-based ionic liquid supported on silica gel for greener Fischer indole synthesis. Catal Lett 146:968–976
15. Kouznetsov V, Zubkov F, Palma A, Restrepo G (2002) A simple synthesis of spiro-C6-annulated hydrocyclopenta[*g*]indole derivatives. Tetrahedron Lett 43:4707–4709
16. Barluenga J, Sanz R, Granados A, Fananas FJ (1998) First intramolecular carbometalation of lithiated double bonds. A new synthesis of functionalized indoles and dihydropyrroles. J Am Chem Soc 120:4865–4866
17. Oskooie HA, Heravi MM, Behbahani FK (2007) A facile, mild and efficient one-pot synthesis of 2-substituted indole derivatives catalyzed by $Pd(PPh_3)_2Cl_2$. Molecules 12:1438–1446

18. Cacchi S, Fabrizi G, Goggiamani A, Lazzetti A, Verdiglione R (2015) A facile palladium-catalyzed route to 2,5,7-trisubstituted indoles. Tetrahedron 71:9346–9356
19. Zhou H-B, Lee JH, Mayne CG, Carlson KE, Katzenellenbogen JA (2010) Imaging progesterone receptor in breast tumors: synthesis and receptor binding affinity of fluoroalkyl-substituted analogues of tanaproget. J Med Chem 53:3349–3360
20. Khoza TA, Makhafola TJ, Mphahlele MJ (2015) Novel polycarbo-substituted imidazo[1,2-*c*] quinazolines: synthesis and cytotoxicity studies. Molecules 20:22520–22533
21. Mphahlele MJ, Makhafola TJ, Mmonwa MM (2016) *In vitro* cytotoxicity of novel 2,5,7-tricarbo-substituted indoles derived from 2-amino-5-bromo-3-iodoacetophenone. Bioorg Med Chem 24:4576–4586
22. Maluleka MM, Mphahlele MJ (2013) 6,8-Dibromo-4-chloroquinoline-3-carbaldehyde as a synthon in the development of novel 1,6,8-triaryl-1*H*-pyrazolo[4,3-*c*]quinolines. Tetrahedron 69:699–704
23. Mphahlele MJ, Khoza TA, Maluleka MM (2014) Suzuki cross-coupling of the 2-aryl-6,8-dibromo-2,3-dihydroquinazolin-4(1*H*)-ones and transformation of the resulting 2,6,8-triaryl-2,3-dihydroquinazolin-4(1*H*)-ones. Bull Chem Soc Ethiop 28:81–90
24. Mphahlele MJ, Khoza TA, Mabeta P (2017) Novel 2,3-dihydro-1*H*-pyrrolo[3,2,1-*ij*] quinazolin-1-ones: synthesis and biological evaluation. Molecules 22:55–68
25. Black DSC, Deb-Das RB, Kumar N (1992) Nitrones and oxaziridines. XLIII. Synthesis of an indol-7-yl-substituted 1-pyrroline 1-oxide and related compounds. Aust J Chem 45:1051–1056
26. Owa T, Yoshino H, Okauchi T, Yoshimatsu K, Ozawa Y, Suki NH, Nagasu T, Koyanagi N, Kitoh K (1999) Discovery of novel antitumor sulfonamides targeting G1 phase of the cell cycle. J Med Chem 42:3789–3799
27. Mohan R, Banerjee M, Ray A, Manna T, Wilson L, Owa T, Bhattacharyya B, Panda D (2006) Antimitotic sulfonamides inhibit microtubule assembly dynamics and cancer cell proliferation. Biochemistry 45:5440–5449
28. Outlaw VK, Townsend CA (2014) A practical route to substituted 7-aminoindoles from pyrrole-3-carboxaldehydes. Org Lett 16:6334–6337
29. Saroj MK, Sharma N, Rastogi RC (2012) Photophysical study of some 3-benzoylmethyleneindol-2-ones and estimation of ground and excited states dipole moments from solvatochromic methods using solvent polarity parameters. J Mol Struct 1012:73–86
30. Kumar D, Kumar NM, Akamatsu K, Kusaka E, Harada H, Ito T (2010) Synthesis and biological evaluation of indolyl chalcones as antitumor agents. Bioorg Med Chem Lett 20:3916–3919
31. Robinson MW, Overmeyer JH, Young AM, Erhardt PW, Maltese WA (2012) Synthesis and evaluation of indole-based chalcones as inducers of methuosis, a novel type of nonapoptotic cell death. J Med Chem 55:1940–1956
32. Gao W, Liu R, Li Y, Cui P (2014) Two efficient methods for the synthesis of novel indole-based chalcone derivatives. Res Chem Intermed 40:3021–3032
33. Özdemir A, Altintop MD, Turan-Zitouni G, Çiftçi GA, Ertorum I, Alataş Ö, Kaplancikli ZA (2015) Synthesis and evaluation of new indole-based chalcones as potential antiinflammatory agents. Eur J Med Chem 89:304–309
34. Tran PH, Tran HN, Hansen PE, Do MHN, Le TN (2015) A simple, effective, green method for the regioselective 3-acylation of unprotected indoles. Molecules 20:19605–19619
35. Faul MM, Winneroski LL (1997) Palladium-catalyzed acylation of a 1,2-disubstituted 3-indolylzinc chloride. Tetrahedron Lett 38:4749–4752
36. Black DSC, Kumar N, Mitchell PSR (2002) Synthesis of pyrroloquinolines as indole analogues of flavonols. J Org Chem 67:2464–2473
37. Watterson SH, Dhar TGM, Ballentine SK, Shen Z, Barrish JC, Cheney D, Fleener CA, Roleau KA, Townsend R, Hollenbaugh DL, Iwanovicz EJ (2003) Novel indole-based inhibitors of IMPDH: introduction of hydrogen bond acceptors at indole C-3. Bioorg Med Chem Lett 13:1273–1276
38. Mphahlele MJ, Maluleka MM (2016) Trifluoroacetylation of indole-chalcones derived from the 2-amino-3-(arylethynyl)-5-bromo-iodochalcones. J Fluorine Chem 189:88–95

Chapter 24
Processability Issue in Inverted Organic Solar Cells

F.J. Lim and A. Krishnamoorthy

Abstract Though impressive progress on the power conversion efficiency of organic solar cells (OSCs) has been made, their practical use is still hampered due to their inherent poor stability. Under ambient conditions the long term stability of non-encapsulated organic solar cells with conventional device architecture is lower than the technical lifetime of devices with an inverted configuration. The removal of the interface between the ITO (indium tin oxide) layer and the acidic PEDOT:PSS layer along with the substitution of a low work function metal electrode with a high work function metal electrode in the inverted device configuration renders relatively higher stability in these devices. Though encouraging device performance (with respect to both stability and efficiency) is seen in inverted organic solar cells, there exists a few technical challenges in the fabrication of these devices namely (1) processability; (2) light-soaking and (3) stability. In this short review we will focus on tackling the processability issue of the device fabrication. Firstly, an overview of recent developments of inverted organic solar cells (IOSC) using various photoactive layers and charge transport layers will be presented. Secondly, the inferior wettability of the hydrophilic PEDOT:PSS hole transport layer onto the photoactive layer such as the P3HT:PCBM blend, which is hydrophobic in nature will be discussed. Thirdly, we will summarize how this issue was addressed successfully and finally, a brief conclusion and an outlook for solution-processed inverted organic solar cells will be presented.

Keywords Inverted organic solar cells • Hole transport layer • PEDOT:PSS • Wettability • Fluorosurfactant

F.J. Lim (✉)
Solar Energy Research Institute of Singapore (SERIS), National University of Singapore, 7 Engineering Drive 1, Singapore 117574, Singapore
e-mail: serlfj@nus.edu.sg

A. Krishnamoorthy (✉)
SRM Research Institute and Department of Chemistry, SRM University, Kattankulathur, Chennai, Tamilnadu 603203, India
e-mail: ananthanarayanan.k@ktr.srmuniv.ac.in; kananthaz@gmail.com

P. Ramasami et al. (eds.), *Emerging Trends in Chemical Sciences*,
DOI 10.1007/978-3-319-60408-4_24

24.1 Introduction

Fossil fuels such as coal, oil and natural gas are the major sources of energy generation in the world [1, 2]. Recent reports indicate that the annual global energy consumption in 2016 is around 153,000 TWh, with the highest consumption being in the Asia region [2]. With these high consumptions, the continual dependence of the energy on the fossil fuels increases the emission of carbon dioxide (CO_2). Renewable energy (solar and wind power) has been highly in demand and has served 35% of global final energy production in 2015 [2]. Furthermore, the cost of solar energy has been continually decreasing over the years; the levelised cost of electricity (LCOE) of solar photovoltaics (PV), i.e. the net unit-cost of electricity over the lifetime of a solar system, has reached to as low as USD 0.126/kWh in 2015 [3]. As a result, the global solar market has been growing at about 30% annually. According to Greentech Media, the total cumulative global installation capacity of solar PV in 2014 was around 175 GW, and it is expected to grow to about 700 GW by 2020 [4], out of which, silicon wafer based solar cells dominate the market share with 90% and remaining market share by thin film solar cells [5]. According to Green et al., the record module efficiency of a monocrystalline silicon solar 120-cells module with an area of 15,140 $cm^2$is 19.9% by Trina Solar [6]. With proper integration of the solar modules and an appropriate energy storage system, it will be feasible to supply base load power, effectively replacing the conventional energy sources.

Although significant improvements have been made in the energy payback time, silicon used per watt and device efficiency, the silicon solar panels are opaque and heavy in weight. The thick p-n junction makes the solar panel appear black, non-aesthetically pleasing and non-transparent, thus only limiting its use on the rooftops. Moreover, the finishing of a silicon solar panel is rigid and generally has a distributed weight of approximately 20 kg/m^2 [7]. These attributes limit their applications on areas such as building-integrated photovoltaics (BIPV) and consumer electronics. Furthermore, typical solar technologies have a negative temperature coefficient (i.e. efficiency decreases when temperature increases) and a poor low-light performance under outdoor conditions. Thus, third generation solar technology like organic solar cells has been developed to overcome the abovementioned drawbacks.

Organic solar cells (OSC) based on solution-processed semiconducting polymers have been a hot topic of research since the 1980s [8, 9]. The evolution of the OSC devices has started from single organic layer [8, 10], bi-layer planar heterojunction [11] to bulk heterojunction (BHJ) [12, 13] designs. BHJ structure has been widely adopted to produce more efficient devices with a world record of 10.8% using thieno[3,4-b]thiophene/benzodithiophene (PTB7), [6,6]-phenyl C_{71} butyric acid methyl ester ($PC_{71}BM$), and an IR-absorbing diketopyrrolopyrrole based porphyrin small molecule (DPPEZnP-TEH) [14].

Organic solar cell presents several advantages over conventional inorganic counterparts: lightweight, flexible, semi-transparent, easy color-tuning, positive

temperature coefficient, low energy intensive fabrication protocols and sensitive to low-light condition [15]. As a result, it can be applied in several niche applications where it is not possible to use conventional silicon solar cells. For instance, the flexible, lightweight and semi-transparent nature enables them to be integrated easily onto a variety of surfaces such as fabrics, mobile electronics and windows. Apart from that, organic semiconductors, which have variety of colors, are also suitable for aesthetically significant application like BIPV. Furthermore, due to the nature of charge hopping transport in organic semiconductors, it has a positive temperature coefficient, i.e. device efficiency increases as the surrounding temperature gets higher. Most importantly, it also has a more superior performance in low-light (diffused-light) conditions [16, 17], which makes it suitable for indoor power generation. Therefore, without directly competing with conventional silicon solar cells, OSC can potentially fill in the areas wherein the silicon solar cells cannot be used.

Even though OSCs have several advantages over silicon solar cells they fall short on two important factors: the device efficiency and the device lifetime. The commercialization of organic solar cells is still largely hampered because of the above mentioned factors. To ensure the feasibility of OSC modules, the costs involving manufacture, packaging, installation and maintenance have to be covered by the revenue proportional to its power output. Thus, it is vital for the cell efficiency to exceed 10% before it can be considered commercially viable [18]. Recently a high device efficiency of 10.6% was achieved by adopting a tandem device architecture using a low band gap polymer [19]. However, to fully achieve a cost-effective OSC, a high-efficiency single junction device is desired. On June 2015, the National Renewable Energy Laboratory (NREL) has updated the solar cell efficiency chart with a breakthrough efficiency exceeding 11% for organic solar cells with morphologically optimized PffBT4T-C_9C_{13}:$PC_{71}BM$ [6, 20–22]. These recent improvements in the efficiency value suggest a good prospect for OSC. From the industry aspect, a breakthrough in device efficiency of 13.2% was announced by Heliatek GmbH in 2016 on multi-junction vacuum-processed small molecules based OSC [23]. Some of the market players who are involved in the production of organic photovoltaics are Heliatek, Sono-tek, Solarmer and Belectric [15, 24–26].

24.1.1 Research Areas in Organic Solar Cells

The research in OSC can be diversified into three main overlapping areas: (1) efficiency; (2) stability; and (3) scalability, as shown in Fig. 24.1. Each area would trigger a series of research directions.

Firstly, boosting the efficiency of OSC towards and surpass 10% is an always-prevalent challenge. According to NREL, the efficiency of OSC has grown since 1980s from 0.8% to a current 11.5% at 2015 [21]. The enhancement of device efficiency is primarily achieved by developing novel photoactive layers. A

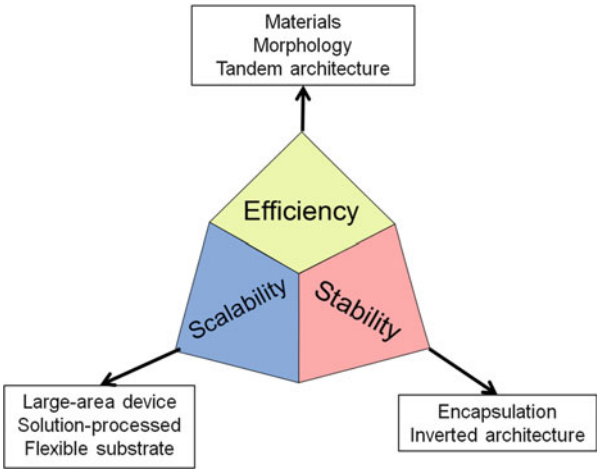

Fig. 24.1 Research areas of organic solar cells

continuous development of low band gap conjugated semiconductor materials, tailoring of donor-acceptor morphology and adopting new device architecture are few of the directions taken by the research community. Achieving the goal may also require an alternative design on the device architecture. Tandem architecture was adopted to harvest a broader spectrum of sunlight with effectively thicker device and a larger open-circuit voltage [27]. However, this design is limited by the effective short-circuit current, which is limited by the absorber layer with the lower current. Various device optimization and material selection are needed in order for the device to deliver its highest capability.

Secondly, the scalability of the device is important to fabricate organic solar cells or solar modules eventually in a large-scale, roll-to-roll and solution-processed way. To do so, the conventional spin coating and thermal evaporation methods on a rigid substrate have to be abandoned as they give low-throughput and are incompatible to large-area, flexible devices [18, 28]. A continuous roll-to-roll processing has to be devised for a high-throughput and large-area compatible capability on flexible substrates. However, the implementation of this method often requires a lot of optimization steps which generally account for the observed lower efficiency [29]. The realization of the processability of OSC is vital to take them one step closer to the road of product manufacturing.

Lastly, apart from achieving high efficiency and roll-to-roll processability in OSC, one must not overlook the device stability. Søndergaard et al. have proposed a goal of 10-10 (10% efficiency and 10 years of stability) as the transcending point of OSC from laboratory scale research to industrial scale production [28]. This goal is, in the authors' opinion, extremely important for the device practicality because the inherent poor stability of the device severely hampers their practical value. The degradation of organic semiconductors in oxygen and moisture remains a key point to be addressed by the research community [30]. These materials degrade rapidly in the presence of oxygen and moisture, hindering the energy harvesting capability of

the device. PEDOT:PSS on top of the indium-doped tin oxide (ITO) is highly sensitive to moisture, only capable to function for 1 h without proper encapsulation [31]. Due to the acidity of PEDOT:PSS, it will often etch into ITO substrate upon moisture, causing degraded contact [32]. Furthermore, the presence of low work function metals such as aluminium (Al) as cathode which oxidizes easily in air will also cause reduced longevity of the device lifetime [33]. Thus, to safeguard the instability of the device, high-cost encapsulation techniques are mandatory. Though glass-glass type encapsulation results in the best device lifetime, it eliminates the flexible characteristics for OSC. Research efforts on developing proper device encapsulations were carried out [34]. However, tackling the problem from the root, i.e. ITO etching by PEDOT:PSS and low-work function Al, is a better strategy.

To this end, inverted organic solar cell (IOSC), which 'inverts' the sequencing of layers, was adopted to address these root causes. The adoption of such architecture could effectively contribute to a significant improvement in the device lifetime [35].

In this short review, we will mainly focus on the scalability of the organic solar cell, in particular inverted organic solar cells (IOSC), due to its wide adoption by the research community. Firstly, an overview of IOSC will be discussed, with a summary of recent developments of such architecture using various photoactive layer materials and transport layers. Secondly, the processability issue of PEDOT:PSS hole transport layer in IOSC will be discussed. Thirdly, the solutions adopted by research community will be summarized and compared. Lastly, the review will end with a brief conclusion and outlook to the future of IOSC.

24.1.2 An Overview of Inverted Organic Solar Cells

IOSC are gaining attention from the research community due to their superior device stability. Since 2006, device efficiency of at least 3% was successfully achieved using P3HT:$PC_{61}BM$ [36, 37]. A stable, solution-processable IOSC on flexible substrate with an efficiency of 3.3% was also achieved [35]. In fact, the record high OSC efficiency of 10.8% using PffBT4T-2OD:$TC_{71}BM$ as photoactive layer has been realized with the inverted architecture [20]. Table 24.1 shows the summary of recent development of device efficiencies for IOSC using various photoactive layer materials.

Many results have indeed proven that the IOSC have longer device stability than conventional devices [35, 45–49]. Yang et al. reported an inverted bulk heterojunction (BHJ) device based on PBDTTT-C-T/$PC_{71}BM$ blend with gold nanoparticles and nanograting design with an efficiency of 8.8% [50]. Hau et al. demonstrated an inverted flexible OSC device using ZnO as an interfacial layer which could retain 80% of the initial device performance after 40 days of exposure in air [35]. McGehee et al. reported a PCDTBT polymer based OSC with an inverted architecture that shows a shelf life of 7 years under encapsulation in

Table 24.1 Summary of recent development of device efficiency for inverted organic solar cells using various photoactive layer materials

ETL	Donor[a]	Acceptor[a]	HTL	Metal	V_{oc} (mV)	j_{sc} (mA/cm^2)	FF (%)	η (%)	Year	Ref.
PFN	PTB-7	$PC_{71}BM$	MoO_3	Ag	740	17.2	72	9.2	2012	[38]
ZnO	PTB-7	$PC_{71}BM$	MoO_3 WO_3	Al	710 720	13.5 14.3	67 64	6.5 6.7	2013	[39]
Zn-C_{60}	PTB7-Th	$PC_{71}BM$	MoO_3	Ag	800	15.7	74	9.4	2013	[40]
ZnO-CsSt	PTB-7	$PC_{71}BM$	MoO_3	Al	730 740	15.9 17.1	62 69	7.0 8.7	2014	[41]
ZnO	PNTz4T	$PC_{61}BM$ $PC_{71}BM$	MoO_x	Ag	729 708	18.2 19.4	74 73	9.6 9.8	2015	[42]
ZnO	PffBT4T-2OD	$TC_{71}BM$	MoO_x	Al	770	18.8	75	10.8	2015	[20]
ZnO-HBPA	PffBT4T-2OD	$PC_{71}BM$	MoO_x	Ag	700	15.2	68	7.6	2016	[43]
ZnO	FBT	$PC_{71}BM$	MoO_x	Ag	720	19.0 [20]	66	8.9	2017	[44]

[a]For full chemical names of the photoactive layer materials and solvents, please refer to the respective journals

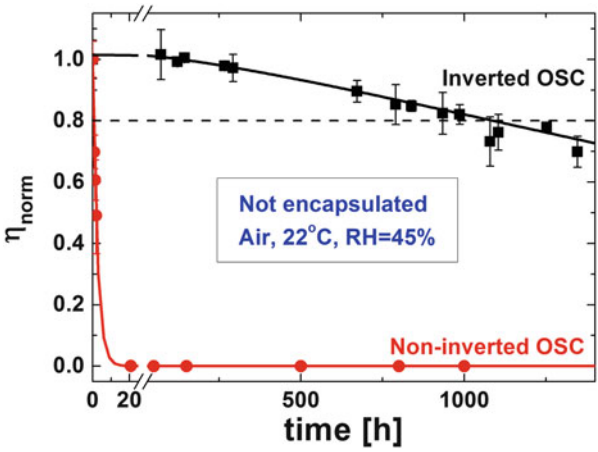

Fig. 24.2 Comparison of the lifetime of conventional and inverted P3HT:$PC_{61}BM$ OSC under exposure to ambient condition without encapsulation

ambient conditions [51]. Park et al. developed a dynamic annealed ZnO electron transport layer with 94% of device efficiency retained after exposure in air for 50 days [52]. Lima et al. also conducted an outdoor stability study of IOSC with V_2O_5 as hole transport layer able to retain 80% of its initial device efficiency for 900 h [49]. In fact, preliminary testing of a conventional and inverted architecture based on P3HT:$PC_{61}BM$ in air without encapsulation in our laboratory also shows similar enhancements in device lifetime (Fig. 24.2).

There are two major modifications in the device structure of inverted OSC: (1) 'inversion' of the transport layers, and (2) the change of metal with higher work function. Firstly, the PEDOT:PSS hole transport layer (HTL) is shifted upwards between the photoactive layer and the metal contact. It is found that the acidity of PEDOT:PSS upon moisture and oxygen contact could be the major cause for the instability of the cell as it etches the ITO [31, 53]. Thus, shifting the PEDOT:PSS layer to the top of the photoactive layer prevents the etching of ITO. Instead of low work function metal, an air-stable high work function metal such as silver (Ag) or gold (Au) is used as the metal electrode. As a result, the direction of carrier extraction is 'inverted' with respect to the conventional architecture. The electrons are now extracted at ITO while holes are extracted at the metal electrode (Fig. 24.3). Such phenomenon can be clearly seen in the energy level diagram for an IOSC shown in Fig. 24.4, where the excitons are generated in the photoactive layer and dissociated at the organic interfaces and are then subsequently extracted to respective contacts.

24.1.3 Transport Layers in Inverted Organic Solar Cells

Similar to its non-inverted counterpart, IOSCs require electron transport layers (ETL) and hole transport layers (HTL) for an effective charge extraction. Efficient

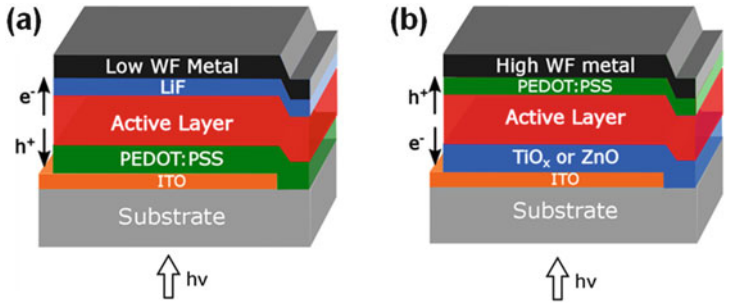

Fig. 24.3 Schematic representation for (**a**) Conventional OSC cell structure and (**b**) inverted OSC. Note the direction of charge collections between the two types of devices

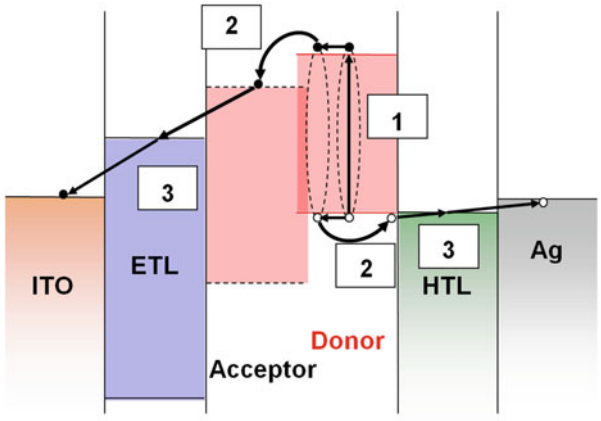

Fig. 24.4 Energy level diagram and charge transport scheme of a typical inverted organic solar cell. The *red lines* and *black dashed lines* correspond to HOMO and LUMO of donor and acceptor, respectively. The charge transport scheme is denoted (1) exciton generation; (2) exciton dissociation and (3) charge extraction

charge extraction would lead to a minimal recombination loss and low leakage current. Several n-type metal oxides such as TiO_x [46, 54], ZnO [43, 55] and Cs_2CO_3 [56, 57] were generally used as ETL. Materials such as poly(3,4-ethylenedioxythiophene):poly(styrene sulfonate) (PEDOT:PSS) [45, 58, 59], p-type metal oxides [39, 49, 60] and nanoparticles [61] were normally used as HTL. Charge transport layers play an extremely vital role in IOSC devices as they affect the energy alignment between the transport layer and photoactive layer interface, tailoring built-in field, improve charge selectivity, and improve device stability.

Although IOSC provides an excellent way to tackle the poor device stability in organic solar cells, it is not yet completely feasible to be used in large-scale manufacturing and practical energy harvesting applications. The main source of

Table 24.2 List of IOSC device performance with various hole transport layer materials and deposition methods

Photoactive material	HTL (formulation)	Additives (for PEDOT:PSS only)	HTL deposition method	Film thickness (nm)	η (%)	Ref.	Year
P3HT: $PC_{71}BM$	MoO_x	n/a	Thermal evaporation	2	4.0	[57]	2011
PTB7: $PC_{71}BM$	MoO_x	n/a	Thermal evaporation	10	6.5	[39]	2013
P3HT: $PC_{61}BM$	PEDOT:PSS (CPP 105 D)	Dynol	Spin coat	250	1.4	[62]	2005
P3HT: $PC_{61}BM$	PEDOT:PSS (unspecified)	Triton X-100	Spin coat	40	4.0	[63]	2010
P3HT: $PC_{61}BM$	PEDOT:PSS (P VP AI 4083)	Unspecified surfactant	Spin coat	50	3.0	[64]	2011
P3HT: $PC_{61}BM$	PEDOT:PSS (P VP AI 4083)	Not reported	Spin coat	30	3.6	[65]	2011
P3HT: $PC_{61}BM$	PEDOT:PSS (Clevios PH)	Isopropanol	Doctor blade	120	2.4	[66]	2011
P3HT: $PC_{61}BM$	PEDOT:PSS (P VP AI 4083)	Capstone FS-31	Spin coat	80	3.1	[37]	2012
P3HT: $PC_{61}BM$	PEDOT:PSS	Surfynol 104 PA	Spin coat	40	4.0	[67]	2013
P3HT: $PC_{61}BM$	VO_x	n/a	Spin coat	25	3.9	[65]	2011
PTB7: $PC_{71}BM$	WO_x	n/a	Thermal evaporation	5	6.7	[39]	2013
P3HT: $PC_{61}BM$	CoO_x	n/a	Thermal evaporation	10	2.7	[68]	2015
P3HT: $PC_{61}BM$	ITO nanoparticle	n/a	Spin coat	16	3.0	[61]	2016

the problem stems from the charge transport layers in the device. The configuration and material used for the charge transport layers give rise to two serious issues: (i) wettability issue of PEDOT:PSS hole transport layer on photoactive layers and (ii) light-soaking issue due to the use of metal oxide electron transport layer. Among the wide range of materials available for HTL in IOSC, PEDOT:PSS is often more preferred due to its ease of solution-processing. This is because metal oxide based HTL is generally deposited by means of thermal evaporation, while PEDOT:PSS can be easily deposited by printing or coating methods (Table 24.2).

24.2 Processability Issue in Inverted Organic Solar Cells

24.2.1 PEDOT:PSS Hole Transport Layer

PEDOT is a conductive polymer which adopts 3,4-dialkoxythiophene structures. Its conductive nature originates from the polymerization of the bicyclic 3,4-ethylenedioxythiophene (EDOT) and its derivatives. From the structure of the polymer shown in Fig. 24.5, the presence of oxygen atoms adjacent to the thiophene ring stabilizes the positively charged EDOT during polymerization. As a result, a conductive PEDOT polymer is formed [69]. Due to the inherent chemical structure and the hydrophilicity of the material, PEDOT:PSS is intrinsically an acidic and hygroscopic compound. Typical conductivity of PEDOT is in the range of 500 S cm^{-1}. However, such high conductivity is not suitable for hole transport action because large lateral conductivity will occur, leading to unwanted device interconnections. When coupled with PSS at various ratios, its conductivity can be tuned to as low as 10^{-3} S cm^{-1} (Table 24.3). PEDOT:PSS with lower conductivity grade (Clevios™ P VP AI 4083) is normally used as the hole transport layer for organic solar cells.

24.2.2 Wettability Issue of PEDOT:PSS in Inverted Organic Solar Cells

Coating of the PEDOT:PSS onto the photoactive layer remains a serious technical challenge involved in the fabrication of these devices. The hydrophobic nature of the underlying photoactive layer (such as P3HT:$PC_{61}BM$) produces high surface tension upon contact with hydrophilic PEDOT:PSS, causing a serious wettability issue. Without the aid of additives, PEDOT:PSS can hardly be coated onto the

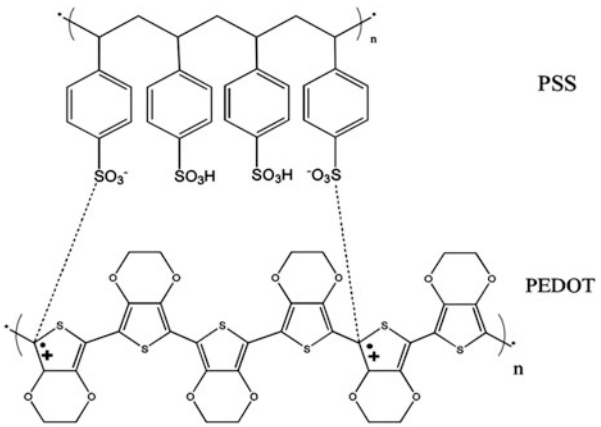

Fig. 24.5 Chemical structure of PEDOT:PSS

Table 24.3 List of PEDOT:PSS and its respective properties [69]

Type of PEDOT:PSS	PEDOT:PSS ratio	Conductivity (S/cm)	Applications
Clevios™ PH1000	1:2.5	850	Transparent electrodes
Clevios™ PH500	1:2.5	300	Transparent electrodes
Clevios™ P VP AI 4083	1:6	10^{-3}	Transport layer
Clevios™ P VP CH 8000	1:20	10^{-5}	Transport layer

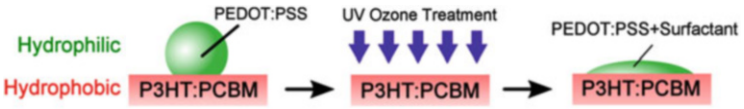

Fig. 24.6 Schematic showing the necessity of UV-ozone treatment on photoactive layers prior to coating PEDOT:PSS with conventional surfactants modification

photoactive layer. Upon contact, PEDOT:PSS solution would form a high surface angle on the photoactive layer surface (Fig. 24.6 (left)). Consequently, this will lead to poor film morphology and inferior device performance. Removal of PEDOT:PSS as a hole transport layer (HTL) is not an option to resolve this issue as this will render the photoactive layer susceptible to oxygen and moisture, causing detrimental effects to the device performance. Furthermore, the absence of HTL will also result in poor device performance [70]. Replacement of PEDOT:PSS with other p-type oxides is also undesired because this would subject the device incompatible for solution-processing (see Table 24.2). Therefore, use of additives is necessary to circumvent this wettability issue.

24.3 Modification of PEDOT:PSS with Additives

To lower the surface energy of PEDOT:PSS, a non-ionic additive should be used. On one hand, anionic additives such as sodium dodecyl sulfate (SDS) could significantly enhance the conductivity by substituting PSS anion by the anions [71]. As shown in Table 24.3, high conductivity PEDOT:PSS is not a suitable HTL as it will cause undesired lateral device connections. On the other hand, cationic additives would neutralize the PSS anion by forming stable complex which could affect the morphology of the PEDOT:PSS film. The addition of non-ionic surfactant neither alters its conductivity significantly, nor affects its morphology to undesired state. As a result, non-ionic additives are generally used to modify the wettability of PEDOT:PSS [62, 63, 72].

In Table 24.2, an overview of the additives into PEDOT:PSS before coating onto the photoactive layer was presented. Isopropyl alcohol (IPA) is the most commonly used additive for PEDOT:PSS to reduce the surface energy [66]. Other alternatives such as Dynol [62], Triton X-100 [63] and Zonyl FS-300 [72] were also used previously. The use of fluorosurfactants such as Zonyl FS-300 is more beneficial

Table 24.4 Device performance of inverted organic solar cells with device architecture ITO/TiO_x/P3HT:$PC_{61}BM$/(PEDOT:PSS + additives)/Ag using various types of additives at TiO_x thickness of ~100 nm

PEDOT:PSS formulation	V_{oc} (mV)	j_{sc} (mA/cm^2)	FF (%)	η (%)	Ref.
PEDOT:PSS + IPA	580	6.3	55	2.1	[58]
PEDOT:PSS + Zonyl FS300	560	7.9	48	2.2	[29]
PEDOT:PSS + CFS-31	610	7.8	65	3.1	[37]

than hydrocarbon based surfactants (Triton X-100) in reducing the surface tension between the two organic layers. This is attributed to the lipophobic nature of the C-F tail which tends to concentrate at liquid-air interface, in contrary to the lipophilic C-H tail that concentrates in condensed phase interfaces [73]. In the fabrication of inverted OSCs, Zonyl FS-300 is often used together with IPA because Zonyl FS-300 or IPA alone is insufficient for PEDOT:PSS to lie within the wetting envelope of P3HT:$PC_{61}BM$ [29]. An undesirable and detrimental UV ozone surface treatment of photoactive layer prior to PEDOT:PSS coating is often required to increase its surface energy (Fig. 24.6). Our group has adopted an alternative fluorosurfactant (Capstone® Dupont™ FS-31) as additive for PEDOT:PSS which could resolve the wettability issue for various photoactive layer materials without the need for detrimental UV-ozone treatment [37, 47]. Such properties of the material greatly enhance the compatibility of the device in roll-to-roll solution-processed capability.

Other than its excellent wettability, Capstone® Dupont™ FS-31 (CFS-31) is a good alternative for common additives such as Zonyl FS-300 in the fabrication of IOSC. CFS-31 is capable of providing remarkably low surface tension (~15 mN/m) compared to Zonyl FS-300 (~23 mN/m) in aqueous or solvent-based products (ideal for PEDOT:PSS) that could enable better wetting. When made into device, it shows a non-destructive property to device efficiency (Table 24.4) [37, 48]. Fourier transform infrared spectroscopy (FTIR) studies have shown that the addition of CFS-31 into PEDOT:PSS does not alter the chemical structure of the coating materials (Fig. 24.7) [37].

24.4 Conclusions and Outlook

A brief review of inverted organic solar cells, with PEDOT:PSS as hole transport layer was presented. Through a review of recent advances in inverted organic solar cells and different types of transport layers materials, it was found that PEDOT:PSS is still the best candidate for solution-processed hole transport layer. However, due to its hydrophilic property, it faces a wettability issue in the fabrication of such device, posing an inherent processability challenge. It is undeniable that the processability issue is one of the main hindrances hampering its adoption as the main design in industry. To this end, a range of additives to PEDOT:PSS have been

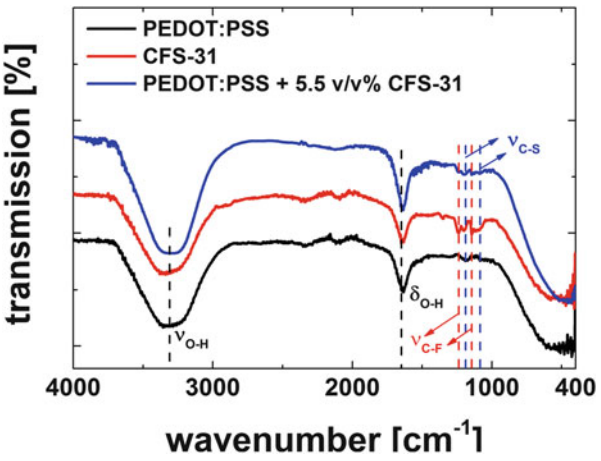

Fig. 24.7 FTIR spectra for PEDOT:PSS (*black*, *bottom*), CFS-31 fluorosurfactant (*red*, *middle*) and combination of PEDOT:PSS and CFS-31 (*blue*, *top*). The demarcated peaks are labeled according to the different associated modes of the chemical bond

outlined and compared, with Capstone® Dupont™ FS-31 (CFS-31) as the best candidate for roll-to-roll, solution-processed inverted organic solar cells.

Moving forward, in view of industry viability and taking reference with major industry players of organic photovoltaics in PV industry such as Heliatek and infinityPV, it is evident that roll-to-roll streamlined cell or module manufacturing process is the sensible direction to point towards to. As a result, other than focusing on improving the device efficiency, researchers should put more emphasis in the processability of the device, which indirectly produces merit to the device stability, increasing the product lifetime of the technology.

References

1. Institute for Energy Research (2015) Fossil fuels
2. Enerdata (2016) Global energy statistical yearbook 2016
3. International Renewable Energy Agency (2015) Power generation summary charts
4. Greentech Media (2015) Global PV demand outlook 2015-2020: exploring risk in downstream solar markets – GTM research
5. Greentech Media (2015) 8 Solar trends to follow in 2015
6. Green MA, Emery K, Hishikawa Y et al (2017) Solar cell efficiency tables (version 49). Prog Photovolt 25:3–13
7. Ranjan S, Balaji S, Panella RA et al (2011) Silicon solar cell production. Comput Chem Eng 35:1439–1453
8. Chamberlain GA (1983) Organic solar cells: a review. Sol Cells 8:47–83
9. Benanti T, Venkataraman D (2006) Organic solar cells: an overview focusing on active layer morphology. Photosynth Res 87:73–81
10. Wöhrle D, Meissner D (1991) Organic solar cells. Adv Mater 3:129–138
11. Tang CW (1986) Two-layer organic photovoltaic cell. Appl Phys Lett 48:183–185
12. Halls JJM, Walsh CA, Greenham NC et al (1995) Efficient photodiodes from interpenetrating polymer networks. Nature 376:498–500

13. Yu G, Gao J, Hummelen JC et al (1995) Polymer photovoltaic cells: enhanced efficiencies via a network of internal donor-acceptor heterojunctions. Science 270:1789–1790
14. Nian L, Gao K, Liu F et al (2016) 11% efficient ternary organic solar cells with high composition tolerance via integrated near-IR sensitization and interface engineering. Adv Mater 28:8184–8190
15. Heliatek (2015) Unique – HeliaFilm® perfectly combines design and functionality
16. You J, Dou L, Yoshimura K et al (2013) A polymer tandem solar cell with 10.6% power conversion efficiency. Nat Commun 4:1446
17. Guo S, Brandt C, Andreev T et al (2014) First step into space: performance and morphological evolution of P3HT:PCBM bulk heterojunction solar cells under AM 0 illumination. ACS Appl Mater Interfaces 6:17902–17910
18. Søndergaard RR, Hösel M, Krebs FC (2013) Roll-to-roll fabrication of large area functional organic materials. J Polym Sci Polym Phys 51:16–34
19. Li G, Zhu R, Yang Y (2012) Polymer solar cells. Science 6:153–161
20. Liu Y, Zhao J, Li Z et al (2014) Aggregation and morphology control enables multiple cases of high-efficiency polymer solar cells. Nature Commun 6293:5293
21. National Center for Photovoltaic Research (2015) Best research-cells efficiencies. National Renewable Energy Laboratory (NREL)
22. Zhao J, Li Y, Yang G et al (2016) Efficient organic solar cells processed from hydrocarbon solvents. Nat Energy 1:15027
23. Heliatek (2016) Heliatek sets new organic photovoltaic world record efficiency of 13.2%. Available at: http://www.heliatek.com/en/press/press-releases/details/heliatek-sets-new-organic-photovoltaic-world-record-efficiency-of-13-2
24. Sono-Tek Corporation (2015) www.sono-tek.com/
25. Solarmer (2015) www.solarmer.com/
26. Belectric (2015) www.belectric.com/
27. Sista S, Hong Z, Chen LM et al (2011) Tandem polymer photovoltaic cells – current status, challenges and future outlook. Energ Environ Sci 4:1606–1620
28. Søndergaard R, Hösel M, Angmo D et al (2012) Roll-to-roll fabrication of polymer solar cells. Mater Today 15:36–49
29. Voigt MM, MacKenzie RCI, Yau CP et al (2011) Gravure printing for three subsequent solar cell layers of inverted structures on flexible substrates. Sol Energ Mat Sol C 95:731–734
30. Espinosa N, García-Valverde R, Urbina A et al (2012) Life cycle assessment of ITO-free flexible polymer solar cells prepared by roll-to-roll coating and printing. Sol Energ Mat Sol C 97:3–13
31. Kawano K, Pacios R, Poplavskyy D et al (2006) Degradation of organic solar cells due to air exposure. Sol Energ Mat Sol C 90:3520–3530
32. Kim H, Nam S, Lee H et al (2011) Influence of controlled acidity of hole-collecting buffer layers on the performance and lifetime of polymer: fullerene solar cells. J Phys Chem C 115:13502–13510
33. Gaynor W, Lee J-Y, Peumans P (2009) Fully solution-processed inverted polymer solar cells with laminated nanowire electrodes. ACS Nano 4:30–34
34. Ahmad J, Bazaka K, Anderson LJ et al (2013) Materials and methods for encapsulation of OPV: a review. Renew Sustain Energy Rev 27:104–117
35. Hau SK, Yip H-L, Baek NS et al (2008) Air-stable inverted flexible polymer solar cells using zinc oxide nanoparticles as an electron selective layer. Appl Phys Lett 92:253301–253303
36. White MS, Olson DC, Shaheen SE et al (2006) Inverted bulk-heterojunction organic photovoltaic device using a solution-derived ZnO underlayer. Appl Phys Lett 89:143517
37. Lim FJ, Krishnamoorthy A, Luther J et al (2012) Influence of novel fluorosurfactant modified PEDOT:PSS hole transport layer on the performance of inverted organic solar cells. J Mater Chem 22:25057–25064
38. He Z, Zhong C, Su S et al (2012) Enhanced power-conversion efficiency in polymer solar cells using an inverted device structure. Nat Photonics 6:593–597

39. Lampande R, Kim GW, Boizot J et al (2013) A highly efficient transition metal oxide layer for hole extraction and transport in inverted polymer bulk heterojunction solar cells. J Mater Chem A 1:6895–6900
40. Liao S-H, Jhuo H-J, Cheng Y-S et al (2013) Fullerene derivative-doped zinc oxide nanofilm as the cathode of inverted polymer solar cells with low-band gap polymer (PTB7-Th) for high performance. Adv Mater 25:4766–4771
41. Wang G, Jiu T, Tang G et al (2014) Interface modification of ZnO-based inverted PTB7: PC71BM organic solar cells by cesium stearate and simultaneous enhancement of device parameters. ACS Sustain Chem Eng 2:1331–1337
42. Vohra V, Kawashima K, Kakara T et al (2015) Efficient inverted polymer solar cells employing favourable molecular orientation. Nat Photonics 9:403–408
43. Juang T-Y, Hsu Y-C, Jiang B-H et al (2016) Highly efficient inverted organic photovoltaics containing aliphatic hyperbranched polymers as cathode modified layers. Macromolecules 49:7837–7843
44. Zhou JC, Zhang G, Zhong C et al (2017) Toward high efficiency polymer solar cells: influence of local chemical environment and morphology. Adv Energ Mater 7:1601081
45. Kanwat A, Jang J (2014) Extremely stable organic photovoltaic incorporated with WOx doped PEDOT:PSS anode buffer layer. J Mater Chem C 2:901–907
46. Lim FJ, Set YT, Krishnamoorthy A et al (2015) Addressing the light-soaking issue in inverted organic solar cells using chemical bath deposited fluorinated TiOx electron transport layer. J Mater Chem A 3:314–322
47. Lim FJ, Krishnamoorthy A, Ho GW (2015) Device stability and light-soaking characteristics of high-efficiency benzodithiophene–thienothiophene copolymer-based inverted organic solar cells with F-TiOx electron-transport layer. ACS Appl Mater Interfaces 7:12119–12127
48. Lim FJ, Krishnamoorthy A, Ho GW (2016) All-in-one solar cell: stable, light-soaking free, solution processed and efficient diketopyrrolopyrrole based small molecule inverted organic solar cells. Sol Energ Mat Sol C 150:19–31
49. Lima FS, Beliatis MJ, Roth B et al (2016) Flexible ITO-free organic solar cells applying aqueous solution-processed V_2O_5 hole transport layer: an outdoor stability study. APL Mater 4:026104
50. Li X, Choy WCH, Huo L et al (2012) Dual plasmonic nanostructures for high performance inverted organic solar cells. Adv Mater 24:3046–3052
51. Peters CH, Sachs-Quitana IT, Kastrop JP et al (2011) High efficiency polymer solar cells with long operating lifetimes. Adv Energy Mater 1:491–494
52. Park H-Y, Lim D, Kim K-D et al (2013) Performance optimization of low-temperature-annealed solution-processable ZnO buffer layers for inverted polymer solar cells. J Mater Chem A 1:6327–6334
53. Norrman K, Madsen MV, Gevorgyan SA et al (2010) Degradation patterns in water and oxygen of an inverted polymer solar cell. J Am Chem Soc 132:16883–16892
54. Ou K-L, Tadytin D, Steirer KX et al (2013) Titanium dioxide electron-selective interlayers created by chemical vapor deposition for inverted configuration organic solar cells. J Mater Chem A 1:6794–6803
55. Trost S, Becker T, Polywka A et al (2016) Avoiding photoinduced shunts in organic solar cells by the use of tin oxide (SnOx) as electron extraction material instead of ZnO. Adv Energy Mater 6:1600347–1600355
56. Liao H-H, Chen L-M, Xu Z et al (2008) Highly efficient inverted polymer solar cell by low temperature annealing of Cs_2CO_3 interlayer. Appl Phys Lett 92:173303
57. Lee YI, Youn JH, Ryu MS et al (2011) Electrical properties of inverted poly (3-hexylthiophene): Methano-fullerene [6,6]-phenyl C71-butyric acid methyl ester bulk hetero-junction solar cell with Cs_2CO_3 and MoO_3 layers. Sol Energy Mater Sol Cells 95:3276–3280
58. Sun H, Weickert J, Hesse HC et al (2011) UV light protection through TiO_2 blocking layers for inverted organic solar cells. Sol Energy Mater Sol Cells 95:3450–3454

59. Ouyang J (2013) Secondary doping methods to significantly enhance the conductivity of PEDOT:PSS for its application as transparent electrode of optoelectronic devices. Displays 34:423–436
60. Stenta C (2013) Study and characterization of ZnPc:C60/MoOx interface in organic solar cells by means of photoelectron spectroscopy. Universidade Nova de Lisboa, Portugal, p 73
61. Wahl T, Zellmer S, Hanisch J et al (2016) Thin indium tin oxide nanoparticle films as hole transport layer in inverted organic solar cells. Thin Solid Films 616:419–424
62. Glatthaar M, Niggemann M, Zimmermann B et al (2005) Organic solar cells using inverted layer sequence. Thin Solid Films 491:298–300
63. Baek WH, Choi M, Yoon TS et al (2010) Use of fluorine-doped tin oxide instead of indium tin oxide in highly efficient air-fabricated inverted polymer solar cells. Appl Phys Lett 96:133506
64. Boix PP, Ajuria J, Pacios R et al (2011) Carrier recombination losses in inverted polymer: fullerene solar cells with ZnO hole-blocking layer from transient photovoltage and impedance spectroscopy techniques. J Appl Phys 109:074514
65. Chen C-P, Chen Y-D, Chuang S-C (2011) High-performance and highly durable inverted organic photovoltaics embedding solution-processable vanadium oxides as an interfacial hole-transporting layer. Adv Mater 23:3859–3863
66. Stubhan T, Oh H, Pinna L et al (2011) Inverted organic solar cells using a solution processed aluminum-doped zinc oxide buffer layer. Org Electron 12:1539–1543
67. Heo SW, Baek KH, Lee TH et al (2013) Enhanced performance in inverted polymer solar cells via solution process: morphology controlling of PEDOT:PSS as anode buffer layer by adding surfactants. Org Electron 14:1629–1635
68. Xiangdong W, Qing P, Weiguo Z et al (2015) High performance of inverted polymer solar cells with cobalt oxide as hole-transporting layer. Semicond Sci Technol 30:055001
69. Brabec CJ, Dyakonov V, Scherf U (2008) Organic photovoltaics: materials, device physics, and manufacturing technologies. Wiley-VCH, Weinheim, p 575
70. Servaites JD, Ratner MA, Marks TJ (2011) Organic solar cells: a new look at traditional models. Energ Environ Sci 4:4410–4422
71. Fan B, Xia Y, Ouyang J (2009) Novel ways to significantly enhance the conductivity of transparent PEDOT: PSS. Proc SPIE 7415:74151Q
72. Lipomi DJ, Tee BCK, Vosgueritchian M et al (2011) Stretchable organic solar cells. Adv Mater 23:1771–1775
73. Mason Chemical Company (2007) Fluorosurfactant – structure and function. Available at: http://www.masonsurfactants.com/Products/Fluorosurfactant.htm